

UNIVERSITÄT KASSEL  
**THEORETISCHE PHYSIK**  
QUANTENDYNAMIK UND KONTROLLE

## **Dissertation**

zur Erlangung des akademischen Grades

**Doktor der Naturwissenschaften**

(Dr. rer. nat.) im Fachbereich Physik

**eingereicht am Fachbereich**

**Mathematik und Naturwissenschaften**

**UNIVERSITÄT KASSEL**

vorgelegt von

**R. ESTEBAN GOETZ**

---

**Quantum optimal control theory of  
photoelectron spectroscopy**

Signature of Chirality and theoretical  
description of multiphoton ionization

---

Betreuerin: PROF. DR. CHRISTIANE P. KOCH

Zweitgutachter: PROF. EM. DR. BURKHARD FRICKE

Eingereicht am: 5. Januar 2018

Disputation am: 13. Juni 2018



# Acknowledgements

First and foremost, I would like to express my sincere gratitude to my advisor Prof. Dr. Christiane Koch, for her exceptional support, patience, invaluable guidance and for providing me with an excellent atmosphere during my doctoral work. She has been an outstanding source knowledge and motivation from the beginning to the end.

I would also like to acknowledge Prof. Dr. Robin Santra, with whom I had the opportunity to work on several projects, for receiving me a couple of times in his group in Hamburg and for his exceptional guidance and comments during our conjoint work. Many of the publications and results presented in this thesis originated as part of this collaboration. My thanks also goes to Antonia Karamatskou, for her engagement and effort in analyzing and interpreting the results obtained during this fruitful cooperation.

I am also grateful to Prof. Dr. Robert Berger for his guidance and for the interesting discussions and constructive feedback during our collaboration. My thanks also goes to Timur Isaev and Behnam Nikoobakht for their commitment and dedication during this worthwhile and productive collaboration.

I would also like to give thanks to Birgitta Whaley for receiving me in her group at Berkely and to Loren Greenman for introducing me the details of the TDCIS code.

Last but not least, my thanks to all the former and present members of the exceptional group in Kassel. They provided me with a friendly and cooperative atmosphere at work. In particular, I would like to acknowledge Michael Goerz for introducing me the Qdyn library and Daniel Reich for his feedback and insightful comments on my work. My special gratitude goes to my family, for their unconditional support over all these years.



TO MY PARENTS



# Contents

<b>0</b>	<b>Zusammenfassung</b>	<b>1</b>
<b>1</b>	<b>Abstract</b>	<b>3</b>
<b>2</b>	<b>Introduction and overview of the thesis</b>	<b>5</b>
<b>I</b>	<b>Theoretical framework:</b>	
	<b>Methods for electron dynamics and quantum control</b>	<b>11</b>
<b>3</b>	<b>Many-body theories for quantum electron dynamics</b>	<b>13</b>
3.1	The Born-Oppenheimer approximation . . . . .	13
3.2	The many-body electron dynamics . . . . .	15
3.3	Single-active-electron model . . . . .	17
3.4	Hartree-Fock and post-Hartree-Fock approximations: An overview . . . . .	19
3.4.1	The Configuration Interaction . . . . .	20
3.4.2	Time-dependent Configuration-Interaction Singles (TDCIS) . . . . .	24
<b>4</b>	<b>Numerical methods for solving the time-dependent Schrödinger equation</b>	<b>27</b>
4.1	Discrete Variable Representation . . . . .	28
4.1.1	Lagrange-mesh method . . . . .	31
4.1.2	Finite-Element Discrete Variable Representation . . . . .	33
4.1.3	The Fourier Hamiltonian Grid and Dynamical Fourier methods . . . . .	36
4.2	Numerical simulation of Quantum Dynamics . . . . .	38
4.2.1	The Chebychev propagation method . . . . .	39
4.2.2	Short iterative Lanczos propagator . . . . .	41
<b>5</b>	<b>Optimal control algorithms in a nutshell</b>	<b>45</b>
5.1	Gradient-based methods . . . . .	47
5.1.1	Gradient Ascent Pulse Engineering . . . . .	47
5.1.2	Krotov's optimization method . . . . .	49
5.2	Gradient-free methods . . . . .	52

5.2.1	Nelder-Mead optimization algorithm . . . . .	53
5.2.2	Brent's principal axis optimization method . . . . .	54
<b>6</b>	<b>Numerical methods for the computation of photoionization observables</b>	<b>57</b>
6.1	Wave function splitting method . . . . .	57
6.2	Photoelectron spectrum and angular distributions . . . . .	59
<b>II</b>	<b>Method development and numerical results</b>	<b>63</b>
<b>7</b>	<b>An efficient mapped pseudospectral propagation method for solving the time-dependent Schrödinger Equation</b>	<b>65</b>
7.1	Introduction and Motivations . . . . .	65
7.2	Time-dependent Schrödinger equation . . . . .	67
7.3	Description of the pseudospectral formalism . . . . .	69
7.4	Numerical Results . . . . .	72
7.4.1	Numerical performance . . . . .	73
7.4.2	Enhancement of the high harmonic yield via coherent superposition	75
7.5	Discussion and Conclusions . . . . .	82
<b>8</b>	<b>Optimal control of photoelectron properties</b>	<b>85</b>
8.1	Introduction and motivations . . . . .	86
8.2	Theoretical background . . . . .	87
8.3	Construction of minimization functionals . . . . .	89
8.3.1	Momentum-resolved photoelectron spectrum . . . . .	89
8.3.2	Angle-resolved photoelectron angular distributions . . . . .	89
8.4	Optimal field constraints . . . . .	90
8.4.1	Propagating electric field . . . . .	91
8.4.2	Electric frequency constraints . . . . .	92
8.4.3	Electric field maximal peak amplitude . . . . .	92
8.5	Krotov's formalism in the framework of wave function splitting method . . . . .	93
8.5.1	Construction of the multi-channel Lagrange multipliers . . . . .	96
8.5.2	Summary of the algorithm . . . . .	99
8.6	Application I: Prescribing the complete photoelectron distribution . . . . .	102
8.7	Application II: Minimizing the probability of emission into the upper hemisphere . . . . .	104
8.8	Application III: Maximizing the difference in the number of electrons emitted into upper and lower hemisphere . . . . .	106
8.8.1	Hydrogen . . . . .	106

8.8.2	Argon . . . . .	112
8.9	Summary of achievements and conclusions . . . . .	117
<b>9</b>	<b>Coherent control of hole dynamics in attosecond ionization</b>	<b>119</b>
9.1	Introduction and motivations . . . . .	119
9.2	Hole dynamics of photoionization . . . . .	121
9.3	Optimization problem . . . . .	122
9.3.1	Alternative optimization algorithms . . . . .	123
9.3.2	Sequential optimization update . . . . .	124
9.4	Minimizing hole decoherence in Argon . . . . .	126
9.4.1	Numerical performance of SPA-optimization . . . . .	127
9.4.2	Optimization using a “pre-optimized” guess field . . . . .	129
9.4.3	Enhancement mechanisms of hole coherence of hole states in ultra- fast photoionization . . . . .	132
9.4.4	Electronic correlations and asymptotic oscillating behavior of the degree of coherence . . . . .	134
9.4.5	Minimization of hole decoherence with prescribed hole population ratio . . . . .	137
9.5	Suppression of hole decoherence in Xenon: A novel mechanism . . . . .	142
9.6	Summary of achievements and conclusions . . . . .	148
<b>10</b>	<b>Theoretical description of photoelectron circular dichroism of randomly ori- ented chiral molecules</b>	<b>151</b>
10.1	Fingerprints of Chirality: Context and Motivation . . . . .	152
10.2	Derivation of the theoretical model . . . . .	155
10.2.1	Single center expansion . . . . .	156
10.2.2	Photoelectron Angular Distributions . . . . .	158
10.2.3	Orientation-dependent two-photon absorption . . . . .	160
10.2.4	Orientation-averaged 2+1 REMPI differential cross-section . . . . .	164
10.3	Symmetry properties of the model . . . . .	167
10.3.1	Parity transformation under handedness exchange: . . . . .	168
10.3.2	Parity transformations under field polarization helicity exchange . .	170
10.3.3	Mixing polarization directions and photoelectron circular dichroism	171
10.4	Anisotropy of photoelectron emission: . . . . .	174
10.4.1	Angular momentum dependence of the intermediate state . . . . .	175
10.4.2	Two-photon absorption tensor dependence of the intermediate state	176
10.5	Numerical Results . . . . .	178
10.5.1	Fenchone . . . . .	178

10.5.2	Camphor . . . . .	184
10.6	Intermediate state dependence of photoelectron circular dichroism in (2+1) REMPI . . . . .	188
10.7	Conclusion and Remarks . . . . .	193
<b>11</b>	<b>New approach for the observation of electroweak parity violation effects</b>	<b>197</b>
11.1	Introduction . . . . .	198
11.1.1	Brief review of atomic parity-nonconservation (PNC) . . . . .	198
11.1.2	Current approaches to the observation of PNC effects . . . . .	202
11.1.3	New proposal. Basic idea . . . . .	204
11.2	Modeling the cesium atom for observation of PNC effects . . . . .	205
11.2.1	Single-active-electron approach with spin-orbit coupling . . . . .	205
11.2.2	Evaluation of the radial wave functions . . . . .	208
11.3	Electron dynamics . . . . .	210
11.4	Observation of the PNC via photoelectron spectroscopy . . . . .	213
11.4.1	Photoelectron spectrum . . . . .	213
11.4.2	Single-photon ionization . . . . .	214
11.4.3	Pump-probe approach . . . . .	215
11.4.4	Time-dependent perturbation theory. Second order corrections . . . . .	218
11.4.5	Effects of second-order processes to the total yield . . . . .	224
11.4.6	Numerical results . . . . .	225
11.5	Relations and differences with previous proposals . . . . .	233
11.6	Conclusions and outlook . . . . .	235
<b>12</b>	<b>Summary and Outlook</b>	<b>239</b>
<b>III</b>	<b>Appendix</b>	<b>245</b>
<b>A</b>	<b>An efficient mapped pseudospectral method for solving the time-dependent Schrödinger equation</b>	<b>247</b>
A.1	Semi-global representation . . . . .	247
A.1.1	Multi-domain weak formulation . . . . .	247
A.1.2	Gauss-Lobatto-Legendre collocation . . . . .	249
A.1.3	Global representation . . . . .	251
A.2	Choice of domain number and collocation order . . . . .	256
A.3	Collocation with Legendre polynomials . . . . .	260
<b>B</b>	<b>Quantum optimal control of photoelectron observables</b>	<b>265</b>

---

<b>C</b>	<b>Theoretical description of photoelectron circular dichroism of randomly oriented chiral molecules</b>	<b>269</b>
C.1	Useful properties . . . . .	269
C.1.1	Radial continuum wavefunctions of the hydrogen atom . . . . .	269
C.1.2	Bound state wavefunctions of the hydrogen atom . . . . .	270
C.1.3	Rotation matrices . . . . .	270
C.1.4	Conversion to complex spherical harmonics . . . . .	272
C.2	Derivations . . . . .	272
C.2.1	One-photon transition rate . . . . .	272
C.2.2	Two-photon absorption tensor . . . . .	274
C.2.3	Cross section for $(2 + 1)$ photoionization . . . . .	276
C.2.4	Non-zero Legendre coefficients for two-photon absorption with circularly polarized light and ionization with linear polarization . . . . .	278
C.2.5	Behavior of Legendre coefficients when changing the helicity of the one-photon photoionization . . . . .	281
C.2.6	Behavior of Legendre coefficients when changing the helicity of the two-photon absorption process . . . . .	283
<b>D</b>	<b>List of publications</b>	<b>287</b>
	<b>Bibliography</b>	<b>289</b>



# Zusammenfassung

Die Entwicklung der Quantenmechanik war zweifellos ein Meilenstein bei der Beschreibung physikalischer Gesetze über das Verhalten von Materie, ihrer Strukturen und deren Interaktion mit Energie auf mikroskopischer Ebene. Durch sie wurde nicht nur die Entwicklung in der modernen Physik, sondern auch unser Verständnis der Natur auf dieser minuskulären Ebene revolutioniert. Durch sie wurde die absolute, ewige, omnipräsente und allmächtige klassische Mechanik bei dem Versuch zur Beschreibung der Materie auf Atom- und Molekularebene durch eine wellenähnliche Gleichung, für das Verhalten von Materie auf zuvor unvorstellbaren Ebenen ersetzt. Hiermit hat die Materie probabilistische wellenähnliche Eigenschaften erhalten, die in jedem Fall nicht nur die moderne Wissenschaft, sondern auch unsere Vorstellung von Wahrnehmung und Realität beeinflusst haben. Die Frage, ob mit der Quantentheorie tatsächlich beschrieben wird, wie die Natur arbeitet oder ob dieses nur abstraktes mathematisches Werkzeug ist, bleibt offen. Auch wenn die philosophischen perplexierenden Implikationen der Quantentheorie manchmal paradox und kontraintuitiv sind, so ist sie doch unzweifelhaft die exakteste Theorie, die jemals entwickelt wurde. Mit der Entdeckung des Lasers und dem außerordentlichen technologischen Fortschritt, der sich in den letzten Jahrzehnten vollzogen hat, wurde die Erforschung der Elektron-Dynamik unter dem Einfluss von Laserfeldern zu einem verheißungsvollen Verfahren zur Prüfung der Voraussage der Theorie. Bis heute hat die mit der Quantentheorie begründete Voraussage sich beständig wieder und wieder bestätigt, sodass sie sogar zur Goldenen Norm in der modernen Wissenschaft geworden ist. Es hat sich dann gezeigt, dass die Entwicklung der neuen Licht- und Attosekunden-Laserpulse, der modernen Spektroskopie, mit der die Photoionisierung von Atomen, Molekülen und Festkörpern studiert werden kann, ein hohes Potential für die Extrahierung von wertvollen Daten zur Elektron-Dynamik und zeitunabhängigen Phänomenen, die ausschließlich aus den wellenähnlichen Eigenschaften der Materie erwachsen, besitzt. Sobald die Gesetze, die die Quanten-Welt bestimmen, akzeptiert worden und die Wege zur Entdeckung der unbekanntenen Welleneigenschaften, der festgestellten Materie, festgelegt worden waren, hat ein enormes Interesse an der Manipulation dieser exotischen Eigenschaften zur Kontrolle der Materie, selbst eingesetzt, welches den Grundstein für die heute als Optimale

Quantenkontrolle bekannte Theorie gelegt hat. Ziel dieser Theorie ist es, die Welleneigenschaften der Materie durch die technische Entwicklung von konstruktiven und destruktiven Quantum-Interferenzen zwischen Licht und Materie in einer spezifischen Form mit dem Zweck, die von Licht indizierte Dynamik in einer gewünschten Form zu steuern. Somit wurde es durch Optimierung der Phasen und Amplituden von unterschiedlichen Frequenz-Komponenten dem optimalen Feld ermöglicht, ein Interferenz-Muster zwischen unterschiedlichen Quantenwegen zu ermitteln, um das gewünschte Ziel zu erreichen. Dieses ist die Fragestellung, welches in dieser Doktorarbeit behandelt wird. Mit der Doktorarbeit werden zwei Ziele verfolgt, und sie kann in zwei unterschiedlich, jedoch untrennbar miteinander verbundenen Kategorien eingestuft werden: (i) Entwicklung von theoretischen Modellen zur Simulation der Elektron-Dynamik und, parallel hierzu (ii) methodische Entwicklung von effizienten Algorithmen für die *Adhoc*-Kontrolle von photoelektronischen und photoionisch-verwandten Beobachtungen. Schwerpunkt der ersten Kategorie ist die Entwicklung von theoretischen Modellvarianten, mit denen die Interaktion von Licht und Materie für die Extraktion und die Kontrolle der quantenmechanischen Beobachtungen beschrieben werden. In diesem Zusammenhang wird in der Doktorarbeit dargestellt, wie spezifische Kontrollbeobachtungen und die Entdeckung, der sich darauf begründenden Kontrollmechanismen, ein besseres Verständnis der damit verbundenen Quanteneigenschaften ermöglichen können. Als Vorbedingung müssen spezifische und gut definierte Optimierungsfunktionale vorhanden sein. Hierbei finden bei der Konstruktion der Optimierungsfunktionalen für die Kontrolle der photoelektronischen Momentum-Verteilung und Kohärenz im Photoion unter gleichzeitiger Berücksichtigung der Einschränkungen durch das System und das Ionenfeld in Verbindung mit den analytischen Techniken zur Erläuterung der asymmetrischen Eigenschaften in dem photoelektronischen Spektrum von chiralen Molekülen besondere Bewertung. Es wird ein neuer Ansatz zur Beobachtung von elektroschwachen Paritätsstörungseffekten besprochen und vorgeschlagen. Außerdem soll mit dieser Doktorarbeit auch gezeigt werden, wie es eine Begrenzung der Kontrollressourcen ermöglicht, neue physikalische Mechanismen, die niemals zuvor erforscht worden sind, festzustellen, dieses resultiert ausschließlich aus der Welleneigenschaft der Materie. Zuletzt wird unbedingt auch eine extensive Methodenentwicklung von numerischen Algorithmen im Rahmen dieser Doktorarbeit benötigt. Hiermit wird die zweite Kategorie beschrieben, durch die der Einsatz eines effizienten pseudospektralen numerischen Propagationansatzes und die Entwicklung einiger neuer Optimierungstechniken zum Zwecke der Kontrolle spezifischer Eigenschaften, der photoelektronischen Momentum-Verteilung und der Kohärenz in dem Photoion, zum Gegenstand gemacht werden.

# Abstract

The development of quantum mechanics unquestionably made a peerless revolution on the path to describe the physical laws describing the behavior of matter, its structure and the interaction with energy at microscopic scales. It revolutionized not only the development of modern physics, but also our understanding of nature at these minuscular scales. It dethroned the absolute, eternal, omnipresent and all-mighty classical mechanics in the quest of describing *matter* at the atomic and molecular level by placing a *wave-like* equation to describe the behavior of matter at scales never imagined before. It endowed matter a probabilistic wave-like character that would definitively revolutionize not only modern science, but also our concept of perception and reality. Whether the quantum theory indeed describes how nature works or whether it is just an abstract mathematical tool remains unanswered. Although the philosophical perplexing implications of the quantum theory tends sometimes to seem paradoxical and counterintuitive, it is undoubtedly the most accurate theory ever developed.

With advent of the laser and the extraordinary technological progress made over the past decades, studying the electron dynamics under the influence of laser fields became the propitious scenario to test the predictions of the theory. Until this day, the prediction invoked by the quantum theory has been unequivocally reproduced again and again, to the point of becoming the Golden standard in modern science. It became then clear that with the development of new light and attosecond laser pulses, modern spectroscopy, which study photoionization in atoms, molecules and solids, possesses a high potential to extract invaluable information about electron dynamics and time-dependent phenomena that arise exclusively from wave-like properties of matter.

Once the laws governing the quantum world were accepted and the ways to unravel the unknown wave properties of matter established, an enormous interest in manipulating such exotic properties, for the control of matter itself, started, giving birth to what is nowadays known as Quantum Optimal Control Theory. This theory is designed to exploit and manipulate the wave properties of matter by engineering constructive and destructive quantum interferences of light and matter in a specific fashion, with the purpose of steering the dynamics induced by light into a desired way. Thus, by optimizing

---

the phases and amplitudes of different frequency components, the optimal field is able to excite an interference pattern among different quantum pathways to achieve the desired target. This is the problem addressed in this thesis.

The object of this doctoral thesis is two-fold and can be classified into two, but intrinsically related categories: (i) development of theoretical models for the simulation of electron dynamics and in parallel to this, (ii) method development of efficient numerical algorithms for *ad hoc* control of photoelectron and photoion-related observables. The first category primarily focuses on the development of a variety of theoretical models describing the interaction of light and matter for the extraction and control of quantum mechanical observables. In this context, this doctoral work describes how controlling specific observables, and unraveling the underlying control mechanisms, allows for a better understanding of the quantum properties that are involved. As precondition, specific and well defined optimization functionals are required. Construction of the optimization functionals for the control of photoelectron momentum distribution and coherence in the photoion while taking into account constraints imposed over the system and ionizing field are particularly emphasized, in conjunction with analytical techniques to explain asymmetry properties in the photoelectron spectrum of chiral molecules. A new approach for the observation of electroweak parity violation effects is discussed and proposed. Furthermore, this thesis also shows how restricting the control resources allows to find novel physical mechanisms, never explored before, which arises exclusively from the wave properties of matter.

Last but not least, extensive method development of numerical algorithms were unavoidably needed over the course of this doctoral thesis. This defines the second category, and introduces the implementation of an efficient pseudospectral numerical propagation approach and development of a pair of new optimization techniques designed for the purpose of controlling specific properties of the photoelectron momentum distribution and coherence in the photoion.

# Introduction and overview of the thesis

With the development of the laser and the advent of new light sources to produce short, coherent electromagnetic radiation of high intensity and broad spectrum, the response of atoms and molecules to controllable electromagnetic fields became a powerful tool to unravel the quantum signature of matter and the fundamental interactions governing scales never explored before. Electronic and nuclear dynamics induced by these ultrafast and intense light sources allows to study the structure of matter at its most fundamental level. In this context, photoelectron spectroscopy became a prime tool for characterizing the light-matter interaction at these timescales. It also designed to study the inherent electronic correlations. In fact, photoelectron momentum distributions contains not only the fingerprints of the interaction of electrons with the ionizing electromagnetic field, but also their interaction and their correlation with each other.

The present thesis is focused on the theoretical investigation of the electron dynamics resulting from the interaction of atomic systems with optimized light pulses in the multi-photon ionization regime. Optimized light pulses are referred to as engineered pulses that steer the dynamics in a specific fashion with the purpose of achieving a desired outcome. This requires the development of theoretical models to simulate the electron dynamics and implementation of optimal control algorithms capable of engineering the ionizing electromagnetic field in order to accomplish the desired “target”. In language of optimal control theory, this is equivalent to a functional minimization problem. In the context of this thesis, the functionals that we have constructed are often written in terms of photoelectron-related quantities, such as photoelectron spectra, photoelectron angular distributions or total yield. Ultimately, inspection of the photoelectron momentum distributions obtained with the optimized pulses serves as a prime tool to unravel the underlying control mechanisms.

This doctoral thesis is partitioned into two main parts, each of them composed of several chapters. **Part I** is intended to present, in general terms, the theoretical framework

of this work, and collects the theoretical approaches and numerical methods utilized over the course of my work for the solution of the many-body time-dependent Schrödinger equation. Additionally, it describes several *state-of-the-art* optimization techniques commonly utilized, while explaining the performances and limitations of each of them. **Part I** and the chapters thereof have been included to this thesis as an attempt to provide an elemental inspection to the general principles behind the improvement accomplished during the preparation of my doctoral work.

**Chapter 3** in **Part I** introduces several theoretical approaches for solving the many-body Schrödinger equation and analyzes the handicap of each of these while outlining the urgent necessity of incorporating the electronic correlations. It also justifies our choice of working in the context of the time-dependent configuration interaction singles.

**Chapter 4** discusses several numerical grid-based approaches for solving the time-dependent Schrödinger equation. Finite-Element-Lagrange-mesh-based methods, also commonly referred to as FE-DVR, for finite-element discrete variable representation, and the Dynamical Fourier method are of particular interest, due to their flexibility for evaluating the representation of operators in their respective basis, as well as for their numerical performances. Chapter 4 closes by covering two complementary approximation methods for wavefunction propagation intensively utilized during my work, namely the Chebychev and the Short Iterative Lanczos propagators, that can be used once the basis for representing the initial state and action of operators have been chosen, e.g. in the framework of the FE-DVR or Dynamical Fourier methods.

**Section 5** presents a concise survey of *state-of-the-art* numerical approaches for scalar function optimization. Their interests, performances and limitations are emphasized. In fact, although very efficient in particular situations, the efficiency of the optimization algorithms can be drastically compromised depending on the complexity of the optimization target. Of particular interest are the monotonically convergent Krotov's optimization method and Brent's principal axis formalism. The goal here is to provide, in general lines, a non-rigorous inspection of the most widely used optimization algorithms. This brief introductory survey has been introduced to justify the modifications and adaptations that have been required to be performed in the context of this thesis to improve their performances in order to accomplish our optimization purposes.

Finally, **Part I** concludes with **Chapter 6**. It describes an efficient numerical formalism for the evaluation of photoelectron momentum distributions. The approach has been adapted to the TDCIS formalism and its efficiency relies on the so-called *wave function splitting method*. The latter allows to significantly enhance the performances of the propagation since the use of extremely large radial grids generally required for the computation of photoelectron-related observables are systematically avoided.

**Part II** is devoted to the most important results obtained during my doctoral work, and discusses, in detail, six different projects in which I was involved. Since method development of numerical algorithms as well as analytical techniques were extensively utilized for the accomplishment of the different projects, they deserve a privilege place in this thesis and therefore they have been carefully included in **Part II** or in the **Appendix**.

**Chapter 7** in **Part II** presents in detail an efficient grid-based approach for solving the time-dependent Schrödinger equation. One of the most striking features of the scheme we have developed is that it outperforms the well-known numerical efficiency of the Dynamical Fourier Method (DFM). The attractiveness of the DFM relies on the fact that it avoids full matrix-vector operations when evaluating the action of the kinetic energy operator by means of the Fast Fourier transformations. This procedure grants the DFM a semi-linear scaling, compared to a cubic scaling for methods using differential operators. The alternative approach we have developed takes ideas of the FE-DVR to construct sparse matrix representations of the kinetic energy operator. Therefore, although our method still relies on matrix-vector multiplications instead of Fourier transformations, these evaluations concern now sparse matrix-vectors operations. For the same accuracy, our propagation method is up-to four times faster, compared to the DFM. A detailed explanation for the optimal choice of the pseudospectral grid parameters in order to achieve such performance is presented. Our scheme then allows to significantly decrease the numerical effort for optimization purposes, since optimization algorithms are generally based on iterative propagation schemes.

The second project is presented in **Chapter 8**. Here, an efficient optimization toolbox for the control of photoelectron momentum distributions is developed. Our formalism is based on the many-body TDCIS approach. This allows to account for the electronic correlation effects which are ultimately inferred from specific patterns in the photoelectron distribution. Importantly, the algorithm is constructed in such a strategic way that explicit knowledge of the final state is not required, only its energy and/or angular distribution. The method is exploited for (i) finding external field that initiate the dynamics in such a way that the resulting photoelectron spectrum coincides with the desired prescribed energy distribution. Alternatively, the method is used for (ii) maximizing of the anisotropy of photoelectron emission between the upper and lower hemispheres. Single- and multiple-channel systems, such as hydrogen and argon are used as paradigms. Scrutinizing the properties of the resulting photoelectron spectrum allows us to elucidate the physical mechanisms for achieving maximal anisotropy of photoelectron emission.

*Projects 3* and *4* are conjointly presented in **Chapter 9**. The purpose here is two-fold: first, we aim to suppress the loss of coherence within the attosecond photoionization

regime. This is achieved by optimizing pulses that create well-defined coherent superposition of states with prescribed population ratio. To characterize pulses that achieve such perfect coherence, an extension of the performances of the standards optimization methods, due to technical specificities of the propagation scheme, become unavoidable. Thus, we introduce and propose an efficient approach relying on a **sequential parametrization technique (SPA)** and based on the principal axis optimization method, due to Brent. Our approach significantly increases the performances of the latter, and thus allows us to accomplish our optimization goals with extreme flexibility. Ultimately, the second goal is to exploit the versatility of the **SPA** technique to inspect the physical mechanisms promoting the suppression of decoherence among hole states. Argon and xenon are used as paradigms. Our optimization technique allows to find well-established and new physical mechanisms involving multi-photon processes that allow to generate perfect coherence among the hole states.

In **Chapter 10**, a theoretical model for the description of **photoelectron circular dichroism (PECD)** of chiral molecules in the (2+1) resonantly enhanced multi-photon ionization (REMPI) regime is derived. Our model is based on two-photon pre-photoselection from randomly oriented chiral molecules and successive one-photon ionization of the photoselected molecules. The model relies on a perturbative treatment of the light-matter interaction within the electric dipole approximation and combines an *ab initio* description of the non-resonant two-photon absorption with a single-center expansion of the photoelectron wavefunction into hydrogenic continuum functions. This allows to account for the Coulomb interaction between photoelectron and photoion as well as electronic correlations in the transition to the intermediate electronically excited state. Making heavy use of the symmetry properties of the Wigner rotation matrices, which describe the frame-transformation between the molecular and laboratory frames of reference while accounting for the randomness of the distribution, we show that our model correctly reproduces the basic symmetry behavior expected under exchange of molecular handedness as well as exchange of light helicity. Fenchone and camphor are utilized as paradigms and semi-quantitative agreement with the experimental data is found.

A proposal based on time-resolved spectroscopy approach for the observation of the signature of electroweak parity violation effects is presented in **Chapter 11**. A direct consequence of the electro-weak interaction is the admixture between different parity states. Here, we show that information about such admixture can be transmitted by the outgoing photoelectron and thus, signature of the parity non-conservation (PNC) can be extracted upon inspection of specific properties of the photoelectron spectrum. The magnitude of such admixture is, however, extremely small. In the hope of detecting such a

small effect, a pump-probe spectroscopy approach is suggested. Ultimately, we show that combination of the pump-probe time-delay-dependent photoelectron yield obtained under electric field reversal (combined signal) allows to separate the admixtures due to the weak Hamiltonian and those generated by the electric field component of the ionizing laser field, thus to isolate the admixture of interest. The combined signal then presents oscillations as a function of the time-delay between the pump and probe pulses with well-defined frequency components. These oscillations vanish if the PNC potential is omitted from the equations of motion. Thus, spectral analysis of the combined signal with observation of spectral components at well defined frequencies irrefutably indicates observation of the PNC effect.

Finally, **Chapter 12** provides a general summary and conclusion of this thesis presenting the main achievements and outlining possible directions for future research in the context of quantum optimal control of photoelectron spectroscopy.



# Part I

## **Theoretical framework: Methods for electron dynamics and quantum control**



# Many-body theories for quantum electron dynamics

---

3.1	The Born-Oppenheimer approximation . . . . .	13
3.2	The many-body electron dynamics . . . . .	15
3.3	Single-active-electron model . . . . .	17
3.4	Hartree-Fock and post-Hartree-Fock approximations: An overview . . . . .	19
3.4.1	The Configuration Interaction . . . . .	20
3.4.2	Time-dependent Configuration-Interaction Singles (TDCIS) . . . . .	24

---

## 3.1 The Born-Oppenheimer approximation

Consider a multi-electron system consisting of a fixed number  $M$  of nucleons and  $N_e$  electrons, such as an atom or molecule in the absence of any external electromagnetic field. If we choose to represent each nucleon and electron by their position  $\mathbf{R} \equiv \mathbf{R}_1, \dots, \mathbf{R}_M$  and  $\mathbf{r} \equiv \mathbf{r}_1, \dots, \mathbf{r}_{N_e}$ , respectively, the full quantum mechanical state of the system, which determines the nuclear and electronic structure and properties of the many-body system in any of its available stationary states, is fully dictated by the many-body time-independent Schrödinger equation,

$$\hat{\mathbf{H}}_0(\mathbf{r}, \mathbf{R})\Psi^N(\mathbf{r}, \mathbf{R}) = E \Psi^N(\mathbf{r}, \mathbf{R}) \quad (3.1)$$

where  $\Psi^N(\mathbf{r}, \mathbf{R}) \equiv \Psi^N(\mathbf{r}_1, \dots, \mathbf{r}_{N_e}, \mathbf{R}_1, \dots, \mathbf{R}_M)$  is said to be the wave function of the system, and where  $\hat{\mathbf{H}}_0$  is the non-relativistic field-free Hamiltonian defined by

$$\hat{\mathbf{H}}_0 = \underbrace{\sum_i^{N_e} -\frac{1}{2m_i} \nabla_i^2}_{\hat{\mathbf{T}}_e} + \underbrace{\sum_I^M -\frac{1}{2M_I} \nabla_I^2}_{\hat{\mathbf{T}}_n} + \underbrace{\frac{1}{2} \sum_{I \neq J}^M \frac{Z_I Z_J}{R_{IJ}}}_{\hat{\mathbf{V}}_{nn}} + \underbrace{\frac{1}{2} \sum_{i \neq j}^{N_e} \frac{1}{r_{ij}}}_{\hat{\mathbf{V}}_{ee}} - \underbrace{\sum_i^{N_e} \sum_I^M \frac{Z_I}{|\mathbf{R}_I - \mathbf{r}_i|}}_{\hat{\mathbf{V}}_{ne}}, \quad (3.2)$$

where  $m_i$  and  $M_I$  denote the mass of the electron and nucleons labelled  $i$  and  $I$ , respectively. The terms  $\mathbf{r}_{ij} \equiv |\mathbf{r}_i - \mathbf{r}_j|$  and  $\mathbf{R}_{IJ} \equiv |\mathbf{R}_I - \mathbf{R}_J|$  refer to the distance between the electrons  $i$  and  $j$  and that between the nucleons  $I$  and  $J$ , respectively. Finally,  $Z_I$  symbolizes the electric charge of the nucleon  $I$ . Note that when relativistic corrections and spin-orbit effects are important, cf. Section 11.2 in Chapter 11, their respective interaction Hamiltonian can be simply added to the Hamiltonian  $\hat{\mathbf{H}}_0$ . The first and second terms in Eq. (3.2) describe the kinetic energy of the electrons and nuclei, respectively. The mutual *electron-electron* and *nucleon-nucleon* electrostatic interaction (repulsion) are symbolized by  $\hat{\mathbf{V}}_{ee}$  and  $\hat{\mathbf{V}}_{nn}$ , respectively. Last but not least, the term  $\hat{\mathbf{V}}_{ne}$  defines the electrostatic attraction between the electrons and the nuclei. It is this term, i.e.  $\hat{\mathbf{V}}_{ne}$ , that couples the electronic and nuclear degrees of freedom, thus preventing from treating the electronic and nuclear motion separately. In particular, this term prevents from writing the solution as a single product of electronic and nuclear parts, i.e.  $\Psi(\mathbf{r}, \mathbf{R}) = \Psi_e(\mathbf{r}) \Psi_n(\mathbf{R})$ . However, assuming the nuclei to be nearly fixed at positions  $\mathbf{R}_I$  with respect to the motion of the electronic cloud, which can be justified by the fact that the nuclei are much more massive than electrons, allows to separate nuclear and electronic degree of freedom and hence to write the total wave function as a simple product of nuclear and electronic states. The validity of the fixed-nucleus model was first established by Born and Oppenheimer [1] and such an approximation is known as the **Born-Oppenheimer approximation**. Within this frozen-core picture, the nuclear positions  $\mathbf{R}_I$  enter merely as fixed parameters in Eq. (3.2). In this approximation, the electronic wave function is obtained upon solution of the so-called **clamped-nuclei Schrödinger equation** [2]

$$\hat{\mathbf{H}}_e(\mathbf{r}) \Psi_e(\mathbf{r}) = E_e \Psi_e(\mathbf{r}), \quad (3.3)$$

where  $\hat{\mathbf{H}}_e(\mathbf{r}) \equiv \hat{\mathbf{H}}_e(\mathbf{r}; \mathbf{R})$ , the electronic wave function  $\Psi_e(\mathbf{r}) \equiv \Psi_e(\mathbf{r}; \mathbf{R})$  and the electronic energy  $E_e = E_e(\mathbf{R})$ <sup>1</sup> are  $\mathbf{R}$ -parametrized. The electronic Hamiltonian reads

$$\hat{\mathbf{H}}_e(\mathbf{r}; \mathbf{R}) = \hat{\mathbf{T}}_e + \hat{\mathbf{V}}_{ee}(\mathbf{r}) + \hat{\mathbf{V}}_{ne}(\mathbf{r}; \mathbf{R}). \quad (3.4)$$

<sup>1</sup>Varying the nuclear positions  $\mathbf{R}$  adiabatically, i.e. by small steps and iteratively solving the clamped-nuclei equation for fixed  $\mathbf{R}$  results in the so-called potential energy surface or adiabatic surface  $E_e(\mathbf{R})$ .

It is customary, although not systematic, to neglect  $\hat{V}_{nn}$  from Eq. (3.3) since it is just a constant that shift  $E_e$  by some constant amount. The Hamiltonian  $\hat{H}_e$  defines the field-free *electronic* Hamiltonian and plays an important when studying the response of the electronic wave function <sup>2</sup> to an external electromagnetic field, i.e. the electron dynamics<sup>3</sup>.

### 3.2 The many-body electron dynamics

Having defined  $\hat{H}_e(\mathbf{r})$  and obtained the many-body electronic wave function  $\Psi_e(\mathbf{r}) \equiv \Psi_e(\mathbf{r}_1, \dots, \mathbf{r}_{N_e})$ , we now focus our attention to the electron dynamics as a result of the response of the system, initially dictated by the Hamiltonian in Eq. (3.2), to an external time-dependent electromagnetic field. At first order, electromagnetic fields induce changes in both, nuclear and electronic distributions [3]. As opposed to what we have previously assumed, the nuclei is now allowed to move from its frozen equilibrium position, which in turn, modifies the electronic density distribution. Furthermore, light-induced modifications of the electronic density may also affect the fixed nuclear geometry assumed by frozen-core approximation, forcing the nuclear distribution to rearrange. Such rearrangements then react back on the electronic distribution, causing the latter to rearrange, which again modifies the nuclear distribution, reacting back again on the electronic distribution, and so on and so forth. In such a vicious circle, changes in the nuclear geometry definitely affect, directly or indirectly, the electron density distribution. In simple terms, the Born-Oppenheimer approximation breaks down. Nevertheless, in specific situations, the frozen-core approximation may still be valid, even in the presence of an external time-dependent excitation [4]. The physical motivation behind the latter assumption relies on the fact that the time-scale of nuclear motion is several orders of magnitude larger compared to that of electrons. In this context, the response of an atom or molecule can be fully considered as a purely electronic process <sup>4</sup> and all relevant details of the atomic and molecular dynamics may still be qualitatively explained in the context of the

---

<sup>2</sup>Having made the clamped-nuclei approximation, the second step in the Born-Oppenheimer approximation consist in evaluating the nuclear wave function  $\Psi_n(\mathbf{R})$ , which is obtained upon solution of  $(\hat{\mathbf{T}}_n + E_e)\Psi_n(\mathbf{R}) = E_T\Psi(\mathbf{R})$ , where  $E_T$  is the total energy of the system, including the contributions from electronic motions, nuclear vibrations, as well as rotation and translations of the system. Finally, the total wave function can be obtained using an expansion of the form  $\Psi(\mathbf{r}, \mathbf{R}) = \sum_k \Psi_{e,k}(\mathbf{r}; \mathbf{R})\Psi_{n,k}(\mathbf{R})$ , where  $k$  runs over all eigenfunctions obtained for a fixed  $\mathbf{R}$ .

<sup>3</sup>assuming a fixed nuclei  $T_n = 0$  and  $V_{nn} = \text{const}$ .

<sup>4</sup>Sensu stricto, a full quantum mechanical treatment of the coupled electronic and nuclear interaction is required for a proper description of the electron- and nuclear dynamics. It has been shown, however, that semi-classical treatment of coupled electronic (quantum) and nuclear (classical) dynamics in the context of the Ehrenfest method [5] does not destroy the relevant picture of the electron dynamics, although it can introduce fast dephasing in the electronic distribution, see e.g. Refs. [3, 6–8] and references therein.

Born-Oppenheimer approximation. Within this picture, all eventual losses of electronic coherence due to the interaction with the ionic core are neglected and electronic motion and electronic density rearrangements are only due to the interaction with the driving external field. This is the context assumed in this work. In this approximation, the electron dynamics of a multi-electron system under the influence of a time-dependent potential  $\hat{\mathbf{H}}_{em}(\mathbf{r}, t)$  generated by an external electromagnetic field is fully dictated by the time-dependent Schrödinger equation

$$i \frac{\partial}{\partial t} \Psi_e(\mathbf{r}_1, \dots, \mathbf{r}_{N_e}, t) = \left[ \sum_i^{N_e} \left( -\frac{\nabla_i^2}{2} + \hat{\mathbf{V}}_{ne}(\mathbf{r}_i) + \hat{\mathbf{H}}_{em}(\mathbf{r}_i, t) \right) + \sum_{j>i}^{N_e} \hat{\mathbf{V}}_{ee}(\mathbf{r}_i, \mathbf{r}_j) \right] \Psi_e(\mathbf{r}_1, \dots, \mathbf{r}_{N_e}, t), \quad (3.5)$$

where  $\hat{\mathbf{V}}_{ee}(\mathbf{r}_i, \mathbf{r}_j)$  refers to the *electron-electron* interaction potential arising from mutual electrostatic repulsion between two electrons pairs, labeled  $i$  and  $j$  and located at  $\mathbf{r}_i$  and  $\mathbf{r}_j$ , respectively, namely

$$\hat{\mathbf{V}}_{ee}(\mathbf{r}_i, \mathbf{r}_j) = \frac{1}{|\mathbf{r}_i - \mathbf{r}_j|}. \quad (3.6)$$

The term  $\hat{\mathbf{V}}_{ne}(\mathbf{r}_i)$  in Eq. (3.5) describes the potential energy arising from the electrostatic interaction of the electron in  $\mathbf{r}_i$  in the field of the charged particles in the nuclei, located at fixed positions  $\mathbf{R}_n$ , namely

$$\hat{\mathbf{V}}_{ne}(\mathbf{r}_i) \equiv \hat{\mathbf{V}}_{ne}(\mathbf{r}_i; \{\mathbf{R}_n\}) = \sum_n^{N_n} \frac{Z_n}{|\mathbf{r}_i - \mathbf{R}_n|}. \quad (3.7)$$

Although the Born-Oppenheimer formalism allows to considerably reduce the numerical effort for both time-dependent and time-independent problems by separating the nuclear and electronic coordinates, and despite the fact that computation power have significantly increased over the last decades, numerical solution of the multi-electron time-dependent Schrödinger equation becomes prohibitively expensive, even for relatively small systems. Fortunately, a plethora of alternative approaches, relying on relatively accurate context-dependent approximations, exists. The following lines are intended to introduce the approximation methods adopted in the context of this thesis for the solution of both, the many-body time-dependent and time-independent Schrödinger equation.

### 3.3 Single-active-electron model

Undoubtedly one of the cheapest numerical approaches for solving the many-body electron dynamics relies in the so-called **single-active-electron** (SAE) approximation [9]. The SAE formalism reduces the entire many-body structure to a *frozen-core single-active electron picture*, whereby only a single protagonist electron is assumed to be exposed to an effective time-independent local potential  $V_{\text{SAE}}(\mathbf{r}; \gamma_j)$ . In the presence of an external interacting electric field  $\mathcal{E}(t)$  and within the strict dipole approximation, the electron dynamics is described by the effective single-particle time-dependent Schrödinger equation, that, in the framework of the SAE takes the form [10]

$$i \frac{\partial}{\partial t} \Psi(t, \mathbf{r}) = \left( \frac{-\nabla^2}{2} + V_{\text{SAE}}(\mathbf{r}; \{\gamma_j\}) - \mathcal{E}(t) \cdot \mathbf{r} \right) \Psi(t, \mathbf{r}), \quad (3.8)$$

where  $\{\gamma_j\}$  denotes a set of system-dependent variables that needs to be adjusted. Construction of the local SAE potential is rather straightforward: in the vicinity of the origin, the local potential is dominated by the nuclear potential [11]

$$\lim_{r \rightarrow 0^+} V_{\text{SAE}}(r; \{\gamma_j\}) \sim -\frac{Z}{r}, \quad (3.9)$$

where  $Z$  stands for the nuclear charge. On the contrary, the behavior for very large distance is determined by the asymptotic expression,

$$\lim_{r \rightarrow \infty} V_{\text{SAE}}(r; \{\gamma_j\}) \sim -\frac{1}{r}. \quad (3.10)$$

In between these two limits, the model is interpolated by exploiting the semi-empirical character of the latter, namely by fitting the parameters  $\gamma_j$  such that the ionization potential and excitation energies reproduces the experimental values [12]. A myriad of parametrization forms for the energy-consistent effective potential are widely available in the literature and they are also known as pseudopotentials<sup>5</sup>. For instance, in the case where the spin-orbit is not resolved, a standard didactic example of such model potentials is given by [14]

$$V_{\text{SAE}}(\mathbf{r}; \alpha, \beta, \gamma) = -\frac{1}{r} - \alpha \frac{e^{-\beta r}}{r} - (Z - 1 - \alpha) \frac{e^{-\gamma r}}{r}. \quad (3.11)$$

---

<sup>5</sup>Historically introduced in Ref. [13] as a “*new approximation method in the problem of many-body electrons*” for closed-shell atoms, whereby the effective potential for potassium was parametrized as  $V(r) = -1/r + (2.74/r) e^{-1.16 r}$

More sophisticated approximations accounting for appropriate short-range background screened interactions arising from core-polarization effects <sup>6</sup> [16, 17], split-orbit couplings [18] and relativistic corrections [19–21] are also available. Consider, for instance [16, 17]

$$V_{\text{SAE}}(\mathbf{r}; \alpha_D; \beta_\ell; B_\ell; \rho) = -\frac{Z}{r} - \frac{\alpha_D}{2r^4} \left(1 - e^{-(r/\rho)^2}\right)^2 + \sum_{\ell=0}^{\ell_{\text{max}}} B_\ell e^{-\beta_\ell r^2} |\ell\rangle\langle\ell|, \quad (3.12)$$

where  $\alpha_D$  is the dipole polarizability of the core, and  $\rho$  a cut-off parameter. The term  $|\ell\rangle\langle\ell|$  denotes the projection operator and  $\ell$  the angular momentum quantum number. In practice, the parameters are  $\alpha_D$ , and  $\rho$  are tabulated, while  $B_\ell$ ,  $\beta_\ell$  are fitted to the experimental atomic valence and Rydberg states [17]. It has been shown that in specific situations, i.e. when the frozen ionic core is a good approximation, the SAE formalism quantitatively reproduces experimental observations such as ATI [22], HGG spectra [23, 24] and single-ionization production [22, 24–26], which makes the SAE one of the most attractive “many-body” approximations. However such attractiveness and simplicity of implementation comes with a price. In fact, the SAE approximation remains a single-channel theory –describing the full dynamics of the valence shell electron while keeping the ionic ground state frozen, therefore still ignoring all electron correlation effects and interaction among different orbitals. Furthermore, it neglects all relevant details associated with the dynamical description of the residual ion, and the dynamical interaction of the latter with the excited electron, focusing only on the wave-packet dynamics of the single electron [10]. Consequently, it usually breaks down when considering molecules or even heavier noble gas atoms, for which the electronic correlations become relevant [10, 25, 27]. An alternative procedure allowing to improve the theoretical calculations consist in extending the **SAE** approach by means of the time-dependent Density Functional Theory (**TDDFT**) in the Kohn-Sham formulation [28]. However, calculation of photoionization of atoms within the latter formulation [29] have shown to be affected by similar limitations [10, 30–34]. In fact, although the **TDDFT** is formally an exact reformulation of quantum theory and undoubtedly represents a good trade-off in terms numerical costs and effectiveness, the current state of the theory relies on non-rigorous non-first principles-based approximations of the exchange-correlation energy functional, therefore failing even qualitatively in certain cases, particularly when considering strong

---

<sup>6</sup>Refers to the response of the ionic core to external electromagnetic fields causing the former to distort from its initially spherically symmetric equilibrium geometry, giving rise to an induced dipole moment proportional to the polarizability of the ion, that in turn interact with the valence electron. The field of the distorted core reacts back on the valence electron, adding to its potential energy a term proportional to  $e^2/2r^4$  [15].

correlated systems [32–34], since relying on a single-determinant ansatz [35].

### 3.4 Hartree-Fock and post-Hartree-Fock approximations: An overview

Unquestionably one of the simplest and naivest approaches for constructing the N-electron wave function is to assume that the latter can be expressed as an ordinary product of non-interacting single particles states wave functions,

$$\Phi_0(\mathbf{r}_1, \dots, \mathbf{r}_N) = \prod_{i=1}^N \varphi_i(\mathbf{r}_i). \quad (3.13)$$

Such an *ansatz* is the founding principle of the Hartree method [36]. The biggest handicap of the Hartree approach is that the many-body wave function is not antisymmetric under electron exchange. This prerequisite arises from the Pauli exclusion principle. The antisymmetry requirement can be fulfilled, however, by invoking the so-called *Self-consistent-Hartree-Fock* formalism. The latter assumes that the exact many-body wave function of a fermionic system can be approximated by **a single Slater determinant**,

$$\Phi_0(\mathbf{r}_1, \dots, \mathbf{r}_N) = \frac{1}{\sqrt{N!}} \begin{vmatrix} \varphi_1(\mathbf{r}_1) & \varphi_1(\mathbf{r}_2) & \dots & \varphi_1(\mathbf{r}_N) \\ \varphi_2(\mathbf{r}_1) & \varphi_2(\mathbf{r}_2) & \dots & \varphi_2(\mathbf{r}_N) \\ \vdots & \vdots & \ddots & \vdots \\ \varphi_N(\mathbf{r}_1) & \varphi_N(\mathbf{r}_2) & \dots & \varphi_N(\mathbf{r}_N) \end{vmatrix}. \quad (3.14)$$

In fact, with this **single-determinant ansatz** in hand, the N-electron wave function indeed fulfills the Pauli exclusion principle, since the resulting wave function is anti-symmetric under exchange of two electrons, namely

$$\Psi(\mathbf{r}_1, \dots, \mathbf{r}_i, \dots, \mathbf{r}_j, \dots, \mathbf{r}_N) = -\Psi(\mathbf{r}_1, \dots, \mathbf{r}_j, \dots, \mathbf{r}_i, \dots, \mathbf{r}_N). \quad (3.15)$$

The accuracy with which the resulting equations, known as Hartree-Fock equations are solved, is directly determined by the completeness of the expansion basis in the Slater determinant, cf. Eq. (3.14). Although the accuracy can be improved by increasing the number of basis, there is still an enormous handicap in the Hartree-Fock theory: by writing the many-body wave function as a *single* Slater determinant, Pauli's exclusion principle for fermions are now fulfilled, but the wavefunction is still written as a *single* product of non-interaction single particle states. However exact wave functions, cannot generally be expressed as single determinants. In fact, writing the wave function as a simple product implies that the N-particle fermion system is formed by single particle states that do not interact with each other, they are uncorrelated. Only correlation effects arising directly

from the antisymmetrization are accounted for. For instance, correlation effects due to the *electron exchange interaction* term, also known as *Fermi correlation*, are accounted for. This term prevent two parallel-spin electrons from being located at the same point in space, and arises, by construction, from the indistinguishability and antisymmetrization *ansatz* that the Hartree-Fock formalism makes uses of.

However, The Hartree-Fock approximation does not account for the Coulomb correlation, due to the fact, as already mentioned, of writing the N-electron wave function as a single (determinant) product. Consequently, the total electronic energies are always above the exact ones, and their difference is known as *correlation energy* [37].

In an attempt to include such Coulomb correlations, many approaches, often referred to as **post-Hartree-Fock methods** have been developed over the past years. Among the most prominent ones, the Coupled Cluster (CC) method [38–40], the **Configuration Interaction (CI)** [41], the Møller-Plesset perturbation theory [42], Multi-configurational self-consistent field (MCSCF) [43] are also available. In this thesis, the treatment of the many-body structure and incorporation of the electronic correlations are described in terms of the **CI** formalism. It is briefly described in the following.

### 3.4.1 The Configuration Interaction

The **CI** formalism makes a striking step forward on the path to include the unavoidable electronic correlations by going beyond the single-determinant wavefunction *ansatz*. The essence of the **CI** relies on expanding the many-body electron wave function in terms of many-body electron basis, which are constructed by performing substitutions from the original Hartree-Fock determinant. The latter describes the ground state of the many-body wave function schematized in Fig. 3.1 (left).

Physically speaking, these substitutions are equivalent to excitations occurring from the Hartree-Fock ground state determinant,  $|\Phi_0^N\rangle$ , to higher unoccupied orbitals. Specifically, the wave function is expanded in terms of singly  $|\Phi_1^N\rangle$ , doubly  $|\Phi_2^N\rangle$ , triply  $|\Phi_3^N\rangle$ , quadruply  $|\Phi_4^N\rangle$  and so forth excited Slater determinants, where electrons are promoted from an occupied orbital to a virtual orbital starting from the Hartree-Fock ground state Slater determinant, namely

$$\begin{aligned}
 |\Psi^N\rangle = & \underbrace{\alpha_0 |\Phi_0^N\rangle}_{\text{Hartree-Fock}} + \underbrace{\sum_{i,a} \alpha_i^a |\Phi_i^a\rangle}_{\text{single}} + \underbrace{\sum_{i<j,a<b} \beta_{i,j}^{a,b} |\Phi_{i,j}^{a,b}\rangle}_{\text{double}} \\
 & + \underbrace{\sum_{i<j<k,a<b<c} \gamma_{i,j,k}^{a,b,c} |\Phi_{i,j,k}^{a,b,c}\rangle}_{\text{triple excitations}} + \dots, \quad (3.16)
 \end{aligned}$$

where the indexes  $i, j, k, l$  exclusively symbolizes the occupied orbitals, whereas their

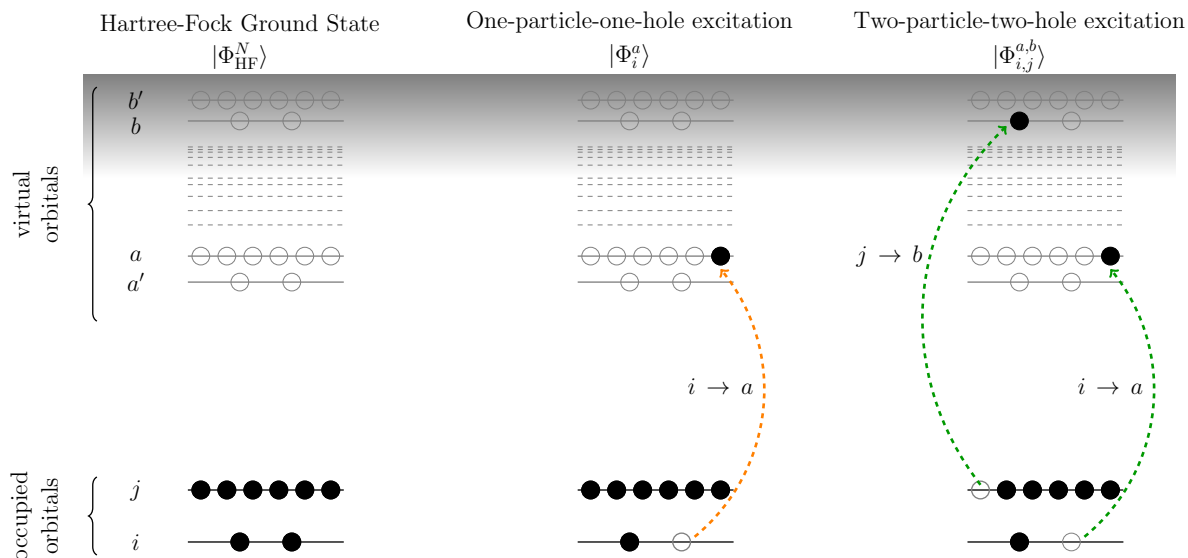


Figure 3.1: **Configuration Interaction:** Schematic representation (not drawn to scale) of the Hartree-Fock ground state (left), one-particle-one-hole (middle) and two-particle-two-hole (right) excitations arising from the substitution of the occupied spin-orbitals in the Hartree-Fock ground state with initially unoccupied spin-orbitals. Filled and unfilled circles symbolize electrons and holes respectively, occupying the different spin-orbitals.

counterparts  $a, b, c, d$  are referred for labeling both, occupied and virtual orbitals.

For the single substitution (or excitation) scenario, each Slater determinant  $|\Phi_i^a\rangle$  is constructed by replacing the spin-orbital  $i$  in  $|\Phi_0\rangle$  with the virtual (not occupied) spin-orbital  $a$ . This substitution describes the excitation from the occupied orbital  $i$  in the Hartree-Fock ground state to an unoccupied orbital  $a$ , cf. Fig. 3.1 (middle). For the double excitation case, two electrons in the Hartree-Fock ground state lying in two different and contiguous spin-orbitals  $i$  and  $j$ , with  $j > i$  are simultaneously promoted to energetically higher orbitals: that on  $i$  being promoted to  $a$  and that on  $j$  to  $b$  with  $b > a$  in order to fulfill the Pauli exclusion principle, cf. Fig. 3.1 (right). The sequence is repeated to account for higher order processes. This set of different orbital occupancies is referred to as **configurations**. The attractiveness of the CI relies on its generality and versatility: the formalism not only applies to closed-shell systems, but also to open-shell atoms, excited states and to complex systems even far from their equilibrium geometries [44]. Furthermore, the formalism is not exclusively restricted to simple atoms, but its domain of applicability can be extended to large molecules [10]. While the *full configuration interaction* contains all possible configurations, calculations accounting for very high order process become very easily computationally prohibited. In order to render calculations manageable, truncation of the configuration-interaction-space becomes unavoidable. Thus, it is almost universally customary, with a few exceptions, to delimit the configuration-space

to single and doubles excitations at the most. These are referred to as **Configuration Interaction Singles (CIS)** and doubles (**CISD**), respectively. The matrix representation of the Hamiltonian operator in the configuration interaction formalism reads [45],

$$\hat{\mathbf{H}}_0^N = \begin{pmatrix} \langle \Phi_0 | \hat{\mathbf{H}} | \Phi_0 \rangle & 0 & \langle \Phi_0 | \hat{\mathbf{H}} | \Phi_2 \rangle & 0 & \dots & 0 \\ 0 & \langle \Phi_1 | \hat{\mathbf{H}} | \Phi_1 \rangle & \langle \Phi_1 | \hat{\mathbf{H}} | \Phi_2 \rangle & \langle \Phi_1 | \hat{\mathbf{H}} | \Phi_3 \rangle & \dots & \langle \Phi_1 | \hat{\mathbf{H}} | \Phi_N \rangle \\ \langle \Phi_2 | \hat{\mathbf{H}} | \Phi_0 \rangle & \langle \Phi_2 | \hat{\mathbf{H}} | \Phi_1 \rangle & \langle \Phi_2 | \hat{\mathbf{H}} | \Phi_2 \rangle & \langle \Phi_2 | \hat{\mathbf{H}} | \Phi_3 \rangle & \dots & \langle \Phi_2 | \hat{\mathbf{H}} | \Phi_N \rangle \\ 0 & \langle \Phi_3 | \hat{\mathbf{H}} | \Phi_1 \rangle & \langle \Phi_3 | \hat{\mathbf{H}} | \Phi_2 \rangle & \langle \Phi_3 | \hat{\mathbf{H}} | \Phi_3 \rangle & \dots & \langle \Phi_3 | \hat{\mathbf{H}} | \Phi_N \rangle \\ \vdots & \dots & \dots & \dots & \ddots & \vdots \\ 0 & \langle \Phi_N | \hat{\mathbf{H}} | \Phi_1 \rangle & \langle \Phi_N | \hat{\mathbf{H}} | \Phi_2 \rangle & \dots & \dots & \langle \Phi_N | \hat{\mathbf{H}} | \Phi_N \rangle \end{pmatrix}, \quad (3.17)$$

where the notation  $|\Phi_I\rangle = |\Phi_I^N\rangle$  has been used to ease reading. It is worth mentioning that the basis  $|\Phi_I\rangle$  correspond to many-body fermionic wave functions, represented by single Slater determinants. Note that in Eq. (3.17), all elements in the block  $\langle \Phi_0 | \hat{\mathbf{H}} | \Phi_1 \rangle$  vanishes. This arises from so-called **Brillouin's theorem**<sup>7</sup>. Application of this theorem to the the matrix elements involving the singly-excited determinants  $|\Phi_i^a\rangle$ , which differs from the Hartree-Fock determinant by only one spin-orbital, and the Hartree-Fock ground states implies  $\langle \Phi_0 | \hat{\mathbf{H}}_0 | \Phi_i^a \rangle = 0$ . Additional vanishing block matrix elements for higher order excitations may appear (for instance  $\langle \Phi_0 | \hat{\mathbf{H}}_0 | \Phi_{i,j,k}^{a,b,c} \rangle = \langle \Phi_0 | \hat{\mathbf{H}}_0 | \Phi_{i,j,k,l}^{a,b,c,d} \rangle = 0$ ) by virtue of the **Slater-Condon Rule**<sup>8</sup> [46–48]. Single excitations do not couple, by virtue of Brillouin's theorem, to the Hartree Fock reference determinant. In fact, by virtue of the Slater-Condon Rule, only double excitations can interact with the HF ground state, i.e.  $\langle \Phi_0 | \hat{\mathbf{H}} | \Phi_2 \rangle \equiv \langle \Phi_0 | \hat{\mathbf{H}}_0 | \Phi_{i,j}^{a,b} \rangle \neq 0$  in Eq. (3.17). Consequently, it is therefore expected double excitations to make the most relevant contributions to the **CI** wave function [45], which is indeed was is observed in numerical simulations [49]. These contributions are particularly relevant when correlations among different orbitals are important. However, when it comes to describe one-electron properties, such as transition moments, *et cetera*, single excitations become crucial, particularly when the laser field driving these transitions are of moderate intensity, such that higher order excitations are less probable to occur. This is the context adopted in this thesis. Also, the so-called *frozen core approximation*, whereby the total and spin angular momenta of the ground state are assumed to be equal to zero, is systematically invoked in our numerical calculations. We recall that the later approxima-

<sup>7</sup>The Brillouin's theorem states that "given two Slater determinants constructed from orthogonal spatial spin-orbitals satisfying the Hartree-Fock equations, if both Slater determinants differ in only one spatial orbital, then the matrix element of the many-body Hamiltonian between both determinants are strictly zero"

<sup>8</sup>The Slater-Condon rule states that "any matrix element of a two-body operator with Slater determinants differing in three or more spin-orbitals vanish"

tion constrains all inner-shell electrons to remain doubly occupied. This approximation, commonly used in the context of many-body calculations [10, 25, 28, 50–53] is found to be justified by considering that the valence electrons are more sensitive to their environment in comparison to their counterpart inner-shell electrons. From a numerical point of view, such an approximation considerably reduces the numerical effort for the evaluation of the matrix elements in the **CIS** picture. The field-free Hamiltonian  $\hat{\mathbf{H}}_0$ , reads [10, 25]

$$\hat{\mathbf{H}}_0 = \hat{\mathbf{F}} + \underbrace{\hat{\mathbf{V}}_C - \hat{\mathbf{V}}_{\text{HF}}}_{\equiv \hat{\mathbf{H}}_1} - E_{\text{HF}}, \quad (3.18)$$

where  $\hat{\mathbf{F}}$  denotes the Fock operator, namely

$$\hat{\mathbf{F}} = -\frac{1}{2}\hat{\nabla}^2 - \frac{Z}{\hat{\mathbf{r}}} + \sum_i (2\hat{\mathbf{J}}_i + \hat{\mathbf{K}}_i), \quad (3.19)$$

such that  $\hat{\mathbf{F}}|\varphi_{p,\sigma}\rangle = \varepsilon_p|\varphi_{p,\sigma}\rangle$ . The four terms defining the Fock operator are described by a kinetic part ( $-\hat{\nabla}^2/2$ ), an attractive Coulomb potential due to the nucleus, direct terms

$$\hat{\mathbf{J}}_j(\mathbf{r}_1)\varphi_i(\mathbf{r}_1) = \left[ \int d\mathbf{r}_2 |\varphi_j(\mathbf{r}_2)|^2 r_{12}^{-1} \right] \varphi_i(\mathbf{r}_1), \quad i \neq j, \quad (3.20)$$

describing the *mean field* created by the remaining electrons, and the so-called exchange terms,

$$\hat{\mathbf{K}}_j\varphi_k(\mathbf{r}_1) = \left[ \int d\mathbf{r}_2 \varphi_j^*(\mathbf{r}_2) r_{12}^{-1} \varphi_i(\mathbf{r}_2) \right] \varphi_j(\mathbf{r}_1), \quad i \neq j, \quad (3.21)$$

which describes the correction that originates from the anti-symmetrization. In Eq. (3.18),  $E_{\text{HF}}$  symbolizes the shift in energy corresponding to the Hartree-Fock ground state energy, namely

$$E_{\text{HF}} = 2 \sum_i \varepsilon_i + \langle \Phi_0 | \hat{\mathbf{H}}_1 | \Phi_0 \rangle \quad \text{where} \quad \langle \Phi_0 | \hat{\mathbf{H}}_1 | \Phi_0 \rangle = - \sum_{i,j} \{ v_{i,j,i,j} - v_{i,j,j,i} \}, \quad (3.22)$$

has been introduced to write the equation in a more compact form [10] and where the matrix elements  $v_{p,q,r,s}$  are given by

$$v_{p,q,r,s} = \langle \varphi_p \varphi_q | 1/r_{12} | \varphi_r \varphi_s \rangle = \int \int d^3r_1 d^3r_2 \varphi_p^*(\mathbf{r}_1) \varphi_q^*(\mathbf{r}_2) \frac{1}{|\mathbf{r}_{12}|} \varphi_r(\mathbf{r}_1) \varphi_s(\mathbf{r}_2). \quad (3.23)$$

The electronic correlation effects are absorbed in the matrix elements of  $\hat{\mathbf{H}}_1$ . In our simulations, and following Refs. [10, 25], these matrix elements are evaluated by means

of the Slater-Condon rules [10],

$$\begin{aligned}\langle \Phi_0 | \hat{\mathbf{H}}_1 | \Phi_i^a \rangle &= 0 \quad \text{Brillouin theorem} \\ \langle \Phi_i^a | \hat{\mathbf{H}}_1 | \Phi_{i'}^{a'} \rangle &= 2v_{a,i',i,a'} - v_{a,i',a',i} + \delta_{i,i'} \delta_{a,a'} \langle \Phi_0 | \hat{\mathbf{H}}_1 | \Phi_0 \rangle,\end{aligned}\tag{3.24}$$

where  $\langle \Phi_0 | \hat{\mathbf{H}}_1 | \Phi_0 \rangle$  is defined in Eq. (3.22).

### 3.4.2 Time-dependent Configuration-Interaction Singles (TDCIS)

Having presented the principles behind the **CI** formalism and explained why it may be suitable in the quest for incorporating the electronic correlations to overcome the limitations of the Hartree-Fock approximation, the extension of the theory to time-dependent problems follows almost immediately. When ignoring magnetic fields and relativistic corrections to the Hamiltonian such as spin-orbit coupling<sup>9</sup>, and assuming the electric field to be linearly polarized along the  $z$  direction, the time-dependent Hamiltonian reads [10, 25],

$$\hat{\mathbf{H}}(t) = \hat{\mathbf{H}}_0 + \hat{\mathbf{H}}_1 - E_{\text{HF}} - \mathcal{E}_z(t) \hat{\mathbf{z}},\tag{3.25a}$$

with  $\hat{\mathbf{H}}_1 = \hat{\mathbf{V}}_{\text{C}} - \hat{\mathbf{V}}_{\text{HF}}$ , and where  $\hat{\mathbf{H}}_0$ ,  $\hat{\mathbf{V}}_{\text{C}}$  and  $\hat{\mathbf{V}}_{\text{HF}}$  are given in Eq. (3.18). Finally,  $\mathcal{E}_z(t)$  and  $\hat{\mathbf{z}}$  refer to the laser electric field and position operator along the electric field polarization direction<sup>10</sup>, respectively [10]. The many-body time-dependent Schrödinger equation reads

$$i \frac{\partial}{\partial t} |\Psi^N(t)\rangle = \hat{\mathbf{H}}(t) |\Psi^N(t)\rangle.\tag{3.25b}$$

Defining the field-free  $N$ -electron wave function in terms of Eq. (3.16) and restricting ourselves to single-particle-hole excitations, the time-dependent CIS wave packet can be written, following the *ansatz* [10, 25, 28]

$$|\Psi(t)^N\rangle = \alpha_0(t) |\Phi_0\rangle + \sum_i \sum_a \alpha_i^a(t) |\Phi_i^a\rangle.\tag{3.25c}$$

In order to solve the coupled equations of motion for the CIS expansion coefficients, the coupling terms due to the dipole operator must be evaluated. The non-diagonal elements

<sup>9</sup>typically, three relativistic corrections are often considered: spin-orbit coupling, s-shift correction and mass-velocity correction [54], plus additional corrections to the magnetic moment of the electron [55, 56]

<sup>10</sup>which can be expressed in terms of the creation and annihilation operators as  $\hat{\mathbf{z}} = \sum_{p,q} z_{p,q} \sum_{\sigma} \hat{\mathbf{c}}_{p\sigma}^{\dagger} \hat{\mathbf{c}}_{q,\sigma}$  with  $z_{\mu,\nu} \equiv \langle \varphi_{\mu} | z | \varphi_{\nu} \rangle$ .

$z_{\mu,\nu} \equiv \langle \varphi_\mu | z | \varphi_\nu \rangle$  are evaluated according to [10, 25]

$$z_{\mu,\nu} = \int d^3r \varphi_\mu(\mathbf{r}) z \varphi_\nu(\mathbf{r}), \quad (3.25d)$$

with  $\varphi_\mu(\mathbf{r})$  a given spin-orbital. Equation (3.25d) is utilized to evaluate the matrix elements in the CIS basis used in Eq. (3.25c). These matrix elements reads [10],

$$\begin{aligned} \langle \Phi_0 | \hat{\mathbf{z}} | \Phi_0 \rangle &= 2 \sum_{i,i'} z_{i,i'} \\ \langle \Phi_0 | \hat{\mathbf{z}} | \Phi_i^a \rangle &= \sqrt{2} z_{i,a} \\ \langle \Phi_i^a | \hat{\mathbf{z}} | \Phi_{i'}^{a'} \rangle &= \delta_{i,i'} z_{a,a'} - \delta_{a,a'} z_{i,i'} + \underbrace{\delta_{i,i'} \delta_{a,a'} \sum_j z_{j,j}}_{\equiv 0, z_{j,j}=0}, \end{aligned} \quad (3.26)$$

where the diagonal elements  $z_{i,i}$  vanish for atomic systems [28]. Following Ref. [10, 25, 28], the equations of motion for  $\alpha_0(t)$  and  $\alpha_i^a(t)$  are obtained by projecting Eq. (3.25c) onto the basis defined by  $|\Phi_0\rangle$  and  $\{|\Phi_i^a\rangle\}$ . The dynamics of the wave packet is obtained by solving the coupled equations of motion [10, 25]

$$\begin{aligned} i\dot{\alpha}_0(t) &= -\sqrt{2} \epsilon(t) \sum_i \sum_a \alpha_i^a(t) z_{i,a} \\ i\dot{\alpha}_i^a(t) &= (\epsilon_a - \epsilon_i) \alpha_i^a(t) + \sum_{i'} \sum_{a'} \alpha_{i'}^{a'}(t) (2v_{ai'ia'} - v_{ai'a'i}) \\ &\quad - \mathcal{E}_z(t) \left\{ \sqrt{2} \alpha_0(t) z_{a,i} + \sum_{a'} \alpha_i^{a'}(t) z_{a,a'} - \sum_{i'} \alpha_{i'}^a z_{i,i'} \right\}, \end{aligned} \quad (3.27)$$

with the initial condition given by  $\alpha_0(t) \rightarrow 1$  and  $\{\alpha_i^a(t)\} \rightarrow 0$  as  $t \rightarrow -\infty$ . In the framework of this thesis, Eq. (3.27) is solved by means of the *Short Iterative Lanczos method*, described in Section 4.2.2.

Finally, as introduced in Ref. [10], a partial summation over all single excitations from each occupied orbital  $|\varphi_i\rangle$  in the rhs in Eq. (3.25c), allows to rewrite the TDCIS formalism in terms of a **“channel wave function”**, namely

$$|\Psi(t)^N\rangle = \alpha_0(t) |\Phi_0\rangle + \sum_i |\varphi_i(t)\rangle \quad \text{with} \quad |\varphi_i(t)\rangle = \sum_a \alpha_i^a |\Phi_i^a\rangle. \quad (3.28)$$

The peculiarity of such “channel wave function” formalism is that it allows to describe and calculate all quantities in a channel-resolved manner [10, 51]. It is this formalism that has adopted throughout this work.



# Numerical methods for solving the time-dependent Schrödinger equation

---

4.1	Discrete Variable Representation . . . . .	28
4.1.1	Lagrange-mesh method . . . . .	31
4.1.2	Finite-Element Discrete Variable Representation . . . . .	33
4.1.3	The Fourier Hamiltonian Grid and Dynamical Fourier methods . . . . .	36
4.2	Numerical simulation of Quantum Dynamics . . . . .	38
4.2.1	The Chebychev propagation method . . . . .	39
4.2.2	Short iterative Lanczos propagator . . . . .	41

---

This chapter is intended to provide an elemental inspection to the general principles behind the *state-of-the art* techniques for the numerical solution of the Schrödinger equation adopted for the preparation of this thesis. Unless otherwise specified, atomic units are used throughout.

In practice, numerical solution of the time-dependent Schrödinger equation consists of three hierarchical steps. The first step consists in determining a suitable representation for the wave function <sup>1</sup> to be propagated. This step is followed by evaluation of the action of operators in this representation and finally, the third step involves the time propagation properly speaking. While a plethora of numerical methods for solving the Schrödinger equation are available [57], numerical efficiency of these techniques plays a critical role when it comes to chose the appropriate method. In the context of this thesis, adaptive grid-based radial representation [58–60] of the wave function allows to

---

<sup>1</sup>generally defined by the ground state, a field-free eigenstate, or a linear combination thereof.

straightforwardly evaluate the action of the operators acting on single-particle and many-body wave functions [25] while considerably reducing the numerical effort required for propagation purposes. In the following lines, standard techniques for efficiently solving both time-independent and time-dependent Schrödinger equation are briefly described.

## 4.1 Discrete Variable Representation

The Discrete Variable representation or **DVR** for short, is a pseudospectral method allowing to represent functions on a discretized quadrature spatial grid, thereby simplifying the representation of certain kind of operators. It is one of the most versatile numerical techniques utilized in the applied mathematics community and has been widely applied to a large class of problems involving polynomials approximation of differential equations: from ordinary and partial differential equations [61, 61–63] to time-dependent problems [64, 65]. It became popular in the physics community after the pioneering work of Light and co-workers [66–72], among others [57, 73–75]. In the context of quantum mechanics, the attractiveness of the DVR relies on two striking features, namely (i) the matrix representation of the potential energy operator  $\hat{\mathbf{V}}$  or any local operator in real space *is diagonal* in this representation whereas (ii) the matrix form of the kinetic matrix operator, although represented by a full matrix,  $\hat{\mathbf{K}}$ , enjoys *simple analytic forms*. These two features together with its pseudospectral accuracy, makes the DVR an accurate numerical formalism easy to implement to quantum mechanical problems.

Generally, the DVR formalism is based on the expansion of a wave function in an orthonormal basis set  $\Phi_n(r)$ ,  $n = 0, N$  and utilization of a Gaussian quadrature rule that depends on the collocation points defining the coordinate grid. More specifically, in the language of the pseudospectral approach, the wave function is evaluated at  $N + 1$  distinct interpolation points of a pseudospectral grid, namely

$$\psi(r_i, t) = \sum_{n=0}^N a_n(t) \Phi_n(r_i), \quad (4.1)$$

where the interpolating points corresponds to the discretized points  $\{r_j\}$  with  $j = 0, \dots, N$ , and where  $\{\Phi_n(r)\}$  are referred to as the *interpolating functions*. It is customary to perform the expansion in terms of functions satisfying the property

$$\sum_{n=0}^N \Phi_n^*(r_i) \Phi_n^*(r_j) = \delta_{i,j}. \quad (4.2)$$

This property allows to find the expression of the expansion coefficients as a function of

the interpolating function  $\psi(r)$ , namely

$$a_n(t) = \sum_{j=0}^N \psi(r_j, t) \Phi_n^*(r_j), \quad (4.3)$$

with the property

$$\psi(r_i, t) = \sum_{j=0}^N \psi(r_j, t) \sum_{n=0}^N \Phi_n^*(r_j) \Phi_n(r_i) \equiv \sum_{j=0}^N \psi(r_j, t) \delta_{i,j}. \quad (4.4)$$

The interpolating functions  $\Phi_n(r)$  are defined in terms of polynomials which are orthogonal to each other with respect to a specific weight function  $\tilde{\omega}(r)$  [76] within a given interval  $\mathcal{D}$ , namely

$$\langle \Phi_n | \Phi_{n'} \rangle = \int_{\mathcal{D}} \tilde{\omega}(r) \Phi_n^*(r) \Phi_{n'}(r) = \delta_{n,n'}, \quad (4.5)$$

where the weight function  $\tilde{\omega}(r)$  ensures a proper decay of the wave function for infinite or semi-infinite intervals [77]. These weight functions depend on the polynomials as well as on the integration interval [76, 78]. For our part, we will limit ourselves to the cases where  $\tilde{\omega}(r) = 1$ , which is the case for the *Lagrange polynomials* and *Legendre cardinal functions*, defined in Eqs. (4.10) and (A.34), respectively, both utilized in the context of this doctoral work. By virtue of the Gaussian quadrature rule, Eq. (4.5) is, for  $\tilde{\omega} = 1$ , exactly equivalent to

$$\sum_{j=0}^N \omega(r_j) \Phi_n^*(r_j) \Phi_{n'}(r_j) = \delta_{n,n'}, \quad (4.6)$$

for any polynomial of degree  $2N - 1$ , and where  $\omega(r_j)$  refers to the Gaussian quadrature weights [77, 78]. The expression of the expansion coefficients become, with  $\omega_j \equiv \omega(r_j)$ ,

$$a_n(t) = \sum_{j=0}^N \omega_j \psi(r_j, t) \Phi_n^*(r_j). \quad (4.7)$$

Inserting Eq. (4.7) into Eq. (4.1), we are now in a position to represent the  $n$  th derivative operator in the DVR formalism, namely

$$\frac{d^n}{dr^n} \psi(r) = \sum_{j=0}^N \omega_j \Phi(r_j) \sum_{i=0}^{N-1} \Phi_i^*(r_j) \frac{d^n \Phi_i(r)}{dr^n}. \quad (4.8)$$

So far, no specific requirements, except for the orthogonality condition, were made on the basis  $\Phi_i(r)$ . Writing Eq. (4.8) in a matrix form, upon renormalization of the basis functions

as we will see later, is a suitable way to solve the time-independent Schrödinger equation. Furthermore, the attractiveness of the DVR approach lies in the fact that Eq. (4.8) can be evaluated analytically for certain kind of basis set. In this case, the expression of the  $n$ -th order derivative depends only on the interpolation polynomials as well as on the domain of integration  $\mathcal{D}$  [78, 79]. Although the choice of the polynomials  $\{\Phi_n(r)\}$  is arbitrary, the error due to the approximation of truncating the series expansion will enjoy different convergence properties depending on the interpolating polynomials [78]. Typically, the strategy consist in making use of the Garlekin method [78], which, for the case of the time-independent Schrödinger, allows to determine the expansion coefficients  $\{a_n\}$  and eigenvalues  $E$  upon solution of a set algebraic equations, namely

$$\sum_{m=0}^N \left( \hat{\mathbf{K}}_{n,m} + \hat{\mathbf{V}}_{n,m} - E \langle \Phi_n | \Phi_m \rangle \right) a_m = 0 \quad \forall m = 0, \dots, N, \quad (4.9a)$$

which is solved by diagonalizing the matrix equation,

$$\left( \hat{\mathbf{H}} - E \hat{\mathbf{1}}_{\tilde{N} \times \tilde{N}} \right) \cdot \mathbf{a} = 0 \quad (4.9b)$$

with  $\tilde{N} = N + 1$ , and where  $\hat{\mathbf{H}} = \hat{\mathbf{K}} + \hat{\mathbf{V}}$  and  $\mathbf{a}$  symbolizes the Hamiltonian and the vector representation of the expansion coefficients  $\{a_n\}$ , respectively. The matrix elements of the *local* potential energy operator reads

$$\hat{\mathbf{V}}_{i,j} = \int_0^\infty \Phi_i(r) V(r) \Phi_j(r) dr. \quad (4.9c)$$

Conversely, the matrix elements of the kinetic matrix operator reads

$$\hat{\mathbf{K}}_{i,j} = -\frac{1}{2m} \int_0^\infty \Phi_i(r) \frac{d^2}{dr^2} \Phi_j(r) dr \quad (4.9d)$$

As already mentioned, DVR-based methods allow for constructing simple non-local analytical forms for the kinetic energy operator, whilst keeping the representation of local operators at a minimum. This is important in a view of exploiting the versatility of the DVR approach in the context of time-dependent calculations, as discussed in Chapter 7. Needless to say, a plethora of choices for the functions  $\Phi_n(r)$  is available. The same applies to the best choice of the interpolation points  $\{r_j\}$ . We briefly introduce and describe a few of the most prominent alternatives commonly utilized. These are briefly outlined in the following.

### 4.1.1 Lagrange-mesh method

In the Lagrange-mesh method, a grid is associated with a basis set with the peculiar characteristic that each continuous basis function spanning the Hilbert space vanishes at all mesh points except at the collocation mesh point to which the basis function is associated [80–82]. Among the family of polynomials enjoying this property, the Lagrange polynomials defined by

$$\begin{aligned}\Phi_j(r) &= \prod_{p=0, p \neq j}^N \frac{r - r_p}{r_j - r_p} \\ &= \frac{(r - r_0)}{(r_j - r_0)} \cdots \frac{(r - r_{j-1})}{(r_j - r_{j-1})} \cdots \frac{(r - r_{j+1})}{(r_j - r_{j+1})} \cdots \frac{(r - r_N)}{(r_j - r_N)},\end{aligned}\quad (4.10)$$

are among the most popular ones. They belong to a class of polynomials fulfilling Eq. (4.2), and they are a particular category of *Cardinal functions* [78]. These functions play an important role in this thesis and they refer to a special class of analytical functions enjoying the remarkable property,

$$\Phi_j(r_i) = \delta_{i,j} = \begin{cases} 1, & i = j \\ 0 & i \neq j. \end{cases}\quad (4.11)$$

It follows that one of the striking properties of the so-called cardinal functions is that the expansion coefficients, i.e. the  $a_n$  in Eq. (4.7), correspond to the value of the wave function at each interpolating point  $r_n$ . Another consequence is that any local operator in coordinate representation such as  $\hat{\mathbf{V}}(r)$  conserves a diagonal representation in the DVR basis, namely

$$\hat{\mathbf{V}}_{i,j} \equiv \int_0^\infty \Phi_i(r) V(r) \Phi_j(r) dr = \sum_{m=0}^N \Phi_i(r_m) V(r_m) \Phi_j(r_m) \omega(r_m) \quad (4.12)$$

$$= \delta_{i,j} V(r_i) \omega_i, \quad (4.13)$$

where we have made use of the Gaussian quadrature rule [78, 83] and where the standard notation  $\omega(r_m) \equiv \omega_m$  is used throughout this work. The matrix representation of the kinetic energy operator  $\hat{\mathbf{T}} = -d^2/dr^2$ , assuming vanishing Dirichlet boundary conditions, reads

$$\begin{aligned}\hat{\mathbf{T}}_{i,j} &= - \int_0^\infty \Phi_i(r) \frac{d^2}{dr^2} \Phi_j(r) dr = \int_0^\infty \frac{d}{dr} \Phi_i(r) \frac{d}{dr} \Phi_j(r) dr \\ &= \sum_{m=0}^N \frac{d}{dr} \Phi_i(r_m) \frac{d}{dr} \Phi_j(r_m) \omega_m,\end{aligned}\quad (4.14)$$

where we made use of the *Green formula* (integration by parts) in order to construct a symmetric matrix<sup>2</sup>. In practice, the matrix elements  $\hat{\mathbf{T}}_{i,j}$  are known analytically [78, 82]. The task consist then in solving the eigenvalue problem via a set of linear algebraic equations

$$\sum_{j=0}^N \left( \frac{1}{2m} \hat{\mathbf{T}}_{i,j} + \hat{\mathbf{V}}_{i,j} - E \underbrace{\langle \Phi_i | \Phi_j \rangle}_{= \omega_i \delta_{i,j}} \right) \psi_j = 0 \quad \forall i = 0, \dots, N. \quad (4.15)$$

However, the eigenvalue problem formulated in the cardinal basis alone results in a generalized eigenvalue problem due to the Gaussian weight arising from the discretization (collocation). In fact, evaluation of the inner product using the Gaussian quadrature rule gives

$$\langle \Phi_i | \Phi_j \rangle \equiv \int_0^\infty \Phi_i(r) \Phi_j(r) dr = \sum_{m=0}^N \Phi_i(r_m) \Phi_j(r_m) \omega(r_m) \quad (4.16)$$

$$= \omega_i \delta_{i,j}. \quad (4.17)$$

The eigenvalue problem can be formulated in the standard form  $\hat{\mathbf{H}} \cdot \mathbf{a} = \lambda \mathbf{a}$  upon *normalization* of the Lagrange polynomials according to

$$\Phi_j(r) = \frac{1}{\sqrt{\omega_j}} \prod_{p=0, p \neq j}^N \frac{r - r_p}{r_j - r_p}, \quad (4.18)$$

which takes into account the collocation weights due to the discretization. Such normalization is also known as **Lagrange condition**. It is worth mentioning that the Gauss quadrature is exact for products of Lagrange functions [80, 81].

An important criterion for minimizing the error due to the discretization consists on properly choosing the collocation points. In fact, for relatively extended grids consisting of evenly spaced collocation points, a well-known pathology consisting in the divergence near the endpoints resulting from the interpolation known as the *Runge-phenomenon* can be avoided by a suitable choice of the distribution of collocation points [78]. In general, the distribution of points consists in a non-evenly spaced set of points concentrated towards the ends or middle of the grid depending on the criteria with which the construction of such distribution of points was based on. For instance, roots of specific polynomials or alternatively, of its derivatives. Among the most commonly employed, the so-called **Legendre-Gauss-Lobatto**, also known as “**extrema plus end-points**”. This set of interpolating points is obtained by fixing the extremities at  $r_0 = -1$  and  $r_N = 1$  while the  $N-1$  remaining points coincides with the extrema of the Legendre polynomials, i.e. the  $N-1$

<sup>2</sup>with respect to the exchange  $i \leftrightarrow j$  in Eq. (4.14)

roots of  $dP_N(x)/dx$  [78]. For a interpolated function defined in a interval different from  $[-1, 1]$ , a linear transformation mapping both intervals is performed [60]. Of course, the choice of such suitable distribution of points is not exclusively restricted to the extrema of  $P_N(x)$ . Alternative ensemble of points, such that the extrema of the Chebychev polynomials also exists [78, 84]. The same applies to the interpolating function which are not restricted to the Lagrange polynomials. In fact, a mesh method fulfilling the Lagrange condition can be associated to every family of orthogonal polynomials [73, 78]. This, combined with the versatility of the finite-element approach, cf. Section 4.1.2, defined the motivation that allowed us to construct a very efficient pseudospectral-finite-element-based propagation approach, described in Ref. [60].

#### 4.1.2 Finite-Element Discrete Variable Representation

The non-local character of the kinetic matrix operator is reflected by the fullness (non-sparseness) of the Hamiltonian matrix representation. The numerical performance for matrix operations involving dense (full) matrices may be seriously compromised, particularly when treating with large Hilbert spaces. This corresponds to the case where large spatial grids are required. Consequently, global methods, such as the DVR approach, characterized by a full matrix representation of the Hamilton operator are in practice computationally demanding, if not prohibited.

Fortunately, the **Finite-Element Discrete Variable representation** [58], or **FE-DVR** for short, makes a considerable step forward on the path to improve the numerical performances by constructing a semi-local representation of the Hamiltonian while conserving the desired accuracy. This is achieved by combining the efficiency of the well established **finite-element method (FEM)** [85, 86] and the spectral accuracy of the pseudospectral approach [87]. The essence of the **FEM** lies in partitioning the entire spatial coordinate into small contiguous **sub-domains**, also referred to as **elements**. On each element, a set of arbitrary functions with compact support<sup>3</sup> on each element, centered around each collocation point is chosen [88]. Because these functions (basis) are compactly supported on each element, the matrix elements involving two basis belonging to the same and different elements, which is required to be computed for the construction of the global representation of the Hamiltonian matrix, takes non-vanishing values only if the operation involves two compactly supported functions belonging to the same element. As a result, the matrix representation of the kinetic energy operator has now a semi-local representation, as opposed to the global representation of the DVR. Consequently, the matrix form of the Hamiltonian in the finite-element basis results in a sparse representation, therefore con-

---

<sup>3</sup>A function has compact support if its support is a compact set, or equivalently, if the function is identically zero outside its compact support.

siderably reducing the numerical effort in terms of storage and matrix-vector operations. Generally speaking, the **FE-DVR** may be viewed as a DVR formalism on each element. It is to outline nonetheless that generally, global representations benefits superior convergence performances with respect to their semi-local counterparts [78]. However, several standard procedures seeking for minimizing the lost of accuracy due to the semi-local representation are available. Such procedures generally involves manipulation of the number of elements, or alternatively, of the number of collocation points per elements, e.g.  $p$ - and  $h$ - refinement, or a better choice of the interpolating polynomial on each element. Herein lies the essence of the **FE-DVR** [58, 83, 89–92], whereby the error of approximation due to the semi-local character is considerably reduced by choosing orthonormal polynomials of arbitrary order with compact support on each element, thus significantly improving the convergence error while benefiting from the sparsity of the representation for storage and matrix-vector operation purposes. In the context of the **Lagrange-mesh method**, the compactly supported polynomials are defined in terms of the *global* Lagrange polynomials defined in Eq. (4.10) which are now *compactly supported* on each element  $m$ , namely

$$\Phi_i^{(m)}(r) = \prod_{k \neq m} \frac{(r - r_i^{(k)})}{(r_i^{(m)} - r_i^{(k)})}, \quad (4.19)$$

where  $m = 1, \dots, M$  is used to label the  $m$ th element. The compactly supported Lagrange functions have the property

$$\Phi_i^{(m)}(r_j^{(m')}) = \delta_{i,j} \delta_{m,m'}, \quad (4.20)$$

where  $r \equiv r_j^{(m')}$  defines a particular discretized point that belongs to the  $m'$  th element. Each element  $\Omega^{(m)}$  is discretized into a set of  $N + 1$  different points,  $r_j$ , with  $j = 0, \dots, N$ . The matrix elements are evaluated and approximated in the usual way, i.e., by means of the Gaussian quadrature rule. Thus, the product of two compactly supported Lagrange polynomials gives

$$\begin{aligned} \int_0^\infty \Phi_i^{(m)}(r) \Phi_j^{(m')}(r) dr &= \sum_{k=1}^M \int_{r_0^{(k)}}^{r_N^{(k)}} \Phi_i^{(m)}(r) \Phi_j^{(m')}(r) dr \\ &\approx \sum_{k=1}^M \sum_{s=0}^{N-1} \Phi_i^{(m)}(r_s^{(k)}) \Phi_j^{(m')}(r_s^{(k)}) \omega_s^{(k)} \\ &= \omega_i^{(m)} \delta_{i,j} \delta_{m,m'}. \end{aligned} \quad (4.21)$$

It follows that, just as for the global DVR formalism, any local operator conserves a

diagonal representation, namely

$$\hat{\mathbf{V}}_{i,j}^{m,m'} \equiv \int_0^\infty \Phi_i^{(m)}(r)V(r)\Phi_j^{(m')} = V(r_i^{(m)})\omega_i^{(m)}\delta_{i,j}\delta_{m,m'}. \quad (4.22)$$

The *global representation* of the Hamiltonian matrix requires assembling of all two contiguous elements. These are “*connected*” at the  $M - 1$  *interelement points*  $r_N^{(m-1)} = r_0^{(m)}$ ,  $\forall m = 2, \dots, M$ . The continuity of the interpolated wave function at each interelement point follows from the continuity of the interpolating basis at these points. Since the global grid has been intentionally split into  $M$  elements, continuity of the basis functions at the  $M - 1$  contiguous points should be performed manually. Continuity at the interelement points  $r_N^{(m-1)} = r_0^{(m)}$  is achieved by re-defining the basis functions according to

$$\zeta_i^{(m)}(r) = \begin{cases} \Phi_i^{(m)}(r), & i = 1, \dots, N - 1 \\ \Phi_N^{(m)}(r) + \Phi_0^{(m+1)}(r), & i = 0, N. \end{cases} \quad (4.23)$$

Again, the Lagrange condition, cf. Eq. (4.18), is employed to solve an ordinary eigenvalue problem of the form  $\hat{\mathbf{H}}\varphi = E\varphi$ . In the framework of the **FE-DVR** the Lagrange condition reads

$$\zeta_i^{(m)}(r) = \begin{cases} \frac{\Phi_i^{(m)}(r)}{\sqrt{\omega_i^{(m)}}}, & i = 1, \dots, N - 1 \\ \frac{\Phi_N^{(m)}(r) + \Phi_0^{(m+1)}(r)}{\sqrt{\omega_N^{(m)} + \omega_0^{(m+1)}}} & i = 0, N. \end{cases} \quad (4.24)$$

The Gaussian weights in Eq. (4.24) are referred to as “*effective weights*”. They take into account the continuity of the basis functions at the interelement points. The matrix elements of the kinetic energy operator in the compactly supported Lagrange [83, 93] basis reads

$$\hat{\mathbf{T}}_{i,j}^{m,m'} = \frac{1}{2}(\delta_{i,j} + \delta_{i,j\pm 1}) \int_0^\infty dr \frac{d}{dr}\zeta_i^{(m)}(r) \frac{d}{dr}\zeta_j^{(m')}(r). \quad (4.25)$$

These matrix elements can be evaluated either numerically or analytically by means of the first order derivatives of the Lagrange polynomials at the quadrature points [78, 83, 93, 96]. By virtue of the compact support on each element, the global representation of the kinetic energy operator is sparse with connections that represent the interelement points of the global grid, see e.g. Figure 7.4 in Section 7.3. Finally, due to the introduction of the “*weighted*” basis set, i.e. Eq. (4.24), proper representation of the eigenvectors requires the

transformation

$$\psi(r_i^m) \rightarrow \psi(r_i^{(m)})/\sqrt{\omega_i^{(m)}} \quad (4.26)$$

where  $\omega$  are the “effective” weights defined in Eq. (4.24) and where the  $\psi(r_i^m)$  is obtained upon diagonalization of the Hamiltonian matrix in the compactly supported Lagrange basis.

### 4.1.3 The Fourier Hamiltonian Grid and Dynamical Fourier methods

The Fourier method is a special case of pseudospectral method resolved in a evenly spaced coordinate grid and whereby the functions  $\{\Phi_n(x)\}$  are chosen to be [57, 94],

$$\Phi_n(x) = \exp[2i\pi nx/L]/\sqrt{L}, \quad \text{with } n = -(N/2 - 1), \dots, 0, N/2 \quad (4.27)$$

with  $-\infty < x < +\infty$  discretized in a box of size  $L$  composed of  $N$  sampling points [94]. There exist two main kinds of implementation of such approach, namely the **Fourier Grid Hamiltonian method**, also referred to as *Cartesian mesh*, as opposite to the Lagrangian-mesh method [73] and the so-called **Dynamic Fourier Method** [94]. While the former requires construction of the full Hamiltonian matrix in the pseudospectral Fourier basis in order to evaluate the action of the momentum operator, the latter avoids any kind of matrix storage by evaluating the action of the kinetic operator via Fast Fourier transform [94].

#### Fourier Hamiltonian Grid method

Historically, in the Fourier Grid Hamiltonian [95] case, the Hamiltonian matrix is constructed in the Fourier basis and diagonalized to obtain eigenvalues and eigenvectors. In the Fourier basis, the matrix representation of any local operator is diagonal in space representation, while the matrix representation of the kinetic energy operator enjoys a simple analytical form, namely [94]

$$\langle \Phi_i | \hat{\mathbf{T}}(p) | \Phi_j \rangle = \frac{1}{m} \begin{cases} \frac{(\pi/\Delta x)^2}{6} & (i = j) \\ \frac{1}{(\Delta x)^2} \frac{(-1)^{j-i}}{(j-i)^2} & (i \neq j), \end{cases} \quad (4.28)$$

where  $m$  and  $\Delta x$  refer to the mass and the interval between two consecutive evenly spaced discretized points, respectively. Despite its simplicity, the Fourier grid Hamiltonian method is not well suited for propagation schemes involving matrix-vector operations,

cf. Section 4.2.1, since the Hamiltonian matrix is represented by a dense (full) matrix due to the non-local character of the momentum operator in space-representation. In fact, for large Hilbert spaces, such an approach may become easily prohibited in terms of storage and propagation effort.

### Dynamic Fourier method

To remedy the limitations of the Fourier Grid Hamiltonian method, the so-called Dynamic Fourier method, due to Feit and Feck [96] and Kosloff and Kosloff [97] makes use of the locality the kinetic energy operator  $\hat{\mathbf{T}}$  in momentum representation. As usual, the action of the position operator in space representation conserves locality. The Dynamic Fourier method exploits the fact that the kinetic operator is local in momentum representation, while any position-dependent operator is local in coordinate space representation. Therefore, a practical application of this approach consist in separating the Hamiltonian in  $\hat{\mathbf{p}}$ -dependent and  $\hat{\mathbf{r}}$ -dependent operators. Generally, such partitioning implies  $\hat{\mathbf{H}} = \hat{\mathbf{T}}(\hat{\mathbf{p}}) + \hat{\mathbf{V}}(\hat{\mathbf{r}})$ . Exploiting the locality of both terms in momentum and coordinates representations, the application of the total Hamiltonian operator is performed in two-parallelizable steps:

1. **action of potential energy operator:** the operation  $\hat{\mathbf{V}}|\psi\rangle$  is merely given by a point-by-point product  $V(r_j)\psi(r_j)$ , since local in spatial representation.
2. **action of the kinetic operator:** is also evaluated locally, but in momentum-representation in a sequence involving three steps, namely
  - (a) Fourier transforming the wave function from spatial to momentum representation.
  - (b) This is followed by multiplying the transformed wave function and the momentum-dependent kinetic operator, ie.  $p^2 \Psi(p)$ , resulting in  $\tilde{\Upsilon}(p)$  by means of Fast-Fourier Transformation (FFT) and finally,
  - (c) transforming back  $\tilde{\Upsilon}(p)$  from momentum to spatial representation.

As a result, the numerical effort scales semi-linearly with the volume of phase-space. The Dynamic Fourier method presents two major advantages with respect to any standard pseudospectral method. First, no prior selection of the expansion basis (polynomials) set is required. This is a non-negligible improvement since it has been shown that different family of orthonormal polynomials commonly used in the framework of the DVR formalism possesses different convergence properties [78]. The second advantage is that it benefits from the efficiency and accuracy of the FFT techniques, therefore being limited only by the machine precision. The only requirement for accuracy is the choice of adequate

sample points in both, space and time domain for the numerical solution, which should fulfill the well-known requirement dictated by the Nyquist sampling theorem to avoid aliasing errors [96]. Compared to the dense matrix-vector operation-based approach, the Dynamical Fourier methods allows to decrease considerably the number of operations from  $\mathcal{O}(N^2)$  to  $N\mathcal{O}(\log(N))/2$  [94, 97], where  $N$  is the dimension of the Hilbert space.

Despite its outstanding efficiency, we show in Chapter 7 that this approach can be outperformed using special techniques based on the **FE-DVR** formalism briefly introduced in Section 4.1.2.

## 4.2 Numerical simulation of Quantum Dynamics

The details revealing the quantum signature imprinted in the electron dynamics of atomic and molecular systems exposed, for instance, to a classical electromagnetic field requires a proper description of the laser-matter interaction and solution of the time-dependent Schrödinger equation becomes unavoidable. Having introduced the DVR and FE-DVR formalisms to represent the atomic or molecular system and the action of operators in this representation, the electron dynamics is obtained by solving the time-dependent Schrödinger equation,

$$i\frac{\partial}{\partial t}|\psi(t)\rangle = \hat{\mathbf{H}}(t)|\psi(t)\rangle, \quad (4.29a)$$

where  $\hat{\mathbf{H}}(t)$  includes the field-free Hamiltonian  $\hat{\mathbf{H}}_0$  and the interaction Hamiltonian  $\hat{\mathbf{H}}_{em}(t)$ , namely

$$\hat{\mathbf{H}}(t) = \hat{\mathbf{H}}_0 + \hat{\mathbf{H}}_{em}(t). \quad (4.29b)$$

A formal solution to Eq. (4.29a) reads

$$|\psi(t)\rangle = \hat{\mathbf{U}}(t; t_0)|\psi(t_0)\rangle \equiv \hat{\mathbf{T}} \exp \left[ -i \int_{t_0}^T \hat{\mathbf{H}}(t') dt' \right] |\psi(t_0)\rangle, \quad (4.30)$$

where  $|\psi(t_0)\rangle$  and  $\hat{\mathbf{U}}(t; t_0)$  denote the initial condition for the initial state and the evolution operator, respectively, and where  $\hat{\mathbf{T}}$  is the time-ordering operator. In practice, solution of Eq. (4.30) has two main difficulties. The first obstacle concerns the analytical expression for the exponentiation of the Hamiltonian operator, and second, the construction of the time-ordering operator.

It is possible, however, to approximate Eq. (4.30) by assuming  $\hat{\mathbf{H}}(t)$  to be piecewise constant over a small time interval  $dt$ . This is equivalent to divide the time grid in very

short segments  $dt$  in which  $\hat{\mathbf{H}}_{em}(t)$  does not change significantly, namely

$$\hat{\mathbf{U}}(t; t_0) \approx \hat{\mathbf{T}} \exp \left[ -i \sum_{j=1}^{N-1} \hat{\mathbf{H}}(t_{j+1/2}) dt \right] = \prod_{j=1}^{N-1} \exp \left[ -i \hat{\mathbf{H}}(t_{j+1/2}) dt \right]. \quad (4.31)$$

with  $t_{j+1/2} = t_j + dt/2$ . From Eq. (4.31), it is apparent that the propagation problem reduces to find an efficient approach to evaluate the operation

$$|\Psi_{j+1}\rangle \equiv \exp \left[ -i \hat{\mathbf{H}}(t_{j+1/2}) dt \right] |\Psi_j\rangle. \quad (4.32)$$

Among the most prominent alternatives, two broad categories are commonly used. The first category is based on a polynomial approximation of the exponential of operators which requires prior knowledge of the polynomial to be used for the expansion. A second method that does not require prior choice of the polynomial is also conceivable [94]. These two alternatives are represented by the Chebychev and short iterative Lanczos propagators, respectively. They are briefly described in sections 4.2.1 and 4.2.2, respectively.

#### 4.2.1 The Chebychev propagation method

The essence of the Chebychev approach [57, 98, 99] relies on approximating every term in the product series of the rhs of Eq. (4.31) by a polynomial expansion of the exponential operator  $\hat{\mathbf{U}}(t_k)$ , namely

$$\begin{aligned} |\Psi_{j+1}\rangle = \hat{\mathbf{U}}_k |\Psi_j\rangle &\equiv \exp \left[ -i \hat{\mathbf{H}}(t_k) dt \right] |\Psi_j\rangle \\ &\approx \sum_{n=0}^{N_C} a_n P_n(\hat{\mathbf{H}}(t_k)) |\Psi_j\rangle \end{aligned} \quad (4.33)$$

with  $k = j + 1/2$  for consistency with the notation of Eq. (4.31) and where  $P_n(\cdot)$  is a polynomial of degree  $n$  and  $\{a_n\}$  the expansion coefficients.

It can be shown that for an analytical scalar function in the interval  $[-1, 1]$ , the polynomial approximation based on the Chebychev polynomials are optimal since the approximation error converges faster in comparison to almost all possible polynomial approximations [57, 78, 98, 99]. The propagation then reduces to a series of repeated applications of the argument of the polynomial, i.e.  $\hat{\mathbf{H}}$  on  $|\Psi\rangle$ . It is for this reason that the Dynamical Fourier grid method, or alternatively sparse matrix representations (FE-DVR) of the Hamiltonian operator together with special libraries for storage and (sparse) matrix-vector operations are suitable when it comes to polynomial approximations of the evolution operator. For the Chebychev polynomials, the necessity of having the argu-

ment in the range  $[-1, 1]$  translates into the requirement of normalizing the Hamiltonian operator according to [57, 98, 99]

$$\hat{\mathbf{H}}_{norm} = 2 \frac{\hat{\mathbf{H}} - E_{min} \mathbb{1}}{\Delta_E} - \mathbb{1}, \quad (4.34)$$

where  $\Delta_E = E_{max} - E_{min}$  denotes the spectral radius and where  $E_{min}$  and  $E_{max}$  refer to the smallest and largest eigenvalue of  $\hat{\mathbf{H}}$ , respectively. A condition for the numerical stability of the propagation is that spectrum of the Hamiltonian lies in  $\Delta_E$  at all times. Therefore, in the case of a time-dependent Hamiltonian, a good empiric procedure consists in defining the spectral radius according to [100],

$$\Delta_E = \left[ \hat{\mathbf{H}}_0 + \min_t \{ \hat{\mathbf{H}}_{em} \}, \hat{\mathbf{H}}_0 + \min_t \{ \hat{\mathbf{H}}_{em} \} \right]. \quad (4.35)$$

With this normalization in hand, the approximated time evolution of the wave packet is obtained via successive applications of the Hamiltonian to the auxiliary vector state  $|\zeta_n(t_j)\rangle$ , namely [98]

$$|\Psi(t_{j+1})\rangle \approx \sum_{n=0}^N a_n |\zeta_n(t_j)\rangle \quad (4.36a)$$

and where we have defined,

$$|\zeta_n(t_j)\rangle \equiv P_n \left[ -i \hat{\mathbf{H}}_{norm}(t_{j+1/2}) \right] |\Psi(t_j)\rangle, \quad (4.36b)$$

with  $P_n(\cdot)$  being the complex Chebychev polynomials of degree  $n$  that takes the complex argument  $-i \hat{\mathbf{H}}_{norm}$ . The expansion coefficients  $a_n$  are evaluated analytically as a function of the Bessel functions  $J_n(\cdot)$ , namely [57, 98, 100]

$$a_n = (2 - \delta_{n,0}) \exp \left[ -i (\Delta_E/2 + E_{min}) dt \right] J_n \left( \frac{\Delta_E dt}{2} \right), \quad (4.37)$$

where the phase shift in the rhs arises from the energy scaling, due to the normalization and where the auxiliary vector states  $|\zeta(t_j)\rangle$  defined in Eq. (4.36b) are computed using the three-term recursion formula

$$|\zeta_n(t_j)\rangle = -2i \hat{\mathbf{H}}_{norm} |\zeta_{n-1}(t_j)\rangle + |\zeta_{n-2}(t_j)\rangle \quad (4.38)$$

with  $|\zeta_s(t_j)\rangle = 0$  for  $s < 0$  and  $|\zeta_0(t_j)\rangle = |\Psi(t_j)\rangle$ . The Chebychev propagator effectively propagates in a single time step of length  $dt$ . Intermediate time results can be cheaply

obtained since the Bessel function coefficients defined in Eq. (4.37) contain information about the time dependency but does not depend on the coordinate discretization [94]. Furthermore, since  $\Psi(0)$  and  $\hat{\mathbf{H}}_{norm}$  are both normalized, the propagation scheme preserves normalization and the error convergence properties of the Chebychev expansion guarantees high levels of accuracy only limited by the machine precision [57, 94].

### 4.2.2 Short iterative Lanczos propagator

The Lanczos method [101] is an extension of the power method<sup>4</sup>[102] to find certain eigenvalues and eigenvectors of a linear system, initially conceived as a method for diagonalizing tridiagonal matrices [103]. It inexorably introduces the notion of **Krylov subspace**. The latter is defined as a sub-space of dimension  $N$  of the full Hilbert space whereby the vectors spanning the sub-space are generated by acting a linear operator on a initial state  $|\Psi(0)\rangle$ ,  $N$  times. If the linear operator is the Hamiltonian, then the vectors spanning the Krylov sub-space are [94]

$$|u_j\rangle = \hat{\mathbf{H}}^j |\psi(0)\rangle. \quad (4.39)$$

The essence of the Lanczos approach consists in constructing a matrix representation of the Hamiltonian taking as a basis the vectors spanning the Krylov sub-space. The Hamiltonian is then diagonalized and the diagonal form is utilized to propagate  $|\Psi(0)\rangle$  within the Krylov sub-space [94]. In order to construct a set of orthogonal basis, each Krylov vector is sequentially orthogonalized with respect to the previous vectors. In practice, the first vector is defined to be the initial state, i.e.,  $|q_0\rangle \equiv |\Psi(0)\rangle$ . The construction of second vector is achieved by acting  $\hat{\mathbf{H}}$  on  $|q_0\rangle$  and subtracting off the component of the first vector [94], namely

$$\hat{\mathbf{H}} |q_0\rangle = \alpha_0 |q_0\rangle + \beta_0 |q_1\rangle, \quad (4.40a)$$

with  $\alpha_0 = \langle q_0 | \hat{\mathbf{H}} | q_0 \rangle$  and  $\beta_0 = \langle q_0 | \hat{\mathbf{H}} | q_1 \rangle$ . This procedure is performed recursively using the *three-term recursion equation* [94, 103, 104]

$$\hat{\mathbf{H}} |q_j\rangle = \beta_{j-1} |q_{j-1}\rangle + \alpha_j |q_j\rangle + \beta_j |q_{j+1}\rangle, \quad (4.40b)$$

where the scalars  $\alpha_j$  and  $\beta_j$  have the following expression

$$\alpha_j = \langle q_0 | \hat{\mathbf{H}} | q_0 \rangle \quad \text{and} \quad \beta_j = \langle q_{j+1} | \hat{\mathbf{H}} | q_j \rangle. \quad (4.40c)$$

---

<sup>4</sup>also known as iteration method or Von Mises iteration method.

A direct consequence of Eq. (4.40b) is that any projection  $\langle q_i | \hat{\mathbf{H}} | q_{j+1} \rangle$  vanishes for  $i \geq 2$ , namely

$$\begin{aligned} \langle q_{j+2} | \hat{\mathbf{H}} | q_j \rangle &= \beta_{j-1} \langle q_{j+2} | q_{j-1} \rangle + \alpha_j \langle q_{j+2} | q_j \rangle + \beta_j \langle q_{j+2} | q_{j+1} \rangle \\ &= 0, \end{aligned} \quad (4.41)$$

since by construction  $\langle q_i | q_j \rangle = \delta_{i,j}$ . As a consequence, the matrix representation of the Hamiltonian  $\hat{\mathbf{H}}$  in the Lanczos basis has a tridiagonal matrix form [94, 103, 104],

$$\hat{\mathbf{H}}_N = \begin{pmatrix} \alpha_0 & \beta_0 & 0 & \dots & \dots & \dots & 0 \\ \beta_0 & \alpha_1 & \beta_1 & 0 & \dots & \dots & 0 \\ 0 & \beta_1 & \alpha_2 & \beta_2 & 0 & \dots & 0 \\ \vdots & \vdots & \ddots & \ddots & \vdots & \vdots & 0 \\ 0 & \dots & \dots & \dots & \beta_{N-3} & \alpha_{N-2} & \beta_{N-2} \\ 0 & \dots & \dots & \dots & \dots & \beta_{N-2} & \alpha_{N-1} \end{pmatrix}. \quad (4.42)$$

Once the matrix representation of  $\hat{\mathbf{H}}$  is obtained, it is diagonalized as follows

$$\hat{\mathbf{D}}_N = \hat{\mathbf{Z}}^\dagger \hat{\mathbf{H}}_N \hat{\mathbf{Z}}, \quad (4.43)$$

and the approximation of the evolution operator reads

$$\hat{\mathbf{U}}(\Delta t) \approx \hat{\mathbf{U}}_N(\Delta t) = \exp \left[ -i\Delta t \hat{\mathbf{H}}_N \right] = \exp \left[ -i\Delta t \hat{\mathbf{Z}} \hat{\mathbf{D}}_N \hat{\mathbf{Z}}^\dagger \right], \quad (4.44a)$$

which can be written in the following form

$$\hat{\mathbf{U}}(\Delta t) \approx \hat{\mathbf{U}}_N(\Delta t) = \hat{\mathbf{Z}} \exp \left[ -i\Delta t \hat{\mathbf{D}}_N \right] \hat{\mathbf{Z}}^\dagger. \quad (4.44b)$$

Finally, propagation from  $t = 0$  to an arbitrary  $t = \Delta t$  is obtained upon operating the approximate  $\hat{\mathbf{U}}_N$  on  $|\Psi(0)\rangle$ , namely

$$|\Psi(\Delta t)\rangle \approx \hat{\mathbf{U}}_N(\Delta t) |\psi(0)\rangle = \hat{\mathbf{Z}} e^{-i\Delta t \hat{\mathbf{D}}_N} \hat{\mathbf{Z}}^\dagger |\Psi(0)\rangle. \quad (4.44c)$$

Having defined the propagation formalism, an important point should be stressed in regard to the dimensionality of the *Krylov space*. As pointed out in Ref. [94], the larger the number of vectors spanning the Krylov space, the longer (larger  $\Delta t$ ) the wave packet can be propagated without leaving such subspace. This opens up two alternatives: (i) generate a large Krylov space (large order) to propagate longer times, or (ii) generate

a smaller number of Krylov vectors (low order) for shorter propagation times with the additional cost of updating it more frequently by generating new Krylov spaces using the propagated vector as initial  $|q_0\rangle$  for the next iterations. The second alternative is referred to as **Short iterative Lanczos method** (SIL) [94]. Apart from inherent errors arising from the approximation properly speaking, external error sources such as those due to the orthogonalization process might also appear, particularly when the dimensionality of the Krylov space becomes relevant. This is why the method is best suited to be applied to short times and relatively low order with successive restarting of the procedure [104]. A detailed comparison of different propagations approaches, such as the Chebychev and the Lanczos schemes among others, can be found in Ref. [104].



# Optimal control algorithms in a nutshell

---

5.1	Gradient-based methods . . . . .	47
5.1.1	Gradient Ascent Pulse Engineering . . . . .	47
5.1.2	Krotov’s optimization method . . . . .	49
5.2	Gradient-free methods . . . . .	52
5.2.1	Nelder-Mead optimization algorithm . . . . .	53
5.2.2	Brent’s principal axis optimization method . . . . .	54

---

Controlling external radiation fields in order to influence the electron dynamics to achieve a desirable outcome is the ultimate goal of quantum control. Typically, the optimization problem is formulated by defining the optimization target containing the desired output, plus eventual constraints<sup>1</sup> on the field  $\epsilon(t)$ , namely

$$J[\varphi, \epsilon] = J_T[\varphi(T), \varphi^\dagger(T)] + \int_0^T g_a[\epsilon(t)] dt + \int_0^T g_b[\varphi(t), \varphi^\dagger(t)] dt, \quad (5.1)$$

where  $\varphi(t) \equiv |\varphi(t)\rangle$  is the state subject to (s.t) the time-dependent Schrödinger equation and where  $\varphi^\dagger(t) \equiv \langle\varphi(t)|$  with  $t = [0, T]$ . In Eq. (5.1),  $J_T[\varphi(T), \varphi^\dagger(T)]$  is referred to as the **final-time cost functional**. It depends exclusively on the propagated state evaluated at the final time  $T$ . In contrast, the term  $g_b[\varphi(t), \varphi^\dagger]$  depends on intermediate times during the propagation. Finally,  $g_a[\epsilon(t)]$  refers to the functional associated to the driving field, i.e. specific constraints that the “optimized” driving field must fulfill, e.g. in view of experimental feasibility.

---

<sup>1</sup>inclusion of the constraints on the field in Eq. (5.1) can be avoided in the context of gradient-free optimization methods by defining a mapping procedure in the parametrization of the control field to constraints the optimization variables in the desired range, cf. Ref. [50]

The optimization problem then reads

$$\arg \min_{\epsilon(t) \in \mathcal{E}} J[\varphi, \epsilon(t)] \quad , \quad (5.2)$$

*s.t.*  $\dot{\varphi}(t) + i\hat{\mathbf{H}}[\epsilon]\varphi(t) = 0$

where  $\mathcal{E}$  denotes the space of feasible solutions, i.e. specific properties required for the optimal field to fulfill such as maximal field peak amplitude, spectral components, smoothness *et cetera*. On the assumption that the optimization problem is to identify a suitable field  $\epsilon(t)$  to steer the dynamics from the initial state  $|\varphi_0\rangle$  to a desired state  $|\Psi_{target}\rangle$  without accounting for the phase, the target functional reads [105, 106],

$$\begin{aligned} J_T[\varphi_T, \varphi_T^\dagger] &= |\langle \Psi_{target} | \varphi(T) \rangle|^2 \\ &= \langle \Psi_{target} | \varphi(T) \rangle \langle \varphi(T) | \Psi_{target} \rangle , \end{aligned} \quad (5.3)$$

with  $\varphi_T \equiv \varphi(T)$ . Of course, the final-time cost functional is not restricted to target-state optimization. In this thesis, construction of functionals for photoelectron spectrum optimization, anisotropy of photoelectron emission as well as suppression of hole decoherence have also been considered, see e.g. Chapters 8 and 9.

Specific constraints on the control field can be incorporated via the second term in Eq. (5.1). For instance, it is customary to define  $g_a$  as a penalty function that minimizes the field intensity while requiring smoothly behavior when the field is switched on and off. This requirement is accomplished by defining

$$g_a[\epsilon(t)] = \frac{\lambda_{a'}}{S(t)} \epsilon^2(t) + \frac{\lambda_a}{S(t)} (\epsilon(t) - \epsilon_{ref}(t))^2 , \quad (5.4)$$

where  $\lambda_{a'}$  and  $\lambda_a$  are optimization weights that stress the relative importance of all the terms in the functional to be minimized. The term  $S(t)$  is a penalty function that takes large (positive) values at times where the maximal peak intensity is constrained to be minimized. Typically, this coincides with times at which the field is switched on and off. The presence of a reference field  $\epsilon_{ref}(t)$  in Eq. (5.4) is used in the esprit of avoiding drastic changes in the updated field during the update procedure. For the update protocol in the context of the monotonically convergent Krotov's method see Section 5.1.2.

The optimization problem may also involve time-dependent constraints imposed on the state  $|\varphi(t)\rangle$  at every intermediate time  $t$ , or alternatively, at a given time interval  $[t_b, t_a]$ . It is possible address such constraints by defining [105, 106]

$$g_b[\varphi(t)] = \frac{\lambda_b}{\Delta_{ba}} \langle \varphi(t) | \hat{\mathcal{P}}(t) | \varphi(t) \rangle \mathbb{1}_{\Delta_{ba}}(t) , \quad (5.5)$$

with  $\Delta_{ba} = t_b - t_a$  and  $\mathbb{1}_{\Delta_{ba}}(t) = 1 \forall t \in [t_b, t_a]$ , 0 otherwise. As usual,  $\lambda_b$  is a optimization weight. The operator  $\hat{\mathcal{P}}$  refers to a time-dependent operator defining the control objective at intermediate times [105, 107], enforcing the dynamics to a predefined trajectory [107]. For instance, it can be introduced to “enforce” the dynamics such that  $|\varphi(t)\rangle$  is allowed to explore (avoid) prescribed desirable (undesirable) subspaces [105, 106].

In order to solve the optimization problem stated in Eq. (5.2), two different basic iterative-based approaches are available: non-variational and variational methods. Non-variational-based methods, also called “*gradient-free*” methods, are extremely versatile since they only require successive evaluations of the functional. They are also straightforward to implement and no adjustments due to specificities of the propagation scheme is required, since as opposite to gradient-base methods, they do not require backward propagation of any Lagrange multiplier or co-state. They require, however, parametrization of the control field. Consequently inequalities and equalities constraints on the control field can be easily incorporated and the second term in Eq. (5.1) can be omitted. Paradoxically, they are prone to converge very slowly or to a local minima for a wrong choice of the parametrization form[50]. For a “good” parametrization form, convergence might also be seriously compromised particularly for a large number of control parameters. Paradoxically, gradient-free methods can suffer from the same limitations for relatively small number of control parameters. As a rule of thumb, direct method should only be used sparingly or when information about the gradient is not accessible. On the other side of the coin, variational or *gradient-based* methods make use of directional derivative information to evaluate the changes in the functional to update the control field. This speeds up considerably the convergence of the algorithm. In the following, a pair of examples of both categories are briefly described.

## 5.1 Gradient-based methods

### 5.1.1 Gradient Ascent Pulse Engineering

The GRAPE method, for Gradient Ascent Pulse Engineering [108] is gradient-based optimization method relying on the analytical evaluation of the minimization functional  $J$  with respect to any control parameter  $\epsilon_j$ . The iterative update of the field is performed according to [108]

$$\epsilon_j^{(i+1)} = \epsilon_j^{(i)} + \alpha \frac{\partial J^{(i)}}{\partial \epsilon_j}, \quad (5.6)$$

where  $\epsilon_j$  denotes the  $j$ th control parameter and  $\alpha$  an arbitrary parameter that controls the descent step. The form of Eq. (5.6) invokes an ordinary application of the well-established

gradient descent method [109], a first order iterative optimization algorithm for finding the minimum of a function. If  $\alpha > 0$ , the displacement is towards the gradient and the algorithm converge towards the minimum.

In the GRAPE formalism, the functional to be minimized is explicitly written in terms of the control parameters  $\{\epsilon_j(t)\}$ . This requires to write the propagated state  $|\varphi(T)\rangle$  in terms of the evolution operator  $\hat{\mathbf{U}}(T, 0)$ . In the case of the functional defined by the projection of the propagated state onto a target state  $|\Psi_{target}\rangle$  the functional to be maximized reads

$$\begin{aligned} J_{T,sm}[\epsilon] &= \langle \Psi_{target} | \varphi(T) \rangle \\ &\equiv \langle \Psi_{target} | \hat{\mathbf{U}}[\epsilon] | \varphi(0) \rangle, \end{aligned} \quad (5.7)$$

which is used to evaluate the gradient with respect to the control parameters  $\epsilon_j$ , namely

$$\frac{\partial J_{T,sm}[\epsilon]}{\partial \epsilon_j} = \left\langle \Psi_{target} \left| \frac{\partial \hat{\mathbf{U}}[\epsilon]}{\partial \epsilon_j} \right| \varphi(0) \right\rangle. \quad (5.8)$$

Alternatively, a time-grid parametrization of the pulse can be envisaged. In this case, every single point in time of the discretized time-grid is iteratively updated following Eq. (5.6), and the gradient reads [100]

$$\begin{aligned} \frac{\partial J_{T,sm}[\epsilon]}{\partial \epsilon(t_k)} &= \frac{\partial}{\partial \epsilon(t_k)} \left\langle \Psi_{target} \left| \hat{\mathbf{U}}_{N-1} \dots \hat{\mathbf{U}}_{k'} \dots \hat{\mathbf{U}}_k \dots \hat{\mathbf{U}}_1 \right| \varphi(0) \right\rangle \\ &= \left\langle \Psi_{target} \left| \hat{\mathbf{U}}_{N-1} \dots \hat{\mathbf{U}}_{k+1} \frac{\partial \hat{\mathbf{U}}_k}{\partial \epsilon(t_k)} \hat{\mathbf{U}}_{k-1} \dots \hat{\mathbf{U}}_1 \right| \varphi(0) \right\rangle \\ &\equiv \left\langle \chi(t_{k+1}) \left| \frac{\partial \hat{\mathbf{U}}_k}{\partial \epsilon(t_k)} \right| \varphi(t_k) \right\rangle, \end{aligned} \quad (5.9)$$

where  $|\chi(t_{k+1})\rangle$  is the backward propagated target state  $|\Psi_{target}\rangle$  that needs to be propagated backwards in time from  $t = T$  to  $t_{k+1} < T$ . It is customary to write exponential of the time-evolution operator as a Taylor expansion, namely

$$\frac{\partial}{\partial \epsilon(t_k)} \hat{\mathbf{U}}_k = \frac{\partial}{\partial \epsilon(t_k)} e^{-\frac{i}{\hbar} \hat{\mathbf{H}}(t_k) dt} \equiv \sum_{n=1}^{\infty} \frac{(-i dt)^n}{n!} \sum_{p=0}^{n-1} \hat{\mathbf{H}}^p(t_k) \left( \frac{\partial \hat{\mathbf{H}}(t_k)}{\partial \epsilon(t_k)} \right) \hat{\mathbf{H}}^{n-p-1}(t_k). \quad (5.10)$$

The GRAPE algorithm is started by choosing any arbitrary guess field. The guess field is used to propagate the initial state and the final-time cost functional is evaluated. Once the gradient is evaluated following the prescription outlined above, the field is iteratively updated using Eq. (5.6), with the proper sign for  $\alpha$  for minimization ( $\alpha > 0$ ) and max-

imization ( $\alpha < 0$ ) of the final-time cost functional. The algorithm needs to be executed until some desired fidelity is achieved. Using the gradient information alone may suffer from slow convergence behavior, in particular near the optimum. This limitation can be circumvented by taking into account the Hessian

$$H_{k,k'} = \frac{\partial^2 J[\epsilon]}{\partial \epsilon(t_k) \partial \epsilon(t'_k)}, \quad (5.11)$$

which is the essence of the Newton method. However, evaluation of the of the Hessian is extremely expensive. To remedy this, the so-called quasi-Newton approaches [110, 111], rely on constructing the Hessian from gradient information instead. Among the most prominent ones, the BFGS [112–115] and a more refined version, the BFGS-B [116] are usually employed.

### 5.1.2 Krotov's optimization method

Let  $J_T = J_T[\varphi_T, \varphi_T^\dagger]$  be the final-time cost functional to be minimized and  $\varphi_T$  the propagated the wave function at the end of the propagation time  $t = T$ . Without loss of generality and following Ref. [105], we employ the notations  $\varphi \equiv |\varphi\rangle$  and  $\varphi^\dagger \equiv \langle\varphi|$  for all the state vectors appearing in the equations below. The essence of the Krotov's monotonically convergent method [106, 117] relies on the introduction of an arbitrary scalar function  $\Phi(t, \varphi, \varphi^\dagger)$  [105] and extended functionals  $G_T[\varphi_T, \varphi_T^\dagger, \Phi_T]$  and  $R[\varphi, \varphi^\dagger, \epsilon, \Phi]$  designed to separate the dependency on  $\varphi$  and  $\epsilon$  of the optimization task. The latter refers to the control field that drives the dynamics to the target path. Let the functionals be defined as,

$$G_T[\varphi_T, \varphi_T^\dagger, \Phi_T] \equiv J_T[\varphi_T, \varphi_T^\dagger] + \Phi[T, \varphi_T, \varphi_T^\dagger] \quad (5.12)$$

and

$$\begin{aligned} R[\varphi, \varphi^\dagger, \epsilon, \Phi] \equiv & -(g_a(\epsilon) + g_b(\varphi, \varphi^\dagger)) + \frac{d}{dt} \Phi(t, \varphi(t), \varphi^\dagger(t)) \\ & -(g_a(\epsilon) + g_b(\varphi, \varphi^\dagger)) + \left( \frac{\partial \Phi}{\partial \varphi} \right) \dot{\varphi} + \left( \frac{\partial \Phi}{\partial \varphi^\dagger} \right) \dot{\varphi}^\dagger, \end{aligned} \quad (5.13)$$

where  $\dot{\varphi}$  denotes the total time-derivative of  $\varphi(t)$ . Minimization of the auxiliary functional  $L[\varphi, \varphi^\dagger, \epsilon, \Phi]$  defined as

$$L[\varphi, \varphi^\dagger, \epsilon, \Phi] = G_T(\varphi_T, \varphi_T^\dagger, \Phi_T) - \Phi(t_0, \varphi_{t_0}, \varphi_{t_0}^\dagger) - \int_{t_0}^T R(\varphi, \varphi^\dagger, \epsilon, \Phi), \quad (5.14)$$

is equivalent to minimization  $J_T = J_T[\varphi_T, \varphi_T^\dagger]$ . In fact, inserting Eq. (5.13) into Eq. (5.14) together with the expression of  $G_T[\varphi_T, \varphi_T^\dagger, \Phi_T]$  in Eq. (5.12), it is straightforward to show that  $L[\varphi, \varphi^\dagger, \epsilon, \Phi] = J[\varphi, \varphi^\dagger]$  for any arbitrary scalar function  $\Phi[t, \varphi, \varphi^\dagger]$ . The question that arises is how to construct the scalar function  $\Phi(t, \varphi, \varphi^\dagger)$ . In the Krotov's optimization formalism, the latter is determined up to a given expansion order, which is accomplished upon requirement of the extremum condition on  $L[\cdot]$ , or equivalently

$$\left(\frac{\partial R}{\partial \varphi}\right) = 0, \quad \left(\frac{\partial R}{\partial \varphi^\dagger}\right) = 0. \quad (5.15)$$

The function  $\Phi(t, \varphi, \varphi^\dagger)$  is constructed by writing the extremum condition in an explicit form [105]<sup>2</sup>

$$0 = \left(\frac{\partial R}{\partial \varphi^\dagger}\right) = -\frac{\partial g_b}{\partial \varphi^\dagger} + \left(\frac{\partial \Phi}{\partial \varphi^\dagger}\right) \frac{\partial \dot{\varphi}}{\partial \varphi^\dagger} + \left(\frac{\partial \dot{\varphi}^\dagger}{\partial \varphi^\dagger}\right) \frac{\partial \Phi}{\partial \varphi^\dagger} + \frac{d}{dt} \left(\frac{\partial \Phi}{\partial \varphi^\dagger}\right). \quad (5.16)$$

As a further step, new functions defining the co-state  $\chi(t)$  and its complex conjugate  $\chi^\dagger(t)$  are defined according to

$$\chi(t) \equiv \frac{\partial \Phi}{\partial \varphi^\dagger} \quad \text{and} \quad \chi^\dagger(t) \equiv \frac{\partial \Phi}{\partial \varphi}, \quad (5.17)$$

which allows to construct  $\Phi = \Phi(t, \varphi, \varphi^\dagger)$  up to first order in terms of  $\varphi$  and  $\varphi^\dagger$ , namely

$$\Phi(t, \varphi, \varphi^\dagger) = \chi^\dagger(t)\varphi(t) + \varphi^\dagger(t)\chi(t). \quad (5.18)$$

Furthermore, Eq. (5.17) allows to rewrite Eq. (5.16) in the following form

$$\frac{d}{dt}\chi(t) = \frac{\partial g_b}{\partial \varphi^\dagger} - \underbrace{\chi^\dagger(t) \frac{\partial \dot{\varphi}}{\partial \varphi^\dagger}}_{=0} - \underbrace{\left(\frac{\partial \dot{\varphi}^\dagger}{\partial \varphi^\dagger}\right)}_{i\hat{\mathbf{H}}(t)} \chi(t). \quad (5.19a)$$

Making use of the Schrödinger equation for  $\varphi(t)$  and  $\varphi^\dagger(t)$ , namely  $\dot{\varphi}(t) = -i\hat{\mathbf{H}}(t)\varphi(t)$  and  $\dot{\varphi}^\dagger(t) = i\varphi^\dagger\hat{\mathbf{H}}^\dagger(t)$ , Eq. (5.19a) becomes

$$\frac{d}{dt}\chi(t) = \frac{\partial g_b}{\partial \varphi^\dagger} - i\hat{\mathbf{H}}(t)\chi(t), \quad (5.19b)$$

where we have made use of the conditions  $\partial \dot{\varphi}^\dagger / \partial \varphi = \partial \dot{\varphi} / \partial \varphi^\dagger = 0$ . Equation (5.19b) describes the equation of motion for  $\chi(t)$ . To fully determine the dynamics of the co-

---

<sup>2</sup>were we have used  $\frac{d}{dt} \left(\frac{\partial \Phi}{\partial \varphi^\dagger}\right) = \dot{\varphi} \frac{\partial}{\partial \varphi^\dagger} \left(\frac{\partial \Phi}{\partial \varphi^\dagger}\right) + \dot{\varphi}^\dagger \frac{\partial}{\partial \varphi^\dagger} \left(\frac{\partial \Phi}{\partial \varphi^\dagger}\right) + \frac{\partial}{\partial t} \left(\frac{\partial \Phi}{\partial \varphi^\dagger}\right)$ .

state  $\chi(t)$ , information about its value at some particular point in time is required. The extremum condition on  $G_T[\varphi_T, \varphi_T^\dagger, \Phi_T]$ , is exploited to evaluate its final time condition, namely [105]

$$\frac{\partial G_T}{\partial \varphi^\dagger} = \frac{\partial J_T}{\partial \varphi^\dagger} + \frac{\partial \Phi}{\partial \varphi^\dagger} \Big|_{t=T} \stackrel{!}{=} 0, \quad (5.20)$$

which gives, using the definition of  $\chi(t)$  in Eq. (5.17), the “initial” condition for the co-state  $\chi(t)$ , namely

$$\chi(T) = - \frac{\partial J_T}{\partial \varphi^\dagger} \Big|_{t=T} \quad (5.21)$$

For  $g_b = 0$ , and hermitian Hamiltonians, the equation for the co-state reduces to an ordinary Schrödinger equation which needs to be solved backwards in time, starting from  $\chi(T)$ . The “initial” condition is then fully determined by the final-time cost functional  $J_T = J_T[\varphi_T, \varphi_T^\dagger]$ . For intermediate-time cost functionals, i.e.  $g_b \neq 0$ , the latter acts as a inhomogeneity and an inhomogeneous Schrödinger equation needs to be solved [118–120].

Once  $\chi(t)$  obtained, it is used to update the control field  $\epsilon(t)$ . Krotov’s update procedure ensures construction of better control fields as the protocol proceeds iteratively. This is, for the minimization case, the updated control field allows for monotonically decreasing the value of the functional as the iteration proceeds. It can be shown that the monotonically convergent update of the control field is given by [106]

$$\begin{aligned} \epsilon^{(i+1)}(t) = \epsilon^{(i)} - \text{Im} \left\{ \left\langle \chi^{(i)}(t) \left| \frac{\partial \hat{\mathbf{H}}}{\partial t} \Big|_{(i+1)} \varphi^{(i+1)}(t) \right\rangle \right. \\ \left. + \frac{1}{2} \sigma(t) \left\langle \Delta \varphi^{(i)}(t) \left| \frac{\partial \hat{\mathbf{H}}}{\partial t} \Big|_{(i+1)} \varphi^{(i+1)}(t) \right\rangle \right\}, \quad (5.22) \end{aligned}$$

with  $\Delta \varphi^{(i)}(t) = \varphi^{(i+1)}(t) - \varphi^{(i)}(t)$  and  $i$  the iteration, and where the Dirac’s *bra-ket* notation have been introduced and will be used in what follows. The expression for  $\sigma(t)$  required to ensure monotonic convergence of the algorithm has been discussed in Ref. [106]. It is to note, however, that the second term alone is necessary to ensure monotonic convergence of the algorithm [106].

A practical application of the algorithm requires, at each iteration  $i$ , forward propagation of the vector state  $|\varphi^{(i)}(t)\rangle$  according to

$$i \frac{\partial}{\partial t} |\varphi^{(i)}(t)\rangle = \hat{\mathbf{H}}[\epsilon^{(i)}(t)] |\varphi^{(i)}(t)\rangle \quad \text{with} \quad |\varphi^{(i)}(0)\rangle = |\varphi(0)\rangle, \quad (5.23)$$

where  $|\varphi(0)\rangle$  refers to the initial condition (usually the ground state) of the state being propagated. Conversely, the co-state  $|\chi^{(i)}(t)\rangle$  is obtained, assuming linearity of the Schrödinger equation in  $\varphi(t)$ , upon backward propagation according to [105, 106]

$$\frac{\partial}{\partial t} |\chi^{(i)}\rangle = -i\hat{\mathbf{H}}^\dagger[\epsilon^{(i)}(i)]|\chi^{(i)}\rangle + \frac{\partial}{\partial \varphi} g_b(\varphi, \varphi^\dagger) \Big|_{\varphi^{(i)}(t)}. \quad (5.24)$$

The "initial condition"  $|\chi^{(i)}(T)\rangle$ , assuming the final-time cost functional in Eq. (5.1) with a *target-state* functional  $J_T[\varphi_T, \varphi_T^\dagger]$  of the form

$$\begin{aligned} J_T[\varphi_T, \varphi_T^\dagger] &= |\langle \Psi_{target} | \varphi(T) \rangle|^2 \\ &= \langle \Psi_{target} | \varphi(T) \rangle \langle \varphi(T) | \Psi_{target} \rangle, \end{aligned} \quad (5.25a)$$

is obtained with the help of Eq. (5.21), namely

$$|\chi^{(i)}(T)\rangle = -\langle \Psi_{target} | \varphi^{(i)}(T) \rangle |\Psi_{target}\rangle. \quad (5.25b)$$

Equations (5.22) and (5.24) together with Eq. (5.23) must be solved simultaneously. The algorithm is started at the iteration  $i = 0$  by solving Eq. (5.23) exposed to some guess field  $\epsilon^{(0)}(t)$  to obtain  $|\varphi^{(0)}(T)\rangle$  and evaluate Eq. (5.25b). Once the expression for  $|\chi^{(0)}(T)\rangle$  is known, the differential equation for  $\chi^0(t)$ , namely Eq. (5.24) must be solved backwards in time. The procedure is followed by sequentially updating the field  $\epsilon^{(1)}(t)$ , by means of Eq. (5.22). The procedure is computed iteratively until reaching the desired tolerance.

## 5.2 Gradient-free methods

In the previous section, we have considered a non-exhaustive list of optimization methods that allows to minimize a given cost function  $f(\mathbf{x})$  provided that  $f(\mathbf{x})$  is differentiable and its gradient  $\nabla f(\mathbf{x})$ , can be evaluated analytically or at least, accurately estimated by finite differences [121]. These methods relies on the necessary condition that for any differentiable function  $f(\mathbf{x})$ , a given minimizer  $\mathbf{x}_0$ , fulfills the condition  $\nabla f(\mathbf{x}_0) = \vec{0}$ , i.e. its gradient vanishes.

In practice, however, analytical expression or numerical approximation of  $\nabla f(\mathbf{x})$  may be inaccessible or untrustworthy. Since numerical stability of gradient-based methods strongly relies on the accuracy of the gradient [122], another kind of optimization methods, often referred to as **direct search methods** or **gradient-free methods** are available. This family of optimization algorithms allows, under certain conditions, to efficiently minimize a differentiable cost function with respect to the design variables without recourse of its

gradient.

### 5.2.1 Nelder-Mead optimization algorithm

The Nelder-Mead method, named after J. Nelder and R. Mead [123], also known as **downhill simplex method** or **amoeba method**, is an heuristic “gradient-free” search method relying on the evaluation of the target functional only, without requiring explicit evaluation of its gradient. It is intended to find the minimum (maximum) of an multidimensional objective function. Typically, it is well suited for optimization problems requiring a relatively small number of optimization parameters and often employed when numerical stable gradient of the target functional is whether not accessible, nor reliable. It exploits the concept of **simplex**, a  $N$ -dimensional polytope provided with  $N + 1$  vertices, which undergoes a set of linear transformations such as contraction and expansion as the algorithm proceeds iteratively, generating new points yielding with improvement in the functional value.

The essence of the method relies in determining the point  $\mathbf{x}_M \in \mathbb{R}^N$  where the function is maximal and to replaced it by its *reflexion* with respect to the center of gravity generated by the  $N$  remaining points [123–125]. If the new point yields to a functional value smaller than that obtained with the  $N$  remaining points, the simplex is expanded along the new point. If not, the simplex is centered at the point where the functional is locally minimal [110, 123]. In detail, for an optimization problem consisting in minimizing  $f(\mathbf{x})$ , with  $\mathbf{x} \in \mathbb{R}^N$ , a standard application of the Nelder-Mead method consists in the implementation of the following steps,

1. **Generation of  $N + 1$  sample points** in  $\mathbb{R}^N$ : Generate a set of *test points*  $\{\mathbf{x}_1, \mathbf{x}_2, \dots, \mathbf{x}_{N+1}\}$
2. **Functional evaluation and ordering**: evaluate the target functional, or cost function  $f(\mathbf{x})$ , and order the resulting values according to  $f(\mathbf{x}_1) \leq f(\mathbf{x}_2) \leq \dots \leq f(\mathbf{x}_{N+1})$ . It is sufficient to know the best and two worst points.
3. **Evaluation of the center of gravity  $\mathbf{x}_0$** : the center of gravity is evaluated using all points except the worst, i.e.  $\mathbf{x}_{N+1}$ .
4. **Reflexion**: Evaluate the reflected point  $\mathbf{x}_r = \mathbf{x}_0 + \gamma_r(\mathbf{x}_0 + \mathbf{x}_{N+1})$ , with  $\gamma_0 > 0$ .
  - (a) If the reflected point is better than the second worst point  $\mathbf{x}_N$ , but not better than the best point, i.e.  $\mathbf{x}_1 \leq \mathbf{x}_r < \mathbf{x}_N$ , then replace the worst point  $\mathbf{x}_{N+1}$  with the reflected one  $\mathbf{x}_r$ , and go to step 2.
  - (b) if not, go to step 5.

5. **Expansion:** If it turns out that the reflected point is the best one, i.e.  $f(\mathbf{x}_r) \leq f(\mathbf{x}_1)$ , then compute the expanded point  $\mathbf{x}_e = \mathbf{x}_0 + \gamma_e(\mathbf{x}_r - \mathbf{x}_0)$  with  $\gamma_e > 1$ 
  - (a) If the expanded point is better than the reflected point, i.e.  $f(\mathbf{x}_e) < f(\mathbf{x}_r)$ , then replace the worst point  $\mathbf{x}_{N+1}$  with the expanded point  $\mathbf{x}_e$  and go to step 2.
  - (b) If not, replace the worst point  $\mathbf{x}_{N+1}$  with the reflected point  $\mathbf{x}_r$  and go to step 2.
6. **Contraction:** At this point  $f(\mathbf{x}_r) \leq f(\mathbf{x}_N)$ . Evaluate the contracted point  $\mathbf{x}_c = \mathbf{x}_0 + \gamma_c(\mathbf{x}_{N+1} - \mathbf{x}_0)$ , with  $0 < \gamma_c \leq 0.5$ .
  - (a) If the contracted point  $\mathbf{x}_c$  is better than the worst point, i.e.  $f(\mathbf{x}_c) < f(\mathbf{x}_{N+1})$ , then replace the worst point  $\mathbf{x}_{N+1}$  with the contracted point  $\mathbf{x}_c$  and go to step 2.
  - (b) If not, go to step 7.
7. **Homothety with respect to the best point :** Replace all points except the best one  $\mathbf{x}_1$  with  $\tilde{\mathbf{x}}_n = \mathbf{x}_n + \gamma_h(\mathbf{x}_1 - \mathbf{x}_n)$  and go to step 2. At this stage the vertices of the new simplex are  $\mathbf{x}_1, \tilde{\mathbf{x}}_2, \dots$ . This stage is alternatively known as **shrink**.

The algorithm proceeds iteratively until the simplex is sufficiently small, eventually converging to a global (local) minimum when the simplex dimension does not change significantly as the iteration proceeds. However, a brief word of caution is in order: the algorithm itself strongly depends on the initial simplex, which is constructed from the *test* or *guess points*  $\mathbf{x}_1, \mathbf{x}_2, \dots, \mathbf{x}_{N+1}$ . In this context, this method frequently gives satisfactory improvements in the very few iterations, producing noticeable reduction in the functional value. However, the lack of convergence theory of the protocol described above is commonly reflected in the stagnation of the algorithm, in particular for large number of iterations. In this case, the algorithm performs a significant number of functional evaluations for an insignificant improvement, even if the simplex is far from a local minimum [112, 126–129]. Needless to say, this pathology strongly penalizes the numerical efficiency of the optimization, particularly when long propagation times are required for the simulation of the electron dynamics. This problem is reviewed in detail in Sec. 9, where we study the limitation the Nelder-Mead method and propose an alternative algorithm that allows to circumvent this limitation.

### 5.2.2 Brent's principal axis optimization method

Brent's principal axis optimization algorithm, due to Richard P. Brent [130] refers to a gradient-free minimization method, based on an adaptive coordinate-descent ap-

proach [131] that iteratively performs a set of transformations of the coordinate system, that are designed to disentangle the updated coordinates as much as possible with respect to the cost function to be minimized<sup>3</sup>. The essence of the method relies on repeatedly updating a set of conjugate search directions<sup>4</sup> allowing the algorithm to move towards the minimum. Brent's principal axis method is a modification of the well established and widely known **Powell's conjugate direction method** [132]. The essence of Powell's method, together with the modifications introduced by Brent [130] to ensure quadratic convergence are briefly described in the following lines and requires the following steps [133],

1. **Set of initial conjugate directions:** the algorithm is started by choosing a guess set of parameters  $\mathbf{x}^{(0)} \in \mathbb{R}^N$ , with  $N$  being the number of optimization parameters. A set of  $N$  search directions  $\mathbf{u}^{(1)}, \dots, \mathbf{u}^{(N)}$  is then arranged to the columns of an identity matrix.
2. **Evaluation of the functional:** the cost function or target functional is evaluated  $N$  times, and the optimization problem

$$\arg \min_{\lambda^{(i)} \in \mathbb{R}} f\left(\mathbf{x}^{(i-1)} + \lambda^{(i)} \mathbf{u}^{(i)}\right) \quad (5.26)$$

is solved and the scalars  $\lambda^{(i)}$  obtained.

3. **update of control parameters:** using the optimized scalars obtained from Eq. (5.26), a first update of the control parameter is performed according to

$$\mathbf{x}^{(i)} = \mathbf{x}^{(i-1)} + \lambda^{(i)} \mathbf{u}^{(i)}, \quad (5.27)$$

for  $i = 1, \dots, N$

4. **Update of the conjugate directions:** upon obtaining  $\lambda^{(i)} \in \mathbb{R}$ , for  $i = 1, \dots, N$ , a set of new directions is judiciously generated upon update of the previous ones,

(a) for  $i = 1, \dots, N - 1$ , each direction  $\mathbf{u}^{(i)}$  is replaced according to  $\mathbf{u}^{(i)} = \mathbf{u}^{(i+1)}$

(b)  $\mathbf{u}^{(N)}$  is replaced with  $\mathbf{u}^{(N)} = \mathbf{x}^{(N)} - \mathbf{x}^{(0)}$ .

<sup>3</sup>assuming quadratic form of the objective function

<sup>4</sup>Let a multivariate scalar function  $f(\mathbf{x}) \in \mathbb{R}$  such that  $\mathbf{x} \in \mathbb{R}^N$ , two vectors  $(\mathbf{u}, \mathbf{v}) \in \mathbb{R}^{2N}$  are said to form a conjugate pair if they fulfill the property  $\mathbf{u}^T \mathbf{A} \mathbf{v} = 0$  together with  $\nabla f \cdot \mathbf{u} = 0$  such that  $\nabla f(\mathbf{x} + \delta \mathbf{x}) = \mathbf{A} \mathbf{x} + \mathbf{b}$ .

5. **Second optimization:** at this point, a second optimization takes place, where the task to be accomplished is to find  $\lambda_B \in \mathbb{R}$  such that

$$\arg \min_{\lambda_B \in \mathbb{R}} f(\mathbf{x}^{(0)} + \lambda_B \mathbf{u}^{(N)}). \quad (5.28)$$

6. Once the optimization problem in Eq. (5.28) is solved, the previous step is followed by updating the guess  $\mathbf{x}^{(0)}$  according to

$$\mathbf{x}^{(new)} = \mathbf{x}^{(0)} + \lambda_B \mathbf{u}^{(N)}. \quad (5.29)$$

7. The procedure is repeated using  $\mathbf{x}^{(new)}$  as guess set of optimization parameters for the next iteration, i.e.  $\mathbf{x}^{(0)} = \mathbf{x}^{(new)}$ , until the minimum is reached according to some predefined tolerance criterion.

In Powell's algorithm described in the above lines, the search directions are iteratively updated until a set of conjugate directions, with respect to a quadratic form, is obtained after  $N$  iterations. As a consequence, a minimum will be found at the next iteration if the cost functional is quadratic. In Ref. [130] Brent formally showed in an accessible form that for a quadratic function, the procedure above will reach a minimum in exactly  $N$  iterations. We recall that  $N$  is the dimensionality of the optimization problem. One of the disadvantages of the algorithm is that when replacing  $\mathbf{u}^{(N)} = \mathbf{x}^{(N)} - \mathbf{x}^{(0)}$  in step 4(b), the updated directions tend to become linearly dependent among them, thereby yielding to a minimum lying only in a subspace of the originally  $N$ -dimensional problem. To fix this and other inherent problems, Brent [130] improved the strategy by (i) incorporating automatic rescaling of the different variables, (ii) randomizing steps into the procedure to avoid "resolution ridge" problems [133] and perhaps more importantly, by (iii) replacing the original matrix of the search direction by its principal axes, thus ensuring that conjugacy was fulfilled [130, 133].

# Numerical methods for the computation of photoionization observables

---

6.1	Wave function splitting method . . . . .	57
6.2	Photoelectron spectrum and angular distributions . . . . .	59

---

## 6.1 Wave function splitting method

Photoelectron spectroscopy [134–136] is a powerful tool to scrutinize and rationalize photoionization processes as a result of the laser-matter interaction. The process of photoionization contains not only the specific details about the electron dynamics triggered by the ionizing field, but also the fingerprints of the inherent interactions of the field-free Hamiltonian, thus revealing crucial information about the underlying electronic structure as well as intrinsic electronic interactions and their correlations with each other [51, 137, 138]. From a theoretical perspective, the photoelectron spectrum can be evaluated upon projection of the propagated wave packet onto the eigenstates of the field-free continuum wave functions after the pulse is over [51]. In the particular context of strong and long ionizing light pulses, the spatial extension of the propagated wave packet poses a particular challenge in terms of numerical efficiency. In fact, numerical propagation under strong fields during long times with subsequent evaluation of the photoelectron-related observables becomes prohibitively expensive due to the extension of the propagated continuum wave packet and large number of basis set required to properly represent the outgoing photoelectron. Furthermore, large coordinate grid sizes are also required to avoid spurious reflections of the propagated wave packet once the latter reaches the boundaries of the

grid [25, 51, 139, 140]. This situation, already detrimental to the numerical performances in terms of storage and CPU time, poses an additional computational challenge in the context of numerical optimization, since typically generic optimization methods rely of iterative schemes demanding a few hundreds, or even more evaluations of the optimization functional requiring non-parallelizable propagations. This significantly compromises the numerical efficiency for the purpose of optimization. In the context of this thesis, this is remedied by extracting the asymptotic photoelectron momentum distribution, which is required for the evaluation of the photoelectron-related observables, in the context of the so-called **wave function splitting method (WFSM)** based on Ref. [141] and extended to a channel-resolved formalism of the **TDCIS** for the calculation of photoelectron spectrum (PES) and photoelectron angular distributions (PAD) proposed in Ref. [51, 142]. Briefly, the essence of the WFSM is based on (i) splitting the overall time grid interval  $[0, T]$  into a set of “splitting times”  $t_j \in [0, T]$ , and (ii) application of a “split operator” to the propagated wave function at each splitting time. At each  $t_j$ , the propagated wave function is split into an inner and an outer part using a smooth radial splitting function defined by the operator [51]

$$\hat{\mathbf{S}} = \left[ 1 + e^{-(\hat{r}-r_c)/\Delta} \right]^{-1}, \quad (6.1)$$

where the “smoothing” parameter  $\Delta$  in Eq. (6.1) controls how steep the slope of the splitting function is. The parameter  $r_c$  denotes the “splitting” radius and defines the distance from which the “split operator” becomes active. Application of  $\hat{\mathbf{S}}$  to a given wave function splits the latter into an inner ( $r \leq r_c$ ) and outer ( $r > r_c$ ) parts. Inner and outer parts are defined by the portion of the split wave function whose radial extension is smaller and larger than  $r_c$ , respectively. In the context of the **TDCIS**, the “channel wave functions”  $|\Psi^N(t)\rangle$ , defined in Eq. (3.28) in Section 3.4.2, are used to calculate the spectral components in a channel-resolved manner. This is accomplished by projecting the resulting outer parts onto the **Volkov states**. In detail, each channel wave function (basis set)  $|\varphi_i(t)\rangle$  is split into inner and outer parts at every splitting time  $t_j$ , namely [51]

$$|\varphi_i(t_j)\rangle = |\varphi_{i,\text{in}}(t_j)\rangle + |\varphi_{i,\text{out}}(t_j)\rangle, \quad (6.2a)$$

where the “channel wave functions”  $|\varphi_i(t)\rangle$  are those defined by the partial trace of the single-particle-single-hole excitation in Eq. (3.28) in Section 3.4. It is worth mentioning that  $\hat{\mathbf{S}}$  does not, and should not, affect the Hartree-Fock ground state  $|\Phi_0\rangle$ . The inner and

outer parts in Eq. (6.2a) are respectively defined by

$$|\varphi_{i,\text{in}}(t_j)\rangle = (1 - \hat{\mathbf{S}})|\varphi_i(t_j)\rangle \quad \text{and} \quad |\varphi_{i,\text{out}}(t_j)\rangle = \hat{\mathbf{S}}|\varphi_i(t_j)\rangle. \quad (6.2b)$$

At each splitting time, the inner part,  $|\varphi_{i,\text{in}}(t_j)\rangle$ , is represented in the CIS basis and further propagated with the "full Hamiltonian", defined in (3.25a) in Section 3.4.2, from  $t_j$  to the next splitting time  $t_{j+1}$ . The outer part having reached a sufficiently large extension of the grid, it is assumed not to be affected by the field-free Hamiltonian. Therefore, it is stored and propagated analytically from  $t_j$  to a large  $T$  by means of the **Volkov Hamiltonian** defined by

$$\hat{\mathbf{H}}_V(\tau) = \frac{1}{2} [\hat{\mathbf{p}} + \mathbf{A}(\tau)]^2, \quad (6.3)$$

where  $\hat{\mathbf{p}}$  and  $\mathbf{A}(\tau)$  refer to the momentum operator and vector potential associated to the driving electric field  $\mathcal{E}(\tau)$ , respectively. This procedure is repeated iteratively for all splitting times. Thus, the outer parts of the wave function that have been stored can be analyzed separately in order to obtain information about the photoelectron momentum distribution and evaluate observables such as (i) **energy-integrated photoelectron angular distribution (PAD)**, (ii) **angle-integrated photoelectron spectrum (PES)**, (iii) **full momentum distribution** and (iv) **total yield**. Furthermore, since the outgoing part of the wave function is absorbed efficiently at the splitting times, large box sizes are avoided in the inner region, which significantly increases the numerical performance of the propagation [51].

## 6.2 Photoelectron spectrum and angular distributions

This section introduces the formal description for the evaluation of the full momentum distribution, **PES** and **PAD** of the emitted photoelectrons in the framework of the WFSM. The spectral coefficient  $\varphi_i(\mathbf{p}, T; t_j)$  describing the continuum part of the propagated wave packet originating from a given channel  $i$  at the splitting time  $t_j$  and evaluated at the final time  $t = T$ , reads [51]

$$\begin{aligned} \varphi_{i,\text{out}}(\mathbf{p}, T; t_j) &= \langle \mathbf{p} | \hat{\mathbf{U}}_V(T, t_j) \hat{\mathbf{S}} | \varphi_i(t_j) \rangle \\ &= \int d^3 \mathbf{p}' \langle \mathbf{p}^V | \hat{\mathbf{U}}_V(T, t_j) | \mathbf{p}'^V \rangle \langle \mathbf{p}'^V | \varphi_{i,\text{out}}(t_j) \rangle, \end{aligned} \quad (6.4)$$

where  $|\mathbf{p}^V\rangle$  refers to the Volkov states and where  $\hat{\mathbf{U}}_V(T, t_j)$  is the evolution operator acting on the outer part of the propagated wave packet. It propagates the outer parts from the

splitting time  $t_j$  to a final time  $t = T$ . The parameter  $T$  must be a sufficiently long time so that all parts of the wave function that are of interest have reached the outer region and therefore contribute to the PES. The evolution operator associated with the Volkov Hamiltonian defined in Eq. (6.3), reads

$$\hat{\mathbf{U}}_V(t_2, t_1) = \exp\left(-i \int_{t_1}^{t_2} \hat{\mathbf{H}}_V(\tau) d\tau\right). \quad (6.5)$$

In the velocity form, the Volkov states  $|\mathbf{p}^V\rangle$  corresponds to plane waves,  $\langle \mathbf{r} | \mathbf{p}^V \rangle = (2\pi)^{-3/2} e^{i\mathbf{p}\cdot\mathbf{r}}$  [51]. Making use of multipole expansion for the exponential function<sup>1</sup> [143–146] allows to rewrite Eq. (6.4) in the following form [51],

$$\varphi_{i,\text{out}}(\mathbf{p}, T; t_j) = \frac{2}{\pi} e^{-i\vartheta_V(\mathbf{p})} \sum_a (-i)^{l_a} \beta_i^a(t_j) Y_{m_a}^{l_a}(\Omega_{\mathbf{p}}) \int_0^\infty r dr u_{l_a}^{n_a}(r) j_{l_a}(pr), \quad (6.6)$$

where  $j_{l_a}(pr)$  and  $u_{l_a}^{n_a}(r) = R_{l_a}^{n_a}(r)/r$  [51] denote the Bessel polynomials and the radial wave functions of the field-free Hamiltonian associated with the virtual orbitals, respectively. The photoelectron momentum is defined by  $\mathbf{p}$  with  $p = |\mathbf{p}|$ . The term  $Y_{m_a}^{l_a}(\Omega_{\mathbf{p}})$  denotes the ordinary spherical harmonics where the orientational unit vector  $\Omega_{\mathbf{p}} = (\theta, \phi)$  is defined by the photoelectron emission direction. The angular coordinates  $\theta$  and  $\phi$  denote the polar and azimuthal angles defining the direction of photoelectron emission with respect to the propagation direction of the driving field. In Eq. (6.6), the sum runs over the virtual orbitals, cf. Section 3.4.1, and the *Volkov phase*  $\vartheta_V(\mathbf{p})$ , reads [51]

$$\vartheta_V(\mathbf{p}) = \frac{1}{2} \int_{t_j}^T d\tau [\mathbf{p} + \mathbf{A}(\tau)]^2. \quad (6.7)$$

Finally,  $\beta_i^a(t_j)$  denotes the projection of the outer part onto the field-free virtual orbital  $|\phi_a\rangle$ , namely

$$\beta_i^a(t_j) = \langle \phi_a | \varphi_{i,\text{out}}(t_j) \rangle \quad \text{with} \quad \phi_a(\mathbf{r}) = \frac{u_{l_a}^{n_a}(r)}{r} Y_{m_a}^{l_a}(\Omega_{\mathbf{r}}). \quad (6.8)$$

The contributions from all splitting times must be added up coherently to form the total spectral coefficient for the channel  $i$ , namely

$$\tilde{\varphi}_{i,\text{out}}(\mathbf{p}, T) = \sum_{t_j} \varphi_{i,\text{out}}(\mathbf{p}, T; t_j). \quad (6.9)$$

---

<sup>1</sup> for plane waves the multipole expansion reads  $e^{i\mathbf{p}\cdot\mathbf{r}} = 4\pi \sum_{l=0}^{\infty} (i)^l j_l(pr) \sum_{m=-l}^l Y_m^{*l}(\Omega_{\mathbf{p}}) Y_m^l(\Omega_{\mathbf{r}})$

Equation (6.9) is utilized to evaluate the photoelectron yield. In detail, incoherent summation over all possible ionization channels  $i$ , yields the **full momentum distribution** [51]

$$\frac{d^2\sigma(\mathbf{p})}{dpd\Omega} = |\tilde{\varphi}_{\text{out}}(\mathbf{p}, T)|^2 = \sum_i |\tilde{\varphi}_{i,\text{out}}(\mathbf{p}, T)|^2, \quad (6.10a)$$

where  $d\Omega \equiv d\Omega_{\mathbf{p}} = \sin\theta d\theta d\phi$  is the differential solid angle.

The **energy-integrated PAD** is obtained by integrating Eq. (6.10a) over energy or, equivalently, momentum, namely

$$\frac{d\sigma}{d\Omega} = \int_0^\infty \frac{d^2\sigma(\mathbf{p})}{dpd\Omega} p^2 dp. \quad (6.10b)$$

Analogously, the **angle-integrated PES** is obtained upon integration over all directions

$$\frac{d\sigma}{d\epsilon} = p \int_0^{2\pi} \int_0^\pi \frac{d^2\sigma(\mathbf{p})}{dpd\Omega} \sin\theta d\theta d\phi \quad (6.10c)$$

with  $p = \sqrt{2\epsilon}$  and  $\epsilon \leq 0$  the photoelectron energy. Last but not least, the **total yield**,  $\sigma$ , defining the probability for photoelectron emission is obtained by integrating the angle-integrated PES, i.e. Eq. (6.10c), over all positive valued energies of the continuum spectrum

$$\sigma = \int_{\epsilon \leq 0} \frac{d\sigma}{d\epsilon} d\epsilon. \quad (6.10d)$$

In the context of this work, full momentum distribution, total yield, PES and PAD are evaluated by means of the formalism detailed in the above lines. This formalism will be further exploited to the development of an monotonically convergent optimal control algorithm allowing to manipulate and control specific properties of continuum-related observables in Chapter 8.



## Part II

# Method development and numerical results



# An efficient mapped pseudospectral propagation method for solving the time-dependent Schrödinger Equation

---

7.1	Introduction and Motivations . . . . .	65
7.2	Time-dependent Schrödinger equation . . . . .	67
7.3	Description of the pseudospectral formalism . . . . .	69
7.4	Numerical Results . . . . .	72
7.4.1	Numerical performance . . . . .	73
7.4.2	Enhancement of the high harmonic yield via coherent superposition	75
7.5	Discussion and Conclusions . . . . .	82

---

## 7.1 Introduction and Motivations

Over the past decades, the field of quantum molecular dynamics has been driven by the development of efficient numerical methods for solving the time-dependent Schrödinger equation [94]. Current applications include studies of quantum optimal control [147] or electron dynamics. The two basic tasks that need to be addressed in quantum molecular dynamics are the representation of the state vector (and operators acting on it) and its time evolution. Ideally, the accuracy with which both tasks are accomplished should

be balanced [57]. High accuracy is required by many state-of-the-art applications, for example in quantum optimal control [147]. At the same time, the exponential scaling of quantum dynamics calculations is a challenge for even the most advanced computer architectures. Efficiency of the methods is therefore also an issue, in addition to accuracy.

Highly accurate methods are obtained by employing pseudospectral approaches based on the expansion in orthogonal polynomials [78]. The representation problem can be solved using discrete variable representations or their unitary equivalent, finite basis representations [148]. The operators acting on the wavefunction are then given as sparse (often diagonal) matrices in one of the representations. The numerical effort is either due to the unitary transformation connecting the two representations or due to sparse matrix-vector multiplications. For a sufficiently large number of basis functions, the error becomes smaller than machine precision [149].

It is also well-established that polynomial approximations yield the most accurate and stable propagation schemes [99]. Again, convergence is exponential with increasing polynomial order. For coherent time evolution, the best polynomial approximation of the evolution operator is obtained by the Chebyshev propagator [98], while Newton polynomials yield an accurate and efficient propagator for open quantum systems [99]. Modifications of polynomial propagators allow to also accurately account for time ordering in case of a time-dependent Hamiltonian [150–152].

The valuable high accuracy of these methods may, however, be compromised in time-dependent studies of dissociation or ionization where a sufficiently large grid, respectively a sufficiently large number of basis functions, becomes computationally prohibitive, both in terms of storage requirements and CPU time. Remedies to this problem include the use of variable grid steps [153–156] or variable-grid boundary conditions [157], wavefunction splitting methods [51, 158, 159], mask functions [160–162] or complex absorbing potentials (CAPs) [139, 140]. While the latter approach allows for calculating physical observables that require long propagation times [25, 28, 163], a CAP can only absorb wavepacket components within a certain frequency range [140]. It is thus rather difficult to completely avoid reflection which compromises accuracy. The problem of reflection also occurs for the mask function approach [157]. Furthermore, A CAP, renders the Hamiltonian non-Hermitian, which results in substantial technical difficulties particularly for quantum optimal control [50, 53, 164] and may even preclude the evaluation of observables of interest [25, 28, 52]. Non-Hermitian Hamiltonians are avoided when using variable grid steps or wavefunction splitting but also in these cases high accuracy and reasonable numerical costs are not always guaranteed. For example, the mapped Fourier grid method [154–156, 165] was developed for long-range potentials that vanish asymptotically as  $1/R^N$ . It allows for an accurate description of most bound states and low-energy scattering states.

However, the calculation of the bound spectrum does not scale favorably with the number of grid points, rendering its application in coupled channel calculations difficult [166, 167]. Moreover, it cannot be used in photoionization studies where high-energy scattering states may come into play. Wavefunction splitting is applicable in this case [51, 138]; it neglects, however, the Coulomb interaction between photoion and photoelectron. Thus, it cannot be used to study processes where recombination of the photoelectron is crucial, such as high harmonic generation.

Needless to mention, the tedious task of choosing the proper parameters for each of these methods such that convergence of the observables of interest is achieved. Furthermore, since such parameters are field dependent, from an optimization perspective nothing warrants that the parameters chosen for the guess field are also valid for the optimized field, without compromising the convergence of the observables, and consequently, the validity of the calculations.

In order to circumvent these technical difficulties, we use a weak formulation [78, 168] of the Schrödinger equation to derive a sparse, yet accurate representation of the Hamiltonian and combine it with the Chebyshev propagation method [98]. The basic idea is to decompose the spatial domain into multiple sub-intervals of increasing size, chosen according to the local de Broglie wavelength, similar to the choice of the variable grid step in the mapped Fourier grid method [154–156, 165]. Within each interval, the wavefunction is expanded into Lagrange polynomials. The resulting representation of the Hamiltonian is sparse which is exploited in storage, diagonalization and matrix-vector operations [169]. Our approach thus combines the high accuracy of pseudospectral methods with the ability to use a very large spatial domain. It is particularly advantageous for quantum dynamics involving long-range potentials and long propagation times. As an example, we consider a laser-driven electron in a soft Coulomb potential, a popular model for high-harmonic generation.

## 7.2 Time-dependent Schrödinger equation

The time-dependent Schrödinger equation reads

$$i\hbar \frac{\partial}{\partial t} \Psi(r, t) = H(r, t) \Psi(r, t), \quad (7.1)$$

with the Hamiltonian found in Eq. (7.11). The formal solution is given by

$$\begin{aligned} \Psi(r, t) &= T \exp \left( -\frac{i}{\hbar} \int_0^t H(r, \tau) d\tau \right) \Psi(r, 0) \\ &= U(t) \Psi(r, 0), \end{aligned} \quad (7.2)$$

where  $T$  denotes the time-ordering operator and  $U(t)$  the evolution operator from time zero to time  $t$ . Polynomial propagators treat  $U(t)$  as a function of the Hamiltonian and expand it into a truncated polynomial series [57, 98, 99, 104, 151, 152, 170]. To this end, the domain of the eigenvalues, i.e., the spectral radius  $\Delta E$  of the Hamiltonian must be known, in order to renormalize the Hamiltonian to the domain of the polynomials [57, 98, 99]. Consider for simplicity first a time-independent Hamiltonian in which case the Chebychev propagator is given by [98]

$$U(t) = e^{-iHt/\hbar} \approx \sum_{n=0}^N a_n T_n(-iHt/\hbar) . \quad (7.3)$$

For the exponential function, the expansion coefficients  $a_n$  are known analytically [98], and Eq. (7.3) can be evaluated using the recursion relation of the Chebyshev polynomials. The solution is thus obtained by subsequent applications of the (renormalized) Hamiltonian to a wavefunction [57, 98, 99]. If the Hamiltonian has a matrix representation, the propagation thus involves a series of matrix-vector multiplications. The number  $N$  of Chebyshev polynomials, i.e., applications of the Hamiltonian, is proportional to the product of spectral radius and time step [57, 98, 99]. The error of the expansion (7.3) can be made arbitrarily small by choosing a sufficiently large  $N$ . This reflects the global nature of the approximation (7.3).

For an explicitly time-dependent Hamiltonian as in Eq. (7.11), time-ordering needs to be accounted for, cf. Eq. (7.2). A global polynomial propagator in this case is given by the  $(t, t')$ -method [171]. Unfortunately, its practical use is hampered by an exponential increase in computational effort, due to treating the time-dependence as an additional degree of freedom ( $t'$ ). An alternative is offered by semi-global propagators [151, 152, 170] that also allow for full error control. They are based on rewriting the explicitly time-dependent term on the right-hand side of Eq. (7.1),  $H_I(r, t)\psi(r, t)$ , as an (unknown) inhomogeneity which is determined iteratively in a self-consistent manner. The formal solution of the inhomogeneous Schrödinger equation (with the remaining time-independent Hamiltonian) can be subjected to a polynomial expansion just like Eq. (7.3) [172]. This follows from *Duhamel's principle* which links the formal solution of an inhomogeneous ordinary differential equation to the solution of the corresponding homogeneous equation. A semi-global approximation of the properly time-ordered solution (7.2) with full error control is important for strongly time-dependent Hamiltonians, as present in HHG.

The high accuracy afforded by global and semi-global polynomial propagators is crucial in particular when coherent effects are examined. For example, second order differentiating schemes are not stable already for intermediate propagation times [149], and the popular split operator preserves the norm which means that the numerical error is entirely

in the phase of the wavefunction where it accumulates [104].

### 7.3 Description of the pseudospectral formalism

For a well-balanced numerical approximation of Eq. (7.2), the representation of the wave function and the Hamiltonian that is acting on it should be of the same accuracy as the propagation scheme [149]. Global representation methods are obtained by collocation and include the Fourier grid [149] as well as discrete variable representations (DVRs) and their unitary equivalent, the finite basis representations [148]. For a sufficiently large number of basis functions in the collocation, the error becomes smaller than machine precision [149].

The high accuracy of these methods is, however, compromised by the numerical effort they require if a very large grid or, respectively, a very large number of basis functions is required. This is the case in time-dependent studies of dissociation and ionization. Global approximations quickly become computationally prohibitive, both in terms of storage requirements and CPU time. Remedies to this problem include the use of variable grid steps [153–156] or variable-grid boundary conditions [157], wavefunction splitting methods [51, 158, 159], mask functions [160–162] or complex absorbing potentials (CAPs) [139, 140]. However, none of these methods is suitable to represent the time-dependent wavefunction in HHG which both involves a long-range potential and requires the accurate description of high-energy scattering states that are accessed during ionization and recombination.

An alternative is provided by a semi-global representation of the Hamiltonian. Based on a decomposition of the spatial domain into multiple sub-intervals and collocation, i.e., expansion into orthogonal polynomials, within each interval, it is commonly referred to as finite element discrete variable representation (FE-DVR) [83, 89, 91, 92]. In Appendix A.1, we use Green’s theorem, i.e., a weak formulation of the Schrödinger equation, to derive this representation. This allows for constructing a symmetric Hamiltonian matrix. Moreover, we modify the original derivation of the FE-DVR by taking the sub-intervals to be of increasing size, chosen according to the local de Broglie wavelength, similar to the choice of the variable grid step in the mapped Fourier grid method [154–156, 165]. The resulting representation of the Hamiltonian is blockwise sparse except for the inter-element points [89], with  $k = 1, \dots, M$  being the number of elements and  $(i, j) = 0, \dots, N$  the number of collocation points per element. Denoting the reduced mass and the potential energy evaluated at the collocation point  $r_i^k$  by  $\mu$  and  $V(r_i^k)$ , respectively, the matrix

$$\hat{H}_0 = \begin{pmatrix} \cdots & \mathbf{a}_{N,N}^{k-2} + \mathbf{a}_{0,0}^{k-1} & a_{0,1}^{k-1} & \cdots & a_{0,N}^{k-1} & 0 & 0 & 0 & 0 & \cdots & 0 & 0 & \cdots \\ \cdots & a_{0,1}^{k-1} & a_{1,1}^{k-1} & \cdots & a_{1,N}^{k-1} & 0 & 0 & 0 & 0 & \cdots & 0 & 0 & \cdots \\ \cdots & \vdots & \vdots & \ddots & \vdots & 0 & 0 & 0 & 0 & \cdots & 0 & 0 & \cdots \\ \cdots & a_{N,0}^{k-1} & a_{N,1}^{k-1} & \cdots & \mathbf{a}_{N,N}^{k-1} + \mathbf{a}_{0,0}^k & a_{0,1}^k & \cdots & a_{0,N}^k & 0 & \cdots & 0 & 0 & \cdots \\ \cdots & 0 & 0 & 0 & a_{1,0}^k & a_{1,1}^k & \cdots & a_{1,N}^k & 0 & \cdots & 0 & 0 & \cdots \\ \cdots & 0 & 0 & 0 & \vdots & \vdots & \ddots & \vdots & 0 & \cdots & 0 & 0 & \cdots \\ \cdots & 0 & 0 & 0 & a_{N,0}^k & a_{N,1}^k & \cdots & \mathbf{a}_{N,N}^k + \mathbf{a}_{0,0}^{k+1} & a_{0,1}^{k+1} & \cdots & a_{0,N}^{k+1} & 0 & \cdots \\ \cdots & 0 & 0 & 0 & 0 & 0 & \cdots & a_{1,0}^{k+1} & a_{1,1}^{k+1} & \cdots & a_{1,N}^{k+1} & 0 & \cdots \\ \cdots & 0 & 0 & 0 & 0 & \vdots & \vdots & \vdots & \vdots & \ddots & \vdots & 0 & \cdots \\ \cdots & 0 & 0 & 0 & 0 & 0 & 0 & a_{N,0}^{k+1} & a_{N,1}^{k+1} & \cdots & \mathbf{a}_{N,N}^{k+1} + \mathbf{a}_{0,0}^{k+2} & a_{0,1}^{k+2} & \cdots \\ 0 & 0 & 0 & 0 & 0 & 0 & 0 & 0 & 0 & 0 & a_{1,0}^{k+2} & a_{1,1}^{k+2} & \cdots \\ 0 & 0 & 0 & 0 & 0 & 0 & 0 & 0 & 0 & 0 & \vdots & \vdots & \ddots \end{pmatrix} \quad (7.4)$$

Figure 7.1: **FE-DVR**: Sparse matrix representation of the Hamilton operator in the FE-DVR basis. Note that the individual matrix elements  $a_{i,j}^k \equiv a^k(v_i, v_j)$  in Eq. (7.5), associated with the last and first points of two contiguous elements,  $r_N^k$  and  $r_0^{k+1}$ , are added up at diagonal coordinates coinciding with interelement points of the global grid, i.e.  $r_N^k = r_0^{k+1}$ , ensuring continuity of the eigenvectors at these points.

elements  $a_{i,j}^k \equiv a^k(v_i, v_j)$  are given by

$$a^k(v_i^k, v_j^k) = \frac{\hbar^2}{2\mu} \mathcal{J}_k^{-1} \frac{S_{i,j}^\Lambda}{\sqrt{\gamma_i^k \gamma_j^k}} + V(r_i^k) \delta_{i,j} \frac{w_j^k}{\sqrt{\gamma_i^k \gamma_j^k}} \quad (7.5)$$

with the Jacobian  $\mathcal{J}_k$ , collocation weights  $w_j^k$  and “global weights”  $\gamma_j^k$  found in Eqs. (A.10b), (A.11), and (A.23b), and the matrix elements  $S_{i,j}^\Lambda$  defined in Eq. (A.14). Due to the DVR character of the representation,  $H_I(r, t)$  corresponds to a diagonal matrix, just as  $V(r)$  does.

The number of non-zero matrix elements is given by

$$\mathcal{N} = (N \times M + 1)(N + 1) - N(N + 1)/2 - 2(N + 1), \quad (7.6)$$

where  $N + 1$  is the number of collocation points and  $M$  denotes the number of intervals. This compares to the  $N_{pts}(N_{pts} + 1)/2$  different matrix elements of a full Hermitian matrix that is obtained in global collocation schemes. The sparsity and band-like structure of Eq. (7.4) can be exploited to reduce storage and CPU time in both diagonalization and time propagation, using standard libraries for sparse matrix-vector operations [169].

The semi-global representation (7.4) based on Gauss-Lobatto-Legendre collocation

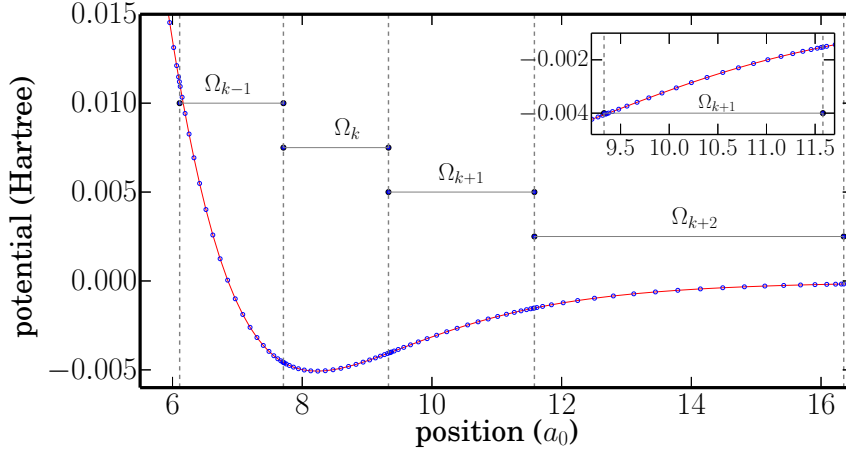


Figure 7.2: Distribution of collocation points with  $N = 21$ . The inset shows a zoom onto the interval labeled by  $\Omega_{k+1}$ . The high density of points close to the edges of the interval is typical for collocation based on Gauss-Lobatto-Legendre points.

in sub-intervals of increasing size is closely related to FE-DVR [83, 89, 90]. The main difference between our derivation of Eq. (7.4) in Appendix A.1 and that of Refs. [83, 89, 90] is our systematic choice of the sub-intervals  $[r_0^k, r_N^k]$ . As explained in Section A.1.1, there is no restriction on the choice of  $r_0^k$  and  $r_N^k$ . We utilize the intuition underlying the Mapped Fourier Grid method [153–156, 165] and adapt the size of each sub-interval to the local de Broglie wavelength. This implies that the sub-intervals get larger in the asymptotic part of the potential which can be achieved as follows. The overall spatial domain starts at  $r_{min}$  and thus  $r_0^{k=1} = r_{min}$ . The end of the first interval,  $r_N^{k=1}$ , is obtained by solving the implicit equation [156]

$$\beta = \frac{\sqrt{2\mu}}{\pi} \int_{r_0^k}^{r_N^k} \sqrt{E_{asy} - V(r)} dr \quad (7.7)$$

for  $k = 1$ , where  $\beta$  and  $E_{asy}$  are two parameters. For all further intervals,  $r_0^{k+1}$  is set equal to  $r_N^k$ , and  $r_N^{k+1}$  is obtained by solving Eq. (7.7). This procedure is repeated until  $r_{max}$  is reached. The two parameters in Eq. (7.7) have a physical meaning that makes their choice straightforward. The parameter  $\beta$  with  $0 < \beta \leq 1$  estimates the local coverage of the phase space volume [154–156]: Smaller values of  $\beta$  result in a higher density of points, and  $\beta = 1$  corresponds to the minimal classical estimation for the phase space discretization. The parameter  $E_{asy}$  specifies the smallest energy up to which the size of the interval is increased, i.e., if  $|V(r)|$  becomes smaller than  $E_{asy}$ , the size of the intervals is not increased any further but kept constant.

Within each interval, the points  $r_j^k$ ,  $j = 0, \dots, N$ , are chosen according to the Leg-

endre quadrature rule, as described in Section A.1.2. Since each interval is discretized by  $N + 1$  collocation points, the density of points per element is constant. The resulting discretization is illustrated in Fig. 7.2 for the  $B^1\Sigma_u^+$  electronically excited state of the  $Ca_2$  molecule [173] which vanishes asymptotically as  $1/R^3$ . Such long-range states support extremely weakly bound vibrationally levels and therefore require large  $r_{max}$  to faithfully represent all (relevant) bound levels [154]. Such levels are important for example in the photoassociation of ultracold atoms, and it was the need to calculate such levels that had prompted the development of the mapped Fourier grid method [154]. We provide a detailed analysis of the dependence of accuracy and computational resources on domain discretization and collocation order in Appendix A.2.

## 7.4 Numerical Results

We focus our attention to the single-atom response leading to high order harmonic generation for linearly polarized light. Besides the physics of the problem, a particular attention will be devoted to the numerical performances with respect to the standard Fourier propagation method. The basic physics of the process can be captured by considering an electron subject to a soft Coulomb potential [174],

$$V(r) = -\frac{1}{\sqrt{a + r^2}}. \quad (7.8)$$

Choosing  $a = 2$  in Eq. (7.8) ensures that the ground state energy coincides with that of the true Coulomb potential, namely 0.5 Hartree. The electron is subject to a linearly polarized electric field of the form

$$E(t) = E_0 G(t) \sin(\omega_0 t), \quad (7.9)$$

where  $G(t)$  is a Gaussian envelope. The interaction of the electron with the electric field is treated in the dipole approximation,

$$H_I(r, t) = -r E(t), \quad (7.10)$$

such that the total Hamiltonian becomes

$$H(r, t) = H_0 + H_I(r, t) = -\frac{\hbar^2}{2m} \nabla_r^2 + V(r) - r E(t). \quad (7.11)$$

The entire information about the harmonic generation process is encoded in the time-

dependent dipole acceleration [175]. It is given by [176]

$$\ddot{d}(t) = \langle \psi(t) | \nabla_r V(r) | \psi(t) \rangle, \quad (7.12)$$

where the dependence on the external field is omitted since it does not contain higher harmonics. The harmonic spectrum  $S(\omega)$  is obtained as [177]

$$S(\omega) = |\ddot{d}(\omega)|^2 / \omega^2, \quad (7.13)$$

where  $\ddot{d}(\omega)$  is the Fourier transform of the dipole acceleration (7.12).

We choose the parameters of the electric field such that  $I_p > U_p > \omega_0$ , where  $I_p$  is the ionization potential and  $U_p$  the ponderomotive energy. Then the high harmonic generation process proceeds in the regime of above threshold ionization (ATI) [178]. Within the quasi-classical three-step model, the harmonic *cutoff* position is given by [23, 179]

$$\omega_c = (I_p + 3.17U_p) / \omega_0. \quad (7.14)$$

For an electron in the ground state, it becomes  $\omega_c = 10.072$ . We minimize the characteristic overestimation of the recollision probability of 1D models with respect to their counterpart 3D models by choosing a few-cycle pulse [176].

### 7.4.1 Numerical performance

For completeness, we compare the numerical performance of the semi-global representation (7.4) to that obtained with the mapped Fourier grid. In both cases, we utilize the Chebychev propagator, Eq. (7.3). In the semi-global representation, the Hamiltonian is applied via sparse matrix-vector multiplications, whereas the mapped Fourier grid method uses fast Fourier transforms together with vector-vector multiplications in real and momentum space.

We assume that initially the electron is in the ground state,  $|\varphi_0\rangle$ , of the field-free Hamiltonian. For the propagation based on the mapped Fourier grid, we use  $R_{max} = 8000$  Bohr, which ensures that there are no spurious reflections at the edges of the grid during propagation. The remaining parameters are chosen to yield fully converged results. Specifically, we find the grid to be converged when using 2047 coordinate points, which leads to a correct representation of continuum states with energies well above  $E_{max} = 0.25$  Hartree, the highest continuum state that gets populated during the dynamics.

The eigenvalues and eigenfunctions are obtained by diagonalization of the field-free Hamiltonian in the mapped Fourier grid representation. The set of eigenvalues from  $E_0$  to

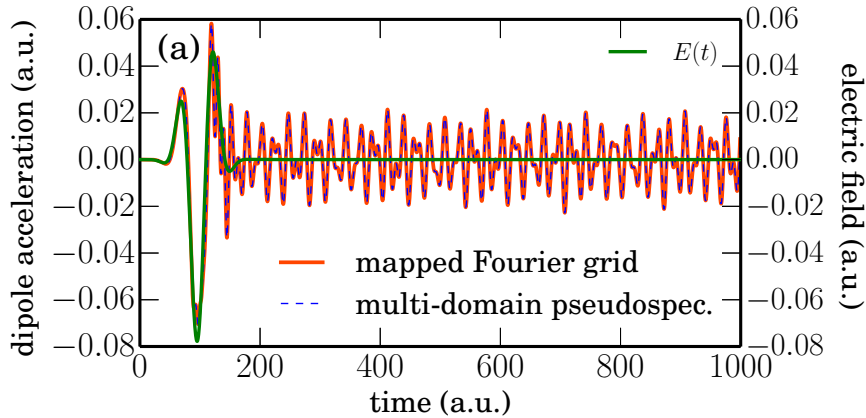


Figure 7.3: Time-dependent dipole acceleration  $\ddot{d}(t)$  obtained with the mapped Fourier grid method and the semi-global representation (7.4) ( $N = 3$ ,  $M = 900$ ). For comparison, the electric field of the driving pulse is also shown.

$E_{max}$  is used as a reference to define the accuracy of the semi-global representation (7.4), when testing several combinations of the number of domains,  $M$ , and collocation order,  $N$ . We find that for a low collocation order, which minimizes the spectral radius, a larger total number of points is needed than with the mapped Fourier grid. For example,  $\mathcal{N} = 2701$  for  $M = 900$  and  $N = 3$ .

The dipole acceleration  $\ddot{d}(t)$  obtained with both propagation approaches is depicted in Fig. 7.3. The few-cycle laser pulse induces a fast dynamics of the electron, and the corresponding harmonic spectrum, cf. Fig. 7.4, shows the characteristic cutoff. Clearly, both methods yield the same dynamics, as expected. The numerical performance is, however, quite different. It is analyzed in Table 7.1. Although the sparse structure of the Hamiltonian matrix (7.4) leads to a larger spectral radius, the CPU time required for propagation may be significantly smaller, depending on the collocation order  $N$ . Thus the semi-global representation using sparse matrix-vector multiplications is numerically more efficient than transforming the propagated wavepacked from coordinate to momentum representation by fast Fourier transforms, provided the parameters  $N$  and  $M$  are chosen judiciously.

The choice of collocation order and number of domains is further analyzed in Table 7.1. The role of the spectral radius becomes particularly apparent for  $N = 10$  and  $M = 270$  which leads to a propagation time 50 per cent longer than that needed with the mapped Fourier grid approach. In this case, the spectral radius is almost ten times larger than the one obtained with the mapped Fourier grid. Correspondingly, the number of applications of the Hamiltonian is ten-fold increased. However, choosing  $N = 6$  and  $M = 450$  reduces the spectral radius considerably, such that the CPU time for propagation is now only

$N$	$M$	spectral radius <sup>†</sup>	CPU time <sup>†</sup>
10	270	973%	152%
6	450	411%	66%
5	540	310%	52%
4	675	227%	40%
3	900	165%	31%

† relative to mapped Fourier grid method

Table 7.1: Numerical effort for wavepacket propagation with the adaptive-size multi-domain pseudospectral approach where  $N$  denotes collocation order and  $M$  the number of domains. The total number of collocation points is  $\mathcal{N} = N \times M + 1 = 2701$ . The reference calculation, using the mapped Fourier grid method and fast Fourier transforms, with 2047 grid points and a spectral radius of 1277.8 Hartree., took 959 s of CPU time.

two thirds of that using the mapped Fourier grid method. Already for this choice of parameters, the semi-global adaptive-size multi-domain pseudospectral approach starts to be more efficient. The efficiency may be further improved by reducing  $N$  and increasing  $M$ , up to a third of the CPU time required with the mapped Fourier grid for  $N = 3$  and  $M = 900$ .

Note that the accuracy in all cases is roughly the same, since the overall number of collocation points is sufficiently large. A low collocation order  $N$  minimizes the spectral radius, and thus the number of times the Hamiltonian is applied. Larger  $N$  does not only lead to a larger spectral radius but also to a less sparse structure of the Hamiltonian, cf. Appendix A.2, i.e., it results in a two-fold increase in the numerical cost. Since small  $N$  allows for highly accurate results, it is the preferable choice. In summary, the best performance of the semi-global multi-domain pseudospectral representation is achieved by choosing a relatively large total number of points, with small  $N$  and large  $M$ , such that the desired accuracy is obtained while minimizing the CPU time.

The advantage of our approach is its stability and accuracy, besides efficiency. These features derive from the pseudospectral treatment of both spatial degree of freedom and time dependence [57, 99]. Our approach is thus particularly suitable for problems where a large grid and long propagation times are needed, for example to calculate spectra in photoionization. It can also be employed in multi-dimensional problems where the sparsity of the Hamiltonian representation will be even more important.

#### 7.4.2 Enhancement of the high harmonic yield via coherent superposition

We now employ the time-dependent semi-global multi-domain pseudospectral representation to analyzing the role of the initial state for the generation of the harmonic spectrum,

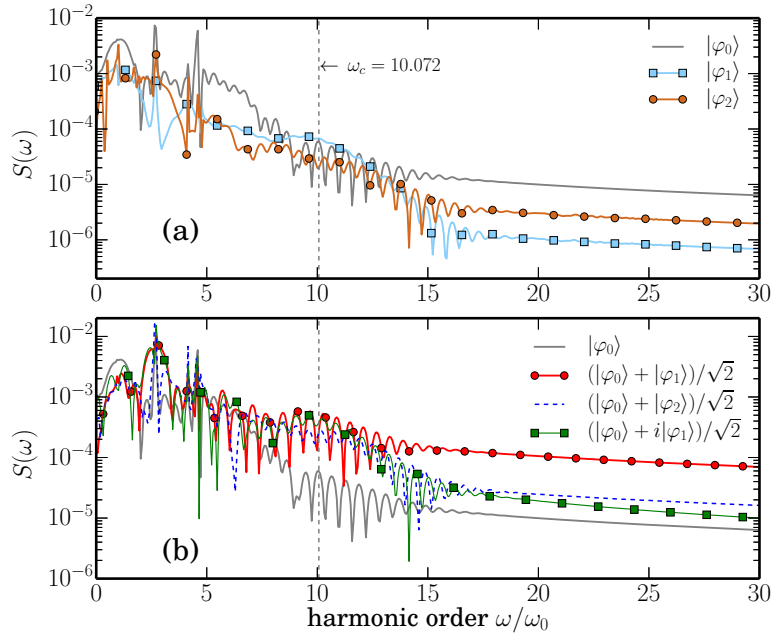


Figure 7.4: Harmonic spectrum for different initial states: (a) Eigenstates of the field-free Hamiltonian and (b) superpositions of two field-free eigenstates.

while keeping the driving pulse fixed. All calculations presented below use a full width at half maximum of  $\tau_{FWHM} = 206.5$  a.u., a maximal field amplitude of  $E_0 = 0.06$  a.u., and a carrier frequency of  $\omega_0 = 0.1$  a.u. These electric field parameters lead to a ponderomotive energy [180] of  $U_p = 0.16$  Hartree such that the Keldysh adiabaticity parameter [181] becomes  $\gamma = 1.25$ . We compare low-lying eigenstates of the field-free Hamiltonian as initial state and superpositions thereof. These different initial states could be prepared by a 'pre-pulse', preceding the pulse that drives the harmonic generation. Figure 7.4(a) shows the harmonic spectra obtained for the first three eigenstates  $|\varphi_0\rangle$ ,  $|\varphi_1\rangle$  and  $|\varphi_2\rangle$  of the field-free Hamiltonian as initial state, with eigenenergies  $-0.500$  Hartree,  $-0.233$  Hartree and  $-0.134$  Hartree. The exponential decay instead of a plateau in Fig. 7.4(a) is characteristic of soft core potentials, the plateau being attributed to the singularity present in the Coulomb potential [182]. Since the ionization potential is the largest for the ground state,  $|\varphi_0\rangle$  results in the largest harmonic cutoff,  $\omega_c/\omega_0 = 10.1$  (indicated by the dashed vertical line in Fig. 7.4), compared to 7.4 and 6.4 for the first first and second excited state, respectively. Figure 7.4(a) also shows that the spectral yield is largest for the ground state for almost all orders in the emission spectrum. Next we consider superpositions of field-free eigenstates as initial state. Some precaution is necessary when evaluating the expectation value (7.12) since a superposition of eigenstates leads to a dipole acceleration even without any driving pulse. For instance, for a superposition of two states, this

“field-free” dipole acceleration is given by

$$\ddot{d}_{ff}(t) = 2|c_i||c_j|\cos(\omega_{i,j}t - \vartheta)\langle\varphi_i|\nabla_x V(x)|\varphi_j\rangle, \quad (7.15)$$

where  $\hbar\omega_{i,j}$  is the energy difference between the superimposed states,  $\vartheta$  their relative phase and  $|c_{i/j}|$  the norm of the expansion coefficients. Equation (7.15) reveals, however, that the harmonics emitted due to the time-dependence of the superposition state are of low order. To make sure that we analyze truly HHG, we focus on the spectral yield for frequencies well above  $\omega_{i,j}$ , for example the yield close to the cutoff frequency.

We start by considering an equal superposition of two field-free eigenstates, allowing for a complex phase. Figure 7.4(b) reveals that, depending on the expansion coefficients in the initial state, the harmonic yields is considerably enhanced compared to the best single eigenstate,  $|\varphi_0\rangle$ . The superposition  $(|\varphi_0\rangle + |\varphi_1\rangle)/\sqrt{2}$  does not only result in a higher harmonic yield at the cutoff, but also in a larger integrated spectrum, i.e., a larger integrated power density, for frequencies higher than  $\omega_c$ . This is true not only for the comparison with the initial states shown in Fig. 7.4(b), but also for other superpositions.

The finding of Fig. 7.4(b) motivates a more thorough control study. Specifically, we use optimization to determine the best combination of eigenstates, such that the power density of the harmonic yield starting from the cutoff  $\omega_c$  is maximized. This choice ensures maximization of the total integrated spectrum for high harmonic orders beyond the cutoff. In detail, we employ the Sequential PARAMetrization update (SPA) technique [50] to determine the expansion coefficients in the initial state,  $c_j \in \mathbb{C}$ , such that propagation of this state maximizes the integrated spectrum [183, 184],

$$J[c_j] = \int_{\omega_c}^{\omega_f} |\ddot{d}(\omega)|^2 d\omega. \quad (7.16)$$

The harmonic *cutoff* position  $\omega_c$  is taken to be the one obtained for the ground state as initial state. The upper limit is defined to be  $\omega_f = 3\omega_c$ . Note that the functional as defined in Eq. (7.16) does not only enhance the spectral yield in  $[\omega_c, \omega_f]$ , but it can also extend the harmonic cutoff as a function of  $\omega_f$ .

We use  $(|\varphi_0\rangle + |\varphi_1\rangle)/\sqrt{2}$  to start the optimization, since this superposition was found to considerably enhance the power spectrum. The SPA technique updates the expansion coefficients, which can take complex values, sequentially: Starting with two guess coefficients,  $c_0 = c_1 = 1/\sqrt{2}$ , additional coefficients are sequentially added, once a plateau is encountered in the optimization [50]. Upon optimization with only two states, we find the optimal initial superposition to be composed of  $|\varphi_0\rangle$  and  $|\varphi_1\rangle$  with coefficients  $c_0 = 0.7215$  and  $c_1 = 0.6924$ . The resulting harmonic yield is very slightly better, by less than 1 per cent, than that obtained with equal weights,  $c_0 = c_1 \approx 0.7071$ , in the initial

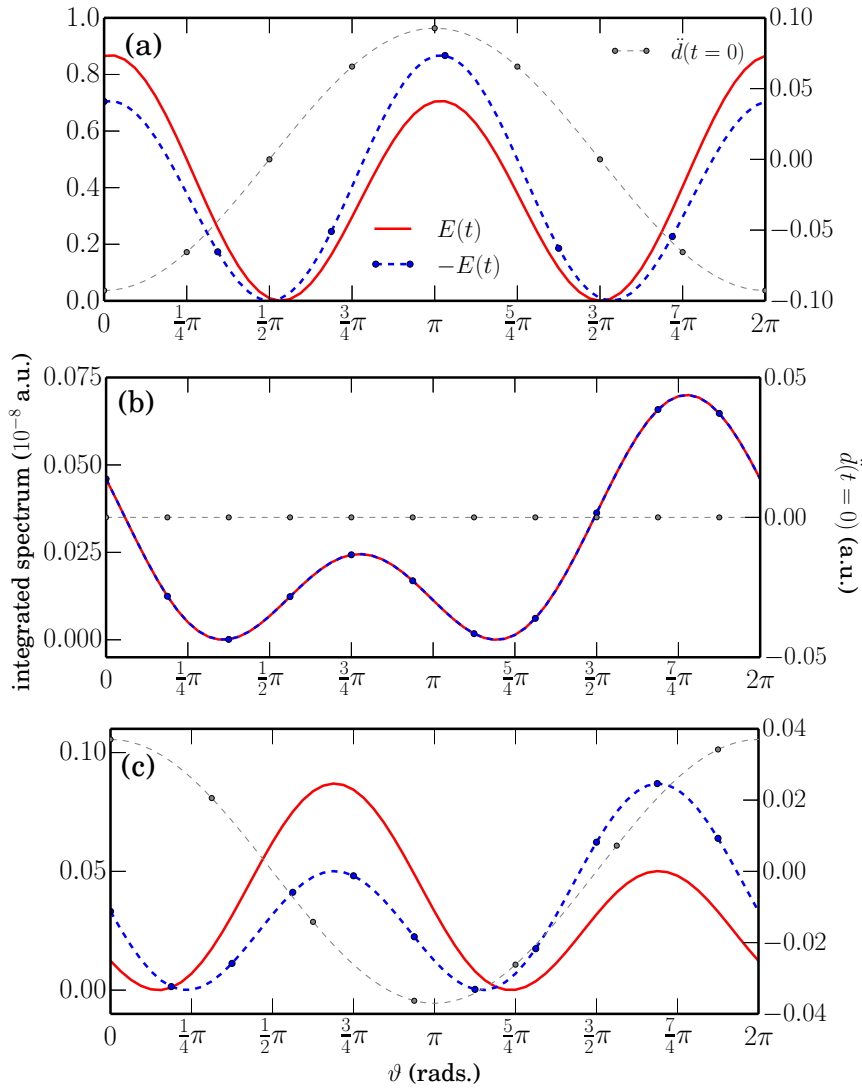


Figure 7.5: Integrated spectrum (red solid and blue dashed curve, left-hand side label), cf. Eq. (7.16), and initial dipole acceleration (grey dotted curve, right-hand side label) as a function of the relative phase  $\theta$  in Eq. (7.17) for initial superpositions of  $|\varphi_0\rangle$  and  $|\varphi_1\rangle$  (a),  $|\varphi_0\rangle$  and  $|\varphi_2\rangle$  (b) and  $|\varphi_0\rangle$  and  $|\varphi_3\rangle$  (c) obtained with driving fields  $E(t)$  (red solid curve) and  $-E(t)$  (blue dashed curve).

superposition. A similarly small improvement is obtained for a superposition involving  $|\varphi_0\rangle$  and  $|\varphi_2\rangle$ . Including up to eight eigenstates in the initial superposition improves the value of the optimization functional (7.16) by 19 per cent compared to the superposition of  $|\varphi_0\rangle$  and  $|\varphi_1\rangle$  with equal weights. This improvement is, however, solely due to the smooth, exponentially decaying region (data not shown), where the harmonic yield is already small.

The role of the phase in the initial superposition is analyzed in Fig. 7.5. It displays the integrated spectrum within the interval  $[\omega_c, 3\omega_c]$  as a function of the relative phase  $\vartheta$  in the superposition

$$|\varphi\rangle = \frac{1}{\sqrt{2}}(|\varphi_0\rangle + e^{i\vartheta}|\varphi_j\rangle) \quad (7.17)$$

for  $j = 1, 2, 3$ . For  $j = 1$ , maxima are found in Fig. 7.5(a) for  $\vartheta \approx \pi/32$  and  $\vartheta \approx 65\pi/64$  which result in the same maximal yield, differing from the yield for  $\theta = 0, 2\pi$  by only

$\approx 0.15$  per cent. In contrast, the minimal yield observed in Fig. 7.5(a) differs by four orders of magnitude.

In order to elucidate the physical origin of the oscillations of the harmonic yield as a function of the relative phase in the initial superposition state, we compare the integrated spectrum (solid red lines in Fig. 7.5(a)) to the initial dipole acceleration (dashed grey line) which is a direct result of the superposition, cf. Eq. (7.15), as explained above. Indeed, the oscillations of the spectral yield as a function of the superposition phase are clearly correlated to the absolute value of the initial dipole acceleration (grey dotted curve). Consider in particular the two initial states  $|\varphi\rangle = (|\varphi_0\rangle \pm |\varphi_1\rangle)/\sqrt{2}$ , i.e.,  $\vartheta = 0$  and  $\vartheta = \pi$ . These states are orthogonal and lead to equal initial dipole accelerations with opposite sign but slightly different spectral yields. This raises the question whether the sign of  $\ddot{d}(t=0)$  determines the maximal value of the harmonic yield. In order to answer this question, we compare the integrated spectrum obtained with driving field  $-E(t)$  to that for  $E(t)$  (blue dashed and red solid lines in Fig. 7.5(a)). The idea is that there is an effective “initial” time which corresponds to the moment  $t_p$  when the driving field starts to become non-zero. The superposition at  $t = 0$  prepares an “initial” wave packet at that time or, classically spoken, the dipole acceleration at  $t = 0$  determines the effective “initial” dipole acceleration at  $t = t_p$ . If HHG depends on both norm and sign of the dipole acceleration at  $t = t_p$ , a symmetric relationship should be found when changing the sign of  $E(t)$  at  $t = t_p$ . This symmetry is indeed observed in Fig. 7.5(a): The harmonic yield obtained with  $\vartheta = \pi$  (giving a positive  $\ddot{d}(0)$ ) and  $-E(t)$ , which matches exactly the yield for  $\vartheta = 0$  (giving a negative  $\ddot{d}(0)$ ) and  $+E(t)$ . Shifting the electric field according to  $E(t - T_s)$  with  $T_s = 2\pi/\omega_{0,1}$  so that  $\ddot{d}_{ff}(t) = \ddot{d}_{ff}(t - T_s)$  does not change the spectral yield (data not shown). This is of course expected for an initial condition at  $t_p - T_s$  that is identical to that at  $t_p$ .

To further investigate the dependence on the initial state, we consider a superposition of eigenstates of the same parity, i.e.,  $|\varphi_0\rangle$  and  $|\varphi_2\rangle$ , cf. Fig. 7.5(b). In fact, because  $\nabla V(r)$  has odd parity, this superposition should lead to a vanishing initial dipole acceleration, cf. Eq. (7.15). Therefore, the harmonic yield obtained with such an initial superposition should not be sensitive to a change of  $E(t)$  to  $-E(t)$ , if the classical picture is still valid. This is indeed observed in Fig. 7.5(b). Similarly, the superpositions with vanishing initial dipole acceleration in Fig. 7.5(a) are also not sensitive to a change of  $E(t)$  to  $-E(t)$ . While for a superposition of  $|\varphi_0\rangle$  and  $|\varphi_1\rangle$ , peaks in the high harmonic yield are found for  $\vartheta = 0$  and  $\vartheta = \pi$ , i.e., for a maximal initial dipole acceleration (in absolute value), such a correlation is not observed for the superposition of  $|\varphi_0\rangle$  and  $|\varphi_2\rangle$ . In this case, the dependence of the high harmonic yield, for example the peak at  $\vartheta = 7\pi/4$ , cannot be explained based on a simple classical argument.

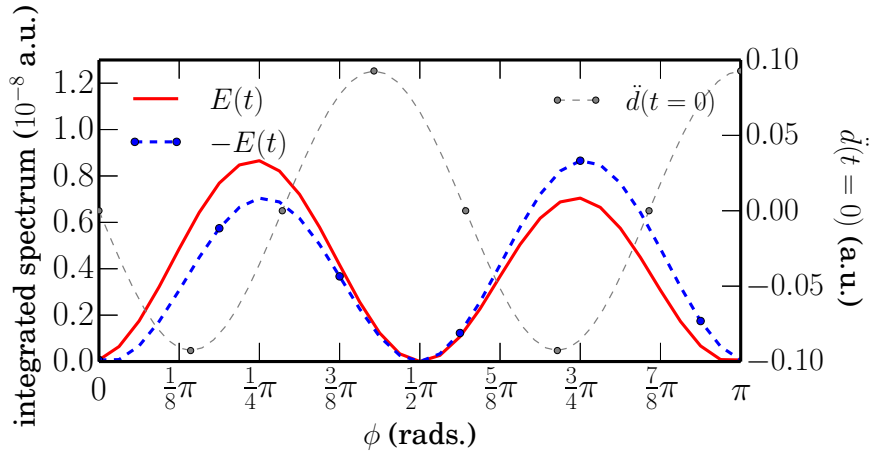


Figure 7.6: Same as Fig. 7.5 but as a function of the relative amplitude of  $|\varphi_0\rangle$  and  $|\varphi_1\rangle$  in the initial superposition state, cf. Eq. (7.18).

Finally, Fig. 7.5(c) displays another example of an initial superposition of even and odd parity states,  $|\varphi_0\rangle$  and  $|\varphi_3\rangle$ . While a similar dependence on the sign of the initial dipole acceleration is observed as in Fig. 7.5(a), in particular when changing the sign of the driving field, there is no one-to-one correlation between the high harmonic yield and the initial dipole acceleration. This shows that not only the initial dipole acceleration contributes to an enhancement of the high harmonic yield, but it also depends on the states involved in such a superposition.

We also consider amplitude control of an initial superposition state. For ease of analysis, we consider a superposition of two field-free eigenstates, which can be expressed as a function of a rotation angle  $\phi$ ,

$$|\varphi\rangle = \cos(\phi)|\varphi_0\rangle + \sin(\phi)|\varphi_1\rangle. \quad (7.18)$$

The high harmonic yield as a function of  $\phi$ , i.e., the relative amplitude of ground and first excited state, is shown in Fig. 7.6. A correlation between the oscillations of the high harmonic yield and the initial dipole acceleration is observed, similar to that found in the dependence on the relative phase. Also, an analogous symmetry when changing the sign of  $E(t)$  is obtained. This shows that the control over the high harmonic yield can equally be achieved by controlling the relative phase or the relative amplitudes in the initial superposition state.

While a coherent superposition of ground and first excited state has earlier been shown to enhance the harmonic yield [185], no phase dependence was found in that study. Our calculations reported above differ from those in Ref. [185] in the spectrum of the Hamiltonian, modeling a hydrogen atom as opposed to a helium ion in which the electron is

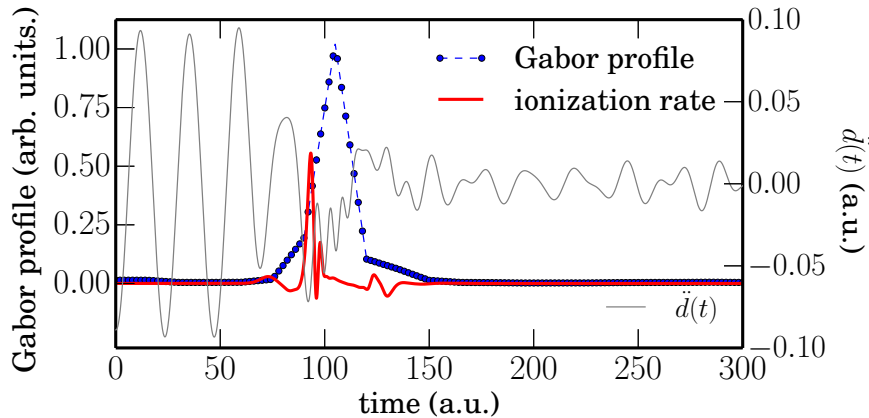


Figure 7.7: Gabor profile of harmonics emitted with  $\omega \in [\omega_c, 3\omega]$  for the initial superposition state  $|\varphi\rangle = (|\varphi_0\rangle + |\varphi_1\rangle)/\sqrt{2}$ . The generation of the high harmonic coincides with the temporal oscillations of the ionization rate, cf. full-red lines (scale not shown), in agreement with the three-step model. The grey line displays the dipole acceleration.

more strongly bound, as well as in the choice of the laser pulse. We have checked the influence of both changes to better understand the origin of the phase dependence. It turns out that, with a different choice of pulse, a dependence of the harmonic yield on the relative phase of the superposition is also observed for the helium ion (data not shown). In contrast, for the pulse considered in Ref. [185], the ionization from the ground state is almost negligible and correspondingly HHG originates from the excited state alone, such that the relative phase becomes irrelevant. The enhancement of the harmonic yield is thus not due to the coherent superposition but rather due to populating the excited state from which it is easier to ionize. Changing the driving field such that both states in the superposition contribute to the ionization turns out to be sufficient to generate a dependence of the harmonic yield on the relative phase. This observation also explains why this phase dependence is more naturally observed in a hydrogen atom where it is more likely that both states participate in ionization (and recollision).

Enhancement of the high harmonic yield due to a purely quantum effect is in contrast to the fact that HHG is usually explained with the three-step model [179], i.e., using a semi-classical picture. We therefore verify whether the three-step model is still valid when starting from a superposition state. To this end, we plot in Fig. 7.7 the temporal Gabor profile of the harmonic yield corresponding to the frequency range above the cutoff and compare it to the ionization probability. The superposition of ground and first excited state, which results in the largest enhancement of the high harmonic yield, cf. Fig. 7.4, is used as initial state. As can be seen from Fig. 7.7, high harmonics are generated during the time interval in which the ionization probability is strongly time-dependent. The

oscillations of the ionization probability (solid red line in Fig. 7.7) indicate that the propagated wavefunction, or part of it, populates the continuum and then returns to the ionic core. This process of ionization and recombination is repeated several times. It is exactly in coincidence with the oscillations in the ionization probability that high harmonics are emitted, as revealed by the peak in the Gabor profile (blue dashed line in Fig. 7.7). We thus find the process of HHG still to be well described by the three-step model, in which semi-classical electron motion leads to the emission of high harmonics [179]. This is in line with earlier findings that coherent control of high harmonic generation reduces to the problem of laser control over classical electron trajectories [23, 184].

## 7.5 Discussion and Conclusions

To conclude, we have developed a highly efficient pseudo-spectral propagation approach for the solution of the time-dependent Schrödinger equation. It relies on the sparse representation of the Hamiltonian matrix in the FE-DVR basis. The coordinate grid is split into  $M$  non-overlapping elements, each of them containing  $N$  collocation points. The FE-DVR basis are defined by means of the cardinal functions based on the Legendre polynomials which are compactly supported on each element. Combined with the Chebyshev propagation formalism, it exploits the efficiency of sparse matrix-vector operations. For an optimal choice of the pseudospectral grid parameters  $N$  and  $M$ , it outperforms the numerical performance of the Dynamical Fourier Grid Method. Optimal pseudospectral grid parameters are obtained by choosing a relatively large total number of grid points, with small number of points per elements ( $N$ ) and large number of elements ( $M$ ), such that the desired accuracy is obtained while minimizing the spectral radius, and thus the CPU time for propagation. Our approach is particularly suitable for problems requiring large grid extension and long propagation times, e.g. calculations involving spectra in photoionization. It can also be employed in multi-dimensional problems where the sparsity of the Hamiltonian representation will be even more important.

We have exploited the numerical efficiency of the pseudospectral propagation approach to investigate the influence of the states involving in a initial coherent superposition of field-free eigenstates for the generation of high order harmonics. We have shown that an initial superposition state may significantly enhance the integrated high harmonic power density, with the relative phase in the superposition controlling the overall yield. In our control scheme, superimposing the lowest two eigenstates with equal weights improves the harmonic yield at the so-called cutoff frequency by one order of magnitude compared to starting from the ground state. Building a superposition between the ground state and a higher excited state does not lead to a further increase of the yield. Equal weights in the

superposition are essentially optimal, and adding more states to the superposition does only increase the yield in the exponentially decaying region of the harmonic spectrum, at the very high frequencies. For a superposition of the two lowest eigenstates, the harmonic yield displays an oscillatory dependence on the relative phase that is clearly connected to the absolute value of the effective initial dipole acceleration. In this case, it is thus straightforward to reconcile the dependence on the relative phase, i.e., a quantum feature, with the semi-classical three-step model. For superpositions involving higher excited states, the effective initial dipole acceleration alone is not sufficient to explain the observed enhancement but the nature of the quantum states making up the superposition matters, too.

Our investigation is complementary to recent demonstrations of coherent control of high harmonic generation that have exploited high lying electronically excited states [186] and nuclear motion [187]. Moreover, our results are in contrast to earlier studies where coherent superposition states were found to extend the high harmonic plateau but no phase dependence was observed [185]. The shift of the harmonic cutoff can be readily attributed to the energy gap between the states making up the superposition [185]. In a semi-classical picture, that type of control can also be rationalized in terms of selecting certain electron paths [188, 189]. Modifications, such as addition of a second color [190, 191] or chirping the fundamental [192, 193], do not change this picture. In fact, these simulations were all carried out for a  $\text{He}^+$  ion, in contrast to our model which mimicks a hydrogen atom. For the helium ion, the difference in the ionization potential of the eigenstates making up the superposition is the key, i.e., the increase in ionization efficiency for the excited compared to the ground state [194]. This is independent of the relative phase in the superposition [185].

The dependence of the high harmonic yield on the relative phase in the initial superposition that we have found points to constructive and destructive interference in the maximization of the dipole acceleration, a hallmark of coherent control. Controlling the harmonic yield by a suitable preparation of the initial state could be realized in an experiment with two pulses, a first pulse that prepares the desired superposition state and a second pulse that drives the harmonic generation. The time delay between the two pulses as well as the Rabi angle produced by the first pulse [195] can be used to adjust the relative phase. To the best of our knowledge, such a strategy has not yet been utilized for maximizing the yield at the cutoff in high harmonic generation.



# Optimal control of photoelectron properties

---

8.1	Introduction and motivations . . . . .	86
8.2	Theoretical background . . . . .	87
8.3	Construction of minimization functionals . . . . .	89
8.3.1	Momentum-resolved photoelectron spectrum . . . . .	89
8.3.2	Angle-resolved photoelectron angular distributions . . . . .	89
8.4	Optimal field constraints . . . . .	90
8.4.1	Propagating electric field . . . . .	91
8.4.2	Electric frequency constraints . . . . .	92
8.4.3	Electric field maximal peak amplitude . . . . .	92
8.5	Krotov's formalism in the framework of wave function splitting method . . . . .	93
8.5.1	Construction of the multi-channel Lagrange multipliers . . . . .	96
8.5.2	Summary of the algorithm . . . . .	99
8.6	Application I: Prescribing the complete photoelectron distribution . . . . .	102
8.7	Application II: Minimizing the probability of emission into the upper hemisphere . . . . .	104
8.8	Application III: Maximizing the difference in the number of electrons emitted into upper and lower hemisphere . . . . .	106
8.8.1	Hydrogen . . . . .	106
8.8.2	Argon . . . . .	112
8.9	Summary of achievements and conclusions . . . . .	117

---

## 8.1 Introduction and motivations

Photoelectron spectroscopy is a powerful tool for studying photoionization in atoms, molecules and solids [196–201]. With the advent of new light sources, photoelectron spectroscopy using intense, short pulses has become available, revealing important information about electron dynamics and time-dependent phenomena [202–205]. In particular, it allows for characterizing the light-matter interaction of increasingly complex systems [196, 198, 200]. Photoelectron spectra (PES) and photoelectron angular distributions (PAD) contain not only fingerprints of the interaction of the electrons with the electromagnetic fields, but also of their interaction and their correlations with each other [137]. PAD in particular can be used to uncover electron interactions and correlations [206, 207].

Tailoring the pulsed electric field in its amplitude, phase or polarization allows to control the coupled electron-nuclear dynamics, with corresponding signatures in the photoelectron spectrum [208–212]. While it is natural to ask how the electron dynamics is reflected in the experimental observables—PES and PAD [208–212], it may also be interesting to see whether one can control or manipulate directly these observables by tailoring the excitation pulse. Moreover, one may be interested in certain features such as directed electron emission without analyzing all the details of the time evolution. This is particularly true for complex systems where it may not be easy to trace the full dynamics all the way to the spectrum. The question that we ask here is how to find an external field that steers the dynamics such that the resulting photoelectron distribution fulfills certain prescribed properties. Importantly, the final state of the dynamics does not need to be known. The desired features may be reflected in the angle-integrated PES, the energy-integrated PAD, or both.

To answer this question, we employ optimal control theory (OCT), using Krotov’s monotonically convergent method [106] and adapting it to the specific task of realizing photoelectron distributions with prescribed features. The photoelectron distributions are calculated within the time-dependent configuration interaction singles scheme (TDCIS) [25], employing the splitting method for extracting the spectral components from the outgoing wavepacket [51, 142]. While OCT has been utilized to study the quantum control of electron dynamics before, in the framework of TDCIS [213] as well as the multi-configurational time-dependent Hartree-Fock (MCTDHF) method [214] or time-dependent density functional theory (TDDFT) [215, 216], the PES and PAD have not been tackled as control targets before. In fact, most previous studies did not even account for the presence of the ionization continuum. A proper representation of the ionization continuum becomes unavoidable [217–221], however, when investigating the interaction with XUV light where a single photon is sufficient to ionize [53], and it is indispensable

for the full description of photoionization experiments.

To demonstrate the versatility of our approach, we apply it to two different control problems: (i) We prescribe the full three-dimensional photoelectron distribution and search for a field that produces, at least approximately, a given angle-integrated PES and energy-integrated PAD. Such a detailed control objective is rather demanding and corresponds to a difficult control problem. (ii) We seek to maximize the relative number of photoelectrons emitted into the upper as opposed to the lower hemisphere, assuming that the polarization axis of the light pulse runs through the poles of the two hemispheres. This implies a condition on the PAD alone, leaving complete freedom to the energy dependence. The corresponding control objective leaves considerable freedom to the optimization algorithm and the control problem becomes much simpler. Maximizing the relative number of photoelectrons emitted into the upper as opposed to the lower hemisphere corresponds to a maximization of the PAD's asymmetry. Asymmetric photoelectron distributions arising in strong-field ionization were studied previously for near-infrared few-cycle pulses where the effect was attributed to the carrier envelope phase [222, 223]. Here, we pose the question whether it is possible to achieve asymmetry in the PAD for multiphoton ionization in the XUV regime and we seek to determine the shaped pulse that steers the electrons into one hemisphere. To ensure experimental feasibility of the optimized pulses, we introduce spectral as well as amplitude constraints. We test our control toolbox for hydrogen and argon atoms, corresponding to a single channel and three active channels, respectively. These comparatively simple examples allow for a complete discussion of our optimization approach, while keeping the numerical effort at an acceptable level.

## 8.2 Theoretical background

This section introduces the many-body formalism and optimization problem that constitute the building blocks of the optimization formalism here developed for the quantum control of specific photoelectron momentum-based observables. Since the fingerprints of the electronic correlations are imprinted in the photoelectron momentum distributions, a many-body approach of the electron dynamics with proper description of the electron-electron correlations becomes unavoidable. In order to fulfill these requirements, we place ourselves in the context of the channel-resolved many-body wave function formalism defined in Section 3.4.2. The multi-channel  $N$ -electron wave function is expanded in the one-particle–one-hole basis

$$|\Psi(t)\rangle = \alpha_0(t)|\Phi_0\rangle + \sum_i \alpha_i|\varphi_i\rangle, \quad (8.1)$$

with  $|\varphi_i(t)\rangle = \sum_a \alpha_i^a(t) |\phi_a\rangle$ , as introduced in Section 3.4.2 and where the index  $i$  denotes an initially occupied orbital,  $a$  stands for a virtual orbital to which the particle can be excited and  $|\Phi_0\rangle$  symbolizes the Hartree-Fock ground state. The  $N$ -electron dynamics is driven by full time dependent Hamiltonian,

$$\hat{H}(t) = \hat{H}_0 + \hat{H}_1 + \hat{\mathbf{p}} \cdot \mathbf{A}(t), \quad (8.2)$$

where  $\hat{H}_0 = \hat{T} + \hat{V}_{\text{nuc}} + \hat{V}_{\text{MF}} - E_{\text{HF}}$  contains the kinetic energy  $\hat{T}$ , the nuclear potential  $\hat{V}_{\text{nuc}}$ , the potential at the mean-field level  $\hat{V}_{\text{MF}}$  and the Hartree-Fock energy  $E_{\text{HF}}$ .  $\hat{H}_1 = \frac{1}{|r_{12}|} - \hat{V}_{\text{MF}}$  describes the Coulomb interactions beyond the mean-field level, and  $\hat{\mathbf{p}} \cdot \mathbf{A}(t)$  is the light-matter interaction within the velocity form in the dipole approximation, assuming linear polarization.

The optimization problem is to find a control vector potential,  $\mathbf{A}_{\text{opt}}(t)$ , that steers the system from a given ground state  $|\Psi(t=0)\rangle = |\Phi_0\rangle$ , defined in Eq. (8.1), to **an unknown final state**  $|\Psi_{\text{opt}}(T)\rangle$  whose **PES** and/or **PAD** display certain desired features. It is worth mentioning that the most well studied problem in OCT concerns state-to-state transitions [105], whereby the task to be accomplished is to find the control field that allows to reach a prescribed final state  $|\Psi_{\text{opt}}(T)\rangle$ , at the end of the propagation. However, in our context, the state  $|\Psi_{\text{opt}}(T)\rangle$ , which displays the desired PES/PAD is not known. To the best of our knowledge, such a *implicit-in-state* optimization problem has not been tackled by the quantum optimal control theory community before. Furthermore, the backward propagation of the Lagrange-multiplier needs to be reviewed since the splitting protocol, cf. Section 6.1, needs to be taken into account while solving the time-dependent Schrödinger equation in forward and backward directions in time.

Finally, we construct the optimization functionals that will allow us to manipulate specific properties of the photoelectron momentum distributions. These are fully characterized by the asymptotic part of the propagated wave function evaluated long time after the pulse is over. *A priori*, these optimization functionals may be expressed mathematically as **final-time cost functionals**  $J_T[\varphi(T), \varphi^\dagger(T)]$  [106], where  $\varphi(T)$  refers to the wave packet evaluated at the end of the propagation, i.e. at  $t = T$ . However, in the context of the channel-resolved wave function splitting method, cf. Section 6.1, the inner part of the propagated wave packet evaluated at  $t = T$  does not contribute to the photoelectron spectrum. Only the asymptotic part contained in the *“outer parts”* of the wave packet, originating at every splitting time  $t_j$  and evaluated at  $t = T$  do contribute to the photoelectron momentum distribution. Therefore, the final-time cost functional to be minimized uniquely depends on the *“asymptotic states”*  $\tilde{\varphi}_{i,\text{out}}(T - t_j)$ , where the index  $i$  refers to the channel from which it originates, and where the difference  $T - t_j$  determines the *Volkov*

*phase* that the each outer part of the wave packet accumulates, from the splitting time  $t_j$  to the final time  $T$ . In this context, the optimization problem reads,

$$\arg \min_{\mathbf{A} \in \mathcal{U}} J_T[\tilde{\varphi}_{i,\text{out}}, \tilde{\varphi}_{i,\text{out}}^\dagger], \quad (8.3)$$

with  $\tilde{\varphi}_{i,\text{out}}$  is defied in Eq. (6.9) in Section 6.2, and where  $\mathcal{U}$  refers to the space of admissible solutions, i.e, specific constraints that the vector potential  $\mathbf{A}(t)$ , or its counterpart electric field  $\mathbf{E}(t)$  must fulfill, such as maximal amplitude, frequency components and smoothness.

It is worth mentioning that since the dynamics is not constrained, this is, the functional to be minimized depends only on the final time  $T$  and not on intermediate times, solution of Eq. (8.3) serves as a powerful tool to interpret the electron dynamics and thus to infer the physical mechanisms to achieve the desired photoelectron feature. It allows not only to understand the physical mechanisms of enhancement of a given observable, but also to find news, sometimes unexpected mechanisms.

## 8.3 Construction of minimization functionals

### 8.3.1 Momentum-resolved photoelectron spectrum

In terms of photoelectron momentum-based observables, we seek first to prescribe the full photoelectron distribution in momentum space. Such an choice is strongly motivated by experimental works in the field of 3D photoelectron momentum distributions reconstruction techniques, based on inverse Abel transforms[224–226], slice imaging [227], time-resolved event counting [228–230] and by tomographic reconstruction [231, 232].

In mathematical therms, final time cost functional to be minimized is defined as

$$J_T^{(1)}[\tilde{\varphi}_{\text{out}}(T), \tilde{\varphi}_{\text{out}}^\dagger(T)] = \lambda_1 \int (\tilde{\sigma}(\mathbf{p}, T) - \tilde{\sigma}_0(\mathbf{p}))^2 d^3p, \quad (8.4)$$

where  $\tilde{\sigma}(\mathbf{p}, T) = d^2\sigma(\mathbf{p})/dp d\Omega$  denotes the actual photoelectron distribution, cf. Eq. (6.10a),  $\tilde{\sigma}_0(\mathbf{p})$  stands for the target distribution, and  $\lambda_1$  is a weight that stresses the importance of  $J_T^{(1)}[\tilde{\varphi}_{\text{out}}, \tilde{\varphi}_{\text{out}}^\dagger]$  compared to additional terms in the total optimization functional. The goal is thus to minimize the squared Euclidean distance between the actual and the desired photoelectron distributions.

### 8.3.2 Angle-resolved photoelectron angular distributions

Alternatively, we would like to control the difference in the number of electrons emitted into the lower and upper hemispheres. This can be expressed via the following final-time

functional

$$\begin{aligned}
J_T^{(2)}[\tilde{\varphi}_{\text{out}}(T), \tilde{\varphi}_{\text{out}}^\dagger(T)] &= \lambda_2^{(-)} \int_{\pi/2}^{\pi} \sin \theta d\theta \int_0^{+\infty} |\tilde{\varphi}_{\text{out}}(\mathbf{p}, T)|^2 p^2 dp \\
&+ \lambda_2^{(+)} \int_0^{\pi/2} \sin \theta d\theta \int_0^{+\infty} |\tilde{\varphi}_{\text{out}}(\mathbf{p}, T)|^2 p^2 dp \quad (8.5) \\
&+ \lambda_2^{\text{tot}} \int_0^{\pi} \sin \theta d\theta \int_0^{+\infty} |\tilde{\varphi}_{\text{out}}(\mathbf{p}, T)|^2 p^2 dp,
\end{aligned}$$

where the first and second term correspond to the probability of the photoelectron being emitted into the lower and upper hemisphere, whereas the third term is the total ionization probability.  $\lambda_2^{(-)}$ ,  $\lambda_2^{(+)}$  and  $\lambda_2^{\text{tot}}$  are weights. The factor of  $2\pi$  resulting from integration over the azimuthal angle has been absorbed into the weights. Directed emission can be achieved in several ways—one can suppress the emission of the photoelectron into the lower hemisphere, without imposing any specific constraint on the number of electrons emitted into the upper hemisphere. This is achieved by choosing  $\lambda_2^{(+)} = \lambda_2^{\text{tot}} = 0$  and  $\lambda_2^{(-)} > 0$ . Alternatively, one can maximize the difference in the number of electrons emitted into the upper and lower hemispheres. To this end, the relative weights need to be chosen such that  $\lambda_2^{(-)} > 0$  and  $\lambda_2^{(+)} < 0$ . If  $\lambda_2^{\text{tot}} = 0$ , the optimization seeks to increase the *absolute* difference in the number of electrons emitted into the upper and lower hemisphere. Close to an optimum, this may result in a strong increase in the overall ionization probability, accompanied by a very small increase in the difference, since only the complete functional is required to converge monotonically, and not each of its parts. This undesired behavior can be avoided by maximizing the relative instead of the absolute difference of electrons emitted into the upper and lower hemispheres. It requires  $\lambda_2^{\text{tot}} > 0$ , i.e., minimization of the total ionization probability in addition to maximizing the difference. Note that  $\lambda_2^{\text{tot}}$  could also be absorbed into the weights for the hemispheres,

$$\begin{aligned}
J_T^{(2)}[\tilde{\varphi}_{\text{out}}(T), \tilde{\varphi}_{\text{out}}^\dagger(T)] &= \lambda_{\text{eff}}^{(-)} \int_{\pi/2}^{\pi} \sin \theta d\theta \int_0^{+\infty} |\tilde{\varphi}_{\text{out}}(\mathbf{p}, T)|^2 p^2 dp \quad (8.6) \\
&+ \lambda_{\text{eff}}^{(+)} \int_0^{\pi/2} \sin \theta d\theta \int_0^{+\infty} |\tilde{\varphi}_{\text{out}}(\mathbf{p}, T)|^2 p^2 dp,
\end{aligned}$$

where  $\lambda_{\text{eff}}^{(+)} = -|\lambda_2^{(+)}| + |\lambda_2^{\text{tot}}|$  and  $\lambda_{\text{eff}}^{(-)} = |\lambda_2^{(-)}| + |\lambda_2^{\text{tot}}|$  are effective weights. Since  $\lambda_{\text{eff}}^{(+)} < 0$  and  $\lambda_{\text{eff}}^{(-)} > 0$  in order to maximize (minimize) emission into the upper (lower) hemisphere, the weights need to fulfill the condition  $|\lambda_2^{(+)}| > |\lambda_2^{\text{tot}}|$ .

## 8.4 Optimal field constraints

In Eq. (8.3),  $\mathcal{U}$  designates the space of feasible solutions. The latter refers to the space of all possible forms for the optimal field, characterized by specific constraints that all

possible candidates in  $\mathcal{U}$  fulfills. If constraints on the driving control are required, the functional as defined in Eq. (8.3) needs to be extended to account for these eventual constraints. This is performed by adding the so-called penalty functionals [106]. The complete functional, that also takes into account eventual constraints imposed on the eventual optimized field, to be minimized reads,

$$J = J_T[\tilde{\varphi}_{\text{out}}(T), \tilde{\varphi}_{\text{out}}^\dagger(T)] + C[\mathbf{A}], \quad (8.7)$$

where the functional  $C[\mathbf{A}]$  are written in terms of the constraints to ensure that the control fulfills the desired restrictions. The constraints may be written for the electric field  $\mathbf{E}(t)$  associated with the vector potential  $\mathbf{A}(t)$ , even though the minimization problem is expressed in terms of  $\mathbf{A}(t)$  and the dynamics is generated by  $\hat{H}[\mathbf{A}]$ , cf. Eq. (8.2).

Among these constraints, the present work focused on three main properties that the vector potential  $\mathbf{A}(t)$ , or its corresponding electric field  $\mathbf{E}(t)$  must fulfill, such that the resulting optimized field may be experimentally reproduced. These concerns the maximal peak amplitude, frequency components and smoothness of the driven electric field.

Because constraints are usually applied to the electric field, an additional step is required to write such constraints in terms of the vector potential instead. To this end, we merely make use of the relation between the vector potential  $\mathbf{A}(t)$  and the electric field  $\mathbf{E}(t)$ , given by

$$\mathbf{A}(t) = - \int_{t_0}^t \mathbf{E}(\tau) d\tau. \quad (8.8)$$

with  $\mathbf{A}(t_0) = \mathbf{0}$ . Without loss of generality, we can write

$$C[\mathbf{A}] = C_a[\mathbf{A}] + C_\omega[\mathbf{A}] + C_e[\mathbf{A}], \quad (8.9)$$

where the independent terms in the rhs. of Eq. (8.9) are described in detail in Sections 8.4.3, 8.4.2 and 8.4.3, respectively.

### 8.4.1 Propagating electric field

The first property that the optimized electric field must fulfill is that its integral over time vanishes, i.e.,

$$\int_{t_0}^T \mathbf{E}(t) dt = 0, \quad (8.10)$$

which implies, according to Eq. (8.8),  $\mathbf{A}(T) = \mathbf{A}(t_0) = 0$ . Therefore, we choose initial guess fields with  $\mathbf{A}(T) = \mathbf{A}(t_0) = 0$  and utilize

$$C_a[\mathbf{A}] = \lambda_a \int s^{-1}(t) (\mathbf{A}(t) - \mathbf{A}_{\text{ref}}(t))^2 dt \quad (8.11)$$

with  $s(T) = 0$  to ensure that Eq. (8.10) is fulfilled. In Eq. (8.11),  $\mathbf{A}_{\text{ref}}(t)$  and  $s(t)$  refer to a reference vector potential and a shape function, respectively, and  $\lambda_a \geq 0$  is a weight that stresses the importance of  $C_a[\mathbf{A}]$  compared to all other terms in the complete functional, Eq. (8.7). The shape function,  $s(t)$ , can be used to guarantee that the control is smoothly switched on and off at the initial and final times.

### 8.4.2 Electric frequency constraints

Alternatively, another important property of the optimized field concerns a limited spectral bandwidth. As a rule of thumb, optimization without spectral constraints leads to pulses with unnecessarily broad spectra, making their experimental realization very hard or literally impossible. In order to restrict the bandwidth of the electric field,  $\mathbf{E}(t)$ , a penalty functional  $C_\omega[\mathbf{A}]$  in frequency domain is constructed, namely

$$C_\omega[\mathbf{A}] = \lambda_\omega \int \tilde{\gamma}(\omega) |\tilde{\mathbf{E}}(\omega)|^2 d\omega \equiv \lambda_\omega \int \tilde{\gamma}(\omega) \omega^2 |\tilde{\mathbf{A}}(\omega)|^2 d\omega, \quad (8.12)$$

with  $\tilde{\mathbf{E}}(\omega)$  being the Fourier transform of the field,

$$\tilde{\mathbf{E}}(\omega) = \int \mathbf{E}(t) e^{-i\omega t} dt. \quad (8.13)$$

It worth mentioning that constraints-based functional of the form of Eq. (8.12) were previously discussed in Refs. [233, 234]: The kernel  $\tilde{\gamma}(\omega)$  plays a role similarly to the inverse shape function  $s^{-1}(t)$  in Eq. (8.11), that is, it takes large values at all undesired frequencies. Additionally, we assume that the symmetry requirement  $\tilde{\gamma}(\omega) = \tilde{\gamma}(-\omega)$  is fulfilled, see Appendix B for details.

### 8.4.3 Electric field maximal peak amplitude

Constraining the maximal peak amplitude of the optimized field to reasonable values is, for evident reasons of experimental feasibility, a key criteria. Due to the relation defined in Eq. (8.8), we construct a constraint that penalizes changes in the first time derivative of  $\mathbf{A}(t)$ . In fact, since  $\mathbf{E}(t) = -\dot{\mathbf{A}}(t)$ , large values in the derivative of the vector potential translate into large amplitudes of the corresponding electric field  $\mathbf{E}(t)$ . To avoid this, we

adopt here a modified regularization condition [235] for  $\mathbf{A}(t)$ , defining

$$C_e[\mathbf{A}] = \lambda_e \int s^{-1}(t) |\mathbf{E}(t)|^2 dt \equiv \lambda_e \int s^{-1}(t) |\dot{\mathbf{A}}(t)|^2 dt.$$

$C_e[\mathbf{A}]$  plays the role of a penalty functional [235], ensuring the regularity of  $\mathbf{A}(t)$ , and, as a consequence, penalizing large values on the electric field amplitude  $\mathbf{E}(t)$ . The choice of the same  $s^{-1}(t)$  in both Eq. (8.11) and Eq. (8.14) will simplify the optimization algorithm as shown below.

## 8.5 Krotov's formalism in the framework of wave function splitting method

Krotov's optimization method for quantum optimal control provides a recipe to construct monotonically convergent optimization algorithms, depending on the type of equation of motion, the target functionals and additional constraints, as well as on the power of the control in the light-matter interaction [106]. The state-of-the-art optimization algorithm consists of a set of coupled equations for the update of the control. Such equations concerns the forward propagation of the state and the backward propagation of the so-called co-state or Lagrange multiplier. This set of equations needs to be solved iteratively. The final-time target functional (or, more precisely, its functional derivative with respect to the propagated state, evaluated at the final time, which reflects the extremum condition on the optimization functional [236]) determines the "initial" condition, at final time, for the backward propagation of the Lagrange multiplier [106]. Additional constraints which depend on the control such as those in Eq. (8.9) appears in the update equation for the control [106, 234] to take into account such a constraints.

The challenge when combining Krotov's method with the wave function splitting approach is due to the fact that splitting in the forward propagation of the state implies "glueing" in the backward propagation of the co-state. We recall, given the Hamiltonian into consideration, the time-dependent Lagrange multiplier is obtained by solving the Schrödinger equation backwards in time, plus, a "glueing" procedure, in the wave function splitting formalism. Here, we present an extension of the optimization algorithm obtained with Krotov's method that takes the splitting procedure into account.

The prescription for monotonically updating the field is given in Refs. [106, 234]. In our context, such an update reads, with  $k$  labeling the iteration step,

$$\mathbf{A}^{(k+1)}(t) = \mathbf{A}^{(k)}(t) + I^{(k+1)}(t) - \frac{\tilde{\lambda}_\omega}{\lambda_a} s(t) \mathbf{A}^{(k+1)} \star h(t) + \frac{\lambda_e}{\lambda_a} \ddot{\mathbf{A}}^{(k+1)}(t), \quad (8.14a)$$

with  $\tilde{\lambda}_\omega = \sqrt{2\pi}\lambda_\omega$ .  $\mathbf{A}^{(k+1)} \star h(t)$  denotes the convolution of  $\mathbf{A}^{(k+1)}$  and  $h(t)$ ,

$$\mathbf{A}^{(k+1)} \star h(t) = \int \mathbf{A}^{(k+1)}(\tau) h(t - \tau) d\tau \quad (8.14b)$$

with  $h(t)$  the inverse Fourier transform of  $\tilde{h}(\omega) = \omega^2 \tilde{\gamma}(\omega)$ . The second term in Eq. (8.14a) is given by

$$\begin{aligned} I^{(k+1)}(t) &= \frac{s(t)}{\lambda_a} \Im \left\{ \left\langle \chi^{(k)}(t) \left| \frac{\partial \hat{H}}{\partial \mathbf{A}} \right| \Psi^{(k+1)}(t) \right\rangle \right\} \\ &= \frac{s(t)}{\lambda_a} \Im \left\{ \langle \chi^{(k)}(t) | \hat{\mathbf{p}} | \Psi^{(k+1)}(t) \rangle \right\}, \end{aligned} \quad (8.14c)$$

where  $|\Psi^{(k+1)}(t)\rangle$  and  $|\chi^{(k)}(t)\rangle$  denote the forward propagated state and backward propagated co-state at iterations  $k + 1$  and  $k$ , respectively and  $\Im\{z\}$  the imaginary part of the argument  $z$ . The explicit derivation of Eqs. (8.14) is fully detailed in Appendix B.

If  $\lambda_\omega = \lambda_e = 0$ , the implicitness of Eq. (8.14) in  $\mathbf{A}^{(k+1)}(t)$  can easily be circumvented by a numerically cheap and stable zeroth-order solution, following the prescription given in [236]. However, for  $\lambda_\omega \neq 0$ , Eq. (8.14) corresponds to a second order Fredholm equation with inhomogeneity  $I^{(k+1)}(t)$  [234]. Numerical solution, although relatively expensive in terms of CPU times, is possible using, for example, the method of degenerate kernels [234]. This is achieved, by first approximating to zeroth order the inhomogeneity  $I^{(k+1)}(t)$ , which depends on  $|\varphi^{(k+1)}(t)\rangle$  and thus on  $\mathbf{A}^{(k+1)}(t)$ . Such approximation is assumed to solve Eq. (8.14) with  $\lambda_\omega = 0$  in the first place that is, without frequency constraints; and the resulting approximation  $I_0^{(k+1)}(t)$  is then used to solve the Fredholm equation. While an iterative procedure to improve the approximation of  $I^{(k+1)}(t)$  may be conceivable, the zeroth order approximation is in practice, sufficient for conserving stability and monotonic convergence of the functional [233, 234].

However, such approach, based on the solution of the Fredholm equation in time domain, may result in a relatively time-consuming approach, in particular when the propagation involves large number of propagation steps. In order to improve the numerical efficiency, we adopt a slightly different procedure, in the sense that the Fredholm equation is not solved in time domain but in frequency domain. This allows us to treat the cases  $\lambda_\omega \neq 0$  and  $\lambda_e \neq 0$  on the same footing. Such procedure can be made possible by assuming that  $s(t)$  in Eqs. (8.11) and (8.14) rises and falls off very quickly at the beginning and end of the optimization time interval. This judicious choice of  $s(t)$  together with the fact that the Fourier transform of a convolution of two functions in time domain, as encountered

in Eq. (8.14), is the product of the functions in frequency domain, allows to approximate

$$\left| \int s(t) \Gamma^{(k+1)}(t) e^{-i\omega t} dt - S_0 \int \Gamma^{(k+1)}(t) e^{-i\omega t} dt \right| \leq \epsilon, \quad (8.15)$$

where  $\epsilon$  is a small, positive number and  $\Gamma^{(k+1)}(t)$  is defined as

$$\Gamma^{(k+1)}(t) = \mathbf{A}^{(k+1)} \star h(t). \quad (8.16)$$

A possible choice for  $s(t)$  to fulfill the condition (8.15) is

$$s(t) = e^{-\beta((t-t_c)/2\sigma)^{2n}}, \quad (8.17)$$

where  $\sigma$  refers to the duration of the pulse centered at  $t = t_c$ . If Eq. (8.15) is satisfied, we can easily take the Fourier transform of both sides of Eq. (8.14a) to get

$$\tilde{\mathbf{A}}^{(k+1)}(\omega) = \frac{\tilde{\mathbf{A}}^{(k)}(\omega) + \tilde{I}^{(k+1)}(\omega)}{1 + \frac{\tilde{\lambda}_\omega}{\lambda_a} \omega^2 \tilde{\gamma}(\omega) + \frac{\lambda_e}{\lambda_a} \omega^2} \quad (8.18a)$$

with  $\mathbf{A}^{(k+1)}(t) = \int \tilde{\mathbf{A}}^{(k+1)}(\omega) e^{+i\omega t} d\omega / \sqrt{2\pi}$ . Note that Eq. (8.18a) becomes exact if  $s(t)$  is constant. Approximating  $\tilde{I}^{(k+1)}(\omega)$  by its zeroth order solution analogously to Ref. [234], Eq. (8.18a) can be expressed as

$$\tilde{\mathbf{A}}^{(k+1)}(\omega) = \tilde{G}(\omega) \tilde{\mathbf{A}}_0^{(k+1)}(\omega), \quad (8.18b)$$

where  $\tilde{\mathbf{A}}_0^{(k+1)}(\omega)$  is the zeroth order solution of the updated control, found by solving Eq. (8.14) with  $\lambda_\omega = \lambda_e = 0$ ,

$$\tilde{\mathbf{A}}_0^{(k+1)}(\omega) = \tilde{\mathbf{A}}^{(k)}(\omega) + \tilde{I}_0^{(k+1)}(\omega), \quad (8.18c)$$

and  $\tilde{G}(\omega)$  is a transfer function given by

$$\tilde{G}(\omega) = \left( 1 + \frac{\lambda_\omega}{\lambda_a} \omega^2 \tilde{\gamma}(\omega) + \frac{\lambda_e}{\lambda_a} \omega^2 \right)^{-1}. \quad (8.18d)$$

Thence, the first order approximation is obtained by (i) updating the control with  $\lambda_\omega = \lambda_e = 0$ , (ii) Fourier transforming it to frequency domain, then (iii) filtering it by means of the transfer function  $\tilde{G}(\omega)$  defined in Eq. (8.18b) and finally Fourier transforming it back to time-domain to propagate the ground state and thus complete the iteration step.

### 8.5.1 Construction of the multi-channel Lagrange multipliers

Finally, in order to evaluate the update defined in Eqs. (8.14), it is required to construct the time-dependent Lagrange multiplier, at the previous iteration,  $|\chi^{(k)}(t)\rangle$ , which is obtained by backward propagation using the old control,  $\mathbf{A}^{(k)}(t)$ . The equation of motion for the Lagrange multiplier is [106]

$$i \frac{\partial}{\partial t} |\chi(t)\rangle = \hat{H}(t) |\chi(t)\rangle. \quad (8.19a)$$

In the context of the multi-channel many-body wavefunction formalism  $|\Psi(t)\rangle$  is decomposed into channels wavefunctions, cf. Eqs. (8.1) and (3.28). The same channel-revolved structure applies to the Lagrange multiplier. The ‘‘initial’’ condition at the final time  $T$  is written separately for each channel,

$$|\tilde{\chi}_{i,\text{out}}(T)\rangle = - \frac{\partial J_T[\tilde{\varphi}_{i,\text{out}}(T), \tilde{\varphi}_{i,\text{out}}^\dagger(T)]}{\partial \langle \tilde{\varphi}_{i,\text{out}}(T) |}. \quad (8.19b)$$

Evaluation of Eq. (8.19b) requires knowledge of the outer part of each channel wavefunction,  $|\tilde{\varphi}_{i,\text{out}}(T)\rangle$ , which is obtained by forward propagation of the initial state, including the splitting procedure.

Defining  $\hat{U}(t', \tau; \mathbf{A}(t))$  as the evolution operator that propagates a given state from time  $t = \tau$  to  $t = t'$  under the control  $\mathbf{A}(t)$ , we make the distinction between the time evolution operators for the inner part,  $\hat{U}_F(t', \tau; \mathbf{A}(t))$ , generated by the full Hamiltonian, Eq. (8.2), and affecting only the outer parts,  $\hat{U}_V(t', \tau; \mathbf{A}(t))$ , which is generated by the Volkov Hamiltonian, Eq. (6.3). Thus, for every channel wave function, the total wave function for forward propagated wave packet reads,

$$|\varphi_i^{(k+1)}(t)\rangle = |\varphi_{i,\text{in}}^{(k+1)}(t)\rangle + |\tilde{\varphi}_{i,\text{out}}^{(k+1)}(t)\rangle, \quad (8.20)$$

which is valid for arbitrary times  $t \geq t_1$  with  $t_1$  the first splitting time.

Within the context of the wave function splitting method, it is natural to define second term in Eq. (8.20) as

$$\begin{aligned} |\tilde{\varphi}_{i,\text{out}}^{(k+1)}(t)\rangle &= \sum_{j=1}^{\lfloor t/t_1 \rfloor} |\varphi_{i,\text{out}}^{(k+1)}(t; t_j)\rangle \\ &\equiv \sum_{j=1}^{\lfloor t/t_1 \rfloor} \hat{U}_V(t, t_j; \mathbf{A}^{(k+1)}) |\varphi_{i,\text{out}}^{(k+1)}(t_j)\rangle \end{aligned} \quad (8.21)$$

with  $\lfloor x \rfloor = \max\{m \in \mathbb{Z}, m \leq x\}$ . Equation (8.21) accounts for the fact that for  $t \geq t_2$ ,

all outer parts  $|\varphi_{i,\text{out}}^{(k+1)}(t; t_j)\rangle$  that originate at splitting times  $t_j \leq t$  must be added up coherently.

Subsequent propagation of the liberated photoelectron, represented by all  $|\varphi_{i,\text{out}}^{(k+1)}(t; t_j)\rangle$  and iterative propagation and splitting of the inner components  $|\varphi_{i,\text{in}}^{(k+1)}(t)\rangle$  eventually yields the state at final time,  $|\varphi_i^{(k+1)}(T)\rangle$ . Its outer part is determined by the contribution to the continuum, upon application of the splitting operator, namely

$$|\tilde{\varphi}_{i,\text{out}}^{(k+1)}(T)\rangle = \sum_{j=1}^N |\varphi_{i,\text{out}}^{(k+1)}(T; t_j)\rangle, \quad (8.22)$$

with  $N$  denoting the total number of splitting times utilized during propagation, and where the last splitting time  $t_N$  is chosen such that  $t_N \leq T$ . It is to mention that the parameters defining the splitting operator must be judiciously chosen to reach convergence when evaluating the observable. The best compromise between size of the spatial grid, time step and duration between two consecutive splitting times is discussed in Ref. [51].

Equation (8.19b) can now be evaluated: Since our final time functionals all involve the product  $\tilde{\varphi}_{\text{out}}(\mathbf{p}, T) \cdot \tilde{\varphi}_{\text{out}}^*(\mathbf{p}, T) = \sigma(\mathbf{p}, T)$ , Eq. (8.19b) can be written, at the  $k$ th iteration of the optimization, as

$$\tilde{\chi}_{i,\text{out}}^{(k)}(\mathbf{p}, T) = \mu(\mathbf{p}) \tilde{\varphi}_{i,\text{out}}^{(k)}(\mathbf{p}, T), \quad (8.23a)$$

where  $\mu(\mathbf{p})$  is a function that depends on the target functional under consideration. It becomes

$$\mu_1^{(k)}(\mathbf{p}) = -2\lambda_1 \left( \tilde{\sigma}^{(k)}(\mathbf{p}, T) - \tilde{\sigma}_0(\mathbf{p}) \right) \quad (8.23b)$$

for  $J_T^{(1)}$  given in Eq. (8.4) and

$$\mu_2(\mathbf{p}) = \lambda_2^- \mathbb{1}_{\vartheta_-}(\theta) + \lambda_2^+ \mathbb{1}_{\vartheta_+}(\theta) \quad (8.23c)$$

for  $J_T^{(2)}$  given in Eq. (8.5). The intervals  $\vartheta_- = [\pi/2, \pi]$  and  $\vartheta_+ = [0, \pi/2]$  denote the lower and upper hemispheres, respectively, and  $\mathbb{1}_{\vartheta_{\pm}}(\theta)$  is the characteristic function on a given interval,

$$\mathbb{1}_{\vartheta_{\pm}}(\theta) = \begin{cases} 1 & \text{if } \theta \in \vartheta_{\pm} \\ 0 & \text{if } \theta \notin \vartheta_{\pm} \end{cases}$$

with  $\theta \in [0, \pi]$  the polar angle with respect to the polarization axis. Since the functionals defined in Eq. (8.4) and Eq. (8.6) depend only on the final time  $T$  but not on intermediate-times, the backward propagated co-state  $|\chi(t)\rangle$  follows the same equation of motion as the forward propagated  $|\Psi(t)\rangle$  state [106]. For that reason, and analogous to  $|\Psi(t)\rangle$ , it is

convenient to define inner and outer parts of  $|\chi(t)\rangle$ , namely

$$|\chi_i^{(k)}(t)\rangle = |\chi_{i,\text{in}}^{(k)}(t)\rangle + |\tilde{\chi}_{i,\text{out}}^{(k)}(t)\rangle. \quad (8.24a)$$

with

$$|\tilde{\chi}_{i,\text{out}}^{(k)}(T)\rangle = \sum_{j=1}^N |\chi_{i,\text{out}}^{(k)}(T; t_j)\rangle. \quad (8.24b)$$

Eq. (8.24b) implies that also  $|\tilde{\chi}_{i,\text{out}}^{(k)}(T)\rangle$  is obtained by coherently summing up the contributions from all splitting times.

Conversely, the outer part of the co-state originating at the splitting time  $t_j$  and evaluated at the same time is given by

$$\chi_{i,\text{out}}^{(k)}(\mathbf{p}, t_j; t_j) = \mu(\mathbf{p})\varphi_{i,\text{out}}^{(k)}(\mathbf{p}, t_j; t_j). \quad (8.25)$$

The next step is to construct the total co-state at an arbitrary time  $t$ ,  $|\chi_i^{(k)}(t)\rangle$ , required in Eq. (8.14), from all  $|\chi_{i,\text{out}}^{(k)}(t_j; t_j)\rangle$  using Eq. (8.25). This is achieved by backward propagation and “glueing” inner and outer parts, as opposite to “splitting” during the forward propagation. However, when reconstructing the co-state by backward propagation, care should be taken to not to perform the “glue” procedure twice or more, at a given splitting time. **The backward propagation of the co-state is explicitly explained in what follows:** Since at the final time  $T$ , the total co-state is given by a coherent superposition of all outer parts originating at the splitting times  $t_j$ , cf. Eq. (8.24b), it suffices to store all  $|\varphi_{i,\text{out}}^{(k)}(t_j; t_j)\rangle$  and apply Eq. (8.25) to evaluate  $|\chi_{i,\text{out}}^{(k)}(t_j; t_j)\rangle$ . We recall that  $|\chi_{i,\text{out}}^{(k)}(t_j; t_j)\rangle$ , respectively  $|\phi_{i,\text{out}}^{(k)}(t_j; t_j)\rangle$ , denote the outer part born exclusively at  $t = t_j$  and evaluated at the same splitting time. Once all outer parts of the co-state are evaluated at every splitting time using Eq. (8.25),  $|\chi_i^{(k)}(t)\rangle$  is obtained for all times  $t$  by backward propagation and “glueing”, with the additional care of not “glueing” twice or more. In detail,  $|\chi_{i,\text{out}}^{(k)}(t_N; t_N)\rangle$  is propagated backwards from  $t_N$  to  $t_{N-1}$  using the full CIS Hamiltonian,  $\hat{H}$ , cf. Eq. (8.2). The resulting wave function at  $t = t_{N-1}$  is  $|\chi_{i,\text{in}}^{(k)}(t_{N-1})\rangle$ . The outer part born exclusively at the splitting time  $t = t_{N-1}$  is obtained using Eq. (8.25), and the “composite” wave function  $|\chi_i^{(k)}(t_{N-1})\rangle$  is obtained by “glueing”  $|\chi_{i,\text{in}}^{(k)}(t_{N-1})\rangle$  and  $|\chi_{i,\text{out}}^{(k)}(t_{N-1}; t_{N-1})\rangle$ ,

$$|\chi_i^{(k)}(t_{N-1})\rangle = |\chi_{i,\text{in}}^{(k)}(t_{N-1})\rangle + |\chi_{i,\text{out}}^{(k)}(t_{N-1}; t_{N-1})\rangle.$$

The procedure is now repeated: the composite co-state  $|\chi_i^{(k)}(t_{N-1})\rangle$  is propagated backwards from  $t = t_{N-1}$  to  $t = t_{N-2}$  using the full CIS Hamiltonian, resulting in  $|\chi_{i,\text{in}}^{(k)}(t_{N-2})\rangle$ ,

and “glueing” yields the composite wave function at  $t = t_{N-2}$ ,

$$|\chi_i^{(k)}(t_{N-2})\rangle = |\chi_{i,\text{in}}^{(k)}(t_{N-2})\rangle + |\chi_{i,\text{out}}^{(k)}(t_{N-2}; t_{N-2})\rangle,$$

with  $|\chi_{i,\text{out}}^{(k)}(t_{N-2}, t_{N-2})\rangle$  given by Eq. (8.25); and so on and so forth for all splitting times  $t_j$ , until  $t = t_0$ , where  $t_0$  refers to the initial time. During the backward propagation, as described above, the resulting co-state is stored in CIS basis. It gives by construction, at an arbitrary time  $t$ , the first term in Eq. (8.24a). The second term in Eq. (8.24a) involving the outer parts “born” at the splitting times  $t = t_j$  and evaluated at  $t > t_j$  is merely given by forward propagating analytically all  $|\chi_{i,\text{out}}(t_j; t_j)\rangle$  using the Volkov Hamiltonian, and summing them up coherently according to Eq. (8.21). This allows to calculate the “total” co-state wavefunction at an arbitrary time  $t$ , analogously to  $|\varphi_i(t)\rangle$ . Finally, Eqs. (8.24a) and (8.20) allow for evaluating Krotov’s update equation for the control, Eq. (8.14), where the iteration label just indicates whether the guess,  $\mathbf{A}^{(0)}(t)$ , the old,  $\mathbf{A}^{(k)}(t)$ , or the new control,  $\mathbf{A}^{(k+1)}(t)$ , enter the propagation of  $|\chi_i(t)\rangle$  and  $|\varphi_i(t)\rangle$ , respectively. A difficulty in solving the update equation for the control, is given by the fact that Eq. (8.14) is implicit in  $\mathbf{A}^{(k+1)}(t)$ . Strategies to overcome this obstacle depend on the additional constraints.

### 8.5.2 Summary of the algorithm

The complete implementation of the optimization within the time-splitting framework of the TDCIS method is summarized as follows:

1. **Choose an initial guess for the vector potential,  $\mathbf{A}^{(k=0)}(t)$ .**
2. **Forward propagation of the state:**
  - (a) Propagate  $|\Psi^{(k=0)}(t = 0)\rangle$ , cf. Eq. (8.1), from  $t = 0$  until the first splitting time,  $t = t_1$ , in the CIS basis. We label the projection of the propagated state onto the *channel wave functions* defined in Eq. (3.28) in Section 3.4.2, by  $i = 1, 2, \dots$ , while  $i = 0$  is reserved for the projection onto the Hartree-Fock ground state.
  - (b) At  $t = t_1$ , apply the splitting function defined in Eq. (6.1) to obtain  $|\varphi_{i,\text{in}}^{(k)}(t_1)\rangle$  and  $|\varphi_{i,\text{out}}^{(k)}(t_1; t_1)\rangle$ . Store the outer part in the CIS representation, before transforming  $|\varphi_{i,\text{out}}^{(k)}(t_1; t_1)\rangle$  to the Volkov representation.
  - (c) Propagate  $|\varphi_{i,\text{in}}^{(k)}(t_1)\rangle$  using  $\hat{H}$  and  $|\varphi_{i,\text{out}}^{(k)}(t_1; t_1)\rangle$  using  $\hat{H}_V$  from  $t = t_1$  to the next splitting time,  $t = t_2$ .
  - (d) At  $t = t_2$ , apply the splitting function to  $|\varphi_{i,\text{in}}^{(k)}(t_2)\rangle$ , again store the resulting outer part in CIS representation, and transform  $|\varphi_{i,\text{out}}^{(k)}(t_2; t_2)\rangle$  to the Volkov representation.

- (e) Propagate  $|\varphi_{i,\text{in}}^{(k)}(t_2)\rangle$  using  $\hat{H}$  and  $|\tilde{\varphi}_{i,\text{out}}^{(k)}(t_2)\rangle = |\varphi_{i,\text{out}}^{(k)}(t_2; t_1)\rangle + |\varphi_{i,\text{out}}^{(k)}(t_2; t_2)\rangle$  using  $\hat{H}_V$  from  $t = t_2$  to the next splitting time  $t = t_3$ .
- (f) Repeat steps (2d) and (2e) for all remaining splitting times  $t_j$  up to  $t_N$ .
- (g) Propagate for each channel wave function,  $|\tilde{\varphi}_{i,\text{out}}^{(k)}(t_N)\rangle = \sum_{t_j=t_1}^{t_N} |\varphi_{i,\text{out}}^{(k)}(t_N; t_j)\rangle$  from the last splitting time,  $t = t_N$ , to the final time,  $t = T$ , to obtain  $|\tilde{\varphi}_{i,\text{out}}^{(k)}(T)\rangle$  and evaluate the target functional  $J_T$ .
- (h) Calculate  $\chi_{i,\text{out}}^{(k)}(\mathbf{p}, T)$  according to Eq. (8.23a).

### 3. Backward propagation of the co-state:

- (a) Calculate  $\mu(\mathbf{p}, T)$  according to Eq. (8.23b) or (8.23c).
- (b) Calculate  $|\chi_{i,\text{out}}^{(k)}(t_N; t_N)\rangle$  from Eq. (8.25) and propagate it backwards using  $\hat{H}$  from  $t = t_N$  to the previous splitting time  $t_{N-1}$ . The resulting state is  $|\chi_{i,\text{in}}^{(k)}(t_{N-1})\rangle$ .
- (c) At  $t = t_{N-1}$ , calculate  $|\chi_{i,\text{out}}^{(k)}(t_{N-1}; t_{N-1})\rangle$  from Eq. (8.25) and 'glue' to obtain  $|\chi_i^{(k)}(t_{N-1})\rangle = |\chi_{k,\text{in}}^{(k)}(t_{N-1})\rangle + |\chi_{i,\text{out}}^{(k)}(t_{N-1}; t_{N-1})\rangle$ . This procedure is performed in the CIS basis for each channel wave function.
- (d) Propagate  $|\chi_i^{(k)}(t_{N-1})\rangle$  from  $t = t_{N-1}$  to  $t_{N-2}$  using  $\hat{H}$  to obtain  $|\chi_{i,\text{in}}^{(k)}(t_{N-2})\rangle$ .
- (e) Repeat steps (3c) and (3d) for all remaining splitting times and propagate backward up to  $t = 0$ . During the backward propagation, the resulting wavefunction is stored in the CIS basis. As previously detailed, this procedure allows for performing the "glueing" procedure only once at every splitting time. It gives gives rises to the first term in Eq. (8.24a). The second term involving the evaluation of the outer part (coherent summation) at any arbitrary time  $t$  is obtained upon application Eq. (8.21) to each of the individual contribution  $|\chi_{i,\text{out}}(t_j; t_j)\rangle$  for all splitting times.

### 4. Forward propagation and update of control:

- (a) Determine the zeroth order approximation of the new control at times  $(n + 1/2)\Delta t$ ,  $\mathbf{A}_0^{(k+1)}(n + 1/2\Delta t)$ , from Eq. (8.14), using the states at times  $n\Delta t$ , i.e., the co-state obtained in step 3,  $|\chi_i^{(k)}(n\Delta t)\rangle$  and  $|\varphi_i^{(k+1)}(n\Delta t)\rangle$  obtained with the control  $\mathbf{A}^{(k+1)}((n - 1/2)\Delta t)$ .
- (b) If  $\lambda_\omega \neq 0$  or  $\lambda_e \neq 0$ , solve Eq. (8.18b) to obtain  $\tilde{\mathbf{A}}^{(k+1)}(\omega)$ , using the approximated  $\mathbf{A}_0^{(k+1)}(t)$ , and Fourier transform  $\tilde{\mathbf{A}}^{(k+1)}(\omega)$  to time domain.

- 5. **Iteration:** Increase  $k$  by one and repeat steps 3 and 4 until convergence of  $J_T$  is reached.

At this point, we would like to stress that the parameters chosen for the momentum grid require particular attention for the optimization algorithm to work. This is due to the transformation from the CIS representation to the Volkov basis (CIS-to- $p$  transformation) at each splitting time, as discussed Section 6.2 of Part I. During the backward propagation, correspondingly, the inverse transformation is required, i.e., the  $p$ -to-CIS transformation. The CIS-to- $p$  transformation of the outer part is evaluated using Eq. (6.4); the inverse of this transformation is straightforwardly derived. Since the dynamics is reversible, forward propagation (involving wavefunction splitting and the CIS-to- $p$  transformation) needs to give identical results to backward propagation (involving wavefunction “glueing” and the  $p$ -to-CIS transformation). This can and needs to be used to check the numerical accuracy of the CIS-to- $p$  transformation and its inverse: Since the inverse transformation involves integration over  $\mathbf{p}$ , a significant error is introduced if the sampling of the momentum grid is insufficient. Consequently, transforming the outer part from the CIS representation to the Volkov basis and then back may not yield exactly the same wave function. While for each  $p$ -to-CIS transformation the error may be relatively small, it accumulates as the optimization proceeds iteratively according to Eq. (8.14). It results in optimized pulses with non-physical and undesirable “jumps” at those splitting times where the accuracy of the  $p$ -to-CIS transformation is insufficient and destroys the monotonic convergence of the optimization algorithm. The jumps disappear when the number of the momentum grid points is increased and  $p_{max}$  is adjusted.

Therefore, a naive solution to this problem would be to considerably enlarge the number of momentum grid points. However, this will significantly increase the numerical effort of the optimization, i.e., evaluation of the inner product in the rhs. of Eq. (8.14c). The inner product involves not only calculation of the overlap of the inner part in the CIS representation and the outer part in the Volkov basis but it also requires evaluation of the mixed terms,  $\langle \chi_{i,in}^{(k)}(t) | \hat{p}_z | \varphi_{i,out}^{(k+1)}(t) \rangle$  and  $\langle \chi_{i,out}^{(k)}(t) | \hat{p}_z | \varphi_{i,in}^{(k+1)}(t) \rangle$  and thus one CIS-to- $p$  transformation and integration over two—perhaps even three—degrees of freedom at every time  $t$ , for each channel  $i$  and in every iteration step  $k + 1$ . Thence, finding the best balance between efficiency and accuracy in the  $p$ -to-CIS transformation is essential for the proper functioning and feasibility of the optimization calculations. Also, reducing the total size of the radial coordinate while simultaneously increasing the number of splitting times translates into a more important number of evaluations of the inner product defined in Eq. (8.14c) in momentum representation. Below, we state explicitly the momentum grid parameters utilized in our simulations which allowed for a good compromise between efficiency and accuracy.

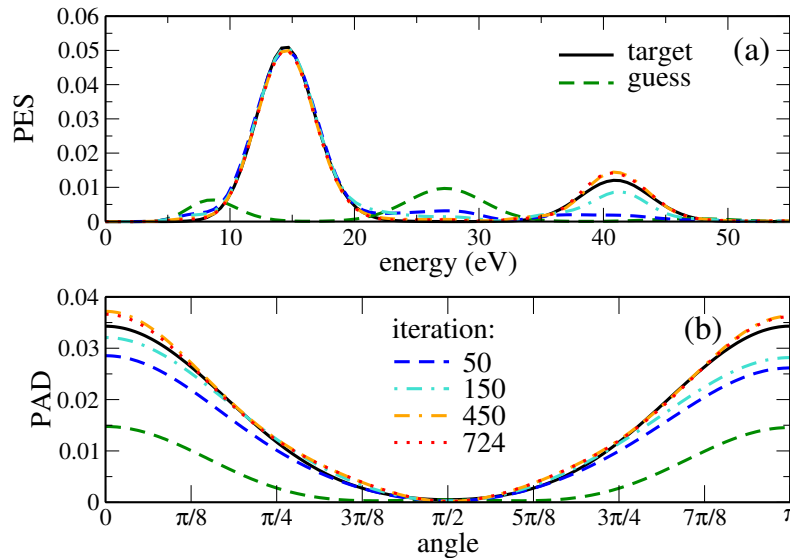


Figure 8.1: **Hydrogen**, optimal control of the complete photoelectron distribution: (a) angle-integrated PES, and (b) energy-integrated PAD. As the optimization proceeds iteratively, the actual photoelectron distribution approaches the desired one (black solid line) in both its energy dependence and angular distribution. The photoelectron distribution obtained with the guess field (green dashed lines) is far from the desired distribution.

## 8.6 Application I: Prescribing the complete photoelectron distribution

We consider, as a first example, the optimization of the complete photoelectron distribution, cf. Eq. (8.4), for a hydrogen atom. The wavepacket is represented, according to Eq. (8.1), in terms of the ground state  $|\Phi_0\rangle$  and excitations  $|\Phi^a\rangle$ . The calculations employed a pseudo-spectral grid with density parameter  $\zeta = 0.50$  [25], a spatial extension of 200 a.u. and 800 grid points. All optimization calculations employed a linearly polarized electric field along the  $z$  axis. This translates into a rotational symmetry of the photoelectron distribution along the  $z$  axis. Therefore, only wave functions of the form  $\Psi_{\text{out}} = \Psi_{\text{out}}(p, \theta)$  need to be considered. For the calculation of the spectral components, the outer parts of the wave functions were projected onto the Volkov basis, defined on a spherical grid in momentum representation  $\mathbf{p}$ . For our calculations, we adopted an evenly spaced grid in  $p$  as well as in the polar coordinate  $\theta$ . The size of the radial component of the spherical momentum grid was set to  $E_{\text{max}} = 6$  a.u., sampled at 301 points. The same number of points was utilized for the polar coordinate. The splitting radius was set to  $r_c = 50$  a.u., the total number of splitting times is  $N = 3$  with a smoothing parameter  $\Delta = 5.0$  a.u. [51]. The splitting procedure was applied every 30 a.u. of time. Finally, a total integration time of 120 a.u. with a time step of 0.05 a.u. was utilized for the time propagation.

We consider first the minimization of the functional  $J^{(1)}[\varphi, \varphi^\dagger]$  defined in Eq. (8.4).

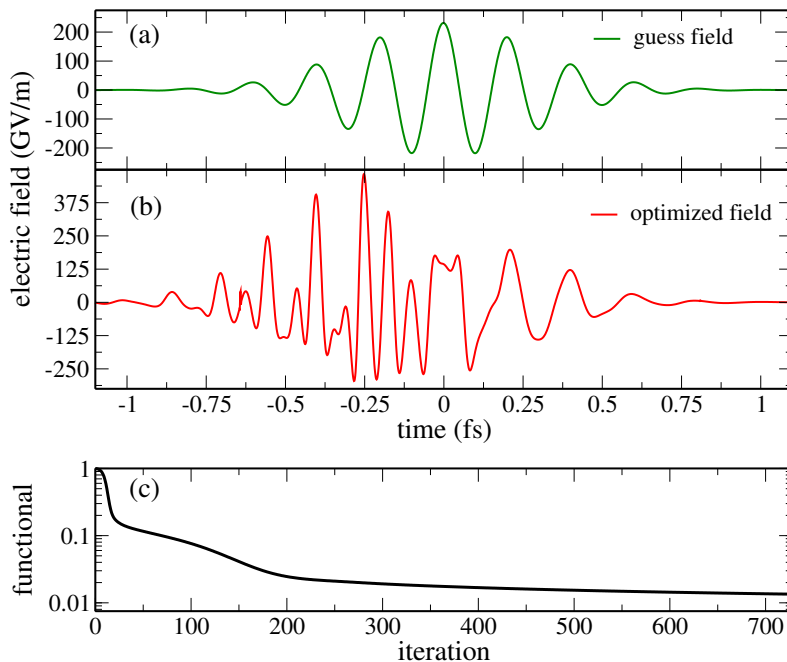


Figure 8.2: **Hydrogen**, optimization of the full photoelectron distribution: (a) Guess field  $E_z^{(0)}(t)$  chosen to start the optimization shown in Fig. 8.1 and (b) optimized electric field obtained after about 700 iterations. (c) The final time cost functional  $J_T^{(1)}$  decreases monotonically, as expected for Krotov’s method.

The goal is to find a vector potential  $A_{z,\text{opt}}(t)$  such that the photoelectron distribution resulting from the electron dynamics generated by  $A_{z,\text{opt}}(t)$  coincides with  $\sigma_0(\mathbf{p})$  at every point  $\mathbf{p}$ , cf. Eq. (8.4). For visualization convenience, we plot the angle-integrated PES and energy-integrated PAD, cf. Eq. (6.10), associated to “target” photoelectron distribution  $\sigma_0(\mathbf{p})$ , as shown by the solid-black lines in Figs. 8.1(a) and 8.1(b), respectively. To simplify the optimization, neither frequency restriction nor amplitude constraint on  $E_z(t)$  is imposed, i.e.,  $\lambda_\omega = \lambda_e = 0$ . The initial guess for the vector potential is chosen in such a way that the fidelity with respect to the target  $\sigma_0(\mathbf{p})$  is poor, see the green dashed lines in Fig. 8.1. Despite the bad initial guess, the optimization quickly approaches the desired photoelectron distribution, converging monotonically, as expected for Krotov’s method and demonstrated in Fig. 8.2(c): After about 700 iterations, the target distribution is realized with an error of 2%. The reason for such a large number of iterations can be understood by considering that the optimized photoelectron distribution must coincide (point-by-point) with a two-dimensional target object. This represents a non-trivial optimization problem. The optimized electric field is shown in Fig. 8.2(b): Compared to the initial guess, cf. Fig. 8.2(a), the amplitude of the optimized field is somewhat increased, and a high-frequency oscillation has been added. The monotonic convergence towards the target distribution in terms of angle-integrated PES and energy-integrated PAD is illus-

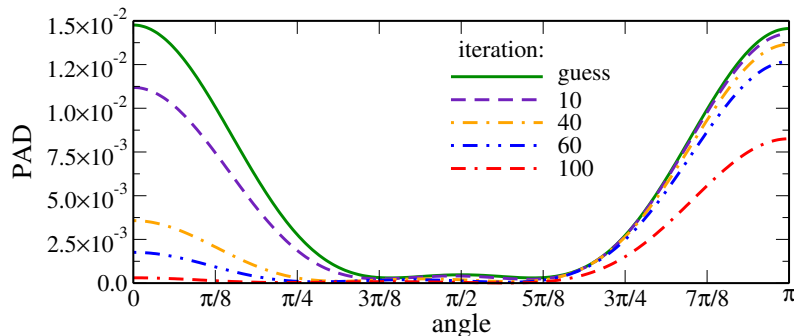


Figure 8.3: **Hydrogen**, minimization of the photoelectron emission into the upper hemisphere: As the optimization proceeds iteratively, the probability of emission into the upper hemisphere decreases monotonically up to almost complete extinction.

trated in Fig. 8.1. We can appreciate that the algorithm first tends to match all points with higher values, starting with the peak near 15 eV, while adjusting the remainder of the spectrum, with lower values, later in the optimization. The slow-down of convergence, observed in Fig. 8.2(c) after about 200 iterations, is typical for optimization methods that rely on gradient information alone: As the optimum is approached, the gradient vanishes [237]. Such a slow-down of convergence can only be avoided by incorporating information from higher order derivatives in the optimization. This is rather non-trivial in the framework of Krotov’s method [237, 238] and beyond the scope of our current study.

## 8.7 Application II: Minimizing the probability of emission into the upper hemisphere

As a second application of our control toolbox, we are interested in minimizing the probability of emission into the upper hemisphere without imposing any specific constraint on the number of electrons emitted into the lower hemisphere. The final time cost functional is given by Eq. (8.5) with  $\lambda_2^+ > 0$  and  $\lambda_2^- = 0$ . We consider again a hydrogen atom and a linearly polarized electric field along the  $z$ -axis, using the same numerical parameters as in Section 8.6.

In contrast to the example discussed in Section 8.6, no particular expression for the target PES and PAD needs to be imposed—we only require the probability of emission into the upper hemisphere to be minimized regardless of the actual shape of angle-integrated PES and energy-integrated PAD. We employ the optimization prescription described in Section 8.5.2 using Eq. (8.23c) in the final time condition for the adjoint state. As the optimization proceeds iteratively, the energy-integrated PAD becomes more and more asymmetric, see Fig. 8.3, minimizing emission into the upper hemisphere, as desired. The

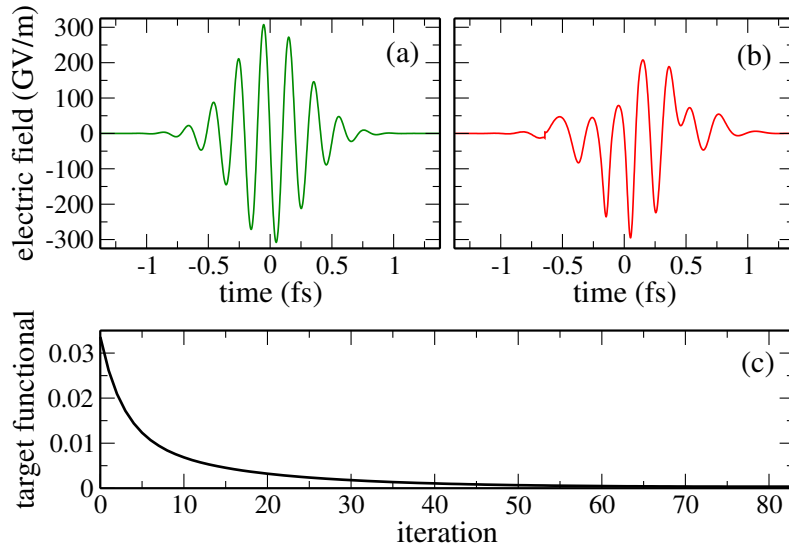


Figure 8.4: **Hydrogen**, minimization of the probability of emission into the upper hemisphere: Guess (a) and optimized (b) electric field for the optimization shown in Fig. 8.3. Also for this target functional, Eq. (8.5), monotonic convergence of the optimization algorithm is achieved (c).

guess and optimized pulses are shown in Fig. 8.4(a) and (b). As illustrated by the solid green line in Fig. 8.3, the guess field was chosen such that it leads to a symmetric probability of emission for the two hemispheres. Again, monotonic convergence of the final time cost functional is achieved, cf. Fig. 8.4(c). At the end of the iteration procedure, the probability of emission into the upper hemisphere vanishes completely. As for the lower hemisphere, the emission probability initially remains almost invariant as the algorithm proceeds iteratively, see Fig. 8.3, while the probability of emission into the upper hemisphere decreases very fast, and monotonically, as expected. However, for a large number of iterations, the probability of emission into the lower hemisphere starts to decrease as well. After about 150 iterations it reaches an emission probability of  $2.3 \times 10^{-4}$ , that is two orders of magnitude smaller than for the guess pulse. Although our goal is only for the probability of emission into the upper hemisphere to be minimized, without specific constraints on the probability of emission into the lower hemisphere, the current results are completely consistent in terms of the optimization problem. More precisely, the optimization does exactly what the functional  $J_T^{(2)}$ , Eq. (8.5) with  $\lambda_2^+ > 0$  and  $\lambda_2^- = 0$ , targets. In fact, since the target functional depends on the upper hemisphere alone, then, by construction, the algorithm calculates the corrections to the field according to Eq. (8.14), regardless of how these changes affect the probability of emission into the lower hemisphere. To keep the probability of emission into the lower hemisphere constant or to maximize it, an additional optimization functional is required. This is investigated in the following section and defines the motivation for the maximization of the anisotropy

of emission discussed in the following lines.

### 8.8 Application III: Maximizing the difference in the number of electrons emitted into upper and lower hemisphere

Finally we maximize the difference in probability for emission into the upper and the lower hemispheres. To this end, we construct the final-time cost functional such that it maximizes emission into the upper hemisphere while simultaneously minimizing emission into the lower hemisphere. This is expressed by the functional (8.5) where both weights are non-zero and have different signs,  $\lambda_2^{(+)} < 0$  and  $\lambda_2^{(-)} > 0$ . The signs correspond to maximization and minimization, respectively. We consider this control problem for two different atoms—hydrogen as a one-channel case and argon as an example with three active channels [51]. The latter serves to underline the appropriateness of our methodology for quantum control of multi-channel problems.

Furthermore, in order to demonstrate the versatility of our optimal control toolbox in constraining specific properties of the optimized electric field, we consider the following options: (i) a spectral constraint, i.e.,  $\lambda_\omega \neq 0$  in Eq. (8.12), and (ii) the constraint to minimize fast changes in the vector potential, with  $\lambda_e \neq 0$  in Eq. (8.14). The latter is equivalent to avoiding large electric field amplitudes.

#### 8.8.1 Hydrogen

We consider a hydrogen atom, interacting with an electric field linearly polarized along the  $z$ -axis, using the same numerical parameters as in Sec. 8.6. The optimization was carried out with and without restricting the spectral bandwidth of  $E_z(t)$ . Figure 8.5(b) displays the symmetric energy-integrated PAD obtained with the Gaussian guess field, shown in Fig. 8.6(b), for which a central frequency  $\omega_0 = 27.2$  eV was used. For the optimization with spectral constraint, the admissible frequency components for  $E_z(t)$  are chosen such that  $|E_z(\omega)|^2 \leq \epsilon$  for all  $|\omega| \geq \omega_{max}$  with  $\omega_{max} = 5$  a.u.  $\approx 136.1$  eV. This requirement translates into the penalty function  $\tilde{\gamma}(\omega)$  shown in Fig. 8.7(c), for which we have used the form

$$\tilde{\gamma}(\omega) = \tilde{\gamma}_0 \left(1 - e^{-(\omega/\alpha)^{2n}}\right), \quad (8.26)$$

where the parameters  $\alpha$ ,  $n$  and  $\tilde{\gamma}_0$  must be chosen such that the term  $\lambda_\omega \hat{\gamma}(\omega)$  in the functional  $C_\omega[\mathbf{A}]$  in Eq. (8.12) takes very large values in the region of undesired frequencies. For our first example,  $\alpha = 25$ ,  $n = 6$  and  $\tilde{\gamma}_0 = 1$  allows for strongly penalizing, and therefore filtering all undesirable frequency components above  $|\omega| \geq \omega_{max}$ , as it is

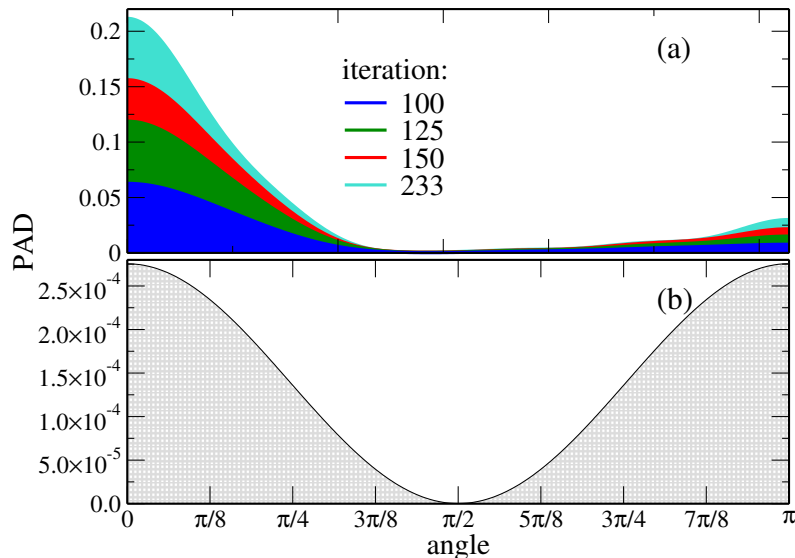


Figure 8.5: **Hydrogen**, maximizing the difference in photoelectron emission into the upper and lower hemisphere: (a) The probability for emission into the upper hemisphere ( $0 \leq \theta \leq \pi/2$ ) increases significantly as the optimization proceeds. Although the probability for emission with angles ( $\pi/2 \leq \theta \leq \pi$ ) also grows somewhat, the overall difference increases. The energy-integrated PAD obtained with the guess pulse is shown in (b). Note the different y-axis scales in (a) and (b).

shown by the corresponding transfer function  $\tilde{G}(\omega)$ , cf. Fig. 8.7(d). Note that it is not the weight  $\lambda_\omega$  alone that determines how strictly the spectral constraint is enforced; it is the ratio  $\lambda_\omega/\lambda_a$  that enters in the transfer function  $\tilde{G}(\omega)$ . This reflects the competition of the different terms in the complete optimization functional, Eq. (8.7).

As in the previous two examples, the optimization approach developed leads to monotonic convergence of the target functional, Eq. (8.5), with and without spectral constraint. This is illustrated in Fig. 8.6(a). Even though the spectra of the fields optimized with and without spectral constraint, are completely different, cf. Fig. 8.7(a) and (b), the speed of convergence is roughly the same, and the maximum values for  $J_T^{(2)}$  reached using both fields are also very similar, cf. Fig. 8.6(a). This means that the algorithm finds two distinct solutions. Such a finding is very encouraging as it implies that the spectral constraint does not put a large restriction onto the control problem. In other words, more than one, and probably many, control solutions exist, and it is just a matter of picking the suitable one with the help of the additional constraint. It also implies that most of the frequency components in the spectrum of the field optimized without spectral constraint are probably not essential. This is verified by removing the undesired spectral components in Fig. 8.7(a), using the same transfer function utilized for the frequency-constrained optimization shown in Fig. 8.7(d). The energy-integrated PAD obtained with

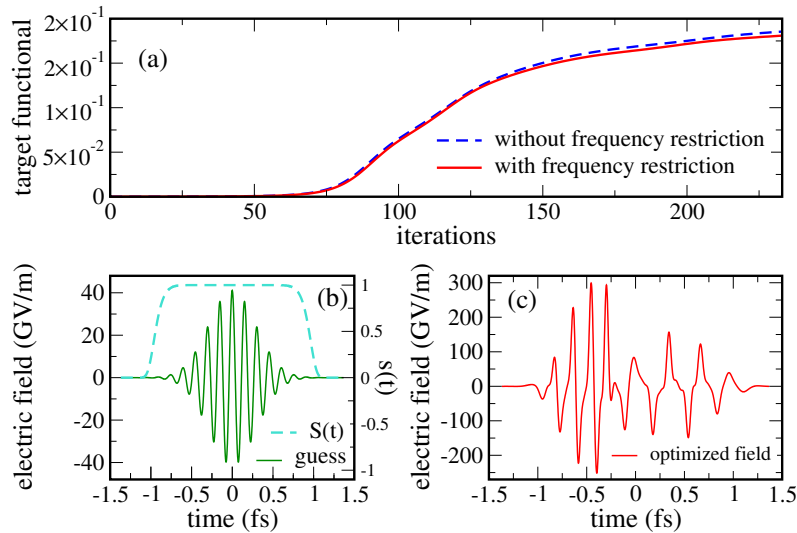


Figure 8.6: **Hydrogen**, maximization of the anisotropy in the PAD: The target functional  $J_T^{(2)}$ , for the optimization shown in Fig. 8.5, measuring the difference in probability for emission into upper and lower hemisphere increases monotonically with  $(\lambda_\omega \neq 0)$  and without  $(\lambda_\omega = 0)$  spectral constraint (a). The guess field (green line) is shown in (b) together with the shape function  $s(t)$  used in both optimizations. The optimized field obtained with the spectral constraint is displayed in (c).

such a filtered optimized pulse remains asymmetric, and the value of the target functional  $J_T^{(2)}$  is decreased by only about 10 per cent.

The peak amplitude of the optimized field is about one order of magnitude larger than that of the guess field, cf. Fig. 8.6(b) and (c). The increase in peak amplitude is connected to the gain in emission probability for the northern hemisphere by almost three orders of magnitude. The optimized pulse thus ionizes much more efficiently than the guess pulse. Figure 8.8(a) compares the electric fields optimized with and without spectral constraints—a huge difference is observed for the two fields. While the electric field optimized without spectral constraint presents very sharp and high peaks in amplitude, beyond experimental feasibility, the frequency-constrained optimized field is characterized by reasonable amplitudes and a much smoother shape. The frequency components of the unconstrained field shown in Fig. 8.7(a) now become clear. Note that the difference in amplitude only appears during the first half of the overall pulse duration, see Fig. 8.8(a). It is a known feature of Krotov’s method to favor changes in the field in an asymmetric fashion; the feature results from the sequential update of the control, as opposed to a concurrent one [239].

Figure 8.8(b) shows the energy-integrated PAD obtained upon propagation with the two fields. One notes that, although the probability of emission into the lower hemisphere is larger for the unconstrained than for the constrained field, the same applies to

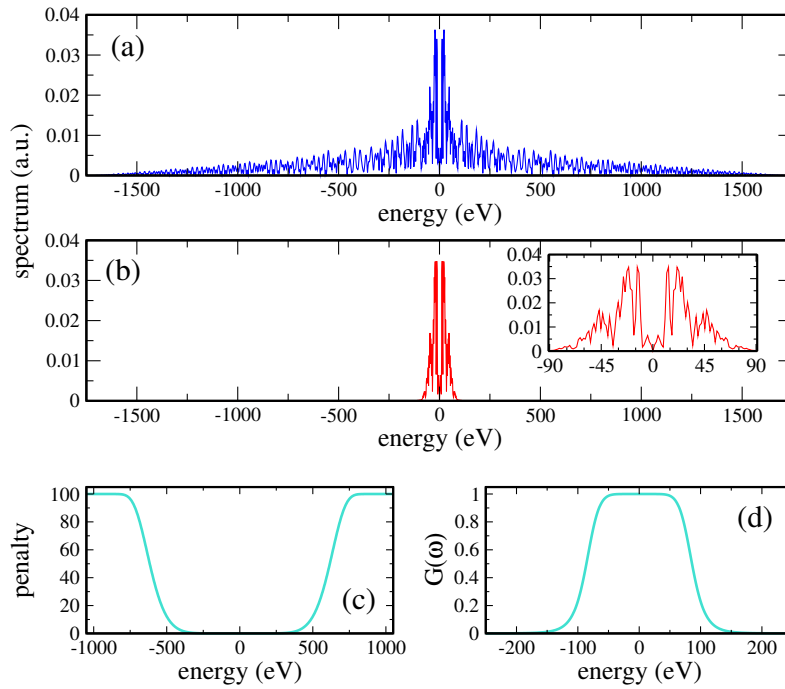


Figure 8.7: **Hydrogen**, maximization of the anisotropy of emission: Spectrum of the optimized electric field for the optimization shown in Figs. 8.5 and 8.6 with (b) and without (a) spectral constraint. The corresponding penalty function  $\tilde{\gamma}(\omega)$  and transfer function  $\tilde{G}(\omega)$ , cf. Eqs. (8.12) and (8.18d), are shown in (c) and (d), respectively.

the probability of emission into the upper hemisphere. Therefore the difference in the number of electrons emitted into upper and lower hemisphere is in the end relatively close, which explains the behavior of the final-time functional observed in Fig. 8.6(a). The electron dynamics generated by the frequency-unconstrained field leads to a larger total probability of emission into both hemispheres, with respect to that obtained with the frequency-constrained field, as shown in Fig. 8.8(c). More precisely, propagation with the unconstrained optimized field results in a total probability of emission of 0.27, i.e., probabilities of 0.23 and  $4.3 \times 10^{-2}$  for emission into the upper and lower hemisphere, respectively. In comparison, a total probability of emission of 0.26 is obtained for the frequency-constrained field, with probabilities of emission into the upper and lower hemispheres of 0.22 and  $3.9 \times 10^{-2}$ , respectively. The fact that the spikes observed in the unconstrained optimized field do not have any significant impact on the asymmetry of the PAD can be rationalized by the short timescale on which the intensity is very high. This time is too short for the electronic system to respond to the rapid variations of the field amplitude.

In order to rationalize how anisotropy of electron emission is achieved by the optimized field, we analyze in Fig. 8.9 the partial wave decomposition of the angle-integrated PES, comparing the results obtained with the guess field to those obtained with the frequency-

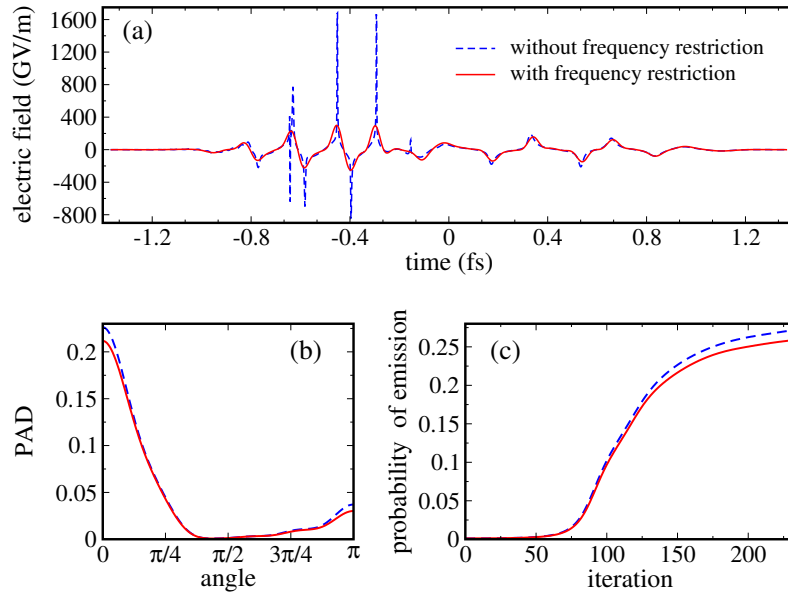


Figure 8.8: (**Hydrogen**, maximization of the difference of photoelectrons emitted into the lower and upper hemispheres: Optimized electric fields with ( $\lambda_\omega \neq 0$ ) and without ( $\lambda_\omega = 0$ ) frequency restriction (a) where the red curve shows the same data as in Fig. 8.6(c). Also compared are the energy-integrated PAD (b) and total emission probability (c) obtained with the frequency-constrained and unconstrained optimized fields.

constrained optimized field. Inspection of Fig. 8.9 reveals that upon optimization, there is a clear transition from distinct ATI peaks, Fig. 8.9(a), to a quasicontinuum energy spectrum, Fig. 8.9(b). Also, the optimized field enhances the contribution of states of higher angular momentum that have the same kinetic energy. In particular, the peaks for  $l = 5$  are dramatically higher than in the PES obtained with the guess field. In fact, the symmetric case, cf. Fig. 8.9(a), shows an energy distribution of partial waves characterized by waves of the same parity at the same energy, whereas the asymmetric case reveals a partial wave distribution of opposite parity at the same energy, cf. Fig. 8.9(b). Figure 8.9 thus demonstrates that the desired asymmetry in the energy-integrated PAD is achieved through the mixing of various partial waves of opposite parity at the same energy. Interestingly, especially lower frequencies are mixed with a considerable intensity into the pulse spectrum which leads to higher order multiphoton ionization leading to comparable final energies in the PES. Thus, more angular momentum states are mixed.

Next, we would like to constrain not only the frequency components but also the maximal field amplitude, as the maximal field amplitude of the electric field, shown in Fig. 8.6(c) is still important. To this end, we employ Eq. (8.18) for  $\lambda_e > 0$ , which penalizes large changes on the derivative of the vector potential, cf. Eq. (8.14), and thus large values of the electric field amplitude. As can be seen in Fig. 8.10(a), the resulting optimized field is one order of magnitude smaller than that for which no amplitude restriction was

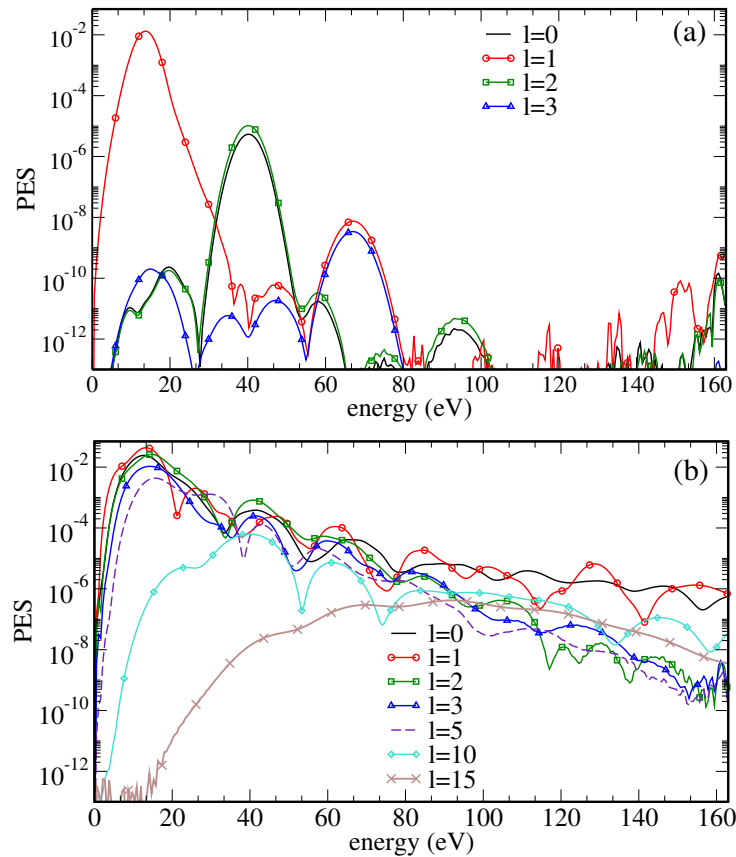


Figure 8.9: **Hydrogen**, maximizing the anisotropy of photoelectron emission: Partial wave contribution to the angle-integrated PES, shown in Fig. 8.5, obtained with the guess (a) and the frequency-constrained optimized field (b).

imposed, cf. Fig. 8.6(c), and of the same order of magnitude as the guess field. Despite the constraint and as shown in Fig. 8.10(c), a perfect top-bottom asymmetry is obtained.

A common feature observed between the amplitude-unconstrained and constrained cases concerns the low frequencies appearing upon optimization, cf. Fig. 8.7(b) and Fig. 8.10(b), respectively. To quantify the role of the frequency components for achieving anisotropy, we start by suppressing all frequency components above 10 eV: the anisotropy of emission is preserved. On the other hand, removing frequencies below the XUV re-establish the initial symmetry of emission into both hemispheres. Therefore, in both cases the top-bottom asymmetry arises from low frequency components of the optimized field and is achieved through the mixing of various partial waves of opposite parity at the same energy.

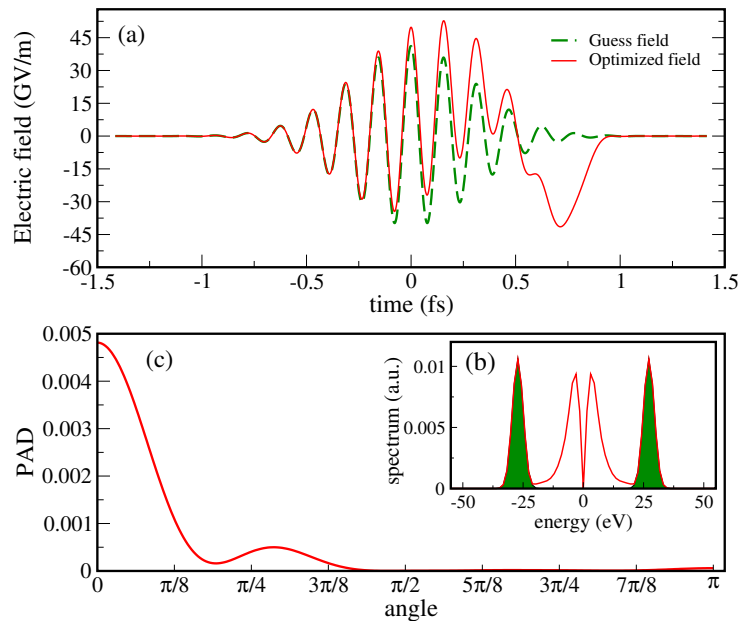


Figure 8.10: **Hydrogen**, maximizing the anisotropy of photoelectron emission: Optimization results obtained when simultaneously constraining the maximal amplitude and frequency components of the electric field for the weights  $|\lambda_{eff}^{(-)}| = 2|\lambda_{eff}^{(+)}|$  with  $|\lambda_{eff}^{(+)}| = 1$ . Guess and optimized electric fields are shown in panel (a), their spectra in panel (b). A perfectly anisotropy of photoelectron emission is obtained with the optimized field, as demonstrated in the photoelectron angular distribution shown in panel (c).

### 8.8.2 Argon

We extend now our quantum control multi-channel approach to the study of electron dynamics in argon, interacting with an electric field linearly polarized along the  $z$ -direction. We consider the  $3s$  and  $3p$  orbitals to contribute to the ionization dynamics and define three ionization channels  $3s$ ,  $3p$  with  $m = 0$  and  $3p$  with  $m = +1$  (the case  $3p$  with  $m = -1$  is symmetric to  $m = +1$  due to the polarization direction of the electric field, linearly polarized along to the  $z$  axis). In order to describe the multi-channel dynamics, a spatial grid of 100 a.u. with 450 grid points and a density parameter of  $\zeta = 0.55$  was utilized. The size of the radial component of the spherical momentum grid was set to  $E_{max} = 12$  a.u., sampled by 601 evenly spaced points, while the polar component  $\theta \in [0, \pi]$  was discretized using 301 points. A splitting radius of  $r_c = 50$  a.u., and a smoothing parameter  $\Delta = 10.0$  a.u. were employed, together with a splitting step of 2.0 a.u. and a total number of  $N_s = 2036$  splitting times. For time propagation, the time step was chosen to be 0.01 a.u., for an overall integration time  $\Delta T \approx 200$  a.u.

Analogously to the results shown for hydrogen in Sec. 8.8.1, the goal is to maximize the difference in the probability for electron emission into the upper and lower hemispheres. To start the optimization, a Gaussian-shaped guess electric field with central frequency

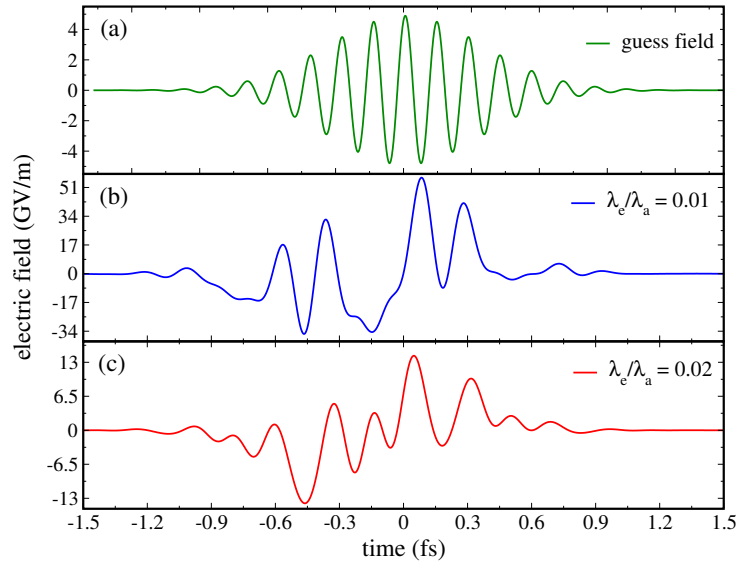


Figure 8.11: **Argon**, maximizing the difference in photoelectron emission into the upper and lower hemisphere: Guess field (a) utilized for the optimization. Optimized fields obtained with an amplitude constraint are depicted in (b) and (c) respectively.

$\omega = 27.2$  eV and maximal amplitude  $E_{max} = 5.14$  GV/m was chosen. It is depicted in Fig. 8.11(a) and yields a symmetric distribution for the upper and lower hemispheres, see Fig. 8.12(a). The total emission probability amounts to only  $1.4 \times 10^{-2}$ . In order to obtain reasonable pulses which result in a maximally anisotropic PAD, we utilize Eq. (8.14) with  $\lambda_e \neq 0$  to minimize fast changes in the vector potential and avoid large peaks of the electric field amplitude.

The optimized pulses for two values of the ratio  $\lambda_e/\lambda_a$ , characterizing the relative weight of minimizing peak values in the electric field compared to minimizing the integrated vector potential, are shown in Figs. 8.11(b) and (c), respectively. As expected, a larger amplitude constraint yields an electric field with a smaller maximal amplitude. In fact, the maximal amplitude for  $\lambda_e/\lambda_a = 0.01$  is one order of magnitude larger than that of the guess field, whereas for  $\lambda_e/\lambda_a = 0.02$  it is only three times larger. Figures 8.12(b) and (c) display the energy-integrated PADs obtained with these fields. A significant top-bottom asymmetry of emission is achieved in both cases, the main difference being the total emission probability of  $2.7 \times 10^{-2}$  for Fig. 8.12(b) compared to  $9.4 \times 10^{-3}$  for Fig. 8.12(c). The spectra of the two optimized fields are examined in Fig. 8.13. Despite the difference in amplitude, both optimized fields are characterized by low frequency components. Note that no frequency restriction was imposed. This finding suggests that the low frequency components are responsible for achieving the top-bottom asymmetry. Indeed, removing all optical and infra-red (IR) components results in a complete loss of the asymmetry. On the other hand, removing frequency components above 10 eV does not affect the top-

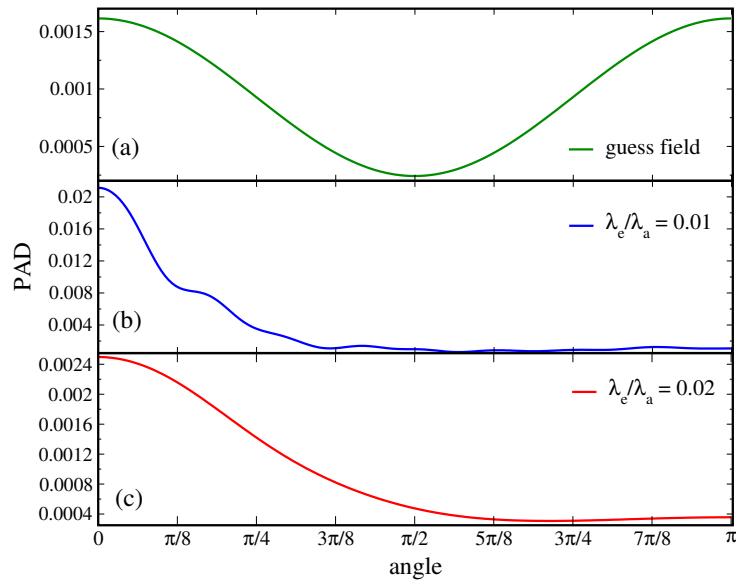


Figure 8.12: **Argon**, maximization of the top-bottom asymmetry: Energy-integrated PAD obtained with the guess pulse (a) and amplitude-constrained cases with  $|\lambda_{eff}^{(-)}| = 2|\lambda_{eff}^{(+)}|$  and  $|\lambda_{eff}^{(+)}| = 1$  in (b) and (c), respectively. Note the different scales for the probability of emission.

bottom asymmetry achieved by both optimized fields considerably.

These optimization results raise the question whether frequency components in the optical and IR range are essential for achieving the top-bottom asymmetry or whether a pure XUV field can also realize the desired control. To answer this question, we now penalize all frequency components in the optical and IR region. The resulting optimized electric field and its spectrum are depicted in Fig. 8.14(a) and (b), respectively. This field indeed possesses frequency components only in the XUV region, cf. Fig. 8.14(b). Nevertheless, a strongly asymmetric top-bottom emission is again achieved, cf. Fig. 8.14(c). Therefore,

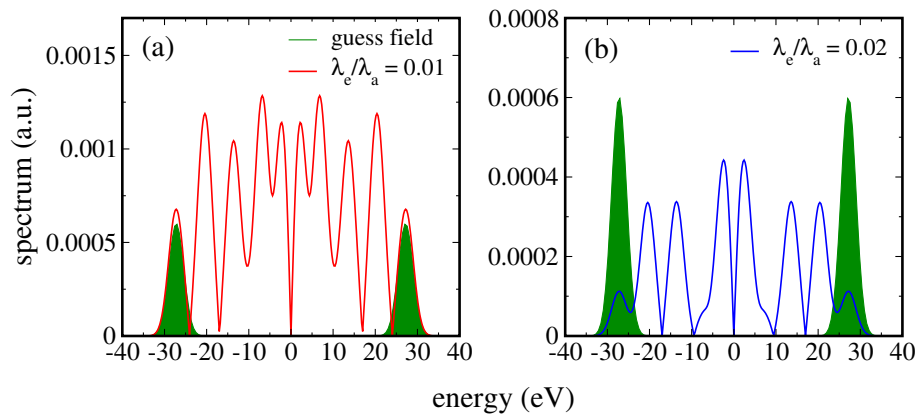


Figure 8.13: **Argon**, maximizing the anisotropy of photoemission in argon: Spectra of the optimized pulses and the guess field for comparison.

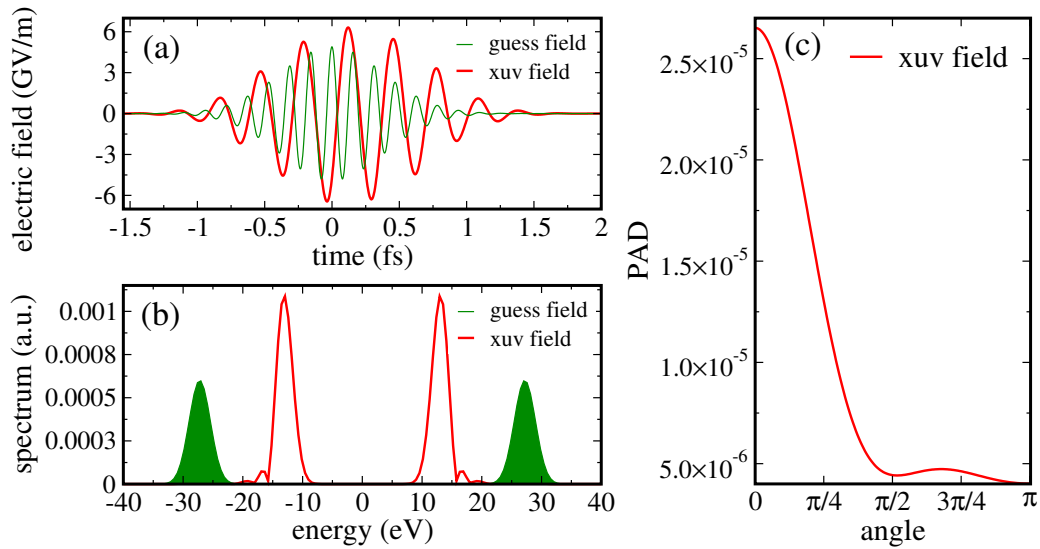


Figure 8.14: **Argon**, top-bottom asymmetry of photoelectron emission: Frequency and amplitude-constrained optimized field and its spectrum in (a) and (b) with the guess field shown for comparison. For obtaining the XUV field, the ratios  $\lambda_e/\lambda_a = 0.02$  and  $\lambda_\omega/\lambda_a = 0.02$  with a penalty function  $\tilde{\gamma}_{XUV} = \tilde{\gamma}(\omega - \omega_0) + \tilde{\gamma}(\omega + \omega_0) - 1 + \epsilon_\omega$  with  $\tilde{\gamma}_o = 100$ ,  $\omega_0 = 27.2$  eV,  $n = 4$  and  $\alpha = 15$  were utilized, cf. Eq. (8.26). The quantity  $\epsilon_\omega = 0.001$  has been introduced in order to avoid numerical instabilities when evaluating the transfer function  $\tilde{G}(\omega)$ , cf. Eq. (8.18d). The resulting asymmetric photoelectron angular distribution obtained with the optimized field is shown in panel (c).

while optical or IR excitation may significantly contribute to achieving anisotropy of the photoelectron emission, fields with frequency components in the XUV alone may also lead to such an asymmetry.

Finally, we would like to understand the physical mechanism from which the anisotropy in the emission into both hemispheres arises. To this end, we consider the partial wave decomposition of the angle-integrated PES. Analogously to our analysis for hydrogen, cf. Section 8.8.1, a symmetric PAD, as obtained with the guess field, is characterized by an energy distribution of partial waves of the same parity at the same energy, cf. Fig. 8.15(a). In contrast, the partial wave decomposition corresponding to the asymmetric PAD reveals an energy distribution of partial waves of different parity at the same energy, cf. Figs. 8.15(b), 8.16(a). For the optimized fields with significant optical and IR components, many partial waves, including those with high angular momentum, contribute to the angle-integrated PES. This suggests that the top-bottom anisotropy of photoelectron emission is achieved by absorbing low-energy photons at relatively high intensity which is accompanied by strong mixing of a number of partial waves of opposite parity at the same energy. The same mechanism had previously been found for hydrogen, cf. Section 8.8.1.

As for the optimized XUV electric field yielding an asymmetric probability for emis-

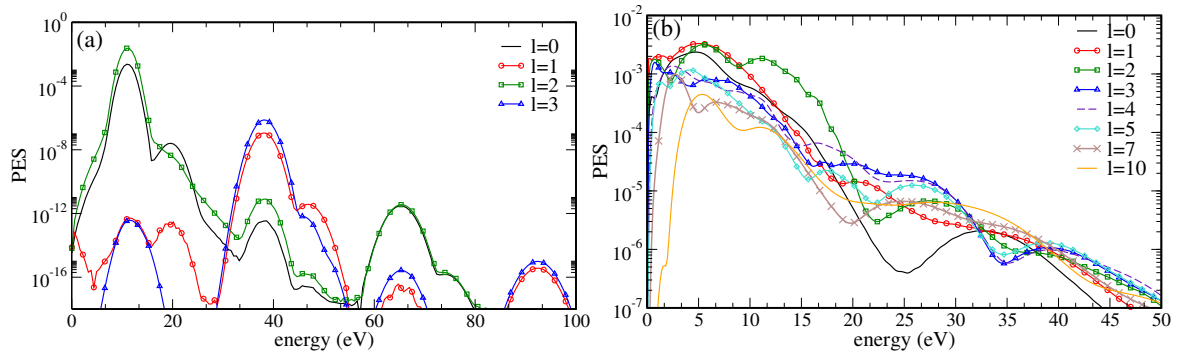


Figure 8.15: **Argon**, maximizing the anisotropy of photoelectron emission: Partial wave contribution to the angle-integrated PES, shown in Fig. 8.12 obtained with the guess (a) and the amplitude-constrained optimized field corresponding to the ratio  $\lambda_e/\lambda_a = 0.01$  in (b).

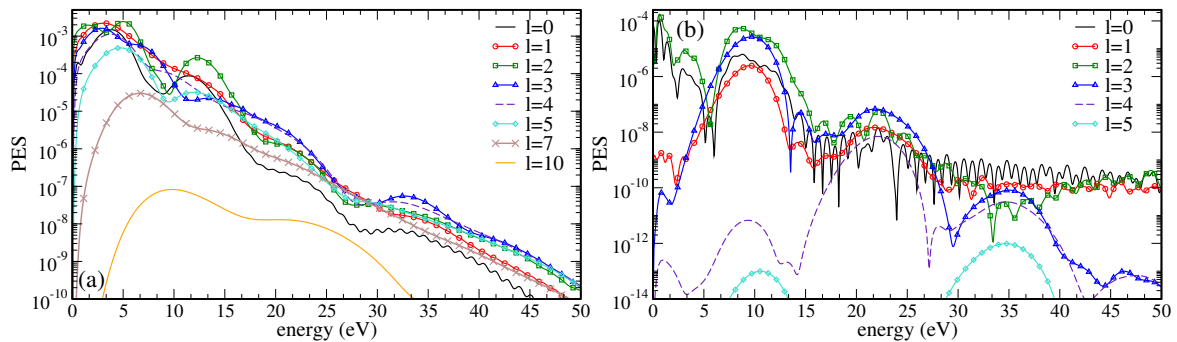


Figure 8.16: **Argon**, maximizing the anisotropy of photoelectron emission: Partial wave contributions to the angle-integrated PES corresponding to the energy-integrated PAD shown in Fig. 8.12(c) obtained amplitude-constrained optimized field for the ratio  $\lambda_e/\lambda_a = 0.02$  and that corresponding to the PAD shown in Fig. 8.14(c) obtained with the optimized XUV pulse in panels (a) and (b), respectively.

sion, shown in Fig. 8.14(c), the same mechanism involving mixing of partial waves of different parity at the same energy is found, cf. Fig. 8.16(b). Nevertheless, a much smaller number of partial waves is involved, cf. Fig. 8.16(a) and (b). For the XUV pulse (Fig. 8.14(b)), it is mainly the components of the continuum wavefunction with angular momentum  $l = 2$  and  $l = 3$  that contribute to the anisotropy of emission.

The reason why partial waves with different parity are always present for anisotropic photoelectron emission can be straightforwardly understood. It lies in the fact that the angular distribution arises from products of spherical harmonics, cf. Eqs. (6.10b), (6.10a) and (6.4), and the product of two spherical harmonics with the same (opposite) parity is a symmetric (antisymmetric) function of  $\theta$ . The optimized pulses take advantage of this property and realize the desired asymmetry by driving the dynamics in such a way that

it results in partial wave components which interfere constructively (destructively) in the upper (lower) hemisphere.

We have also investigated whether channel coupling plays a role in the generation of the anisotropy. While switching off the interchannel coupling in the dynamics under the optimized pulse shown in Fig. 8.14(a) decreases the resulting anisotropy slightly, overall it still yields an anisotropic PAD. This shows that interchannel coupling in argon is not a key factor in achieving top-bottom asymmetry in photoelectron angular distributions.

## 8.9 Summary of achievements and conclusions

To summarize, we have developed a quantum optimal control toolbox to target specific features in photoelectron spectra and photoelectron angular distributions that result from the interaction of a closed-shell atom with strong XUV radiation. To this end, we have combined Krotov's method for quantum control [106] with the time-dependent configuration interaction singles approach to treat the electron dynamics [25] and the wave-function splitting method to calculate photoelectron spectra [51, 142]. We have presented here the algorithm and its implementation in detail. While currently based on the time-dependent configuration interaction singles approach, it is straightforward to adapt the algorithm to different time-dependent electronic structure methods, provided they are compatible with wavefunction splitting to calculate the photoelectron spectrum. To the best of our knowledge, our work is the first to directly target photoelectron observables in quantum optimal control.

We have utilized this toolbox to identify, for the benchmark systems of hydrogen and argon atoms, photoionization pathways which result in asymmetric photoelectron emission. Our optimization results show that efficient mechanisms for achieving top-bottom asymmetry exist in both single-channel and multi-channel systems. We have found the channel coupling to be beneficial, albeit not essential for achieving asymmetric photoelectron emission. Since typically the solution to a quantum control problem is not unique, additional constraints are useful to ensure certain desired properties of the control fields, such as limits to peak amplitude and spectral width. We have demonstrated how such constraints allow to determine solutions characterized by low or high photon frequency. In the low frequency regime, our control solutions require relatively high intensities. Correspondingly, the anisotropy of the photoelectron emission is realized by strong mixing of many partial waves. In contrast, for pure XUV pulses, we have found low to moderate peak amplitudes to be sufficient for asymmetric photoelectron emission. In both cases, we have identified the top-bottom asymmetry to originate from mixing, in the photoelectron wavefunction, various partial waves of opposite parity at

the same energy. The corresponding constructive (destructive) interference pattern in the upper (lower) hemisphere yields the desired asymmetry of photoelectron emission. Whereas many partial waves contribute for control fields characterized by low photon energy and high intensity, interference of two partial waves is found to be sufficient in the pure XUV regime. In all our examples, we have found surprisingly simple shapes of the optimized electric fields. In the case of hydrogen, tailored electric fields to achieve asymmetric photoelectron emission have been discussed before and we can compare our results to those of Refs. [223, 240]. Our work differs from these studies in that we avoid a parametrization of the field and allow for complete freedom in the change the electric field, whereas Refs. [223, 240] considered only the carrier-envelope phase, intensity and duration of the pulse as control knobs. The additional freedom of quantum optimal control theory is important, in particular when more complex systems are considered.

The set of applications that we have presented here is far from being exhaustive, and our current work opens many perspectives for both photoionization studies and quantum optimal control theory. On the one hand, we have shown how to develop optimization functionals that target directly an experimentally measurable quantity obtained from continuum wavefunctions. On the other hand, since our approach is general, it can straightforwardly be applied to more complex examples. In this respect it is desirable to lift the restriction to closed-shell systems. This would pave the way to studying the role of electron correlation in maximizing certain features in the photoelectron spectrum. Similarly, allowing for circular or elliptic polarization of the electric field, one could envision, for example, to maximize signatures of chirality in the photoelectron angular distributions. This requires, however, substantial further development on the level of the time-dependent electronic structure theory.

# Coherent control of hole dynamics in attosecond ionization

---

9.1	Introduction and motivations . . . . .	119
9.2	Hole dynamics of photoionization . . . . .	121
9.3	Optimization problem . . . . .	122
9.3.1	Alternative optimization algorithms . . . . .	123
9.3.2	Sequential optimization update . . . . .	124
9.4	Minimizing hole decoherence in Argon . . . . .	126
9.4.1	Numerical performance of SPA-optimization . . . . .	127
9.4.2	Optimization using a “pre-optimized” guess field . . . . .	129
9.4.3	Enhancement mechanisms of hole coherence of hole states in ultra-fast photoionization . . . . .	132
9.4.4	Electronic correlations and asymptotic oscillating behavior of the degree of coherence . . . . .	134
9.4.5	Minimization of hole decoherence with prescribed hole population ratio . . . . .	137
9.5	Suppression of hole decoherence in Xenon: A novel mechanism . . . . .	142
9.6	Summary of achievements and conclusions . . . . .	148

---

## 9.1 Introduction and motivations

In Chapter 8 we have formally demonstrated the possibility of controlling the momentum distribution of the liberated photoelectron. Manipulating photoelectron-related observ-

ables allowed us to unravel the underlying the physical mechanism involved to achieve, for instance, the desired angular anisotropy of photoelectron emission, regardless of the coherence properties in the photoion created during the photoionization process [138].

This time, we shift the direction of our research from manipulating the photoelectron momentum distribution, to controlling the hole correlation dynamics. Such a choice is manifestly motivated by the increasing progress in the observation of hole dynamics in the photoion [241–244] which is initiated by the photoionization itself.

Such a coherent superposition has been in the focus of research in chemistry and physics for many decades [245–248] since it plays an important role in the quest of control over matter: it is the starting point for time-dependent spectroscopy of electron dynamics, for example via pump-probe studies to investigate hole alignment [241] or interchannel coupling [244]. As with any coherent spectroscopy, the degree of coherence of the state that will be transiently probed is a crucial resource [249].

It is well established that the physical mechanisms inducing coherent superposition of states, might be mediated via two possible pathways: by one-photon ionization— using a pulse with sufficiently large bandwidth, for instance [52] or alternatively, through multiphoton processes [242, 243].

In practice, a necessary requirement for hole coherence is ionization into photoelectron states with the same angular momentum and energy. Because of the dipole selection rules, however, creating coherence between a pair of hole states through one-photon ionization may not be possible even if the spectral bandwidth of the ionizing pulse exceeds the energy separation of the two hole states.

Although for multiphoton processes it may be possible to generate hole coherence by ionization from occupied orbitals of opposite parity, the transient interaction between the photoion and the liberated photoelectron introduces decoherence, or loss of coherence, of the hole states detrimental to the control process. This applies even in one-photon ionization with attosecond pulses [52]. In optical tunnel ionization, the observed degree of coherence is also limited, so far to about 85 per cent [243]. In that regime, even the shortest ionizing pulses do not allow to realize perfect coherence among the hole states [250]. Moreover, only outer-valence hole states are accessible and it is very hard to vary the population ratio of the hole states.

Despite the importance of the phase characterization for coherent control, it is often assumed, however, that a coherent wave packet has been prepared in a sudden and unspecified manner, such that it constitutes a well-defined coherent superposition of states. However, the question remains how to generate such a coherent superposition in the first place. In view of utilizing the coherent superposition in time-dependent spectroscopy, the challenge is thus to identify suitable experimentally feasible pulses that create a pre-

scribed superposition of hole states with predefined population ratio, satisfying practical constraints. This is the control problem that we consider here.

The use of quantum optimal control theory allows for exploring both regimes and, moreover, finding novel mechanisms for achieving high hole coherence.

## 9.2 Hole dynamics of photoionization

The electron dynamics of photoionization is simulated by solving the time-dependent Schrödinger equation,

$$i\frac{\partial|\Psi(t)\rangle}{\partial t} = \hat{\mathbf{H}}(t)|\Psi(t)\rangle \quad (9.1)$$

where the time dependent Hamiltonian  $\hat{\mathbf{H}}(t)$  governing the dynamics, reads

$$\hat{\mathbf{H}}(t) = \hat{\mathbf{H}}_0 + \hat{\mathbf{H}}_1 + E(t)\hat{\mathbf{z}} - i\eta\hat{\mathbf{W}}(\hat{\mathbf{r}}), \quad (9.2)$$

with  $\hat{\mathbf{H}}_0$  and  $\hat{\mathbf{H}}_1$  being the mean-field Fock operator and the residual Coulomb interaction, respectively. The latter takes the form,

$$\hat{\mathbf{H}}_1 = \hat{\mathbf{V}}_C - \hat{\mathbf{V}}_{MF}, \quad (9.3)$$

with  $\hat{\mathbf{V}}_C$  and  $\hat{\mathbf{V}}_{MF}$  being the electron-electron interaction and the mean-field potential, respectively. The third term on the right-hand side of Eq. (9.2) describes the electric dipole interaction of the atom with an external electric field, assumed to be linearly polarized.

The fourth term on the rhs of Eq. (9.2), denotes a complex absorbing potential (CAP) [139, 140] of the form [25, 28, 251, 252],

$$-i\eta\hat{\mathbf{W}}(\hat{\mathbf{r}}) = -i\eta h(\hat{\mathbf{r}} - r_c) \times (\hat{\mathbf{r}} - r_c)^2 \quad (9.4)$$

that has been incorporated in order to avoid numerical artifacts due to reflection on the edges of the numerical grid as the TDCIS wavefunction propagates over time. In Eq. (9.4),  $h(\cdot)$ ,  $r$  and  $r_c$  refer to the Heavyside distribution, the distance from the origin and the critical distance at which the CAP starts absorbing, respectively.

The time-dependent wavepacked is expressed in terms of the multi-channel time-dependent configuration interaction singles (TDCIS) formalism [25, 51, 52, 253]. Specifically, the TDCIS  $N$ -electron wavefunction reads

$$|\Psi(t)\rangle = \alpha_0(t)|\Phi_0\rangle + \sum_{i,a} \alpha_i^a(t)|\Phi_i^a\rangle, \quad (9.5)$$

where  $|\Phi_0\rangle$  and  $|\Phi_i^a\rangle$  denote the Hartree-Fock ground state and the single particle-hole excitation from an initially occupied orbital, labeled  $i$ , to an initially unoccupied orbital  $a$ . The binding energies utilized in the present work are those obtained from the Hartree-Fock formalism using Koopmans' theorem [254, 255].

The photoion corresponds to a reduced system that is obtained by integrating out the photoelectron and thus needs to be described by a density matrix [250]. To study the hole dynamics, we use the ion density matrix approach of Refs. [25, 52],

$$\rho_{i,j}^{IDM}(t) = \text{Tr}_a [|\Psi(t)\rangle\langle\Psi(t)|]_{i,j} = \sum_a \langle\Phi_i^a|\Psi(t)\rangle\langle\Psi(t)|\Phi_j^a\rangle, \quad (9.6)$$

where the trace is carried out over the virtual channels which are occupied by the photoelectron. The CAP, cf. Eq. (9.4), affects all virtual orbitals and thus also the ion density matrix, which therefore must be corrected according to [25, 28]

$$\rho_{i,j}^{IDM}(t) = \tilde{\rho}_{i,j}^{IDM}(t) + 2\eta e^{(\varepsilon_i - \varepsilon_j)t} + \sum_{a,b} w_{a,b} \int_{-\infty}^t dt' \alpha_i^a(t') \alpha_j^{*b}(t') e^{(\varepsilon_i - \varepsilon_j)t'}, \quad (9.7a)$$

where the ‘‘uncorrected’’ matrix elements of ion density matrix  $\tilde{\rho}^{IDM}(t)$  read [25, 28]

$$\tilde{\rho}_{i,j}^{IDM}(t) = \sum_a (\Phi_i^a|\Psi(t)\rangle\langle\Psi(t)|\Phi_j^a), \quad (9.7b)$$

with  $|\Phi_j^a\rangle = |\Phi_j^a\rangle$  and  $|\Phi_j^a\rangle$  and  $(\Phi_j^a|$  referring to the right and left eigenvectors of  $\hat{F} - i\eta\hat{W}$ , where  $\hat{F}$  is the Fock operator. Note that, due to the CAP,  $(\Phi_j^a|$  and  $|\Phi_j^a\rangle$  are not orthogonal [25].

Equation (9.7a) provides the starting point for defining a measure of hole coherence: The positive semidefinite quantity

$$g_{i,j}(t) = \frac{|\rho_{i,j}^{IDM}(t)|}{\sqrt{\rho_{i,i}^{IDM}(t)\rho_{j,j}^{IDM}(t)}} \quad (9.8)$$

defines the degree of coherence between the hole states in the atomic orbitals  $i$  and  $j$  [52]. For a totally incoherent statistical mixture  $g_{i,j} = 0$ , whereas  $g_{i,j} = 1$  for perfect coherence between the states  $i$  and  $j$ .

### 9.3 Optimization problem

Our optimization targets maximization of hole coherence. In a first stage, we maximize the degree of coherence between the  $3s$  and  $3p_0$  hole states in argon at the final time  $T$ , regardless of the final hole population ratio in the  $3s$  and  $3p_0$  orbitals. It is customary to

minimize rather than maximize, such that the final-time cost functional reads

$$J_T^{(1)} = (g_{3s,3p_0}(T) - 1)^2. \quad (9.9)$$

It takes values between 0 and 1 with  $J_T^{(1)} = 0$  corresponding to perfectly coherent  $3s$  and  $3p_0$  hole states. Additionally, when the target is not only to maximize hole coherence but also to prescribe a certain ratio  $\mathcal{R}$  between the hole populations, which is suitable in view of utilizing such a coherent superposition for time-dependent spectroscopy, the final time cost functional takes the form,

$$J_T^{(2)} = w_{pop} \left( \frac{\rho_{3p_0,3p_0}(T)}{\rho_{3s,3s}(T)} - \mathcal{R} \right)^2 + w_{coh} (g_{3s,3p_0}(T) - 1)^2, \quad (9.10)$$

where  $w_{pop}$  and  $w_{coh}$  are optimization weights that can be used to stress the relative importance of each term in Eq. (9.10).

### 9.3.1 Alternative optimization algorithms

It is worth mentioning that because of the correction performed to the ion density matrix, due to the CAP, the equation of motion for the Lagrange multiplier, or co-state, results in a linear non-homogeneous Schrödinger equation that needs to be solved backwards in time. The inhomogeneous term is attributed to the correction, cf. second term in Eq. (9.7a), the latter being performed sequentially in time. This, combined to the presence of a denominator in Eq. (9.8) results in an extremely unstable backward propagation. Consequently, it translates into a systematic loss of monotonic convergence after a few number of iterations. Consequently, an alternative gradient-free and robust optimization method must be utilized.

As a alternative approach to the Krotov's optimization method, we opt, because of the form of the functional in Eq. (9.10), for gradient-free optimization which only requires evaluation of the functional but not its gradient. This avoids backward propagation of an adjoint state that is typical for gradient-based optimization approaches [106]. In our case, backward propagation involves an inhomogeneous Schrödinger equation with the inhomogeneity originating from the correction of the ion density matrix due to the presence of the CAP, cf. Eq. (9.7a). While a numerically exact solution of inhomogeneous Schrödinger equations is possible [172], it becomes challenging if the source term gets large. This is the case here.

A plethora of available methods for gradient-free optimization exists. A popular approach, and notably the only one employed in quantum optimal control so far [256, 257], is due to Nelder and Mead [123]. It minimizes a function of  $n$  optimization parameters

(therefore gradient-free approaches are sometimes referred to as parameter optimization) by comparing function evaluations at the  $n + 1$  vertices of a general simplex, and updating the worst vertex by moving it around a new vertex that is an average of the remaining (best) vertices [123, 125]. While the approach often works well, it may become ill-conditioned, particularly when non-convex forms of the function are involved. As an alternative to the Nelder-Mead simplex approach, we consider the principal axis optimization method [130] which is based on an inverse parabolic interpolation.

In the context of gradient-free methods, additional constraints in functional form, that are customary in gradient-based optimization and often cumbersome to implement [233, 234], to fulfill the desired constraints, such as field duration, frequency components, maximal electric field peak intensity, are not needed: The bandwidth of the field, field duration range and the maximal amplitudes of the Fourier components can be directly confined by mapping the optimization variables, updated by the algorithm, to a specific sampling range of choice. This, combined with the advantage of avoiding backward propagation of the adjoint state with gradient-free optimization is nonetheless balanced by two critical drawbacks—the requirement for prior parametrization of the field, and the convergence not being monotonic. Gradient-free optimization may lead to poor fidelities if (i) the parametrization of the field is not properly chosen, (ii) the number of parameters is too small, or, paradoxically, (iii) the number of parameters exceeds a certain threshold. In the latter case, a saturation effect causes the functional to reach an asymptote very quickly and the optimization gets stuck. As a rule of thumb, although gradient-free optimization does not require any particular adaptation when including special techniques avoiding grid reflexions, such as CAP or Splitting methods, these gradient-free approaches should be used only in the ideal context of dealing with very an inexpensive propagation, assuming of course that the solution only requires a moderate number of control parameters. Unfortunately, such a particular context is certainly not the case here. In order to circumvent this problem, we introduce and propose a sequential parametrization update-based methodology which is explained in the following.

### 9.3.2 Sequential optimization update

The poor performance of gradient-free optimization due to a too large number of optimization parameters can be avoided by a sequential update of the number of optimization parameters [258]. Here, we adopt this approach to optimization methods beyond a Nelder-Mead simplex search and allow for treating the circular frequencies themselves as optimization parameters while still maintaining a prespecified bandwidth. The optimization is started with a minimal number of parameters, and additional parameters are included *on-the-fly* as the algorithm proceeds iteratively, i.e., every time the value of the

optimization functional reaches a plateau.

As an example of the SPA technique, let the parametrization of the field be defined by Fourier components,

$$E_{NI}(t) = \sum_{n=1}^N \sum_{i=1}^I s_n(t, \sigma_n) \left\{ f_n(a_{n,i}) \cos(\omega_{n,i} t) + f_n(b_{n,i}) \sin(\omega_{n,i} t) \right\},$$

with the Fourier amplitudes  $a_{n,i}$  and  $b_{n,i}$  as optimization parameters. The double sum notation was chosen to ease implementation of a field that consists of  $N$  subpulses. In Eq. (9.11),  $s_n(t, \sigma_n)$  is a fixed envelope, for example Gaussian or  $\sin^2$ -shaped. The durations  $\sigma_n$  of the subpulses as well as the circular frequencies  $\omega_{n,i}$  can be fixed or considered as additional optimization parameters. The functions  $f_n(\cdot)$  are introduced in order to constrain the Fourier amplitudes  $a_{n,i}$  and  $b_{n,i}$  to within a prespecified range. For instance, a function of the form

$$f_n(\zeta_i) = \zeta_o \int_0^{\zeta_i} e^{-t^2} dt \quad (9.11a)$$

ensures that the Fourier coefficient does not exceed a given maximum absolute value  $\zeta_o$ , avoiding large amplitudes for the resulting optimized field. Equivalently, a hyperbolic tangent form,

$$f_n(\zeta_i) = \zeta_{n,o} \frac{e^{\zeta_i} - e^{-\zeta_i}}{e^{\zeta_i} + e^{-\zeta_i}}, \quad (9.11b)$$

may be utilized to control the maximal amplitude of the optimized field. Alternatively, one could also apply the transformations (9.11) to the overall electric field instead of each Fourier component separately. This may, however, result in additional low frequency components arising from the transformation in question. Such artifact frequencies might be undesirable, in particular when the solution shall be constrained to a specific spectral range.

For simplicity purposes, we choose a single pulse,  $N = 1$ , with two Fourier amplitudes,  $I = 2$ , and fixed or variable circular frequencies to start the optimization properly speaking. When using fixed circular frequencies, a set of circular frequency values is specified in the very beginning, which are successively added during the parametrization updates. If the circular frequencies are treated as optimization parameters, the spectral range can be simply controlled by restricting the circular frequencies to an interval via the mapping

$$\omega^{new} = \frac{1}{2}(\omega_{max} - \omega_{min}) \tanh(\omega) + \frac{1}{2}(\omega_{max} + \omega_{min}), \quad (9.12)$$

where  $\omega \in \mathbb{R}$  is the circular frequency returned by the optimization algorithm, whereas  $\omega^{new}$ , which is guaranteed to be in the interval  $[\omega_{min}, \omega_{max}]$  by Eq. (9.12), is the one used for the propagation.

Consider for simplicity the example of fixed circular frequencies, treating the pulse duration (full width at half maximum (FWHM) of the intensity profile), Fourier amplitudes and relative phases as optimization parameters. The procedure consists of two loops, an outer loop over generations (with each generation corresponding to a parametrization with  $m$  parameters), and an inner loop, iterating for a given parametrization. The inner loop proceeds until  $N_c$  evaluations of the functional, i.e. propagations of the wavefunction, are reached. It then checks whether the overall minimization threshold is reached. If so, the complete procedure is stopped; if not, it checks whether the value of the functional has changed significantly during the  $N_c$  iterations. If so, another  $N_c$  iterations are carried out, if not, then the algorithm increases the number of optimization parameters, and restarts the optimization for the new generation, using the best previous field as guess field for the new parametrization with all new optimization parameters set to zero. This procedure of updating the parametrization of the field is repeated every time that the functional gets stuck, allowing it to escape from the plateau. The user needs to specify the maximal number of generations  $\mathcal{G}_{max}$ , or new parametrizations, together with  $N_c$ , the maximum number of evaluations of the functional, i.e. propagations, and the tolerance thresholds.

In the following, we show that such a sequential parametrization update is more efficient than choosing a large number of parameters from the beginning. In a sense, the optimization is “driven” efficiently and does not get stuck in a final plateau since every time the functional reaches a saturation plateau, the additional parameters introduced allow for escaping from such an asymptotic region. This is in line with the findings of Ref. [258] where the frequencies are randomized within a prespecified interval. Furthermore, we show that updating the parametrization is particularly efficient when combined with the principal axis method, due to Brent [130], as compared to the Nelder-Mead optimization algorithm [123], employed in Ref. [258].

## 9.4 Minimizing hole decoherence in Argon

The goal is to maximize the degree of coherence  $g_{i,j}(T)$  between the  $3s$  and  $3p_0$  hole-population in argon. Note that the  $3s$  hole state in argon would be inaccessible in tunnel ionization.

The ionizing external electric field is assumed to be linearly polarized along the  $z$  direction, in the XUV regime and with maximal field amplitude not exceeding 0.02 a.u. Correspondingly, the target functional is the one defined in Eq. (9.9). The wavepacket is

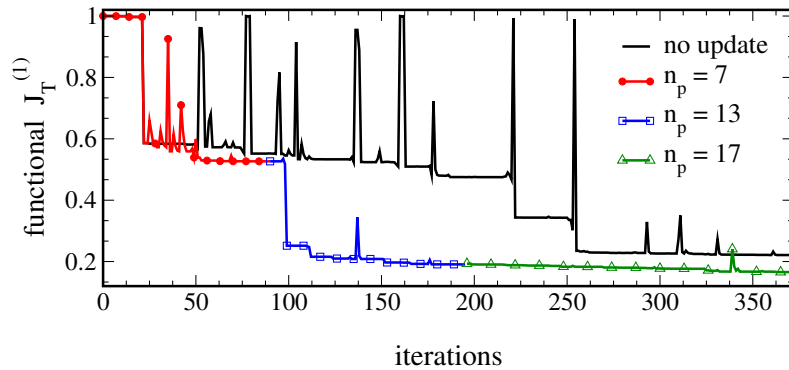


Figure 9.1: Efficiency of optimization using the principal axis method of Brent with fixed parametrization (black line,  $n_p = 13$ ) and with sequential parametrization update (SPA-optimization, colored lines).

represented, according to Eq. (9.5), in terms of the ground state  $|\Phi_0\rangle$  and excitations  $|\Phi_i^a\rangle$ , from which the corrected form of the IDM, due to the CAP, cf. Eq. (9.7a), is calculated.

#### 9.4.1 Numerical performance of SPA-optimization

We first compare our sequential parametrization update (SPA) technique to optimization with a standard fixed parametrization, using the principal axis method in both cases to determine the change in parameters. Figure 9.1 shows the optimization efficiency for the two methods, started with the same guess field. The optimization parameters are the pulse duration and the Fourier components. The circular frequencies, taken to be fixed on an evenly spaced frequency grid, are chosen in the XUV regime. For the standard version, the entire frequency grid is used from the beginning of the optimization, while for SPA-optimization circular frequencies from the grid are successively added. The standard non-updated version (full black line), for which the field is defined by 13 optimization parameters, decreases quasi-monotonically but very slowly during the first 210 iterations. Then the functional considerably decreases between the iterations 210 to 250 before reaching a plateau with final value  $J_T^{(1)} = 0.21$ . SPA-optimization is started by defining at first a pulse characterized by 7 circular frequencies, which coincide with the first seven circular frequencies from the overall set of circular frequencies.

After 50 iterations with these parameters, SPA-optimization reaches already a functional value slightly below that reached by the non-sequential version after the same number of iterations. Once the plateau for the field containing 7 optimization parameters is reached, the new generation is started by adding 6 additional optimization parameters. As can be seen from Fig. 9.1, such an update allows the functional to considerably decrease, reaching after just 100 iterations the same value that is obtained with the non-sequential version in 255 iterations. Furthermore, it also shows that there are some frequency com-

ponents resulting from the non-update version, that are not necessarily required for the optimization. The different colors in Fig. 9.1 illustrate the increase in the number of optimization parameters as a function of the number of propagations. From Fig. 9.1, it is clear that the sequential parametrization update version is more efficient than standard optimization: It allows not only to reach higher fidelities at the end of the optimization, but also converges faster. The comparison shown in Fig. 9.1 does not depend on the specific choice of the initial guess. That is, we have carried out the comparison for several guess fields and observed always a better performance of SPA-optimization compared to optimization with fixed parametrization.

It is clear that the SPA-approach can be extended to other gradient-free optimization methods. A particularly popular method is the widely used Nelder-Mead downhill simplex approach, which we now compare to the principal axis method. The convergence behavior of the two methods, when using the SPA-technique, is shown in Fig. 9.2. Both Nelder-Mead simplex and principal axis method are again started with 7 parameters, as described above, using the same guess for both methods. The principal axis method is found to clearly outperform the Nelder-Mead simplex: Indeed, with only 7 optimization parameters, the principal axis method reaches a value of  $J_T^{(1)} = 0.50$  already after 100 iterations, whereas the simplex method requires almost 400 iterations to reach the same value. Moreover, the simplex algorithm tends to reach a plateau more easily than the principal axis method, and after 600 iterations, the functional does not decrease even upon increasing the number of parameters. This behavior is typical, and we only show representative results in Fig. 9.2. For example, changing the number of critical iterations does not change this observation—the Nelder-Mead simplex method tends to get stuck more rapidly and the optimization cannot escape from the plateau, cf. the blue triangles in Fig. 9.2(a). In contrast, as seen from Fig. 9.2(b), with the principal axis method the functional continues to decrease, albeit slowly, when the number of optimization parameters is increased. According to our numerical experiments, this behavior is again independent of the guess field. We thus find that SPA-optimization based on the principal axis method represents a promising alternative not only to the widely used Nelder-Mead simplex approach, but also to the principal axis method itself, when used in the standard version with a fixed number of optimization parameters. The resulting degree of coherence amounts asymptotically to  $g_{3s_0,3p_0} = 0.989$  after 1500 iterations, which is induced by an driving field fulfilling, by construction, both, maximal peak amplitude and frequency components requirements. All numerical experiments that we have carried out reproduced the relative advantage of SPA-optimization over optimization with a fixed number of optimization parameters (Fig. 9.1) and of the principal axis method over Nelder-Mead simplex (Fig. 9.2). However, they also revealed a rather high sensitivity of the optimization success, both in terms of

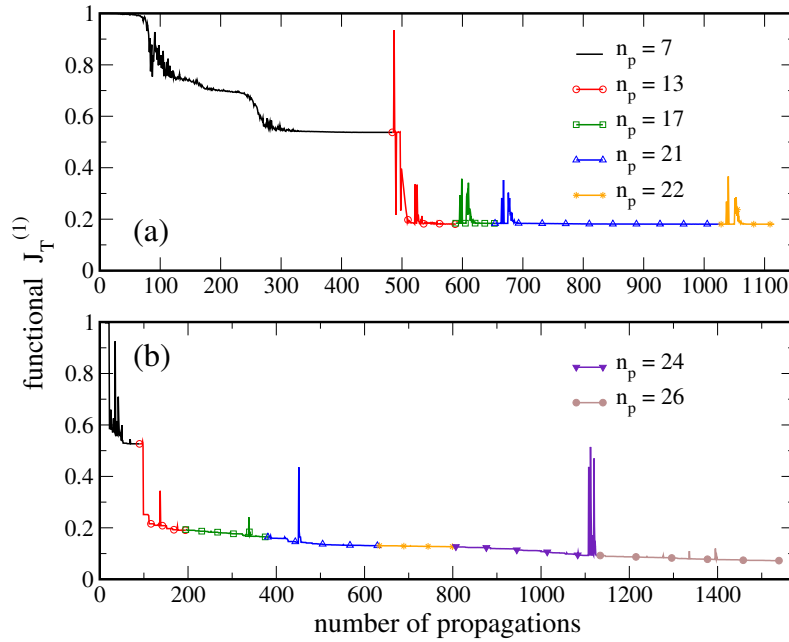


Figure 9.2: SPA-optimization based on the principal axis method (b) converges significantly faster and yields a better hole coherence than with the Nelder-Mead (a) simplex search.

convergence speed and final hole coherence achieved, on the initial guess. This suggests to pre-scan the parameters of the initial guess, as studied next.

### 9.4.2 Optimization using a “pre-optimized” guess field

The idea is to identify a small number of key parameters whose values are scanned in a prespecified range. While this does not constitute optimization in itself, it is related in spirit to the hybrid optimization approach of Ref. [259] which combines a cheap, low-level parameter “pre-optimization” with a numerically more expensive, high-level gradient-based optimization. Once the parameter scan has been carried out, the best parameters resulting from the scanning procedure, i.e the ones that minimize, at least locally, the functional of interest, are chosen to define the guess for the actual SPA-optimization. As a result, the actual optimization is started with a minimal number of optimization parameters at an already relatively good fidelity.

This approach is particularly useful when no a priori physical insight into the best choice of the field parameters is available. The required calculations are independent of each other and can thus be carried out in parallel. Nevertheless, the number of parameters to be scanned should be kept at a minimum. Furthermore, it is not necessary to perform the scan with very high resolution since small changes in the parameters that significantly improve the target will be readily identified by the subsequent optimization. We thus start by evaluating the degree of coherence by scanning three parameters of a transform-limited

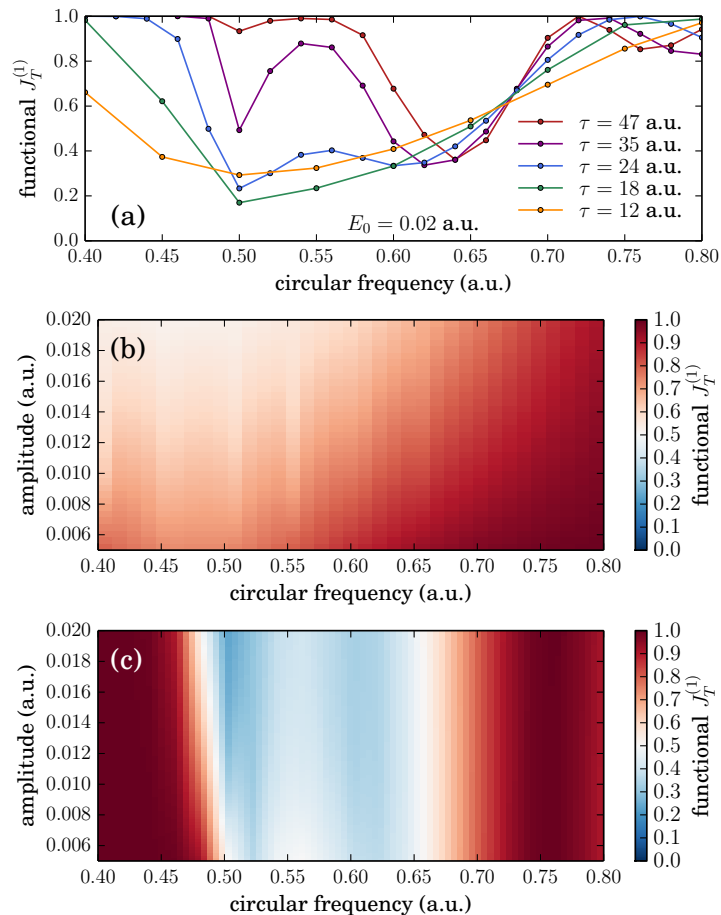


Figure 9.3: Parameter scanning prior to optimization: Frequency / peak amplitude scans for fixed pulse durations  $\tau = 6$  a.u. (b) and  $\tau = 23$  a.u. (c). Favorable parameters for the initial guess field can clearly be identified.

Gaussian pulse—its peak amplitude, central frequency, and duration or, equivalently, spectral width. The numerical results are shown in Fig. 9.3. Keeping the peak amplitude fixed at  $E_0 = 0.02$  a.u., which corresponds to the maximal peak amplitude allowed, and varying the pulse frequency, one broad minimum of the functional is observed in Fig. 9.3 (top) for short (spectrally broad) pulses near  $\omega_{ph} = 0.50$  a.u. This minimum is shifted to  $\omega_{ph} = 0.64$  a.u. for the longest pulse, whereas both minima occur for intermediate pulse durations. Note that  $\tau$  refers to the FWHM of the intensity profile.

A relatively complete picture is obtained when scanning both frequency and peak amplitude of the field, keeping only the duration fixed. The results are shown in Figs. 9.3(b) and (c) for pulse durations of  $\tau = 6$  a.u. and  $\tau = 23$  a.u., respectively: Apparently, spectrally too broad pulses are not suitable for the maximization of hole coherence, cf. Fig. 9.3(b). The best pulses are obtained for  $\tau = 23$  a.u. (light-blue area in Fig. 9.3(c)) where a distinct window of favorable central circular frequencies occurs between  $\omega_{ph} = 0.50$  a.u. and  $\omega_{ph} = 0.65$  a.u. Interestingly, good hole coherences are ob-

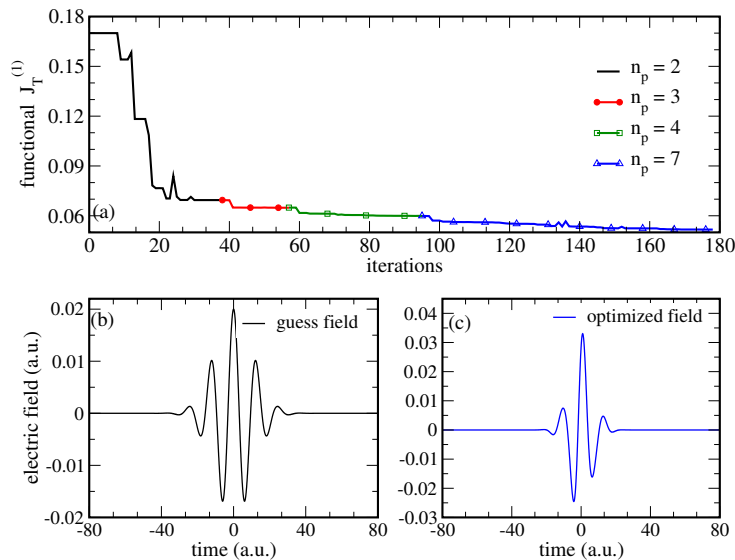


Figure 9.4: SPA-optimization with the principal axis method, using favorable initial parameters in the guess pulse: The convergence is significantly accelerated (a). Guess and optimized fields are shown in (b) and (c).

tained even for weak fields. One has to keep in mind, however, that these come with low overall ionization probabilities.

Once we have scanned the basic parameters of the field, we use the best values to start the actual SPA-optimization, increasing the number of parameters once the change in the functional,  $J_T^{(1)}$ , becomes too small, as before. Figure 9.4 shows the corresponding results. The parameter scan allows to find an already good guess field, depicted in Fig. 9.4(b), such that SPA-optimization starts with a value of  $J_T^{(1)} = 0.17$ , cf. Fig. 9.4(a), to be compared with the poor starting fidelity in Figs. 9.1 and 9.2. After only 180 iterations,  $J_T^{(1)}$  has dropped to 0.04. At this stage, 7 optimization parameters are used, resulting in a comparatively simple shape of the optimized field, cf. Fig. 9.4(c). For comparison, the lowest value of  $J_T^{(1)}$  obtained in Sec. 9.4.1 without a prior parameter scan amounts to 0.07. Thus, the sequential update technique based on the principal axis method, with prior scanning of the optimal parameters for the guess field reveals itself to be a very efficient optimization method. It allows for reaching high fidelities while minimizing the number of optimization parameters as well as the numerical effort. The dynamics obtained with various guess and optimized fields are analyzed in Fig. 9.5, which displays the degree of coherence as a function of time. Figures 9.5(a) and (b) compare  $g_{3s,3p_0}(t)$  for a randomly chosen guess field with a large number of parameters (black line) and for the optimized field obtained from this guess (red line). The fields are shown in grey (not scaled). Whereas the guess field yields a very poor fidelity, cf. the y-axis scale, the maximized degree of coherence between the hole states  $3s$  and  $3p_0$ , reaches a value

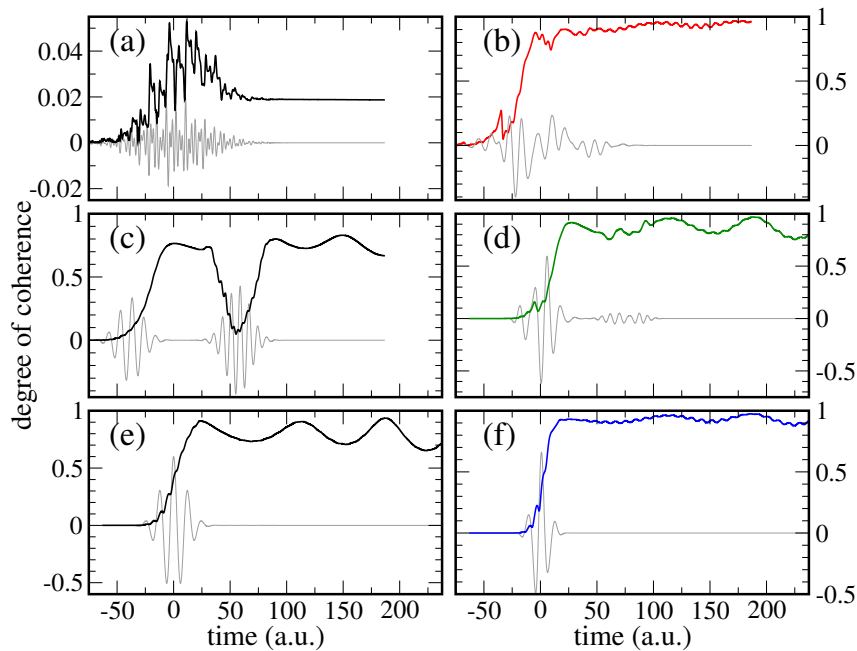


Figure 9.5: Degree of coherence as a function of time obtained with guess (left) and optimized (right) fields: (a) randomly chosen initial parameters ( $n_p = 26$ ); (b) corresponding optimized field with  $g_{3s,3p_0}(T) = 0.989$  ( $n_p = 26$ ); (c) initial guess field consisting of two time-delayed Gaussians ( $n_p = 8$ ) (d) corresponding optimized field for which the degree of coherence oscillates between  $g_{3s,3p_0}(t) = 0.97$  and  $0.75$  with a final value of  $g_{3s,3p_0}(T) = 0.80$  ( $n_p = 16$ ); (e) initial monochromatic guess field with favorable parameters identified by parameter scan, (f) corresponding optimized field ( $n_p = 7$ , the same as shown in Fig. 9.4(c)) for which the degree of coherence oscillates between  $g_{3s,3p_0}(t) = 0.98$  and  $g_{3s,3p_0}(T) = 0.90$ .

of  $g_{3s,3p_0} = 0.989$ . Figures 9.5(c) and (d) answer the question whether a time-delayed sequence of two Gaussian pulses is suitable for maximizing hole coherence. We treat the amplitudes, circular frequencies and delay as a optimization parameters. Since the sub-pulse structure essentially disappears upon optimization, we conclude that time-delayed pulses are not suitable for maximizing hole coherence. Finally, Figs. 9.5(e) and 9.5(f) display the degree of coherence obtained with the guess constructed after parameter scan and the corresponding optimized field, also shown in Fig. 9.4(b) and (c).

### 9.4.3 Enhancement mechanisms of hole coherence of hole states in ultrafast photoionization

The benefits of scanning the field parameters are two-fold. Not only it allows to find an educated guess field to start the optimization while reducing considerably the numerical effort, but also, by evaluating the functional defined by the degree of coherence

as a function of the field parameters, together with the inspection of the photoelectron spectrum allows already to unravel the physical mechanisms that allows to minimize the decoherence. In fact, the results displayed in Fig. 9.3 (top) already provide an insight into possible mechanisms for enhancing the degree of coherence between the  $3s$  and  $3p_0$  hole states. For perfect hole coherence, it is required that photoelectrons from the  $3s$  and  $3p_0$  orbitals to be **energetically indistinguishable**. The binding energy is 1.272 a.u. for  $3s$  and 0.591 a.u. for  $3p_0$  at the Hartree-Fock level. Therefore, a photon with  $\omega_{ph} = 0.50$  a.u. might create, via three-photon ionization of the  $3s$  orbital, a photoelectron at an energy of  $\omega_{e-(3s)} = 0.228$  a.u. while two-photon ionization of the  $3p_0$  orbital would create a photoelectron at  $\omega_{e-(3p_0)} = 0.409$  a.u. **This is the first scenario**, where the minimum bandwidth required for energetic indistinguishability corresponds to a maximum  $\tau = 30.7$  a.u. This scenario corresponds to the minimum in Fig. 9.3 (top) near  $\omega_{ph} = 0.50$  a.u. for  $\tau$  up to 35 a.u. For shorter pulses, the minimum becomes broader but remains centered at  $\omega_{ph} = 0.50$  a.u. The second minimum, near  $\omega_{ph} = 0.64$  a.u., observed for long and spectrally narrow pulses, cannot be explained by this first scenario. For example,  $\tau = 47$  a.u. corresponds to a spectral bandwidth of 0.06 a.u. However, a central frequency of  $\omega_{ph} = 0.64$  a.u. is not too far from the transition frequency between the parent orbitals,  $\delta\omega_{3s,3p_0} = 0.681$  a.u. This first scenario describing the three-photon ionization of the  $3s$  and two-photon ionization of the  $3p_0$  is schematized in Fig. 9.6 (left panel).

**A second conceivable scenario** thus consists in the one-photon ionization of the  $3p_0$  orbital together with the resonant excitation of a  $3s$  electron into the  $3p_0$  hole, as depicted in Fig. 9.6 (right panel). In this scenario, one-photon ionization of the  $3p_0$  orbital with a photon of  $\omega_{ph} = 0.64$  a.u. would lead to a photoelectron at  $E_{e-(3p)} = 0.049$  a.u., whereas a photoelectron originating from the  $3s$  orbital that absorbed two such photons would have an energy of  $E_{e-(3s)} = 0.008$  a.u. In order to check whether these scenarios are indeed responsible for the structure observed in Fig. 9.3 (top), channel-resolved photoelectron spectra (PES) are shown in Fig. 9.7. Indeed, for  $\omega_{ph} = 0.64$  a.u. and  $\tau = 47$  a.u. (yellow lines), the channel-resolved PES reveal for  $3s$  a peak in the vicinity of  $\omega_{e-(3s)} = 0.01$  and for  $3p_0$  one at  $\omega_{e-(3p_0)} = 0.05$  a.u. Given our resolution, these peaks essentially coincide with the expected ones at 0.008 a.u. and 0.049 a.u., confirming the creation of hole coherence by resonant transition from the  $3s$  into the  $3p_0$  orbital. The same mechanism is seen to be at work for the pulse with  $\tau = 35$  a.u. and  $\omega_{ph} = 0.64$  a.u. (dark blue line in Fig. 9.7). The larger width of the blue peaks compared to the yellow ones ( $\tau = 47$  a.u.) simply reflects the larger bandwidth of the field. Completely different PES are obtained for a central frequency of  $\omega_{ph} = 0.50$  a.u. (red and cyan lines in Fig. 9.7). Assuming here the first scenario to be relevant, i.e., a simultaneous three-photon ionization of  $3s$  and

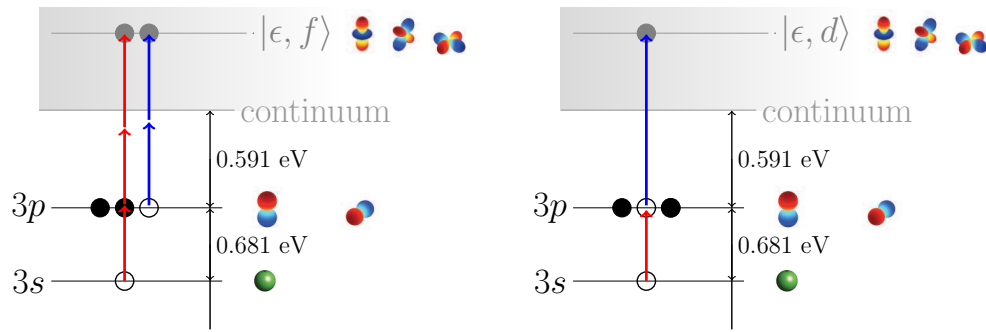


Figure 9.6: **Schematic control mechanism for hole decoherence suppression:** Three-photon ionization of the  $3s$  and two-photon ionization of the  $3p_o$  orbital (left) defines the first scenario. A second conceivable scenario is the one-photon ionization of the  $3p_o$  orbital together with the resonant excitation (refilling) of a  $3s$  electron into the  $3p_o$  hole (right panel).

two-photon ionization of  $3p_o$ , we expect peaks at  $\omega_{e^{\hat{a}}_{Az}(3s)} = 0.228$  a.u. in the  $3s$ -PES and at  $\omega_{e^-(3p)} = 0.409$  a.u. in the  $3p_o$ -PES. These peaks are indeed observed for the red and cyan curves in Fig. 9.7. Even if for  $\tau = 47$  a.u. (cyan line in Fig. 9.7) the spectral bandwidth is too small to really render the  $3s$  and  $3p_o$  photoelectrons indistinguishable, the mechanism of simultaneous three-photon ionization of  $3s$  and two-photon ionization of  $3p_o$  explains the small dip at  $\omega_{ph} = 0.50$  a.u. in the brown line in Fig. 9.3. This holds of course also for the deeper minima observed for shorter, i.e., spectrally broader pulses. We thus conclude that the first scenario, of simultaneous three-photon ionization of  $3s$  and two-photon ionization of  $3p_o$ , is at work for  $\omega_{ph} = 0.50$  a.u.

#### 9.4.4 Electronic correlations and asymptotic oscillating behavior of the degree of coherence

The impact of the Coulomb interaction on the hole coherence is analyzed by comparing hole coherence dynamics within the “full” (or **interchannel**) model and **intrachannel approximations**. Within the “full” model, the photoelectron may couple to all hole states in the parent ion which mediates a coupling between different channels. In contrast, within the intrachannel approximation, the photoelectron can only interact with the hole in the orbital from which it originates [52].

Remarkably, the degree of coherence oscillates as a function of time in Fig. 9.5, even after the field is over. These oscillations may be the direct manifestation of two possible mechanisms: On one hand, the oscillations might be related to how fast the photoelectron leaves the parent ion since the interaction between any outgoing photoelectron and the remaining ion creates entanglement and thus decreases the hole coherence. Alternatively,

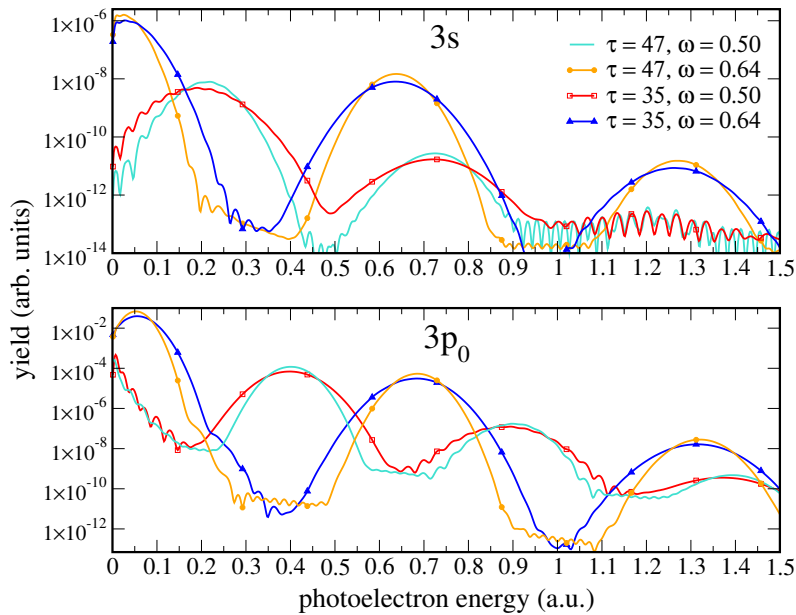


Figure 9.7: upper panel: Frequency scan with fixed peak amplitude for several pulse durations (FWHM of the intensity) and resulting channel-resolved PES in middle and lower panels.

they may be caused by excitation of Rydberg states, which would allow the electron-ion interaction to persist even long after the pulse is over. In both cases, the excited electron reaches a sufficiently large spatial extension such that it is affected by the CAP.

Therefore, in order to quantify how fast a photoelectron leaves the parent ion, we can exploit the loss of norm, due to the CAP. In fact, since the CAP acts only to the virtual orbitals, it might serve as a sensor for the excited electron, or eventually, the photoelectron that reaches the asymptotic region, where the CAP is active. Such an indicator is given by the loss of norm, due to the CAP namely,

$$\Delta_{\rho}(t) = 1 - \left( \text{Tr}_i [\tilde{\rho}^{IDM}(t)] + |\alpha_0(t)|^2 \right), \quad (9.13)$$

since  $\text{Tr}_i[\tilde{\rho}^{IDM}(t)] + |\alpha_0(t)|^2$  is not equal to one, due to the CAP (only  $\text{Tr}_i[\rho^{IDM}(t)] + |\alpha_0(t)|^2$  is) and the CAP does not affect the coefficients  $\alpha_0(t)$ .

To inspect how fast the excited electron reaches the region of the CAP, Fig. 9.8 shows the loss of norm for the three different optimized fields shown on the right-hand side of Fig. 9.5. The optimized field, for which the degree of coherence shows the fastest oscillations with the smallest amplitude (red line in Fig. 9.5), produces the more energetically excited electrons (the ones reaching large spatial domain first), whereas the slowest oscillations of the degree of coherence with the largest amplitude (green line in Fig. 9.5) are associated with the less energetically excited electrons reaching the CAP region, cf.

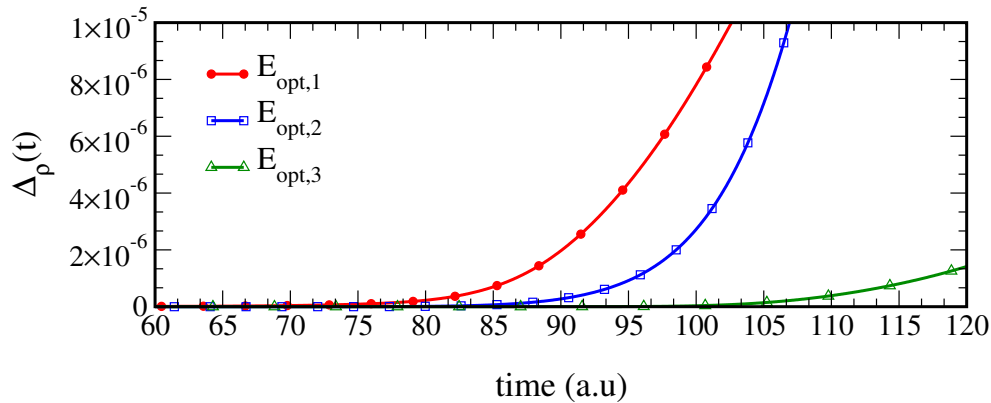


Figure 9.8: **Argon**: Photoionization probability, obtained in terms of the absorbed part of the ion density matrix, cf. Eq. (9.13), as a function of time for the three optimized fields depicted in Fig. 9.5(b), (d) and (f). The color code is the same as in Fig. 9.5.

Fig. 9.8. From these observations we may conclude that the oscillations arise from the interaction between the remaining ion and the excited electron, which perturbs the coherence of the ion density matrix. Thus, the fastest excited electrons interact the least with the remaining ion whereas the slowest (or bound) ones, which interact with the remaining ion during longer times, lead to a larger perturbation of the degree of coherence. A similar conclusion regarding the interaction between the photoelectron and the photoion was previously drawn for hole decoherence in the photoionization of xenon [52].

This interpretation is relevant for the “full” model including interchannel coupling where a fast departure of the photoelectron minimizes the interaction with the remaining ion. In contrast, within the intrachannel model, the excited electron can interact only with the electrons remaining in the channel from which it originates. One should therefore expect that the oscillations in this case become less important. In Fig. 9.9, we compare the degree of coherence as well as the hole populations as a function of time for the “full” model and the intrachannel approximation. We have used the optimized field, depicted in Fig. 9.5(b), that produces the fastest photoelectrons (within the “full” model), so that the oscillations in  $g_{3s,3p_0}$  are minimal. As can be seen in Fig. 9.9(a), the oscillations at times larger than 50 a.u., due to the interaction between the excited electron and the parent ion, disappear completely if we allow the excited electron to interact only with the orbital from which it originates. Furthermore, the interchannel coupling is also found to be responsible for the oscillations in the hole populations after the pulse is over, cf. Fig. 9.9(b) and Fig. 9.9(c).

In Fig. 9.10, we carry out the same analysis of the interchannel coupling, this time using the optimized field depicted in Fig. 9.5(f), which produces slower photoelectrons, cf. Fig. 9.8. Again, the oscillations in  $g_{3s,3p_0}(t)$  and the hole populations, observed for

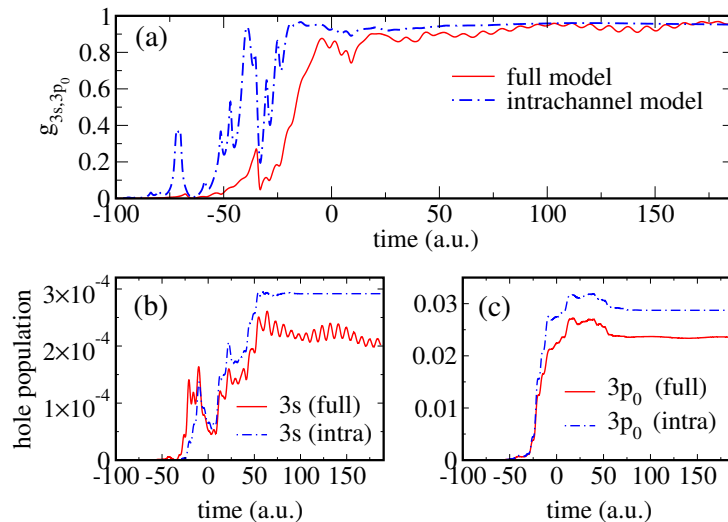


Figure 9.9: **Argon**: Degree of coherence (a) and hole populations (b,c) as a function of time, obtained with the optimized field shown in Fig. 9.5(b), for the interchannel (‘full’) and intrachannel models.

the “full” model, disappear in the intrachannel approximation. Despite the modified dynamics, the final value for the degree of coherence remains almost the same for both optimized fields when switching off the interchannel coupling. In contrast, the final hole populations are considerably changed, cf. the lower panels in Figs. 9.9 and 9.10. This strongly suggests that the oscillations present in the degree of coherence as well as in the hole populations are induced by the interchannel interaction.

#### 9.4.5 Minimization of hole decoherence with prescribed hole population ratio

One of the most striking features of the optimization results presented in the previous section concerns the population difference between the hole states. Specifically, the population of the  $3p_0$  hole exceeds that of the  $3s$  hole by at least two orders of magnitude in all examples studied. Such a large population difference is undesirable in view of utilizing the coherent superposition in time-dependent spectroscopy. We therefore address now the question whether it is possible to maximize the degree of coherence between the  $3s$  and  $3p_0$  hole states while simultaneously controlling the final hole population.

We consider all possible scenarios, i.e., equal populations,  $\rho_{3p_0,3p_0} > \rho_{3s,3s}$ , and  $\rho_{3p_0,3p_0} < \rho_{3s,3s}$ . To be specific, we ask for the corresponding population ratio  $\mathcal{R}$  to be equal to 0.7 in the last two cases and utilize the optimization functional  $J_T^{(2)}$ , cf. Eq. (9.10). Starting with equal populations, Fig. 9.11 shows the degree of coherence, hole populations and optimized field as a function of time, demonstrating success of SPA-optimization also for this more challenging control target. Figure 9.11 also analyzes the role of the interchannel coupling, cf. red and blue lines, as well as the role of direct transitions between the  $3s$

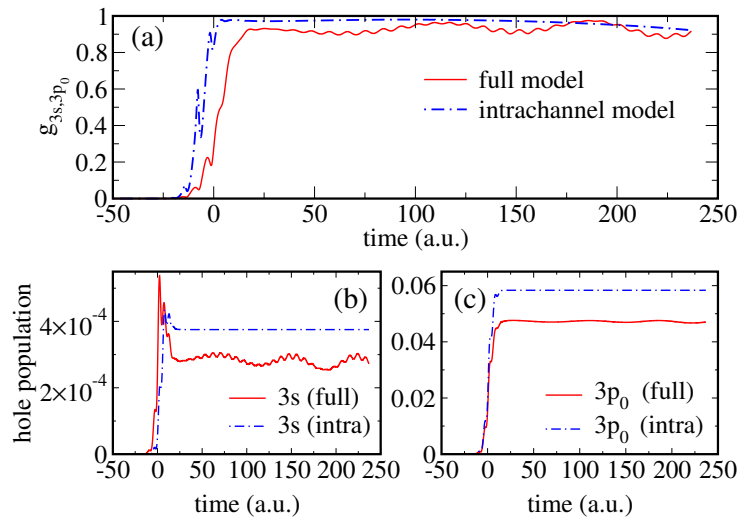


Figure 9.10: **Argon**: Degree of coherence (a) and hole populations (b,c) as a function of time, obtained with the optimized field shown in Fig. 9.5(f), for the interchannel ('full') and intrachannel models.

and  $3p_0$  states, cf. red and green lines. The interchannel coupling is seen to affect the hole coherence only during the first half of the pulse, whereas the final coherence is identical with and without interchannel coupling, cf. Fig. 9.11(a). In contrast, suppressing the excitation of a  $3s$  electron into the  $3p_0$  orbital strongly modifies the degree of coherence. It reduces the final value from 0.98 to 0.39, indicating that sequential ionization of  $3s$  electrons is important here.

As for the population dynamics, Fig. 9.11(b) reveals the  $3p_0$  hole population to always be larger than the  $3s$  population until the two populations reach the same value. This is true both with and without interchannel coupling. The interchannel coupling is seen to only affect the final populations, by an amount that is not very large. While the  $3s$  hole population increases monotonically, the  $3p_0$  hole population reaches a maximum value at the same time that the degree of coherence becomes stationary. After that time, the  $3p_0$  hole population decreases to the target value. In contrast to the degree of coherence that becomes stationary already while the pulse is still on, the hole populations do so only at the end of the pulse. The population dynamics confirms the importance of excitations from  $3s$  electrons to  $3p_0$ : When this transition is switched off, the  $3s$  hole population drops to essentially zero, cf. the green line in Fig. 9.11(b). We can thus conclude that the decrease of the  $3p_0$  hole population and simultaneous increase of the  $3s$  hole population, seen for the "full" model, is due to a dipole transition between these two states. In other words, Rabi oscillations occur between these orbitals, as indicated by the oscillatory pattern of the red and blue lines in Fig. 9.11(b) for  $-10 \leq t \leq 15$  a.u. This interpretation is confirmed by the fact that these oscillations occur with the same frequency, but a phase

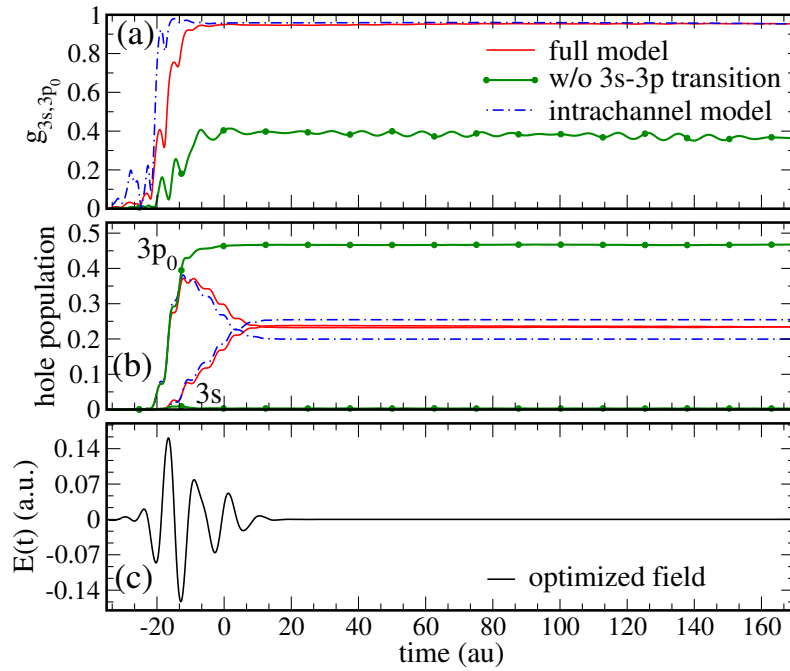


Figure 9.11: **Argon**: Maximization of the degree of coherence between the  $3p_0$  and  $3s$  hole states while simultaneously optimizing for a hole population ratio of one: degree of coherence (a), hole populations (b) and optimized electric field (c) as a function of time.

shift of  $\pi$  (data not shown).

Next, we target the case  $\rho_{3p_0,3p_0} > \rho_{3s,3s}$  with a population ratio of  $\mathcal{R} = 0.7$ . Given the fact that the  $3p_0$  hole population always turned out to be larger than the  $3s$  hole one for the cases previously described, this is the simplest of the three cases. The results are shown in Fig. 9.12. Similarly to the case of equal hole populations, the interchannel coupling does not affect the final degree of coherence and the final populations. However, in contrast to the case of equal populations, both the hole population and the degree of coherence become stationary at the same time, once the pulse is over, cf. Fig. 9.12(a) and (b). Direct transitions between the  $3s$  and  $3p_0$  orbitals are found to play again an important role, cf. the green lines in Fig. 9.12(a) and (b).

Finally, we maximize the degree of coherence constraining the hole populations such that  $\rho_{3p_0,3p_0} < \rho_{3s,3s}$ . This is the most difficult target, but it is successfully addressed by SPA-optimization and the results are shown in Fig. 9.13. Again, the interchannel coupling is found to affect the degree of coherence only during the pulse, but neither the final coherence nor the population dynamics, cf. red and blue lines in Fig. 9.13(a) and (b). Compared to the cases of equal population and larger  $3p_0$  hole population, the population dynamics is more intricate, showing a crossing in order to reach the desired population ratio and a number of distinct oscillations. We again check whether these oscillations correspond to Rabi cycling between the  $3s$  and  $3p_0$  orbitals by switching

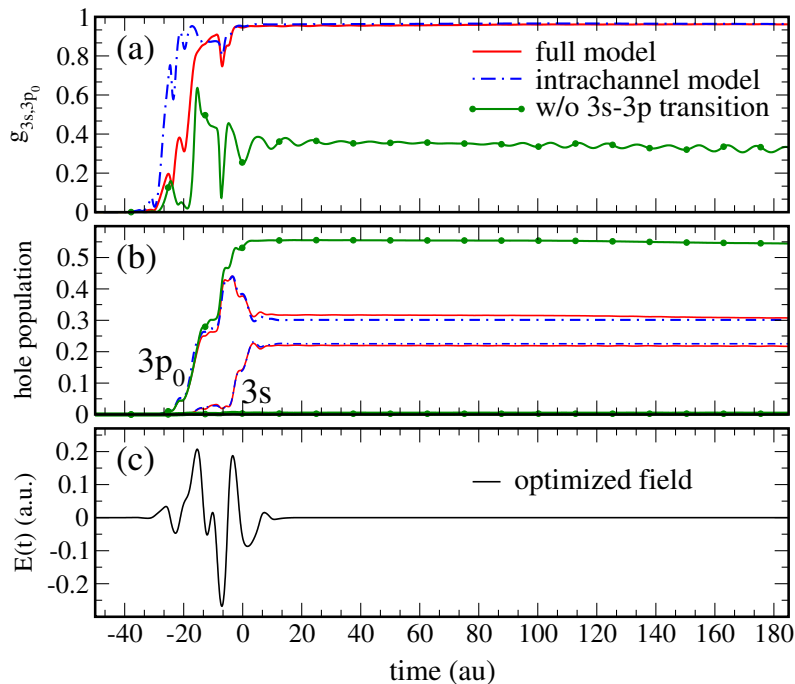


Figure 9.12: **Argon**: Maximization of the degree of coherence between the  $3p_0$  and  $3s$  orbitals while simultaneously optimizing for a hole population ratio of  $\rho_{3s,3s}/\rho_{3p_0,3p_0} = 0.7$ : degree of coherence (a), hole populations (b) and optimized electric field (c) as a function of time.

off the transition dipole matrix elements. We find that, when  $3s$  to  $3p_0$  transitions are not allowed, no oscillations are present in the population dynamics, and the  $3s$  hole population drops to essentially zero. Moreover, analysis of the population oscillations reveals again their identical frequency and a phase shift of  $\pi$  (data not shown). For all three variants of the  $3s$  to  $3p_0$  hole population ratio, the corresponding optimized fields were successfully identified by SPA-optimization. Their spectra are shown in Fig. 9.14. The circular frequencies were treated as optimization parameters, using Eq. (9.12) to constrain them to  $\omega_{min} = -4$  a.u. and  $\omega_{max} = 4.0$  a.u. The most difficult optimization target results in the broadest spectrum, cf. blue line in Fig. 9.14. It is a common observation that more difficult optimization problems result in more complex control fields. Overall, the optimized spectra are too broad to identify one of the two control mechanisms, based on photon energies of 0.50 a.u. versus 0.68 a.u., as discussed in the previous section, by inspection of the spectra alone. The numerical effort, in terms of optimization parameters is comparable for all three cases—the final number of optimization parameters amounts to 28. The most difficult optimization target required the largest number of iterations. In this case, the value of the functional  $J_T^{(2)}$  decreased with a slower rate, compared to the other two cases. For all three population ratios, SPA-optimization was started with the same guess field, using four optimization parameters: the FWHM, a frequency, a Fourier

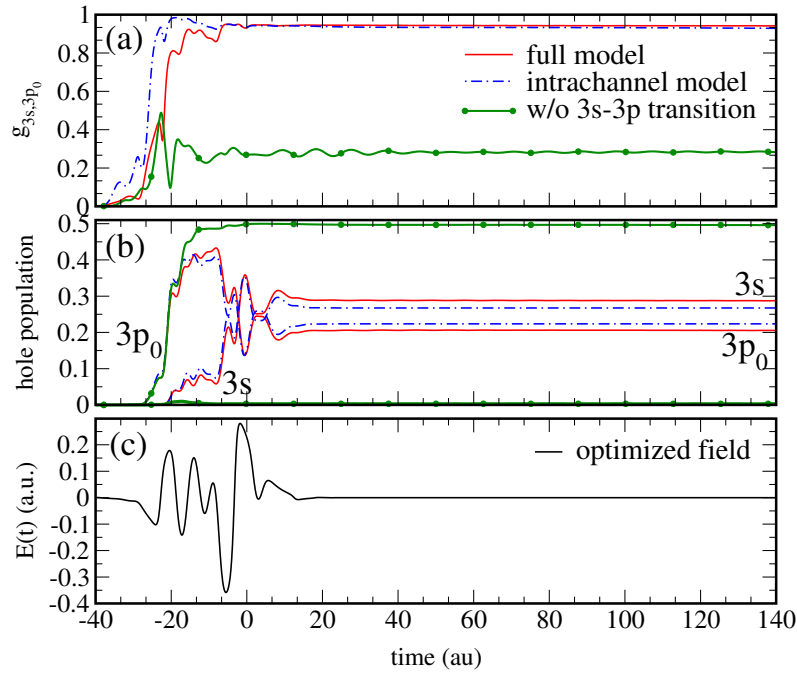


Figure 9.13: **Argon**: Maximization of the degree of coherence between the  $3p_0$  and  $3s$  hole states while simultaneously optimizing for a hole population ratio of  $\rho_{3p_0,3p_0}/\rho_{3s,3s} = 0.7$ : degree of coherence (a), hole populations (b) and optimized electric field (c) as a function of time.

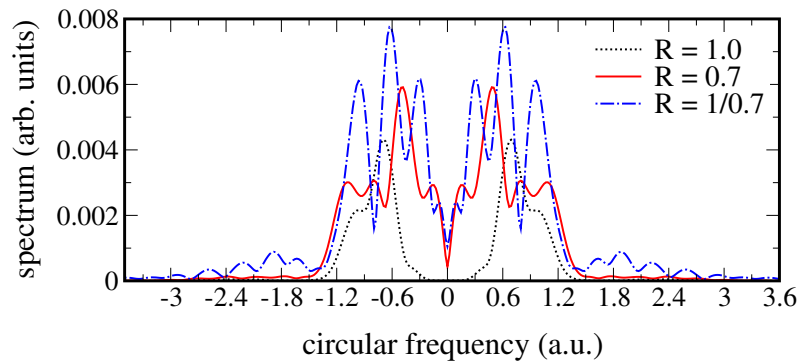


Figure 9.14: **Argon**: Maximization of the degree of coherence between the  $3p_0$  and  $3s$  hole states while simultaneously optimizing for a given hole population ratio. Spectra of the optimized fields for the three different hole population ratios,  $\mathcal{R} = \rho_{3s,3s}/\rho_{3p_0,3p_0}$ .

amplitude and a phase shift. At the end of the procedure, the FWHM, nine frequency components, nine Fourier amplitudes and nine phases were optimized.

## 9.5 Suppression of hole decoherence in Xenon: A novel mechanism

As previously discussed in Section 9.4.4, an enhancement pathway to achieve decoherence suppression consist in (i) increasing the photon energy in order to reduce the interaction time between the ionized photoelectron and the photoion. The same enhancement mechanism was previously discussed in Ref. [52] in the context of one-photon ionization in xenon. In the context of our photoionization studies in argon, cf. Section 9.4.3, we have found that ionization of the  $3p_0$  followed by (ii) refilling of the created  $3p_0$  hole from the  $3s$  orbital leads a to a notorious enhancement of the degree of coherence between the both holes states.

These two observations define the motivation of this section. We apply our **SPa** optimization approach to *a more challenging* atomic many-body situation, namely the maximization of the degree of coherence between the  $4d_0$  and  $5s$  hole states in Xenon. In fact, the simple enhancement mechanism found for argon– of ionizing the  $3p_0$  orbital and refilling it by excitation from the  $3s$  orbital, fails in this case since the  $4d_0$  and  $5s$  orbitals cannot be coupled by one-photon excitation, in the context of the strict dipole approximation.

Furthermore, in order to avoid the “trivial” solution of avoiding entanglement by reducing the interaction between the freed photoelectron and ionic hole, which is accomplished merely by increasing the photon energy as prescribed in Ref. [52], we limit the photon energies to below  $\omega_{\max} = 130$  eV, which corresponds to the photon energy for which a maximal degree of coherence was found in Ref. [52]. The idea behind is to exploit the versatility of the SPA technique to find new enhancement mechanisms that violates the observations in Ref. [52].

Additionally, given the Auger lifetime of 2.6 fs for the  $4d_0$  hole, we restrict our analysis to the attosecond photoionization timescale and constrain the pulse duration to a few hundred attoseconds. Note that the lifetime of the  $4d_0$  nor final  $f$ – stated were not considered in Ref. [52]. Furthermore, by restricting ourselves to maximal field peak amplitudes up to  $52$  GV m<sup>-1</sup>, for which the probability for multiple ionization remains small, the validity of the calculations in the context of the **TDCIS**, is ensured. From a practical prospective, such upper bound for the peak amplitude avoid the final ground state depletion to be outside the 0.2 and 0.3 range . The former bound ensures reasonably high ionization probabilities for the purpose of experimental detection of photoelectron yield, while the latter warranties ionization of predominantly one single electron.

Finally, in a view of practical applications in the context of time-dependent spectroscopy, we also optionally allow for a constraint in the optimization procedure prescribing a specific hole population ratio,  $\mathcal{R} = \rho_{5s,5s}^{\text{IDM}}/\rho_{4d_0,4d_0}^{\text{IDM}}$ , such that a superposition with significant contributions from both states is obtained.

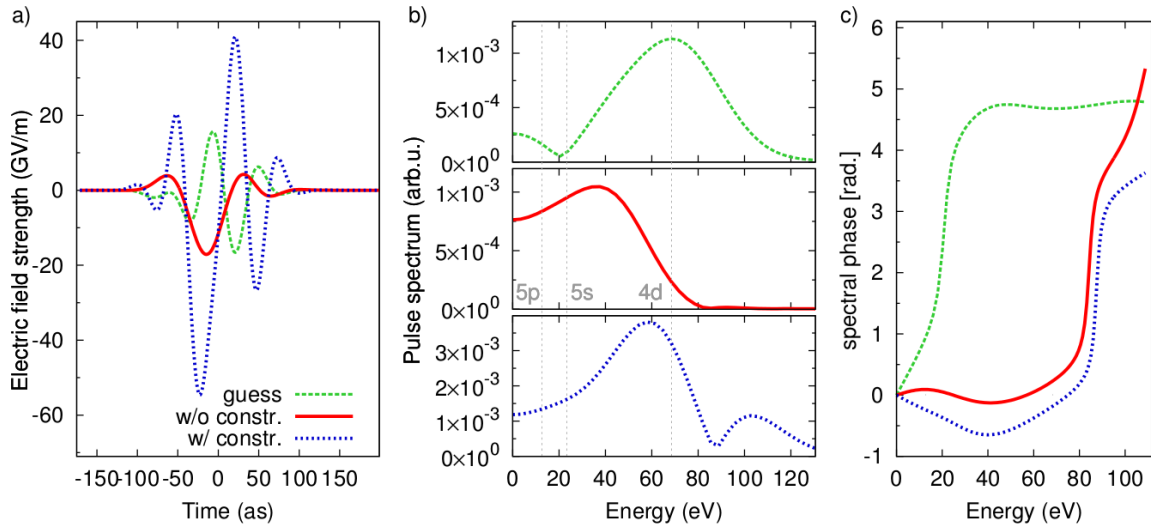


Figure 9.15: **Suppression of hole decoherence in Xenon:** (a) Electric field of the guess pulse (green dashed) and two optimized pulses, obtained with (blue dotted) and without (red solid) a hole-population ratio constraint of  $\mathcal{R} = 1$ . (b) Corresponding spectra, and (c) spectral phases with the same color coding. The gray-dotted lines in panel (b) denote the binding energies of the three outermost shells.

To scrutinize the enhancement mechanism, we choose a arbitrary guess field such that it leads to a very low degree of coherence and compare to that resulting from the optimized field. Guess and optimized fields are shown in Fig. 9.15(a). Besides the guess field (solid green), two optimized fields are shown, corresponding to the optimization with (dotted blue) and without (solid red) hole population ratio. As observed in Fig. 9.15(b), all three spectra spans the binding energies of the xenon  $4d$ ,  $5s$  and  $5p$  orbitals. Because of the red shifting, the optimized guess produce slower photoelectrons from ionization of the valence shells than the guess pulse, which is in striking contradiction, to the enhancement mechanisms found for xenon in Ref. [52], namely of reducing the interaction time between the liberated photoelectron and the photoion by increasing the photoelectron's kinetic energy found in Ref [52], that would result in a blue shift of the optimized pulses, with respect to the guess pulse, instead.

Figure 9.15(c) depicts the spectral phases for all three pulses. While the guess pulse exhibits a linear chirps in the relevant spectral region, non-linear cubic and quadratic chirps characterize the optimized unconstrained and constrained fields, respectively, indicating that besides the power spectrum, interference play a critical role for achieving the control. The presence of non-linear chirp can be straightforwardly understood since it allow to manipulate the shape, by broadening or focusing wave packets [210], controlling the wave packet's energy distribution, leading to a controlled evolution of the different energy components.

The optimized hole population as well as the degree of coherence as a function of time are shown in Fig. 9.16(b), panels (a) and (b), respectively. As opposite to the hole dynamics driven by the guess pulse, ionization of the  $5s$  and  $5d$  orbital is increased and decreased, respectively, for the optimized pulses. While the guess pulse result in almost no coherence for the  $5s$  and  $4d_0$  holes, the unconstrained field prepares the hole in such a superposition that long after the pulse is over, the degree of coherence reaches a asymptotic value of 0.85. This, however, comes at the expense of a relatively small hole population in the  $4d$  orbital, which allows to suppress the unavoidable loss of population induced by the Auger decay. To support this, the same optimization are performed without accounting for the Auger decay, resulting, an almost perfect DOC,  $g_{4d_0,5s} \approx 1$ , instead of 0.85. The Auger decay also explains the  $\text{DOC} \approx 0.5$  obtained in the constrained case, cf. Fig.9.16(b), blue lines. In fact, the increasing  $4d_0$  hole population implies a larger impact of the Auger refilling, such that it only reaches a DOC of 0.5, in comparison to  $\approx 0.82$  when the lifetime of the  $5d_0$  is manually switched off. To understand the impact of the electronic correlation on the coherence, we compare the results within the inter- and intra-channel approximations. While ignoring electronic correlation leads to unchanged holes once created, accounting for correlation arising from all orbitals (inter-channel) result in holes that can be changed through channel interaction, and in particular via atomic resonances that can potentially be driven by the ionizing field. This implies that the entanglement between the ejected photoelectron and the hole in the ion is created only by the electronic correlation in the full correlated scenario. Surprisingly, the optimization succeed in reproducing a significantly enhanced DOC in both scenarios. This can be explained upon analysis of the mechanism by which the optimized pulse achieve such enhancement. In fact, avoiding photon energies between  $75 - 140$  eV., the influence of the many-body interaction is diminished, since the latter range correspond to the region of the giant dipole resonance, which is known to be caused by electronic correlations. Therefore, for both correlated and uncorrelated scenarios, the optimization is able to find the proper pathway that lead to a very high DOC, when no hole-population ratio is constrained.

To rationalize the physical mechanism induced by the optimized to strongly suppress decoherence, which is the main purpose if the work, Fig. 9.17 compares the angle-integrated partial photoelectron spectra (PES) for the  $4d_0$  and  $5s$ . The guess field drives the dynamics in such a way such that the contribution of the  $4d_0$  orbital dominates the yield, with respect to the contribution arising from the  $5s$ . While the  $5s$  contributes to continuum wavefunction with angular momentum  $l = 0$ , the  $4d_0$  contribution to  $l = 1$  for low energies, and  $l = 3$  for high energies. Furthermore, the contribution to  $l = 3$  of the  $4d_0$  exceeds that to  $l = 1$ . In opposition, for the unconstrained pulse reaching  $g_{5d,4d_0} \approx 0.85$ , photoelectron energies in the range  $5 - 40$  eV originating mainly from the  $4d_0$  are sup-

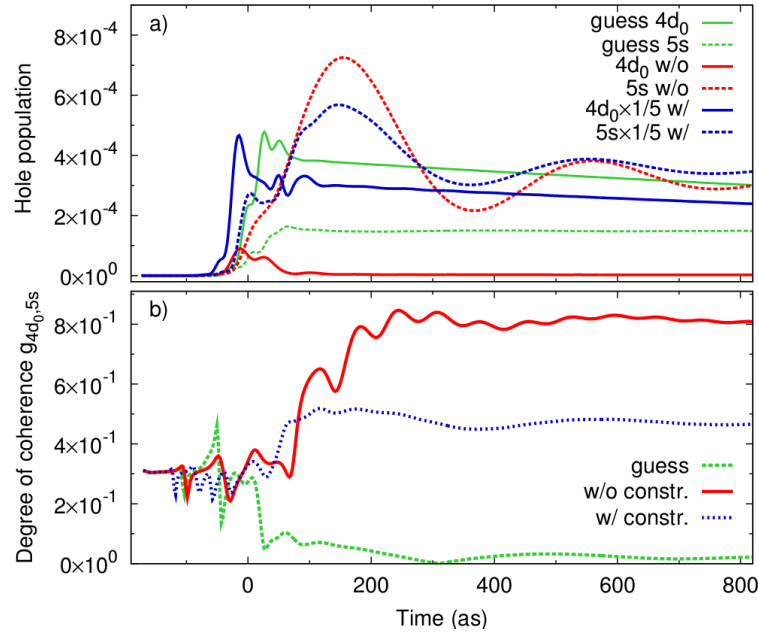


Figure 9.16: **Suppression of hole decoherence in Xenon:** (a) Hole populations of the  $4d_0$  (solid curves) and  $5s$  (dashed curves) orbitals resulting from the guess pulse (green curves) and the optimized pulses with (blue curves) and without (red curves) constraining the hole populations to be equal. The hole populations obtained with the constraint  $\mathcal{R} = 1$  are scaled down by a factor of five. Note that all pulses are over at 100 as, cf. Fig. 9.15. (b) DOC as a function of time. While the guess pulse results in an almost vanishing DOC, a maximum DOC of 0.85 is achieved without hole-population ratio constraint. Including the constraint  $\mathcal{R} = 1$  leads to a DOC of  $\sim 0.5$  which is limited by the Auger decay of the  $4d_0$  orbital ( $g_{4d_0,5s} \approx 0.82$  is obtained in this case when neglecting the Auger decay).

pressed. As alluded to the above lines, the optimized pulse tends to avoid the impact of the many-body correlations in the range of the giant dipole resonance. As a consequence, photoelectrons with lower kinetic energy are liberated and the main photoelectron peaks of both  $4d_0$  and  $5s$  are red shifted to the 0.1 – 0.5 eV range instead.

Additionally, while the low kinetic energy are dominated by contributions from  $4d_0$  and  $5s$  hole states to  $l = 1$ , the contribution from  $4d_0$  to  $l = 3$  dominates the higher portion of the photoelectron spectrum, albeit  $l = 1$  contribute the most to the total yield. Inspection of the field's spectrum in Fig. 9.15(b) (full red lines), indicates that, as a consequence of the red-shifting spectrum, the probability of one-photon ionization from the  $4d_0$  is not very probable. Such a shift leads to a peak position around  $\Omega = 20 - 40$  eV, below the  $4d_0$  binding energy. Alternatively, three-photon ionization induced by high intensity field at the photon energy  $\omega \approx 23 \in \Omega$  eV with from the  $4d_0$  to continuum states with angular momentum  $l = 1$  would result in a photoelectron with angular momentum

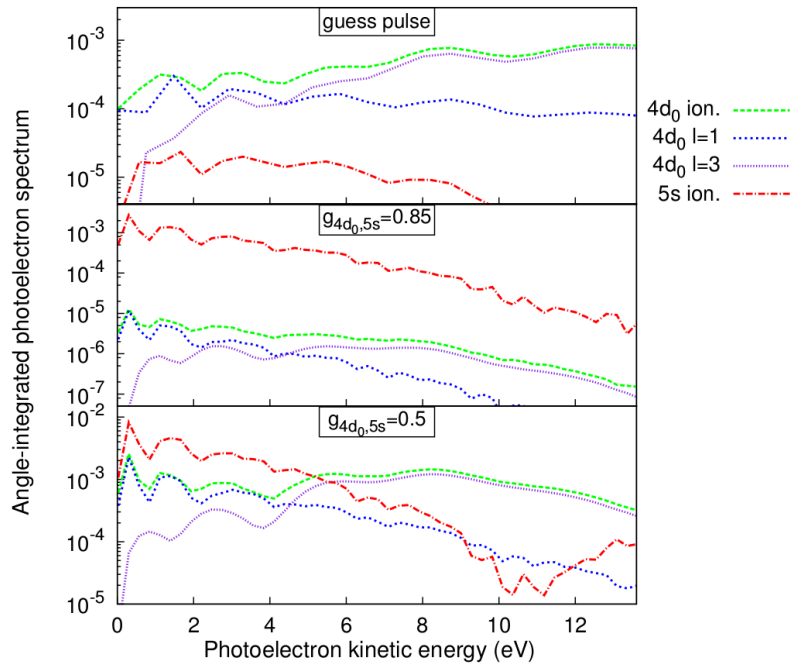


Figure 9.17: **Suppression of hole decoherence in Xenon:** Partial angle-integrated PES for the guess pulse and the optimized pulses (cf. Fig. 9.15). For the guess pulse ionization of  $4d_0$  electrons dominates, the contribution of a final  $l = 3$  continuum state is significant.  $5s$  ionization is less probable. The optimized pulse without hole-population ratio constraint enhances the  $5s$  ionization and leads to very similar shapes of the partial spectra of both  $4d_0$  and  $5s$  photoelectrons over the whole energy range. The pulse increases the ionization of  $4d_0$  electrons into a final state with  $l = 1$  compared to  $l = 3$  exploiting three-photon ionization, such that a more coherent superposition of the ionic hole in  $4d_0$  and  $5s$  hole states is generated. The constraint  $\mathcal{R} = 1$  leads to higher total ionization and enhanced  $4d_0$  spectra by generating more one-photon ionized electrons, but the shapes of the  $4d_0$  and  $5s$  spectra coincide less.

$l = 1$  at  $\omega_{e-(5s)} = 0.5$  eV, which is corroborated upon inspection of the partial yield spectrum, cf. Fig. 9.17, (dotted blue lines). Furthermore, consulting the unconstrained field's spectrum suggests that, single photon-ionization of the  $5s$  is highly probable. Such a mechanism would originate a photoelectron with the same angular momentum  $l = 1$  at the same photoelectron energy, namely  $\omega = 0.5$  eV, which is again corroborated by Fig. 9.17, (dotted red lines).

A common feature observed in the calculations is that for the unconstrained case, the  $5s$  hole population is larger than that of the  $5d_0$ , e.g. Fig. 9.16. In order to fulfill the constraint  $\mathcal{R} = 1$ , while simultaneously fulfilling the constraints on the total ionization of the ground state as mentioned before, a conceivable scenario consists in increasing the ionization of the  $4d_0$  orbital, which would require higher electric field strength as well

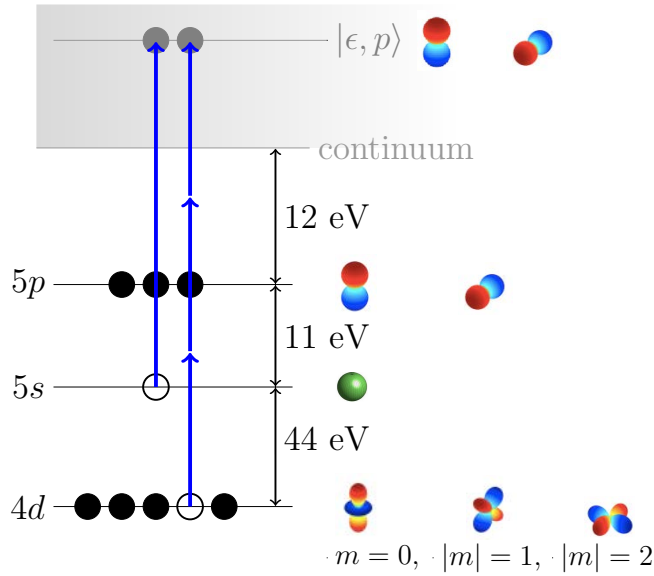


Figure 9.18: **Suppression of hole decoherence in xenon:** Schematic representation (not drawn to scale) of the physical mechanism for hole-decoherence suppression in Xenon – single photon ionization of the 5s orbital together with three-photon ionization of the 4d<sub>0</sub> promoting the 5s and 4d<sub>0</sub> electrons into the same final electronic continuum state with same angular momentum  $\ell = 2$  at the same relatively low photoelectron energy.

as a blue shift of the photon energy distribution, which would significantly increase the photoelectron population with angular momentum  $l = 1$  and  $l = 3$ . This is indeed what is observed in Figs. 9.15 and 9.16 – the electric field strength is significantly increased and blue-shifted, and the  $p$  and  $f$  photoelectron population have increased by two orders of magnitude, cf. 9.17(c) as compared to the results obtained with the unconstrained case. However, due to the blue shifting towards the 4d<sub>0</sub> binding energy, two mechanisms particularly detrimental to the coherence occur: (i) the optimized field also drives one-photon excitation from the bound 4d<sub>0</sub> to the continuum  $l = 3$ , therefore promoting photoelectrons to the wrong  $l = 3$  final state, and (ii), the photoelectron's kinetic energy distribution is also blue-shifted toward the giant dipole resonance range Fig. 9.15(b), which leads to entanglement caused by many-body correlations, and thus lowering the DOC as compared to the unconstrained scenario. Therefore, by virtue of the observations given in the above lines, we are in a position to conclude that the physical mechanism for strong hole decoherence suppression is accomplished by *appropriate combination on predominant single photon ionization of the 5s orbital together with three-photon ionization of the 4d<sub>0</sub> at relatively low photoelectron energies thus promoting the 5s and 4d<sub>0</sub> electrons into the same final electronic continuum state with same angular momentum at the same relatively low photoelectron energy*, which is required to avoid the impact of many-body correlation in the range of the giant dipole resonance. Simultaneously, one-photon ionization to continuum states with  $l = 3$  is strongly suppressed therefore promoting the photoelectron to the same final continuum state. The physical mechanism for suppression of hole decoherence in xenon is depicted in Fig. 9.18 – both 5s and 4d<sub>0</sub> electrons are promoted to the same final electronic continuum state via single- and multi-photon ionization, respectively. De-

spite the fact that the freed photoelectron still interacts with the ionic parent during the irradiation process, which unavoidable leads to decoherence, the appropriate non-linear chirps introduced by the optimization algorithm allows for preparing a significant part of the final state in a superposition of the  $5s$  and  $4d_0$  hole states which enhance coherence between both hole states. Making use of the SPa technique and intentionally restricting the spectrum of the eventual optimized pulses, we have thus discovered a novel control mechanism that exploits simultaneous single- and multi-photon ionization to noticeably enhance the degree of coherence between the  $5s$  and  $4d_0$  hole states in xenon at low photoelectron kinetic energy, in contrast to the result of Ref. [52] where the mean photon energy had to be increased.

## 9.6 Summary of achievements and conclusions

To summarize, we have introduced a sequential update of the pulse parametrization to ease implementation of gradient-free parameter optimization in quantum control. The versatility of this technique, and its efficiency compared to the standard optimization techniques without sequential update allowed us to maximize the coherence of hole state superpositions in the photoionization of argon while significantly decreasing the numerical effort. A sequential update of the pulse parametrization, which adds more terms to the parametrization once the optimization gets stuck, allows for faster convergence and better final results. Such a sequential update can be combined with any method for parameter optimization, and we have tested it here for the principal axis method and the Nelder Mead downhill simplex approach. The principal axis method which so far has not been employed in quantum control turns out to be clearly more efficient than the widely used Nelder Mead approach. Thus, the principal axis method, in particular when combined with a sequential parametrization update, represents an efficient and viable tool for quantum control.

Admittedly, parameter optimization comes with the disadvantage of depending, sometimes critically, on the chosen parametrization. This is outweighed in our case by the ease of implementation, even for a non-Hermitian Hamiltonian. The latter is due to the fact that the long propagation times for photoionization require the use of a complex absorbing potential. For comparison, the alternative approach of gradient-based optimization always involves backward-in-time propagation of Lagrange multiplier wave functions, and the CAP becomes, in the adjoint equation, a source term which can easily give rise to numerical instability.

The technique introduced here can be further improved by scanning key parameters prior to optimization. The numerical effort required for the scan is more than paid off by the reduction in the number of iterations. It also allows for an identification of possible

control mechanisms. In our example, determination of the photon energy turned out to be the most important step. Two favorable energies were identified that correspond to two different scenarios—three-photon ionization of the  $3s$  orbital simultaneously with two-photon ionization of the  $3p_0$  orbital for pulses with sufficiently large spectral bandwidth to render the photoelectrons energetically indistinguishable and one-photon ionization of the  $3p_0$  orbital combined with transitions between  $3s$  and  $3p_0$ .

In argon, when only the hole coherence is optimized, without any restriction on the hole population, the population of the  $3p_0$  hole is found to exceed that of the  $3s$  hole by two orders of magnitude or more. We have therefore extended the optimization functional to include a term that prescribes the population ratio. An equal or similar population of both hole states would be required when using the hole state superposition in time-dependent spectroscopy studies. SPA-optimization has addressed also this more challenging control task very successfully, yielding hole coherences close to one for exactly the population ratio desired, no matter whether the population of the  $3s$  hole should exceed that of the  $3p_0$  or vice versa or whether the populations should be equal. The resulting pulse shapes were found to be fairly simple, with their spectra indicating the second control scenario to be at work.

In all optimizations for hole creation in argon, channel coupling was found not to play any role. This is in contrast to photoionization in xenon where channel coupling is expected to be the main source of decoherence [52]. It may explain why, for argon, hole coherences very close to the absolute maximum can be achieved. Of course, this raises the question as to what the maximum hole coherence is in a case where channel coupling is known to be important.

The SPa-optimization formalism developed in the present work was found to be an versatile tool and a perfect candidate to address this question. Therefore, it has been applied to the suppression of hole decoherence in xenon. In order to explore new mechanisms for the suppression of hole decoherence, we have restricted the frequency components of the optimized pulse and limit the photon energies to avoid the “trivial” solution of reducing the interaction time between photoelectron and ionic hole by increasing the photon energy [52]. that can be accomplished by increasing the photon energies.

The optimization results along with the inspection of the resulting photoelectron spectrum allowed us to find that the physical mechanism leading to a high DOC is the predominant ionization of  $4d_0$  and  $5s$  electrons into the same final electronic continuum state with  $p$ -character at low photoelectron energies. This is accomplished by optimized pulses which enable and appropriately combine one- and three-photon ionization, such that the ionization of a  $4d$  electron into  $f$ -states is strongly suppressed since this process leads to decoherence. Despite the fact that the optimized pulses produce predominantly slow

photoelectrons which leave the parent ion at low velocity, the DOC can be effectively increased. During the ionization process the freed electron can still interact with the ionic system which always leads to decoherence. Nevertheless, introducing appropriate chirps the pulse is capable of preparing a significant part of the final state in a superposition of the  $4d_0$  and  $5s$  hole states which enhances the coherence. We have thus discovered a control mechanism which exploits multiphoton ionization and leads to a noticeable enhancement of the DOC at low photoelectron kinetic energies, in contrast to the results of Ref. [52] where the high mean photon energies are critical to ensure short interaction times between the freed electrons and ionic core.

Using xenon as paradigm atom with many ionization channels, we have demonstrated that the challenge of preparing coherent superpositions can be met by optimized pulses which interfere single- and multiphoton ionization pathways in the attosecond photoionization process. Therefore ionization occurs at comparatively low photon energies and into the same partial waves of the final photoelectron state which dramatically increases the coherence in the final ionic state. Since the optimized pulses are of reasonable intensity and shape and Auger decay was taken into account in the calculations, a comparison of our results with experimental coherence measurements seems feasible, e.g., by probing the ionic hole state in a similar fashion as in Ref. [243] on an attosecond timescale.

The multiphoton mechanism found in the present work can be generalized to other complex systems and the conclusions drawn for xenon may be applied to other materials. The availability of ultrashort pulses in combination with pulse shapers and the resulting amazing controllability in the generation of light pulses regarding their amplitude, bandwidth, phase and polarization have enabled substantial progress in experiments, see, e.g., Ref. [210]. In view of the discussed coherent wave packet preparation, the development of such technologies is of particular interest for various applications in chemistry and materials science since they will enable the utilization of specific coherence properties of atoms and molecules. Using modern attosecond light sources, see, e.g., Ref. [260], which might soon advance to generate tailored light pulses similar to the optimized pulses found in this work, the presented paradigm could be tested experimentally and coherent states could be produced and controlled in the laboratory.

# Theoretical description of photoelectron circular dichroism of randomly oriented chiral molecules

---

10.1	Fingerprints of Chirality: Context and Motivation . . . . .	152
10.2	Derivation of the theoretical model . . . . .	155
10.2.1	Single center expansion . . . . .	156
10.2.2	Photoelectron Angular Distributions . . . . .	158
10.2.3	Orientation-dependent two-photon absorption . . . . .	160
10.2.4	Orientation-averaged 2+1 REMPI differential cross-section . . . . .	164
10.3	Symmetry properties of the model . . . . .	167
10.3.1	Parity transformation under handedness exchange: . . . . .	168
10.3.2	Parity transformations under field polarization helicity exchange . .	170
10.3.3	Mixing polarization directions and photoelectron circular dichroism	171
10.4	Anisotropy of photoelectron emission: . . . . .	174
10.4.1	Angular momentum dependence of the intermediate state . . . . .	175
10.4.2	Two-photon absorption tensor dependence of the intermediate state	176
10.5	Numerical Results . . . . .	178
10.5.1	Fenchone . . . . .	178
10.5.2	Camphor . . . . .	184
10.6	Intermediate state dependence of photoelectron circular dichroism in (2+1) REMPI . . . . .	188
10.7	Conclusion and Remarks . . . . .	193

---

## 10.1 Fingerprints of Chirality: Context and Motivation

The term “chiral”, derived from the Greek  $\chi\epsilon\lambda\rho$ , “hand” was first introduced by Lord Kelvin in 1893 to refer an object that is distinguishable from its own mirror image[261]. A chiral molecule refers to a molecule that cannot be superimposed with its mirror image by pure translation and rotation operations. The term enantiomer, from the Greek *enantiomorph*, “opposite forms”, designates the left and right mirror images of the chiral molecule. In the context of nowadays available technology, enantiomers of a chiral molecule can be distinguished, for instance, by their interaction with left- or right-handed circularly polarized photons, defining the polarization of the electromagnetic field.

Another important terminology, that reflects the interaction of chiral molecules with light, is circular dichroism (CD), and it is intrinsically related to chiral activity. In fact, the term CD refers to the differential absorption of left and right circularly polarized light by different enantiomers, and when such difference in absorption exist, it is said that the molecule presents a chiral activity.

Although chiral activity can be measured by direct absorption, in practice, however, experimental conditions usually involves low optical densities, and therefore such measurements are experimentally challenging to perform. Consequently, the necessity of an equivalent method for measuring chiral activity in gas phase, less challenging from a practical perspective, becomes unavoidable.

An alternative approach is based on photoelectron spectroscopy in gas phase. It consist of gas phase photoionization with subsequent measurement of photoionization-related quantities. Within this alternative approach, intense short laser pulses for the ionization, which easily drive multi-photon transitions, allow to observe effects in table-top experiments that otherwise would require synchrotron radiation. In such experiments, the normalized difference in the ion yield of the photoelectron circular dichroism (PECD) is measured. The latter defines the laboratory-frame forward/backward asymmetry of photoelectron emission with respect to the propagation axis of the beam that ionizes a randomly oriented ensemble of chiral molecules [262]. Historically, PECD effect was demonstrated experimentally in the framework of one-photon [263] and resonantly enhanced multi-photon ionization (REMPI) [264–267].

A recent example that motivated the present theoretical work is the photoelectron circular dichroism (PECD) of chiral molecules [264, 265, 267–269]. It refers to the forward/backward asymmetry with respect to the light propagation axis in the photoelectron angular distribution (PAD) obtained after excitation with circularly polarized light [263, 270–272]. When the resulting PAD is expanded in Legendre polynomials, the PECD is characterized by the expansion coefficients of the odd-order polynomials with the highest order polynomial being determined by the order of the process, i.e., the number

of absorbed photons [270, 273].

A theoretical description of such experiments with intense femtosecond laser pulses requires proper account of the multi-photon excitation pathways. In this context, a first pioneering model accounting for simultaneous absorption of two photons including the corresponding modified molecular selection rules was formulated by McClain and co-workers in the early seventies [274–276] and a theory of two-photon circular dichroism was developed in an independent work in Ref. [277], where the effect was attributed to a difference in the absorption coefficient for the two left and two right polarized photons. Both approaches are based on a perturbation expansion of the light-matter interaction, which requires relatively low intensity fields. A complementary alternative description is provided by the so-called strong-field approximation, which is particularly suited for very intense fields [278, 279].

Generally speaking, multi-photon transitions driven by strong femtosecond laser pulses may or may not involve intermediate states. In recent experiments with bicyclic ketones [264, 265, 267–269], a 2+1-REMPI process was employed for the measurement of PECD in chiral molecules. The nature of the intermediate state, populated prior to ionization, as well as the fingerprints of the latter in the PECD, remains yet to be elucidated. In particular, randomly oriented molecules of fenchone and camphor molecules in gas phase served as a prototype for the measurement of the photoelectron angular distributions and photoelectron circular dichroism resulting from ionization with circularly polarized femtosecond laser pulses in Ref. [264, 265], .

From a theoretical point of view, the validity of a physical model is irrevocably sentenced by its capability of reproducing experimental results. In an attempt to model the photoionization process and reproduce the experimental observations referenced in the above lines, a first theoretical study, based on the so-called strong-field approximation, was proposed in Ref. [280]. While the standard strong-field approximation using a purely plane wave basis for the photoelectron fails to describe any chiral activity, i.e. no difference in PAD for circularly right and left polarized fields, it was found that accounting for the Coulomb interaction between photoelectron and photoion within the Born approximation allowed for observation of PECD. However, the resulting Legendre coefficients, as well as overall PECD obtained from the calculated angular distribution of photoelectrons did not agree with the experimental ones. When analyzing the theoretical treatment in Ref. [280], it becomes obvious that the discrepancy between theory and experiment may be explained, to a large extent, by the role of the intermediate excited state in the REMPI process which is unavoidable ignored in the strong-field approximation [280].

Motivated by the dichotomy between the experimental [264] and theoretical [280] results, we construct and propose an alternative and novel approach based on perturbation

theory treatment of the multi-photon process. For a fair comparison with experiment, our model is constructed exclusively for a 2 + 1 REMPI process, therefore taking into account the geometrical properties of the resonant intermediate excited state. Within our model, ionization is viewed as a (weak) one-photon transition into the continuum spectrum, from the 'initial' state, which is prepared by non-resonant two-photon absorption. Justification of such a perturbative approach is based on the moderate intensities, of the order of  $10^{12}$  W/cm<sup>2</sup>, used in the experiments [264, 265, 267–269]. Although clearly in the multi-photon regime, such intensities can be described comparatively well by low order perturbation theory [249, 281, 282].

It is well established that the non-resonant two-photon preparation step yields an important difference compared to pure one-photon excitation [270]. In the latter case, the first order Legendre polynomial alone accounts for the PECD [283–285]. This results from the random orientation of the molecules, or, in more technical terms, from integrating the differential cross section over the Euler angles. In contrast, non-resonant two-photon excitation may lead to an orientation-dependent probability distribution of the molecules in the resonant intermediate state [267, 286]. In this case, the maximum order of Legendre polynomials contributing to the PAD is not limited to 2, but 6 for a 2+1 process. Whether the two-photon absorption is orientation-dependent is determined by the two-photon transition matrix elements. In order to compare our theoretical results with the experimental counterparts, the two-photon transition matrix elements are calculated using state of the art *ab initio* methods.

As a rule of thumb, modeling the complete photoionization process for molecules as complex of camphor and fenchone from first principles is extremely challenging, even when using the most advanced *ab initio* methods. We therefore split the theoretical description into two parts.

First, as long as all electrons remain bound, state of the art quantum chemical approaches, for example the coupled cluster methods, can be used to accurately determine the electronic wave functions. However, once an electron starts to leave the ionic core, the standard basis sets of electronic structure theory are not well adapted. An alternative is offered by a single-center expansion into eigenfunctions of a hydrogen-like atom for which both bound and continuum functions are known analytically. The hydrogenic continuum functions properly account for the long-range Coulomb interaction between ionic core and ejected electron but neglect the effect of short-range correlations in the ionization step. Second, the basis functions for the single center expansion are chosen such as to yield the simplest possible model that is able to reproduce the laboratory-frame photoelectron angular distributions (LF-PADs) resulting from a 2+1-REMPI process in randomly oriented chiral molecules. The two descriptions are matched at the resonant, electronically

excited intermediate state by projecting the numerically calculated wavefunction onto the basis functions of the single center expansion.

To conclude, our approach of calculating the PAD as a one-photon absorption cross section for an effective “initial” state in a single center expansion, while neglecting dynamical effects, provides a simple, yet rather general model for PECD in randomly oriented chiral molecules after 2+1 REMPI. It allows us to analyze, beyond the examples of fenchone or camphore and independent of details specific to those molecules, the role of the laser polarization for each step in the 2+1 ionization process and the conditions on the two-photon absorption matrix elements for yielding PECD.

## 10.2 Derivation of the theoretical model

In an attempt to reproduce the experimental observations [264, 265, 267–269], we construct a first principles-based model, in which we explicitly model the resonantly enhanced multi-photon photoionization as a 2+1 process [286]. Specifically, we assume the last photon to constitute a weak probe of the molecular state that is prepared by non-resonant two-photon absorption. Justified by the orders of magnitude stated in the above lines, the strict electric dipole approximation is employed. Therefore, contributions from magnetic dipole terms, which are important for circular polarization dependent differences in absorption cross sections, as well as higher order electric and magnetic multipole terms are neglected.

In order to derive the PAD in the laboratory frame of reference, two coordinate systems, namely the molecular frame of reference  $\mathcal{R}$  and the laboratory frame  $\mathcal{R}'$ , are defined. Respectively,  $\epsilon'_{\varrho_2}$  denotes the polarization of the laser field with respect to the laboratory frame (where we distinguish the polarization of the ionizing photon,  $\epsilon'_{\varrho_2}$  from that of the first two photons,  $\epsilon'_{\varrho_1}$ ). In order to easily extract symmetry information from the Wigner symbols latter in the derivations, we work in the spherical basis. Thus,  $\epsilon'_{\varrho_2}$  and  $\epsilon'_{\varrho_1}$  refer to the spherical unit vectors in the laboratory frame, with  $\varrho_{1,2} = \pm 1, 0$  denoting left/right circular and linear polarization of the laser beam which propagates in the positive  $z'$  direction (the relation between the spherical and Cartesian unit vectors is found in Eq. (C.7)). Primed (unprimed) coordinates refer the laboratory (molecular) frame of reference throughout. Both frames,  $\mathcal{R}'$  and  $\mathcal{R}$ , are related by an arbitrary coordinate rotation  $D(\alpha\beta\gamma)$ , where  $\omega = (\alpha, \beta, \gamma)$  denote the Euler angles defining the orientation of  $\mathcal{R}$  with respect to  $\mathcal{R}'$ .

Consider a one-photon (1P) transition in a molecule whose orientation with respect to  $\mathcal{R}'$  is given by the Euler angles  $\omega$ . The corresponding differential photoionization cross section, when measured in the molecular frame  $\mathcal{R}$ , reads, within perturbation theory and

the electric dipole approximation and in SI units [287],

$$\frac{d^2\sigma_{\text{IP}}}{d\omega d\Omega_{\mathbf{k}}} = c_0 \left| \langle \Psi_{\mathbf{k}} | \epsilon'_{\varrho_2} \cdot \mathbf{r} | \Psi_o \rangle \right|^2, \quad (10.1)$$

where  $c_0 = 4\pi^2\alpha\hbar\omega_{\text{ph}}$  with  $\alpha$  being the fine-structure constant,  $\hbar\omega_{\text{ph}}$  the energy of the ionizing photon,  $\hbar$  the reduced Planck constant and  $\mathbf{r}$  the position operator of the electron (or a sum of the various position operators in the multi-electron case). The polarization of the electric field in the laboratory frame of reference is specified by  $\epsilon'_{\varrho_2}$ , where  $\varrho_2$  takes the value 0 for linear and  $+1(-1)$  for left (right) circular polarization, respectively.  $|\Psi_{\mathbf{k}}\rangle$  denotes an energy normalized molecular state with one electron transferred to the ionization continuum with asymptotic electron linear momentum  $\mathbf{k}$ .  $|\Psi_o\rangle$  is the (bound, unity normalized) molecular state prepared by the non-resonant two-photon absorption, which is defined in the molecular frame of reference. In Eq. (10.1), the standard notation for doubly differential cross sections in the molecular frame of reference [285, 288, 289] that depend not only on the solid angle  $\Omega_{\mathbf{k}}$  but also on the orientation of the molecule via the Euler angles  $\omega$ , is employed. A single-center approximation [290] is employed. This allows to calculate the matrix elements in Eq. (10.1) explicitly. In other terms, we project the multi-electron wave function obtained from *ab initio* calculations,  $|\Psi_o\rangle$ , on one-electron basis functions and neglect electron correlations in the continuum description.

### 10.2.1 Single center expansion

The “initial” state for the one-photon ionization is a multi-electron wavefunction which is usually expanded in specially adapted basis functions developed in quantum chemistry. In contrast, the single center expansion is based on the fact that any molecular wavefunction can be written as a linear combination of functions about a single arbitrary point [290]. Of course, such an ansatz will converge very slowly, if the multi-center character of the wavefunction is important. Writing the wavefunction of the electronically excited state of the neutral molecule, that is prepared by the two-photon absorption process, as  $\langle \mathbf{r} | \Psi_o \rangle = \Psi_o(\mathbf{r})$ , we expand it into eigenfunctions of a hydrogen-like atom,

$$\Psi_o(\mathbf{r}) = \sum_{n_o=0}^{\infty} \sum_{\ell_o=0}^{n_o-1} \sum_{m_o=-\ell_o}^{\ell_o} a_{m_o}^{\ell_o}(n_o) R_{\ell_o}^{n_o}(r) Y_{m_o}^{\ell_o}(\Omega_{\mathbf{r}}). \quad (10.2)$$

Here,  $a_{m_o}^{\ell_o}(n_o)$  stands for the unknown expansion coefficients,  $R_{\ell_o}^{n_o}(r)$  denotes the radial eigenfunctions of the hydrogen-like atom, and  $Y_{m_o}^{\ell_o}(\Omega_{\mathbf{r}})$  are the ordinary spherical harmonics.  $\Omega_{\mathbf{r}} = (\vartheta_{\mathbf{r}}, \phi_{\mathbf{r}})$  refers to the polar and azimuthal angles of the position vector  $\mathbf{r}$  in the molecular frame of reference. Note that all information about the geometry and

the symmetry properties of the “initial” electronically excited state is contained in the expansion coefficients  $a_{m_o}^{\ell_o}(n_o)$ . The number of basis functions must be truncated in any actual calculation, i.e.,

$$\Psi_o(\mathbf{r}) \approx \sum_{n_o=n_o^{\min}}^{n_o^{\max}} \sum_{\ell_o=0}^{n_o-1} \sum_{m_o=-\ell_o}^{\ell_o} a_{m_o}^{\ell_o}(n_o) R_{\ell_o}^{n_o}(r) Y_{m_o}^{\ell_o}(\Omega_{\mathbf{r}}). \quad (10.3)$$

Strictly speaking, all molecular orbitals that are involved in Slater determinants describing the excited state should be subject to the single center expansion. In the present model, we employ an effective one-electron picture by expanding only one representative virtual orbital around the single center, namely the one that is additionally occupied in the supposedly leading configuration for the respective excited state.

We will also ask what the simplest possible model is that gives rise to PECD. In this case, we assume a single quantum number  $n$ ,  $n = n_o$ , to contribute to Eq. (10.2), i.e.,

$$\Psi_o^s(\mathbf{r}) \approx \sum_{\ell_o=0}^{L_{o,\max}} \sum_{m_o=-\ell_o}^{\ell_o} a_{m_o}^{\ell_o} R_{\ell_o}^{n_o}(r) Y_{m_o}^{\ell_o}(\Omega_{\mathbf{r}}), \quad (10.4)$$

where  $L_{o,\max}$  refers to the highest angular momentum state appearing in the “initial” wavefunction. It follows from basic symmetry arguments that the minimal value of  $L_{o,\max}$  for which a PECD can be expected is  $L_{o,\max} = 2$ , that is, at least  $d$ -orbitals are required.

We model the photoionization as a one-electron process arising from a hydrogenic-like system exclusively, which allows for neglecting the bound molecular part (the remaining molecular parent ion) in  $|\Psi_{\mathbf{k}}\rangle$ . Thus, the resulting continuum wave functions,  $\Psi_{\mathbf{k}}(\mathbf{r})$ , are expanded into partial waves in a way that allows for an explicit expression of the photoionization cross section in terms of the scattering solid angle  $\Omega_{\mathbf{k}}$  [284, 288, 289, 291],

$$\Psi_{\mathbf{k}}(\mathbf{r}) = 4\pi \sum_{l=0}^{\infty} \sum_{m=-l}^l i^l \phi_{k,\ell,m}(r) Y_m^{*\ell}(\Omega_{\mathbf{k}}) Y_m^{\ell}(\Omega_{\mathbf{r}}). \quad (10.5)$$

Here,  $Y_m^{\ell}(\Omega_{\mathbf{r}})$  and  $Y_m^{\ell}(\Omega_{\mathbf{k}})$  correspond to the spherical harmonics describing the orientation of the photoelectron position and momentum, respectively, and  $\phi_{k,\ell,m}(r)$  is the radial part of the photoelectron wavefunction. For simplicity, we use here and in the following  $Y_m^{*\ell}(\Omega_{\mathbf{k}})$  as an abbreviation for  $(Y_m^{\ell}(\Omega_{\mathbf{k}}))^*$ . Modeling photoionization as a one-electron process, we can approximate

$$\phi_{k,\ell,m}(r) \approx e^{-i\delta_{\ell}} G_{k,\ell}(r), \quad (10.6)$$

where  $G_{k,\ell}(r)$  are the well-known radial continuum wavefunctions of the hydrogen atom,

recalled in Appendix C.1.1, and  $\delta_\ell$  stands for the Coulomb phase shift of the  $\ell$ -th scattered partial wave, with  $\delta_\ell = \Gamma(\ell + 1 - i/k)$  [285, 289, 291]. Note that we expect the phase shift for molecules to depend on  $\ell_o$  and  $m_o$  since the molecular potential of chiral molecules is not spherically symmetric. Neglecting the  $m_o$ -dependence of the phase shift involves no approximation when using Eq. (10.2) since the hydrogen eigenfunctions form a complete orthonormal basis. However, this is not true anymore when truncating the basis, cf. Eq. (10.3). Our ansatz thus involves an additional approximation, namely Eq. (10.6).

By construction, Eq. (10.6) yields orthogonality between bound and unbound wavefunctions which is required to avoid spurious singularities [288] and reproduce the correct threshold behavior of the photoionization cross-sections [292]. With the approximation of Eq. (10.6), we account for the long-range Coulomb interaction between photoelectron and a point charge representing the ionic core but neglect the short-range static exchange. Also, dynamic changes in the electron distribution, such as adjustments of the electronic cloud due to nuclear motion, as well as the interaction of the outgoing photoelectron with the driving electric field upon photoionization are neglected.

Inserting Eq. (10.6) into Eq. (10.5) yields

$$\Psi_{\mathbf{k}}(\mathbf{r}) = 4\pi \sum_{l=0}^{\infty} \sum_{m=-l}^l i^\ell e^{-i\delta_\ell} G_{k,\ell}(r) Y_m^{*\ell}(\Omega_{\mathbf{k}}) Y_m^\ell(\Omega_{\mathbf{r}}), \quad (10.7)$$

and we can evaluate the matrix element in Eq. (10.1).

### 10.2.2 Photoelectron Angular Distributions

Because the wavefunctions are given in the molecular frame of reference, we need to rotate the spherical unit vector  $\epsilon'_{\varrho_2}$  in Eq. (10.1) into that frame [285]. Expanding the rotation operator  $D(\alpha\beta\gamma)$  connecting  $\mathbf{r}$  and  $\mathbf{r}'$  into irreducible rank 1 tensor representations, cf. Appendix C.1.3, Eq. (10.1) becomes

$$\frac{d^2\sigma_{\text{1P}}}{d\omega d\Omega_{\mathbf{k}}} = c_0 \sum_{q=-1}^1 \sum_{q'=-1}^1 (-1)^{q'-\varrho_2} \mathcal{D}_{q,\varrho_2}^{(1)}(\omega) \mathcal{D}_{-q',-\varrho_2}^{(1)}(\omega) \langle \Psi_{\mathbf{k}} | \mathbf{r}_q | \Psi_o \rangle \langle \Psi_{\mathbf{k}} | \mathbf{r}_{q'} | \Psi_o \rangle^*. \quad (10.8)$$

Inserting Eqs. (10.4) and (10.7) to evaluate the overlap integrals yields

$$\begin{aligned} \frac{d^2\sigma_{\text{1P}}}{d\omega d\Omega_{\mathbf{k}}} &= c_0 \sum_{\substack{\ell,m \\ n_o \ell_o, m_o}} \sum_{\substack{\ell',m' \\ n'_o \ell'_o, m'_o}} \sum_{q=-1}^1 \sum_{q'=-1}^1 (-i)^{\ell-\ell'} e^{i(\delta_\ell - \delta_{\ell'})} \mathcal{S}_{\ell_o, m_o}^{\ell, m}(q) \mathcal{S}_{\ell'_o, m'_o}^{*\ell', m'}(q') \\ &\quad \times a_{m_o}^{\ell_o}(n_o) a_{m'_o}^{*\ell'_o}(n'_o) I_k^{n_o}(\ell, \ell_o) I_k^{n'_o}(\ell', \ell'_o) Y_m^\ell(\Omega_{\mathbf{k}}) Y_{m'}^{*\ell'}(\Omega_{\mathbf{k}}) \mathcal{D}_{q,\varrho_2}^{(1)}(\omega) \mathcal{D}_{q',\varrho_2}^{*(1)}(\omega) \end{aligned} \quad (10.9)$$

In Eq. (10.9), we have introduced radial and angular integrals  $I_k(\ell, \ell_o)$  and  $\mathcal{S}_{\ell_o, m_o}^{\ell, m}(q)$ , given by

$$I_k^{n_o}(\ell, \ell_o) = I_o \int_0^{+\infty} r^3 G_{k, \ell}(r) R_{\ell_o}^{n_o}(r) dr \quad (10.10a)$$

for a fixed  $n_o$  in Eq. (10.2) with  $I_o = 4\pi/3$ , and

$$\mathcal{S}_{\ell_o, m_o}^{\ell, m}(q) = \int Y_m^{\ell*}(\Omega_r) Y_q^1(\Omega_r) Y_{m_o}^{\ell_o}(\Omega_r) d\Omega_r \quad (10.10b)$$

$$= (-1)^{-m} b_{\ell, \ell_o} \begin{pmatrix} \ell & 1 & \ell_o \\ 0 & 0 & 0 \end{pmatrix} \begin{pmatrix} \ell & 1 & \ell_o \\ -m & q & m_o \end{pmatrix} \quad (10.10c)$$

with

$$b_{\ell, \ell_o} = \sqrt{3(2\ell + 1)(2\ell_o + 1)/4\pi}$$

and using Wigner  $3j$  symbols [143–146]. The angular integral  $\mathcal{S}_{\ell_o, m_o}^{\ell, m}(q)$  determines, for each spherical unit vector  $q = 0, \pm 1$ , the selection rules between the angular components of the bound excited electronic state with quantum numbers  $\ell_o, m_o$  and the partial wave components of the continuum wavefunction with quantum numbers  $\ell, m$ . Equation (10.10b) implies that transitions are allowed if and only if  $\ell + 1 + \ell_o$  is even and  $m_o + q - m = 0$  for all  $|\ell_o - 1| \leq \ell \leq \ell_o + 1$ . This is a special case of the more general rule for multipole transitions derived in Ref. [273]. The angular integrals can be evaluated analytically using the standard angular momentum algebra, whereas the radial integrals in Eq. (10.10a) are computed numerically.

The choice of basis to describe the radial part of the continuum wavefunction determines the weight with which each excited state expansion coefficient  $a_{m_o}^{\ell_o}(n_o)$  contributes to the PAD, cf. Eqs. (10.9) and (10.10a). Thus, choosing for example plane waves, i.e., the eigenfunctions of the “free” photoelectron, which is described in terms of the Bessel functions [143, 145, 146], and does not take into account the Coulomb interaction between the outgoing photoelectron and the remaining ion, would translate into a PAD different from the one obtained with the hydrogenic continuum wavefunctions of Eq. (10.7) [293]. Whether or not the model is able to reproduce the measured Legendre coefficients will to some extent depend on the choice of basis for the radial part in Eq. (10.5).

The missing ingredient to determine the differential photoionization cross section, Eq. (10.1), are the expansion coefficients,  $a_{m_o}^{\ell_o}(n_o)$ , of the intermediate excited state wavefunction. In the framework of this work, they are determined from *ab initio* calculations, cf. Ref. [294].

Two more steps are then required to connect the differential ionization cross section to the experimentally measured PAD. First, the PAD is measured in the laboratory frame and the differential ionization cross section thus needs to be rotated from the molecular into the laboratory frame. Second, the orientation of the molecule with respect to the laboratory frame, defined by the polarization axis of the laser electric field, is arbitrary. We therefore need to average over all possible orientations, i.e., integrate over the Euler angles  $\omega = (\alpha, \beta, \gamma)$ , as we consider a randomly oriented initial ensemble of molecules [270, 271, 295].

Rotating the differential cross section from the molecular into the laboratory frame requires rotation of the continuum state  $|\Psi_{\mathbf{k}}\rangle$  into  $|\Psi_{\mathbf{k}'}\rangle$  using the inverse of Eq. (C.4). This leads to

$$\begin{aligned} \frac{d^2\sigma_{\text{IP}}}{d\omega d\Omega_{\mathbf{k}'}} &= c_0 \sum_{\ell, m} \sum_{n_o, \ell_o, m_o} \sum_{\ell', m'} \sum_{n'_o, \ell'_o, m'_o} \sum_{q, q'} (-i)^{\ell-\ell'} (-1)^{m'+q'-\varrho_2} e^{i(\delta_\ell - \delta_{\ell'})} \\ &\times a_{m_o}^{\ell_o}(n_o) a_{m'_o}^{*\ell'_o}(n'_o) I_k^{n_o}(\ell, \ell_o) I_k^{n'_o}(\ell', \ell'_o) \\ &\times \sum_{\mathcal{L}=|\ell-\ell'|}^{\ell+\ell'} (2\mathcal{L}+1) \begin{pmatrix} \ell & \ell' & \mathcal{L} \\ 0 & 0 & 0 \end{pmatrix} \begin{pmatrix} \ell & \ell' & \mathcal{L} \\ m & -m' & -(m-m') \end{pmatrix} \mathcal{D}_{q, \varrho_2}^{(1)}(\omega) \mathcal{D}_{-q', -\varrho_2}^{(1)}(\omega) \\ &\times \sum_{\mu=-\mathcal{L}}^{\mathcal{L}} e^{i\mu\vartheta'_k} \mathcal{D}_{m'-m, -\mu}^{(\mathcal{L})}(\omega) P_{\mathcal{L}}^{\mu}(\cos \vartheta'_k) \zeta_{\mathcal{L}}^{\mu}(\ell, \ell') \mathcal{S}_{\ell_o, m_o}^{\ell, m}(q) \mathcal{S}_{\ell'_o, m'_o}^{*\ell', m'}(q'), \quad (10.11) \end{aligned}$$

where  $\zeta_{\mathcal{L}}^{\mu}(\ell, \ell')$  is defined in Eq. (C.15) in Appendix C.2.1.  $P_{\mathcal{L}}^{\mu}(\cos \vartheta'_k)$  denotes the associate Legendre polynomials. A detailed derivation of Eq. (10.11) is found in Appendix C.2.1. Equation (10.11) provides the explicit expression for the differential photoionization cross section of the 2+1 REMPI process.

### 10.2.3 Orientation-dependent two-photon absorption

When averaging over all orientations in the second step, we need to account for the fact that the probability for non-resonant two-photon absorption from the ground state to the intermediate electronically excited state is, depending on the properties of the two-photon absorption tensor, not isotropic [286]. The differential ionization cross section in the laboratory frame therefore needs to be weighted by the probability of the electronically excited state to be occupied after absorption of the first two (identical) photons. In fact, since every molecule possesses a given (different) orientation  $\omega$ , the projection of the electric field polarization direction onto each molecular frame  $\omega$  may differ. Consequently, the strength of the dipole interaction between the molecule and driving field depends on

the orientation of the molecule with respect to the electric field polarization. Therefore, the probability of two-photon transition is orientation-dependent and should be taken into account when calculating the probability of ionization from the excited state.

The orientation-dependent probability to reach the intermediate excited state,  $\rho_{2P}(\omega)$ , is obtained from the transition probability for two-photon absorption from the ground state  $|\Psi_g\rangle$  to the intermediate electronically excited state  $|\Psi_o\rangle$  [286]. The latter in general is defined as [296]

$$A_{o,g}^{(2)} = \tilde{\mathcal{N}}_0(\omega_{\text{ph}}) |\mathcal{M}|^2, \quad (10.12a)$$

where  $\mathcal{M}$ , in the strict electric dipole approximation,  $\exp(i\mathbf{k} \cdot \mathbf{r}) \approx 1$ , reads

$$\mathcal{M} = \sum_n \left\{ \frac{(\mathbf{e}_1 \cdot \langle \Psi_o | \mathbf{r} | \Psi_n \rangle)(\langle \Psi_n | \mathbf{r} | \Psi_g \rangle \cdot \mathbf{e}_2)}{\hbar\omega_g - \hbar\omega_n + \hbar\omega_{\text{ph},2}} + \frac{(\mathbf{e}_1 \cdot \langle \Psi_o | \mathbf{r} | \Psi_n \rangle)(\langle \Psi_n | \mathbf{r} | \Psi_g \rangle \cdot \mathbf{e}_2)}{\hbar\omega_g - \hbar\omega_n + \hbar\omega_{\text{ph},1}} \right\}. \quad (10.12b)$$

In Eq. (10.12b),  $\mathbf{e}_j$  denotes the polarization direction (without specifying a certain frame of reference) of photon  $j$  ( $j = 1, 2$ ) with energy  $\hbar\omega_{\text{ph},j}$ . To shorten notation, the polarization independent quantity  $\tilde{\mathcal{N}}_0(\omega_{\text{ph}})$  in Eq. (10.12a) contains all prefactors,

$$\tilde{\mathcal{N}}_0(\omega_{\text{ph}}) = \frac{2\pi e_0^4}{\hbar^3 c^2} (F_1 \hbar\omega_{\text{ph},1}) I(\omega_{\text{ph},2}),$$

with  $e_0$  being the elementary charge, and where  $F_1$  and  $I(\omega_{\text{ph},2})$  refer to the incident laser-photon-flux (of type 1) and the energy flux per unity frequency (of type 2), respectively [296]. Evaluation of Eq. (10.12b) requires a frame transformation, since the wavefunctions involved in the two-photon transition matrices are known in the molecular frame whereas the polarization directions of the photons are given in the laboratory frame of reference. As before, transformation of the polarization directions from the laboratory frame to the molecular frame is carried out by means of the Wigner rotation matrices around the Euler angles  $\omega = (\alpha, \beta, \gamma)$ . Consequently, the orientation dependent two-photon absorption probability is obtained as

$$\rho_{2P}(\omega) = \left( \frac{8\pi^2 \hbar}{3} \right)^2 \tilde{\mathcal{N}}_0(\omega_{\text{ph}}) \left| \sum_{q_1, q_2} \mathcal{D}_{q_1, \varrho_1}^{(1)}(\omega) \mathcal{D}_{q_2, \varrho_2}^{(1)}(\omega) T_{q_1, q_2} \right|^2, \quad (10.13a)$$

where we have applied the properties of the rotation matrices between both frames, detailed in Appendix C.1.3, to Eq. (10.12b). In Eq. (10.13a),  $T_{q_1, q_2}$  denotes the two-photon

absorption tensor in the molecular frame of reference, whose tensor elements read

$$T_{q_1, q_2} = \sum_n \frac{\langle \Psi_o | r_{q_1} | n \rangle \langle n | r_{q_2} | \Psi_g \rangle}{\hbar\omega_g - \hbar\omega_n + \hbar\omega_{\text{ph},2}} + \frac{\langle \Psi_o | r_{q_2} | n \rangle \langle n | r_{q_1} | \Psi_g \rangle}{\hbar\omega_g - \hbar\omega_n + \hbar\omega_{\text{ph},1}}, \quad (10.13b)$$

and  $\varrho_1$  denotes the polarization direction in the laboratory frame of reference, i.e.,  $\varrho_1 = \pm 1, 0$ , driving the two-photon absorption process, both photons having the same polarization direction. Additionally, the indexes  $q_1$  and  $q_2$  take the values  $\pm 1, 0$ . Finally,  $r_{q_k}$  denotes the spherical component of the position operator  $\hat{\mathbf{r}}$ , with  $q_k = \pm 1, 0$ . The correspondence between the spherical and Cartesian components of  $r_k$  are detailed in Eq. (C.7). The correspondences are detailed in Eq. (C.8), in Appendix C.1.3.

A further step consist of normalizing the probability density, such that the normalization condition,

$$\int \rho_{2P}(\omega) d\omega = 1 \quad (10.14)$$

is fulfilled. Using the properties of addition of angular momenta, it is straightforward to find that the normalization factor reads, upon integration of Eq. (10.13a) over the Euler angles,

$$\tilde{\mathcal{N}}_0(\varrho_1) = \tilde{\gamma}(\omega_{\text{ph}})\mathcal{B}(\varrho_1) \quad (10.15a)$$

where we have defined,

$$\begin{aligned} \mathcal{B}(\varrho_1) = & \sum_{\substack{q_1, q_2 \\ q'_1, q'_2}} T_{q_1, q_2} T_{q'_1, q'_2}^* \sum_{\mathcal{Q}=0}^2 (2\mathcal{Q} + 1) \begin{pmatrix} 1 & 1 & \mathcal{Q} \\ q'_1 & q'_2 & -q'_1 - q'_2 \end{pmatrix} \begin{pmatrix} 1 & 1 & \mathcal{Q} \\ \varrho_1 & \varrho_1 & -2\varrho_1 \end{pmatrix} \\ & \times \begin{pmatrix} 1 & 1 & \mathcal{Q} \\ q_1 & q_2 & -q_1 - q_2 \end{pmatrix} \begin{pmatrix} 1 & 1 & \mathcal{Q} \\ \varrho_1 & \varrho_1 & -2\varrho_1 \end{pmatrix}, \end{aligned} \quad (10.15b)$$

with  $\tilde{\gamma}(\omega_{\text{ph}}) \equiv (8\pi^2\hbar/3)^2 \tilde{\mathcal{N}}_0(\omega_{\text{ph}})$ . To retrieve Eqs. (10.15b), we have made use of the properties involving the product of two Wigner rotations matrices, as well as the integration involving a product of three Wigner rotations matrices, and apply them to Eq. (10.13a). These properties are outlined in Eq. (C.9) and Eq. (C.26), in Appendix C.1.3 and Appendix C.2.3, respectively.

Finally, the orientation dependent probability density reads

$$\rho_{2P}(\omega) = \mathcal{N}_0(\varrho_1) \left| \sum_{q_1, q_2} \mathcal{D}_{q_1, \varrho_1}^{(1)}(\omega) \mathcal{D}_{q_2, \varrho_1}^{(1)}(\omega) T_{q_1, q_2} \right|^2 \quad (10.16)$$

with  $\mathcal{N}_0(\varrho_1) = \mathcal{B}^{-1}(\varrho_1)$ . In order to alleviate notations, and unless otherwise stated, we write  $\mathcal{N}_0 = \mathcal{N}_0(\varrho_1)$ . It is important to note, however, that in practice, computation of  $\mathcal{N}_0$  is not required, since this factor is common to all Legendre coefficients, and all of them are given normalized with respect to  $c_0$ , which is also customary for the presentation of experimental data [264, 265]. Equations (10.19) and (10.16) provide a prescription for calculating the partial alignment of molecules in multi-photon ionization. This effect has been widely discussed in the literature, see e.g. Refs. [267, 283], but without stating an explicit way for quantifying it.

Each component of the second-rank tensor  $T_{q_1, q_2}$  determines a property of the system, namely, the average transition rate. As a result of that the tensor  $T_{q_1, q_2}$  has two types of symmetry properties. The first one is due to an intrinsic symmetry originated from the property itself. For instance,  $T_{q_1, q_2}$  defines the probability of a absorption of two identical photons. Since two photons of the same energy and polarization are not the same,  $T_{q_1, q_2}$  has to be symmetric. The second type of symmetry comes from the geometric symmetry of the molecule, and that specifies which of tensor components have to be zero [297, 298].

In the isotropic case,  $\rho_{2P}(\alpha, \beta, \gamma) = 1$ , and evaluation of Eq. (10.19) is analogous to integrating over Eq. (10.11), resulting in the standard expressions for the differential photoionization cross section [268, 283–285, 288, 299]: If the weak probe photon is linearly polarized ( $\epsilon'_{\varrho_2} = \epsilon'_0$ ), only the Legendre coefficients  $c_0$  and  $c_2$  can become non-zero, whereas for circularly polarized light,  $c_0$ ,  $c_1$  and  $c_2$  can have non-vanishing values. Moreover, the laboratory frame PAD preserves the cylindrical symmetry with respect to the propagation direction of the light  $z'$ , i.e.,  $\mu = \varrho_2 - \varrho_2 = 0$  in Eq. (10.11).

The situation changes dramatically if the probability to populate the intermediate electronically excited state becomes anisotropic. If this probability depends on the initial orientation of the molecule, given in terms of the Euler angles  $\omega$  with respect to the laboratory frame  $\mathcal{R}'$ , the Wigner rotation matrices in Eq. (10.13a) couple to those in Eq. (10.11). Upon integration over the Euler angles in Eq. (10.19), this gives rise to higher order Legendre polynomials in the PAD, as we show now. In order to evaluate the angular momentum coupling in Eq. (10.19), we expand the norm squared in Eq. (10.13a). Making use of the product rule for Wigner rotation matrices, Eq. (10.13a) then becomes

$$\rho_{2P}(\omega) = \mathcal{N}_0 \sum_{\substack{q_1, q_2 \\ q_3, q_4}} (-1)^{q_3 + q_4} T_{q_1, q_2} T_{q_3, q_4}^* \sum_{K=0}^4 g_{q_1, q_2, q_3, q_4}^{(K)} \mathcal{D}_{s, 0}^{(K)}(\omega), \quad (10.17a)$$

with  $s = q_1 + q_2 - q_3 - q_4$ , and where we have defined

$$\begin{aligned}
 g_{q_1, q_2, q_3, q_4}^{(K)}(\varrho_1) = & \sum_{Q=0}^2 \sum_{Q'=0}^2 \sum_{K=|Q-Q'|}^{Q+Q'} \gamma_{Q, Q'}^{(K)} \begin{pmatrix} 1 & 1 & Q \\ q_1 & q_2 & -q_1 - q_2 \end{pmatrix} \begin{pmatrix} 1 & 1 & Q \\ \varrho_1 & \varrho_1 & -2\varrho_1 \end{pmatrix} \\
 & \times \begin{pmatrix} 1 & 1 & Q' \\ q_3 & q_4 & -q_3 - q_4 \end{pmatrix} \begin{pmatrix} 1 & 1 & Q' \\ \varrho_1 & \varrho_1 & -2\varrho_1 \end{pmatrix} \\
 & \times \begin{pmatrix} Q & Q' & K \\ q_1 + q_2 & -q_3 - q_4 & -s \end{pmatrix} \begin{pmatrix} Q & Q' & K \\ 2\varrho_1 & -2\varrho_1 & 0 \end{pmatrix}
 \end{aligned} \tag{10.17b}$$

with  $\gamma_{Q, Q'}^{(K)} = (2Q + 1)(2Q' + 1)(2K + 1)$ . In Eq. (10.17a), the orientation dependence is contained in  $\mathcal{D}$ , the polarization dependence in  $g$  and the dependence on molecular parameters in  $T$ . The derivation of Eqs. (10.17), employing the standard angular momentum algebra, is rigorously detailed in Appendix C.2.2. We make once more use of the product rule for two rotation matrices, namely those involving the laser polarization in Eq. (10.11), cf. Eq. (C.9a) in Appendix C.2.3. Thus, a product of three rotation matrices is obtained when inserting Eqs. (10.17) and (C.23), into Eq. (10.18).

#### 10.2.4 Orientation-averaged 2+1 REMPI differential cross-section

Having derived the expression for the orientation-dependent probability density,  $\rho_{2P}(\omega)$ , we are now in a position to define the orientation-averaged differential cross-section for a 2+1 REMPI photoionization. In fact, as stated earlier, the differential ionization cross section in the laboratory frame requires averaging over the orientation-dependent probability of the electronically excited state to be occupied after absorption of the first two (identical) photons. In this context, the differential cross section for photoemission into a solid angle  $d\Omega_{\mathbf{k}'}$  around the axis  $\mathbf{k}'$  in the laboratory frame, after resonant one-photon transition from the electronically excited intermediate state, reads

$$\frac{d^2\sigma_{2+1}}{d\omega d\Omega_{\mathbf{k}'}} = \rho_{2P}(\omega) \frac{d^2\sigma_{1P}}{d\omega d\Omega_{\mathbf{k}'}} \tag{10.18}$$

where  $\rho_{2P}(\omega)$  is the orientation-dependent probability to reach the intermediate excited state by absorption of two identical photons from the ground state, derived in Section 10.2.3. Equation (10.18) assumes a molecule to have, in its electronic ground state, an initial orientation of  $\omega = (\alpha, \beta, \gamma)$  with respect to the laboratory frame of reference. Note that Eq. (10.18) makes an additional assumption, namely the relative phase between

the two-photon and one-photon steps to be irrelevant for the photoelectron spectrum and angular distribution. This is motivated by the fact that only contributions to photoelectron spectrum arising from the probed resonantly excited state, is assumed. As a consequence, relative phase between both process becomes irrelevant. For a discussion of similar approximations in related multiphoton transitions between bound states, see for instance Refs. [274, 275]. For a practical example where relative phases are (ir)relevant in the context of a pump-probe set-up, see Refs. [185] and [60].

The experimentally measured PAD contains contributions from all molecules in the isotropic sample, each of them with a specific orientation  $\omega$ . The total photoelectron signal is therefore obtained by an incoherent summation over the contributions from all molecules. This is equivalent to integrating Eq. (10.18) over the Euler angles weighted by the probability of two-photon absorption. The ‘‘averaged’’ photoionization cross section in the laboratory frame therefore reads,

$$\frac{d\sigma_{2+1}}{d\Omega_{\mathbf{k}'}} = \int \rho_{2P}(\omega) \frac{d^2\sigma_{1P}}{d\omega d\Omega_{\mathbf{k}'}} d\omega, \quad (10.19)$$

where the integration is carried over the Euler angles  $\alpha, \beta, \gamma$ .

Evaluating the products of the Wigner  $3j$  symbols, the differential cross section, Eq. (10.18), for a specific orientation  $\omega$  of the molecule becomes

$$\frac{d^2\sigma_{2+1}}{d\omega d\Omega_{\mathbf{k}'}} = c_o \sum_{\mathcal{L}=0}^{\infty} \sum_{\mu=-\mathcal{L}}^{+\mathcal{L}} b_{\mathcal{L}}^{\mu}(\omega) P_{\mathcal{L}}^{\mu}(\cos \vartheta'_k) e^{i\mu\phi'_k}, \quad (10.20a)$$

where the only orientation-dependent quantity,  $b_{\mathcal{L}}^{\mu}(\omega)$ , is given by

$$b_{\mathcal{L}}^{\mu}(\omega) = \sum_{\lambda} \kappa(\lambda) \mathcal{D}_{s,0}^K(\omega) \mathcal{D}_{q-q',0}^{\nu}(\omega) \mathcal{D}_{m'-m,-\mu}^{\mathcal{L}}(\omega). \quad (10.20b)$$

Note that the summation in Eq. (10.20b) runs over all possible indices, except  $\mathcal{L}$  and  $\mu$ , i.e.,  $\lambda = \{K, \nu, Q, Q', q, q', q_k, n_o, n'_o, \ell, \ell', \ell_o, \ell'_o\}$ , with  $K = 1, 2, 3, 4$  and  $\nu = 0, 1, 2$  appearing from the coupling of the first and second Wigner rotation matrices in Eq. (10.11), cf. Eq. (C.21). The specific form of  $\kappa_{\mathcal{L}}^{\mu}(\lambda)$  is detailed in Eq. (C.25), in Appendix C.2.3.

We can now use the integral properties of a product of three Wigner rotation matrices [143, 145, 146], cf. Eq. (C.26) in Appendix C.2.3. Integration of  $b_{\mu,\nu}^{\mathcal{L}}(\omega)$  over the Euler

angles then yields

$$\begin{aligned}\tilde{c}_{\mathcal{L}}^{\mu} &\equiv \sum_{\lambda} \int b_{\mathcal{L},\lambda}^{\mu}(\omega) d^3\omega = \sum_{\lambda} \kappa_{\mathcal{L}}^{\mu}(\lambda) \begin{pmatrix} K & \nu & \mathcal{L} \\ s & q - q' & m' - m \end{pmatrix} \begin{pmatrix} K & \nu & \mathcal{L} \\ 0 & 0 & -\mu \end{pmatrix} \\ &= \sum_{\lambda} \kappa_{\mathcal{L}}^{\mu}(\lambda) \begin{pmatrix} K & \nu & \mathcal{L} \\ s & q - q' & m' - m \end{pmatrix} \begin{pmatrix} K & \nu & \mathcal{L} \\ 0 & 0 & 0 \end{pmatrix} \delta_{\mu,0}.\end{aligned}$$

Note that the second Wigner symbol in the right-hand side of Eq. (10.21) is non-zero only if  $\mu = 0$  and  $K + \nu + \mathcal{L}$  is even with  $|K - \nu| \leq \mathcal{L} \leq K + \nu$ . Because  $\mu = 0$ , the terms depending on the azimuthal angle in Eq. (10.11) do not contribute and we retrieve cylindrical symmetry for the PAD of Eq. (10.19) which can therefore be expressed in terms of the ordinary Legendre polynomials  $P_{\mathcal{L}}(\cos \vartheta'_{\mathbf{k}})$ . Furthermore, according to the fifth and sixth Wigner symbols in Eq. (10.17b),  $K = 0, \dots, 4$ , because  $|Q - Q'| \leq K \leq Q + Q'$ , and  $0 \leq Q \leq 2$  according to the first and second Wigner symbols in Eq. (10.17b). The same applies to  $Q'$ , reflecting the addition of angular momentum in a two-photon absorption process.

Making use, in Eq. (10.21), of the fact that the non-zero contributions for  $\nu$  are given by  $\nu = 0, 1, 2$ , cf. Eq. (C.21), one obtains that  $\mathcal{L}$  runs from 0 to 6, and higher orders give only vanishing contributions. Therefore, the highest order Legendre polynomial that contributes to the PAD is  $\mathcal{L}_{\max} = 6$ , as expected for a 2+1 process from the  $2(m+n) - 1$  rule [283].

Finally, evaluating Eq. (10.19) with the help of Eq. (10.21) yields the experimentally measured PAD that is obtained for an initial ensemble of randomly oriented molecules,

$$\frac{d\sigma_{2+1}}{d\Omega_{\mathbf{k}'}} = \sum_{\mathcal{L}=0}^6 c_{\mathcal{L}} P_{\mathcal{L}}(\cos \vartheta'_{\mathbf{k}}). \quad (10.21a)$$

Defining  $c_{\mathcal{L}} \equiv \tilde{c}_{\mathcal{L}}^{\mu=0}$  with  $\tilde{c}_{\mathcal{L}}^{\mu=0}$  defined in Eq. (10.21), the Legendre coefficients finally reads,

$$\begin{aligned}c_{\mathcal{L}}(\varrho_1, \varrho_2) &= \tilde{\mathcal{N}}_0 \sum_{\substack{\ell, m \\ n_o, \ell_o, m_o}} \sum_{\substack{\ell', m' \\ n'_o, \ell'_o, m'_o}} \sum_{q, q'} \sum_{\substack{q_1, q_2 \\ q_3, q_4}} \sum_{\nu=0}^2 \sum_{K=0}^4 (-1)^{q_3+q_4} (2\nu+1)(2\mathcal{L}+1) \mathcal{S}_{\ell_o, m_o}^{\ell, m}(q) \mathcal{S}_{\ell'_o, m'_o}^{\ell', m'}(q') \\ &\times (-i)^{\ell-\ell'} (-1)^{m'-q-\varrho_2} e^{i(\delta_{\ell}-\delta_{\ell'})} g_{q_1, q_2, q_3, q_4}^{(K)}(\varrho_1) I_k^{n_o}(\ell, \ell_o) I_k^{n'_o}(\ell', \ell'_o) \hat{\zeta}(\ell, \ell') \\ &\times \begin{pmatrix} \ell & \ell' & \mathcal{L} \\ m & -m' & m' - m \end{pmatrix} \begin{pmatrix} \ell & \ell' & \mathcal{L} \\ 0 & 0 & 0 \end{pmatrix} \begin{pmatrix} 1 & 1 & \nu \\ q & -q' & q' - q \end{pmatrix} \begin{pmatrix} 1 & 1 & \nu \\ \varrho_2 & -\varrho_2 & 0 \end{pmatrix} \\ &\times \begin{pmatrix} K & \nu & \mathcal{L} \\ s & q - q' & m' - m \end{pmatrix} \begin{pmatrix} K & \nu & \mathcal{L} \\ 0 & 0 & 0 \end{pmatrix} a_{m_o}^{\ell_o}(n_o) a_{m'_o}^{*\ell'_o}(n'_o) T_{q_1, q_2} T_{q_3, q_4}^*. \quad (10.21b)\end{aligned}$$

with  $\tilde{\mathcal{N}}_0 = \tilde{c}_0 \mathcal{N}_0$  and  $\tilde{c}_o = 4\pi c_o$ , and where  $\hat{\zeta}(\ell, \ell') = \sqrt{(2\ell + 1)(2\ell' + 1)}$ . Derivation of Eq. (10.21) is explicitly detailed in Appendix C.2.3. Note that the coefficients  $c_{\mathcal{L}}(\varrho_1, \varrho_2)$  depend on the expansion coefficients  $a_{m_o}^{\ell_o}(n_o)$  describing the intermediate electronically excited state, the two-photon absorption tensor elements,  $T_{q_1, q_2}$ , and the laser polarization directions of the two-photon absorption step,  $\varrho_1$ , and of the one-photon ionization,  $\varrho_2$ . Equation (10.21b) is the central result of our perturbation theory treatment of the photoelectron angular distribution, based on separating non-resonant two-photon absorption and one-photon ionization. We recall that it intrinsically connects the electronic structure of the molecule directly to the Legendre coefficients of the PAD which is accessible in experiment.

It is important to note that, according to the model herein presented, contributions of Legendre polynomials with order higher than 2 in Eq. (10.21) are exclusively due to the *orientation dependence of populating the intermediate electronically excited state* by two-photon absorption from the electronic ground state. In other terms, the density  $\rho(\omega)$  expresses the fact that molecules with a certain orientation  $\omega = \omega_1$  have a larger probability to undergo non-resonant two-photon absorption than molecules with some other different orientation  $\omega = \omega_2$ . So although the molecules are assumed to be completely randomly oriented with respect to the laser beam axis when they are in their electronic ground state, *an effective alignment* results for those molecules that absorb two photons. Such an effective alignment results from selection of certain orientations rather than rotational dynamics which would occur on a much slower timescale. The contribution of higher order Legendre polynomials to the PAD is then entirely determined by the properties of the two-photon absorption tensor and the electronically excited state, i.e., the missing link in Ref. [280]. In order to interpret the experimentally observed PADs for fenchone and camphor in terms of their expansion in Legendre polynomials, at least qualitatively, we estimate  $a_{m_o}^{\ell_o}(n_o)$  and  $T_{q_1, q_2}$  using *ab initio* calculations or via fitting. The details about the *ab initio* calculations are given in Ref. [294], we discuss below the basic symmetry properties of these parameters of our model as well as the dependence on the laser polarization directions  $\varrho_1, \varrho_2$ .

### 10.3 Symmetry properties of the model

By definition, PECD is obtained if the sign of the odd Legendre coefficients change when the helicity of the electric field changes. Analogously, for fixed electric field circular helicity, the odd Legendre coefficients change sign when enantiomers are interchanged. Checking such parity transformations under enantiomer and helicity exchange are crucial, since the present model, albeit based perturbation theory treatment of the multi-photon

process, should reproduce such minimal parity transformations, which is confirmed by experimental observations [264, 265]. We therefore first inspect sign changes in the Legendre coefficients for molecules of opposite handedness within our one-center expansion framework. The relation between a given enantiomer and its mirror image is given by the parity operator, which changes the coordinates  $\mathbf{r}$  to  $-\mathbf{r}$ . We therefore check, in the following lines, that our model transforms properly under parity.

Moreover, we determine the role that the excited state coefficients  $a_{m_o}^{\ell_o}(n_o)$  and two-photon absorption tensor elements play for each Legendre coefficient that contributes to the PAD. This is important in order to understand the effect of the geometric properties of the resonantly excited electronic state on the obtained Legendre coefficients. To this end, we rewrite Eq. (10.21b), expressing each  $c_{\mathcal{L}}(\varrho_1, \varrho_2)$  explicitly in terms of the  $a_{m_o}^{\ell_o}(n_o)$  and  $T_{q,q'}$ ,

$$c_{\mathcal{L}}(\varrho_1, \varrho_2) = \sum_{\substack{n_o, \ell_o, m_o \\ n'_o, \ell'_o, m'_o}} \sum_{\substack{q_1, q_2 \\ q_3, q_4}} \gamma_{q_1, q_2, q_3, q_4}^{n_o, \ell_o, m_o, n'_o, \ell'_o, m'_o}(\mathcal{L}, \epsilon'_{\varrho_1}, \epsilon'_{\varrho_2}) a_{m_o}^{\ell_o}(n_o) a_{m'_o}^{\ell'_o}(n'_o) T_{q_1, q_2} T_{q_3, q_4}^* \quad (10.22)$$

Equation (10.22) allows for determining each Legendre coefficient as a function of the intermediate electronically excited state via  $a_{m_o}^{\ell_o}(n_o)$  and  $T_{q,q'}$ . In other words, it connects the measured Legendre coefficients to the electronic structure properties. We can thus compare the contribution of different  $a_{m_o}^{\ell_o}(n_o)$  to different Legendre coefficients  $c_{\mathcal{L}}$ , and explain differences, observed e.g. for different molecules, in terms of the electronic structure. This is important because investigation of camphor and fenchone revealed, for example, the same order of magnitude for the first and third Legendre coefficient in camphor, in contrast to fenchone where  $c_3$  is about one order of magnitude smaller than  $c_1$  [264, 265]. This observation suggests a significantly different electronic structure despite the fact that the two bicyclic monoketones are constitutional isomers which differ only in the position of the geminal methyl groups [300].

In the following, we discuss the behavior under parity and the contribution of the  $a_{m_o}^{\ell_o}(n_o)$  and  $T_{q,q'}$  to the  $c_{\mathcal{L}}(\varrho_1, \varrho_2)$  separately for the excited state coefficients, the two-photon absorption tensor and the laser polarization.

### 10.3.1 Parity transformation under handedness exchange:

#### Role of the excited state expansion coefficients

In this section, we explicitly show that our single-center expansion for the  $(2+1)$  REMPI process properly transforms under parity. Note that the two-photon absorption process conserves parity, which implies that exchanging enantiomers results in a parity change of

the expansion coefficients of the intermediate electronically excited state, from  $a_{m_o}^{\ell_o}(n_o)$  to  $(-1)^{\ell_o} a_{m_o}^{\ell_o}(n_o)$ . For practical convenience, we define the following quantity present in Eq. (10.21b) depending on  $\ell_o$  and  $m_o$ ,

$$\mathcal{P}_{\mathcal{L}} = a_{m_o}^{\ell_o}(n_o) a_{m'_o}^{\ell'_o}(n'_o) \mathcal{S}_{\ell_o, m_o}^{\ell, m}(q) \mathcal{S}_{\ell'_o, m'_o}^{\ell', m'}(q') \begin{pmatrix} \ell & \ell' & \mathcal{L} \\ 0 & 0 & 0 \end{pmatrix}. \quad (10.23)$$

Upon application of the parity operator, Eq. (10.23) becomes

$$\tilde{\mathcal{P}}_{\mathcal{L}} = (-1)^{\ell_o + \ell'_o} a_{m_o}^{\ell_o}(n_o) a_{m'_o}^{\ell'_o}(n'_o) \mathcal{S}_{\ell_o, m_o}^{\ell, m}(q) \mathcal{S}_{\ell'_o, m'_o}^{\ell', m'}(q') \begin{pmatrix} \ell & \ell' & \mathcal{L} \\ 0 & 0 & 0 \end{pmatrix}. \quad (10.24)$$

Furthermore, we make use of the following property of the Wigner  $3j$  symbols [143, 145, 146, 287],

$$\begin{pmatrix} j & j' & J \\ m & m' & M \end{pmatrix} = (-1)^{j+j'+J} \begin{pmatrix} j & j' & J \\ -m & -m' & -M \end{pmatrix}, \quad (10.25)$$

and apply it to the first Wigner  $3j$  symbol in the expressions for  $\mathcal{S}_{\ell_o, m_o}^{\ell, m}(q)$  and  $\mathcal{S}_{\ell'_o, m'_o}^{\ell', m'}(q')$ , i.e., Eq. (10.10b), containing triple zeros in the second row. The parity-transformed  $\mathcal{P}_{\mathcal{L}}$  thus becomes

$$\tilde{\mathcal{P}}_{\mathcal{L}} = (-1)^{\ell_o + \ell'_o} (-1)^{\ell + \ell_o + \ell' + \ell'_o} \mathcal{S}_{\ell_o, m_o}^{\ell, m}(q) \mathcal{S}_{\ell'_o, m'_o}^{\ell', m'}(q') \begin{pmatrix} \ell & \ell' & \mathcal{L} \\ 0 & 0 & 0 \end{pmatrix}. \quad (10.26)$$

Applying Eq. (10.25) once more to the Wigner  $3j$  symbol in Eq. (10.26) allows for eliminating the explicit dependence of  $\tilde{\mathcal{P}}_{\mathcal{L}}$  on the partial waves  $\ell$  and  $\ell'$ ,

$$\begin{aligned} \tilde{\mathcal{P}}_{\mathcal{L}} &= (-1)^{\ell_o + \ell'_o} (-1)^{\ell + \ell_o + \ell' + \ell'_o} \mathcal{S}_{\ell_o, m_o}^{\ell, m}(q) \mathcal{S}_{\ell'_o, m'_o}^{\ell', m'}(q') (-1)^{\ell + \ell' + \mathcal{L}} \begin{pmatrix} \ell & \ell' & \mathcal{L} \\ 0 & 0 & 0 \end{pmatrix} \\ &= (-1)^{\mathcal{L}} \mathcal{S}_{\ell_o, m_o}^{\ell, m}(q) \mathcal{S}_{\ell'_o, m'_o}^{\ell', m'}(q') \begin{pmatrix} \ell & \ell' & \mathcal{L} \\ 0 & 0 & 0 \end{pmatrix} \\ &= (-1)^{\mathcal{L}} \mathcal{P}_{\mathcal{L}}. \end{aligned} \quad (10.27)$$

Because  $\mathcal{P}_{\mathcal{L}}$  and  $\tilde{\mathcal{P}}_{\mathcal{L}}$  refer, by construction, to enantiomers of opposite handedness, Eq. (10.27) implies a change of sign for  $\mathcal{L}$  odd, cf. Eq. (10.21), when interchanging enantiomers, and no sign change for  $\mathcal{L}$  even. Our model properly reproduces this basic symmetry behavior. The corresponding behavior under change of the light helicity, keeping the same enantiomer, is checked below in Sec. 10.3.2.

### 10.3.2 Parity transformations under field polarization helicity exchange

#### Role of Polarizations $\varrho_1$ and $\varrho_2$

Having shown sign inversion for the odd Legendre coefficients for enantiomers of opposite handedness and a fixed circular polarization direction, we outline, in the following, an analogous symmetry property that is relevant when considering the same enantiomer but inverting the polarization direction. By definition, PECD requires all odd Legendre expansion coefficients for a given enantiomer to change sign when changing circular polarization from left to right, and vice versa. In order to show that our approach also properly reproduces this behavior, we employ again the symmetry properties of the Wigner  $3j$  symbols in Eq. (10.21b), similarly to Sec. 10.3.1. For the sake of completeness, we consider the general case of independent polarizations for the two-photon absorption and the one-photon ionization processes.

First, we consider all terms in Eq. (10.21b) depending on  $\epsilon'_{\varrho_2}$ . We apply Eq. (10.25) to the fourth and sixth Wigner  $3j$  symbol in Eq. (10.21b) for  $c_{\mathcal{L}}(-\varrho_1, -\varrho_2)$ . This yields

$$\begin{pmatrix} 1 & 1 & \nu \\ -\varrho_2 & +\varrho_2 & 0 \end{pmatrix} = (-1)^{2+\nu} \begin{pmatrix} 1 & 1 & \nu \\ \varrho_2 & -\varrho_2 & 0 \end{pmatrix} \quad (10.28a)$$

for the fourth Wigner  $3j$  symbol, and

$$\begin{pmatrix} K & \nu & \mathcal{L} \\ 0 & 0 & 0 \end{pmatrix} = (-1)^{K+\nu+\mathcal{L}} \begin{pmatrix} K & \nu & \mathcal{L} \\ 0 & 0 & 0 \end{pmatrix} \quad (10.28b)$$

for the sixth Wigner  $3j$  symbol in Eq. (10.21b) when the polarization direction driving the ionization process is  $-\varrho_2$ . Next, we evaluate the expression containing the information about the polarization direction driving the two-photon absorption process. For  $\epsilon_{-\varrho_1}$ , the term  $g_{\varrho_1}^K(q_1, q_2, q_3, q_4)$ , defined in Eq. (10.17b), reads

$$g_{-\varrho_1}^K(q_1, q_2, q_3, q_4) = (-1)^K g_{+\varrho_1}^K(q_1, q_2, q_3, q_4), \quad (10.28c)$$

when changing  $\varrho_1$  to  $-\varrho_1$ . In Eq. (10.28c), we have applied Eq. (10.25) to the sec-

ond, fourth and sixth Wigner  $3j$  symbols in Eq. (10.17b). The Legendre coefficient  $c_{\mathcal{L}}(-\varrho_1, -\varrho_2)$  involves, according to Eq. (10.21b), the triple product of Eqs. (10.28), that is,

$$g_{-\varrho_1}^K(q_{\{j\}}) \begin{pmatrix} 1 & 1 & \nu \\ -\varrho_2 & +\varrho_2 & 0 \end{pmatrix} \begin{pmatrix} K & \nu & \mathcal{L} \\ 0 & 0 & 0 \end{pmatrix} = (-1)^{\mathcal{L}} g_{+\varrho_1}^K(q_{\{j\}}) \begin{pmatrix} 1 & 1 & \nu \\ +\varrho_2 & -\varrho_2 & 0 \end{pmatrix} \begin{pmatrix} K & \nu & \mathcal{L} \\ 0 & 0 & 0 \end{pmatrix}, \quad (10.29)$$

with  $g_{-\varrho_1}^K(q_{\{j\}}) \equiv g_{-\varrho_1}^K(q_1, q_2, q_3, q_4)$ . Equation (10.29) implies, according to Eq. (10.21b),

$$c_{\mathcal{L}}(-\varrho_1, -\varrho_2) = (-1)^{\mathcal{L}} c_{\mathcal{L}}(+\varrho_1, +\varrho_2), \quad (10.30)$$

i.e., indeed, only odd Legendre coefficients change sign when changing simultaneously the polarization directions  $\varrho_1$  and  $\varrho_2$ , whereas all even coefficients remain unchanged.

To conclude, making use of the symmetry properties of the Wigner  $3j$  symbols, we have demonstrated that the theoretical model herein derived, reproduce the parity transformations under handedness and helicity exchange, observed experimentally.

### 10.3.3 Mixing polarization directions and photoelectron circular dichroism

The parity transformations under helicity exchange derived in Section 10.3.2 are not limited to the same polarization directions, i.e.,  $\epsilon'_{\varrho_1}$  and  $\epsilon'_{\varrho_2}$  for the two-photon excitation and photoionization process, respectively. In fact, we can go further and derive the predictions of our model for different, i.e., mixed, polarization directions. In particular, such analysis allows to determine the role that the two-photon excitation and photoionization processes play in the sign of the resulting Legendre coefficients. This is, it allows to elucidate which process, two-photon excitation or one-photon ionization, is responsible for changing the sign of the odd Legendre coefficients, when the polarization direction in question is exchanged. Also, it allows to understand the role of a linearly polarized electric field, in the generation of PECD if combined with circular polarization direction. As it will be shown, the order, of the polarization directions, i.e.  $\epsilon'_{\varrho_1} = 0$  followed by  $\epsilon'_{\varrho_2} = \pm 1$  or vice-versa is crucial to generate circular dichroism when mixing different polarization directions. For the sake of simplicity, important results requiring long lines of calculations are just stated in the following lines, but the lecturer may find their explicit derivations in Appendix C.2.4.

In order to derive the properties involving mixing polarization directions, and therefore understand the role the excitation and ionization processes play for the generation of PECD, we evaluate all non-vanishing Legendre coefficients as a function of the polarization

directions  $\varrho_1$  and  $\varrho_2$  without making any assumptions on the two-photon absorption tensor  $T$ . At a first state, we may consider the case where the two-photon absorption process is driven by linearly polarized light,  $\varrho_1 = 0$ . The second Wigner  $3j$  symbol in Eq. (10.17b) then becomes

$$\begin{pmatrix} 1 & 1 & Q \\ \varrho_1 & \varrho_1 & -2\varrho_1 \end{pmatrix} = \begin{pmatrix} 1 & 1 & Q \\ 0 & 0 & 0 \end{pmatrix}.$$

It does not vanish if and only if  $Q = 0, 2$ ; and analogously for the fourth Wigner symbol in Eq. (10.17b) involving  $Q'$ . Furthermore, the sixth Wigner  $3j$  symbol in Eq. (10.17b) becomes

$$\begin{pmatrix} Q & Q' & K \\ 0 & 0 & 0 \end{pmatrix},$$

which is non-zero only if  $K$  is even, because  $Q$  and  $Q'$  are even, and  $K + Q + Q' = 2n$  with  $|Q - Q'| \leq K \leq Q + Q'$ . As a consequence, because both  $Q$  and  $Q'$  are restricted to 0 and 2,  $K$  must be equal to 0, 2 or 4. Now, we consider the fourth Wigner  $3j$  symbol in Eq. (10.21b), namely

$$\begin{pmatrix} 1 & 1 & \nu \\ \varrho_2 & -\varrho_2 & 0 \end{pmatrix}, \tag{10.31}$$

which contains the information about the photoionization transition. If the photoionization process is driven by linearly polarized light ( $\varrho_2 = 0$ ), the allowed values for  $\nu$  in Eq. (10.31) are  $\nu = 0, 2$ . Therefore, the last Wigner symbol in Eq. (10.21b),

$$\begin{pmatrix} K & \nu & \mathcal{L} \\ 0 & 0 & 0 \end{pmatrix}, \tag{10.32}$$

has non-vanishing values only for  $|K - \nu| \leq \mathcal{L} \leq K + \nu$  and  $K + \nu + \mathcal{L}$  must be even due to the triple zeros in the second row. Because  $K = [0, 2, 4]$  for  $\varrho_1 = 0$  and  $\nu = 0, 2$  for  $\varrho_2 = 0$ , the maximal order of Legendre coefficients is  $\mathcal{L}_{\max} = 6$  and the non-vanishing Legendre coefficients are those for  $\mathcal{L} = 0, 2, 4, 6$ , i.e., there are no odd Legendre polynomials in the PAD for  $\varrho_1 = \varrho_2 = 0$ .

On the other hand, if we keep  $\varrho_1 = 0$  but the photoionization transition is driven by circularly polarized light ( $\varrho_2 = \pm 1$ ), the non-vanishing values in Eq. (10.31) are not

anymore restricted to even  $\nu$ , but instead to  $\nu = 0, 1, 2$ . Using these values for  $\nu$  together with the requirement  $|K - \nu| \leq \mathcal{L} \leq K + \nu$  in Eq. (10.32), we obtain, for  $K = 0, 2, 4$  (due to  $\varrho_1 = 0$ ), even as well as odd Legendre polynomials in the PAD, i.e.,  $\mathcal{L} = 0, 1, \dots, 6$ .

Next we check whether PECD can arise, i.e., whether the non-zero odd coefficients change sign under changing the light helicity, for  $\varrho_1 = 0$  and  $\varrho_2 = \pm 1$ . To this end, we explicitly write out the dependence of Eq. (10.21b) on the polarization direction  $\varrho_2$  driving the ionization step and define

$$\zeta_{\mathcal{L}}^{K,\nu}(\varrho_2) = \begin{pmatrix} 1 & 1 & \nu \\ \varrho_2 & -\varrho_2 & 0 \end{pmatrix} \begin{pmatrix} K & \nu & \mathcal{L} \\ 0 & 0 & 0 \end{pmatrix}, \quad (10.33a)$$

corresponding to the fourth and sixth Wigner  $3j$  symbol in Eq. (10.21b). For the opposite polarization direction  $-\varrho_2$ , this quantity becomes

$$\begin{aligned} \zeta_{\mathcal{L}}^{K,\nu}(-\varrho_2) &= \begin{pmatrix} 1 & 1 & \nu \\ -\varrho_2 & \varrho_2 & 0 \end{pmatrix} \begin{pmatrix} K & \nu & \mathcal{L} \\ 0 & 0 & 0 \end{pmatrix} \\ &= (-1)^{2\nu+K+\mathcal{L}} \begin{pmatrix} 1 & 1 & \nu \\ \varrho_2 & -\varrho_2 & 0 \end{pmatrix} \begin{pmatrix} K & \nu & \mathcal{L} \\ 0 & 0 & 0 \end{pmatrix} \\ &= (-1)^{\mathcal{L}} \zeta_{\mathcal{L}}^{K,\nu}(\varrho_2), \end{aligned} \quad (10.33b)$$

where we have applied Eq. (10.25) to both Wigner  $3j$  symbols in Eq. (10.33b), together with the fact that  $K$  is even for  $\varrho_1 = 0$ , as previously discussed. Finally, inserting Eq. (10.33b) into Eq. (10.21b) yields

$$c_{\mathcal{L}}(\varrho_1 = 0, -\varrho_2) = (-1)^{\mathcal{L}} c_{\mathcal{L}}(\varrho_1 = 0, +\varrho_2). \quad (10.34)$$

As a consequence, also for linearly polarized light driving the two-photon absorption process, odd Legendre coefficients change sign when the polarization direction of the ionizing field is changed from right to left, and vice versa. Whereas  $K$  must be even for  $\varrho_1 = 0$ ,  $\nu$  is  $\nu = 0, 1, 2$  for  $\varrho_2 = \pm 1$ , allowing  $\mathcal{L}$  to take odd and even values in Eq. (10.33b). This implies that there is no need for circular polarization to drive the two-photon absorption process: Two-photon absorption driven by linearly polarized light followed by photoionization with circularly polarized light is sufficient for observing PECD in chiral molecules. In Section 10.4.2 we investigate the specific role of the two-photon absorption tensor for all the cases discussed above. Conversely, the two-photon transition may be driven by circularly polarized light followed by photoionization with linearly polarized light, i.e.,

$\varrho_1 = \pm 1$  and  $\varrho_2 = 0$ . As shown in Eq. (C.36) in Appendix C.2.4, such a configuration leads to a PAD consisting exclusively of even Legendre contributions.

In Eq. (10.30) we have shown that only odd Legendre coefficients change sign when changing simultaneously the polarization direction driving the two-photon absorption and the one-photon ionization. In Appendix C.2.5, we show that

$$c_{\mathcal{L}}(\varrho_1, \varrho_2) = (-1)^{\mathcal{L}} c_{\mathcal{L}}(\varrho_1, -\varrho_2), \quad (10.35)$$

i.e., odd Legendre coefficients change sign when the polarization direction of the photoionization transition is changed, whereas the polarization of the field driving the two-photon absorption is kept fixed. This suggests the polarization direction of the ionizing field alone to impose the sign for all odd Legendre coefficients; the polarization direction in the two-photon absorption process plays no role. In order to verify this statement, we calculate  $c_{\mathcal{L}}(-\varrho_1, \varrho_2)$  in Appendix C.2.6 and find indeed

$$c_{\mathcal{L}}(-\varrho_1, \varrho_2) = c_{\mathcal{L}}(+\varrho_1, \varrho_2). \quad (10.36)$$

That is, the two-photon process determines only the degree of anisotropy prior to ionization.

To summarize, using linearly polarized light for both two-photon absorption and one-photon ionization results in a PAD consisting only of even Legendre polynomials, i.e., vanishing PECD. In contrast, when the  $(2 + 1)$  REMI process is driven by circularly polarized light, higher order odd Legendre polynomials may contribute, depending on the geometric properties of the resonantly excited state. The occurrence of non-zero Legendre coefficients for all polarization combinations is summarized in Table 10.1 below.

## 10.4 Anisotropy of photoelectron emission:

As shown in Section 10.2.4, the orientation-averaged differential cross section for  $2 + 1$  photoionization relies on two families of parameters: On one hand, the expansion coefficients of the intermediate excited state  $a_{m_o}^{\ell_o}(n_o)$ , and on the other hand, on the two-photon absorption tensor  $T_{q_1, q_2}$ . In this section, we investigate the requirements on the partial wave decomposition of the expansion coefficients, via their partial wave decomposition in order to achieve PECD. Analogously, important results regarding the combination of different polarization direction, for different partial wave decomposition of the expansion coefficients, for isotropic and anisotropic tensor elements  $T_{q_1, q_2}$  are discussed.

### 10.4.1 Angular momentum dependence of the intermediate state

Next we check the dependence of the non-zero Legendre coefficients contributing to the PAD on the maximum order  $L_{o,\max}$  of the excited state coefficients,  $a_{m_o}^{\ell_o}(n_o)$ , cf. Eq. (10.4). According to Equation (10.21b), a non-zero projection of the electronically excited state onto  $d$ -orbitals ( $\ell_o = 2$ ) is required to ensure that higher orders  $c_{\mathcal{L}}$  are non-zero. In fact, an additional requirement to reach  $\mathcal{L}_{\max} = 6$  is that  $L_{o,\max} \geq 2$ . This is straightforward to see by inspecting the term

$$\begin{pmatrix} \ell & \ell' & \mathcal{L} \\ 0 & 0 & 0 \end{pmatrix}$$

in Eq. (10.21b), defining the PAD for a  $(2 + 1)$  REMPI process. This term vanishes unless  $\ell + \ell' + \mathcal{L}$  is even and  $|\ell - \ell'| \leq \mathcal{L} \leq \ell + \ell'$ . In order to reach  $\mathcal{L}_{\max} = 6$ , the minimal requirement in terms of the angular momentum for the continuum wavepacket is  $\ell_{\max} = 3$ . Together with the selection rule  $\ell_{\max} = L_{o,\max} + 1$ , cf. Eq. (10.10b), this implies  $L_{o,\max} = 2$ , i.e., presence of  $d$ -waves in the resonantly excited state. Note that a contribution from higher partial waves only modifies the algebraic value of the Legendre coefficients, but does not lead to higher orders because, as we have already pointed out, the maximal order of the Legendre coefficients is also limited by the term

$$\begin{pmatrix} K & \nu & \mathcal{L} \\ 0 & 0 & 0 \end{pmatrix}$$

in Eq. (10.21b).

Perhaps even more interestingly, for circular polarization direction ( $\varrho_1 = \varrho_2 = \pm 1$ ),  $c_5$  vanishes if the projection of the electronically excited state onto  $\ell_o = 3$  is zero. In other words, expansion of the electronically excited state in terms of  $s$ ,  $p$  and  $d$  orbitals results in non-zero Legendre coefficients  $c_{\mathcal{L}}$  for  $\mathcal{L}$  up to 6, except for  $c_5$ . In fact, we found  $c_5$  to appear only in presence of a non-vanishing contribution of  $f$  orbitals. This does not result from selection rules as discussed before, but rather from an accidental compensation of terms in the summations in Eq. (10.21b) which arises from the central symmetry of our single center basis functions. Conversely, small  $f$ -wave contribution resulting from the intermediate excited state results in small amplitudes for  $c_5$ .

Given the experimental observation of Ref. [264, 265], we expect the electronically excited state for fenchone and camphor to have non-vanishing projections onto  $s$ -,  $p$ -,  $d$ - and possibly  $f$ -orbitals. Also, the eventual expansion coefficients of the electronically excited state will most likely be different for fenchone and camphor to account for the

different ratios of  $c_3$  and  $c_1$  observed for the two molecules [264, 265].

### 10.4.2 Two-photon absorption tensor dependence of the intermediate state

The number of Legendre coefficients contributing to PECD in our model of the 2+1 REMPI process is also determined by the degree of anisotropy of the ensemble of electronically excited molecules. Such a statement follows from the properties of the two-photon absorption tensor. In the following lines, we check the conditions that  $T_{q_1, q_2}$  shall fulfill in order to give rise to any anisotropy in the photoelectron emission. To this end, we introduce the two-photon absorption amplitude  $\mathcal{A}_{2P}(\omega)$ , where for convenience the multiplying factor in Eq. (10.16) has been dropped out,

$$\mathcal{A}_{2P}(\omega) = \sum_{q_1} \sum_{q_2} \mathcal{D}_{q_1, \varrho_1}^{(1)}(\omega) \mathcal{D}_{q_2, \varrho_1}^{(1)}(\omega) T_{q_1, q_2}, \quad (10.37)$$

i.e.,  $\rho_{2P}(\omega) \propto |\mathcal{A}_{2P}(\omega)|^2$ , cf. Eq. (10.16). For simplicity, we define  $\tilde{\mathcal{A}}_{2P}(\omega)$  such that  $\mathcal{A}_{2P}(\omega) = \frac{4\pi}{3} \tilde{\mathcal{A}}_{2P}(\omega)$ . We first check the 'trivial' case of an isotropic two-photon absorption tensor, i.e., a two-photon tensor that is diagonal in the Cartesian basis with equal elements. In this case,  $\tilde{\mathcal{A}}_{2P}(\omega)$  becomes

$$\begin{aligned} \tilde{\mathcal{A}}_{2P}(\omega) = & +\mathcal{D}_{0, \varrho_1}^{(1)}(\omega) \mathcal{D}_{0, \varrho_1}^{(0)}(\omega) T_{zz} - \frac{1}{2} \mathcal{D}_{-1, \varrho_1}^{(1)}(\omega) \mathcal{D}_{+1, \varrho_1}^{(1)}(\omega) (T_{xx} + T_{yy}) \\ & - \frac{1}{2} \mathcal{D}_{+1, \varrho_1}^{(1)}(\omega) \mathcal{D}_{-1, \varrho_1}^{(1)}(\omega) (T_{xx} + T_{yy}), \end{aligned}$$

where the transformation between spherical and Cartesian basis has been employed, cf. Eq. (C.7). Taking the elements to be equal,  $T_{xx} = T_{yy} = T_{zz} = 1$  without loss of generality,  $\tilde{\mathcal{A}}_{2P}(\omega)$  can be written as

$$\begin{aligned} \tilde{\mathcal{A}}_{2P}(\omega) &= \mathcal{D}_{0, \varrho_1}^{(1)}(\omega) \mathcal{D}_{0, \varrho_1}^{(1)}(\omega) - 2\mathcal{D}_{-1, \varrho_1}^{(1)}(\omega) \mathcal{D}_{+1, \varrho_1}^{(1)}(\omega) \\ &= \sum_{\mu=0, \pm 1} (-1)^\mu \mathcal{D}_{\mu, \varrho_1}^{(1)}(\omega) \mathcal{D}_{-\mu, \varrho_1}^{(1)}(\omega) \\ &= \sum_{\mu=0, \pm 1} (-1)^{-\varrho_1} \mathcal{D}_{\mu, \varrho_1}^{(1)}(\omega) \mathcal{D}_{\mu, -\varrho_1}^{*(1)}(\omega) \\ &= (-1)^{-\varrho_1} \delta_{\varrho_1, -\varrho_1}, \end{aligned} \quad (10.38)$$

where we have used Eq. (C.20). That is, for an isotropic two-photon tensor, it is not possible to reach an anisotropic distribution by absorption of two identical photons. The PAD for the (2 + 1) REMPI process then reduces to the well-known one for one-photon ionization of randomly oriented molecules, i.e., only  $P_0$  and  $P_2$  contribute if  $\varrho_2 = 0$ , and  $P_0$ ,  $P_1$  and  $P_2$  are non-zero for  $\varrho_2 = \pm 1$ .

	$\epsilon'_0/\epsilon'_{\pm 1}$				$\epsilon'_{\pm 1}/\epsilon'_0$				$\epsilon'_0/\epsilon'_0$				$\epsilon'_{\pm 1}/\epsilon'_{\pm 1}$				$\epsilon'_{\pm 1}/\epsilon'_{\mp 1}$															
	isotropic		<i>s</i>	<i>p</i>	<i>d</i>	<i>f</i>	isotropic		<i>s</i>	<i>p</i>	<i>d</i>	<i>f</i>	isotropic		<i>s</i>	<i>p</i>	<i>d</i>	<i>f</i>	isotropic		<i>s</i>	<i>p</i>	<i>d</i>	<i>f</i>	isotropic		<i>s</i>	<i>p</i>	<i>d</i>	<i>f</i>		
$c_0$	•	•	•	•	–	–	–	–	•	•	•	•	–	–	–	–	–	–	–	–	–	–	–	–	–	–	–	–	–	–	–	–
$c_1$	–	–	•	•	–	–	–	–	–	–	–	–	–	–	–	–	–	–	–	–	–	–	–	–	–	–	–	–	–	–	–	–
$c_2$	•	•	•	•	–	–	–	–	•	•	•	•	–	–	–	–	–	–	–	–	–	–	–	–	–	–	–	–	–	–	–	–
$c_3$	–	–	–	–	–	–	–	–	–	–	–	–	–	–	–	–	–	–	–	–	–	–	–	–	–	–	–	–	–	–	–	–
$c_4$	–	–	–	–	–	–	–	–	–	–	–	–	–	–	–	–	–	–	–	–	–	–	–	–	–	–	–	–	–	–	–	–
$c_5$	–	–	–	–	–	–	–	–	–	–	–	–	–	–	–	–	–	–	–	–	–	–	–	–	–	–	–	–	–	–	–	–
$c_6$	–	–	–	–	–	–	–	–	–	–	–	–	–	–	–	–	–	–	–	–	–	–	–	–	–	–	–	–	–	–	–	–

	$\epsilon'_0/\epsilon'_{\pm 1}$				$\epsilon'_{\pm 1}/\epsilon'_0$				$\epsilon'_0/\epsilon'_0$				$\epsilon'_{\pm 1}/\epsilon'_{\pm 1}$				$\epsilon'_{\pm 1}/\epsilon'_{\mp 1}$															
	anisotropic		<i>s</i>	<i>p</i>	<i>d</i>	<i>f</i>	anisotropic		<i>s</i>	<i>p</i>	<i>d</i>	<i>f</i>	anisotropic		<i>s</i>	<i>p</i>	<i>d</i>	<i>f</i>	anisotropic		<i>s</i>	<i>p</i>	<i>d</i>	<i>f</i>	anisotropic		<i>s</i>	<i>p</i>	<i>d</i>	<i>f</i>		
$c_0$	•	•	•	•	•	•	•	•	•	•	•	•	•	•	•	•	•	•	•	•	•	•	•	•	•	•	•	•	•	•	•	•
$c_1$	–	–	•	•	–	–	–	–	–	–	–	–	–	–	•	•	–	–	•	•	–	–	•	•	–	–	•	•	–	–	•	•
$c_2$	•	•	•	•	•	•	•	•	•	•	•	•	•	•	•	•	•	•	•	•	•	•	•	•	•	•	•	•	•	•	•	•
$c_3$	–	–	•	•	–	–	–	–	–	–	–	–	–	–	•	•	–	–	•	•	–	–	•	•	–	–	•	•	–	–	•	•
$c_4$	–	•	•	•	–	•	•	•	–	•	•	•	–	•	•	•	–	•	•	•	–	•	•	•	–	•	•	•	–	•	•	•
$c_5$	–	–	–	•	–	–	–	–	–	–	–	–	–	–	–	•	–	–	–	•	–	–	–	•	–	–	–	•	–	–	–	•
$c_6$	–	–	•	•	–	–	•	•	–	–	•	•	–	–	•	•	–	–	•	•	–	–	•	•	–	–	•	•	–	–	•	•

• contributing to the PAD

– not contributing to the PAD

Table 10.1: Contribution of Legendre coefficients to the PAD as a function of the partial wave cut-off in Eq. (10.4) and the polarizations  $\epsilon'_{\rho_1}$  and  $\epsilon'_{\rho_2}$  of two-photon absorption and photoionization, respectively, for an isotropic and anisotropic two-photon absorption tensor  $T$  within the strict electric dipole approximation.

In what follows, we discuss a general two-photon absorption tensor, decomposing it as

$$\begin{aligned}
T &= \alpha_o 1_{3 \times 3} + \begin{pmatrix} \beta_{xx} & 0 & 0 \\ 0 & \beta_{yy} & 0 \\ 0 & 0 & \beta_{zz} \end{pmatrix} + \begin{pmatrix} 0 & T_{xy} & T_{xz} \\ T_{xy} & 0 & T_{yz} \\ T_{xz} & T_{yz} & 0 \end{pmatrix} \\
&\equiv T_{\text{Id}} + T_{\text{d}} + T_{\text{nd}}, \tag{10.39}
\end{aligned}$$

where we have split the diagonal elements into  $T_{\text{Id}}$  and  $T_{\text{d}}$  in order to differentiate between isotropic and anisotropic two-photon tensors. The contributions of odd and even Legendre polynomials to the PAD as a function of  $L_{o,\text{max}}$ , the number of partial waves in the electronically excited state, the polarizations  $\epsilon'_{\rho_1}$  and  $\epsilon'_{\rho_2}$ , and the two-photon absorption tensor are summarized in Table 10.1. If the complete  $(2 + 1)$  REMPI process is driven by linearly polarized light and only  $\alpha_0 \neq 0$ , then  $P_o$  and  $P_2$  contribute to the PAD as just discussed. If the two-photon absorption tensor is anisotropic, even Legendre polynomials of higher order can appear. For a molecule characterized by such a two-photon absorption tensor, odd Legendre polynomials can contribute to the PAD if the polarization of the ionization step is circular ( $\epsilon'_{\rho_2} = \epsilon'_{\pm 1}$ ). Analogously, both even and odd Legendre polynomials can appear if  $\epsilon'_{\rho_1} = \epsilon'_{\rho_2} = \epsilon'_{\pm 1}$ . Note that anisotropy of the

two-photon tensor is sufficient, i.e., it does not matter whether the anisotropy is due to diagonal or non-diagonal elements of the Cartesian tensor. The latter case is the one discussed in Ref. [267], where a “nearly” diagonal two-photon absorption tensor was used. In other words, an anisotropic tensor with non-zero off-diagonal elements in the Cartesian basis also yields the pattern in the lower part of Table 10.1.

As indicated, the point group symmetry of the molecule determines which tensor components of  $T_{q_1, q_2}$  must be zero. This tensor pattern is a property of the states involved in the transition and is determined by the symmetry of the initial and final states. For instance, in molecular systems with point groups T and O, the photon absorption tensor becomes more selective. The 2+1 process between two states that transform like the totally symmetric representation of these point groups will only take place with linearly polarized laser light. In this case the isotropic part  $T_{Id}$  of Eq. (10.39) can remain nonzero. If the 2+1 process involves initial and final states that transform like non-totally symmetric representations of the point group, the tensor pattern changes and thus the tensor might have isotropic or anisotropic parts. This determines whether the 2+1 process is allowed or not. We refer the reader to Refs. [297, 298] for more detailed discussion of this issue.

## 10.5 Numerical Results

### 10.5.1 Fenchone

We start by addressing the question of how many partial waves are required in the intermediate electronically excited state to yield odd Legendre coefficients with  $\mathcal{L} > 1$ , as observed experimentally. To this end, we consider the expansion of the intermediate electronically excited state, cf. Eq. (10.3), with  $L_{o, \max} = 2$  and  $L_{e, \max} = 3$ , i.e., up to  $d$  and  $f$  waves, for the states B and C, and employ the two-photon tensor elements from the CCSD/Rydberg-TZ calculations outlined in Ref. [294]. The results are presented in Table 10.2. Presence of  $f$ -waves is required to obtain a non-zero coefficient  $c_5$ , as expected from Table 10.1. Allowing for  $f$  waves (with  $n_0=4$ ) results in a perfect match for the odd coefficients for states C1, C2 and C3, cf. the upper part of Table 10.2. In contrast, for state B,  $c_3$  and  $c_5$ , while having the correct sign, are off by an order of magnitude. Modifying the optimization weights improves  $c_5$  for state B, but only at the expense of the agreement for  $c_1$  and  $c_3$ . State B can therefore be ruled out as intermediate electronically excited state. This is further confirmed by the lower part of Table 10.2, showing the results for both odd and even Legendre coefficients in the optimization target. For state B, the sign of  $c_6$  does not match the experimental one. Fitting both odd and even Legendre coefficients also allows to differentiate between the C states—only state C3 reproduces

coeffs.	exp. [265]	state B		state C1		state C2		state C3	
		<i>d</i> waves	<i>f</i> waves						
$c_1$	-0.067	-0.067	-0.067	-0.067	-0.067	-0.067	-0.067	-0.067	-0.067
$c_3$	+0.008	+0.080	+0.080	+0.008	+0.008	+0.008	+0.008	+0.008	+0.008
$c_5$	+0.004	-	+0.0005	-	+0.004	-	+0.004	-	+0.004
$c_1$	-0.067	-0.028	-0.041	-0.045	-0.036	-0.040	-0.048	-0.045	-0.046
$c_2$	-0.580	-0.076	-0.102	-0.274	-0.176	-0.146	-0.226	-0.224	-0.246
$c_3$	+0.008	+0.006	+0.005	+0.006	+0.008	+0.003	+0.004	+0.006	+0.005
$c_4$	-0.061	-0.004	-0.004	-0.021	-0.012	-0.012	-0.011	-0.012	-0.019
$c_5$	+0.004	-	+0.0001	-	+0.001	-	+0.002	-	+0.001
$c_6$	-0.008	+0.0002	+0.0003	+0.0007	+0.0001	+0.0006	+0.001	-0.002	-0.002

Table 10.2: Legendre coefficients for the **PAD of fenchone** (calculated at a photoelectron energy of 0.56 eV and normalized with respect to  $c_0$ ), obtained by fitting to the experimental values with the excited state coefficients  $a_{m_o}^{\ell_o}$  as free parameters. Only odd (top) and both odd and even (bottom) contributions were accounted for in the fitting procedure. The Rydberg states B, C1, C2 and C3 of fenchone are characterized by their two-photon absorption tensor obtained from *ab initio* calculations, cf. Ref. [294].

the correct sign of  $c_6$ . For all other Legendre moments, signs and order of magnitude of the coefficients match the experimental ones for all three C states. Fitting to all and not just the odd Legendre coefficients decreases the agreement between theoretical and experimental results for all C states. This may indicate that the model, with a single  $n_o$ , is not capable of reproducing the full complexity of the process, or it may be due to different experimental error bars for even and odd Legendre coefficients. In our fitting procedure, we have neglected the experimental error bars to keep the calculations manageable. The experimental error bars for the even Legendre coefficients are much larger than for the odd ones [265], and ignoring them may introduce a bias into the optimization procedure that could also explain the decreased agreement.

While already Table 10.2 suggests that C3 is likely the intermediate electronically excited state state probed in the 2+1 photoexcitation process, the ultimate test consists in using *ab initio* results for all parameters in Eq. (10.21), i.e., the excited state expansion coefficients and the two-photon tensor elements, and compare the resulting Legendre coefficients to the experimental data. The results are shown in Table 10.3 (“fixed tensor elements”). Choosing a slightly larger photoelectron energy, specifically 0.58 eV instead of 0.56 eV, with the shift of 0.02 eV well within the error bars of the calculated excitation energies, considerably improves the agreement between theoretical and experimental values, in particular for the  $c_1$  coefficient. Additionally, we allow the tensor elements to vary within a range of  $\pm 20\%$  to account for unavoidable errors in the electronic structure cal-

coeffs.exp. [265]	state B		state C1		state C2		state C3	
	fixed	error bars	fixed	error bars	fixed	error bars	fixed	error bars
$c_1$	-0.067	+0.003 +0.003	-0.004	-0.003	-0.002	-0.001	-0.013	-0.015
$c_2$	-0.580	-0.238 -0.193	-0.272	-0.217	-0.409	-0.358	-0.250	-0.213
$c_3$	+0.008	-0.039 -0.029	+0.050	+0.038	+0.033	+0.025	+0.008	+0.010
$c_4$	-0.061	-0.095 -0.113	-0.084	-0.105	+0.010	-0.015	-0.023	-0.048
$c_5$	+0.004	-0.001 -0.001	+0.003	+0.002	-0.004	+0.003	-0.0004	-0.00004
$c_6$	-0.008	-0.003 -0.005	+0.003	-0.001	-0.004	-0.017	-0.013	-0.007

Table 10.3: Legendre coefficients for the **PAD of fenchone** (calculated at a photoelectron energy of 0.58 eV and normalized with respect to  $c_0$ ), obtained by employing the excited state coefficients and two-photon tensors from the *ab initio* calculations. When including error bars, the tensor elements are allowed to vary within  $\pm 20\%$ .

culations. The best tensor elements within the error range are obtained by minimization. The corresponding functional is defined as

$$\Gamma = \frac{1}{\Gamma^{(0)}} \sum_{j=1}^6 \omega_j \left( \frac{c_j - c_j^{\text{exp}}}{c_j^{\text{exp}}} \right)^2, \quad (10.40)$$

where  $\omega_j$  are optimization weights and  $\Gamma^{(0)}$  is the value of the functional using the fixed tensor elements. Table 10.3 confirms state B to be ruled out, since it does not reproduce correctly even a single sign of the odd coefficients. For all states C, the correct signs are obtained for the lower order Legendre coefficients, up to  $c_4$ . State C1 yields the correct sign of  $c_6$  only if the tensor elements are allowed to vary within  $\pm 20\%$ ; the same holds for C2 and the sign of  $c_5$ . C3 does not reproduce the correct sign of  $c_5$ , but the value of  $c_5$  is very small and close to zero when accounting for the error bars. In terms of PECD, the most important coefficient for fenchone is  $c_1$ , since its experimental value is an order of magnitude larger than that of the other odd coefficients. For  $c_1$ , the best agreement is obtained for state C3, differing from the experimental value by a factor of five. In contrast, the difference is by a factor of about twenty for state C1, and even larger for state C2. While  $c_1$  is too small by more than an order of magnitude for states C1 and C2,  $c_3$  is overestimated by a factor of five for C1 and a factor of three for C2. For states C1 and C2, the largest odd Legendre coefficient is thus  $c_3$ , unlike the experimental result where it is  $c_1$ . In contrast, the theoretical result for  $c_3$  is in quantitative agreement for state C3 which therefore yields the correct ordering of the odd Legendre coefficients in terms of their magnitude. We thus conjecture that for fenchone, state C3 is most likely the intermediate electronically state probed in the experiment, despite the fact that  $c_5$  is very close to zero. The reason for the discrepancy exclusively for  $c_5$ , while all other coefficients match the experimental ones at least qualitatively, is not entirely clear. A necessary

coefficient	exp. [265]	fixed	$\pm 20\%$	$\pm 30\%$	$\pm 50\%$	$\pm 20\%$	$\pm 30\%$	$\pm 50\%$
$c_1$	-0.067	-0.012	-0.015	-0.016	-0.016	-0.015	-0.018	-0.022
$c_2$	-0.580	+0.250	-0.213	-0.210	-0.212	-0.223	-0.227	-0.268
$c_3$	+0.008	+0.008	+0.010	+0.010	+0.010	+0.010	+0.011	+0.014
$c_4$	-0.061	-0.023	-0.045	-0.048	-0.048	-0.045	-0.0504	-0.033
$c_5$	+0.004	-0.0004	-0.00004	-0.00001	+0.00002	+0.00004	+0.0004	+0.001
$c_6$	-0.008	-0.013	-0.007	-0.007	-0.007	-0.006	-0.001	-0.001
$\Gamma$ (equal $\omega_j$ )		1.0	0.714	0.711	0.705	–	–	–
$\Gamma$ (unequal $\omega_j$ )		1.0	–	–	–	0.775	0.710	0.686

Table 10.4: Legendre coefficients for the **PAD of fenchone** (calculated at a photoelectron energy of 0.58 eV and normalized with respect to  $c_0$ ), obtained by employing the excited state coefficients and two-photon tensor elements from the *ab initio* for state C3 and increasing error bars of the two-photon tensor elements. Minimization of the functional in Eq. (10.40) carried out with equal (top) and unequal (bottom,  $\omega_5 = 10\omega, \omega_{j=1,\dots,4,6} = \omega$ ) optimization weights.

condition for non-vanishing  $c_5$  is, according to Table 10.1, that the  $f$ -wave contribution of the intermediate state to be non-vanishing. The results shown in Table 10.3 thus suggest that our calculations underestimate the  $f$ -wave character of C3. This may be caused by an improper description of long-range interaction between the photoelectron and the remaining ion, i.e., by the fact that the true potential felt by the photoelectron is neither central nor point-like, or by the interaction between the laser field and the photoelectron whose time dependence is neglected in our model. Finally, the error bars of the two-photon tensor elements may be larger than 20%. Indeed, allowing error bars of  $\pm 50\%$  in the two-photon absorption tensor elements removes the disagreement for  $c_5$  and state C3. At the same time, these error bars do not significantly improve the agreement for the other two states. For example, the coefficient  $c_1$  is  $-0.0061$  for state C1 and  $-0.0045$  for state C2, leaving the conclusion that state C3 is the intermediate resonance unchanged. A systematic increase of the two-photon tensor error bars for state C3 is presented in Table 10.4. We compare minimization of the functional (10.40) with equal weights for all Legendre coefficients (upper part of Table 10.4) to that with a ten times larger weight of  $c_5$  (lower part of Table 10.4). The motivation behind the second choice is to see whether the correct sign can be obtained for  $c_5$  without the need to increase the error bars to a very high value. When increasing the error bars of the two-photon tensor elements, while using the same optimization weights in Eq. (10.40), the value of  $c_5$  is increased until it changes sign. The overall value of the functional decreases monotonically, as expected. When the optimization weight of  $c_5$  is taken 10 times larger than those of all other Legendre coefficients, assuming an error range of  $\pm 20\%$  for the two-photon tensor elements of state

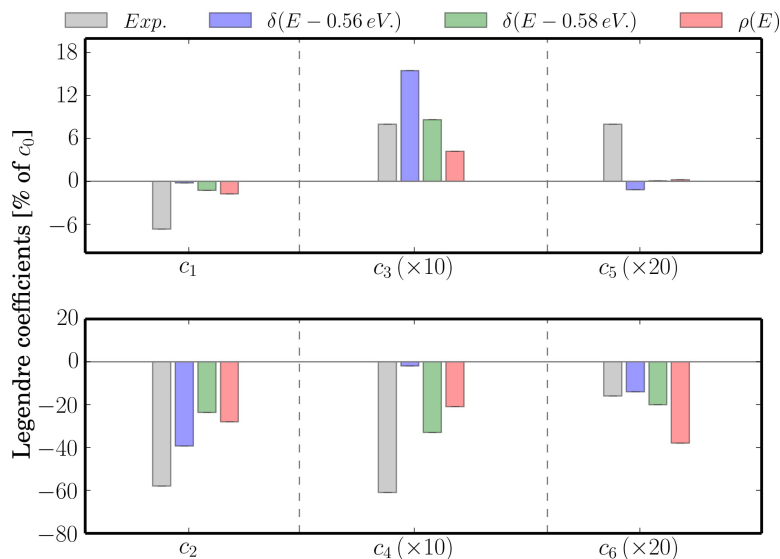


Figure 10.1: **Fenchone**: Comparison of experimentally obtained and theoretically calculated Legendre coefficients in the PAD for *S*-(+)-fenchone, using state C3 and right circular polarization. The calculations were carried out for a fixed photoelectron energy of 0.56 eV, respectively 0.58 eV, as well as integrating over a Gaussian distribution of photoelectron energies (denoted by  $\rho(E)$ ) centered at 0.56 eV with a FWHM of 200 meV.

C3 already yields the correct sign for all Legendre coefficients. Increasing the error range in this case further improves the magnitude of  $c_5$ , until it differs from the experimental one by a factor of four for error bars of  $\pm 50\%$ . However, this comes at the expense of the agreement for all other Legendre coefficients except  $c_1$ . It is quantified by evaluating  $\Gamma$  in Eq. (10.40) with equal weights, using the optimized two-photon tensor elements obtained with unequal weights.

Overall, already the two-photon tensor elements taken directly from the *ab initio* calculations yield a satisfactory agreement for the PAD between theory and experiment for state C3. The agreement is further improved by allowing the two-photon tensor elements to vary within a range of  $\pm 20\%$  to account for the error bars of the *ab initio* calculations. All Legendre coefficients except  $c_3$  are sensitive to a variation within this range. Except for  $c_5$ , i.e., underestimation of the excite state *f*-wave character, a surprisingly good agreement between theoretical and experimental values is obtained, with the numerical values differing from the experimental ones up to a factor of five. The semi-quantitative agreement between theory and experiment is further illustrated in Fig. 10.1, left panel, where we compare calculation results for two specific photoelectron energies, 0.56 eV and 0.58 eV, to the experimentally obtained Legendre coefficients. The differences for the Legendre coefficients for 0.56 eV and 0.58 eV indicates the dependence of our results on the error bar of the calculated excitation energy of the intermediate electronically excited

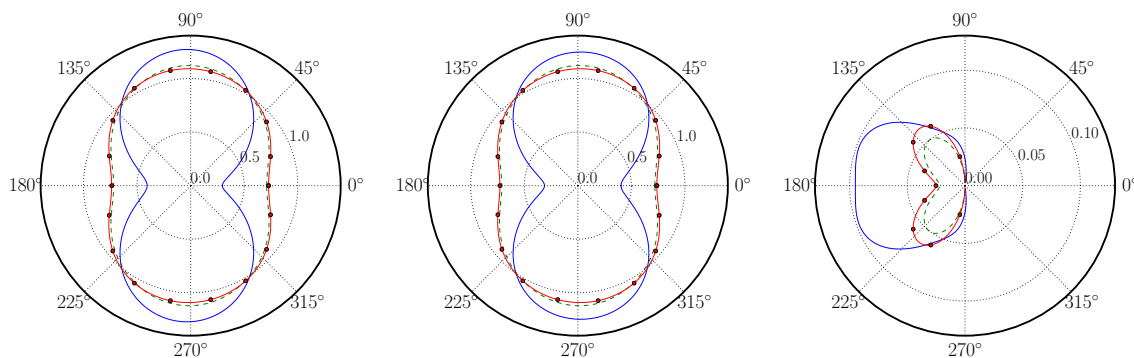


Figure 10.2: **Fenchone**: Photoelectron angular distributions obtained with left circularly polarized light for ionization from the state C3 of S-(+)-fenchone (**left panel**) and of R-(-)-fenchone (**middle**) employing the fixed two-photon absorption tensor elements (dashed green lines) and two-photon absorption tensor elements with  $\pm 20\%$  error bars (solid red lines with black circles). The theoretical curves are compared to those obtained for the experimentally determined Legendre coefficients of Ref. [265] (blue solid lines). The differences between the PAD for the two enantiomers are shown in the right panel. The calculated difference (**right panel**) is scaled by a factor of 2.5 times in order to have theoretical and experimental curves on the same scale.

state. Additionally, left panel in Fig. 10.1 also shows the result of integrating over a normal distribution of photoelectron energies centered at 0.56 eV with a full width at half maximum (FWHM) of 200 meV. This accounts for the experimental averaging over photoelectron energies [265]. The disagreement between theoretical and experimental results amounts to a factor of about two which translates into a “mean” PECD of 3% and 4% for the fixed and  $\pm 20\%$  adjustable tensor elements, respectively, compared to the experimental value of 10.1% [265]. Figure 10.2 displays the photoelectron angular distributions (PAD) for both enantiomers (S-(+) and R-(-)) of fenchone, corresponding to state C3, which was identified as being the most likely resonantly excited state in the 2+1 process. The experimental Legendre coefficients are taken from Ref. [265] left circularly polarized light is assumed. Also shown is the difference between the PAD of the two enantiomers (bottom panel of Fig. 10.2). Overall, the shapes obtained with the theoretical and experimental Legendre coefficients are similar, illustrating the semi-quantitative agreement between the calculated and experimental results. The main difference between theoretical and experimental curves arises from the factor of four between the experimentally obtained and calculated coefficient  $c_1$  (which is one order of magnitude larger than the other odd coefficients).

The dependence of the calculated Legendre coefficients on the photoelectron energy is further investigated in Fig. 10.3. A non-monotonic behavior is observed for all orders.

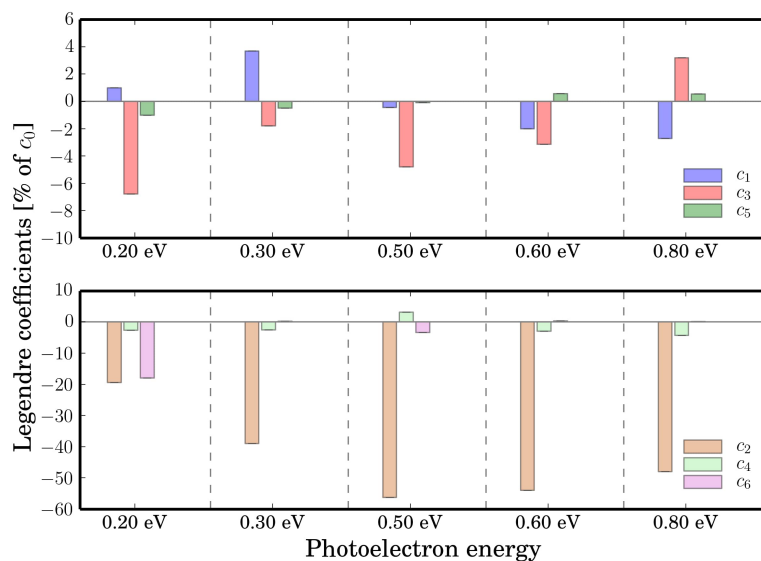


Figure 10.3: **Fenchone**: Dependence of the calculated Legendre coefficients on photoelectron energy for the PAD of state C3 for *S*-(+)-fenchone, using right circular polarization.

Such a non-monotonic behavior of the Legendre coefficients as a function of the photoelectron energy has already been reported for  $c_1$  in the one-photon ionization of randomly oriented molecules [301]. It reflects the dependence of the Legendre coefficients on the radial part of the photoelectron wavefunction.

### 10.5.2 Camphor

This section is devoted to the application of our 2+1 REMPI-based model to camphor. Numerical results and experimental results, the latter referenced in Ref. [265], are compared. For camphor, the experimentally recorded photoelectron spectrum peaks at 0.52 eV. [265]. As for fenchone, the ultimate test to rule out a given state, in the framework of our model, consists in using both two-photon tensor elements and excited state expansion coefficients obtained from the *ab initio* calculations. The corresponding results are shown in Table 10.5. Already Table 10.5 confirms that states C2 and C3 are not the intermediate resonance probed in the experiment, since both states yield the wrong sign for both  $c_1$  and  $c_3$ . By comparing the remaining two candidates, namely states B and C1, it is clear that a much better agreement is observed for C1 which yields the correct signs for all Legendre coefficients. In contrast, state B only yields correct signs for the lower orders,  $c_1$ ,  $c_2$ , and  $c_3$ . When accounting for the error bars in the two-photon tensor, a correct sign is additionally obtained for  $c_4$ , but the signs for  $c_5$  and  $c_6$  still cannot properly be reproduced with state B as intermediate resonance. As to the state C1, not only all signs but also the correct order of magnitude for  $c_2$ ,  $c_3$  and  $c_4$  are properly reproduced,

coeffs. exp. [265]	state B		state C1		state C2		state C3		
	fixed	error bars	fixed	error bars	fixed	error bars	fixed	error bars	
$c_1$	+0.026	+0.003	+0.002	+0.002	+0.001	-0.002	-0.002	-0.001	-0.001
$c_2$	-0.678	-0.384	-0.383	-0.389	-0.401	-0.395	-0.395	-0.421	-0.425
$c_3$	-0.053	-0.025	-0.022	-0.020	-0.017	+0.005	+0.008	+0.004	+0.003
$c_4$	+0.012	-0.066	-0.050	+0.020	+0.023	+0.004	-0.002	-0.008	+0.0001
$c_5$	+0.008	-0.002	-0.001	+0.0001	+0.0001	+0.001	+0.001	+0.0003	+0.001
$c_6$	-0.001	+0.043	+0.035	-0.026	-0.023	-0.008	-0.001	+0.005	-0.0004

Table 10.5: **Camphor**: Legendre coefficients for the PAD of camphor (calculated at a photoelectron energy of 0.52 eV and normalized with respect to  $c_0$ ), obtained by employing the excited state coefficients and two-photon tensor elements from the *ab initio* calculations. When including error bars, the tensor elements are allowed to vary within  $\pm 20\%$ .

coeffs. exp. [265]	state B		state C1		state C2		state C3		
	fixed	error bars	fixed	error bars	fixed	error bars	fixed	error bars	
$c_1$	+0.026	+0.033	+0.030	+0.026	+0.027	-0.005	-0.009	-0.004	-0.002
$c_2$	-0.678	-0.450	-0.498	-0.477	-0.502	-0.431	-0.427	-0.432	-0.437
$c_3$	-0.053	-0.029	-0.031	-0.024	-0.022	-0.003	-0.0002	+0.001	-0.003
$c_4$	+0.012	-0.074	-0.034	+0.003	+0.009	-0.022	-0.036	-0.026	-0.018
$c_5$	+0.008	-0.001	-0.001	+0.0001	+0.0001	+0.0002	+0.001	+0.0002	+0.0001
$c_6$	-0.001	+0.030	+0.024	-0.015	-0.011	-0.020	-0.010	+0.0001	+0.003

Table 10.6: **Camphor**: The same as Table 10.5 but for a photoelectron energy of 0.58 eV.

whereas the values are too small by one order of magnitude for  $c_1$  and by two orders for  $c_5$  and too large by one order of magnitude for  $c_6$ . Allowing the two-photon absorption tensor for state C1 to vary within an error range of  $\pm 20\%$  does not yield any significant improvement. It therefore does not seem to be the unavoidable error in the two-photon tensor elements that is important. Analogously to fenchone, a second source of error in the *ab initio* calculations is found in the excitation energy of the intermediate electronically excited state. This is reflected in the photoelectron energy. We thus present results for a second photoelectron energy, namely 0.58 eV in Table 10.6. For state C1, all signs still match, and the correct order of magnitude is now obtained for  $c_1$  to  $c_4$ . In particular,  $c_1$  is now in quantitative agreement with the experimental value, and  $c_2$  and  $c_3$  differ by less than factor of 1.5, respectively 2.5. Despite the disagreement in the numerical values for  $c_5$  and  $c_6$ , C1 is clearly the state the best matches the experimental data—the results obtained for states B, C2 and C3 show the same deficiencies as in Table 10.5. The agreement with the experimental data obtained for state C1 can be further improved by allowing for larger error bars in the two-photon tensor elements. This is demonstrated in

coeffs.	exp. [265]	fixed	$\pm 20\%$	$\pm 30\%$	$\pm 50\%$
$c_1$	+0.026	+0.026	+0.027	+0.026	+0.022
$c_2$	-0.678	-0.477	-0.502	-0.515	-0.529
$c_3$	-0.053	-0.024	-0.022	-0.020	-0.014
$c_4$	+0.012	+0.003	+0.009	+0.012	+0.012
$c_5$	+0.008	+0.0001	+0.0001	+0.0001	+0.0003
$c_6$	-0.001	-0.015	-0.011	-0.008	-0.001
$\Gamma$ (equal $\omega_j$ )		1.0	0.50	0.26	0.01

Table 10.7: **Camphor**: Legendre coefficients for the PAD of camphor (calculated at a photoelectron energy of 0.58 eV ) for increasing error bars of the two-photon tensor elements. *Ab initio* data for state C3 was used.

Table 10.7. In fact, the agreement can be made fully quantitative, except for  $c_5$ , when increasing the error bars up to  $\pm 50\%$ , as indicated by the small value of the optimization functional.

In comparison to fenchone, cf. Table 10.4, minimization results in significantly smaller values for  $\Gamma$ , as the error range is increased. Also, the higher order Legendre coefficients are found to be more sensitive to modifications of the two-photon tensor elements than the lower ones. This is not surprising since the higher order coefficients depend more strongly on the anisotropy induced by the two-photon absorption. Analogously to fenchone,  $c_5$  has the correct sign but remains too small by one order of magnitude. This indicates once more that we underestimate significantly the *d*-wave contribution to the intermediate electronically excited state. It amounts to just 6% for both fenchone and camphor in our calculations. The discussion above is summarized and illustrated in Fig. 10.4, left panel, which shows, besides the Legendre coefficients for photoelectron energies of 0.52 eV and 0.58 eV, those obtained when integrating over a normal distribution of photoelectron energies, centered at 0.52 eV, with a FWHM of 200 meV. The latter mimicks the spectral bandwidth in the experiment. Introducing a distribution of photoelectron energies slightly worsens the agreement between theory and experiment. This can be attributed to the striking sensitivity of the Legendre coefficients on photoelectron energy, as shown in Fig. 10.4, right panel. A further improvement of the theoretical model would thus require experimental data for more than one photoelectron energy and with better energy resolution.

Figure 10.5 displays the photoelectron angular distributions (PAD) for ionization from those intermediate states in camphor that were identified as the most likely resonances in the 2+1 process, namely state C1 for camphor. Experimental Legendre coefficients are taken from Ref. [265] and assuming left circularly polarized light. Angular distributions

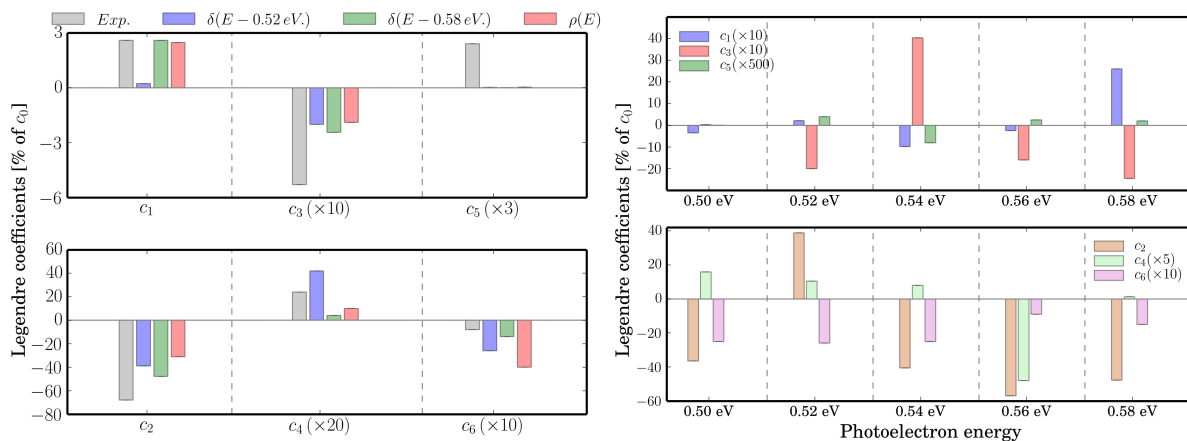


Figure 10.4: **Camphor**. **Left panel**: Comparison of experimentally obtained and theoretically calculated Legendre coefficients in the PAD for *R*-(+)-camphor, using state C1 and right circular polarization. The calculations considered fixed photoelectron energies of 0.52 eV and 0.58 eV as well as an integration over a Gaussian distribution of energies centered at 0.58 eV with a FWHM of 200 meV. **Right panel**: Dependence of the calculated Legendre coefficients in the PAD of camphor, state C1, on the photoelectron energy within the range of 0.50 eV to 0.58 eV using right circularly polarized light.

obtained from both enantiomers of camphor (*R*-(+) and *S*-(-)) are shown. Also shown is the difference between the PAD of the two enantiomers (right panel of Fig. 10.5). As for fenchon, the overall shapes obtained with the theoretical and experimental Legendre coefficients are similar, illustrating the semi-quantitative agreement between the calculated and experimental results. For camphor, the main difference between the theoretical and numerical curves relies in the  $c_3$  coefficient (-0.022 instead of -0.053). Because  $c_3$  is of the same order of magnitude as  $c_1$ , the overall scale is correctly reproduced for the theoretical curves. The theoretical curve fails to reproduce, however, the left lobe. To be able to properly reproduce this feature, a larger value of the numerical  $c_3$  coefficient is required. For example, increasing  $c_3$  from -0.022 to -0.042 would introduce the left lobe, while keeping the shape of the right part of the plot almost unchanged. It is worth mentioning, nevertheless, that for the experimentally obtained odd Legendre coefficients, the moduli are not exactly identical when changing the enantiomer (as one would expect in the ideal case). If they were, the left lobe in the difference PAD for camphor would be smaller. Such an artifact of experimental nature, introduces further differences to its theoretical counterpart, for which a only the sign of the odd Legendre changes, while keeping the same moduli.

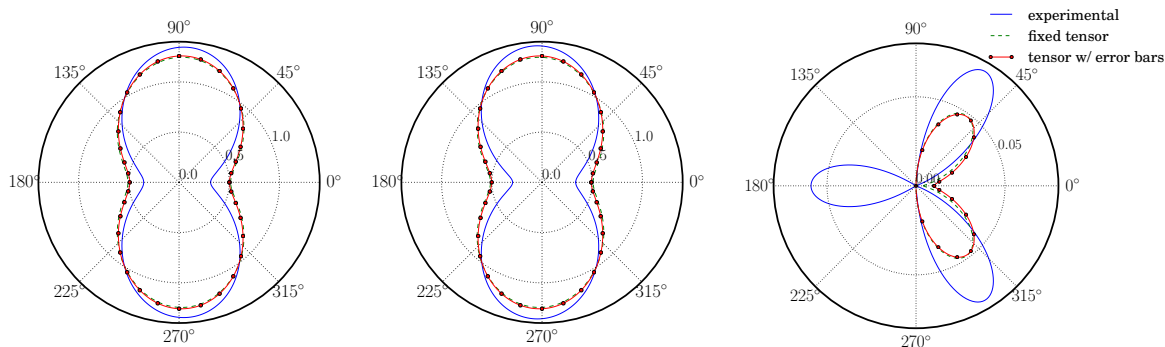


Figure 10.5: **Camphor**: Photoelectron angular distributions obtained with left circularly polarized light for ionization from the state C1 of R-(+)-camphor (**left panel**) and of S-(-)-camphor (**middle panel**), employing the fixed two-photon absorption tensor elements (dashed green lines) and two-photon absorption tensor elements with  $\pm 20\%$  error bars (solid red lines with black circles). The theoretical curves are compared to those obtained for the experimentally determined Legendre coefficients of Ref. [265] (blue solid lines). The differences between the PAD for the two enantiomers are shown in the **right panel**. Note that for the experimentally determined Legendre coefficients, the moduli are not exactly identical when changing the enantiomer. If they were, the lobe on the left-hand side in the bottom right panel for camphor would be smaller.

## 10.6 Intermediate state dependence of photoelectron circular dichroism in (2+1) REMPI

Motivated by recent experimental work [302], we study the intermediate state dependence of the PECD in (2+1) resonance-enhanced multi-photon ionization of randomly oriented fenchone molecules. In Ref. [302], the experimental Legendre coefficients are averaged over a set of measurements characterized by a particular central laser frequency. The central laser frequency can be used as a  $x$ -coordinate to plot the corresponding Legendre coefficients,  $c_j$ . In detail, the “averaged” Legendre coefficients are calculated according to the following formula

$$c_j \equiv \langle c_j(E_k) \rangle = \int \omega(E) \tilde{c}_j(E) dE, \quad (10.41)$$

where  $\omega(E)$ , and  $\tilde{c}_j(E)$  refer to the weight and the  $j$ -th Legendre coefficient obtained with a given the photoelectron energy  $E$ , respectively. In Eq. (10.41),  $E_k$  denotes the energy peak of the (Gaussian) distribution  $\omega(E)$ . The calculations are performed using the weights provided by the authors [303] of Ref. [302]. Further details about the average procedure (weighting protocol, peak positions and FWHM of the Gaussian weight) are

found in Sections III.B.1 and III.B.2 of Ref. [302].

The goal of the present work is to test the perturbative approach for a (2+1) REMPI of randomly oriented chiral molecules developed in Ref. [294] for varying the central laser frequency. Analogously to Section 10.5, the goal is to answer the question whether we can infer which orbital is the one populated prior to ionization. The Legendre coefficients  $\tilde{c}_j(E)$  are obtained with the help of the formalism developed in Ref. [294]. Their “averaged” counterpart  $c_j \equiv c_j(E_k)$  are obtained using Eq.(10.41). The expansion coefficients  $a_{m_o}^{\ell_o}$  and tensor elements  $T_{q_1, q_2}$  associated with each orbital are obtained in the context of the *ab initio* technique described in Ref. [294]. In this section, the orbital 47 correspond to the state C3 in Section 10.5.1, which was found to be the most likely populated according to the numerical calculations of Ref. [294]. Here, we extend our previous calculations in the framework of Eq. (10.41) to the orbital 47 and to orbitals of higher binding energies, labeled 48 to 51.

The scan of the laser wavelength performed in the experiment is such that it leads to photoelectron energies ranging from 0.4 to 1.4 eV [302]. These photoelectron energies serve as a  $x$  axis in Fig. 10.6. Experimental coefficients [302, 303] together with the numerical ones are shown in Fig. 10.6. The numerical results for the orbitals 47 to 50 are shown in panels (a) to (d), i.e. red and blue data points for the coefficients  $c_1$  and  $c_3$ , respectively. The same experimental data (gray and green data points) is shown in all four panels for comparison. As can be observed, there is a sudden jump between 0.9 and 1.0 eV in the experimental data, i.e. a gap between gray and green data points. According to Ref. [302], this is due to the fact that, in addition to the resonantly excited state in Ref. [265], another intermediate state of higher binding energy is excited above 1.0 eV. The low photoelectron spectrum is interpreted to result from excitation an intermediate state having **S** character, while the high photoelectron energy part of the spectrum is generated from excitation of an intermediate state with **P** character. This interpretation is corroborated in Fig. 10.6(a). In fact, in the region of moderate photoelectron energy, i.e. specifically at 0.9 eV, just when the jump is observed, the contribution of both **S** and **P** characters coexists. For the experimental  $c_3$ , this is reflected by the simultaneous presence of the gray empty-circles (S-character) and gray filled-circles (P-character). An analogous behavior is encountered for the  $c_1$  coefficients, i.e. it corresponds to the gray empty-squares (S-character) and their counterparts gray filled-squares (P-character) in Figs. 10.6(a-d).

We compare the behavior of the theoretical “averaged” coefficients, namely  $c_1(\text{th})$  and  $c_3(\text{th})$  in Fig. 10.6, to the experimental ones. In particular, we focus our attention to the “low” ( $< 0.9$  eV) and “high” ( $> 1.1$  eV) energy parts of the photoelectron spectrum. In fact, the region of moderate photoelectron energy ( $0.9 < E < 1.1$  eV.), might be, according

to Ref. [302], characterized by the contribution from a superposition of two intermediate excited states that are simultaneously excited while performing the scanning procedure, which is not reproduced by our model (we would need previous knowledge of the respective weights, phases). A brief description of the numerical results is outlined in the following:

### 1. Photoelectron energies up to 0.9 eV:

- (a) **Orbital 47**, cf. Fig. 10.6(a): For  $c_3$ , it describes the proper signs, order of magnitude as well as general behavior, i.e. decreasing  $c_3$  towards negative values as the photoelectron energies increases. It starts from positive values and cross to negatives ones, just as the experimental case [302]. However, near 0.9 eV, the sign of the averaged (numerical)  $c_3$  changes (from negative to positive again), which is not observed experimentally. This can be explained under the assumption that close to 0.9 eV, a single orbital might not contribute alone, to the photoionization process [302]. For  $c_1$ , the general tendency is qualitatively reproduced, i.e. increasing values as the photoelectron energy increases, despite, however, some differences in sign near 0.85 eV.
- (b) **Orbital 48**, cf. Fig. 10.6(b): For  $c_1$ , it describes proper signs as well as the behavior of increasing values as the photoelectron energy increases. It presents, however, a more oscillating character, compared to that obtained with the orbital 47. For  $c_3$ , it also reproduces the overall tendency, however, it conserves mostly a positive sign over the interval, which is not the case in the experimental case.
- (c) **Orbital 49**, cf. Fig. 10.6(c): For  $c_1$ , it starts with the wrong tendency, but it redress itself to the proper one after  $\approx 0.5$  eV. From 0.5 to 0.85, it reproduces the experimental order of magnitude, signs and behavior, i.e. increasing values of  $c_1$  as the photoelectron energy increases. For  $c_3$ , it reproduces the overall tendency, i.e.  $c_3$  decreases as the photoelectron energy increases, however, and analogously to orbital 48,  $c_3$  keeps positive values almost over the entire domain, contrary to the experimental ones, that cross from positives to negatives values as the photoelectron energy increases.
- (d) **Orbital 50**, cf. Fig. 10.6(d): For  $c_1$ , it starts with the wrong sign and wrong slope/tendency. It matches the experimental signs in general, however, the tendency is far different from the experimental case. For  $c_3$ , the overall tendency is reproduced, i.e.  $c_3$  decreases as the photoelectron energy increases, however, it conserves positive sign almost over the entire interval, which is

in contradiction to the experimental data. Orbital 51 suffers from the same limitations and has not been included in Fig. 10.6.

- (e) **Conclusion:** Taking into account the lines above, we conclude that among all orbitals here considered, it is the orbital 47 the one that reproduces (qualitatively) the best the experimental results.

## 2. High photoelectron energies $> 1.0$ eV.

- (a) For the sake of comparison, we define the following properties,
- i. **Experimental 3P1 band:** (i) the  $c_1$  coefficients are small (amplitude) and negative (sign) over the entire interval. (ii) On the contrary, the  $c_3$  counterparts are positives and of the same order of magnitude.
  - ii. **Experimental 3P2 band:** (iii) Both,  $c_1$  and  $c_3$  have positive values, and are of the same order of magnitude.
- (b) **Orbital 47:** The numerical  $c_1$  takes mostly negative values as the photoelectron energy increases (from moderate to high energies), while  $c_3$  oscillates changing sign with a tendency of becoming larger as the photoelectron energy increases. This is in contradiction to properties (i), (ii) and (iii). Therefore, orbital 47 (alone) fails to reproduce either the **3P1** nor the **3P2** bands.
- (c) **Orbital 48:** Both,  $c_1$  and  $c_3$  have a similar behavior—starting with negative values, they become positive and then negative again. This does not reproduce properties (i), (ii) nor (iii).
- (d) **Orbital 49:** With the exception of  $c_3$  at 1.05 eV (which is fine since we cannot expect to reproduce the experimental behavior for moderate photoelectron energies), both  $c_1$  and  $c_3$  have positive values entire the interval (high energies), therefore reproducing the property (iii) for the **3P2** band. However, both coefficients have a stronger oscillatory character, compared to the experimental counterparts.
- (e) **Orbital 50:** If we consider energies above 1 eV,  $c_1$  is negative while  $c_3$  is positive. satisfying property (i) and (ii) for the 3P1 band. However, for energies ranging from 0.9 to 1.0 eV., (4 calculated points) these properties are not longer fulfilled, because the sings of  $c_1$  and  $c_3$  differs from the experimental ones. Also, their behavior differs from the experimental counterparts for higher photoelectron energies.

To summarize, we find that, among all orbitals considered in the present calculations, orbital 47 reproduce the best the experimental points, but only for the low energy part

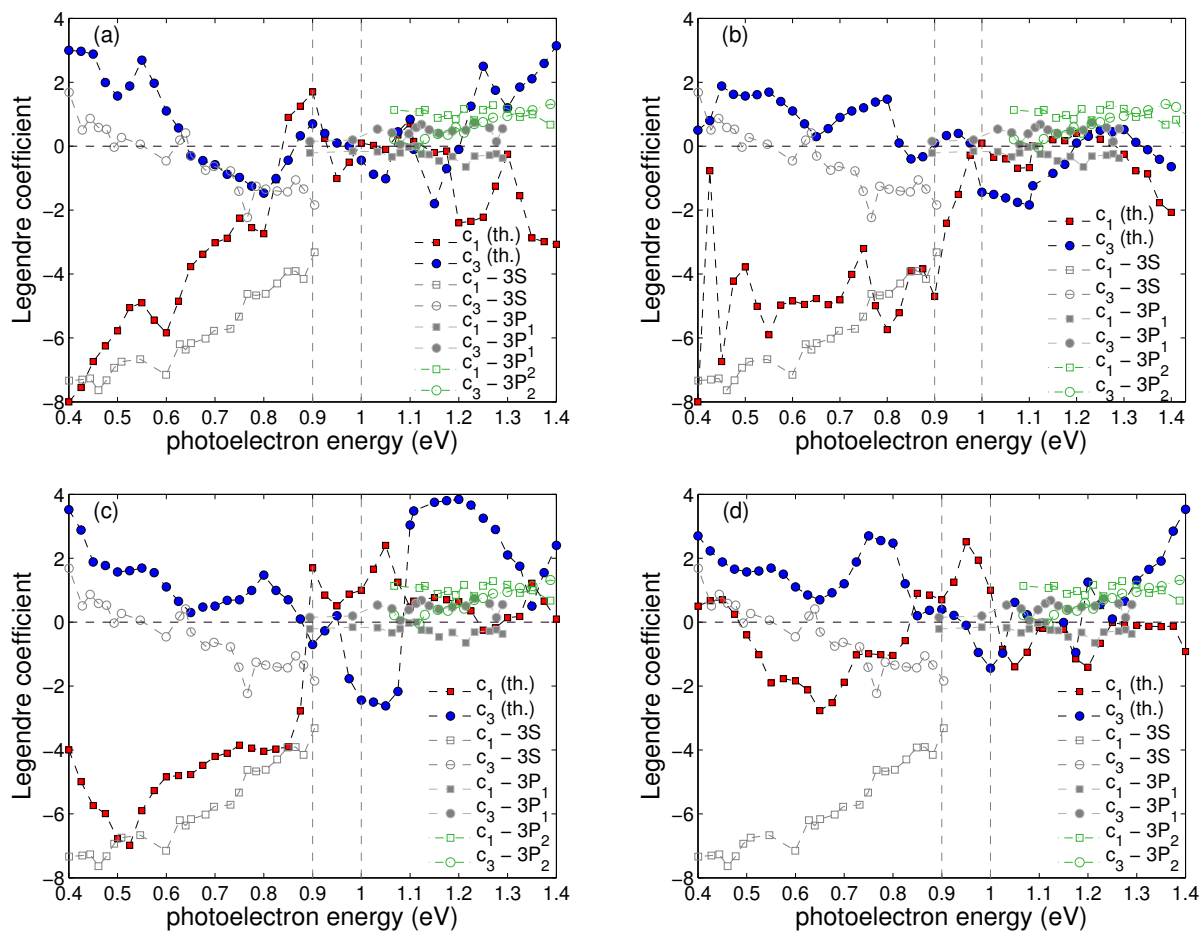


Figure 10.6: **Intermediate state dependence of PECD:** Numerical averaged  $c_1$  (red-squared lines) and  $c_3$  (blue-circled lines) coefficients (in percentage of  $c_0$ ) for orbitals 47 to 50 shown in panels (a) to (d), respectively. Experimental data [302, 303] corresponds to all gray and green data points. For comparison, the same experimental data are shown in all four panels.

of the spectrum. In fact, it reproduces (semi) qualitatively orders of magnitude, sign and general behavior of the experimental coefficients for the 3S band in the lower part of the photoelectron spectrum. It is to note however, that despite the fact that behavior, signs and order of magnitude are mostly reproduced, the numerical values, however, differ from the experimental ones. Regarding the higher part of the spectrum, some (qualitative) similarities, such that positive signs of  $c_1$  and  $c_3$ , would suggest the orbital 49 to roughly reproduce the behavior for  $c_1$  and  $c_3$  associated with the 3P2 band. Also orbital 50 seems to have some points in common with the 3P1 band. The difference with the experimental points, in both cases, occurs in the medium (to moderate) part of the photoelectron spectrum. Furthermore, the main difficulty concerns the small magnitude of the experimental  $c_1$  and  $c_3$  in the high-energy part of the spectrum. Consequently,

the qualitative agreement is much worse than in the low energy part. Also, the overall tendency, i.e. the asymptotic behavior for high photoelectron energies differs that of the experimental data points. It is therefore difficult to make a clear concluding statement when only a single orbital is assumed to be ionized.

To remedy this, two approaches might be envisioned. On one hand, if we consider that more than one state indeed contribute to the ionization while performing the laser-frequency scanning procedure, a full time-dependent description of the (2+1) REMPI process becomes unavoidable. This would allow to account for the relative population ratios and phases between the ionized states which are not described by the theoretical model presented in this work. In fact, our theoretical description is based on Refs. [264, 265] where only the (single) resonantly excited state contributes to the photoelectron spectrum. On the other hand, a more relevant role of the chirality of the continuum should be considered. In fact, the theoretical model derived in this work takes into account only the chiral structure of the bound states. The information about chirality is then contained in the expansion coefficients and two-photon absorption tensors of the bound states, while the continuum spectrum is constructed from continuum hydrogenic wave functions, cf. Eq. (10.6), where their respective phase shift is only  $\ell$ - but not  $m_\ell$ - dependent. In fact, the extraction of expansion coefficients and two-photon absorption tensors are limited by the *ab-initio* technique utilized in this work, which only allows to have access to a given range of bound states within a reasonable accuracy [294]. Furthermore, expanding the the molecular continuum wave functions as a linear superposition of continuum hydrogenic wave functions for *a posteriori* optimization of the expansion coefficients is not the best solution, due to the large dimensionality of the optimization problem. Instead, an alternative approach consists in constructing a  $m_\ell$ -dependent phase shift function and optimizing the  $m_\ell$  components of the latter such that the chirality of the continuum is effectively taken into account, while reducing the dimensionality of the optimization problem. This is the current direction of this work. This would might also allow to explain the non-symmetric behavior of the *absolute value* of the Legendre coefficients when changing the helicity of the light polarization.

## 10.7 Conclusion and Remarks

Throughout this chapter, we have derived a theoretical model to study PECD after (2+1) resonantly enhanced multi-photon ionization in randomly oriented chiral molecules. The model is based on a perturbative treatment of the light-matter interaction within the electric dipole approximation. In order to take into account for the Coulomb interaction between photoelectron and photoion as well as electronic correlations in the transition to

the intermediate electronically excited state, the model relies on an *ab initio* description of the non-resonant two-photon absorption with a single-center expansion of the photoelectron wavefunction into hydrogenic continuum functions. Assuming that the contribution to the photoelectron spectra is due exclusively to resonantly photoionization of the intermediate excited state, the model is constructed upon the assumption of separability of the 2+1 process into an initial two-photon photoselection step with subsequent one-photon photoionization. As an extension of the first order time-dependent approximation of the photoionization dynamics, it naturally neglects all possible static exchanges and dynamic correlations in the interaction of the photoelectron with the parent ion as well as the time-dependence of the laser pulse. Based on a single-center expansion of the intermediate excited state, possible multi-center character of the continuum wavefunction are neglected. Despite these approximations, the model has shown to not only to correctly reproduce the basic symmetry behavior expected under exchange of handedness and exchange of light helicity, but also to satisfactorily reproduce experimental data, improving the current theoretical attempts to reproduce, at least quantitatively, the experimental observations.

The potential of the model has been tested to successfully verify the parity transformation under parity and helicity exchange experimentally observed. Making use of the symmetry properties of the Wigner  $3j$  symbols, reflecting the fundamental selection rules for two-photon absorption and one-photon ionization, we have shown which Legendre coefficients may be expected in the photoelectron angular distributions, depending on the basic geometric properties in the electronic structure of the molecules as well as the possible combinations of polarization for two-photon absorption and one-photon ionization. Complementary, we have identified the role of the two-photon absorption tensor and intermediate state wavefunction—it is the partial wave decomposition of the latter which determines PECD whereas the two-photon absorption tensor (in the electronic dipole approximation) merely introduces an anisotropic distribution of photoexcited molecules. Notably, the anisotropy is achieved by selection and not by rotational dynamics which would occur on a much slower timescale than that of femtosecond laser excitation.

As an application, we have tested our theoretical framework to fenchone and camphor, which have been studied extensively in recent experiments [264, 265, 267–269]. The *ab initio* calculations employed the coupled cluster method as well as density functional theory. Due to the Rydberg-like character of the intermediate electronically excited state, diffuse basis functions needed to be added to the standard basis sets. This has allowed to reach a reasonable agreement with experimental values for the excited state energies.

Electronic structure data has been utilized to calculate the photoionization cross section. Accounting for the basic structure of the two-photon absorption tensor alone has

already allowed us to qualitatively reproduce the experimental results for fenchone and camphor. Among the minimal requirements to reproduce PECD, a contribution of  $d$ -waves in the intermediate electronically excited state is crucial. Such a contribution can be expected if the two-photon absorption tensor is anisotropic. Overall, employing the *ab initio* data in the calculation of the photoelectron angular distribution, allowed us to semi-quantitatively reproduce the experimental Legendre coefficients characterizing the photoelectron angular distribution.

Despite the simplicity of the model herewith constructed, the satisfactory agreement with experimental data encourages a number of follow-up studies. It is to note, nevertheless, that a fully time-dependent description should be employed, following the lines of Ref. [304], because the photoelectron angular distributions depend on the polarization as well as the dynamics [301]. Based on the model developed here, an extension to time-dependent studies is straightforward, but will require substantial numerical effort. Such time-dependent simulations will then be possible to model excitation where the pump and ionization pulses occur at a time delay such that the intermediate state structure and dynamics as well as possible non-radiative relaxation pathways can be probed. A time-dependent extension of the basic model presented here will also allow to investigate the dependence of the photoelectron angular distribution on the laser parameters, including intensity, central frequency, spectral bandwidth and varying polarization. The latter being of great interest, since it will consolidate a first step towards the coherent control of PECD.

As important as taking into consideration time-dependent effects, it is worth to mention that the electronic structure treatment on which our model has been tested, may be improved. In particular, the multi-center character of the continuum wavefunction should be accounted for by employing Dyson orbitals, for instance, in the calculation of the photoionization cross section [292, 305–307].

As for the time-independent structure of the model, a perturbative treatment of the static exchange for the photoelectron as well as an extension to beyond the electric dipole approximation should be envisaged and straightforward to implement. While the former would allow for a detailed study of the dependence of the angular distribution on the photoelectron energy, including low photoelectron kinetic energies, the latter would allow for a unified theoretical treatment of further observables beyond PECD, such as circular dichroism in laser mass spectrometry of photoions [308–310], as well as comparison with different levels of electronic structure theory [311].



# New approach for the observation of electroweak parity violation effects

---

11.1	Introduction . . . . .	198
11.1.1	Brief review of atomic parity-nonconservation (PNC) . . . . .	198
11.1.2	Current approaches to the observation of PNC effects . . . . .	202
11.1.3	New proposal. Basic idea . . . . .	204
11.2	Modeling the cesium atom for observation of PNC effects . . . . .	205
11.2.1	Single-active-electron approach with spin-orbit coupling . . . . .	205
11.2.2	Evaluation of the radial wave functions . . . . .	208
11.3	Electron dynamics . . . . .	210
11.4	Observation of the PNC via photoelectron spectroscopy . . . . .	213
11.4.1	Photoelectron spectrum . . . . .	213
11.4.2	Single-photon ionization . . . . .	214
11.4.3	Pump-probe approach . . . . .	215
11.4.4	Time-dependent perturbation theory. Second order corrections . . .	218
11.4.5	Effects of second-order processes to the total yield . . . . .	224
11.4.6	Numerical results . . . . .	225
11.5	Relations and differences with previous proposals . . . . .	233
11.6	Conclusions and outlook . . . . .	235

---

## 11.1 Introduction

### 11.1.1 Brief review of atomic parity-nonconservation (PNC)

The standard model of unifying the electromagnetic and the weak interaction predicts parity nonconservation (**PNC**) in atoms. Such violation of parity arises from interference between the neutral weak and electromagnetic interactions induced by neutral currents [312, 313]. It results in a mixing of atomic eigenstates with opposite parity [313–316]. Three decades after Eugene Wigner formalized the principle of conservation of parity [317], pioneering work on electron scattering by Zel'dovich [313] suggested that parity might not be conserved and that it would lead to a mixture of atomic levels of different parity. A more detailed and comprehensible theoretical analysis in the language of low energy physics was presented in 1974 by Marie-Anne Bouchiat and Claude Bouchiat [314, 315]. The current interpretation of the weak interaction is based on the exchange of weak neutral  $Z_0$  bosons between the electrons and the nucleus of the atom [318]. Quantum electrodynamics (QED) prohibits the existence of electric dipole moments between atomic states of equal parity. However, the weak  $Z_0$  exchange interactions violates this rule and grant same parity states a small non-vanishing electric dipole amplitude. Particularly for atomic systems, the perturbation describing the short-range weak interaction between the nucleus and the (outermost) electron can be mathematically defined by means of the **point-like** parity-violating scalar potential  $\hat{\mathbf{h}}_{\text{pv}}(\mathbf{r})$  [319]. In the non-relativistic limit, the single-electron form of the latter reads [314, 315]

$$\hat{\mathbf{h}}_{\text{pv}}(\mathbf{r}) = \frac{G_F}{4\sqrt{2}m_e c} Q_w \hat{\boldsymbol{\sigma}} \cdot \left[ \hat{\mathbf{p}} \delta^3(\mathbf{r}) + \delta^3(\mathbf{r}) \hat{\mathbf{p}} \right], \quad (11.1a)$$

where  $m_e$  symbolizes the mass of the electron,  $c$  the speed of light, and where  $\hat{\boldsymbol{\sigma}}$ ,  $\hat{\mathbf{p}}$  and  $\hat{\mathbf{r}}$  refer to electron's spin, momentum and position operators, respectively. For molecular systems, the effective description of the PNC potential, accounting for additional degrees of freedom, reduces to a scalar effective point-like expression analogous to Eq. (11.1a) [320–322]. In Eq. (11.1a),  $G_F$  denotes Fermi's constant which is given by

$$G_F \approx 3 \times 10^{-12} m_e c^2 \left( \frac{h}{m_e c} \right)^3 \quad (11.1b)$$

$$= 3\alpha \times 10^{-12} \text{ a.u.} \quad (11.1c)$$

with  $\alpha = 1/137.035999139(31)$ , the fine structure constant<sup>1</sup>. Finally, the so-called *weak charge*  $Q_w$  is a model-dependent dimensionless constant that represents the most general

<sup>1</sup>also known as Sommerfeld's constant. Although it is often referred to as a physical fundamental *constant*, noticeable evidences for its cosmological evolution can be found in e.g. Ref. [323].

form of a zero-range parity violating potential (where the nuclear and spin momenta have been neglected) and that is invariant under time reflection [314]. It can be derived from the Weinberg model [324] and to lowest order reads

$$Q_W(N, Z) = -N + Z(1 - 4 \sin^2(\theta_W)), \quad (11.1d)$$

where  $\theta_W$  is the weak mixing angle, often referred to as Weinberg angle, and where  $N$  and  $Z$  refer to the number of neutrons and protons, respectively. In particular,  $Q_W \approx -75$  for cesium [319]. The perturbation caused by the weak interaction leads to an admixture of atomic levels with opposite parity. The matrix elements defining such admixture can be straightforwardly evaluated. In fact, because the short-range weak Hamiltonian is a scalar operator that can be very well approximated by a “point-like” operator in position as defined in Eq. (11.1a)– which is a good approximation particularly for atomic systems [319], it can only couple different parity states with  $\ell = 0$  and  $\ell = 1$  with the same total angular momentum  $j = 1/2$  and with the same projection  $m_j = 1/2$ . The non-vanishing matrix elements of  $\hat{\mathbf{h}}_{\text{pv}}$  in the  $(\ell, j)$  basis read [314, 315, 319]

$$\begin{aligned} \langle nS_{1/2} | \hat{\mathbf{h}}_{\text{pv}} | n'P_{1/2} \rangle &= \frac{3i}{16\pi m_e c} \left( \frac{G_F}{\sqrt{2}} \right) Q_W(N, Z) \\ &\times R_{n,\ell=0}(0) \left. \frac{\partial}{\partial r} R_{n',\ell=1}(r) \right|_{r=0}, \quad (11.2) \end{aligned}$$

where  $R_{n,\ell}(r)$  refers to the radial wavefunction associated to the state with principal quantum number  $n$  and orbital angular momentum  $\ell$ . Defining the *perturbed states* as  $|\widetilde{n_o S_{1/2}}\rangle$  and  $|\widetilde{n_1 P_{1/2}}\rangle$ , in contrast to the unperturbed counterparts  $|nS_{1/2}\rangle$  and  $|n'P_{1/2}\rangle$ , the first order time-independent perturbation expansion gives the correction, due to  $\hat{\mathbf{h}}_{\text{pv}}$ , that contains the mentioned admixture, namely

$$\begin{aligned} |\widetilde{nS_{1/2}}\rangle &= |nS_{1/2}\rangle + \sum_{n'} \frac{\langle n'P_{1/2} | \hat{\mathbf{h}}_{\text{pv}} | nS_{1/2} \rangle}{\varepsilon_{S_{1/2}}^n - \varepsilon_{P_{1/2}}^{n'}} |n'P_{1/2}\rangle \\ &+ \int_0^\infty d\epsilon \frac{\langle \epsilon P_{1/2} | \hat{\mathbf{h}}_{\text{pv}} | nS_{1/2} \rangle}{\varepsilon_{S_{1/2}}^n - \epsilon} |\epsilon P_{1/2}\rangle, \quad (11.3a) \end{aligned}$$

where  $\varepsilon_{S_{1/2}}^n < 0$ , and  $\varepsilon_{P_{1/2}}^{n'} < 0$  refer to the eigenenergies for bound  $S_{1/2}$  and  $P_{1/2}$  states, respectively, whereas  $\epsilon > 0$  refers to their counterpart positive valued energies for continuum

states. For  $\ell = 1, j = 1/2$ , i.e.  $P_{1/2}$  states, the perturbed states take the form,

$$\begin{aligned} |\widetilde{nP_{1/2}}\rangle &= |nP_{1/2}\rangle + \sum_{n'} \frac{\langle n'S_{1/2} | \hat{\mathbf{h}}_{pv} | nP_{1/2} \rangle}{\varepsilon_{P_{1/2}}^n - \varepsilon_{S_{1/2}}^{n'}} |n'S_{1/2}\rangle \\ &+ \int_0^\infty d\epsilon \frac{\langle \epsilon S_{1/2} | \hat{\mathbf{h}}_{pv} | nP_{1/2} \rangle}{\varepsilon_{P_{1/2}}^n - \epsilon} |\epsilon S_{1/2}\rangle. \end{aligned} \quad (11.3b)$$

It can be noted from Eq. (11.3), that the weak interaction violates parity by transferring a (small) amount of the  $P_{1/2}$  character to all  $S_{1/2}$  states and vice-versa. The mixing amplitude between states of different parity is remarkably small. In fact, the leading terms characterizing the parity admixture are of the order of  $10^{-11}$  (or smaller) in the case of cesium and depend on the principal quantum numbers  $n$  and  $n'$ . Hence, by virtue of such “*parity transfer*” between states of opposite parity, parity-based electric dipole **E1** and non-relativistic magnetic dipole **M1** transition moments are no longer *strictly* forbidden. In particular, **E1** electric dipole transitions of the type  $|nS\rangle \rightarrow |n'S\rangle$  are henceforth (weakly) allowed. In fact, the admixture of opposite parity states results in an extremely small **E1** electric dipole transition amplitude between states of the same parity, for instance[315],

$$\begin{aligned} \mathcal{E}_{\text{PNC}}(n, n') &= \mathbf{e}_\mu \langle \widetilde{n'S} | \hat{\mathbf{d}} | \widetilde{nS} \rangle \\ &= \mathbf{e}_\mu \left\{ \sum_{n''} \left( \frac{\langle n'S_{1/2} | \hat{\mathbf{d}} | n''P_{1/2} \rangle \langle n''P_{1/2} | \hat{\mathbf{h}}_{pv} | nS_{1/2} \rangle}{E_{nS_{1/2}} - E_{n''P_{1/2}}} \right) \right. \\ &\quad \left. + \sum_{n''} \left( \frac{\langle n'S_{1/2} | \hat{\mathbf{h}}_{pv} | n''P_{1/2} \rangle \langle n''P_{1/2} | \hat{\mathbf{d}} | nS_{1/2} \rangle}{E_{n'S_{1/2}} - E_{n''P_{1/2}}} \right) \right\}, \end{aligned} \quad (11.4)$$

where  $\mathbf{e}_\mu$  refers to the polarization direction of the driving field,  $\hat{\mathbf{h}}_{pv}$  the short range scalar parity-violating potential, cf. (11.1a), and  $\hat{\mathbf{d}} = -|e|\hat{\mathbf{r}}$  the dipole operator, and where the summation is carried out over the bound and unbound states [314, 315]. It is this violation of the standard selection rules that is typically exploited in **PNC** experiments[314–316, 319, 325–329] despite the fact that the order of magnitude involved in such measurements is extremely challenging even for the best techniques.

In 1974 the Bouchiat’s demonstrated that the *mixing amplitude* between states of different parity is proportional to the cube of the atomic number  $Z$  [314, 315]. The amplitude of the parity-mixing being extremely small, the  $Z^3$ -law greatly favors heavy atoms for the measurement of such extremely small **PNC** effects. Hence, they proposed low-energy experiments in heavy atoms, taking cesium (Cs) with  $Z = 55$  and thallium (Tl) as a paradigms, establishing a new era for the test of the standard model with AMO physics in the low-energy regime. However, even for Cs with  $Z = 55$ , the amplitude of

the admixture is extremely small and consequently the weak  $\mathcal{E}_{\text{PNC}}(n, n')$  transition is extremely small compared to the standard allowed **E1** transitions. In detail, for cesium, the weakly allowed  $\mathcal{E}_{\text{PNC}}(n, n')$  transitions are of the order of [315]

$$\begin{aligned}\mathcal{E}_{\text{PNC}}(n, n') &\equiv \langle \widetilde{7S_{1/2}} | \hat{\mathbf{d}}_z | \widetilde{6S_{1/2}} \rangle \\ &\approx -1.7i \times 10^{-11} ea_0,\end{aligned}\tag{11.5a}$$

with  $n' = 7$  and  $n = 6$  for the doubly forbidden  $|6S_{1/2}\rangle \rightarrow |7S_{1/2}\rangle$  transition, and

$$\begin{aligned}\mathcal{E}_{\text{PNC}}(n, n') &\equiv \langle \widetilde{8S_{1/2}} | \hat{\mathbf{d}}_z | \widetilde{6S_{1/2}} \rangle \\ &\approx -0.65i \times 10^{-11} ea_0,\end{aligned}\tag{11.5b}$$

for  $|n = 6, S_{1/2}\rangle \rightarrow |n' = 8, S_{1/2}\rangle$  transition, to be compared to  $\approx 1ea_0$  for the  $|nS_{1/2}\rangle \rightarrow |n'P_{1/2,3/2}\rangle$  allowed electric dipole **E1** transitions. Despite the extremely small amplitude involved, experimental observation of the fingerprints of the weak interaction is nowadays possible and can be inferred from the interference between the allowed parity-conserving and the much smaller parity-violating contributions [314, 316]. Thus, the pioneering work of the Bouchiat's defined an unexplored and complementary approach to high-energy experiments for the observation of **PNC** effects. Furthermore, observation of PNC in atomic systems can be strategically designed to extract valuable information beyond the standard model, since they are performed to probe mechanisms in a very different regime from that probed in the framework of high-energy experiments. In this context, low-energy experiments may be viewed as an alternative model-independent approach to determine electron-quark weak coupling constants [330].

Typically, the predictions of the standard model are tested by confronting the value of the forbidden transition predicted by the standard model, that has been referred here to as  $\mathcal{E}_{\text{PNC}}(n, n')$ , and the same quantity inferred from experimental observations. Given the extremely small quantities involved in the admixture of opposite parity states, this comparison unavoidably requires extremely high precision experiments as well as an accurate description of the electronic structure of the species under consideration. Although **PNC** effects have been observed in atomic systems other than Cs [316, 325–328, 330] such as Tl [312], the former is, from a theoretical prospective, of particular interest because its electronic structure is one of the most accurately known [330]. This results in a non-negligible reduction in the number of sources of discrepancies. In fact, Cs enjoys a highly single-electron character having only one S-state electron outside a fully filled closed shell core [329], rendering the numerical calculations relatively tractable. From an experimental prospective, the interest of using Cs as prototype – besides enjoying a large

$Z$ , relies on the availability of a tunable laser at the right frequency to excite the doubly forbidden  $|6S_{1/2}\rangle \rightarrow |7S_{1/2}\rangle$  **M1** transition as suggested by the Bouchiat's [314].

### 11.1.2 Current approaches to the observation of PNC effects

#### Atomic Parity violation measurements

As previously discussed, the essence of any **PNC** experiment relies on the admixture of different parity states induced by the (weak) parity-violating interaction between the nucleus and the electrons. As a result, electric dipole **E1** transition between states of the same parity are not longer strictly forbidden, but weakly allowed. Observation of such a forbidden transitions may concern  $|nS_{1/2}\rangle \rightarrow |n'S_{1/2}\rangle$  as in cesium or  $|nP_{1/2}\rangle \rightarrow |n'P_{1/2}\rangle$  in case of tallium [314]. The question is then how to properly choose  $n$  and  $n'$  to maximize the effect taking into account experimental constraints. In an extensive work [314], the Bouchiat's reviewed a series of preliminary attempts to detect parity mixing in atomic states and proposed to excite a doubly forbidden magnetic transition such as  $|(n-1)S_{1/2}\rangle \rightarrow |nS_{1/2}\rangle$ . In particular, they proposed excitation of the doubly forbidden  $|6S_{1/2}\rangle \rightarrow |7S_{1/2}\rangle$  transition in Cesium, mediated by means of one-photon absorption at  $\lambda = 539.5$  nm.

The essence of the proposed experiment relies on the excitation of the doubly forbidden transition  $|6S_{1/2}\rangle \rightarrow |7S_{1/2}\rangle$  in cesium, followed by fluorescence mediated by stimulated emission resulting from the decay  $|7S_{1/2}\rangle \rightarrow |7P_{1/2}\rangle$ . The changes in the polarization of the of “probe” beam under field reversal are then scrutinized to infer the value of the weak charge  $Q_W$ , which provides direct evidence of the PNC effect [314]. The experimental value is then compared to the theoretical counterpart, predicted by the standard model.

In this context, two experimental approaches have emerged and are historically referred to as the *Paris* [325–328] and *Boulder* [316, 329–331] experiments. Both groups are constantly improving their measurements in the quest of reducing the signal-to-noise ratio as well as refining their experimental setup to improve the sensitivity of their measurements [325–327, 330].

In order to distinguish the current approaches and the one we propose in this work, we start by quoting the principles of the experiment carried out by the Paris group as described in Ref. [325] and published in 2007. In this recent version of the Paris experiment, the fingerprints of the PNC is obtained by combining stimulated-emission detection and asymmetry amplification. In detail, a pulsed 539 nm laser beam is utilized to excite the “forbidden”  $|6S_{1/2,F=3}\rangle \rightarrow |7S_{1/2,F=4}\rangle$  hyperfine transition in atomic cesium together with a longitudinal electric field  $E_l$ , which is applied for a duration of 100ns. After excitation of the forbidden transition, a weak infrared beam is used to stimulate

emission on the  $|7S_{1/2, F=4}\rangle \rightarrow |6P_{3/2, F=4}\rangle$  allowed transition for 20 ns. The propagation direction of the pump and probe beams are superposed, with same (linear) polarization direction. The essence of the experiment relies on measuring the change of the probe polarization associated to the excitation of the forbidden transition. In fact, the cesium vapor acts on the probe pulse as an amplifier with *eigen-axes* [325] tilted, with respect to the polarization of the probe pulse, by a small angle of  $\theta^{pv} \approx 10^{-6}$  radian [325]. Despite the small magnitude,  $\theta^{pv}$  is odd under  $E_l$  reversal, indicating the signature of the PNC effect.

### High-resolution spectroscopy for measurement of PNC in chiral molecules

Another option to explore the PNC effects concerns the energy difference between two molecular enantiomers due to the short-range parity violating potential, that can also be exploited to infer the signature of the electro-weak interaction in chiral molecules [322]. In fact, the existence of PNC interaction unequally modifies the energy of the two enantiomers at their equilibrium structure, such that their difference  $\Delta_{pv}E$ , does not vanish [332–334].

Analogously to the detection protocols for atomic PNC measurements such as the Paris and Boulder approaches, proposals for spectroscopic experiments for the detection of molecular parity violation are nowadays well established [322]. The first proposals were already based on **high-resolution spectroscopy** and theorized by the pioneering works of Quack *et al.* [321, 322, 332–334]. Because the proposal presented in this work also relies on a pump-probe spectroscopy, we outline in a few lines, for the sake of transparency, the experimental principles for the detection of parity violation in chiral molecules.

In a nutshell, the protocol idealized in Refs. [321, 322, 332–334] starts by conceiving a **first (pump) pulse** to excite, from the ground state, a molecular eigenstate of well-defined parity. A **second pulse** is then introduced to transfer the population of the previously excited state to a superposition state  $\chi(t)$  composed of two chiral eigenstates, other than the ground state. Because  $\chi(t)$  is not an eigenstate of the molecular Hamiltonian, it evolves, changing its parity, under the field-free Hamiltonian. “*Snapshots*” of such parity changes are obtained as a function of time, by introducing a **third pulse (probe)** that probes the parity-changing wave packet to a (bound) high-lying molecular eigenstate of well-defined parity. This transition has a time dependent-probability  $p_D(t)$ , which is initially forbidden by the regular parity selection rules, but becomes allowed due to the changes of parity of  $\chi(t)$  [321]. Under this condition, the probability of the “forbidden” high-lying state to be populated follows  $p_D(t) = \sin^2(\pi\Delta_{pv}Et/h)$  [321, 332, 333]. This high-lying state is detected with very high sensitivity by resonantly-enhanced multiphoton ionization (REMPI) technique, whose sensitivity is limited by the background signals [321]. In

practice, the value of  $\Delta_{pv}E$  being significantly small, the period of the oscillations is of the order of several seconds. Consequently, in order to mitigate the detrimental effects of collisions, practical application the detection is restricted to the millisecond time scale and the corresponding signal fitted according to  $(\pi\Delta_{pv}Et/h)^2$  [321], which allows to extract the parity violating energy difference  $\Delta_{pv}E$ .

### 11.1.3 New proposal. Basic idea

This section introduces an alternative approach for the detection of **PNC** effects in a time-dependent perspective. The essence of our approach exploits the versatility of photoelectron spectroscopy [135] that allows to extract valuable information on the photoion by scrutinizing the properties of the photoelectron momentum distributions. In fact, the photoelectron momentum distribution contains not only the fingerprints of the interaction of the electron with the driving electromagnetic field, but also the signature of its interaction with the ionic core [135, 137]. Here, the signature of interest concerns the weak parity-violating interaction described by  $\hat{\mathbf{h}}_{pv}(\mathbf{r})$ . The approach we propose exploits the weakly induced admixture between different parity states. Extraction of the information on the underlying **PNC** is inferred from specific properties in the momentum distribution of the liberated photoelectron, in particular from the ionization yield.

In detail, a time-dependent pump-probe scheme is envisioned such that the pump pulse prepares the wave packet in a well-defined superposition of field-free eigenstates. The field-free eigenstates contain information about the weak interaction described by  $\hat{\mathbf{h}}_{pv}$ , since they are perturbed by the latter. The prepared wave packet evolves under the field-free Hamiltonian during a time interval  $\tau_p$ , which defines the **time delay** between the pump and the probe pulses. After  $\tau_p$ , the probe pulse is introduced to ionize the wave packet. The resulting photoelectron spectrum is measured, stored and the total yield, which defines the probability of photoemission, calculated. The procedure is performed  $N_p$  times, by incremented values of  $\tau_p$ , and repeated  $N_p$  times with electric field reversal for the probe pulse. The time-delay difference  $\delta\tau_p \equiv \tau_{p+1} - \tau_p$  defines the *sampling rate*<sup>2</sup> and the stored data (total yield) defines a discretized sample of points (signal) that oscillates as a function of the pump-to-probe time-delay. The time-delay dependent signal manifests oscillations containing several frequencies components. They are associated to (1) the admixture between different parity states caused by the regular dipole allowed transitions due to the electric field and to (2) those much weaker induced by  $\hat{\mathbf{h}}_{pv}$ . In order to separate the parity admixture induced by both sources, both stored signals obtained with electric field reversal are added up (combined signal). A spectral analysis of the resulting “combined signal” is performed via Fast Fourier Transform (FFT) and

<sup>2</sup>subject to the Nyquist-Shannon sampling theorem

small but well-defined spectral components reveals the signature of the PNC potential. Importantly, such peaks disappear when the **PNC potential** is omitted from the equations of motion describing the interaction of the cesium atom and the driving time-dependent electromagnetic field. Hence, spectral analysis of the combined signal with observation of specific frequency components at the “*right position*” unambiguously indicates observation of the **PNC effect** in atomic systems, in this case, in cesium.

## 11.2 Modeling the cesium atom for observation of PNC effects

### 11.2.1 Single-active-electron approach with spin-orbit coupling

Accounting for spin-orbit coupling is essential to properly describe the doublet levels of the cesium atom [335, 336]. In particular, these levels are well determined in the context of the non-relativistic **single-active electron** (SAE) approximation with the spin-orbit term [336], which allows to keep the calculations tractable. Following Ref. [337], only nuclear-spin-independent **PNC** effects, i.e. without accounting for different hyperfine components, are considered in the present work. As alluded to the above, we model the cesium atom in the context of SAE formalism, previously detailed in Section 3.3, while incorporating the spin-orbit interaction. Following the notation of Section 3.3, the effective potential in the framework of the SAE approximation will be referred to as  $V_{\text{SAE}}(r; j; \ell)$ . Given the spherical symmetry of the latter [18], it is possible to separate radial and angular parts. The radial part of the time-independent Schrödinger equation in atomic units reads [18]

$$\left( -\frac{1}{2m_e} \frac{\partial^2}{\partial r^2} + \frac{\ell(\ell+1)}{2m_e r^2} + V_{\text{SAE}}(r; j; \ell) \right) R_{n,\ell,j}(r) = E_{n,j,\ell} R_{n,\ell,j}(r), \quad (11.6)$$

where  $V_{\text{SAE}}(r; j; \ell)$  describes the effective screened potential within the frozen-core **SAE** picture when the fine structure is resolved. It will be defined later in the text. The general solution of the time-independent Schrödinger equation, accounting for radial and angular parts, reads

$$\psi_{n,\ell,j,m_j}(\mathbf{r}) = \frac{R_{n,\ell,j}(r)}{r} \Omega_{j,m_j}^{(\ell)}(\vartheta, \phi), \quad (11.7)$$

which are eigenfunctions of  $\hat{\mathbf{J}}^2$  and  $\hat{J}_z$ ,  $\hat{\mathbf{L}}^2$  and  $\hat{\mathbf{S}}^2$ . The second term in the product represents the functions describing the angular dependency that takes into account the

fine structure. These correspond to the spherical spinors [143, 314],

$$\Omega_{j,m_j}^{(\ell)}(\vartheta, \phi) = \sum_{\mu=-\ell}^{\ell} \sum_{\nu=1/2}^{1/2} \left\langle j, m_j \middle| \ell, \mu, \frac{1}{2}, \nu \right\rangle Y_{\mu}^{\ell}(\theta, \phi) \chi_{\nu}, \quad (11.8)$$

where the terms in brackets are the Clebsch-Gordon coefficients and  $\chi_{\nu}$  the ordinary Pauli spinor [314],  $\chi_{\nu} = (\delta_{1/2,\nu}, \delta_{-1/2,\nu})^t$ . Since  $j = \ell + 1/2$  or  $j = \ell - 1/2$ , Eq. (11.8) can be simplified to a two-component representation,

$$\Omega_{\ell+1/2,m_j}^{(\ell)}(\vartheta, \phi) = \begin{pmatrix} \sqrt{\frac{\ell + m_j + 1/2}{2\ell + 1}} Y_{m_j-1/2}^{\ell}(\vartheta, \phi) \\ \sqrt{\frac{\ell - m_j + 1/2}{2\ell + 1}} Y_{m_j+1/2}^{\ell}(\vartheta, \phi) \end{pmatrix},$$

for  $j = \ell + 1/2$ , and

$$\Omega_{\ell-1/2,m_j}^{(\ell)}(\vartheta, \phi) = \begin{pmatrix} -\sqrt{\frac{\ell - m_j + 1/2}{2\ell + 1}} Y_{m_j-1/2}^{\ell}(\vartheta, \phi) \\ \sqrt{\frac{\ell + m_j + 1/2}{2\ell + 1}} Y_{m_j+1/2}^{\ell}(\vartheta, \phi) \end{pmatrix},$$

for  $j = \ell - 1/2$ . Knowledge of  $R_{n,j,\ell}(r)$  and  $\Omega_{j,m_j}^{(\ell)}(\vartheta, \phi)$  allows to evaluate the *unperturbed* doublet levels of the cesium atom. It is worth mentioning that given the small admixture introduced by the **PNC** Hamiltonian, the *perturbed* states  $|\widetilde{nS_{1/2}}\rangle$  and  $|\widetilde{n'P_{1/2}}\rangle$  can be evaluated as a perturbation expansion in terms of the *unperturbed* eigenstates, as outlined in Eqs. (11.3). Therefore, we first concentrate on the evaluation of the perturbation-free eigenstates –in particular the radial wavefunctions, and as a second step, use them to include the corrections due to the weak Hamiltonian  $\hat{\mathbf{h}}_{\text{pv}}$ .

The first step concerns the evaluation of the effective  $V_{\text{SAE}}(r; j; \ell)$ . To this end, we utilize a refined version of the statistical Thomas-Fermi theory [338, 339], as prescribed in Ref. [18]. This approach allows to describe the interaction between the outermost single electron and the ionic nuclear core [18] by means of an effective potential function while taking into account the spin-orbit interaction. It relies on the position-dependent spherically symmetric and semi-empirical effective potential,  $V_{\text{eff}}(r; l)$  which has been developed by Marinescu *et al.* [12] to describe the motion of the valence electron in alkali-metal atoms. This effective potential depends parametrically on the orbital angular momentum  $\ell$ , namely [12, 18]

$$V_{\text{eff}}(r; \ell) = - \left[ \frac{Z_{\text{eff}}(r; \ell)}{r} + V_{\text{pol}}(r; \ell) \right], \quad (11.9a)$$

with

$$Z_{\text{eff}}(r; \ell) = 1 + (Z - 1)e^{-r a_1(\ell)} - r e^{-r a_2(\ell)} \left[ a_3(\ell) + r a_4(\ell) \right], \quad (11.9b)$$

and where the potential describing the static electric polarizability of the ionic core reads

$$V_{\text{pol}}(r; \ell) = \frac{\alpha_c}{2} \frac{1 - e^{-(r/r_c(\ell))^6}}{r^4}. \quad (11.9c)$$

Typically, the parameters  $a_p(\ell)$ ,  $\alpha_c$  and  $r_c(\ell)$  need to be optimized, this is, they are parametrically fitted to reproduce one-electron energies [12, 18]. A further step consists in introducing the spin-orbit interaction. In order to describe the fine splitting of the excitation spectrum of the outermost electron of Cs, we follow Ref. [18] and define the effective spin-orbit term,

$$\mathcal{V}_{SO}(r; j; \ell) = \frac{V_{SO}(r; j; \ell)}{\left(1 - \alpha^2 V_{\text{eff}}(r; \ell)\right)^2}, \quad (11.10a)$$

where  $V_{\text{eff}}(r; \ell)$  is defined in Eq. (11.9a) and

$$V_{SO}(r; j; \ell) = \alpha^2 \frac{1}{r} \left( \frac{\partial}{\partial r} V_{\text{eff}}(r; \ell) \right) \left[ \frac{j(j+1) - \ell(\ell+1) - 3/4}{2} \right], \quad (11.10b)$$

which vanishes for  $\ell = 0$ . In Eq. (11.10),  $\alpha$  denotes the fine structure constant, and  $j > 0$  the total angular momentum, such that  $j \in [\ell - 1/2, \ell + 1/2]$ . Care should be taken with Eqs. (11.10), particularly when evaluating the wave function **near** and **at the origin**, which is required for the matrix elements of  $\hat{\mathbf{h}}_{\text{pv}}$ , cf. Eq. (11.2). In fact, the spin-orbit expression as defined in Eq. (11.10b) is non-relativistic and therefore not valid at small radii [336]. Therefore, we follow the guidelines of Ref. [18] and describe the effective single-electron potential (the parity violating potential is treated separately), by means of the following expression,

$$V_{\text{SAE}}(r; j; \ell) = \begin{cases} V_{\text{eff}}(r; \ell), & \text{if } 0 \leq r \leq r_{SO}(\ell), \\ V_{\text{eff}}(r; \ell) + \mathcal{V}_{SO}(r; j; \ell), & \text{if } r > r_{SO}(\ell), \end{cases} \quad (11.11)$$

where  $r_{SO}(\ell)$ , for  $\ell = 1, 2, \dots$  are optimized in the fitting procedure. The latter, together with  $a_k(\ell)$ ,  $\alpha_c$ ,  $r_c(\ell)$  with  $k = 1, \dots, 4$  defined in Eq. (11.9) are hereafter referred to as *semi-empirical parameters*, and need to be adjusted to reproduce the doublet levels of the cesium atom.

### 11.2.2 Evaluation of the radial wave functions

#### Evaluation of the wave function at small radii

Accurate knowledge of the behavior of the radial wavefunctions at the origin<sup>3</sup> of the radial grid are crucial to properly evaluate the mixing terms. However, the equation for the radial wave function, as defined in Eq. (11.6) introduces a further numerical difficulty that concerns the singular nature of the effective potential  $V_{\text{eff}}(r; j; \ell)$  at the origin. In simple terms, numerical integration of Eq. (11.6) becomes extremely unstable for small radii and information of the radial wave function is completely lost for such short distances, particularly at the origin. In order to get information of the radial wave function at the origin while avoiding singular potentials, we follow Ref. [12] and use a logarithmic grid [340], defined by the transformation  $x = \ln(r)$  together with a transformation of the radial wave function that allows the use of the Numerov method [341] for solving the modified radial equation. It also removes the initial singularity at the origin, therefore avoiding any kind of numerical instability.

As described in Ref. [12], the use of the logarithmic grid increases the density of points near the origin, which allows to (potentially) evaluate the wave functions at very small radii accurately. If the integration needs to be performed within the interval  $r \in [10^{-14}, 3 \cdot 10^3]$ , for instance, it results in  $x \in [-32, 8]$  in the logarithmic grid. A further step consists in parametrizing the original solution, namely  $R_{n,j,\ell}(r(x))$ , according to the transformation

$$\zeta_{n,\ell,j}(x) = \frac{R_{n,j,\ell}(r(x))}{\sqrt{r}}. \quad (11.12)$$

This transformation in conjunction with the logarithmic grid allows to avoid the singularity while accurately representing the radial wave function **near** and **at the origin**, which is of our particular interest. In fact, upon the above transformation, Eq. (11.6) becomes

$$\frac{\partial^2}{\partial x^2} \zeta_{n,\ell,j}(x) = \left[ \frac{2m_e}{\hbar^2} r^2(x) \left( V_{\text{SAE}}(r(x); j; \ell) - E_{n,\ell,j} \right) + \left( \ell + \frac{1}{2} \right)^2 \right] \zeta_{n,\ell,j}(x). \quad (11.13)$$

Equation (11.13) can be straightforwardly solved using the Numerov approach [341, 342] according to the guidelines in Ref. [12], and where

$$V_{\text{SAE}}(r(x)) \underset{r \rightarrow 0}{\sim} -\frac{Z}{r(x)}, \quad (11.14)$$

---

<sup>3</sup>they have non-vanishing values for S-waves due to the absence of the centrifugal barrier for  $\ell = 0$ , while for P-waves, they have non-vanishing first derivatives

is not longer singular since  $1/r(x) = \exp(-x)$  with  $x \in [-32, 8]$  according to our example. Instead, it can take very large values which are counterbalanced by the  $r^2(x)$  term that appears in the rhs of Eq. (11.13). Finally,  $\zeta_{n,\ell,j}(r)/\sqrt{r}$  gives the original radial wave function  $R_{n,\ell,j}/r$  required in Eq. (11.7) with the proper behavior at the origin and for small radii.

### Accuracy of the radial wave functions

In references [12, 18], the semi-empirical parameters are fitted to reproduce the one-electron doublet levels of the outermost valence electron, which are obtained via numerical integration of Eq. (11.6). In addition to the “properly” fitted semi-empirical parameters, this procedure gives, upon convergence, the approximated radial wave functions  $R_{n,\ell,j}(r)$  and one-electron energy spectrum  $E_{n,j,\ell}$ , defined in Eq. (11.6), that reproduces the ground and excited energies in cesium, for each pair of  $j$  and  $\ell$ .

In the context of the effective potentials, however, convergence of the eigenenergies alone does not guarantee a proper representation of the radial wave function [343], which is unfortunate for our purposes. In fact, it is apparent from Eq. (11.2) that precise knowledge of the radial wave function  $R_{n,j,\ell}(r)$  and of its derivative at the origin is required to evaluate the matrix elements of  $\hat{\mathbf{h}}_{\text{pv}}$  giving rise to the mixing terms. Here, in an attempt to render the calculations as realistic as possible, we make a further step and include not only the one-electron energy spectrum, but also the oscillator strengths [336, 344, 345] in the fitting procedure. In fact, given the amount of fitting variables, it is quite straightforward to find two different configurations that give the same energy spectrum, for each  $j$  and  $\ell$ , with slightly different radial wave functions. Imposing additional constraints in the optimization procedure, namely the oscillator strengths, reduces the degree of freedom of the fitting parameters. In our calculations, the semi-empirical parameters are optimized using the procedure described in Ref. [50], by setting a fixed number of optimization variables, for each  $j$  and  $\ell$ . Optimization is carried out by minimizing the Euclidean distance between the calculated eigenenergies and oscillator strengths with respect to their experimental counterparts. The values for the experimental energies and oscillator strengths are taken from Ref. [336] and references therein. Both eigenenergies and radial wave functions are obtained by solving the radial Schrödinger equation defined in Eq. (11.6) and iteratively adjusting the semi-empirical parameters until the desired convergence is obtained. The procedure is independently performed for each set of  $\{j, \ell\}$  with  $j = \ell \pm 1/2$ , which gives  $n$  converged eigenenergies and radial wave functions. The two-component spherical spinors [143] together with the converged radial functions  $R_{n,j,\ell}(r)$  are used to evaluate the oscillators strengths, following Refs. [336, 344].

### Evaluation of the perturbed eigenstates

The action of the **PNC** Hamiltonian still needs to be introduced. Once the radial parts  $R_{n,\ell,j}(r)$  are evaluated according to Eqs. (11.13) and (11.12), the unperturbed wave functions are obtained in accordance with Eq. (11.7). The perturbed states –which contain the admixture of opposite parity states, are obtained by introducing the first order corrections of each (unperturbed) partial wave component  $|n\ell_j\rangle$ . This results in the states  $|\widetilde{nS_{1/2}}\rangle, |\widetilde{nP_{1/2}}\rangle, |nP_{3/2}\rangle, |nD_{3/2}\rangle, \dots$  *et cetera*, cf. Eq. (11.3), which define the eigenfunctions of the field-free Hamiltonian, and that now includes the parity violating potential. The reason for introducing the **PNC** potential *a posteriori* allows for avoiding eventual systematic errors, that might arise from numerical integration (numerical diagonalization, Numerov method) of the time-independent Schrödinger equation due to the small value of effective numerical pre-factor associated with the **PNC** Hamiltonian in Eq. (11.1a).

### 11.3 Electron dynamics

In this section, we model the interaction of a cesium atom and an external electromagnetic field in the SAE approximation while taking into account the **PNC** potential. We derive the equations of motion describing the dynamics of the outermost valence electron. The interaction of the latter with an external radiation field in the strict dipole approximation reads <sup>4</sup> [314]

$$\hat{\mathbf{H}}_{\text{em}}(t) = -\mathcal{E}(t) \cdot \hat{\boldsymbol{\mu}}_{\mathcal{E}} - \mathcal{B}(t) \cdot \hat{\boldsymbol{\mu}}_{\mathcal{M}}, \quad (11.15)$$

where  $\hat{\boldsymbol{\mu}}_{\mathcal{E}}$  and  $\hat{\boldsymbol{\mu}}_{\mathcal{M}}$  refer to the electric and magnetic dipole moments, respectively. The former is defined as  $\hat{\boldsymbol{\mu}}_{\mathcal{E}} = -e\hat{\mathbf{r}}$  with  $\mathbf{r}$  being the position operator, whereas the latter can be expressed in terms of the non-relativistic magnetic dipole moment,  $\hat{\boldsymbol{\mu}}_0 = -e(\hat{\mathbf{L}} + 2\hat{\mathbf{S}})/2m_e c$ , plus first order corrections due to relativistic and spatial effects, namely [314]

$$\hat{\boldsymbol{\mu}}_{\mathcal{M}} = -\frac{e}{2m_e c}(\hat{\mathbf{L}} + 2\hat{\mathbf{S}}) + \hat{\boldsymbol{\mu}}_{\text{rel}} + \hat{\boldsymbol{\mu}}_{\text{ret}}. \quad (11.16)$$

The terms  $\hat{\boldsymbol{\mu}}_{\text{rel}}$  and  $\hat{\boldsymbol{\mu}}_{\text{ret}}$  represent relativistic and retardation corrections to the magnetic dipole moment  $\hat{\boldsymbol{\mu}}_0$ . While these effects might have a negligible impact on light atoms, they may be noticeable for cesium [314], in particular for calculations involving photoelectron momentum distributions such as cross sections [55]. The first such correction is due to the so-called **retardation effects**, described by  $\hat{\boldsymbol{\mu}}_{\text{ret}}$ . It originates from the phase difference

---

<sup>4</sup>homogeneous electric and magnetic fields over the total volume they are assumed, i.e.  $\mathcal{E}(\mathbf{r}, t) \approx \mathcal{E}(\mathbf{0}, t) \equiv \mathcal{E}(t)$  and  $\mathcal{B}(\mathbf{r}, t) \approx \mathcal{B}(\mathbf{0}, t) \equiv \mathcal{B}(t)$

between the waves emitted at different points of the atomic volume and it is defined as [314]

$$\hat{\boldsymbol{\mu}}_{\text{ret}} = -\frac{k^2 r^2}{6} \mu_B \hat{\boldsymbol{\sigma}}, \quad (11.17)$$

where  $\mu_B = e\hbar/2m_e$  is the *Bohr magneton*,  $r$  the radial coordinate of the valence electron in the **SAE** approximation,  $\hat{\boldsymbol{\sigma}}$  the spin operator and  $k = 2\pi/\lambda$  the photon wave number [56, 314]. As opposed to the non-relativistic magnetic dipole moment  $\hat{\boldsymbol{\mu}}_0$ , Eq. (11.17) is  $r$ -dependent. As a consequence, the forbidden magnetic dipole transitions defined by  $\Delta n \neq 0$ , where  $\Delta n = |n_f - n_i|$  is the difference between principal quantum numbers describing the initial  $n_i$  and final  $n_f$  states determined by the transition, are not longer strictly forbidden [314, 346]. Additionally, relativistic effects in heavy atoms such as cesium also break down the  $\Delta n = 0$  selection rule. The relativistic correction to the magnetic dipole moment is given by [314]

$$\hat{\boldsymbol{\mu}}_{\text{rel}} = -\frac{2}{3m_e c^2} \left( \hat{\mathbf{p}}^2 - \frac{2Ze^2}{r} \right) \hat{\boldsymbol{\sigma}}. \quad (11.18)$$

Having defined the operators involved in Eq. (11.15), as well as the procedure to obtain the semi-empirical parameters and the approach to treat the radial part of the wave function, we are now in a position to solve the time-dependent Schrödinger equation,

$$i\hbar \frac{\partial}{\partial t} \widetilde{|\psi(t)\rangle} = \left( -\frac{\hbar^2}{2m_e} \nabla^2 + \frac{\ell(\ell+1)}{2m_e r^2} + \hat{\mathbf{V}}_{\text{SAE}}(\mathbf{r}; j; \ell) + \hat{\mathbf{h}}_{\text{pv}}(\mathbf{r}) + \boldsymbol{\epsilon}(t) \cdot \hat{\boldsymbol{\mu}}_{\text{elec}}(\mathbf{r}) \right) \widetilde{|\psi(t)\rangle} \\ + \left[ -\frac{e}{2m_e c} (\hat{\mathbf{L}} + 2\hat{\mathbf{S}}) + \hat{\boldsymbol{\mu}}_{\text{rel}} + \hat{\boldsymbol{\mu}}_{\text{ret}} \right] \cdot \mathbf{B}(t) \widetilde{|\psi(t)\rangle}. \quad (11.19)$$

The field-free eigenstates contain the parity admixture due to the **PNC** interaction<sup>5</sup> and the time-dependent wave packet is projected as a linear combination thereof, namely

$$\widetilde{|\psi(t)\rangle} = \sum_n a_n(t) e^{-i\varepsilon_{S_{1/2}}^n t} \widetilde{|nS_{1/2}\rangle} + \sum_n b_n(t) e^{-i\varepsilon_{P_{1/2}}^n t} \widetilde{|nP_{1/2}\rangle} \\ + \sum_n c_n(t) e^{-i\varepsilon_{P_{3/2}}^n t} \widetilde{|nP_{3/2}\rangle} + \sum_{n,j} d_{n,j}(t) e^{-i\varepsilon_{D_j}^n t} \widetilde{|nD_j\rangle} \quad (11.20) \\ + \sum_{n,j} f_{n,j}(t) e^{-i\varepsilon_{F_j}^n t} \widetilde{|nF_j\rangle} + \dots$$

The summation in Eq. (11.20) runs over bound and unbound states and  $j$  refers to the total angular momentum with  $j = \ell \pm 1$ . As in Eq. (11.3a) and (11.3b),  $\varepsilon$  refers to the doublet energy levels of the cesium atom, where the upper and lower scripts denote the

<sup>5</sup>only the eigenstates  $\widetilde{|nS_{1/2}\rangle}$  and  $\widetilde{|n'P_{1/2}\rangle}$

principal and angular momentum quantum numbers, respectively. For unbound states, the counterpart energy will henceforth be referred to as  $\epsilon$ . Inserting Eq. (11.20) into Eq. (11.19) and projecting both sides of the resulting equation onto field-free eigenstates allows to obtain the relevant equations of motion for the time-dependent expansion coefficients,

$$\begin{aligned} \dot{a}_n(t) = & i \sum_{n'} \left\{ e\mathcal{E}_z(t) \left[ a_{n'}(t) e^{-i\epsilon_{S_{1/2}}^{n'} t} \langle \widetilde{nS_{1/2}} | \hat{\mathbf{z}} | \widetilde{n'S_{1/2}} \rangle + b_{n'}(t) e^{-i\epsilon_{P_{1/2}}^{n'} t} \langle \widetilde{nS_{1/2}} | \hat{\mathbf{z}} | \widetilde{n'P_{1/2}} \rangle \right. \right. \\ & \left. \left. + c_{n'}(t) e^{-i\epsilon_{P_{3/2}}^{n'} t} \langle \widetilde{nS_{1/2}} | \hat{\mathbf{z}} | \widetilde{n'P_{3/2}} \rangle + d_{n',3/2}(t) e^{-i\epsilon_{D_{3/2}}^{n'} t} \langle \widetilde{nS_{1/2}} | \hat{\mathbf{z}} | \widetilde{n'D_{3/2}} \rangle \right] \right. \\ & \left. + \mathcal{B}_y(t) a_{n'}(t) e^{-i\epsilon_{S_{1/2}}^n t} \langle nS_{1/2} | \hat{\boldsymbol{\mu}}_{\mathcal{M}} | n'S_{1/2} \rangle \right\} e^{i\epsilon_{S_{1/2}}^n t}, \end{aligned} \quad (11.21a)$$

describing the dynamics of the  $|\widetilde{n'S_{1/2}}\rangle$  states. The first and second lines in the rhs of Eq. (11.21a) describe the coupling due to the electric component of the electromagnetic field in the dipole approximation, whereas the third line arises due to the magnetic component. Also, note that by virtue of Eq. (11.3a) and the magnetic dipole selection rules, we find the following approximation,

$$\begin{aligned} \langle \widetilde{nS_{1/2}} | \hat{\boldsymbol{\mu}}_{\mathcal{M}} | \widetilde{n'S_{1/2}} \rangle &= \langle nS_{1/2} | \hat{\boldsymbol{\mu}}_{\mathcal{M}} | n'S_{1/2} \rangle + \sum_{m,m'} \frac{\langle mP_{1/2} | \hat{\mathbf{h}}_{\text{pv}} | nS_{1/2} \rangle}{\epsilon_{P_{1/2}}^m - \epsilon_{S_{1/2}}^n} \\ &\quad \times \frac{\langle m'P_{1/2} | \hat{\mathbf{h}}_{\text{pv}} | n'S_{1/2} \rangle}{\epsilon_{S_{1/2}}^n - \epsilon_{P_{1/2}}^{m'}} \langle mP_{1/2} | \hat{\boldsymbol{\mu}}_{\mathcal{M}} | m'P_{1/2} \rangle \\ &\approx \langle nS_{1/2} | \hat{\boldsymbol{\mu}}_{\mathcal{M}} | n'S_{1/2} \rangle \end{aligned} \quad (11.21b)$$

and similarly for the  $|\widetilde{nP_{1/2}}\rangle$  states. For the  $\ell = 1$  states, the dynamics obeys the following equations of motion,

$$\begin{aligned} \dot{b}_n(t) = & i \sum_{n'} \left\{ e\mathcal{E}_z(t) \left[ a_{n'}(t) e^{-i\epsilon_{S_{1/2}}^{n'} t} \langle \widetilde{nP_{1/2}} | \hat{\mathbf{z}} | \widetilde{n'S_{1/2}} \rangle + b_{n'}(t) e^{-i\epsilon_{P_{1/2}}^{n'} t} \langle \widetilde{nP_{1/2}} | \hat{\mathbf{z}} | \widetilde{n'P_{1/2}} \rangle \right. \right. \\ & \left. \left. + c_{n'}(t) e^{-i\epsilon_{P_{3/2}}^{n'} t} \langle \widetilde{nP_{1/2}} | \hat{\mathbf{z}} | \widetilde{n'P_{3/2}} \rangle + d_{n',3/2}(t) e^{-i\epsilon_{D_{3/2}}^{n'} t} \langle \widetilde{nP_{1/2}} | \hat{\mathbf{z}} | \widetilde{n'D_{3/2}} \rangle \right] \right. \\ & \left. + \mathcal{B}_y(t) \left[ b_{n'}(t) e^{-i\epsilon_{P_{1/2}}^{n'} t} \langle nP_{1/2} | \hat{\boldsymbol{\mu}}_{\mathcal{M}} | n'P_{1/2} \rangle \right. \right. \\ & \left. \left. + c_{n'}(t) e^{-i\epsilon_{P_{3/2}}^{n'} t} \langle nP_{1/2} | \hat{\boldsymbol{\mu}}_{\mathcal{M}} | n'P_{3/2} \rangle \right] \right\} e^{i\epsilon_{P_{1/2}}^n t}. \end{aligned} \quad (11.21c)$$

and

$$\begin{aligned}
 \dot{c}_n(t) = & i \sum_{n'} \left\{ e\mathcal{E}_z(t) \left[ a_{n'}(t) e^{-i\varepsilon_{S_{1/2}}^{n'} t} \langle nP_{3/2} | \hat{\mathbf{z}} | n'S_{1/2} \rangle + b_{n'}(t) e^{-i\varepsilon_{P_{1/2}}^{n'} t} \langle nP_{3/2} | \hat{\mathbf{z}} | n'P_{1/2} \rangle \right. \right. \\
 & \left. \left. + \sum_{j'} d_{n',j'}(t) e^{-i\varepsilon_{D_{j'}}^{n'} t} \langle nP_{3/2} | \hat{\mathbf{z}} | n'D_{j'} \rangle \right] \right. \\
 & \left. + \mathcal{B}_y(t) \left[ b_{n'}(t) e^{-i\varepsilon_{P_{1/2}}^{n'} t} \langle nP_{3/2} | \hat{\boldsymbol{\mu}}_{\mathcal{M}} | n'P_{1/2} \rangle \right. \right. \\
 & \left. \left. + c_{n'}(t) e^{-i\varepsilon_{P_{3/2}}^{n'} t} \langle nP_{3/2} | \hat{\boldsymbol{\mu}}_{\mathcal{M}} | n'P_{3/2} \rangle \right] \right\} e^{i\varepsilon_{P_{3/2}}^n t}. \tag{11.21d}
 \end{aligned}$$

for  $j = 1/2$  and  $j = 3/2$ , respectively and where  $\langle nP_{3/2} | \hat{\mathbf{z}} | n'P_{1/2} \rangle = \langle nP_{3/2} | \hat{\mathbf{z}} | n'S_{1/2} \rangle$ . Finally, a key component of the present work is given by the equation of motion obeyed by the  $d$ -wave components, namely

$$\begin{aligned}
 \dot{d}_{n,j}(t) = & i \sum_{n'} \left\{ e\mathcal{E}_z(t) \left[ a_{n'}(t) e^{-i\varepsilon_{S_{1/2}}^{n'} t} \langle nD_j | \hat{\mathbf{z}} | n'S_{1/2} \rangle + b_{n'}(t) e^{-i\varepsilon_{P_{1/2}}^{n'} t} \langle nD_j | \hat{\mathbf{z}} | n'P_{1/2} \rangle \right. \right. \\
 & \left. \left. + c_{n'}(t) e^{-i\varepsilon_{P_{3/2}}^{n'} t} \langle nD_j | \hat{\mathbf{z}} | n'P_{3/2} \rangle + \sum_{j'} f_{n',j'}(t) e^{-i\varepsilon_{F_{j'}}^{n'} t} \langle nD_j | \hat{\mathbf{z}} | n'F_{j'} \rangle \right] \right. \\
 & \left. + \mathcal{B}_y(t) \sum_{j'} d_{n',j'}(t) e^{-i\varepsilon_{D_{j'}}^{n'} t} \langle nD_j | \hat{\boldsymbol{\mu}}_{\mathcal{M}} | n'D_{j'} \rangle \right\} e^{i\varepsilon_{D_j}^n t}, \tag{11.21e}
 \end{aligned}$$

which holds for bound and unbound states within the SAE approximation.

## 11.4 Observation of the PNC via photoelectron spectroscopy

### 11.4.1 Photoelectron spectrum

The essence of our approach consists in detecting the fingerprints of the parity violation in the photoelectron spectrum. The probability of photoemission, henceforth referred to as total yield, reads

$$\sigma(t_f) = \int_0^\infty \rho(\epsilon) d\epsilon, \tag{11.22}$$

where  $\rho(\epsilon) = |\langle \widetilde{\Psi}_\epsilon(t_f) | \widetilde{\Psi}_\epsilon(t_f) \rangle|^2$  is the probability density for photoelectron emission which is evaluated after a long time  $t_f$  after the driving field is over, and  $\langle \mathbf{r} | \widetilde{\Psi}_\epsilon(t_f) \rangle$  is the unbound part of the propagated wavefunction with energy  $\epsilon > 0$ . In particular, for positive energies,

the probability for the photoelectron to have an energy between  $\epsilon$  and  $\epsilon + d\epsilon$  reads

$$\rho(\epsilon) d\epsilon = \rho(k) d^3k = \rho(k) k^2 dk d\Omega_k \quad (11.23)$$

with  $k = \sqrt{2\epsilon}$  and  $d\Omega_k = \sin(\theta_k) d\theta_k d\phi_k$  referring to the solid angle of photoemission and where

$$\rho(k) = \left| \int e^{-i\mathbf{k}\cdot\mathbf{r}} \Psi(\mathbf{r}, t_f) d^3r \right|^2, \quad (11.24)$$

describes the probability distribution in  $k$ -space with  $\Psi(\mathbf{r}, t) = \langle \mathbf{r} | \widetilde{\Psi}(t) \rangle$ . The state vector  $|\widetilde{\Psi}(T)\rangle$  is obtained by solving Eq. (11.19) and each partial wave contribution obeys the equations of motion defined in Eq. (11.21). The photoelectron spectrum is evaluated by projecting the propagated wave function onto the continuum eigenstates of the field-free Hamiltonian. We can thus analyze each partial wave contribution independently. For instance, the ***d-wave contribution to the total yield*** reads

$$\sigma_d(t_f) = \sum_j \int_0^\infty |d_{\epsilon,j}(t_f)|^2 d\epsilon, \quad (11.25)$$

where  $d_{\epsilon,j}(t)$  corresponds to the solution of Eq. (11.21e) for positive-valued energies. It is apparent from Eq. (11.21e) that not only  $\ell = 1$  and  $\ell = 3$  contribute to the *d-wave* component of the total yield, cf. Eq. (11.25), but also  $\ell = 0$  contributes, via  $|\widetilde{nS_{1/2}}\rangle$ , due to the parity mixing. The latter statement defines the motivation of our approach, and will be exploited to infer the signature of the PNC potential, which are imprinted in the photoelectron yield, more specifically, in the *d-wave* component of the latter.

### 11.4.2 Single-photon ionization

Single-photon ionization refers to the ejection of an electron from its initial state to the continuum. Perhaps the most intuitive and naive approach to infer the contribution of bound  $\ell = 0$  states to the *d-wave* component of the total yield would consist in measuring the probability of photoemission from the  $|\widetilde{6S_{1/2}}\rangle$  ground state in cesium, via single-photon ionization. In fact, it is apparent from Eq. (11.3a) that **non only *E1 bound-bound***, but also ***bound-continuum one-photon*** transitions of the type  $|\widetilde{nS_{1/2}}\rangle \rightarrow |\epsilon, D_{3/2}\rangle$ , are no longer strictly forbidden, since  $|\widetilde{nS_{1/2}}\rangle$  enjoys a small  $P_{1/2}$  component, proportional to  $\gamma_{pv}$ , where  $\gamma_{pv}$  refers to the leading term of the mixing amplitude, cf. Eq. (11.3a). For the case of cesium, it corresponds to the mixing amplitude between the  $|\widetilde{6S_{1/2}}\rangle$  and  $|\widetilde{6P_{1/2}}\rangle$  states,

and its value is given by

$$\gamma_{pv} \equiv i \frac{\langle 6P_{1/2} | \hat{\mathbf{h}}_{pv} | 6S_{1/2} \rangle}{\varepsilon_{6S_{1/2}} - \varepsilon_{6P_{1/2}}} \simeq 4.3i \times 10^{-12}. \quad (11.26)$$

Having stated the general idea, the limitation of such an approach is discussed next. The initial state is assumed to be the ground state in cesium, namely the  $|\widetilde{6S_{1/2}}\rangle$  state. In order to obtain a clear picture of this approach, and in particular of its limitations, we consider a harmonic perturbation with frequency  $\omega$  and we make use of first order time-dependent perturbation theory to evaluate the contribution of the ground state to the  $d$ -component of the photoelectron yield. The transition probability per unit of time is, according to the Fermi's Golden Rule,

$$\mathcal{P}_{6S_{1/2} \rightarrow D_{3/2}} = 2\pi \int_0^{+\infty} d\epsilon \varrho(\epsilon) \left| \langle \epsilon D_{3/2} | \hat{\mathbf{z}} | \widetilde{6S_{1/2}} \rangle \right|^2 \delta(\omega_{if} - \omega), \quad (11.27a)$$

where  $\omega_{if} = \epsilon - \varepsilon_i$  with  $\varepsilon_i = \varepsilon_{6S_{1/2}}$  is the ground state energy, and  $\varrho(\epsilon)$  refers to the density of states (included here to account for eventual multiplicities). The transition amplitudes  $\langle \epsilon D_{3/2} | \hat{\mathbf{z}} | \widetilde{6S_{1/2}} \rangle$  exhibit non-vanishing values due to the parity violating potential and read

$$\left| \langle \epsilon D_{3/2} | \hat{\mathbf{z}} | \widetilde{6S_{1/2}} \rangle \right|^2 = \left| \sum_n \langle \epsilon D_{3/2} | \hat{\mathbf{z}} | nP_{1/2} \rangle \frac{\langle nP_{1/2} | \hat{\mathbf{h}}_{pv} | 6S_{1/2} \rangle}{\varepsilon_{S_{1/2}}^6 - \varepsilon_{P_{1/2}}^n} \right|^2. \quad (11.27b)$$

Accounting only for the dominant term in the summation, defined in Eq. (11.26), allows to obtain a good estimate for Eq. (11.27b), namely

$$\left| \langle \epsilon D_{3/2} | \hat{\mathbf{z}} | \widetilde{6S_{1/2}} \rangle \right|^2 \approx |\gamma_{pv}|^2 \left| \langle \epsilon D_{3/2} | \hat{\mathbf{z}} | 6P_{1/2} \rangle \right|^2. \quad (11.27c)$$

The transition amplitude in Eq. (11.27c) being proportional to  $|\gamma_{pv}|^2$ , the contribution of the  $\ell = 0$  state –and thus the fingerprint of the PNC potential is negligible to be experimentally detected by any available means. Given the extremely weak character of the parity exchange, an alternative approach must be conceived in the hope of detecting the fingerprints of the PNC in the photoelectron spectrum.

### 11.4.3 Pump-probe approach

In an effort to observe the fingerprints of **PNC**, we show in the following an alternative approach that allows to describe the contribution of the parity admixture in terms of  $|\gamma_{pv}|$  instead of  $|\gamma_{pv}|^2$ . To this end, we suggest pump-probe spectroscopy and we define

the wavepacket prepared by the pump pulse according to

$$|\psi_0\rangle = a_0 e^{-i\phi_0} |\widetilde{n_o S_{1/2}}\rangle + b_0 e^{-i\phi_1} |n_1 P_{1/2}\rangle + c_0 e^{-i\phi_2} |n_1 P_{1/2}\rangle, \quad (11.28)$$

where  $a_0$ ,  $b_0$  and  $c_0$  are real-valued normalized weights and  $\phi_j$  are the phases that depend on the pump pulse. In practice, we choose  $n_0 = n_1 = n_2 = 6$ . The reason for choosing a superposition involving the perturbed ground  $|\widetilde{6S_{1/2}}\rangle$  and one or both P states relies on the fact that if only the state  $|\widetilde{6S_{1/2}}\rangle$  were used and the P states were omitted, the contribution to the  $d$ -wave component of the total yield arising from the **relevant one-photon process** would not be sensitive to the pump-to-probe time-delay  $\tau_p$ . The same applies if a  $D$  state were defined instead of the  $P$  states in Eq. (11.28). If only two (or more)  $|\widetilde{nS_{1/2}}\rangle$  states were used as a linear combination instead, the  $d$ -wave component would indeed be sensitive to the time delay but still proportional to  $|\gamma_{pv}|^2$ . Thus, choosing a linear superposition between the cesium ground state and one P state, for instance the  $|n_1 P_{3/2}\rangle$  state, guarantees the  $d$ -wave component of the yield to be sensitive to  $\tau_p$  while being proportional to  $\gamma_{pv}$  instead of  $|\gamma_{pv}|^2$ . Hence, introducing one additional states with regular non-vanishing one-photon transition matrix elements to the  $d$ -continuum, e.g. P states, allows the latter to be modulated and thus carry the small contribution arising from the perturbed  $|\widetilde{n_o S_{1/2}}\rangle$ , which also can be coupled to the  $d$ -continuum via one-photon absorption. This will become clearer in Section 11.4.4, where the dynamics of the prepared wave packet is scrutinized by approximating its time evolution in the context of the second order time-dependent perturbation theory. Additionally, second order processes effects on the other wave components of the total yield will be discussed in Section 11.4.5.

After the delay  $\tau_p$ , the second pulse interacts with wave packet prepared by the pump pulse. Within this time interval, the dynamics of the prepared wave packet is dictated by the field-free time evolution, and at time  $t = \tau_p$ , for  $p = 1, 2, \dots$  the  $p$  th probe pulse finds the wave packet given by

$$\begin{aligned} |\psi(\tau_p)\rangle &= \exp[-i\hat{\mathbf{H}}_0 \tau_p] |\psi_0\rangle \\ &= a_0 e^{-i(\varepsilon_{S_{1/2}}^{n_0} \tau_p + \phi_0)} |\widetilde{n_o S_{1/2}}\rangle + b_0 e^{-i(\varepsilon_{P_{1/2}}^{n_1} \tau_p + \phi_1)} |\widetilde{n_1 P_{1/2}}\rangle \\ &\quad + c_0 e^{-i(\varepsilon_{P_{3/2}}^{n_2} \tau_p + \phi_2)} |n_2 P_{3/2}\rangle. \end{aligned} \quad (11.29)$$

For a reason that will become clear later, it is ideal for the **pump pulse** to excite only one of the D-lines in neutral cesium. This implies that only the  $|\widetilde{n_1 P_{1/2}}\rangle$  or the  $|n_2 P_{3/2}\rangle$  state in Eq. (11.29) needs to be efficiently populated. In the framework of this work, we have chosen  $n_0 = n_1 = n_2 = 6$ , such that, as discussed earlier, the matrix elements of the **PNC** Hamiltonian are maximized. The D1-line in cesium is characterized by an

energy separation of  $\omega_{D1} = \omega_{P_{1/2}}^6 - \omega_{S_{1/2}}^6 = 894$  nm while the D2-line corresponds to  $\omega_{D2} = \omega_{P_{1/2}}^6 - \omega_{S_{3/2}}^6 = 852$  nm. To efficiently create a linear superposition between only the  $6S_{1/2}$  and  $6P_{3/2}$  states, for instance, a resonant laser excitation at  $\omega_{D2}$  with a bandwidth  $\Delta\omega_{\text{FWHM}} < 42$  nm is necessary, which excludes very short pulses. Therefore, we consider here a combination of both  $j = 1/2$  and  $j = 3/2$  for the P state. Also, note that only the  $n = 6$  is considered in Eq. (11.28). In fact, the energy separation between the  $6S_{1/2}$  and  $7P_{1/2}$  is  $\omega_{6S_{1/2}-7P_{1/2}} \approx 457.988$  nm, and that of the  $7P_{3/2}$  is  $\omega_{6S_{1/2}-7P_{3/2}} \approx 455.698$  nm, both well above  $\omega_{D1}$  and  $\omega_{D2}$ . Hence, undesirable population transfer to higher  $|nP_j\rangle$  levels with  $n \geq 7$  can easily be avoided in practice.

As briefly introduced in Section 11.1.3, our approach consists in inferring the weak parity admixture, due to the parity violation, from specific properties of the photoelectron spectrum. The principle of the proposed pump-probe approach rests on detecting the fingerprint of such parity admixture from the oscillations of the total yield, as a function of the pump-to-probe time delay. In particular, we seek to observe oscillations of the d-wave component of the total yield, i.e.  $\sigma_d(t_f)$  in Eq. (11.25), as a function of  $\tau_p$  that originate from the  $|\widetilde{6S_{1/2}}\rangle$  perturbed state. Regarding this point, however, a word of caution should be particularly stressed. The point to be stressed concerns the role of the electric field component of the laser field on the observable we are interested in, in particular one and multi-photon process induced by the electric field.

To illustrate the precautions to be taken, let's consider, for the sake of simplicity that the prepared state is obtained upon resonant excitation of the D2 line, with equal probability density  $a_0 = c_0 = 1/\sqrt{2}$ . In this case, not only  $|\widetilde{6S_{1/2}}\rangle$  but also the  $|6P_{3/2}\rangle$  state contributes to d-wave component of the spectrum via **one-photon absorption**. This means that, even in the absence of the **PNC Hamiltonian**, i.e.  $|\widetilde{6S_{1/2}}\rangle = |6S_{1/2}\rangle$ , oscillations of the photoelectron signal as a function of the pump-to-probe delay are observed. Furthermore, since not only  $\hat{\mathbf{h}}_{pv}$  but also the electric field component of the laser field couples states of opposite parity, **two-photon excitation** from the  $|6P_{3/2}\rangle$  to the  $d$ -continuum can *mimick* the contribution of the  $|\widetilde{6S_{1/2}}\rangle$ , even in the absence of the weak parity-violating Hamiltonian. Consequently, it is imperative to find a procedure that allows to isolate the contributions to the spectrum due to the **PNC** potential from those induced by the driving field, **which also couples opposite parity states**.

To this end, we scrutinize the electron dynamics generated by the probe pulse by approximating the time evolution of the prepared wave packet to second order in time-dependent perturbation theory in Section 11.4.4.

#### 11.4.4 Time-dependent perturbation theory. Second order corrections

In order to distinguish the contributions due to the weak Hamiltonian and those due to the laser field, we approximate the electron dynamics, i.e. the coefficients of the prepared state in Eq. (11.21) up to a second order in time-dependent perturbation theory. As previously emphasized, first and second order corrections are required to account for one and two-photon transitions. The former is required to describe, for instance, the contribution of the  $|6P_{3/2}\rangle$  state in Eq. (11.28) to the  $d$ -continuum, while the latter describes second order processes, that in the case of the  $|6P_{3/2}\rangle$  state, compete with the (very small) contribution of the single-photon excitation from the  $\widetilde{|6S_{1/2}\rangle}$  to the continuum. For the sake of simplicity and to avoid cumbersome notation, only the electric field component within the strict dipole approximation is accounted for in the perturbation expansion – it is the admixture of states of different parity mediated by the latter that is in competition with that caused by the PNC potential. In this sense, the magnetic component<sup>6</sup> and quadrupole transitions<sup>7</sup> only introduce systematic effects of minor importance in the overall description.

The second order approximation of the partial yield in Eq. (11.25) reads

$$\begin{aligned} \sigma_d(t_f) &\approx \sum_j \int_0^\infty |d_{\epsilon,j}^{(0)}(t_f) + d_{\epsilon,j}^{(1)}(t_f) + d_{\epsilon,j}^{(2)}(t_f)|^2 d\epsilon \\ &\approx \sum_j \int_0^\infty \left\{ |d_{\epsilon,j}^{(1)}(t_f)|^2 + |d_{\epsilon,j}^{(2)}(t_f)|^2 \right. \\ &\quad \left. + d_{\epsilon,j}^{(1)*}(t_f)d_{\epsilon,j}^{(2)}(t_f) + d_{\epsilon,j}^{(1)}(t_f)d_{\epsilon,j}^{(2)*}(t_f) \right\} d\epsilon, \end{aligned} \quad (11.30)$$

where  $d_{\epsilon,j}^{(k)}(t_f)$  denotes the  $k$ -th order correction to the  $d$ -wave component of the wave function with energy  $\epsilon$ . In particular, according to the expression of the “prepared” state in Eq. (11.28)  $d_{\epsilon,j}^{(0)} = d_{\epsilon,j}(\tau_p) = 0$ . Higher order corrections are obtained in the standard fashion, for instance

$$\begin{aligned} d_{\epsilon,j}^{(2)}(t_f) &= ie \sum_{n'} \int_{\tau_p}^{t_f} \left\{ a_{n'}^{(1)}(t) e^{-i\epsilon_{S_{1/2}}^{n'} t} \langle \epsilon D_j | \hat{\mathbf{z}} | \widetilde{n'} S_{1/2} \rangle \right. \\ &\quad + b_{n'}^{(1)}(t) e^{-i\epsilon_{P_{1/2}}^{n'} t} \langle \epsilon D_j | \hat{\mathbf{z}} | n' P_{1/2} \rangle \\ &\quad \left. + c_{n'}^{(1)}(t) e^{-i\epsilon_{P_{3/2}}^{n'} t} \langle \epsilon D_j | \hat{\mathbf{z}} | n' P_{3/2} \rangle \right\} e^{i\epsilon t} \mathcal{E}_z(t) dt \end{aligned} \quad (11.31)$$

<sup>6</sup>the relativistic magnetic components coupling only states with  $\Delta\ell = 0$  and  $\Delta j = \pm 1$

<sup>7</sup> electric-quadrupole **E2** transitions only coupling equal parity states with  $\ell = 0, \pm 2$  and  $j = 0, \pm 1, \pm 2$ , does not interfere directly with the admixture of different parity states induced by  $\hat{\mathbf{h}}_{pv}$  and electric-dipole **E1** transitions

where  $a^{(1)}(t)$ ,  $b^{(1)}(t)$  and  $c^{(1)}(t)$  refer to the first order correction of the expansion coefficients. Note that the  $f$  states do not contribute to  $d_{\epsilon,j}^{(2)}(t_f)$  since its zeroth and first order approximations vanish i.e.  $f_{n,j}^{(1)}(t) = f_{n,j}^{(0)}(t) = 0$ . The first order approximations are evaluated following the same perturbation protocol. For instance, the first order correction for  $a(t)$  reads

$$a_n^{(1)}(t) = ib_0 e^{-i(\epsilon_{P_{1/2}}^{n_1} \tau_p + \phi_1)} \langle \widetilde{nS_{1/2}} | \widetilde{\mathbf{z}} | \widetilde{n'P_{1/2}} \rangle \int_{\tau_p}^t e^{-i(\epsilon_{P_{1/2}}^{n_1} - \epsilon_{S_{1/2}}^{n_0})t'} \mathcal{E}(t') dt' \\ + ic_0 e^{-i(\epsilon_{P_{3/2}}^{n_2} \tau_p + \phi_2)} \langle \widetilde{n_0S_{1/2}} | \widetilde{\mathbf{z}} | \widetilde{n'P_{3/2}} \rangle \int_{\tau_p}^t e^{-i(\epsilon_{P_{3/2}}^{n_2} - \epsilon_{S_{1/2}}^{n_0})t'} \mathcal{E}(t') dt', \quad (11.32)$$

where we have made use of the properties  $\langle \widetilde{nS_{1/2}} | \widetilde{\mathbf{z}} | \widetilde{n'S_{1/2}} \rangle = 0$  if  $n = n'$  and  $\langle \widetilde{nS_{1/2}} | \widetilde{\mathbf{z}} | \widetilde{n'P_{3/2}} \rangle = \langle nS_{1/2} | \mathbf{z} | n'P_{3/2} \rangle$ ,

$$b_n^{(1)}(t) = ia_0 e^{-i(\epsilon_{S_{1/2}}^{n_0} \tau_p + \phi_0)} \langle \widetilde{nP_{1/2}} | \widetilde{\mathbf{z}} | \widetilde{n'S_{1/2}} \rangle \int_{\tau_p}^t e^{-i(\epsilon_{S_{1/2}}^{n_1} - \epsilon_{P_{1/2}}^{n_1})t'} \mathcal{E}(t') dt' \\ + ic_0 e^{-i(\epsilon_{P_{3/2}}^{n_2} \tau_p + \phi_2)} \langle \widetilde{nP_{1/2}} | \widetilde{\mathbf{z}} | \widetilde{n'P_{3/2}} \rangle \int_{\tau_p}^t e^{-i(\epsilon_{P_{3/2}}^{n_2} - \epsilon_{S_{1/2}}^{n_0})t'} \mathcal{E}(t') dt', \quad (11.33)$$

and analogously for  $c^{(1)}(t)_n$  and  $d^{(1)}(t)$ . The first order correction to the quantity of interest reads,

$$d_{\epsilon,j}^{(1)}(t) = ia_0 e^{-i(\epsilon_{S_{1/2}}^{n_0} \tau_p + \phi_0)} \langle \epsilon D_j | \widetilde{\mathbf{z}} | \widetilde{n'S_{1/2}} \rangle \int_{\tau_p}^t e^{-i(\epsilon_{P_{1/2}}^{n_0} - \epsilon)t'} \mathcal{E}(t') dt' \\ + ib_0 e^{-i(\epsilon_{P_{1/2}}^{n_1} \tau_p + \phi_1)} \langle \epsilon D_j | \mathbf{z} | n_1 P_{1/2} \rangle \int_{\tau_p}^t e^{-i(\epsilon_{P_{1/2}}^{n_1} - \epsilon)t'} \mathcal{E}(t') dt' \\ + ic_0 e^{-i(\epsilon_{P_{3/2}}^{n_2} \tau_p + \phi_2)} \langle \epsilon D_j | \mathbf{z} | n_2 P_{3/2} \rangle \int_{\tau_p}^t e^{-i(\epsilon_{P_{3/2}}^{n_2} - \epsilon)t'} \mathcal{E}(t') dt', \quad (11.34)$$

so that the first relevant quantity of interest in Eq. (11.30) becomes

$$|d_{\epsilon,j}^{(1)}(t_f)|^2 = |\mathcal{E}_0|^2 \left\{ a_0 b_0 \sin(\omega_{01} \tau_p + \phi_{01}) \text{Im} \left[ \langle \epsilon d_j | \widetilde{\mathbf{z}} | \widetilde{n_0 S_{1/2}} \rangle \langle \epsilon d_j | \mathbf{z} | n_1 P_{1/2} \rangle \mathcal{R}_{n_0 S_{1/2}}^{\epsilon,j} \mathcal{R}_{n_1 P_{1/2}}^\epsilon \right. \right. \\ \left. \left. + a_0 c_0 \sin(\omega_{02} \tau_p + \phi_{02}) \text{Im} \left[ \langle \epsilon d_j | \widetilde{\mathbf{z}} | \widetilde{n_0 S_{1/2}} \rangle \langle \epsilon d_j | \mathbf{z} | n_2 P_{3/2} \rangle \mathcal{R}_{n_0 S_{1/2}}^{\epsilon,j} \mathcal{R}_{n_2 P_{3/2}}^\epsilon \right. \right. \right. \\ \left. \left. + b_0 c_0 \sin(\omega_{12} \tau_p + \phi_{12}) \langle \epsilon d_j | \mathbf{z} | n_1 P_{1/2} \rangle \langle \epsilon d_j | \mathbf{z} | n_2 P_{3/2} \rangle \mathcal{R}_{n_1 P_{1/2}}^{\epsilon,j} \mathcal{R}_{n_2 P_{3/2}}^\epsilon \right] \right\} \\ + S_{dc}^{(1)}, \quad (11.35)$$

with  $S_{dc}^{(1)}$  being a non-oscillating DC component proportional to  $\mathcal{E}_0^2$  and where we have defined  $\omega_{01} = \epsilon_{S_{1/2}}^{n_0} - \epsilon_{P_{1/2}}^{n_1}$ ,  $\omega_{02} = \epsilon_{S_{1/2}}^{n_0} - \epsilon_{P_{3/2}}^{n_2}$  and  $\omega_{12} = \epsilon_{P_{1/2}}^{n_1} - \epsilon_{P_{3/2}}^{n_2}$ . The relative phases

are given by  $\phi_{01} = \phi_0 - \phi_1$ , etc. Assuming the probe pulse delayed by  $\tau_p$  to be of the form

$$\mathcal{E}(t)_z = \mathcal{E}_0 e^{-(t-t_p)^2/2\sigma^2} \cos(\omega(t-t_p)) \quad (11.36)$$

with  $t_p = \tau_p + n\sigma$  and ideally,  $n > 5$  to avoid any superposition of the pump and probe pulses,  $\mathcal{R}_{n,\ell_{j'}}^\epsilon$  reads

$$\mathcal{R}_{n,\ell_{j'}}^\epsilon = \sqrt{2} \int_{-n\sigma}^{+n\sigma} e^{-t^2/2\sigma^2} \cos(\omega t') \cos((\epsilon_{\ell_{j'}}^n - \epsilon)t') dt'. \quad (11.37)$$

Note from Eq. (11.35), that even in the absence of the PNC potential, which implies that only the third line is non-zero, oscillations occurs. The second quantity of interest in Eq. (11.30) is the norm squared of the second order correction of  $d_{\epsilon,j}(t_f)$ . It has the following expression

$$\begin{aligned} |d_{\epsilon,j}^{(2)}(t_f)|^2 &= |\mathcal{E}_0|^4 a_0 b_0 \left\{ \left( \cos(\omega_{01}\tau_p + \phi_{01}) \operatorname{Im}[\tilde{G}_{1,\epsilon,j}^* R_{\epsilon,j}] \right) - \sin(\omega_{01}\tau_p + \phi_{01}) \operatorname{Re}[\tilde{G}_{1,\epsilon,j}^* R_{\epsilon,j}] \right\} \\ &\quad + |\mathcal{E}_0|^4 a_0 c_0 \left\{ \left( \cos(\omega_{02}\tau_p + \phi_{02}) \operatorname{Im}[\tilde{G}_{2,\epsilon,j}^* R_{\epsilon,j}] \right) - \sin(\omega_{02}\tau_p + \phi_{02}) \operatorname{Re}[\tilde{G}_{2,\epsilon,j}^* R_{\epsilon,j}] \right\} \\ &\quad + S_{dc}^{(2)}, \end{aligned} \quad (11.38)$$

Again, the small DC component  $S_{dc}^{(2)}$  is proportional to  $|\mathcal{E}_0|^4$  and has no oscillatory behavior. The negligible terms proportional to  $|\gamma_{pv}|^2$  have been systematically omitted from the equation. In Eq. (11.38), the term

$$\begin{aligned} \tilde{G}_{k,\epsilon,j} \equiv \tilde{G}_{k,\epsilon,j}(t_f) &= \sum_n \left\{ \operatorname{Im}[\langle \epsilon d_j | \hat{\mathbf{z}} | n S_{1/2} \rangle] \langle S_{1/2} | \hat{\mathbf{z}} | n_k P_{k-1/2} \rangle \right. \\ &\quad \times \int_{\tau_p}^{t_f} e^{-i(\epsilon_{S_{1/2}}^n - \epsilon)t'} \int^{t'} e^{-i(\epsilon_{P_{k-1/2}}^{n_k} - \epsilon_{S_{1/2}}^n)t''} h(t') h(t'') dt' dt'', \end{aligned} \quad (11.39)$$

describes the second order process via the *weakly allowed transition* mediated by  $\hat{\mathbf{h}}_{pv}$ , when  $\operatorname{Im}[\langle \epsilon d_j | \hat{\mathbf{z}} | n S_{1/2} \rangle] \neq 0$  and where  $h(t) = e^{-(t-t_p)^2/2\sigma^2} \cos(\omega(t-t_p))$  is defined in Eq. (11.36). Finally, the term  $R_{\epsilon,j} = R_{\epsilon,j}(t_f)$  given by

$$R_{\epsilon,j} = \sum_{n,j'} \langle \epsilon d_j | \hat{\mathbf{z}} | n P_{j'} \rangle \langle n P_{j'} | \hat{\mathbf{z}} | n_0 S_{1/2} \rangle \int_{\tau_p}^{t_f} e^{-i(\epsilon_{P_{1/2}}^n - \epsilon)t'} \int^{t'} e^{-i(\epsilon_{S_{1/2}}^{n_0} - \epsilon_{P_{j'}}^n)t''} h(t') h(t'') dt' dt'',$$

describes the regular dipole allowed second order process. After some cumbersome algebra, we find that the oscillating components in the second line in the rhs of Eq. (11.30)

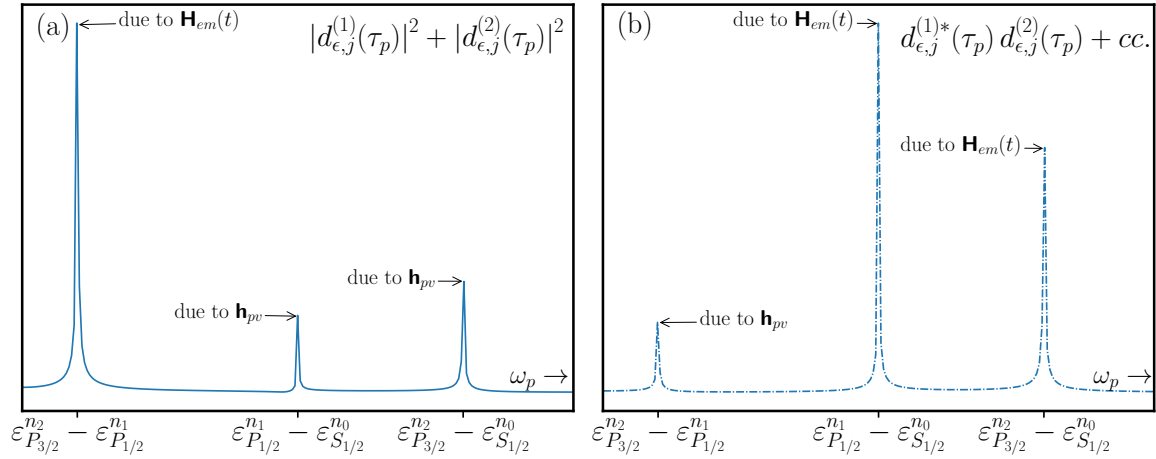


Figure 11.1: Schematic representation (not drawn to scale) of the spectral components of the d-wave contribution to the total yield due to the terms  $|d_{\epsilon,j}^{(1)}(\tau_p)|^2 + |d_{\epsilon,j}^{(2)}(\tau_p)|^2$  and  $d_{\epsilon,j}^{(1)*}(\tau_p) d_{\epsilon,j}^{(2)}(\tau_p) + cc.$  Note that the much smaller contributions due to  $\hat{\mathbf{h}}_{pv}$  are *overshadowed* by those due the external electric field when the components are added up.

read

$$\begin{aligned}
 & d_{\epsilon,j}^{(1)*}(t_f) d_{\epsilon,j}^{(2)}(t_f) + d_{\epsilon,j}^{(1)}(t_f) d_{\epsilon,j}^{(2)*}(t_f) \tag{11.40} \\
 &= \mathcal{E}_0 |\mathcal{E}_0|^2 b_0 c_0 \left\{ \left( \cos(\omega_{12}\tau_p + \phi_{12}) \text{Im}[\tilde{Q}_{1,\epsilon,j}^* K_{\epsilon,j}] \right) - \sin(\omega_{01}\tau_p + \phi_{01}) \text{Re}[\tilde{Q}_{1,\epsilon}^* K_{\epsilon,j}] \right\} \\
 & \quad + \mathcal{E}_0 |\mathcal{E}_0|^2 a_0 b_0 \left\{ \left( \cos(\omega_{01}\tau_p + \phi_{01}) \text{Im}[G_{1,\epsilon,j}^* F_{\epsilon,j}] \right) - \sin(\omega_{01}\tau_p + \phi_{01}) \text{Re}[G_{1,\epsilon}^* F_{\epsilon,j}] \right\} \\
 & \quad + \mathcal{E}_0 |\mathcal{E}_0|^2 a_0 b_0 \left\{ \left( \cos(\omega_{02}\tau_p + \phi_{02}) \text{Im}[G_{1,\epsilon,j}^* M_{\epsilon,j}] \right) - \sin(\omega_{02}\tau_p + \phi_{02}) \text{Re}[G_{1,\epsilon}^* M_{\epsilon,j}] \right\},
 \end{aligned}$$

where  $\tilde{Q}_{1,\epsilon,j}$ ,  $K_{\epsilon,j}$ ,  $G_{1,\epsilon,j}$ , *etc.* contain the product of terms describing first and second order processes. Among these terms, only  $\tilde{Q}_{1,\epsilon,j}$  appearing in the first line of the rhs in the above equation vanishes if the PNC potential is not included in the equations of motion.

### Isolating the PNC signature

Having defined each term appearing in Eq. (11.30), we now present the strategy that allows to isolate the PNC effect from that due to the parity mixing mediated by the electric field. For the present discussion, we will assemble all contributing terms appearing in Eq. (11.30) into three relevant terms that we have conveniently defined in Eqs. (11.35), (11.38) and (11.40). These three terms together define the d-wave component of the photoelectron spectrum defined in Eq. (11.30), and their individual contribution to the latter is represented in a schematic form in Fig. 11.1. In detail, we first note, according to Eq. (11.35), (11.38) and (11.40), together with Eq. (11.30), that the d-wave components

of the total yield oscillates periodically as a function of the pump-to-probe time delay,  $\tau_p$ , i.e.  $\sigma_d(t_f) = \sigma_d(t_f; \tau_p)$ , with specific frequency components. The spectral analysis of the oscillatory time-delay dependent signal reveals the signature of the **PNC effect** as well as that due to the electric dipole coupling. In detail, if a discrete Fourier transform of such a signal is performed<sup>8</sup>, one should expect, according to the first and second lines in Eq. (11.35), to find small Fourier peaks precisely at  $\omega_{10} = \varepsilon_{P_{1/2}}^{n_1} - \varepsilon_{S_{1/2}}^{n_0}$ , and  $\omega_{20} = \varepsilon_{P_{3/2}}^{n_2} - \varepsilon_{S_{1/2}}^{n_0}$ , which would be a clear evidence of the fingerprints of the PNC effect. Indeed, these peaks disappear if  $|\widetilde{6S_{1/2}}\rangle = |6S_{1/2}\rangle$ . The other peak at  $\omega_{21} = \varepsilon_{P_{3/2}}^{n_2} - \varepsilon_{P_{1/2}}^{n_1}$  will be found if both  $P_{1/2}$  and  $P_{3/2}$  states are prepared by the pump pulse. The peak at  $\omega_{21}$  is the signature of the standard one-photon transition from each of the P states to the *d-continuum* caused by the E1 dipole transition.

As for the second relevant term in Eq. (11.30), namely  $|d_{\epsilon,j}^{(2)}(t_f)|^2$ , it also contributes, although to a weaker extent, to the peaks at  $\omega_{10}$  and  $\omega_{20}$ . This can be clearly seen in Eq. (11.38) and (11.39). These contributions are attributed to the “forbidden” second order processes. The above observations concerning the peak contributions arising from the term  $|d_{\epsilon,j}^{(1)}(\tau_p)|^2$  together with those due to  $|d_{\epsilon,j}^{(2)}(\tau_p)|^2$  are schematically depicted in Fig. 11.1(a). The small peaks at  $\omega_p = \varepsilon_{P_{1/2}}^{n_1} - \varepsilon_{S_{1/2}}^{n_0}$  and at  $\omega_p = \varepsilon_{P_{3/2}}^{n_2} - \varepsilon_{S_{1/2}}^{n_0}$  in Fig. (11.1)(a) are entirely due to the PNC Hamiltonian. The large peak at much lower frequency  $\omega_p = \varepsilon_{P_{3/2}}^{n_2} - \varepsilon_{P_{1/2}}^{n_1}$ , is, according to Eq. (11.35), the signature of the parity mixing due to the electric component of the electromagnetic field.

The peak contribution due to the mixed terms, cf. Eq. (11.40) is schematized in Fig. 11.1(b). The terms  $d_{\epsilon,j}^{(1)*}(t_f; \tau_p)d_{\epsilon,j}^{(2)}(t_f; \tau_p) + cc$ , which describe the two-photon absorption process from the P states to the *d-continuum*, contribute in the opposite way. This is, the corresponding peak due to the PNC is now located at  $\omega_p = \varepsilon_{P_{3/2}}^{n_2} - \varepsilon_{P_{1/2}}^{n_1}$ , while the signature of the coupling due to the laser field is now manifested at the (more prominent) peaks  $\omega_p = \varepsilon_{P_{1/2}}^{n_1} - \varepsilon_{S_{1/2}}^{n_0}$  and  $\omega_p = \varepsilon_{P_{3/2}}^{n_2} - \varepsilon_{S_{1/2}}^{n_0}$ .

The effective final peak distribution is obtained by adding up the individual contributions depicted in Fig. 11.1(a) and Fig. 11.1(b). This gives rise to an overlap between peaks arising from different mechanisms, namely the parity mixing due to the driving electric field, and the negligible PNC induced admixture of different parity states. Due to small magnitude of the PNC effect, such peak overlap is detrimental for direct detection of the PNC effect alone, since the contribution associated to the PNC effect is overshadowed by the peaks associated to the electric field when both contributions (left and right panels in Fig. 11.1) are combined.

<sup>8</sup> assuming that the sampling rate, i.e.  $\tau_{p+1} - \tau_p$ , fulfills the **Nyquist-Shannon sampling theorem**, this is  $\tau_{p+1} - \tau_p \leq 1/2\nu_{max}$ , where  $\nu_{max} = \omega_{max}/2\pi$  is the highest frequency component of the signal to be properly resolved

To remedy this, let us rewrite Eq. (11.30) in the following way,

$$\sigma_d(t_f; \tau_p) = \sigma_d^{(1)} + \sigma_d^{(2)} + \sigma_d^{(1,2)}, \quad (11.41)$$

where we have defined

$$\sigma_d^{(1)} + \sigma_d^{(2)} = \sum_j \int_0^{+\infty} \left\{ |d_{\epsilon,j}^{(1)}(t_f)|^2 + |d_{\epsilon,j}^{(2)}(t_f)|^2 \right\} \quad (11.42a)$$

and

$$\sigma_d^{(1,2)} = \sum_j \int_0^{+\infty} \left\{ d_{\epsilon,j}^{(1)*}(t_f) d_{\epsilon,j}^{(2)}(t_f) + d_{\epsilon,j}^{(1)}(t_f) d_{\epsilon,j}^{(2)*}(t_f) \right\}. \quad (11.42b)$$

The strategy is to separate the peaks due to  $|d_{\epsilon,j}^{(1)}(t_f)|^2 + |d_{\epsilon,j}^{(2)}(t_f)|^2$  and those arising from of the mixed terms  $d^{(1)*}(t_f)d^{(2)}(t_f) + d^{(1)}(t_f)d^{(2)*}(t_f)$ , cf. Fig. 11.1. This implies separation of  $\sigma_d^{(1)} + \sigma_d^{(2)}$  and  $\sigma_d^{(1,2)}$ . Furthermore, it is necessary, for the purpose of experimental realization, to translate such a separation into a physical observable. Separation of the peak contribution due to the terms  $\sigma_d^{(1)} + \sigma_d^{(2)}$ , cf. Fig. 11.1(a), while fulfilling the observable requirement is achieved by noticing that, for a given  $\tau_p$ ,

$$\begin{aligned} \sigma_d^{\text{PNC}}(\tau_p) &\equiv \sigma_d^{(1)}(\tau_p) + \sigma_d^{(2)}(\tau_p) \\ &= \frac{1}{2} \left[ \sigma_d(\tau_p; \mathcal{E}_0) + \sigma_d(\tau_p; -\mathcal{E}_0) \right], \end{aligned} \quad (11.43)$$

where  $\sigma_d(\tau_p; \pm\mathcal{E}_0) = \sigma_d(t_f; \tau_p; \pm\mathcal{E}_0)$  refers to  $d$ -wave component of the total yield for which the probe pulse has a peak amplitude of  $\pm\mathcal{E}_0$ , respectively.

By construction,  $\sigma_d^{(1)}(\tau_p) + \sigma_d^{(2)}(\tau_p)$  in Eq. (11.43) is the quantity that is obtained by adding the  $d$ -wave components of the total yield,  $\sigma_d(\tau_p)$  obtained under electric field reversal. This erases all information from **regular dipole** external field induced second order processes which manifest themselves in Fourier components located at the same peak position as those originating from the PNC effect.

Conversely, we may want to isolate the peak contribution due to  $\sigma_d^{(1,2)}(t_f) = \sigma_d^{(1,2)}(t_f; \tau_p)$ , cf. Fig. 11.1(b), while fulfilling the observable requirement. This can be achieved by subtracting the  $d$ -wave components of the total yield  $\sigma_d(t_f)$  obtained with electric field reversal, namely

$$\sigma_d^{(1,2)}(\tau_p) = \frac{1}{2} \left[ \sigma_d(\tau_p; \mathcal{E}_0) - \sigma_d(\tau_p; -\mathcal{E}_0) \right]. \quad (11.44)$$

Given that the expression in Eq. (11.44) is proportional of the matrix elements for two-

photon absorption, is preferable to measure the observable defined in Eq. (11.43), which is proportional to the larger one-photon transition matrix elements, as can be seen from Eq. (11.35).

#### 11.4.5 Effects of second-order processes to the total yield

So far, we have restricted our discussion to the impact of the PNC on the  $d$ -wave component of the photoelectron spectrum and how to isolate the PNC effect from the laser-induced admixture between different parity states.

The motivation behind this approach relies on the fact that due to  $\hat{\mathbf{h}}_{pv}$ , the perturbed  $|\widetilde{6S_{1/2}}\rangle$  state can be weakly coupled to the  $d$ -continuum via one-photon absorption. However, it is apparent from Eq. (11.32) that the perturbed  $|\widetilde{6S_{1/2}}\rangle$  ground state can also be excited to the (perturbed)  $S$ -continuum states by the same one-photon absorption mechanism. Thus, one-photon processes reveal not only the fingerprints of the PNC imprinted in  $d$ -wave component of the photoelectron spectrum, but also in the  $s$ -component of the latter. These two one-photon absorption mediated mechanisms are schematically depicted by the segments  $|\widetilde{n_oS}\rangle \rightarrow |\widetilde{\epsilon D}\rangle$  and  $|\widetilde{n_oS}\rangle \rightarrow |\widetilde{\epsilon S}\rangle$  in Fig 11.2, respectively. It is also to note that not only the perturbed  $|\widetilde{n_oS}\rangle$  can be coupled to the  $|\epsilon D\rangle$  continuum state, but also to the  $|nD\rangle$  bound state, which in turn can be

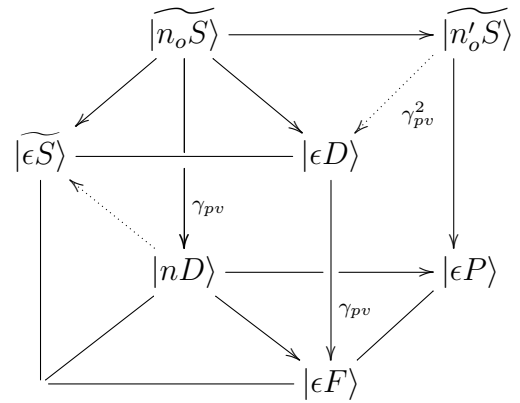


Figure 11.2: **First and second order processes:** "Forbidden" bound-continuum and bound-bound transitions due the  $\hat{\mathbf{h}}_{pv}$  potential. The "forbidden" bound-bound transitions are utilized by the regular dipole allowed transition to populate different wave-components of the continuum spectrum.

excited via the regular electric dipole allowed transition to the  $|\epsilon F\rangle$  and  $|\epsilon P\rangle$  continuum states. These processes are illustrated by the segments  $|\widetilde{n_oS}\rangle \rightarrow |nD\rangle \rightarrow |\epsilon F\rangle$  and  $|\widetilde{n_oS}\rangle \rightarrow |nD\rangle \rightarrow |\epsilon P\rangle$  in Fig. 11.2, respectively. Hence, second order processes reveal the fingerprints of the PNC potential in the  $p$ - and  $f$ -wave components of the photoelectron spectrum.

As for the remaining relevant second order contribution, the perturbed ground state  $|\widetilde{n_oS}\rangle$  with  $n_o = 6$ , can be excited to different perturbed  $|\widetilde{nS}\rangle$  states with  $n_o \neq n$ , which in turn can be promoted to the  $|\epsilon P\rangle$  continuum i.e.  $|\widetilde{n_oS}\rangle \rightarrow |\widetilde{nS}\rangle \rightarrow |\epsilon P\rangle$ <sup>9</sup> in Fig. 11.2.

<sup>9</sup>It is straightforward to show that  $|\widetilde{nS}\rangle \rightarrow |\epsilon P\rangle$  is equivalent to  $|\widetilde{nS}\rangle \rightarrow |\epsilon P\rangle$  since  $\langle \widetilde{nS_{1/2}} | \hat{\mathbf{z}} | \epsilon P_j \rangle =$

These processes are all proportional to  $\gamma_{pv}$ <sup>10</sup>.

The effects on the total photoelectron yield will be confirmed by the non-perturbative numerical wave packet dynamics simulation in Section 11.4.6. In conclusion, the fingerprints of the PNC potential are ultimately imprinted not only in the  $s$ - and  $d$ -wave components of the photoelectron spectrum, but in all partial components of the latter. Thus, it is the entire yield,  $\sigma_{tot}(\tau_p)$  that contains the signature of the parity admixture due to  $\hat{\mathbf{h}}_{pv}$ , in particular when the intensity of the driving laser field is enough to generate second order processes. For much weaker fields, the signature is mainly contained in the  $s$ - and  $d$ - wave components of the photoelectron spectrum. However, since the amplitude of the oscillations arising from the relevant one-photon processes are proportional to  $|\mathcal{E}|^2$ , see e.g. Eq. (11.35), it is suitable, given the small amplitude of the parity admixture, to use moderate-to-intense laser fields to ionize the prepared wave packet. This allows to observe the PNC signature in the wave components of the photoelectron spectrum that are populated by higher-order processes.

To summarize, extraction and isolation of the fingerprints of the **PNC effect** is achieved by measuring the  $d$ -wave component of the photoelectron spectrum (or alternatively the total ionization yield) as a function of the pump-to-probe time delay. The stored data forms a finite sequence of equally-spaced samples. The condition for the time interval between two consecutive time delays  $\tau_p$  and  $\tau_{p+1}$  are assumed to fulfill the Nyquist-Shannon sampling theorem and will be given in Section 11.4.6. The procedure is repeated with electric field reversal for the probe pulse. Ultimately both time-delay-dependent signals obtained under electric field reversal are added up and Fourier transformed. Observation of the resulting peaks according to Fig. 11.1(a) irrevocably indicates observation of the **PNC effect**.

### 11.4.6 Numerical results

In the following, we apply the partial wave analysis of the photoelectron spectrum to the extraction of the PNC signature in the cesium atom. The electron dynamics is obtained by non-perturbative treatment of the Schrödinger equation. Numerical integration of the expansion coefficients in Eq. (11.21) is performed by means of the Chebyshev propagator [152].

As a first intermediate state in the pump-probe process, we consider resonant excitation at the **D2 line** in cesium. The pump pulse utilized in our numerical simulations consists of a  $\pi/2$  pulse with  $\Delta t_{FWHM} = 265$  fs. It allows to create the desired super-

---

$\langle S_{1/2} | \hat{\mathbf{z}} | \epsilon P_j \rangle + \mathcal{O}(|\gamma_{pv}|^2)$

<sup>10</sup>It is worth mentioning that other possible pathways are possible, for instance  $|\widetilde{n_o S}\rangle \rightarrow |\widetilde{n S}\rangle \rightarrow |\epsilon D\rangle$  and  $|\widetilde{n_o S}\rangle \rightarrow |\widetilde{n S}\rangle \rightarrow |\epsilon S\rangle$ . However, they are proportional to  $|\gamma_{pv}|^2$  and thus negligible

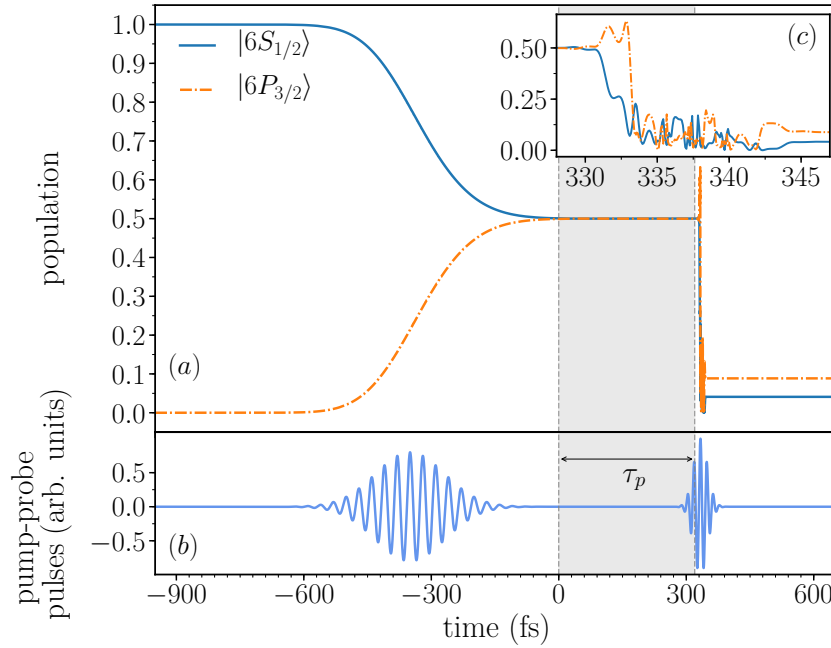


Figure 11.3: **Pump-probe spectroscopy:** The electron dynamics is started from the cesium  $\widetilde{|6S_{1/2}\rangle}$  ground state and the pump pulse prepares the wave packet as a coherent superposition of  $\widetilde{|6S_{1/2}\rangle}$  and  $\widetilde{|6P_{3/2}\rangle}$  states with equal probability (a). After a time-delay  $\tau_p$  the second pulse (b) ionizes the prepared wavepacket (c). The resulting continuum spectrum is further analyzed to extract the PNC signature. Pump and probe pulses not drawn to scale (b).

position after a time  $t_0 = (n + 1/2)\pi/\Omega_R$ , where  $\Omega_R = 2\mathcal{E}_0\langle 6P_{3/2}|\hat{\mathbf{z}}|6S_{1/2}\rangle$  refers to the Rabi frequency and where  $n$  is an integer that is chosen such that  $t_0 \geq 3\Delta t_{FWHM}$ , for a given  $\mathcal{E}_0$ . The numerical results concerning the preparation of the wave packet are shown in Fig. 11.3. The electron dynamics is simulated starting from the cesium ground state  $\widetilde{|6S_{1/2}\rangle}$ , cf. Fig. 11.3(a) and the pump-pulse interacts with the latter, cf. Fig. 11.3(b). After the pump pulse is over, the prepared state is in a coherent superposition of  $\widetilde{|6S_{1/2}\rangle}$  and  $\widetilde{|6P_{3/2}\rangle}$  states with equal probability. In fact, it is apparent from Eq. (11.35), that weights  $a_0 = c_0 = 1/\sqrt{2}$  maximize the amplitude of the oscillations. The impact of the relative phases will be discussed later. Finally, the probe pulse ionizes the prepared wave packet. At the end of the propagation, both ground and excited state are mostly depopulated, cf. 11.3(c) and the resulting photoelectron spectrum is scrutinized for extraction of the PNC signature, according to the protocol based on the time-dependent second order perturbation approximation previously described. To test the validity of our second order perturbation approach, the electron dynamics is simulated *with* and *without* the PNC potential. As suggested by the rhs of Eq. (11.43), for each time delay  $\tau_p$ , the contribution of the partial wave components to the total yield is evaluated with electric field reversals

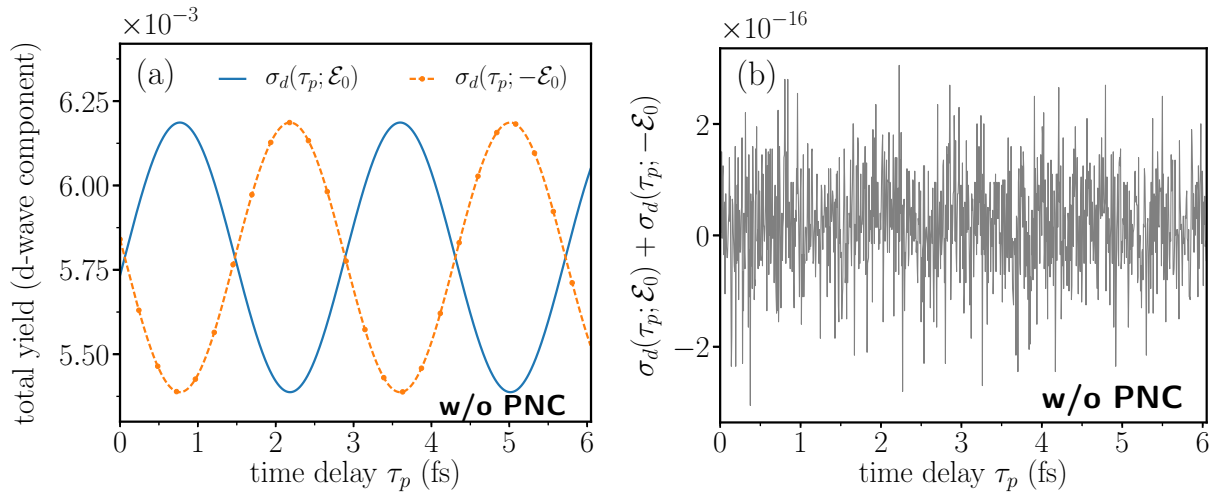


Figure 11.4: Exclusion of the PNC potential: Time-delay dependence of the sampled  $d$ -character of the total yield in (a). Combined signal obtained with field reversals in (b). Note the no oscillations are present if PNC potential is not included.

and added up. The sampling frequency is given by  $1/\Delta\tau_p$  with  $\Delta\tau_p = \tau_{p+1} - \tau_p \approx 0.012$  fs. The choice of the sampling rate is relevant and a good trade-off between required rate  $\Delta\tau$  and experimental feasibility should be made. For the chosen sampling rate, on one hand, the Nyquist-Shannon theorem allows to resolve frequencies up to  $\approx 170$  eV, well above  $\omega_p = \varepsilon_{P_{3/2}}^6 - \varepsilon_{S_{1/2}}^6 \approx 1.45$  eV, which corresponds to the frequency that, according to Fig. 11.1 we are looking for. On the other hand, such a time delay difference is experimentally achievable [347]. A short 10 fs (FWHM) probe pulse with maximal electric field amplitude  $\mathcal{E}_0 = 41$  GVm $^{-1}$  and circular frequency  $\omega = 2.7$  eV is utilized. The reason for such a short pulse will be motivated later.

Figure 11.4 summarizes the numerical results for which the PNC Hamiltonian is not included in the equations of motion. As previously discussed, oscillations in the observable  $\sigma_d(\tau_p; \pm\mathcal{E}_0)$  occur, even in the absence of the PNC potential, cf. Fig. 11.4(a). These oscillations correspond to the one- and two-photon processes that contribute to the population of the  $d$ -wave continuum. However, as shown in Fig. 11.4(b), the combination of the  $d$ -components of the yield obtained under field reversal results in a vanishing signal, well below the machine precision, just as expected.

The same calculation is now repeated with the **PNC potential**. The results are depicted in Fig. 11.5. Although the individual  $d$ -wave components  $\sigma_d(\tau_p; \mathcal{E}_0)$  and  $\sigma_d(\tau_p; -\mathcal{E}_0)$  resemble those obtained without  $\hat{\mathbf{h}}_{pv}$ , cf. Figs. 11.5(a) and 11.4(a), their combination under field reversal now shows, contrary to the previous case, a clear oscillatory structure, confirming the validity of the second order perturbation approach. The oscillatory behavior is shown in Fig. 11.5(b). A discrete Fourier transform of the combined signal, shown below, will confirm that the oscillations correspond to the frequency predicted by the second or-

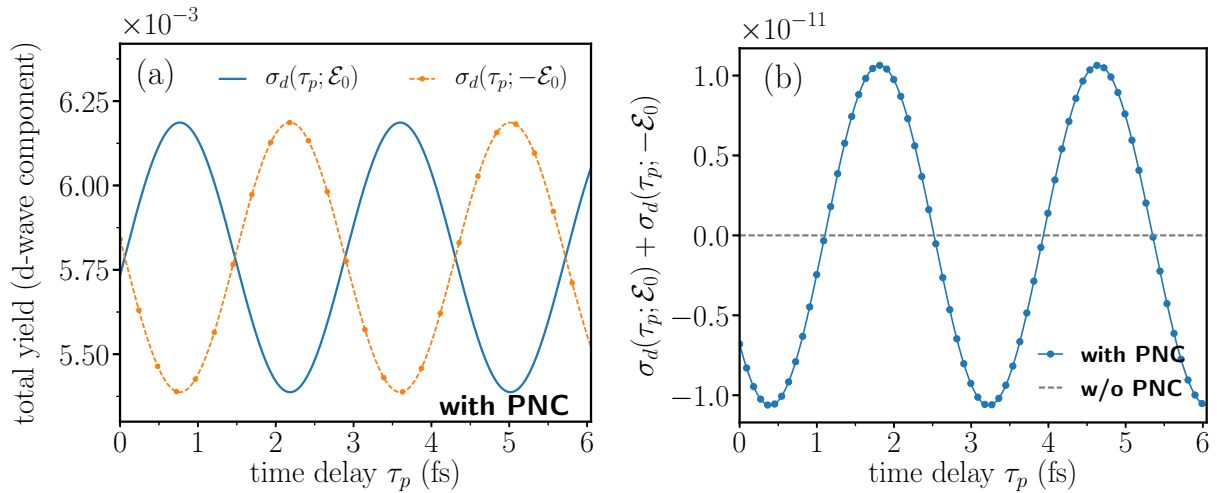


Figure 11.5: Inclusion of the PNC potential: Time-delay dependence of the sampled d-character of the total yield in (a). Combined signal obtained with field reversals in (b). Note the oscillations are only present if PNC potential is accounted for.

der approximation, namely  $\omega_{02}$ . Figure 11.5(b) also compares the combined signal under field reversal obtained with (blue-dotted lines) and without PNC (gray dashed lines). It is clear that the observed oscillations are a clear evidence of the **PNC interaction**. These numerical results reinforce the validity of the perturbative derivations outlined above. They also confirm the efficiency of the procedure based on the partial-wave analysis of the combined photoelectron spectrum under field reversal. Such a procedure, as confirmed by the numerical simulations, allows to eliminate the contribution, at the relevant peaks, originating from the regular dipole coupling due to the probe pulse and extract only the one of interest. Thus, the signature of the PNC potential is entirely extracted from the electron dynamics.

At this point, an important observation is worth being considered. According to Eq. (11.35), it is the **frequency components of the oscillations** in the combined signal  $\sigma_d(\tau_p; \mathcal{E}_0) + \sigma_d(\tau_p; -\mathcal{E}_0)$ , not its amplitude, that **unambiguously** defines the fingerprints of the **PNC effect**. In fact, the amplitude of the oscillations of the combined signal is not uniquely characterized by PNC but also depends on the driving time-dependent electric field. The peak positions, however, are field-independent<sup>11</sup>, and only depend on the states involved in the "prepared" wave packet. To expand this observation, let us consider Fig. 11.5(b). It is clear that the amplitude of the oscillations observed in Fig. 11.5(b) is rather small. This is largely, but not uniquely due to the weak strength of  $\hat{\mathbf{h}}_{pv}$  and the admixture contained in the term  $\text{Im}[\langle \epsilon d_j | \hat{\mathbf{z}} | n_0 S_{1/2} \rangle]$  in the rhs of Eq. (11.35), which is rather small. This small value, however, is multiplied by the integral factors defined in

<sup>11</sup>for a non-zero electric field and for a non-zero PNC effect, i.e.  $\gamma_{pv} \neq 0$

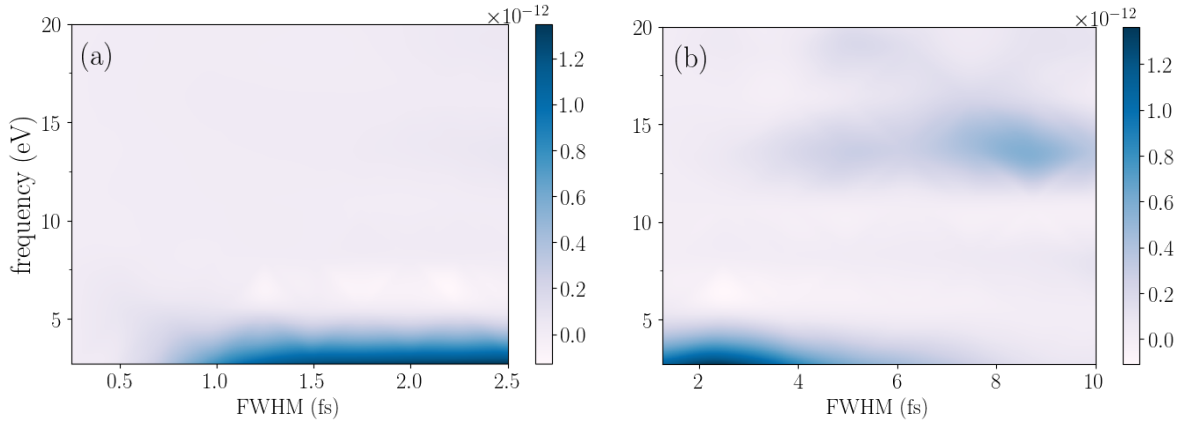


Figure 11.6: **Electric field parameters:** Amplitude of the oscillations due to the PNC interaction as a function of the driving electric field FWHM and circular frequency for a fixed maximal field amplitude of  $\mathcal{E}_0 = 7.65 \text{ GVm}^{-1}$  of the probe pulse. Short pulse durations at low photon energies increases the oscillation amplitude of the combined signal (a). For longer pulse durations (smaller spectral bandwidth) at higher photon energies, the amplitude of the PNC signal is weaker, which is detrimental to its observation. Conversely, a small enhancement can be obtained at photon energies lying in the 12 – 15 eV range for a pulse duration of FWHM of about 8 – 10 fs (b). The “best” field parameter are those for which both  $|6S_{1/2}\rangle$  and  $|\widetilde{6P_{3/2}}\rangle$  are ionized and thus contribute to the photoelectron spectrum.

Eqs. (11.37), which are field-dependent. Hence, it is the product of the PNC effect and the field-dependent integral in Eq. (11.35) that “*effectively and ultimately*” defines the amplitude of the oscillation. In this context, we can ask whether specific electric fields may ‘enhance’ the value of the integral factors so that the peak height in Fig. 11.5(b) is increased.

In a attempt to find a good choice for the electric field parameters that increase the amplitude of the oscillations in Eq. (11.43), we evaluate the amplitude as a function of the circular frequency, FWHM and maximal peak amplitude of the probe pulse. From Fig. 11.6 it is apparent that for a fixed peak field amplitude of  $\mathcal{E}_0 = 7.65 \text{ GVm}^{-1}$ , it is possible to enhance the chances for the observation the PNC effect by means of short pulses at low photon energies. A further analysis confirms that the best field parameters are those for which both  $|\widetilde{6S_{1/2}}\rangle$  and  $|\widetilde{6P_{3/2}}\rangle$  bound states defining the “*prepared*” wave packet are highly ionized via one-photon absorption. In fact, the spectrum of long pulses ( $> 6 \text{ fs}$ ) at high photon energies ( $> 5 \text{ eV}$ ) does not simultaneously overlap with the ionization energies of the ground  $|\widetilde{6S_{1/2}}\rangle$  and  $|\widetilde{6P_{3/2}}\rangle$  states. However, simultaneous ionization of both states is achieved by employing shorter pulses (broader spectrum) with FWHM ranging from 1 to 4 fs and photon energies up to  $< 5 \text{ eV}$ , which guarantees such an overlap. Consequently,

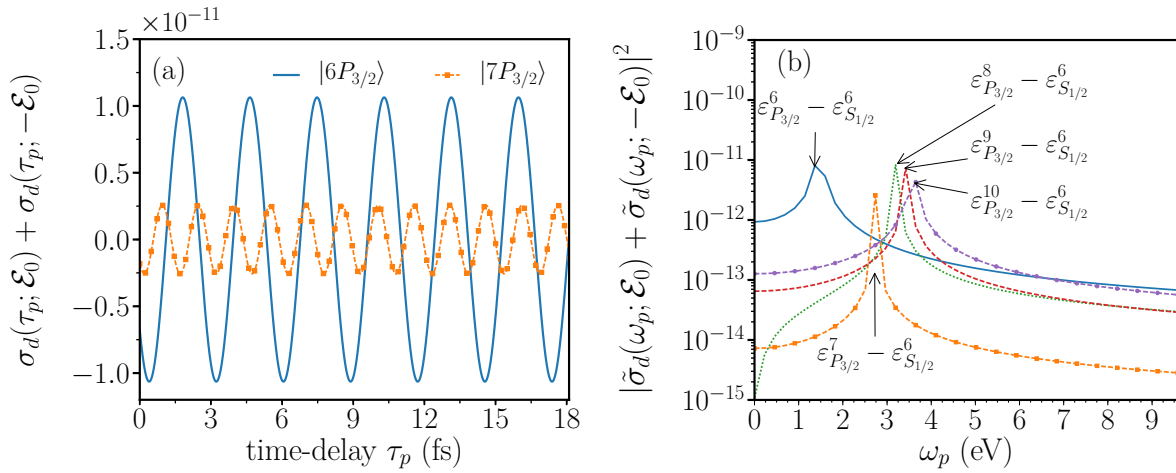


Figure 11.7: (a) Combined signal  $\sigma_d(\tau_p; \mathcal{E}_0) + \sigma_d(\tau_p; -\mathcal{E}_0)$  for a linear superposition between the states  $|6S_{1/2}\rangle$  and  $|6P_{3/2}\rangle$  (solid lines) and between the states  $|6S_{1/2}\rangle$  and  $|7P_{3/2}\rangle$  (dashed-dotted lines) for a fixed probe pulse. Spectral analysis of the combined signal for the different configurations for the prepared state  $|\psi_0\rangle = (|6S_{1/2}\rangle + |n_2P_{3/2}\rangle)\sqrt{2}$ , with  $n_2 = 6, 7, 8, 9$  and  $10$  in (b).

both states are ionized and thus contribute to the d-component of photoelectron spectrum via one-photon ionization. Ultimately, for shorter pulses (FWHM  $< 1$  fs), second order processes are favored, which weakens the strength of the relevant one-photon “forbidden” excitation to the d-continuum. In particular, this is detrimental to the “forbidden” *s-to-d* bound-continuum transition of interest. Therefore, intense and short (10 fs) femtosecond pulses at photon energies not exceeding 5 eV are used for the numerical calculations.

It is worth mentioning, however, that the enhancement due to the probe-pulse parameters eventually reaches a saturation limit, which is of course only determined by the magnitude of  $\gamma_{pv}$ , thus by the strength of  $\hat{\mathbf{h}}_{pv}$ , which depends on the atomic system under consideration. Note also that the numerical simulations for the pump-probe approach with the prepared state defined in Eq. (11.28) confirms the **linear dependence** on the PNC mixing amplitude predicted by the time-dependent second order perturbation approximation of the measured signal. Hence, the observation of the PNC effect in the photoelectron spectrum is only proportional to  $\gamma_{pv}$  for the case of the superposition in Eq. (11.28), instead of  $|\gamma_{pv}|^2$  which characterizes the one-photon ionization from the  $6S_{1/2}$  cesium ground state alone.

So far, a linear superposition between the states  $|n_0S_{1/2}\rangle$  and  $|n_2P_{3/2}\rangle$  with  $n_2 = n_0 = 6$  has been considered. In Fig. 11.7, the role of the  $|n_2P_{3/2}\rangle$  state in the linear superposition prepared by the pump pulse is further investigated. Figure 11.7(a) compares, for a fixed probe pulse, the amplitude and frequency of the oscillations for  $n_2 = 6$  and  $n_2 = 7$ . It is apparent that the amplitude of the oscillations is smaller for the  $n_2 = 7$  case and that

the corresponding signal oscillates faster compared to that related to the  $n_2 = 6$  case. The difference in amplitude can be explained by the characteristics of the pump field, as previously discussed. In fact the perturbed state  $\widetilde{|6S_{1/2}\rangle}$  is kept the same for both scenarios. Thus, changing  $|n_2P_{3/2}\rangle$  may reduce the efficiency of the probe pulse to ionize the  $|n_2P_{3/2}\rangle$  state, compared to the efficiency to ionize the  $n_2 = 6$  state.

However, the oscillation frequency is electric field-independent and only depends on the states involved in the linear superposition. In fact, the difference in frequency between the  $n_2 = 6$  and  $n_2 = 7$  in Fig. 11.7(a) is straightforwardly explained by the second order time-dependent perturbation approximation in Eq. (11.35), where the combined signal oscillates as a function of  $\sin((\varepsilon_{P_{3/2}}^{n_2} - \varepsilon_{S_{1/2}}^6)\tau_p)$ . The energy separation for both cases corresponds to  $\varepsilon_{P_{3/2}}^6 - \varepsilon_{S_{1/2}}^6 \approx 1.451$  eV and  $\varepsilon_{P_{3/2}}^7 - \varepsilon_{S_{1/2}}^6 \approx 2.712$  eV. Therefore, faster oscillations are expected for  $n_2 = 7$ , compared to the  $n_2 = 6$  case.

Analogously to the  $n_2 = 6$  case, the position of the peaks coincides with that predicted by the second order time-dependent perturbation theory. Also in Fig. 11.7(b) are shown different peak positions for several  $n_2$ . Every time, the peak position for different  $n_2$  obtained by numerical simulation coincides with that predicted by the our model. We also stress that the oscillations, and therefore the frequency components of the combined signal  $\sigma_d(\tau_p; \mathcal{E}_0) + \sigma_d(\tau_p; -\mathcal{E}_0)$  are completely absent when the PNC potential is not included in the total Hamiltonian. This is important in order exclude any possible contribution due to the admixture of different parity states induced by the electric component of the laser field. Hence, observation of such peaks at the *"right position"* is a clear and unambiguous indication of the observation of the **PNC effect**. As schematized in Fig. 11.2, the fingerprints of the PNC admixture revealed by **one-photon processes** are imprinted in the  $s$ - and  $d$  components of the photoelectron spectrum. In addition, the PNC interaction can also be revealed by higher order processes. When second order process becomes important,  $p$ - and  $f$ - wave components of the photoelectron spectrum also contain the signature of the PNC potential. Consequently it is not only the  $d$ -wave component but the entire yield that contains the signature of the PNC effect. This is confirmed by the non-perturbative numerical simulations shown in Fig. 11.8. In detail, Fig. 11.8(a) shows the time-delay-dependent  $s$ -wave component of the photoelectron spectrum (upper panel) and combined signal (lower panel). The latter is obtained by adding up the  $s$ -components obtained under electric field reversal. Analogously,  $d$ -wave components of the photoelectron spectrum, cf. Fig. 11.8(c), also contains the PNC fingerprints. Both  $s$ - and  $d$ - components of the total yield are revealed by one-photon absorption process.

For second order processes, the PNC signature are imprinted in the  $p$ - and  $f$ - components, as shown in Figs. 11.8(b),(d). As expected, these second-order-induced oscillations are smaller, although not vanishing, compared to the ones related to the one-photon ion-

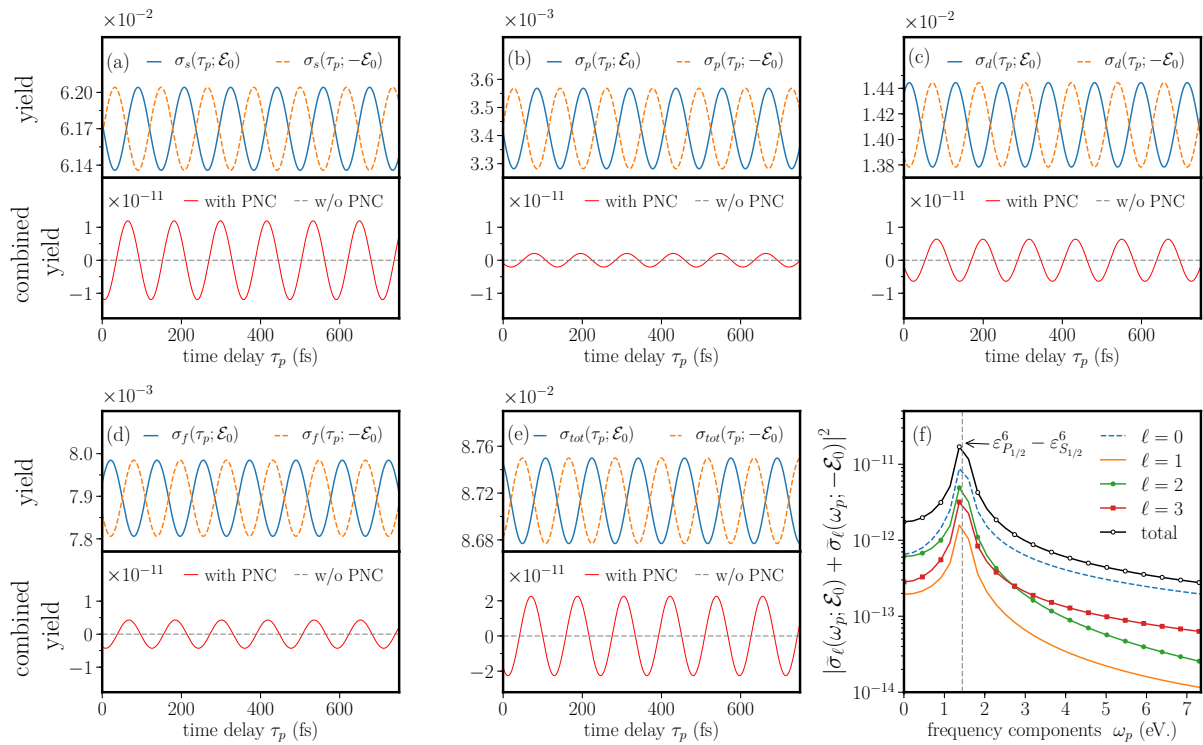


Figure 11.8: **Fingerprints of the PNC potential:** Partial  $s$ ,  $p$   $d$  and  $f$ –wave components of the time-delay dependent signal in the upper panels of (a),(b),(c) and (d), respectively. The corresponding lower panels show the combined signal obtained under electric field reversal. Fingerprints of the PNC admixture in the partial  $p$  and  $f$ –components are due to second order processes. Thus, it is the entire spectrum that reveals the information about the PNC potential, shown in (e), favoring the possibility of detection as the overall amplitude is increased. The peak position remains unchanged (f).

ization processes, cf. Figs. 11.8(a),(c). Consequently, the signature of the PNC admixture is contained in the entire spectrum, cf. Figs. 11.8(e). This favors the chances for experimental detection as the overall amplitude is increased compared to the  $d$ –component alone. Remarkably, the associated peak (frequency component) remains unchanged, as can be seen in Fig. 11.8(f), the latter being solely determined by the energy difference of the perturbed  $|6S_{1/2}\rangle$  and  $|6P_{3/2}\rangle$  states defining the prepared wave packet. These oscillations evanesce when the PNC potential is omitted from the Hamiltonian.

Finally, we consider a prepared wave packet consisting of a linear superposition involving all three terms in Eq. (11.28). According to Eq. (11.35), Eq. (11.38) and Fig. 11.1 the combined signal  $\sigma_d(\tau; \mathcal{E}_0) + \sigma_d(\tau; -\mathcal{E}_0)$  should be composed of three well defined frequency components. The lowest frequency corresponds to the energy difference  $\omega_p = \varepsilon_{P_{3/2}}^6 - \varepsilon_{P_{1/2}}^6 \approx 0.069$  eV and is the signature of mixture of different parity states caused by the field-induced E1 dipole transition between the S and P states. The higher

frequency components, on the other hand, are entirely due to the PNC potential and are located at  $\omega_p = \varepsilon_{P_{1/2}}^6 - \varepsilon_{S_{1/2}}^6 \approx 1.393$  eV and  $\omega_p = \varepsilon_{P_{3/2}}^6 - \varepsilon_{S_{1/2}}^6 \approx 1.462$  eV. The numerical results are depicted in Fig. 11.9. The “time-delay” dependence of  $\sigma_d(\tau_p; \pm\mathcal{E}_0)$  has a much more complicated structure due to the additional low frequency. The lower frequency of the combined data corresponds to the electric-field induced one-photon processes and thus its amplitude dominates the data. The remaining two higher frequencies are entirely due to the PNC effect and thus of considerably weaker amplitude. This observation is indeed observed in Fig. 11.9. Each peak position, characterizing the two different mechanisms, namely the allowed E1 one-photon processes and the parity admixture due to the PNC potential are centered at the positions predicted by the second order time-dependent perturbation theory. Compared to the mixture of different parity states induced by the electric field component of the laser field, the contribution due to the PNC potential is so weak that the oscillations of the three-frequency signal, cf. Fig. 11.9(b), dotted-red lines, are dominated by the contribution of the former. This is, the oscillations due to the PNC are overshadowed by the contribution due to the electric field and thus not appreciable at first glance. Only a frequency decomposition of the combined signal reveals the very small contribution due to the PNC potential, cf. Fig. 11.9(c).

We also note that the amplitude of the peaks associated to the PNC effect is roughly one order of magnitude smaller compared to the case defined by only two states in the prepared state. This can be explained by the weights involved in such a superposition, i.e.  $|\widetilde{6S_{1/2}}\rangle$  contributes less to the d-wave continuum component of the spectrum when more states are included in the prepared state. As alluded to the above, it is suitable to generate a pump pulse that prepares a wave packet consisting of a superposition of  $|\widetilde{6S_{1/2}}\rangle$  and  $|\widetilde{6P_{3/2}}\rangle$ , followed by a probe pulse that ionizes the prepared wave packet, making sure that both states in the superposition participate in the population of the continuum. Experimental feasibility of such superposition is nowadays achievable [348] and it is discussed more in detail in Section 11.6.

## 11.5 Relations and differences with previous proposals

Conceptually speaking, PNC-based experiments rely on the observation of the admixture of different parity states induced by weak neutral currents. Observation of such an effect is inferred from forbidden transitions that become weakly allowed due to the PNC potential. Such an observation is the building block of the Paris [325–328] and Boulder experiments [316, 329–331], as well as the principle for the measurement of parity violation energy difference in chiral molecules [321, 322, 332–334]. In this respect, our proposal also seeks for the detection of such a fingerprints, based on the detection of “forbidden”

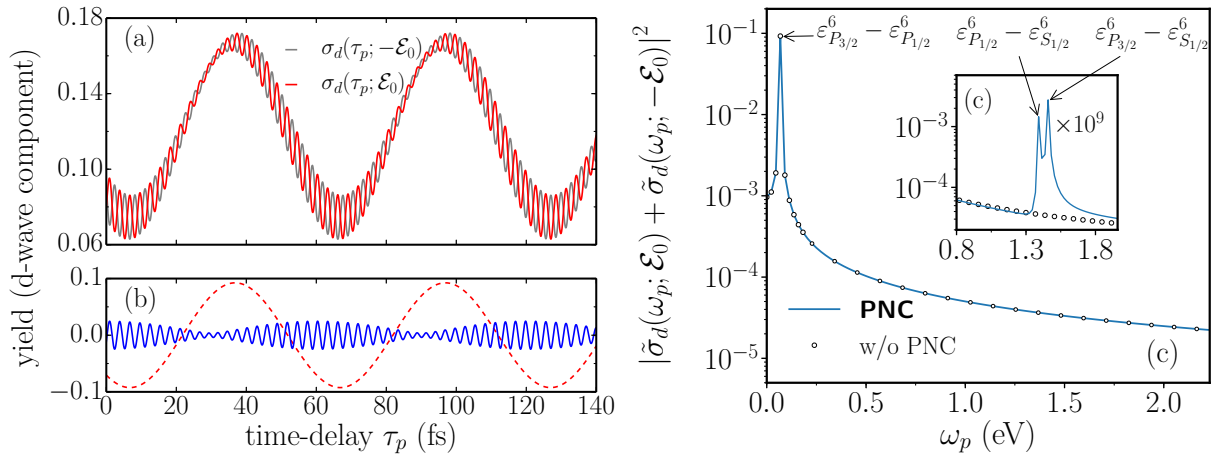


Figure 11.9: **Fingerprints of the PNC potential:** Time-delay dependent d-wave components of the total yield in (a). In panel (b), the dashed and filled lines corresponds to the added (Eq. (11.43)) and subtracted (Eq. (11.44)) signals obtained under field reversals, respectively. In (c) the spectral component of the added signal is depicted. The much larger peak at  $\varepsilon_{P_{3/2}}^6 - \varepsilon_{P_{1/2}}^6$  is due to the admixture induced by the electric field while the much smaller ones are the fingerprints of the PNC potential.

transitions, but utilizes a very different approach.

In comparison to the Paris experiment [325], that also utilizes cesium as prototype, our approach does not explicitly populate a forbidden transition via a “pump” pulse, nor infer such a forbidden population transfer from the change of polarization of the amplified pump pulse that follows the induced allowed transition as outlined in Section 11.1.2. Instead of looking at the polarization properties of the stimulated photon emission in a one-pump-probe step scheme, our approach is based on **time-resolved photoelectron spectroscopy** that extracts information about the PNC admixture based on the properties of the **photoelectron spectrum**.

With respect to the high-resolution spectroscopy approach proposed by Quack *et al.* [321, 322, 332–334], our approach shares a pump-to-probe delay measurement scheme. However, it does not utilize the probe pulse to explicitly populate a “forbidden” bound state nor seeks to infer the energy difference that results from the parity violating potential. Regarding this point, the implementation of this approach in the context of our proposal would be completely hopeless since the lowest order of the energy correction of the  $S_{1/2}$  and  $P_{1/2}$  states due to  $\hat{\mathbf{h}}_{pv}$ , scales as  $|\gamma_{pv}|^2$ . A further difference is that, due to the small value of  $\Delta_{pv}E$ , cf. Section 11.1.2, the period of parity change in Quack’s scheme is relatively large. Thus, that approach is limited by the inherent lifetimes that becomes relevant at the required time scales. Consequently, the latter scheme is restricted just to a few milliseconds time window and fit of the signal becomes unavoidable [321].

On the contrary, no fit procedure is required in the context of our approach. Instead, the limitation of our technique arises from the small magnitude of the amplitude of the PNC-induced oscillations, not from constraints imposed by the frequency of these small oscillations. Furthermore, detection of the PNC signature is inferred from specific frequency components of the photoelectron spectrum and a post-processing technique of the signal, consisting in adding up the time-delay-dependent yields obtained under electric field reversal is required to exclude the contributions arising from the parity admixture caused the driving field. Such a procedure is absent in Quack's approach.

In summary, our technique differs from the previous proposals but also contains a few common points from both approaches. With the Boulder and Paris experiments, it shares the field reversal technique to extract information about the PNC effect. Regarding this point, it is also worth mentioning that such a technique is widely utilized for the observation of dichroism in the photoelectron angular distribution, cf. Section 10. In this work, we have analytically shown why this technique works and gave an complementary solution for discriminating the contribution due to the electric field component of the laser field. With Quack's high-resolution approach for the extraction the the parity violating energy difference in chiral molecules, it shares the time-resolved pump-probe spectroscopy measurement principle. These already existent techniques, in conjunction with the photoelectron spectroscopy-based approach and signal analysis techniques here presented make our approach a complementary alternative for the detection of PNC effect in atomic and molecular systems.

## 11.6 Conclusions and outlook

In this work, we have investigated the effect of the parity violation on the photoelectron spectrum. Motivated by the Bouchiat's pioneering work, we have modeled the cesium atom and utilized it as paradigm system. Ultimately, we have theorized a pump-pump spectroscopy to identify and extract the signature of the parity violating weak interaction mediated by the exchange of weak neutral bosons between the electrons and the nucleus [318].

Due to this interaction, small admixture between different parity states occurs. The information about this admixture is contained in all bound and continuum states and can be transmitted by an outgoing photoelectron. Therefore, signature of PNC interaction can be extracted upon inspection of specific properties of the photoelectron spectrum.

However, the magnitude of such admixture (information) is so small that observation of the PNC effect is challenging for experimental detection. To circumvent this, we have approximated the time evolution of the prepared wavepacked using second-order

time-dependent perturbation theory and algebraic manipulations of the photoelectron spectrum-related quantities enabled us to separate the admixtures due to the PNC potential and those generated by the electric field component of the laser field.

The second order time-dependent approximation allowed us to understand how and why a pump-probe spectroscopy with a well defined “prepared” superposition of states allows to dramatically increase the hope for detecting the contribution due to the PNC potential. In the language of signal transmission, the auxiliary state, i.e. the  $|6P_{3/2}\rangle$  state, involved in the prepared superposition may be interpreted as a “carrier” that is modulated by the perturbed  $|\widetilde{6S_{1/2}}\rangle$  state which contains the (small) information of interest to be conveyed. In fact, as we have shown in our derivations, introducing the auxiliary state allows to write the d-wave component of the photoelectron as a function of  $\gamma_{pv}$  as leading term, instead of  $|\gamma_{pv}|$  alone while making the total yield time-delay dependent. The fingerprint of interest to be conveyed is the PNC interaction and is extracted from small frequency components in photoelectron spectrum as a function of the pump-to-probe time-delay. In this configuration, the pump-to-probe time-dependent “combined signal” defined as the combination of the total ionization signal obtained under field reversal for the *probe* pulse is characterized by an oscillatory behavior consisting of well defined frequencies. Such oscillations are absent if the PNC potential is omitted from the equations of motion. Thus, spectral analysis of the combined signal with observation of spectral components at well defined frequencies irrefutably indicates observation of the **PNC effect**.

Realization of a coherent superposition exclusively defined by the  $|\widetilde{6S_{1/2}}\rangle$  and  $|6P_{3/2}\rangle$  states in cesium with subsequent ionization is experimentally feasible using currently available experimental techniques. In a recent experimental work [348], a pump-probe technique using ultrafast laser pulses was performed for the experimental measurement of the cesium  $|6P_{3/2}\rangle$  lifetime. In this experiment, a 852 nm single mode-locked **pump pulse** was utilized to excite the  $|6P_{3/2}\rangle$  state from the ground state while keeping the excitation of  $|\widetilde{6P_{1/2}}\rangle$  negligible [348]. Ultimately, a frequency-doubled **probe pulse** served to ionize the population remaining in the  $|6P_{3/2}\rangle$  excited state. In the context of our proposal though, it is required that both ground and excited states to be ionized. This can be achieved by a broadband XUV pulse or by two phase-locked pulses that are spectrally more narrow.

An actual experimental setup of the proposal presented in this work can be accomplished by means of an ion-detection technique that allows to detect single ions generated as a by-product of the ionization process. To this end, we shall consider a high-repetition rate femtosecond-laser pulse interacting with a transversal cesium atomic beam, for instance, similar to the experimental setup in Ref. [348]. In detail, the *pump pulse* prepares

the state in the desired superposition while a broadband (or two phase-locked) ionizing *probe pulse*, delayed by  $\tau_p$ , ionizes the cesium atom while making sure that both states in the superposition contribute to the ionization signal. The resulting **photoions** are collected and counted. The detection sensitivity of such ion-detection technique is in practice limited by background signals [321]. To mitigate the background signal, a coincidence detection technique [349] may also be envisaged. However, this will require considerably larger times of signal accumulation. Given the small contribution to the ionization probability associated to the PNC potential, which is of the order of  $\sigma_{pv} \equiv 10^{-12}$ , a large number of counts per pulse repetition is needed in order to maintain the accumulation time, for a fixed pump-to-probe time-delay,  $\tau_p$ , reasonable. This demands high-repetition rate laser pulses as well as high-density atomic cesium beams. High-repetition rate femtosecond laser pulses at 1 GHz are commercially available [350]. Other laser sources with lower repetition rates can be used, depending on the spectral band needed. At such 1 GHz repetition rates, 100 ion counts per shot can be obtained with reasonable high-density cesium beams, along with an accumulation time of 2 min. Thus, in this configuration, there are 8 – 10 ion counts due to the PNC potential, for a total number of ion counts of  $\approx 10^{12}$ . These few PNC-induced ion counts oscillate as a function of the time-to-probe time-delay and can be isolated from the total number of events (total ion counts) by adding up the photoion signal obtained under electric field reversal. As shown in our numerical calculations, the period of these oscillations is of the order of  $T_{pv} = 1.45$  fs. Hence, a  $\delta\tau_p = 0.145$  fs time-delay step allows to construct a time-delay dependent signal containing 10 different points within the oscillation period  $T_{pv}$ . In this scenario, this is, for 10 time-delays, a total of  $\approx 20$  min of total signal accumulation is required for a single statistical measurement. The same procedure needs to be repeated under electric field reversal for the ionizing pulse. Adding up the time-dependent signals obtained under electric field reversal then reveals the oscillations in the combined signal predicted by our model. Specifically, the small number of counts that *"survive"* the addition of the photoion signal obtained under electric field reversal are due to the PNC potential and oscillate as a function of the pump-to-probe time-delay. The frequency components of the combined signal can be obtained by Fourier transforming the latter, and a single frequency component at  $\omega_{pv} = 1.49$  eV should be found for a superposition involving the  $|\widetilde{6S_{1/2}}\rangle$  and  $|6P_{3/2}\rangle$  states.

For the statistics, this sequence can be repeated  $N = 100$  times, which gives a partial count time of 34 hours. Repeating the procedure under field reversal would require a total of 68 hours of signal accumulation. In this scenario, the measurement error can be decreased by a factor of 10 as the uncertainty  $\sigma$  decreases as the squared root of  $N$ . Of course, a larger number of repetitions  $N$  will be required if the measurement

error is comparable to the mean of the measurement. If this is the case, the total time of signal accumulation can be drastically increased. Higher pulse-repetition rates and higher density atomic beams would considerably reduce the total accumulated count time for the measurements. To conclude, the technique presented in this work may be viewed as complementary approach for the detection of PNC effect in atomic and molecular systems.

# Summary and Outlook

This thesis covered the theoretical description, numerical simulation and quantum optimal control of the electron dynamics of complex systems in the multi-photon ionization regime. Among the most relevant contributions of this thesis, we have combined quantum optimal control theory and photoelectron spectroscopy to infer the underlying mechanisms that allow to manipulate a given photoelectron-related observable. To this end, we have constructed a non-exhaustive list of optimization functionals to control specific properties the photoelectron momentum distribution.

Numerical simulation of the electron dynamics of complex systems subject to strong ionizing pulses becomes computationally demanding, if not prohibited. Not only special techniques for time-propagation such as the wave function splitting method (WFSM) become unavoidable, but also the use of numerically efficient optimization algorithms is crucial. In this context, we have extended the monotonically convergent Krotov's optimization formalism to the WFSM. The resulting algorithm is designed to take into account the splitting procedure backwards in time, which is required to construct the Lagrange multiplier while ensuring the monotonically convergence of the algorithm. Importantly, also the optimization functionals are written in the context of the WFSM, this is, the final-time cost functionals do not depend on a specific target state, only the contribution of the outer parts needs to strategically be included in the functional. This allowed, for instance, to maximize the anisotropy of photoemission and rationalize the physical mechanism leading to such anisotropy. In this case, we have shown that the optimized pulses achieve the desired asymmetry by driving the dynamics in such a way that the photoelectron spectrum is composed of partial wave components which interfere constructively (destructively) in the upper (lower) hemisphere. Our optimization algorithm also takes into account specific constraints on the optimized field, such as frequency restriction and smoothness. This makes a substantial contribution for the optimal control of photoelectron spectroscopy.

To mitigate the numerical effort for propagation even further, we have developed a highly efficient multi-domain pseudospectral propagation approach for the solution of the time-dependent Schrödinger equation. Our approach is based on the efficiency of the well-

established FE-DVR and the Chebychev propagation formalism, which approximates the time-evolution operator as a polynomial series expansion in terms of the Chebychev polynomials. The propagation method then relies on the efficiency of numerical routines for sparse matrix-vector operations. For an optimal choice of the pseudospectral grid parameters, i.e. large number of grid points with small number of collocation points per element and large number of elements, our method outperforms the numerical performance of the Dynamical Fourier Grid Method for time propagation.

In the second part of this thesis, we have shifted the direction of our research from manipulating the photoelectron momentum distribution, to controlling the hole correlation dynamics. The motivation here was to minimize the decoherence between hole-states resulting from the transient interaction between the photoion and the outgoing photoelectron. The observable of interest concerned the degree of coherence between hole states, which defined the final-time cost functional to be maximized. In this case, however, the expression of the optimization functional does not allow the use of gradient-based optimization methods. In fact, the gradient cannot be either analytically nor numerically evaluated without compromising the stability of the optimization. Furthermore, the non-convex character of the functional strongly penalizes the efficiency of gradient-free methods. To circumvent the well known limitations of gradient-free optimization methods, we have introduced a sequential parametrization (SPa) update of the pulse parametrization which was implemented in the framework of the Brent's principal axis optimization method. In terms of efficiency, we have shown that the sequential update technique outperforms their non-sequential counterparts. For argon, our approach allowed to suppress the decoherence between the  $3s$  and  $3p_0$  hole states and to study the role of the intra- and interchannel couplings. Interestingly enough, the SPa technique allowed to find optimized pulses that completely suppress the decoherence even when the transient interchannel couplings are present. To rationalize our findings, we have study the photoelectron spectrum and identified that the mechanisms for hole-decoherence suppression correspond to two different scenarios: (i) three-photon ionization of the  $3s$  orbital simultaneously with two-photon ionization of the  $3p_0$  orbital for pulses with sufficiently large spectral bandwidth to render the photoelectrons energetically indistinguishable and (ii) one-photon ionization of the  $3p_0$  orbital combined with  $3s - 3p_0$  resonant excitation that fills the created  $3p_0$  hole. Motivated by these results, we have applied the SPa technique to the suppression of hole decoherence in xenon. In fact, the resonant excitation mechanism found in argon does not apply to the  $4d_0$  and  $5s$  channels in xenon due to the electric dipole selection rules. Furthermore, we have exploited the flexibility of the SPa technique to restrict the frequency components of the optimized pulses in order to avoid the "trivial" solution of reducing the interaction time between photoelectron and

ionic hole by increasing the photon energy as discussed elsewhere. In this case, the physical mechanism that allows to suppress the decoherence, almost completely, relies in the predominant ionization of  $4d_0$  and  $5s$  electrons into the same final electronic continuum state with  $p$ -character at low photoelectron energies. The mechanism is accomplished by appropriately combining one- and three-photon ionization of the  $5s$  and  $4d_0$ , respectively, while strongly suppressing single photon ionization of the  $4d_0$  to the  $f$  continuum since this process leads to decoherence. By construction, the optimized pulses produce predominantly slow photoelectrons which leave the photoion with low kinetic energies, in clear contrast to the “trivial case”. Thus, despite the limitations due to the non-convex character of the optimization functional, the SPa approach allowed to find an efficient control mechanism which exploits multi-photon ionization and leads to a noticeable suppression of the decoherence, even at low photoelectron kinetic energies.

In this work, we have also explored a non-exhaustive list of complementary applications of photoelectron spectroscopy. In particular, it can be applied to study the most fundamental properties arising from the spatial distribution of atoms in molecules as well as interactions at the sub-atomic level, such as molecular chiral activity and atomic parity violation effects. In the first case, the signature of chiral activity is reflected in the angular distribution of the emitted photoelectrons, which exhibits circular dichroism (CD). Resonantly enhanced multi-photon ionization is a well-established and appropriate tool to study CD since it allows to probe specific molecular states and thus rationalize the role of each of the resonantly excited states that contribute to the ionization process. However, the role of the intermediate excited state remains yet to be elucidated. Of course, interpretation of experimental observations in the context of photoelectron spectroscopy in gas phase requires sophisticated numerical techniques to fully describe the electron dynamics of the ionization process. However, at low ionizing photon energies, the dynamics, and thus the ionization process, can be approximated using perturbation techniques in the hope of interpreting the experimental observations. These observations typically concern symmetric and antisymmetric properties of the photoelectron angular distributions under enantiomer exchange or, alternatively, under helicity exchange (reversal). Among the contributions of this thesis, we have derived a theoretical model to study PECD after  $(2+1)$  resonantly enhanced multi-photon ionization in randomly oriented chiral molecules. Our model is based on a perturbative treatment of the light-matter interaction within the electric dipole approximation and relies on an *ab initio* description of the non-resonant two-photon absorption with a single-center expansion of the photoelectron wavefunction into hydrogenic continuum functions. Making heavily use of the symmetry properties of the Wigner rotation matrices appearing in the analytical expression of the Legendre coefficients, we have shown that the model correctly reproduces the basic symmetry behavior

expected under exchange of molecular handedness and light helicity. We have applied the formalism to fenchone and camphor and obtained semi-quantitative agreement with the experimental data. We have shown that a sufficient  $d$  wave character of the electronically excited intermediate state is crucial to reproduce the experimental observations, namely correct sign and order of magnitude of the Legendre coefficients while a  $f$  character allows to observe non-vanishing  $c_5$  coefficients. A first step towards coherent control of PECD requires a full time-dependent extension of the basic model presented here, or at least, inclusion of higher order terms in the perturbation expansion. This is essential in order to investigate the dependence of the photoelectron angular distribution on the laser-field parameters. Of the same importance is the multi-center character of the continuum wave function that should be accounted for by employing more sophisticated techniques such that, for instance, Dyson orbitals. Ultimately, an extension the light-matter interaction to beyond the electric dipole approximation should be envisaged and straightforward to implement for direct comparison with different levels of electronic structure theory.

The asymmetric response of matter to laser fields under electric field polarization reversal is not restricted to chiral molecules. In fact, a new application of photoelectron spectroscopy conceived in this thesis concerns the observation of atomic parity violation effects, that exploits such asymmetry of response under electric field reversal. Parity non-conservation (PNC) arises from the interference between the neutral weak and electromagnetic interactions induced by neutral currents. The current interpretation of the weak interaction relies in the exchange of weak neutral  $Z_0$  bosons between the electrons and the nucleus of the atom, leading to a mixture of atomic levels of different parity. In this thesis, we have shown that the information about the admixture of different parity states can be transmitted by the outgoing photoelectron and thus, signature of PNC interaction can be extracted upon inspection of specific properties of the photoelectron spectrum. We have shown that observation of PNC effects via photoelectron spectroscopy requires, however, a two-fold challenge to be faced. The first challenge concerns the extremely small magnitude of the admixture. In this regard, we have shown that any attempt to extract the signature of the PNC effect via ionization from the ground state is, in practice, hopeless. To dramatically increase the chances of detection, we have conceived a pump-probe spectroscopy approach. It is based on a strategical preparation of a wave packet consisting of a coherent superposition of well-defined field-free eigenstates, followed by ionization. The second challenge consists in separating the parity admixture due to the weak neutral currents and those induced by the ionizing electromagnetic field. To this end, we have approximated the electron dynamics of the prepared wave packet using second-order time-dependent perturbation theory and algebraic manipulations of the photoelectron spectrum obtained under electric field reversal enabled us to separate the

admixture due to the PNC potential and those generated by the electric field component of the laser field. Combination of the time-delay-dependent signal obtained under electric field reversal gives rise to small oscillations with well-defined frequency components that are only present if the PNC potential is included in the equations of motion. In order to test the predictions of our analytical formalism, we have performed a non-perturbative treatment of the electron dynamics by solving the time-dependent Schrödinger equation numerically, with and without the PNC potential. Indeed, oscillations as a function of the pump-to-probe time-delay are only observed if the PNC potential is included in the Hamiltonian and the spectral components coincide with those predicted by our analytical model. Furthermore, the oscillations vanish when the PNC potential is omitted from the equations of motion. Thus, spectral analysis of the combined signal with observation of spectral components at well defined frequencies irrefutably indicates observation of the PNC effect.

To conclude, this thesis provides a comprehensive framework of the systematic method developments conceived for the quantum optimal control of photoelectron spectroscopy. It also provides a detailed description of (i) the derivation of the models, (ii) the algorithms constructed to circumvent the limitations in terms of numerical efficiency encountered throughout this thesis as well as (iii) a non-exhaustive list of applications.

The results presented in this thesis required non-negligible effort that has been spent to extend the TDCIS method in the context of the gradient-based and gradient-free optimization methods developed to accomplish our optimization purposes, as well as development of a multi-domain pseudospectral propagation approach that allowed to push further the limits of the propagation efficiency. These techniques were implemented as part of XCID [253] and QDYN [351] Fortran 90 libraries, respectively.

The application of the tools described in this thesis is by far from being exhausted. On a long-term perspective, the range of applicability of these tools should be extended to beyond closed-shell atoms while improving the description of the electronic correlations: from open-shell atoms to molecular systems, which might enable to find new interesting mechanisms to achieve a desired outcome. From a control perspective, extension of the light-matter interaction to beyond the (simplistic) linear polarization scenario is the perfect candidate to study the effects of angular momentum mixing as well as of their magnetic quantum numbers due to the break of cylindrical symmetry about the light polarization axis. Last but not least, implementation of accurate and numerically efficient methods for the representation of the many-body continuum wave function is of great interest, particularly in the context of photoelectron spectroscopy and quantum control. In order to keep the calculation tractable in the framework of these implementations, a more efficient description of the many-body electronic structure as well as implementation

of numerically efficient propagation and optimization methods become unavoidable.

# Part III

## Appendix



# An efficient mapped pseudospectral method for solving the time-dependent Schrödinger equation

## A.1 Semi-global representation

Here, we derive a sparse representation of the Hamiltonian (7.11). It is based on domain decomposition, the variational or weak solution [168] of the Schrödinger equation, Lagrange interpolation, and polynomial series expansions of operators [78]. The concept of the local de Broglie wavelength, central to the mapped Fourier grid Hamiltonian [154–156], is used to determine the size of the domains. The pseudospectral multi-domain representation of the Hamiltonian is derived from the weak formulation of the Schrödinger equation in Section A.1.1. Within each domain, a Gauss-Lobatto-Legendre collocation is employed, as described in Section A.1.2, and a global representation of the Hamiltonian is derived in Section A.1.3 by assembling all domains.

### A.1.1 Multi-domain weak formulation

In order to derive a matrix representation of the Hamiltonian  $H_0$ , cf. Eq. (7.11), we consider the time-independent radial Schrödinger equation,

$$-\frac{\hbar^2}{2\mu}\nabla^2 u(r) + V(r)u(r) = \lambda u(r) \quad (\text{A.1})$$

with  $r \in \Omega = [r_{min}, r_{max}]$  and  $\lambda$  an eigenvalue. Note that a multi-dimensional problem may be mapped onto Eq. (A.1) by representing all degrees of freedom other than  $r$  in basis sets [92]. We employ domain decomposition for  $\Omega$ . The main idea behind this method

is to split the domain of (spatial) integration  $\Omega$  into  $M$  non-overlapping intervals  $\Omega_k$  of arbitrary size. The total domain,  $\Omega$ , is given by the union,

$$\Omega = \bigcup_{k=1}^M \Omega_k \text{ with } \Omega_k \cap \Omega_{k'} = \begin{cases} \{r_N^k\} & \text{if } k' = k + 1, \\ \emptyset & \text{otherwise,} \end{cases} \quad (\text{A.2})$$

where  $r_N^k = r_0^{k+1}$ . Each interval  $\Omega_k = [r_0^k, r_N^k]$  is discretized using  $N + 1$  points, and the constraint  $r_N^k = r_0^{k+1}$  ensures connection of all  $\Omega_k$ . Within each interval  $\Omega_k$ , Eq. (A.1) becomes

$$-\frac{\hbar^2}{2\mu} \nabla^2 u^k(r) + V(r)u^k(r) = \lambda u^k(r). \quad (\text{A.3})$$

In order to derive the weak solution of the Schrödinger equation for a given  $\Omega_k$ , we multiply both sides of Eq. (A.3) by an arbitrary test function  $v^k(r)$  defined on the Sobolev space  $H^1(\Omega^k) = \{\phi \in L^2(\Omega^k), \nabla \phi \in L^2(\Omega)\}$ . Integrating over the domain  $\Omega_k$  and applying Green's theorem, we find

$$\begin{aligned} -\frac{\hbar^2}{2\mu} \int_{\Omega_k} \nabla v^k(r) \nabla u^k(r) dr + \int_{\Omega_k} v^k(r) V(r) u^k(r) dr &+ \frac{\hbar^2}{2\mu} \oint_{\partial\Omega_k} v^k(r) \nabla_n u^k(r) d\Gamma \\ &= \lambda \int_{\Omega_k} v^k(r) u^k(r) dr, \end{aligned} \quad (\text{A.4})$$

where  $\nabla$  denotes the usual gradient and  $\nabla_n$  stands for the normal derivative. The solution  $u^k(r)$  satisfying Eq. (A.4) is called the *weak solution* on  $\Omega_k$ , as opposed to the strong solution, i.e.,  $u^k(r)$  satisfying Eq. (A.3). Note that  $u^k(x) \in H^1(\Omega_k)$ . It is obtained from

$$\begin{cases} a^k(u, v) = \lambda(u, v)_{\Omega_k} \\ u(r) = \tilde{u}(r) \quad \text{in} \quad \partial\Omega_k, \end{cases} \quad (\text{A.5a})$$

where  $\tilde{u}(r)$  stands for the boundary condition of  $u^k$  at the domain boundary,  $\partial\Omega_k$ , and the bilinear forms  $a^k(\cdot, \cdot)$  and  $(\cdot, \cdot)_{\Omega_k}$  are defined as

$$\begin{aligned} a^k(u, v) &= \frac{\hbar^2}{2\mu} \int_{\Omega_k} \nabla v^k(r) \nabla u^k(r) dr + \int_{\Omega_k} v^k(r) V^k(r) u^k(r) dr \\ &\quad + \frac{\hbar^2}{2\mu} \oint_{\partial\Omega_j} v^k(r) \nabla_n u^k(r) d\Gamma, \end{aligned} \quad (\text{A.5b})$$

$$(u, v)_{\Omega_k} = \int_{\Omega_k} u^k(r) v^k(r) dr. \quad (\text{A.5c})$$

In order to derive an explicit representation of the Hamiltonian from the weak formulation of the Schrödinger equation, we rewrite the bilinear forms as a linear operator equation in

dual space. To this end, we employ a Galerkin-type method based on piecewise cardinal functions with bounded support in  $\Omega_k$ ,  $\delta^k(r - r_j)$  where  $r_j \in \Omega_k$ .

### A.1.2 Gauss-Lobatto-Legendre collocation

Consider the vector space spanned by  $N + 1$  cardinal functions defined within  $\Omega_k$  and denote the set of basis functions by  $\{v_j^k\}_{j=0,\dots,N}$ . We can expand  $u^k(r)$  in this basis,

$$u^k(r) = \sum_{j=0}^N u^k(r_j) v_j^k(r) = \sum_{j=0}^N u^k(r_j) \delta^k(r - r_j). \quad (\text{A.6})$$

Inserting Eq. (A.6) into Eq. (A.4), multiplying both sides of Eq. (A.4) by one of the cardinal functions and integrating over  $\Omega_k$ , we obtain a set of  $N + 1$  algebraic equations,

$$\sum_{j=0}^N u_j^k a^k(v_i, v_j) = \lambda \sum_{j=0}^N u_j^k (v_i, v_j)_{\Omega_k}, \quad (\text{A.7})$$

where  $i = 0, \dots, N$ ,  $u_j^k = u^k(r_j)$  and  $r_j \in \Omega_k$  by construction.

In the particular case of a discrete variable representation [148], the expansion coefficients  $u^k(r_j)$  in Eq. (A.6) correspond to the wavefunction amplitudes at every collocation point, and the error is only due to the Gaussian quadrature approximation. In other words, in each domain  $\Omega_k$ ,  $u^k(r)$  is approximated at the collocation points by the interpolant in Eq. (A.6). Correspondingly, we can evaluate the integrals in Eq. (A.5b) by means of a Gaussian quadrature rule within each interval  $\Omega_k$ ,

$$\int_{\Omega_k} f(r) dr = \sum_{j=0}^N f^k(r_j) w_j^k. \quad (\text{A.8})$$

This leads to

$$a^k(v_i, v_j) \approx \frac{\hbar^2}{2\mu} \sum_{q=0}^N \nabla v_i^k(r_q) \nabla v_j^k(r_q) w_q^k + \sum_{j=0}^N v_i^k(r_q) V(r_q) v_j^k(r_q) w_q^k + \frac{\hbar^2}{2\mu} \left( \nabla u^k(r_0^k) \delta_{0,i} - \nabla u^k(r_N^k) \delta_{N,i} \right). \quad (\text{A.9a})$$

Using Gauss-Lobatto sampling points, i.e., sampling points that include the boundary of the domain  $\Omega_k$ , by definition  $v_i^k(r_0^k) = \delta_{0,i}$  and  $v_j^k(r_N^k) = \delta_{N,i}$  for  $k = 2, \dots, M - 1$ , i.e., for all domains except those containing  $r_{min}$  and  $r_{max}$ . Analogously, for Eq. (A.5c) we use

the discrete inner product in  $\Omega_k$  which is given by

$$(v_i, v_j)_{\Omega_k} \approx \sum_{q=0}^N w_i^k(r_q) v_j^k(r_q) w_q^k = w_i^k \delta_{i,j}. \quad (\text{A.9b})$$

We employ Gaussian quadrature based on Legendre polynomials. Since Legendre polynomials are defined on the interval  $\Lambda = [-1, 1]$ , we need an affine transformation,

$$\begin{aligned} \Phi^k &: \Lambda \longrightarrow \Omega_k \\ \xi_i &\longmapsto \xi_i (r_N^k - r_0^k) / 2 + (r_N^k + r_0^k) / 2 \end{aligned} \quad (\text{A.10a})$$

with Jacobian

$$\mathcal{J}_k = (r_N^k - r_0^k) / 2 \quad (\text{A.10b})$$

and  $\xi_i$  the standard Gauss-Lobatto-Legendre sampling points, cf. Eq. (A.31). Integration in  $\Omega_k$  can then be directly connected to integration in  $\Lambda$ ,

$$\int_{\Omega_k} f(r) dr = \int_{-1}^{+1} f \circ \Phi^k(\xi) \mathcal{J}_k d\xi = \mathcal{J}_k \sum_{j=0}^N f(r_j) w_j^\Lambda.$$

Comparing this to Eq. (A.8), we obtain

$$w_j^k = \mathcal{J}_k w_j^\Lambda \quad (\text{A.11})$$

with  $w_j^\Lambda$  that standard Legendre quadrature weights, cf. Eq. (A.31).

Next, we evaluate the derivatives in Eq. (A.9a) in terms of derivatives of the cardinal functions,

$$\frac{\partial}{\partial r} f^k(r) = \sum_{j=0}^N f(r_j) \frac{\partial}{\partial r} \delta^k(r - r_j). \quad (\text{A.12})$$

The first order differentiation matrix for Legendre cardinal functions reads [78]

$$\frac{\partial}{\partial \xi} \delta^{(\Lambda)}(\xi_i - \xi_j) = \begin{cases} -N(N+1)/4 & \text{if } i = j = 0 \\ N(N+1)/4 & \text{if } i = j = N \\ 0 & \text{if } 1 \leq i = j \leq N-1 \\ \frac{L_N(\xi_i)}{L_N(\xi_j)(\xi_i - \xi_j)} & \text{if } j \neq i. \end{cases} \quad (\text{A.13})$$

This can be easily checked using the properties of the Legendre polynomials and the cardinal functions, cf. Appendix A.3. Together with the affine transformation (A.10), Eq. (A.13) allows to determine the derivatives in Eq. (A.9a) with an error that is solely due to the Gaussian quadrature approximation. Moreover, a useful expression to evaluate the first term in Eq. (A.9a), i.e., to construct the matrix representation of the kinetic operator, is given by

$$S_{\mu,\nu}^k = \int_{\Omega_k} \frac{\partial}{\partial r} \delta^k(r - r_\mu) \frac{\partial}{\partial r} \delta^k(r - r_\nu) dr^k$$

with  $\mu, \nu = 0, \dots, N$ . It is straightforward to show that

$$S_{\mu,\nu}^k = \mathcal{J}_k^{-1} S_{\mu,\nu}^\Lambda,$$

where

$$\begin{aligned} S_{\mu,\nu}^\Lambda &= \int_\Lambda \frac{\partial}{\partial \xi} \delta^\Lambda(\xi - \xi_\mu) \frac{\partial}{\partial \xi} \delta^\Lambda(\xi - \xi_\nu) d\xi \\ &\approx \sum_{j=0}^N \frac{\partial}{\partial \xi} \delta^\Lambda(\xi_j - \xi_\mu) \frac{\partial}{\partial \xi} \delta^\Lambda(\xi_j - \xi_\nu) w_j^\Lambda \end{aligned} \quad (\text{A.14})$$

and the first order differentiation matrix elements,  $\frac{\partial}{\partial \xi} \delta^\Lambda(\xi_i - \xi_j)$ , are given in Eq. (A.13).

Recall that at the Gauss-Lobatto-Legendre points, the cardinal functions obey

$$\delta^k(r_i - r_j) = \delta_{i,j},$$

where  $\delta_{i,j}$  stands for the Kronecker delta, cf. Eq. (A.34). This, together with Eq. (A.14), yields the following algebraic expression for the weak form of the Schrödinger equation, Eq. (A.7), within the interval  $\Omega_k$ ,

$$\begin{aligned} \sum_{j=0}^N u_j^k \left( \frac{\hbar^2}{2\mu} \mathcal{J}_k^{-1} S_{i,j}^\Lambda + V(r_j) \delta_{i,j} w_j^k \right) + \frac{\hbar^2}{2\mu} \nabla u(r_0^k) \delta_{0,i} - \frac{\hbar^2}{2\mu} \nabla u(r_N^k) \delta_{N,i} \\ = \lambda \sum_{i=0}^N u^k(r_i) w_j^k \delta_{i,j}. \end{aligned} \quad (\text{A.15})$$

### A.1.3 Global representation

An algebraic expression for the Schrödinger equation (A.1) in the complete spatial domain and thus a matrix representation of the Hamiltonian is obtained by assembling all intervals  $\Omega_k$ . Since  $\Omega = \bigcup_{k=1}^M \Omega_k$ , this can simply be done by adding the multi-domain bilinear forms

defined in Eqs. (A.5),

$$a(u, v) = \sum_{k=1}^M a^k(u, v),$$

$$\lambda(u, v) = \sum_{k=1}^M \lambda(u, v)_{\Omega_k},$$

provided that the correct boundary conditions are ensured at the intersection of two contiguous elements,

$$r_N^k = r_0^{k+1}, \quad (\text{A.16a})$$

$$u^k(r_N^k) = u^{k+1}(r_0^{k+1}), \quad (\text{A.16b})$$

$$\nabla u^k(r) \Big|_{r=r_N^k} = \nabla u^{k+1}(r) \Big|_{r=r_0^{k+1}}. \quad (\text{A.16c})$$

Continuity and differentiability of the global solution need to be enforced since the global cardinal basis, defined as  $v^k(r - r_N^k) \cup v^{k+1}(r - r_0^{k+1})$ , is not differentiable at the  $M - 1$  interelement points. Consider the sum of  $a^k(u, v)$  for two contiguous elements,

$$a^k(u^k, v^k) + a^{k+1}(u^{k+1}, v^{k+1}) = \frac{\hbar^2}{2\mu} \int_{\Omega_k} \nabla u^k(r) \nabla v^k(r) dr + b_{\Omega_k \cup \Omega_{k+1}} \quad (\text{A.17})$$

$$+ \frac{\hbar^2}{2\mu} \int_{\Omega_{k+1}} \nabla u^{k+1}(r) \nabla v^{k+1}(r) dr$$

$$+ \frac{\hbar^2}{2\mu} \left( v^k(r_0^k) \nabla u^k(r_0^k) - v^{k+1}(r_N^{k+1}) \nabla u^{k+1}(r_N^{k+1}) \right)$$

$$+ \frac{\hbar^2}{2\mu} \left( v^{k+1}(r_0^{k+1}) \nabla u^{k+1}(r_0^{k+1}) - v^k(r_N^k) \nabla u^k(r_N^k) \right),$$

where we have defined

$$b_{\Omega_k \cup \Omega_{k+1}} = b^k(u^k, v^k) + b^{k+1}(u^{k+1}, v^{k+1}) \quad \text{with} \quad b^k(u^k, v^k) = \int_{\Omega_k} u^k(r) V(r) v^k(r) dr.$$

For the bilinear form  $a(u, v)$ , resulting from the integration by parts [89, 91], the condition of differentiability implies that the last term in Eq. (A.18) vanishes. Thus, when adding the bilinear forms for all intervals  $\Omega_k$ , the interelement boundary conditions cancel out, as desired.

Analogously to Eq. (A.16) for the bilinear forms, we introduce the global interpolant  $u(r)$  as

$$u(r) = \sum_{k=1}^M u^k(r) = \sum_{k=1}^M \sum_{j=0}^N u^k(r_j^k) v_j^k(r). \quad (\text{A.18})$$

Then, just as the basis set expansion of  $u^k(r)$ , Eq. (A.6), has led to  $N + 1$  algebraic equations within the interval  $\Omega_k$ , Eq. (A.18) results in  $M \times (N + 1)$  algebraic equations for the total domain  $\Omega$ ,

$$\sum_{k=1}^M \sum_{k'=1}^M \sum_{j=0}^N u_j^{k'} a^k(v_j^{k'}, v_i^q) = \lambda \sum_{k=1}^M \sum_{k'=1}^M \sum_{j=0}^N u_j^{k'} (v_j^{k'}, v_i^q)_{\Omega_k} \quad (\text{A.19})$$

with  $i = 0, \dots, N$ ,  $q = 1, \dots, M$ . Note that the subscripts  $i, j$  run over the collocation points whereas the superscripts  $k, k', q$  indicate the intervals. Since the cardinal functions  $\delta^k(r - r_j)$  are non-zero only within their own interval  $\Omega_k$ , we obtain

$$a^k(v_j^p, v_i^q) = a^k(v_j^k, v_i^k) \delta_{k,p} \delta_{p,q} \quad (\text{A.20})$$

and

$$(v_j^p, v_i^q)_{\Omega_k} = w_i^k \delta_{k,p} \delta_{p,q} \delta_{i,j}. \quad (\text{A.21})$$

Therefore, Eq. (A.19) takes the same form as Eq. (A.16) but with  $(N + 1) \times (M - 1)$  vanishing terms. In other words, the global representation, by construction, is equivalent to writing the elemental equation (A.16)  $M \times (N + 1)$  times, while accounting for the boundary conditions (A.16). Specifically, when adding the two algebraic equations for  $q = k, j = N$  and  $q = k + 1, j = 0$ , for  $k = 1, M - 1$ , in Eq. (A.19), the last (vanishing) term in Eq. (A.18) is retrieved at the  $M - 1$  connection points. We thus obtain a system of  $M \times (N + 1) - (M - 1) = N \times M + 1$  algebraic equations, in accordance with the number of collocation points in the global representation, i.e., without any repetition of points. Solving the linear system of equations (A.19) with the boundary conditions (A.16) is then equivalent to solving the generalized eigenvalue problem

$$A u = \lambda \mathcal{M}(w) u, \quad (\text{A.22})$$

where  $\mathcal{M}(w)$  is a  $(N \times M + 1) \times (N \times M + 1)$  diagonal matrix, referred to as the *global mass matrix*. Its matrix elements are given in terms of the Gaussian quadrature weights  $w_j^k$ , cf. Eq. (A.11),

$$\mathcal{M}_{i,i}(w) = \gamma_j^k(w), \quad i = N(k - 1) + j + 1, \quad (\text{A.23a})$$

with  $j = 0, \dots, N$ ,  $k = 1, \dots, M$ , and

$$\gamma_j^k(w) = \begin{cases} w_j^k & \text{if } k < M \text{ and } 0 < j < N, \\ w_N^k + w_0^{k+1} & \text{if } k \leq M \text{ and } j = 0, \\ w_N^{k-1} + w_0^k & \text{if } k < M \text{ and } j = N, \\ w_0^1 & \text{if } k = 1 \text{ and } j = 0, \\ w_N^M & \text{if } k = M \text{ and } j = N. \end{cases} \quad (\text{A.23b})$$

Note that the weights defined at the interelement points, i.e.,  $x_N^k$  and  $x_0^{k+1}$ , are defined as  $w_N^k + w_0^{k+1}$ . This can be easily shown using the additivity theorem of integration for continuous functions. The matrix  $A$  corresponds to the global representation of the bilinear form  $a(u, v)$ . Because of the compact support of the basis functions  $v_j^k(r)$ ,  $A$  is characterized by a sparse structure, with matrix elements

$$A_{i,j} = \begin{cases} a^k(v_{i'}^k, v_{j'}^k) & \text{if } i' \neq j' \neq 0 \text{ or } i' \neq j' \neq N, \\ a^1(v_0^1, v_0^1) & \text{if } k = 1, \\ a^M(v_N^M, v_N^M) & \text{if } k = M, \\ a^{k,k+1} & \text{if } k < M \text{ and } i' = j' = N, \\ a^{k-1,k} & \text{if } k \geq 2 \text{ and } i' = j' = 0, \\ 0 & \text{otherwise,} \end{cases} \quad (\text{A.24a})$$

and global indices

$$i = N(k-1) + i' + 1 \text{ and } j = N(k-1) + j' + 1, \quad (\text{A.24b})$$

such that  $1 \leq i, j \leq NM + 1$  for  $i', j' = 0, \dots, N$  and

$$a^{k,k+1} = a^k(v_N^k, v_N^k) + a^{k+1}(v_0^{k+1}, v_0^{k+1}). \quad (\text{A.24c})$$

The *elemental* bilinear form  $a^k(v_{i'}^k, v_{j'}^k)$ , is given by

$$a^k(v_{i'}^k, v_{j'}^k) = \frac{\hbar^2}{2\mu} \mathcal{J}_k^{-1} S_{i',j'}^\Lambda + V(r_{i'}) \delta_{i',j'} w_{j'}^k + \frac{\hbar^2}{2\mu} \left( \nabla u(r_0^k) \delta_{0,j'} - \nabla u(r_N^k) \delta_{N,j'} \right), \quad (\text{A.24d})$$

where  $S_{i,j}^\Lambda$  is defined in Eq. (A.14) and  $\mathcal{J}_k^{-1}$  refers to the inverse of the Jacobian (A.10b).

Solution of Eq. (A.22) requires significantly less numerical effort, if  $\mathcal{M}$  can be transformed into identity. To this end, it suffices to renormalize the basis functions [89, 352],

$$\tilde{v}_j^k(r) = \delta^k(r - r_j)/\sqrt{\gamma_j^k},$$

Then Eq. (A.6) takes the form

$$u^k(r) = \sum_{j=0}^N \tilde{u}_j^k(r) \tilde{v}_j^k(x), \quad (\text{A.25})$$

with  $\tilde{u}_j^k = u_j^k/\sqrt{\gamma_j^k}$ . Using Eq. (A.25), the linear system of equations (A.19) becomes

$$\sum_{k=1}^M \sum_{k'=1}^M \sum_{j=0}^N \tilde{u}_j^{k'} a^k(\tilde{v}_j^{k'}, \tilde{v}_i^q) = \lambda \sum_{k=1}^M \sum_{k'=1}^M \sum_{j=0}^N \tilde{u}_j^{k'} (\tilde{v}_j^{k'}, \tilde{v}_i^q)_{\Omega_k},$$

which corresponds to the eigenvalue problem

$$\tilde{A} \tilde{u} = \lambda \tilde{u} \quad (\text{A.26})$$

with matrix elements

$$\tilde{A}_{i,j} = \frac{A_{i,j}}{\sqrt{\gamma_{i'}^k \gamma_{j'}^k}},$$

and  $A_{i,j}$  given in Eq. (A.24a). The actual value of the eigenfunction at  $r = r_j^k$  is obtained as  $u_j^k = \tilde{u}_j^k/\sqrt{\gamma_j^k}$ .

In order to explicitly state the global boundary conditions, it is convenient to rewrite Eq. (A.26) in the following form,

$$\tilde{H} \tilde{u} = \lambda \tilde{u} + \tilde{A}^{(0)} \tilde{u}, \quad (\text{A.27})$$

where  $\tilde{A} = \tilde{H} - \tilde{A}^{(0)}$  and  $\tilde{A}^{(0)} \tilde{u}$  is the boundary condition vector,

$$\begin{aligned} \left( \tilde{A}^{(0)} \tilde{u} \right)_i &= \frac{\hbar^2}{2\mu} \left( -\nabla u(r_{i'}^k) \delta_{0,i'} \delta_{1,k} + \nabla u(r_N^k) \delta_{N,i'} \delta_{M,k} \right) \\ &= \frac{\hbar^2}{2\mu} \left( \nabla u(r_1) \delta_{i,1} - \nabla u(r_{NM+1}) \delta_{i,NM+1} \right) \end{aligned}$$

with  $i = i'(i', k)$  found in Eq. (A.24b). For bound states and eigenstates in a box,  $u_0^1 = u_N^M = 0$ , which can be ensured by the choice of basis functions,  $v_0^1 = 0$  and  $v_N^M = 0$ . A simple implementation is achieved by taking  $j = 1, \dots, N$  for  $k = 1$  and  $j = 0, \dots, N - 1$  for  $k = M$  instead of  $j = 0, \dots, N$ . The matrix representation of the Hamiltonian is then

given by

$$\tilde{H}_{i-1,j-1} = \tilde{A}_{i,j}, \quad i, j = 2, \dots, NM.$$

For Dirichlet boundary conditions, Eq. (A.27) takes thus the form

$$\tilde{H} \tilde{u} = \lambda \tilde{u}.$$

Despite the dense structure of the matrix representation of the kinetic operator in each interval  $\Omega_k$ , the local support of the basis functions  $v_j^k(r)$  translates into a global kinetic energy matrix that is blockwise sparse except for the interelement points, cf. Eq. (7.4).

## A.2 Choice of domain number and collocation order

The two parameters which are crucial for the analysis of accuracy and efficiency of the multi-domain pseudospectral approach are the number of intervals,  $M$ , and the number of collocation points within each interval  $N+1$ , or equivalently, the order of the interpolation polynomial,  $N$ . If  $M$  and  $N$  are chosen optimally, the calculation will be highly accurate while minimizing at the same the requirements on storage and CPU time. The role of  $M$  and  $N$  in our approach is similar to the parameters  $h$  and  $p$  in finite element methods [78], where the standard  $h$ -version, also referred to as  $h$ -refinement, consists in keeping the degree of the interpolating polynomials, usually of low degree,  $p = 1, 2$ , unchanged while modifying the size of each subdomain. Alternatively, the  $p$ -version, consists in keeping the size of each element unchanged while increasing the order of the interpolating polynomials. Finally, the  $h$ - $p$ -version of the finite element method modifies the size of each element only in regions where high resolution is needed [78].

As a first practical example, we consider the calculation of a weakly bound level of the  $\text{Ca}_2$   $B^1\Sigma_u^+$  electronically excited state. The overall spatial domain is chosen with  $r_{min} = 4.5 a_0$ ,  $r_{max} = 50000 a_0$ . For the mapped Fourier grid Hamiltonian, we take the total number of grid points to be  $\mathcal{N} = 20000$  which corresponds to  $\beta = 0.029$ . Choosing the eigenvalue labeled by  $v_{ref} = 229$  with  $E_{ref} = -2.2640249 \times 10^{-10}$  Hartree, we treat the result obtained with the mapped Fourier grid Hamiltonian and this very large number of points as a reference to benchmark the accuracy of the multi-domain spectral method for increasing the total number of collocation points, see Fig. A.1. We find the calculation using the multi-domain spectral method to be converged to machine precision (with an arbitrary choice of  $N$  and  $M$ ) if the total number of points,  $N \times M + 1$ , exceeds 3000. The overall precision in Fig. A.1 is determined by the eigenvalue with the largest magnitude, which is the ground state of the Hamiltonian, with magnitude of the order of  $10^{-2}$  Hartree. Machine precision relative to this value amounts to  $10^{-17}$  Hartree.

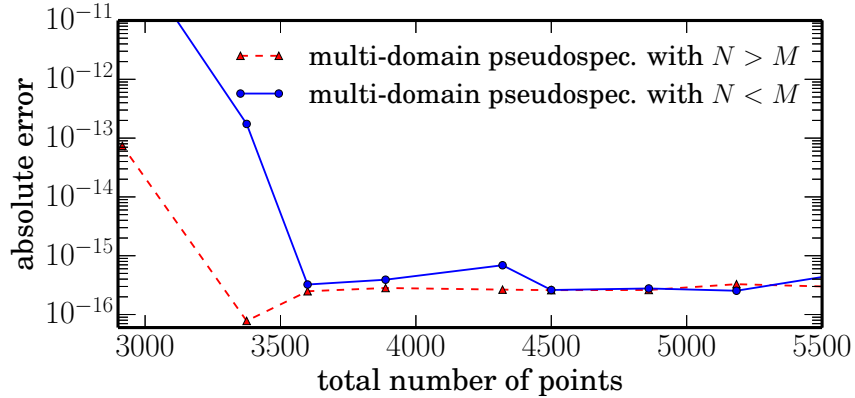


Figure A.1: Accuracy of the eigenvalue of a weakly bound level, calculated with the multi-domain pseudospectral method, referenced to the result obtained with the mapped Fourier grid Hamiltonian using a large number of points,  $\mathcal{N} = 20000$ . The reference eigenvalue is  $E_{ref} = -2.2640245 \times 10^{-10}$  Hartree, compared to  $E_0 \approx -2.607 \times 10^{-2}$  Hartree which is the eigenvalue with largest magnitude. When the total number of collocation points is sufficiently large, the accuracy of the multi-domain pseudospectral method is independent of the choice of the number of domains  $M$  and the collocation order  $N$ .

The accuracy of the pseudospectral method saturates somewhere about  $10^{-16}$  Hartree. The missing digit is most likely due to different numerical routines for diagonalization in the multi-domain spectral method (with a sparse Hamiltonian matrix) and the mapped Fourier grid method (with a fully occupied Hamiltonian matrix). The ease with which we find the semi-global representation to produce highly accurate results is in line with an earlier analysis of the FE-DVR using Gauss-Lobatto Legendre collocation for studying scattering wavefunctions [91].

An important question concerns the best choice of the parameters  $M$  and  $N$ . The same total number of points,  $N \times M + 1$ , can be realized by two different choices of  $M$  and  $N$ . Accuracy, storage requirement and spectral radius are, however, not the same between one configuration and the other. It is known from finite-element methods, that the  $p$ -refinement shows better convergence than the  $h$ -version [78]. In particular when just a small number of points is used, the accuracy may be improved by choosing  $N > M$  [78]. Nevertheless, the imbalance between  $N > M$  and  $N < M$  is removed when the overall number of points becomes sufficiently large, as shown in Fig. A.1. Remarkably, the accuracy reaches a stationary value and remains independent of the choice of  $M$  and  $N$ . The corresponding flexibility in the choice of  $N$  and  $M$  is crucial for choosing optimal values for time propagation. On one hand, choosing larger  $N$ , i.e., a higher degree of the interpolation polynomial, and smaller  $M$  considerably reduces the total number of

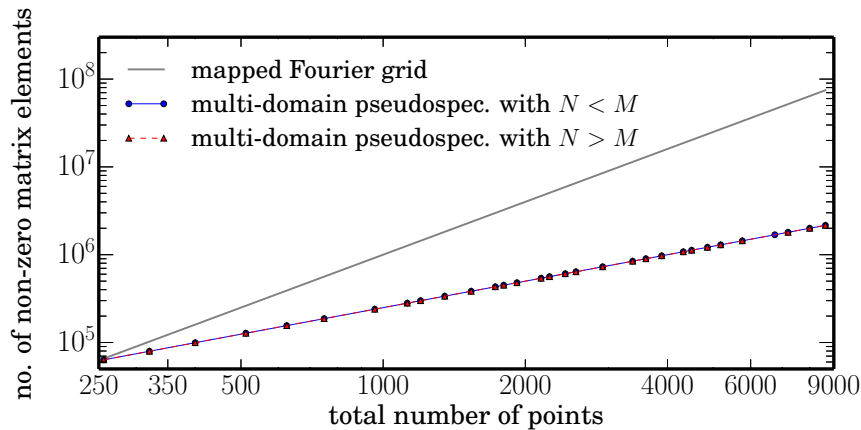


Figure A.2: Number of non-zero matrix elements of the Hamiltonian that need to be stored in memory. The mapped Fourier grid leads to a full kinetic energy matrix, whereas the Hamiltonian is sparse in the multi-domain pseudospectral representation. Note the log-log scale.

grid points,  $\mathcal{N}$ , for a given accuracy. Smaller  $\mathcal{N}$  decreases the spectral radius. On the other hand, our numerical tests show that the decrease of the spectral radius is actually even faster for the case of larger  $M$  and smaller  $N$  (with a correspondingly larger total number of points  $\mathcal{N}$ ). We therefore focus on this second option and see in what follows that choosing a larger total number of points  $\mathcal{N}$  (with smaller  $N$  and larger  $M$ ) does not compromise the efficiency of the Chebychev propagation nor increase the storage requirements for the Hamiltonian matrix.

The corresponding number of non-zero matrix elements of the Hamiltonian, i.e., the storage requirement, is shown in Fig. A.2 as a function of the total number of points. Again,  $N$  and  $M$  have been chosen arbitrarily. Due to the sparsity of the Hamiltonian, the multi-domain pseudospectral representation requires significantly less storage than the mapped Fourier grid Hamiltonian. Given the fact, that the accuracy of both methods is the same for  $\mathcal{N} > 3000$ , the multi-domain pseudospectral representation allows for a dramatic reduction in the memory required to calculate the spectrum without compromising accuracy. This opens new perspectives for obtaining highly accurate weakly bound states as well as scattering states for long-range potentials, for example in coupled channels calculations, where the memory required for storing the mapped Fourier Hamiltonian quickly becomes a limiting issue [166, 167].

While different choices of  $N$  and  $M$  correspond to different storage requirements, this does not show up on the scale of Fig. A.2. The sparsity of the Hamiltonian is therefore further analyzed in Fig. A.3 by comparing the cases  $N > M$  and  $N < M$  for a fixed number of points allowing, this time,  $N$  and  $M$  to be significantly different. As can be

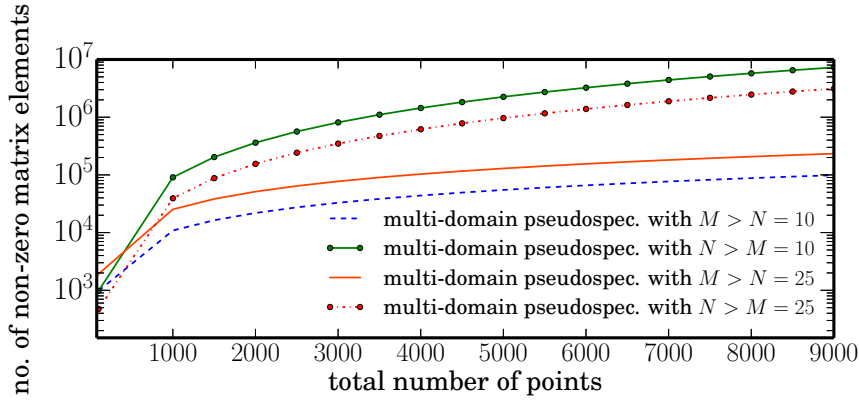


Figure A.3: Number of non-zero matrix elements of the Hamiltonian that need to be stored in memory for specific choices of  $N$  and  $M$ .

seen from Eq. (7.6), for a fixed number of points  $N \times M + 1$ , the case  $N > M$  leads to a less sparse representation of the Hamiltonian matrix. However, both cases,  $N > M$  and  $N < M$ , lead to a significant improvement in terms of storage, requiring only a few percent of the memory needed for the full matrix obtained with the mapped Fourier grid method.

Finally, we compare the spectral radius,  $\Delta E$ , obtained with the mapped Fourier grid Hamiltonian and the adaptive multi-domain pseudospectral approach in Fig. A.4. This is important because the spectral radius determines the number of terms in the Chebychev expansion of the time evolution operator, cf. Section 4.2.1, i.e., the number of times the Hamiltonian is applied to a wavefunction. As a rule of thumb, the spectral radius of the mapped Fourier grid Hamiltonian is smaller than that obtained with the adaptive multi-domain pseudospectral approach for the same number of points. Moreover, we find that for the same total number of points  $\mathcal{N}$ , the spectral radius for  $N > M$  is larger than that for  $N < M$ . This is somewhat unfortunate since for a given total number of points better accuracy is obtained with  $N > M$ . However, since, for sufficiently large  $\mathcal{N}$ , the accuracy is independent of the choice of  $N$  and  $M$ , cf. Fig. A.1, and time propagation will be most efficient for  $\Delta E$  as small as possible, it is convenient to choose a relatively large total number of points with a low order  $N$  of the interpolation polynomial. This allows to reduce the numerical effort of the multi-domain pseudospectral method compared to the mapped Fourier grid Hamiltonian while keeping the level of accuracy, even though the total number of grid points required for the multi-domain pseudospectral approach is larger than that required for the mapped Fourier grid.

To summarize, it is optimal to (i) choose a low order of the interpolation polynomial or, equivalently, number of collocation points per element, e.g.  $N = 3, 4, 5$ , since it results in a small spectral radius, (ii) increase the total number of points such that the

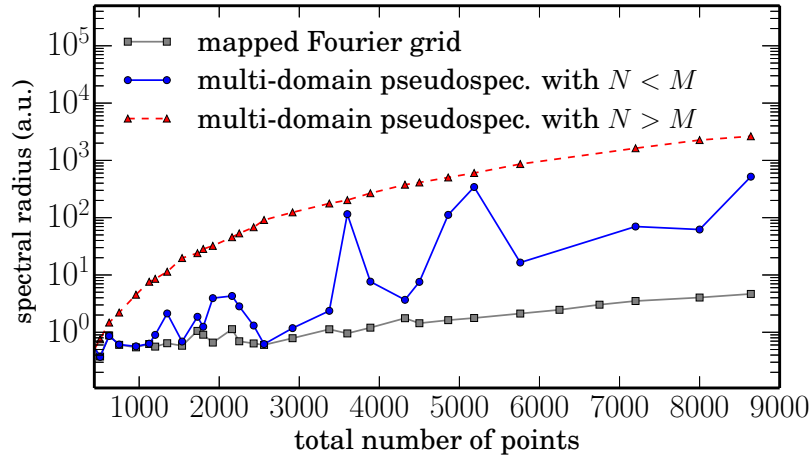


Figure A.4: Spectral radius as a function of the total number of points. The spectral radius determines the number of the times the Hamiltonian needs to be applied for time evolution with the Chebychev propagator.

desired accuracy is obtained and (iii) define the number of intervals  $M$  according to  $\mathcal{N} = N \times M + 1$ .

Note that for a low order of the interpolation polynomials, e.g.  $N = 3$ , the sparse band-like structure of the kinetic energy matrix is quite similar to what is obtained using second and fourth order finite differences. We therefore compare the accuracy obtained with the multi-domain pseudospectral approach for low order of the interpolation polynomials to that of the second and fourth order finite differences. As shown in Fig. A.5, the multi-domain pseudospectral representation yields a significantly better accuracy than finite differences. This reflects the *global* approximation of the derivatives within each interval and emphasizes the superiority of pseudo-spectral approaches over methods based on the Taylor expansion.

### A.3 Collocation with Legendre polynomials

For completeness, we recall the basic properties of Legendre collocation. The Legendre polynomials [78, 353] are the solutions of the second order differential equation

$$\left( (1 - \xi^2)L'_n(\xi) \right)' + n(n+1)L_n(\xi) = 0, \quad (\text{A.28})$$

where  $'$  denotes the first derivative with respect to the argument of  $L_n(\cdot)$ . In the interval  $\Lambda = [-1, 1]$ , the Legendre polynomials are orthogonal with respect to the  $L_2$  inner product

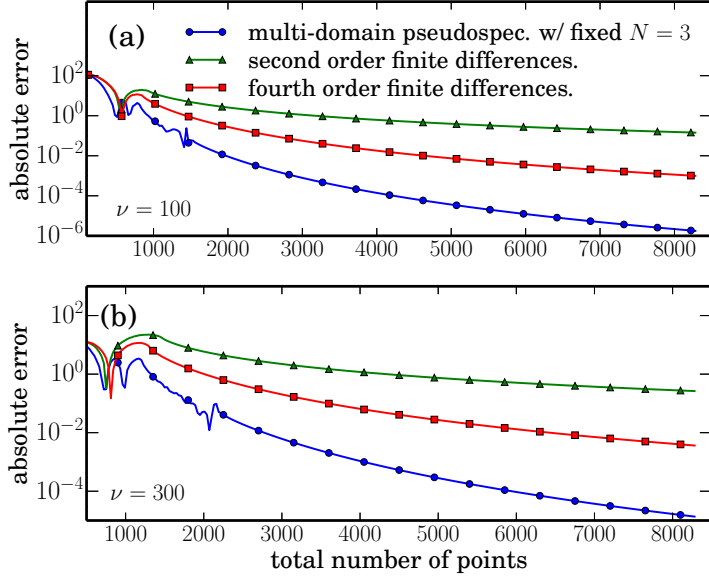


Figure A.5: Accuracy of the multi-domain pseudospectral approach for a low collocation order ( $N = 3$ ) compared to second and fourth orders finite differences for the levels  $\nu = 100$  (a) and  $\nu = 300$  (b) of the Morse potential with eigenvalues  $E_{100} = -112.1253125$  a.u. and  $E_{300} = -12.3753125$  a.u., respectively. Despite the similar structure of the Hamiltonian matrix, the pseudospectral approach is significantly more accurate.

and they obey the three-term recurrence relation

$$(n + 1)L_{n+1}(\xi) = (2n + 1)\xi L_n(\xi) - nL_{n-1}(\xi), \quad n \geq 1, \tag{A.29}$$

with  $L_0 = 1$ ,  $L_1 = \xi$ , where  $\xi \in \Lambda$ . Another useful recurrence relation reads [353]

$$(2n + 1)L_n(\xi) = L'_n(\xi) - L'_{n-1}(\xi), \quad n \geq 1. \tag{A.30}$$

In the interval  $\Lambda = [-1, 1]$ , the set  $\{\xi_j, \omega_j^\Lambda\}$  is defined as the set of Gauss-Lobatto-Legendre nodes  $\xi_j$  and Gaussian quadrature weights  $w_j^\Lambda$ . It is given by [78]

$$\begin{cases} \{\xi_j\}_{0 \leq j \leq N} &= \text{zeros of } \zeta(\xi) = (1 - \xi^2)L'_N(\xi) \\ \omega_j^\Lambda &= \frac{2}{N(N-1)(L'_N(\xi_j))^2}. \end{cases} \tag{A.31}$$

For moderate order collocation, the  $N - 1$  interior points of the Gauss-Lobatto-Legendre grid in  $\Lambda = [-1, 1]$  can be generated with the help of the Golub-Welsh algorithm [354]. In detail, Eqs. (A.29)-(A.31) yield the recursion relation

$$\beta_n L'_{n+1}(\xi) + \alpha_n L'_{n-1}(\xi) - \xi L'_n(\xi) = 0, \tag{A.32a}$$

where the recursion coefficients  $\alpha_n$  and  $\beta_n$  are given by

$$\alpha_n = \frac{n+1}{2n+1} \quad \text{and} \quad \beta_n = \frac{n}{2n+1}. \quad (\text{A.32b})$$

Taking into account Eq. (A.31), i.e.,  $L'_N(\xi_j) = 0$  for all  $j = 1, \dots, N-1$ , the tridiagonal Jacobian matrix reads

$$\begin{pmatrix} 0 & \beta_1 & 0 & 0 & \dots & 0 \\ \alpha_2 & 0 & \beta_2 & 0 & \dots & 0 \\ \vdots & \ddots & 0 & \ddots & & 0 \\ 0 & \dots & \alpha_n & 0 & \beta_n & 0 \\ \vdots & 0 & \dots & \ddots & \ddots & 0 \\ 0 & \dots & \dots & 0 & \alpha_{N-1} & 0 \end{pmatrix} \begin{pmatrix} L'_1(\xi_j) \\ L'_2(\xi_j) \\ \vdots \\ L'_n(\xi_j) \\ \vdots \\ L'_{N-1}(\xi_j) \end{pmatrix} = \xi_j \begin{pmatrix} L'_1(\xi_j) \\ L'_2(\xi_j) \\ \vdots \\ L'_n(\xi_j) \\ \vdots \\ L'_{N-1}(\xi_j) \end{pmatrix}, \quad (\text{A.32c})$$

where the eigenvalues correspond to the  $N-1$  roots of  $L'_N(\xi_j)$  which define, according to Eq. (A.31), the interior points of the Gauss-Lobatto grid. The extrema are given by  $\xi_0 = -1$  and  $\xi_N = 1$ . Alternatively, in particular for a high-order quadrature, it is suitable to use a Newton-root-finding iterative method in order to avoid round-off errors that may occur during the diagonalization of the Jacobian matrix.

A first order Taylor expansion of  $\zeta(\xi)$ , defined in Eq. (A.31), around the  $j$ th Gauss-Lobatto-Legendre point, i.e., the  $j$ th root of  $\zeta(\xi)$ , gives

$$\begin{aligned} \zeta(\xi) &\simeq \zeta(\xi_j) + \zeta'(\xi_j)(\xi - \xi_j) + \mathcal{O}(|\xi - \xi_j|)^2 \\ &= \zeta'(\xi_j)(\xi - \xi_j), \end{aligned} \quad (\text{A.33})$$

since, by definition,  $\zeta(\xi)$  vanishes at the Gauss-Lobatto-Legendre points,  $\zeta(\xi_j) = 0$ . Equations (A.31) and (A.33) yield an explicit expression of the Legendre cardinal function  $\delta^\Lambda(\xi - \xi_j)$ ,

$$\delta^{(\Lambda)}(\xi - \xi_j) = \frac{\zeta(\xi)}{\zeta'(\xi_j)(\xi - \xi_j)} = \frac{L'_N(\xi)(1 - \xi^2)}{(L'_j(\xi)(1 - \xi^2))'} \frac{1}{\xi - \xi_j},$$

where  $\zeta(\xi)$  is defined in Eq. (A.31) and  $L_j$  denotes the  $j$ th Legendre polynomial. Together with Eq. (A.28), this yields

$$\delta^{(\Lambda)}(\xi - \xi_j) \equiv -\frac{L'_N(\xi)(1 - \xi^2)}{N(N+1)L_N(\xi_j)} \frac{1}{\xi - \xi_j} \quad (\text{A.34})$$

Moreover, we have  $\delta^{(\Lambda)}(\xi_i - \xi_j) = \delta_{ij}$  at each  $\xi_j$  by construction which results in the first order differentiation matrix for Legendre cardinal functions, cf. Eq. (A.13).



# Quantum optimal control of photoelectron observables

## Frequency and Amplitude Restriction

In the following, we present the derivation of Krotov's update equation for the control, Eq. (8.14a) using the approximation for  $s(t)$  previously described. This allows for a more compact expression for Krotov's equation for the specific constraints on the field used in this work. It is obtained following Ref. [106]: We seek to minimize the complete functional, Eq. (8.7). In order to evaluate the extremum condition, we start by evaluating the functional derivative of the penalty functional with respect to the changes in the control field  $\mathbf{A}(t)$  in Eq. (8.11),

$$\frac{\delta C_a[\mathbf{A}]}{\delta \mathbf{A}(t)} = 2\lambda_a s^{-1}(t) (\mathbf{A}(t) - \mathbf{A}_{\text{ref}}(t)). \quad (\text{B.1})$$

Next, we evaluate the functional derivative of Eq. (8.12). Abbreviating  $\omega^2 \tilde{\gamma}(\omega)$  by  $\tilde{h}(\omega)$  in Eq. (8.12), the functional derivative reads

$$\begin{aligned} \frac{\delta C_\omega[\mathbf{A}]}{\delta \mathbf{A}(t)} &= \lambda_\omega \int \mathbf{A}^*(\omega) \frac{\delta \tilde{\mathbf{A}}(\omega)}{\delta \mathbf{A}(t)} \tilde{h}(\omega) d\omega \\ &+ \lambda_\omega \int \tilde{\mathbf{A}}(\omega) \frac{\delta \tilde{\mathbf{A}}^*(\omega)}{\delta \mathbf{A}(t)} \tilde{h}(\omega) d\omega. \end{aligned} \quad (\text{B.2})$$

Using the fact that  $\tilde{\mathbf{A}}(\omega)$  is the Fourier transform of  $\mathbf{A}(t)$ ,

$$\tilde{\mathbf{A}}(\omega) = \int \mathbf{A}(t) e^{-i\omega t} dt,$$

the functional derivative becomes,

$$\frac{\delta \tilde{\mathbf{A}}(\omega)}{\delta \mathbf{A}(t')} = e^{-i\omega t'},$$

such that

$$\begin{aligned} \frac{\delta C_\omega[\mathbf{A}]}{\delta \mathbf{A}(t)} &= \lambda_\omega \int \tilde{\mathbf{A}}^*(\omega) e^{-i\omega t} \tilde{h}(\omega) d\omega \\ &+ \lambda_\omega \int \tilde{\mathbf{A}}(\omega) e^{+i\omega t} \tilde{h}(\omega) d\omega . \end{aligned}$$

This can be rewritten as

$$\begin{aligned} \frac{\delta C_\omega[\mathbf{A}]}{\delta \mathbf{A}(t)} &= \lambda_\omega \int \tilde{\mathbf{A}}^*(-\omega) e^{+i\omega t} \tilde{h}(-\omega) d\omega \\ &+ \lambda_\omega \int \tilde{\mathbf{A}}(\omega) e^{+i\omega t} \tilde{h}(\omega) d\omega . \end{aligned} \quad (\text{B.3})$$

Since the control  $\mathbf{A}(t)$  is a real function of time,  $\tilde{\mathbf{A}}^*(-\omega) = \tilde{\mathbf{A}}(\omega)$ . Moreover, by construction  $\tilde{h}(\omega) = \tilde{h}(-\omega)$ . Therefore, Eq. (B.3) becomes

$$\begin{aligned} \frac{\delta C_\omega[\mathbf{A}]}{\delta \mathbf{A}(t)} &= 2\lambda_\omega \int \tilde{\mathbf{A}}(\omega) e^{+i\omega t} \tilde{h}(\omega) d\omega \\ &= 2\lambda_\omega \int \tilde{\mathbf{A}}(\omega) e^{i\omega t} d\omega \int h(\tau) e^{-i\omega\tau} d\tau \\ &= 2\lambda_\omega \int h(\tau) d\tau \int \tilde{\mathbf{A}}(\omega) e^{+i\omega(t-\tau)} d\omega \\ &= 2\tilde{\lambda}_\omega \int h(\tau) \mathbf{A}(t-\tau) d\tau = 2\tilde{\lambda}_\omega \mathbf{A} \star h(t) , \end{aligned} \quad (\text{B.4})$$

with  $\tilde{\lambda}_\omega = \sqrt{2\pi}\lambda_\omega$ , and  $h(t) = \int \tilde{h}(\omega) \exp(+i\omega t) d\omega / \sqrt{2\pi}$  and where  $f \star g(t)$  refers to the convolution product of  $f$  and  $g$ .

We now calculate the functional derivative of the constraint penalizing large values of  $\dot{\mathbf{A}}(t)$ , Eq. (8.14). Assuming vanishing boundary conditions for  $\mathbf{A}(t)$ , we find, upon integration by parts,

$$\frac{\delta C_e[\mathbf{A}]}{\delta \mathbf{A}(t)} = -2\lambda_e s^{-1}(t) \ddot{\mathbf{A}}(t) . \quad (\text{B.5})$$

Using Eqs. (B.1), (B.4) and (B.5), the extremum condition with respect to a variation in the control becomes

$$\begin{aligned} 0 &= \lambda_a s^{-1}(t) (\mathbf{A}(t) - \mathbf{A}_{ref}(t)) - \lambda_e s^{-1}(t) \ddot{\mathbf{A}}(t) \\ &+ \tilde{\lambda}_\omega \mathbf{A} \star h(t) - \mathfrak{Im} \left\{ \left\langle \chi(t) \left| \frac{\partial \hat{H}}{\mathbf{A}} \right| \Psi(t) \right\rangle \right\} . \end{aligned}$$

where the last term has been previously introduced in Eq. (8.14). It can be straightforwardly derived from variational principles, ie. Euler-Lagrange Lagrange equation, or in the context of Pontriagin's maximum/minimum principle or in the context of Krotov's

optimization method, cf. Refs. [106, 234]. It stresses the dynamics to which the forward propagated state is subject to. Solving for  $\mathbf{A}(t)$  gives us the update rule for the optimized pulse,

$$\begin{aligned} \mathbf{A}(t) = & \mathbf{A}_{ref}(t) + \frac{s(t)}{\lambda_a} \Im \left\{ \left\langle \chi(t) \left| \frac{\partial \hat{H}}{\partial \mathbf{A}} \right| \Psi(t) \right\rangle \right\} \\ & - \frac{\tilde{\lambda}_\omega}{\lambda_a} s(t) \mathbf{A} \star h(t) + \frac{\lambda_e}{\lambda_a} \ddot{\mathbf{A}}(t), \end{aligned} \quad (\text{B.6})$$

i.e., we retrieve Eq. (8.14a). Using the property

$$\int \ddot{\mathbf{A}}(t) e^{-i\omega t} dt = -\omega^2 \tilde{\mathbf{A}}(\omega),$$

together with Eq. (8.17) for  $s(t)$ , it is straightforward to write Krotov's equation in frequency domain. To this end, we merely take the Fourier transform of Eq. (B.6) and utilize the well-known property that the Fourier transform of a convolution of two functions in time domain is the product of the functions in frequency domain. We thus find

$$\begin{aligned} \tilde{\mathbf{A}}^{(k+1)}(\omega) \approx & \tilde{\mathbf{A}}^{(k)}(\omega) + \tilde{I}^{(k+1)}(\omega) \\ & - \frac{\tilde{\lambda}_\omega}{\lambda_a} \tilde{\mathbf{A}}^{(k+1)}(\omega) \tilde{h}(\omega) - \omega^2 \frac{\lambda_e}{\lambda_a} \tilde{\mathbf{A}}^{(k+1)}(\omega), \end{aligned} \quad (\text{B.7})$$

which yields Eq. (8.18a).



# Theoretical description of photoelectron circular dichroism of randomly oriented chiral molecules

## C.1 Useful properties

In the following, for completeness we summarize the properties of the continuum wavefunctions, rotation matrices and complex spherical harmonics in Secs. C.1.1, C.1.3 and C.1.4.

Furthermore, we provide details of the derivation of the one-photon transition rate, two-photon absorption tensor and the photoionization cross section in Secs. C.2.1 to C.2.3 as well as the behavior of the Legendre coefficients under change of helicity in the one-photon photoionization and two-photon absorption processes in Secs. C.2.4 to C.2.6.

### C.1.1 Radial continuum wavefunctions of the hydrogen atom

An explicit expression of the radial continuum wavefunctions is given in terms of the Kummer confluent hypergeometric functions [287],

$$G_{k,\ell}(r) = C_{E,\ell} (2kr)^\ell e^{-ikr} F_1(\ell + 1 + i/k, 2\ell + 2, 2ikr). \quad (\text{C.1})$$

The factor

$$C_{E,\ell} \equiv \sqrt{\frac{2\mu k}{\pi \hbar^2}} \frac{|\Gamma(\ell + 1 - i/k)|}{(2\ell + 1)!} e^{\pi/2k},$$

where  $\Gamma(\cdot)$  refers to the Euler Gamma function, ensures proper normalization such that

$$\int_0^\infty G_{E,\ell}(r) G_{E',\ell}(r) r^2 dr = \delta(E - E').$$

In order to avoid numerical instabilities when generating the radial continuum wavefunctions, Eq. (C.1) may be written in integral form [355],

$$G_{k,\ell}(r) = \sqrt{\frac{2\mu k}{\pi\hbar^2}} |\Gamma(\ell + 1 - i/k)|^{-1} e^{\pi/2k} (2kr)^\ell e^{-ikr} \times \int_0^1 s^{\ell+i/k} (1-s)^{\ell-i/k} e^{2ikrs} ds. \quad (\text{C.2})$$

### C.1.2 Bound state wavefunctions of the hydrogen atom

As for the radial part of bound states for hydrogenic wavefunctions,  $R_{\ell_o}^{n_o}(r)$ , cf. Eq. (10.2), they can also be expressed in terms of the Kummer confluent hypergeometric functions [355],

$$R_{\ell_o}^{n_o}(r) = \left( 4k_{n_o}^3 \frac{(n_o + \ell_o - 1)!}{[(n_o + \ell_o)!]^3} \right)^{1/2} (2k_{n_o} r)^\ell \times F_1(\ell_o + 1 - n_o, 2\ell_o + 1, 2k_{n_o} r) e^{-k_{n_o} r}, \quad (\text{C.3a})$$

with

$$k_{n_o} \equiv \frac{1}{1 + \frac{m_e}{M_n}} \frac{1}{n_o a_o} \approx \frac{1}{n_o a_o} \quad (\text{C.3b})$$

where  $m_e$ ,  $M_n$  and  $a_o$  refer to the masses of the electron and that of the nucleus and the Bohr's radius, respectively.

### C.1.3 Rotation matrices

We summarize here some useful properties that are utilized in the derivation of the photoionization cross section, following the standard angular momentum algebra as found in Refs. [143–146, 287]. Any irreducible tensor field  $f_{m_k}^k$  of rank  $k$  is transformed from the molecular frame to the laboratory frame as follows [145, 146]:

$$f_{m_k}^k(\mathbf{r}') = D(\alpha\beta\gamma) f_{m_k}^k(\mathbf{r}) \equiv \sum_{m'_k=-k}^{+k} f_{m'_k}^k(\mathbf{r}) \mathcal{D}_{m'_k, m_k}^{(k)}(\alpha\beta\gamma), \quad (\text{C.4})$$

where  $\mathcal{D}_{m'_j, m_j}^{(j)}(\alpha\beta\gamma) = \langle j, m' | D(\alpha\beta\gamma) | j, m \rangle$  refers to the Wigner rotation matrix of rank  $j$ , and the subscripts  $m_k$  and  $m'_k$  stand for the projection of the total angular momentum  $k$  onto the  $z$  axis in the molecular, respectively laboratory, frame. Conversely, the inverse

of the transformation (C.4) is given by

$$f_{m_k}^k(\mathbf{r}) = D^{-1}(\alpha\beta\gamma)f_{m_k}^k(\mathbf{r}') \equiv \sum_{m'_k=-k}^{+k} f_{m'_k}^k(\mathbf{r}') \mathcal{D}_{m'_k, m_k}^{\dagger, (k)}(\alpha\beta\gamma). \quad (\text{C.5})$$

We express all vector quantities in spherical coordinates,

$$\mathbf{r}' = \sqrt{\frac{4\pi}{3}} r \sum_{\mu=0, \pm 1} (-1)^\mu Y_\mu^1(\Omega_{\mathbf{r}'}) \epsilon'_{-\mu}, \quad (\text{C.6})$$

where  $\epsilon'_{-\mu}$  refers to the spherical unit vector in the laboratory frame, and  $\mu = 0, \pm 1$  denotes linear, left and right unit components, respectively. The correspondence between the components of a arbitrary vector operator  $\mathcal{V}$  in spherical and cartesian basis is given by [145, 146, 353],

$$\begin{aligned} \mathcal{V}_{-1} &= \frac{1}{\sqrt{2}} (\mathcal{V}_x - i\mathcal{V}_y) \\ \mathcal{V}_0 &= \mathcal{V}_z \\ \mathcal{V}_{+1} &= -\frac{1}{\sqrt{2}} (\mathcal{V}_x + i\mathcal{V}_y) \end{aligned} \quad (\text{C.7})$$

The standard *ab initio* calculations [294] were performed in the Cartesian basis  $T_{\alpha, \beta}$ , with  $\alpha, \beta = x, y, z$ . However, in order to render the analytical expressions more manageable, the use of spherical basis is suitable. Transforming the spherical components  $\mathbf{r}_q$ , with  $q = \pm 1, 0$  in to the Cartesian basis using Eq. (C.7), we find the two-photon absorption tensor in the spherical basis,

$$\begin{aligned} T_{-1, -1} &= \frac{1}{2} (T_{xx} - 2iT_{xy} - T_{yy}) \\ T_{-1, 0} &= \frac{1}{\sqrt{2}} (T_{xz} - iT_{yz}) \\ T_{-1, +1} &= -\frac{1}{2} (T_{xx} + T_{yy}) \\ T_{0, 0} &= T_{zz} \\ T_{0, +1} &= -\frac{1}{\sqrt{2}} (T_{zx} + iT_{zy}) \\ T_{+1, +1} &= \frac{1}{2} (T_{xx} + 2iT_{xy} - T_{yy}) \end{aligned} \quad (\text{C.8})$$

Because  $T_{\alpha, \beta} = T_{\beta, \alpha}$ , cf. Ref. [294], it can be straightforwardly shown, using Eq. (C.7), that  $T_{q_1, q_2} = T_{q_2, q_1}$ .

In the derivations we make heavily use of the product rule for two Wigner rotations

matrices of ranks  $k$  and  $k'$ ,

$$\mathcal{D}_{\mu,\nu}^{(k)}(\omega)\mathcal{D}_{\mu',\nu'}^{(k')}(\omega) = \sum_{J=|k-k'|}^{k+k'} (2J+1)\mathcal{D}_{-\mu-\mu',-\nu-\nu'}^{*(J)}(\omega) \begin{pmatrix} k & k' & J \\ \mu & \mu' & -\mu-\mu' \end{pmatrix} \begin{pmatrix} k & k' & J \\ \nu & \nu' & -\nu-\nu' \end{pmatrix}, \quad (\text{C.9a})$$

together with the following symmetry property,

$$\mathcal{D}_{\mu,\nu}^{(k)} = (-1)^{\mu-\nu}\mathcal{D}_{-\mu,-\nu}^{*(k)}(\omega), \quad (\text{C.9b})$$

where (\*) denotes the complex conjugate.

### C.1.4 Conversion to complex spherical harmonics

The standard complex spherical harmonics  $Y_m^\ell(\Omega)$  are related to the real spherical harmonics  $\Upsilon_{\ell,|m|}(\Omega)$  by

$$Y_m^\ell(\Omega) = \begin{cases} \frac{1}{\sqrt{2}}\left(\Upsilon_{\ell,|m|}(\Omega) - i\Upsilon_{\ell,-|m|}(\Omega)\right) & \text{if } m \leq 0, \\ \Upsilon_{\ell,0}(\Omega) & \text{if } m = 0, \\ \frac{(-1)^\ell}{\sqrt{2}}\left(\Upsilon_{\ell,|m|}(\Omega) + i\Upsilon_{\ell,-|m|}(\Omega)\right) & \text{if } m \geq 0. \end{cases}$$

Therefore the excited state expansion coefficients  $a_{m_o}^{\ell_o}(n)$ , defined in Eq. (10.2), are connected to the coefficients in the basis of real spherical harmonics by

$$a_{m_o}^{\ell_o}(n) = \begin{cases} \frac{1}{\sqrt{2}}\left(\tilde{a}_{m_o}^{\ell_o}(n) + i\tilde{a}_{m_o}^{\ell_o}(n)\right) & \text{if } m \leq 0, \\ \tilde{a}_0^{\ell_o}(n) & \text{if } m = 0, \\ \frac{(-1)^{\ell_o}}{\sqrt{2}}\left(\tilde{a}_{m_o}^{\ell_o}(n) - i\tilde{a}_{m_o}^{\ell_o}(n)\right) & \text{if } m \geq 0. \end{cases}$$

## C.2 Derivations

### C.2.1 One-photon transition rate

This section is devoted to deriving the rate for the photoionization transition from the intermediate electronically excited state to the continuum, driven by an electric field with polarization  $\epsilon'_{\varrho_2}$ . The starting point is the doubly differential cross section in the molecular frame given in Eq. (10.7). It contains the laboratory-frame product  $\epsilon'_{\varrho_2} \cdot \mathbf{r}'$ , which, using

Eq. (C.6), becomes

$$\epsilon'_{\varrho_2} \cdot \mathbf{r}' = \sqrt{\frac{4\pi}{3}} r Y_{\varrho_2}^1(\Omega_{\mathbf{r}'}) \equiv \mathbf{r}'_{\varrho_2}. \quad (\text{C.11})$$

This is rotated into the molecular frame, employing Eq. (C.4), resulting in

$$\epsilon'_{\varrho_2} \cdot \mathbf{r}' = \sqrt{\frac{4\pi}{3}} r \sum_{q=0,\pm 1} \mathcal{D}_{q,\varrho_2}^{(1)}(\omega) Y_q^1(\Omega_{\mathbf{r}}). \quad (\text{C.12})$$

Inserting Eq. (C.12) into Eq. (10.7) yields the photoionization cross section in the molecular frame as a function of the Euler angles  $\omega \equiv (\alpha, \beta, \gamma)$ , cf. Eq. (10.8). Evaluating Eq. (10.8) requires evaluation of the product  $\langle \Psi_{\mathbf{k}} | \mathbf{r}_q | \Psi_o \rangle \langle \Psi_{\mathbf{k}} | \mathbf{r}_{q'} | \Psi_o \rangle^*$ . Inserting Eqs. (10.4) and (10.7) yields, for a fixed polarization direction  $q$ ,

$$\langle \Psi_{\mathbf{k}} | \mathbf{r}_q | \Psi_o \rangle = \sum_{\substack{\ell, m \\ n_o, \ell_o, m_o}} (-i)^\ell e^{i\delta_\ell} I_k^{n_o}(\ell, \ell_o) S_{\ell_o, m_o}^{\ell, m}(q) a_{m_o}^{\ell_o}(n_o) Y_m^\ell(\Omega_{\mathbf{k}})$$

with  $I_k^{n_o}(\ell, \ell_o)$  and  $S_{\ell_o, m_o}^{\ell, m}(q)$  defined in Eqs. (10.10a) and (10.10b) such that Eq. (10.8) comprises the product  $Y_m^\ell(\Omega_{\mathbf{k}}) Y_{m'}^{\ell'}(\Omega_{\mathbf{k}})$ . Using the symmetry properties of the spherical harmonics, we can write

$$\begin{aligned} Y_m^\ell(\Omega_{\mathbf{k}}) Y_{m'}^{\ell'}(\Omega_{\mathbf{k}}) &= (-1)^{m'} Y_m^\ell(\Omega_{\mathbf{k}}) Y_{-m'}^{\ell'}(\Omega_{\mathbf{k}}) \\ &= (-1)^{-m} \sum_{\mathcal{L}=|\ell-\ell'|}^{\ell+\ell'} \tilde{\gamma}(\ell, \ell', \mathcal{L}) \begin{pmatrix} \ell & \ell' & \mathcal{L} \\ m & -m' & m' - m \end{pmatrix} \begin{pmatrix} \ell & \ell' & \mathcal{L} \\ 0 & 0 & 0 \end{pmatrix} Y_{m-m'}^{\mathcal{L}}(\Omega_{\mathbf{k}}) \end{aligned} \quad (\text{C.13a})$$

with

$$\tilde{\gamma}(\ell, \ell', \mathcal{L}) = \sqrt{(2\ell+1)(2\ell'+1)(2\mathcal{L}+1)/4\pi} \quad (\text{C.13b})$$

and  $\Omega_{\mathbf{k}} = (\vartheta_{\mathbf{k}}, \phi_{\mathbf{k}})$  referring to polar and azimuthal angles of the momentum vector in the molecular frame of reference. In order to express the photoionization direction in the laboratory frame, we need to apply the inverse transformation (C.5) to  $Y_{m-m'}^{\mathcal{L}}(\Omega_{\mathbf{k}'})$ , i.e.,

$$\begin{aligned} Y_{m-m'}^{\mathcal{L}}(\Omega_{\mathbf{k}}) = D^{-1}(\omega) Y_{m-m'}^{\mathcal{L}}(\Omega_{\mathbf{k}'}) &= \sum_{\mu=-\mathcal{L}}^{\mathcal{L}} \mathcal{D}_{\mu, m-m'}^{\dagger(\mathcal{L})}(\omega) Y_{\mu}^{\mathcal{L}}(\Omega_{\mathbf{k}'}) \\ &= \sum_{\mu=-\mathcal{L}}^{\mathcal{L}} (-1)^{m'-m-\mu} \mathcal{D}_{m'-m, -\mu}^{(\mathcal{L})}(\omega) Y_{\mu}^{\mathcal{L}}(\Omega_{\mathbf{k}'}) \end{aligned} \quad (\text{C.14a})$$

which can be expressed in terms of the Generalized Legendre polynomials  $P_{\mathcal{L}}^{\mu}(\cos \vartheta'_k)$ ,

$$Y_{m-m'}^{\mathcal{L}}(\Omega_{\mathbf{k}}) = \sum_{\mu=-\mathcal{L}}^{\mathcal{L}} \sqrt{\frac{(2\mathcal{L}+1)(\mathcal{L}-\mu)!}{4\pi(\mathcal{L}+\mu)!}} (-1)^{m'-m} \times \mathcal{D}_{m'-m,-\mu}^{(\mathcal{L})}(\omega) P_{\mathcal{L}}^{\mu}(\cos \vartheta'_k) e^{i\mu\varphi'_k} \quad (\text{C.14b})$$

It follows that, using Eq. (C.14b), Eq. (C.13b) then becomes,

$$Y_m^{\ell}(\Omega_{\mathbf{k}}) Y_{m'}^{*\ell'}(\Omega_{\mathbf{k}}) = (-1)^{m'} \sum_{\mathcal{L}=|\ell-\ell'|}^{\ell+\ell'} (2\mathcal{L}+1) s_{\mathcal{L}}^{\mu}(\ell, \ell') \begin{pmatrix} \ell & \ell' & \mathcal{L} \\ m & -m' & m'-m \end{pmatrix} \begin{pmatrix} \ell & \ell' & \mathcal{L} \\ 0 & 0 & 0 \end{pmatrix} \times \sum_{\mu=-\mathcal{L}}^{\mathcal{L}} \mathcal{D}_{m'-m,-\mu}^{(\mathcal{L})}(\omega) P_{\mathcal{L}}^{\mu}(\cos \vartheta'_k) e^{i\mu\varphi'_k} \quad (\text{C.14c})$$

with

$$s_{\mathcal{L}}^{\mu}(\ell, \ell') = \sqrt{\frac{(2\ell+1)(2\ell'+1)(\mathcal{L}-\mu)!}{16\pi^2(\mathcal{L}+\mu)!}} \quad (\text{C.15})$$

In Eq.(C.14), we have used the equality between spherical harmonics and associate Legendre polynomials, including the Condon-Shortley phase convention [146, 287, 353],

$$Y_{\mu}^{\mathcal{L}}(\vartheta'_k, \varphi'_k) = (-1)^{\mu} \sqrt{\frac{(2\mathcal{L}+1)(\mathcal{L}-\mu)!}{4\pi(\mathcal{L}+\mu)!}} P_{\mathcal{L}}^{\mu}(\cos \vartheta'_k) e^{i\mu\varphi'_k}. \quad (\text{C.16})$$

Inserting Eq. (C.14) into Eq. (10.9), we obtain the differential one-photon cross section in the laboratory frame of reference for a fixed molecular orientation defined in Eq. (10.11).

### C.2.2 Two-photon absorption tensor

The probability of two-photon absorption, Eq. (10.13a), of a molecule that is oriented with angles  $\omega = (\alpha, \beta, \gamma)$  with respect to the laboratory frame of reference contains the product

$$\mathcal{D}_{q_1, \varrho_1}^{(1)}(\omega) \mathcal{D}_{q_2, \varrho_2}^{(1)}(\omega) \mathcal{D}_{q_3, \varrho_3}^{*(1)}(\omega) \mathcal{D}_{q_4, \varrho_4}^{*(1)}(\omega)$$

. Using Eqs. (C.9), we obtain

$$\begin{aligned} \mathcal{D}_{q_1, \varrho_1}^{(1)}(\omega) \mathcal{D}_{q_2, \varrho_1}^{(1)}(\omega) &= (-1)^{q_1+q_2} \sum_{Q=0}^2 (2Q+1) \mathcal{D}_{q_1+q_2, 2\varrho_1}^{(Q)}(\omega) \\ &\times \begin{pmatrix} 1 & 1 & Q \\ q_1 & q_2 & -q_1 - q_2 \end{pmatrix} \begin{pmatrix} 1 & 1 & Q \\ \varrho_1 & \varrho_1 & -2\varrho_1 \end{pmatrix}, \end{aligned} \quad (\text{C.17a})$$

and analogously for  $\mathcal{D}_{q_3, \varrho_1}^{*(1)}(\omega) \mathcal{D}_{q_4, \varrho_1}^{*(1)}(\omega)$ ,

$$\begin{aligned} \mathcal{D}_{q_3, \varrho_1}^{*(1)}(\omega) \mathcal{D}_{q_4, \varrho_1}^{*(1)}(\omega) &= \sum_{Q'=0}^2 (2Q'+1) \mathcal{D}_{-q_3-q_4, -2\varrho_1}^{(Q')}(\omega) \\ &\times \begin{pmatrix} 1 & 1 & Q' \\ q_3 & q_4 & -q_3 - q_4 \end{pmatrix} \begin{pmatrix} 1 & 1 & Q \\ \varrho_1 & \varrho_1 & -2\varrho_1 \end{pmatrix}. \end{aligned} \quad (\text{C.17b})$$

Inserting Eqs. (C.17) into (10.13a) and using

$$\begin{aligned} \mathcal{D}_{q_1+q_2, 2\varrho_1}^{(Q)}(\omega) \mathcal{D}_{-q_3-q_4, -2\varrho_1}^{(Q')}(\omega) &= \sum_{K=0}^4 (2K+1) \mathcal{D}_{s,0}^{*(K)}(\omega) \\ &\times \begin{pmatrix} Q & Q' & K \\ q_1+q_2 & -q_3-q_4 & -s \end{pmatrix} \begin{pmatrix} Q & Q' & K \\ 2\varrho_1 & -2\varrho_1 & 0 \end{pmatrix}, \end{aligned}$$

with  $s = q_1 + q_2 - q_3 - q_4$ , the orientation-dependent probability of two-photon absorption becomes,

$$\begin{aligned} \rho_{2P}(\omega) &= \sum_{q_1, q_2} T_{q_1, q_2} \sum_{q_3, q_4} T_{q_3, q_4}^* (-1)^{q_3+q_4} \sum_{Q=0}^2 (2Q+1) \begin{pmatrix} 1 & 1 & Q \\ q_1 & q_2 & -q_1 - q_2 \end{pmatrix} \begin{pmatrix} 1 & 1 & Q \\ \varrho_1 & \varrho_1 & -2\varrho_1 \end{pmatrix} \\ &\times \sum_{Q'=0}^2 (2Q'+1) \begin{pmatrix} 1 & 1 & Q' \\ q_3 & q_4 & -q_3 - q_4 \end{pmatrix} \begin{pmatrix} 1 & 1 & Q' \\ \varrho_1 & \varrho_1 & -2\varrho_1 \end{pmatrix} \\ &\times \sum_{K=0}^4 (2K+1) \begin{pmatrix} Q & Q' & K \\ q_1+q_2 & -q_3-q_4 & -s \end{pmatrix} \begin{pmatrix} Q & Q' & K \\ 2\varrho_1 & -2\varrho_1 & 0 \end{pmatrix} \mathcal{D}_{s,0}^{(K)}(\omega) \\ &\equiv \sum_{q_1, q_2} T_{q_1, q_2} \sum_{q_3, q_4} (-1)^{q_3+q_4} T_{q_3, q_4}^* \sum_{K=0}^4 g_{q_1, q_2, q_3, q_4}^{(K)} \mathcal{D}_{s,0}^{(K)}(\omega), \end{aligned} \quad (\text{C.18})$$

cf. Eq. (10.17). Two useful properties of the Wigner  $3j$  symbols utilized throughout this work, involve odd permutations of two columns [143],

$$\begin{pmatrix} j & j' & J \\ m & m' & M \end{pmatrix} = (-1)^{j+j'+J} \begin{pmatrix} j' & j & J \\ m' & m & M \end{pmatrix}, \quad (\text{C.19})$$

as well as the unitary condition for the Wigner rotation matrices [143],

$$\sum_{M=-J}^J \mathcal{D}_{M,M'}^{(J)}(\omega) \mathcal{D}_{M,\tilde{M}'}^{*(J)}(\omega) = \delta_{M',\tilde{M}'}. \quad (\text{C.20})$$

### C.2.3 Cross section for $(2 + 1)$ photoionization

In order to simplify the expression of the cross section for the  $(2+1)$  REMPI process, we utilize the properties defined in Eq. (C.9), to the product involving the first and second Wigner  $3j$  symbols in Eq. (10.11),

$$\mathcal{D}_{q,\varrho_2}^{(1)}(\omega) \mathcal{D}_{-q',-\varrho_2}^{(1)}(\omega) = (-1)^{q'-q} \sum_{\nu=0}^2 (2\nu+1) \mathcal{D}_{q-q',0}^{(\nu)}(\omega) \begin{pmatrix} 1 & 1 & \nu \\ q & -q' & q'-q \end{pmatrix} \begin{pmatrix} 1 & 1 & \nu \\ \varrho_2 & -\varrho_2 & 0 \end{pmatrix}. \quad (\text{C.21})$$

The rhs of Eq. (C.21) will allow for exploiting, while integrating over the Euler angles, the well-known properties for integrating over a product of three Wigner  $3j$  symbols. With Eq. (C.21), Eq. (10.11) takes the following form,

$$\begin{aligned} \frac{d^2\sigma_{\text{1P}}}{d\omega d\Omega_{\mathbf{k}'}} &= c_o \sum_{\substack{\ell,m \\ \ell_o,m_o}} \sum_{\substack{\ell',m' \\ \ell'_o,m'_o}} \sum_{q,q'} (-i)^{\ell-\ell'} e^{i(\delta_\ell-\delta_{\ell'})} a_{m_o}^{\ell_o} a_{m'_o}^{\ell'_o} I_k(\ell, \ell_o) I_k(\ell', \ell'_o) \mathcal{S}_{\ell_o,m_o}^{\ell,m}(q) \mathcal{S}_{\ell'_o,m'_o}^{\ell',m'}(q') \\ &\times \sum_{\mathcal{L}=|\ell-\ell'|}^{\ell+\ell'} (2\mathcal{L}+1) \begin{pmatrix} \ell & \ell' & \mathcal{L} \\ 0 & 0 & 0 \end{pmatrix} \begin{pmatrix} \ell & \ell' & \mathcal{L} \\ m & -m' & -(m-m') \end{pmatrix} (-1)^{m'-q-\varrho_2} \\ &\times \sum_{\nu=0}^2 (2\nu+1) \begin{pmatrix} 1 & 1 & \nu \\ q & q' & q'-q \end{pmatrix} \begin{pmatrix} 1 & 1 & \nu \\ \varrho_2 & -\varrho_2 & 0 \end{pmatrix} \\ &\times \sum_{\mu=-\mathcal{L}}^{\mathcal{L}} \mathcal{S}_{\mathcal{L}}^{\mu}(\ell, \ell') \mathcal{D}_{q-q',0}^{(\nu)}(\omega) \mathcal{D}_{m'-m,-\mu}^{(\mathcal{L})}(\omega) P_{\mathcal{L}}^{\mu}(\cos \vartheta'_k) e^{i\mu\varphi'_k}. \end{aligned} \quad (\text{C.22})$$

Inserting Eq. (C.18) and Eq. (C.23) into Eq. (10.18), the PAD measured in the laboratory frame, resulting from a fixed molecular orientation  $\omega$  reads,

$$\begin{aligned}
 \frac{d^2\sigma_{2+1}}{d\omega d\Omega_{\mathbf{k}'}} &= \mathcal{N}_0 c_o \sum_{\substack{\ell, m \\ \ell_o, m_o}} \sum_{\substack{\ell', m' \\ \ell'_o, m'_o}} \sum_{q, q'} (-i)^{\ell-\ell'} e^{i(\delta_\ell - \delta_{\ell'})} a_{m_o}^{\ell_o} a_{m'_o}^{*\ell'_o} I_k(\ell, \ell_o) I_k(\ell', \ell'_o) \mathcal{S}_{\ell_o, m_o}^{\ell, m}(q) \mathcal{S}_{\ell'_o, m'_o}^{\ell', m'}(q') \\
 &\times \sum_{\mathcal{L}=|\ell-\ell'|}^{\ell+\ell'} (2\mathcal{L}+1) \begin{pmatrix} \ell & \ell' & \mathcal{L} \\ 0 & 0 & 0 \end{pmatrix} \begin{pmatrix} \ell & \ell' & \mathcal{L} \\ m & -m' & -(m-m') \end{pmatrix} \\
 &\times \sum_{\nu=0}^2 (2\nu+1) \begin{pmatrix} 1 & 1 & \nu \\ q & q' & q'-q \end{pmatrix} \begin{pmatrix} 1 & 1 & \nu \\ \varrho_2 & -\varrho_2 & 0 \end{pmatrix} \\
 &\times \sum_{\mu=-\mathcal{L}}^{\mathcal{L}} \zeta_{\mathcal{L}}^{\mu}(\ell, \ell') (-1)^{m'-q-\varrho_2} P_{\mathcal{L}}^{\mu}(\cos \vartheta'_k) e^{i\mu\varphi'_k} \\
 &\times \sum_{q_1, q_2} T_{q_1, q_2} \sum_{q_3, q_4} (-1)^{q_3+q_4} T_{q_3, q_4}^* \sum_{K=0}^4 g_{q_1, q_2, q_3, q_4}^{(K)} \mathcal{D}_{s,0}^{(K)}(\omega) \mathcal{D}_{q-q',0}^{(\nu)}(\omega) \mathcal{D}_{m'-m,-\mu}^{(\mathcal{L})}(\omega),
 \end{aligned} \tag{C.23}$$

with  $s = q_1 + q_2 - q_3 - q_4$ . Equation (C.23) may be written in the more compact form of Eqs. (10.20), namely,

$$\frac{d^2\sigma_{2+1}}{d\omega d\Omega_{\mathbf{k}'}} = \mathcal{N}_0 c_o \sum_{\mathcal{L}=0}^{\infty} \sum_{\mu=-\mathcal{L}}^{+\mathcal{L}} b_{\mathcal{L}}^{\mu}(\omega) P_{\mathcal{L}}^{\mu}(\cos \vartheta'_k) e^{i\mu\varphi'_k}, \tag{C.24a}$$

In Eq. (C.24a), the only orientation-dependent quantity,  $b_{\mathcal{L}}^{\mu}(\omega)$ , is given by

$$b_{\mathcal{L}}^{\mu}(\omega) = \sum_{\lambda} \kappa_{\mathcal{L}}^{\mu}(\lambda) \mathcal{D}_{s,0}^K(\omega) \mathcal{D}_{q-q',0}^{\nu}(\omega) \mathcal{D}_{m'-m,-\mu}^{\mathcal{L}}(\omega). \tag{C.24b}$$

with  $\kappa_{\mathcal{L}}^{\mu}(\lambda)$  defined as

$$\begin{aligned}
 \kappa_{\mathcal{L}}^{\mu}(\lambda) &= (-i)^{\ell-\ell'} e^{i(\delta_\ell - \delta_{\ell'})} a_{m_o}^{\ell_o} a_{m'_o}^{\ell'_o} I_k(\ell, \ell_o) I_k(\ell', \ell'_o) \mathcal{S}_{\ell_o, m_o}^{\ell, m}(q) \mathcal{S}_{\ell'_o, m'_o}^{\ell', m'}(q') \zeta_{\mathcal{L}}^{\mu}(\ell, \ell') \\
 &\times T_{q_1, q_2} (-1)^{q_3+q_4} T_{q_3, q_4}^* g_{q_1, q_2, q_3, q_4}^{(K)} (2\nu+1)(2\mathcal{L}+1) (-1)^{m'-q-\varrho_2} \\
 &\times \begin{pmatrix} \ell & \ell' & \mathcal{L} \\ 0 & 0 & 0 \end{pmatrix} \begin{pmatrix} \ell & \ell' & \mathcal{L} \\ m & -m' & -(m-m') \end{pmatrix} \begin{pmatrix} 1 & 1 & \nu \\ q & q' & q'-q \end{pmatrix} \begin{pmatrix} 1 & 1 & \nu \\ \varrho_2 & -\varrho_2 & 0 \end{pmatrix}
 \end{aligned} \tag{C.25}$$

where  $\lambda$  comprises all summation indices, except for  $\mathcal{L}$  and  $\mu$ , as described in Sec. C.2.3. Next, according to Eq. (10.19), we need to average over all initial orientations, i.e., integrate the doubly differential cross section over the Euler angles. To this end, we uti-

lize the following integration property involving the product of three Wigner  $3j$  symbols [143, 145, 146],

$$\int \mathcal{D}_{s,0}^{(K)}(\omega) \mathcal{D}_{q-q',0}^{(\nu)}(\omega) \mathcal{D}_{m'-m,-\mu}^{(\mathcal{L})}(\omega) d^3\omega = \begin{pmatrix} K & \nu & \mathcal{L} \\ s & q-q' & m'-m \end{pmatrix} \begin{pmatrix} K & \nu & \mathcal{L} \\ 0 & 0 & -\mu \end{pmatrix} \quad (\text{C.26})$$

with  $d^3\omega \equiv d^3(\alpha, \beta, \gamma) = d\alpha d(\cos(\beta)) d\gamma/8\pi^2$ . Finally, following Eq. (10.19), integration of Eq. (C.23) over the Euler angles  $\omega \equiv (\alpha, \beta, \gamma)$ , using Eq. (C.26), gives the expression of the laboratory frame PAD resulting from a randomly ensemble of molecules in the context of a  $(2+1)$  REMPI process, defined in Eq. (10.21). In particular, due to the second Wigner  $3j$  symbol in Eq. (C.26), it is clear that the integral vanishes if  $\mu \neq 0$ . As a consequence, this requirement translates into cylindrical symmetry of the PAD measured in the laboratory frame, as  $\mu$  also appears in the azimuthal angle dependent term  $e^{i\mu\varphi'_k}$  in Eq. (C.23). Thus, we retrieve the expression defined in Eq. (10.21).

#### **C.2.4 Non-zero Legendre coefficients for two-photon absorption with circularly polarized light and ionization with linear polarization**

In this section, we show that a  $(2+1)$  REMPI process for which the two-photon absorption process is driven by circular polarized light, followed by linearly polarized light for the radiative process, lead within the electric dipole approximation exclusively to even Legendre coefficients. To this end, we exploit the symmetry as well as invariance properties of Eq. (10.21b), by making a change of variables for  $q_1, q_2, q_3$  and  $q_4$  in Eq. (10.21b) that preserves  $c_{\mathcal{L}}(\varrho_1, \varrho_2)$  unchanged and also keeps  $s = q_1 + q_2 - q_3 - q_4$  invariant (in order to keep the fifth Wigner  $3j$  symbol in Eq. (10.21b) unchanged). A change of variables fulfilling this property reads,

$$\begin{pmatrix} q'_1 \\ q'_2 \\ q'_3 \\ q'_4 \end{pmatrix} = \begin{pmatrix} 0 & 0 & -1 & 0 \\ 0 & 0 & 0 & -1 \\ -1 & 0 & 0 & 0 \\ 0 & -1 & 0 & 0 \end{pmatrix} \begin{pmatrix} q_1 \\ q_2 \\ q_3 \\ q_4 \end{pmatrix}, \quad (\text{C.27})$$

i.e., it interchanges  $q_1 \rightleftharpoons -q_3$  and  $q_2 \rightleftharpoons -q_4$ .

For simplicity, we define the quantity,

$$\Lambda_{\theta}(\varrho_1) = \sum_K \sum_{q_1, q_2} \sum_{q_3, q_4} (-1)^{q_3+q_4} g_{q_1, q_2, q_3, q_4}^K(\varrho_1) T_{q_1, q_2} T_{q_3, q_4}^* W_{\theta}(s) \quad (\text{C.28a})$$

with

$$W_{\theta}(s) = \begin{pmatrix} K & \nu & \mathcal{L} \\ s & q - q' & m' - m \end{pmatrix} \quad (\text{C.28b})$$

Eqs. (C.28) appear in Eq. (10.21b). In Eq. (C.28),  $s = q_1 + q_2 - q_3 - q_4$  and  $\theta$  stands for the indices ( $\theta \equiv K, \nu, m, m', q, q', \mathcal{L}$ ). Analogously,  $\Lambda'_{\theta}(\varrho_1)$  is defined using the primed dummy variables  $q'_k$ , for  $k = 1, \dots, 4$  with the symmetry property  $\Lambda_{\theta}(\varrho_1) = \Lambda'_{\theta}(\varrho_1)$ . Of course, we have

$$c_{\mathcal{L}}(\varrho_1, 0) = c'_{\mathcal{L}}(\varrho_1, 0) \quad (\text{C.29})$$

Using Eq. (C.27), the tensor elements appearing in Eq. (10.21b) then transform according to

$$T_{q'_1, q'_2} = T_{-q_3, -q_4} = (-1)^{q_3+q_4} T_{q_3, q_4}^* \quad (\text{C.30a})$$

and

$$T_{q'_3, q'_4}^* = T_{-q_1, -q_2}^* = (-1)^{q_1+q_2} T_{q_1, q_2}, \quad (\text{C.30b})$$

Using Eq. (C.30), Eq. (C.28) reads, upon transformation,

$$\Lambda'_{\theta}(\varrho_1) = \sum_{q_1, q_2} \sum_{q_3, q_4} (-1)^{q_3+q_4} g_{-q_3, -q_4, -q_1, -q_2}^K(\varrho_1) T_{q_1, q_2} T_{q_3, q_4}^* W_{\theta}(s), \quad (\text{C.31})$$

with  $\Lambda_{\theta}(\varrho_1) = \Lambda'_{\theta}(\varrho_1)$ . Next, evaluation of the quantity  $g_{-q_3, -q_4, -q_1, -q_2}^K(\varrho_1)$  present in Eq. (C.31) using Eq. (10.17b), gives

$$\begin{aligned} g_{-q_3, -q_4, -q_1, -q_2}^{(K)}(\varrho_1) &= \sum_{Q'=0}^2 \begin{pmatrix} 1 & 1 & Q' \\ -q_3 & -q_4 & q_3 + q_4 \end{pmatrix} \begin{pmatrix} 1 & 1 & Q' \\ \varrho_1 & \varrho_1 & -2\varrho_1 \end{pmatrix} \\ &\times \sum_{Q=0}^2 \begin{pmatrix} 1 & 1 & Q \\ -q_1 & -q_2 & q_1 + q_2 \end{pmatrix} \begin{pmatrix} 1 & 1 & Q \\ \varrho_1 & \varrho_1 & -2\varrho_1 \end{pmatrix} \\ &\times \sum_{K=|Q-Q'|}^{Q+Q'} \begin{pmatrix} Q' & Q & K \\ -q_3 - q_4 & q_1 + q_2 & s \end{pmatrix} \begin{pmatrix} Q' & Q & K \\ 2\varrho_1 & -2\varrho_1 & 0 \end{pmatrix} \gamma_{Q, Q'}^{(K)}, \end{aligned} \quad (\text{C.32})$$

where we have interchanged the dummy indices  $Q$  and  $Q'$ . Application of Eq. (10.25) to

the first and third Wigner  $3j$  symbol in Eq. (C.32) gives,

$$\begin{pmatrix} 1 & 1 & Q' \\ -q_3 & -q_4 & q_3 + q_4 \end{pmatrix} = (-1)^{Q'} \begin{pmatrix} 1 & 1 & Q' \\ q_3 & q_4 & -q_3 - q_4 \end{pmatrix} \quad (\text{C.33a})$$

and

$$\begin{pmatrix} 1 & 1 & Q \\ -q_1 & -q_2 & q_1 + q_2 \end{pmatrix} = (-1)^Q \begin{pmatrix} 1 & 1 & Q \\ q_1 & q_2 & -q_1 - q_2 \end{pmatrix}, \quad (\text{C.33b})$$

respectively. Next, we permute the first and second column in the fifth Wigner  $3j$  symbol in Eq. (C.32), following Eq. (C.19), which yields

$$\begin{pmatrix} Q' & Q & K \\ -q_3 - q_4 & q_1 + q_2 & s \end{pmatrix} = \begin{pmatrix} Q & Q' & K \\ q_1 + q_2 & -q_3 - q_4 & s \end{pmatrix} (-1)^{Q+Q'+K} \quad (\text{C.33c})$$

Finally, inserting Eqs. (C.33) into Eq. (C.32) together with the property  $\Lambda_\theta(\varrho_1) = \Lambda'_\theta(\varrho)$ , we find

$$\begin{aligned} & \sum_K \sum_{q_1, q_2} \sum_{q_3, q_4} (-1)^{q_3+q_4} g_{q_1, q_2, q_3, q_4}^K(\varrho_1) T_{q_1, q_2} T_{q_3, q_4}^* W_\theta(s) \\ & = \sum_K \sum_{q_1, q_2} \sum_{q_3, q_4} (-1)^{q_3+q_4} g_{q_1, q_2, q_3, q_4}^K(\varrho_1) (-1)^K T_{q_1, q_2} T_{q_3, q_4}^* W_\theta(s) \end{aligned} \quad (\text{C.34})$$

with  $W_\theta(s)$  invariant as  $s$  invariant, and where  $g_{q_1, q_2, q_3, q_4}^K(\varrho_1)$  is defined in Eq. (10.17b). Equation (C.34) means that the summations over  $K$  and  $q_k$  is invariant under the trans-

formation  $g^K \rightarrow (-1)^K g^K$ . Using Eq. (C.34), we find for  $\varrho_1 = \pm 1$  and  $\varrho_2 = 0$ ,

$$\begin{aligned}
 c'_{\mathcal{L}}(\varrho_1, 0) &= \mathcal{N}_0 \tilde{c}_o \sum_{\substack{\ell, m \\ n_o, \ell_o, m_o}} \sum_{\substack{\ell', m' \\ n'_o, \ell'_o, m'_o}} \sum_{q, q'} \sum_{\substack{q_1, q_2 \\ q_3, q_4}} \sum_{\nu=0}^2 \sum_{K=0}^4 (-1)^{q^3+q^4} (2\nu+1)(2\mathcal{L}+1) \\
 &\times a_{m_o}^{\ell_o}(n_o) a_{m'_o}^{*\ell'_o}(n'_o) T_{q_1, q_2} T_{q_3, q_4}^* \mathcal{S}_{\ell_o, m_o}^{\ell, m}(q) \mathcal{S}_{\ell'_o, m'_o}^{\ell', m'}(q') \hat{\zeta}(\ell, \ell') \\
 &\times (-i)^{\ell-\ell'} (-1)^{m'-q-\varrho_2} e^{i(\delta_\ell - \delta_{\ell'})} g_{q_1, q_2, q_3, q_4}^{(K)}(\varrho_1) I_k^{n_o}(\ell, \ell_o) I_k^{n'_o}(\ell', \ell'_o) \\
 &\times \begin{pmatrix} \ell & \ell' & \mathcal{L} \\ m & -m' & m' - m \end{pmatrix} \begin{pmatrix} \ell & \ell' & \mathcal{L} \\ 0 & 0 & 0 \end{pmatrix} \begin{pmatrix} 1 & 1 & \nu \\ q & -q' & q' - q \end{pmatrix} \begin{pmatrix} 1 & 1 & \nu \\ 0 & 0 & 0 \end{pmatrix} \\
 &\times \begin{pmatrix} K & \nu & \mathcal{L} \\ s & q - q' & m' - m \end{pmatrix} \begin{pmatrix} K & \nu & \mathcal{L} \\ 0 & 0 & 0 \end{pmatrix} (-1)^K (-1)^{K+\nu+\mathcal{L}} \\
 &= (-1)^{\mathcal{L}} c_{\mathcal{L}}(\varrho_1, 0). \tag{C.35}
 \end{aligned}$$

In Eq. (C.35), the factors  $(-1)^K$  and  $(-1)^{\nu+K+\mathcal{L}}$  arise from Eqs. (C.34) and from application of the property defined in Eq. (10.25) to the sixth Wigner  $3j$  symbol in Eq. (C.35), respectively. Furthermore, we used the property that  $\nu$  is even, i.e. only even  $\nu$  contribute to the summation, due to the triple zeros in the second row of the fourth Wigner  $3j$  symbol. Finally, using Eq. (C.29), it follows that for  $\varrho_2 = 0$ ,

$$c_{\mathcal{L}}(\varrho_1, 0) = (-1)^{\mathcal{L}} c_{\mathcal{L}}(\varrho_1, 0). \tag{C.36}$$

Because no assumptions have been made on the polarization direction  $\varrho_1$ , Eq. (C.36) shows that only even Legendre coefficients are present in the PAD if the radiative photoabsorption is driven by linearly polarized light, i.e.  $\varrho_2 = 0$ , independently of the polarization direction,  $\varrho_1$ , driving the non-resonant two-photon absorption process. As a consequence, only even Legendre orders contribute to the PAD if  $\varrho_1 = \pm 1, 0$  and  $\varrho_2 = 0$ , translating into a vanishing PECD.

### C.2.5 Behavior of Legendre coefficients when changing the helicity of the one-photon photoionization

The easiest way to prove Eq. (10.35) consists of making the change of variables defined in Eq. (C.27), and evaluate  $c'_{\mathcal{L}}(\varrho_1, -\varrho_2)$ , using the property

$$c_{\mathcal{L}}(\varrho_1, -\varrho_2) = c'_{\mathcal{L}}(\varrho_1, -\varrho_2), \tag{C.37}$$

where the unprimed (primed) quantities in Eq. (C.37) refer to the Legendre coefficients before (after) the change of variables, respectively. Keeping  $\epsilon_{\varrho_1}$  fixed while changing the polarization direction  $\varrho_2$  transforms the fourth Wigner  $3j$  symbol in Eq. (10.21b) according to,

$$\begin{pmatrix} 1 & 1 & \nu \\ -\varrho_2 & \varrho_2 & 0 \end{pmatrix} = (-1)^\nu \begin{pmatrix} 1 & 1 & \nu \\ \varrho_2 & \varrho_2 & 0 \end{pmatrix}, \quad (\text{C.38})$$

where we have used Eq. (10.25). Inserting Eqs. (C.34) and (C.38) to Eq. (10.21b), for  $c'_{\mathcal{L}}(\varrho_1, -\varrho_2)$  gives

$$\begin{aligned} c'_{\mathcal{L}}(\varrho_1, -\varrho_2) &= \mathcal{N}_0 \tilde{c}_o \sum_{\substack{\ell, m \\ n_o, \ell_o, m_o}} \sum_{\substack{\ell', m' \\ n'_o, \ell'_o, m'_o}} \sum_{q, q'} \sum_{\substack{q_1, q_2 \\ q_3, q_4}} \sum_{\nu=0}^2 \sum_{K=0}^4 (-1)^{q_3+q_4} (2\nu+1)(2\mathcal{L}+1) \\ &\times a_{m_o}^{\ell_o}(n_o) a_{m'_o}^{*\ell'_o}(n'_o) T_{q_1, q_2} T_{q_3, q_4}^* \mathcal{S}_{\ell_o, m_o}^{\ell, m}(q) \mathcal{S}_{\ell'_o, m'_o}^{\ell', m'}(q') \hat{\zeta}(\ell, \ell') \\ &\times (-i)^{\ell-\ell'} (-1)^{m'-q-\varrho_2} e^{i(\delta_\ell-\delta_{\ell'})} g_{q_1, q_2, q_3, q_4}^{(K)}(\varrho_1) I_k^{n_o}(\ell, \ell_o) I_k^{n'_o}(\ell', \ell'_o) \\ &\times \begin{pmatrix} \ell & \ell' & \mathcal{L} \\ m & -m' & m'-m \end{pmatrix} \begin{pmatrix} \ell & \ell' & \mathcal{L} \\ 0 & 0 & 0 \end{pmatrix} \begin{pmatrix} 1 & 1 & \nu \\ q & -q' & q'-q \end{pmatrix} \begin{pmatrix} 1 & 1 & \nu \\ \varrho_2 & -\varrho_2 & 0 \end{pmatrix} \\ &\times \begin{pmatrix} K & \nu & \mathcal{L} \\ s & q-q' & m'-m \end{pmatrix} \begin{pmatrix} K & \nu & \mathcal{L} \\ 0 & 0 & 0 \end{pmatrix} (-1)^K (-1)^\nu (-1)^{K+\nu+\mathcal{L}} \\ &= (-1)^\mathcal{L} c_{\mathcal{L}}(\varrho_1, +\varrho_2). \end{aligned} \quad (\text{C.39})$$

In Eq. (C.39), the factors  $(-1)^K$  and  $(-1)^\nu$  arise from the invariance property defined in Eq. (C.34) for the transformation defined in Eq. (C.27), and (C.38), respectively. Application of the property defined in Eq. (10.25) to the sixth Wigner  $3j$  symbol in Eq. (C.39) gives rise to the factor  $(-1)^{K+\nu+\mathcal{L}}$ . The terms in  $K$  and  $\nu$  compensates, giving rise to the factor in  $(-1)^\mathcal{L}$  alone. Finally, using (C.37) and comparing Eq. (10.21b) for  $\varrho_1$  and  $\varrho_2$  and Eq. (C.39) for  $\varrho_1$  and  $-\varrho_2$ , determines the proof for Eq. (10.35), i.e.,

$$c_{\mathcal{L}}(\varrho_1, -\varrho_2) = (-1)^\mathcal{L} c_{\mathcal{L}}(\varrho_1, +\varrho_2) \quad (\text{C.40})$$

### C.2.6 Behavior of Legendre coefficients when changing the helicity of the two-photon absorption process

In this section, we present the proof of Eq. (10.36). To verify that it is the polarization direction of the ionizing field alone which imposes the sign for all odd Legendre coefficients, whereas the polarization direction of the two-photon absorption plays no role, we define the following transformation

$$\begin{pmatrix} q'_1 \\ q'_2 \\ q'_3 \\ q'_4 \end{pmatrix} = \begin{pmatrix} 0 & 0 & 0 & -1 \\ 0 & 0 & -1 & 0 \\ 0 & -1 & 0 & 0 \\ -1 & 0 & 0 & 0 \end{pmatrix} \begin{pmatrix} q_1 \\ q_2 \\ q_3 \\ q_4 \end{pmatrix} \quad (\text{C.41})$$

which interchanges the indices  $q_1 \rightleftharpoons -q_4$  and  $q_2 \rightleftharpoons -q_3$  while keeping Eq. (10.21b) unchanged and  $s$  invariant. In particular, the tensor elements appearing in Eq. (10.21b) then transform according to,

$$\begin{aligned} T_{q'_1, q'_2} &= T_{-q_4, -q_3} = (-1)^{q_3+q_4} T_{q_4, q_3}^* \\ &= (-1)^{q_3+q_4} T_{q_3, q_4}^* \end{aligned} \quad (\text{C.42a})$$

and

$$\begin{aligned} T_{q'_3, q'_4}^* &= T_{-q_2, -q_1}^* = (-1)^{q_1+q_2} T_{q_2, q_1} \\ &= (-1)^{q_1+q_2} T_{q_1, q_2}, \end{aligned} \quad (\text{C.42b})$$

where we have made use of the correspondence between the components of a vector operator in spherical and cartesian basis, defined in Eq. (C.7) in Appendix C.1.3, in  $T_{q_k, q_{k'}}$ , for  $q_k, q_{k'} = \pm 1, 0$ , together with the fact that the two-photon absorption tensor is symmetric in cartesian coordinates, i.e.,  $T_{i,j} = T_{j,i}$  for  $i, j = (x, y, z)$ .

We define  $\Lambda_\theta(\varrho_1)$ , according Eq. (C.28) and we study the symmetry properties of  $\Lambda'_\theta(\varrho_1)$  upon transformation defined in Eq. (C.41). In particular, because the quantity given by

$$(-1)^{q'_1+q'_3} T_{q'_1, q'_2} T_{q'_3, q'_4} W_\theta(s') \quad (\text{C.43})$$

is (as for the earlier transformation defined in Eq. (C.27)) invariant under transformation defined in Eq. (C.41), we may neglect it in the following, avoiding cumbersome notations. We outline, however, that a full notation was used in Section C.2.4. Therefore, given

such invariance properties, we may consider the behavior of  $g^K$  under exchange  $\varrho_1 \rightarrow -\varrho_1$  alone, and neglect the extra terms depending on  $K, q_1, \dots, q_4$  in the expression for  $\Lambda'_\theta(s)$ . Because  $\varrho_1$  is changed to  $-\varrho_1$  while  $\varrho_2$  is kept fixed, we consider  $g^K(-\varrho_1)$  which becomes, upon transformation defined in Eq. (C.41),

$$g_{q'_1, q'_2, q'_3, q'_4}^{(K)}(-\varrho_1) = \sum_{Q=0}^2 \sum_{Q'=0}^2 \begin{pmatrix} 1 & 1 & Q' \\ -q_4 & -q_3 & q_4 + q_3 \end{pmatrix} \begin{pmatrix} 1 & 1 & Q' \\ -\varrho_1 & -\varrho_1 & +2\varrho_1 \end{pmatrix} \begin{pmatrix} 1 & 1 & Q \\ -q_2 & -q_1 & q_2 + q_1 \end{pmatrix} \\ \times \sum_{K=|Q-Q'|}^{Q+Q'} \begin{pmatrix} 1 & 1 & Q \\ -\varrho_1 & -\varrho_1 & +2\varrho_1 \end{pmatrix} \begin{pmatrix} Q' & Q & K \\ -q_4 - q_3 & q_3 + q_2 & s \end{pmatrix} \begin{pmatrix} Q' & Q & K \\ -2\varrho_1 & +2\varrho_1 & 0 \end{pmatrix} \gamma_{Q, Q'}^{(K)}, \quad (\text{C.44})$$

where we have interchanged the indexes  $Q$  and  $Q'$ . Next we apply the symmetry property given in Eq. (10.25), followed by an odd permutation of the first and second columns, according to Eq. (C.19), to the first Wigner  $3j$  symbol in Eq. (C.44). We find

$$\begin{pmatrix} 1 & 1 & Q' \\ -q_4 & -q_3 & q_4 + q_3 \end{pmatrix} = \begin{pmatrix} 1 & 1 & Q' \\ q_3 & q_4 & -q_3 - q_4 \end{pmatrix}. \quad (\text{C.45a})$$

The same procedure is applied to the third symbol in Eq. (C.44), i.e.,

$$\begin{pmatrix} 1 & 1 & Q \\ -q_2 & -q_1 & q_2 + q_1 \end{pmatrix} = \begin{pmatrix} 1 & 1 & Q \\ q_1 & q_2 & -q_1 - q_2 \end{pmatrix}. \quad (\text{C.45b})$$

Next, odd permutation of the first and second columns in the fifth Wigner  $3j$  symbol gives,

$$\begin{pmatrix} Q' & Q & K \\ -q_4 - q_3 & q_2 + q_1 & s \end{pmatrix} = \begin{pmatrix} Q & Q' & K \\ q_1 + q_2 & -q_4 - q_3 & s \end{pmatrix} (-1)^{Q+Q'+K}. \quad (\text{C.45c})$$

Application of Eq. (10.25), followed by permutation of the first two rows leaves the sign of the second Wigner  $3j$  symbol unchanged for all  $Q'$ , namely

$$\begin{pmatrix} 1 & 1 & Q' \\ -\varrho_1 & -\varrho_1 & -2\varrho_1 \end{pmatrix} = \begin{pmatrix} 1 & 1 & Q' \\ +\varrho_1 & +\varrho_1 & +2\varrho_1 \end{pmatrix} \quad (\text{C.45d})$$

and analogously for the fourth Wigner symbol involving  $Q$ . It is to note that, the left side of Eq. (C.45d) is related to  $g^K(-\varrho_1)$  while the right side is related to  $g^K(+\varrho_1)$ . Permuting

the first two rows of the fifth Wigner symbol in Eq. (C.44) gives

$$\begin{pmatrix} Q' & Q & K \\ -2\varrho_1 & +2\varrho_1 & 0 \end{pmatrix} = (-1)^{Q+Q'+K} \begin{pmatrix} Q & Q' & K \\ 2\varrho_1 & -2\varrho_1 & 0 \end{pmatrix}. \quad (\text{C.45e})$$

Inserting the symmetry transformations (C.45) into Eq. (C.44), leads to a compensation of the terms  $(-1)^{Q+Q'+K}$  in Eqs. (C.45c) and (C.45e). Finally, comparing Eq. (C.44) and Eq. (10.17b) gives the following property,

$$\sum_K \sum_{\substack{q_1, q_2 \\ q_3, q_4}} g_{q_1, q_2, q_3, q_4}^K(-\varrho_1) = \sum_K \sum_{\substack{q_1, q_2 \\ q_3, q_4}} g_{q_1, q_2, q_3, q_4}^K(+\varrho_1), \quad (\text{C.46})$$

which implies  $c_{\mathcal{L}}(-\varrho_1, \varrho_2) = c_{\mathcal{L}}(\varrho_1, \varrho_2)$  according to Eq. (10.21b), cf. Eq. (10.36).



# List of publications

1. **R. Esteban Goetz**, Andrea Simoni and Christiane P. Koch  
*An adaptive-size multi-domain pseudospectral approach for solving the time-dependent Schrödinger equation*  
arXiv:1611.09034
2. **R. Esteban Goetz**, Antonia Karamatskou, Robin Santra and Christiane P. Koch  
*Quantum optimal control of photoelectron spectra and angular distributions*  
Phys. Rev. A **90**, 013413 (2016)
3. **R. Esteban Goetz**, Maximilian Merkel, Antonia Karamatskou, Robin Santra and Christiane P. Koch  
*Maximizing hole coherence in ultrafast photoionization of argon with an optimization by sequential parametrization update*  
Phys. Rev. A **94**, 023420 (2016)
4. **R. Esteban Goetz**, Timur A. Isaev, Behnam Nikoobakht, Robert Berger and Christiane P. Koch  
*Theoretical description of circular dichroism in photoelectron angular distributions of randomly oriented chiral molecules after multi-photon photoionization*  
The Journal of Chemical Physics **146**, 024306 (2017)
5. Antonia Karamatskou, **R. Esteban Goetz**, Robin Santra and Christiane P. Koch  
*Suppression of hole decoherence via quantum optimal control*  
Submitted to PRL.
6. **R. Esteban Goetz** and Christiane P. Koch  
*New approach for the observation of electroweak parity violation effects*  
to be submitted



# Bibliography

- [1] M. Born, Ann. Physik **84**, 8 (1927).
- [2] D. W. Schwenke, The Journal of Physical Chemistry A **105**, 2352 (2001).
- [3] M. Vacher, M. J. Bearpark, M. A. Robb, and J. P. Malhado, Physical Review Letters **118**, 083001 (2017).
- [4] N. Zettili and F. M. Villars, Nuclear Physics A **469**, 93 (1987).
- [5] M. Vacher, D. Mendive-Tapia, M. J. Bearpark, and M. A. Robb, Theoretical Chemistry Accounts **133**, 1505 (2014).
- [6] M. Vacher, M. J. Bearpark, and M. A. Robb, “Communication: Oscillating charge migration between lone pairs persists without significant interaction with nuclear motion in the glycine and Gly-Gly-NH-CH<sub>3</sub> radical cations,” (2014).
- [7] D. Mendive-Tapia, M. Vacher, M. J. Bearpark, and M. A. Robb, The Journal of chemical physics **139**, 044110 (2013).
- [8] A. J. Jenkins, M. Vacher, M. J. Bearpark, and M. A. Robb, The Journal of chemical physics **144**, 104110 (2016).
- [9] B. H. Bransden and C. J. Joachain, *Physics of atoms and molecules* (Pearson Education India, 2003).
- [10] N. Rohringer, A. Gordon, and R. Santra, Phys. Rev. A **74**, 043420 (2006).
- [11] J. Higuete, H. Ruf, N. Thiré, R. Cireasa, E. Constant, E. Cormier, D. Descamps, E. Mével, S. Petit, B. Pons, *et al.*, Physical Review A **83**, 053401 (2011).
- [12] M. Marinescu, H. Sadeghpour, and A. Dalgarno, Physical Review A **49**, 982 (1994).
- [13] H. Hellmann, The Journal of Chemical Physics **3**, 61 (1935).
- [14] H. G. Muller, Phys. Rev. A **60**, 1341 (1999).
- [15] J. Callaway, Physical Review **106**, 868 (1957).

- [16] P. Fuentealba, H. Preuss, H. Stoll, and L. Von Szentpály, *Chemical Physics Letters* **89**, 418 (1982).
- [17] P. Fuentealba, *Journal of Physics B: Atomic and Molecular Physics* **15**, L555 (1982).
- [18] A. Sanayei, N. Schopohl, J. Grimm, M. Mack, F. Karlewski, and J. Fortágh, *Physical Review A* **91**, 032509 (2015).
- [19] M. Dolg and X. Cao, *Chem. Rev* **112**, 403 (2012).
- [20] P. Schwerdtfeger, in *Theoretical chemistry and physics of heavy and superheavy elements* (Springer, 2003) pp. 399–438.
- [21] X. Cao and M. Dolg, in *Relativistic methods for chemists* (Springer, 2010) pp. 215–277.
- [22] J. L. Krause, K. J. Schafer, and K. C. Kulander, *Phys. Rev. Lett.* **68**, 3535 (1992).
- [23] M. Lewenstein, P. Balcou, M. Y. Ivanov, A. L’Huillier, and P. B. Corkum, *Phys. Rev. A* **49**, 2117 (1994).
- [24] K. J. Schafer, B. Yang, L. F. DiMauro, and K. C. Kulander, *Phys. Rev. Lett.* **70**, 1599 (1993).
- [25] L. Greenman, P. J. Ho, S. Pabst, E. Kamarchik, D. A. Mazziotti, and R. Santra, *Phys. Rev. A* **82**, 023406 (2010).
- [26] K. C. Kulander, *Phys. Rev. A* **36**, 2726 (1987).
- [27] A. Gordon, F. X. Kärtner, N. Rohringer, and R. Santra, *Phys. Rev. Lett.* **96**, 223902 (2006).
- [28] N. Rohringer and R. Santra, *Phys. Rev. A* **79**, 053402 (2009).
- [29] V. Vénier, R. Taieb, and A. Maquet, *Laser physics* **13**, 465 (2003).
- [30] N. Rohringer, S. Peter, and J. Burgdörfer, *Physical Review A* **74**, 042512 (2006).
- [31] V. Vénier, R. Taieb, and A. Maquet, *Laser physics* **13**, 465 (2003).
- [32] C. J. Cramer and D. G. Truhlar, *Physical Chemistry Chemical Physics* **11**, 10757 (2009).
- [33] A. J. Cohen, P. Mori-Sánchez, and W. Yang, *Science* **321**, 792 (2008).
- [34] A. J. Cohen, P. Mori-Sánchez, and W. Yang, *Chemical Reviews* **112**, 289 (2011).

- [35] J. Kim, K. Hong, S. Choi, S.-Y. Hwang, and W. Y. Kim, *Physical Chemistry Chemical Physics* **17**, 31434 (2015).
- [36] D. R. Hartree, in *Mathematical Proceedings of the Cambridge Philosophical Society*, Vol. 24 (Cambridge University Press, 1928) pp. 89–110.
- [37] P.-O. Löwdin, *Physical review* **97**, 1509 (1955).
- [38] G. D. Purvis III and R. J. Bartlett, *The Journal of Chemical Physics* **76**, 1910 (1982).
- [39] K. Raghavachari, G. W. Trucks, J. A. Pople, and M. Head-Gordon, *Chemical Physics Letters* **157**, 479 (1989).
- [40] T. Van Voorhis and M. Head-Gordon, *The Journal of Chemical Physics* **115**, 5033 (2001).
- [41] M. Spanner and P. Brumer, *Physical Review A* **78**, 033840 (2008).
- [42] C. Møller and M. S. Plesset, *Physical Review* **46**, 618 (1934).
- [43] B. O. Roos, P. R. Taylor, P. E. Si, *et al.*, *Chemical Physics* **48**, 157 (1980).
- [44] C. D. Sherrill, School of Chemistry and Biochemistry, Georgia Institute of Technology (1995).
- [45] A. Szabo and N. S. Ostlund, NY: McGraw-Hill (1989).
- [46] J. C. Slater, *Physical Review* **34**, 1293 (1929).
- [47] E. Condon, *Physical Review* **36**, 1121 (1930).
- [48] J. C. Slater, *Physical Review* **38**, 1109 (1931).
- [49] R. Harrison and N. Handy, *Chemical Physics Letters* **95**, 386 (1983).
- [50] R. E. Goetz, M. Merkel, A. Karamatskou, R. Santra, and C. P. Koch, *Phys. Rev. A* **94**, 023420 (2016).
- [51] A. Karamatskou, S. Pabst, Y.-J. Chen, and R. Santra, *Phys. Rev. A* **89**, 033415 (2014).
- [52] S. Pabst, L. Greenman, P. J. Ho, D. A. Mazziotti, and R. Santra, *Phys. Rev. Lett.* **106**, 053003 (2011).
- [53] L. Greenman, C. P. Koch, and K. B. Whaley, *Phys. Rev. A* **92**, 013407 (2015).

- [54] J. Appel, Phys. Rev. **133**, A280 (1964).
- [55] A. Ron, I. Goldberg, J. Stein, S. T. Manson, R. Pratt, and R. Yin, Physical Review A **50**, 1312 (1994).
- [56] C. Cohen-Tannoudji, *Atoms in electromagnetic fields*, Vol. 1 (World scientific, 1994).
- [57] R. Kosloff, J. Chem. Phys. **92**, 2087 (1988).
- [58] A. Scrinzi and N. Elander, The Journal of chemical physics **98**, 3866 (1993).
- [59] L. Greenman, R. R. Lucchese, and C. W. McCurdy, arXiv:1708.03679 (2017).
- [60] R. Esteban Goetz, A. Simoni, and C. P. Koch, arXiv:1611.09034 (2017).
- [61] D. Funaro, *Polynomial approximation of differential equations*, Vol. 8 (Springer Science & Business Media, 2008).
- [62] C. G. Canuto, M. Y. Hussaini, A. Quarteroni, and T. A. Zang, *Spectral methods: Fundamentals in single domains* (Springer, 2010).
- [63] D. A. Kopriva, *Implementing spectral methods for partial differential equations: Algorithms for scientists and engineers* (Springer Science & Business Media, 2009).
- [64] J. S. Hesthaven, S. Gottlieb, and D. Gottlieb, *Spectral methods for time-dependent problems*, Vol. 21 (Cambridge University Press, 2007).
- [65] E. Tadmor, *Spectral methods for time dependent problems* (PN, 1990).
- [66] R. G. Littlejohn, M. Cargo, T. Carrington Jr, K. A. Mitchell, and B. Poirier, The Journal of chemical physics **116**, 8691 (2002).
- [67] J. Lill, G. Parker, and J. Light, Chemical Physics Letters **89**, 483 (1982).
- [68] J. Lill, G. A. Parker, and J. C. Light, The Journal of chemical physics **85**, 900 (1986).
- [69] Z. Bačić and J. Light, The Journal of chemical physics **85**, 4594 (1986).
- [70] J. Light and Z. Bačić, The Journal of chemical physics **87**, 4008 (1987).
- [71] Z. Bačić and J. Light, The Journal of chemical physics **86**, 3065 (1987).
- [72] S. E. Choi and J. Light, The Journal of Chemical Physics **90**, 2593 (1989).
- [73] D. Baye and P.-H. Heenen, Journal of Physics A: Mathematical and General **19**, 2041 (1986).

- [74] J. Tennyson and J. R. Henderson, *The Journal of chemical physics* **91**, 3815 (1989).
- [75] E. Fattal, R. Baer, and R. Kosloff, *Physical Review E* **53**, 1217 (1996).
- [76] J. C. Light and T. Carrington Jr, *Advances in Chemical Physics* **114**, 263 (2000).
- [77] B. I. Schneider and N. Nygaard, *Physical Review E* **70**, 056706 (2004).
- [78] J. P. Boyd, *Chebyshev and Fourier Spectral Methods*, 2nd ed. (Dover Publications, Inc., New York, 2000).
- [79] D. T. Colbert and W. H. Miller, *The Journal of chemical physics* **96**, 1982 (1992).
- [80] D. Baye, *physica status solidi (b)* **243**, 1095 (2006).
- [81] D. Baye, *Physics reports* **565**, 1 (2015).
- [82] M. Hesse, J. Roland, and D. Baye, *Nuclear Physics A* **709**, 184 (2002).
- [83] T. N. Rescigno and C. W. McCurdy, *Phys. Rev. A* **62**, 032706 (2000).
- [84] D. Gottlieb, M. Hussaini, and S. Orszag, SIAM, Philadelphia (1984).
- [85] A. Hrennikoff, *Journal of applied mechanics* **8**, 169 (1941).
- [86] R. Courant, *Bulletin of the American mathematical Society* **49**, 1 (1943).
- [87] S. A. Orszag, *Studies in Applied Mathematics* **51**, 253 (1972).
- [88] J. N. Reddy, *An introduction to the finite element method*, Vol. 2 (McGraw-Hill New York, 1993).
- [89] B. I. Schneider, L. A. Collins, and S. X. Hu, *Phys. Rev. E* **73**, 036708 (2006).
- [90] A. Scrinzi, *Phys. Rev. A* **81**, 053845 (2010).
- [91] J. Power and G. Rawitscher, *Phys. Rev. E* **86**, 066707 (2012).
- [92] A. Simoni, A. Viel, and J.-M. Launay, arXiv:1705.04102 (2017).
- [93] D. Manolopoulos and R. Wyatt, *Chemical physics letters* **152**, 23 (1988).
- [94] D. J. Tannor, *Introduction to Quantum Mechanics: A Time-Dependent Perspective* (Univ. Science Books, Sausalito, Calif., 2007).
- [95] C. C. Marston and G. G. Balint-Kurti, *The Journal of Chemical Physics* **91**, 3571 (1989).

- [96] M. Feit, J. Fleck, and A. Steiger, *Journal of Computational Physics* **47**, 412 (1982).
- [97] D. Kosloff and R. Kosloff, *Journal of Computational Physics* **52**, 35 (1983).
- [98] H. Tal-Ezer and R. Kosloff, *J. Chem. Phys.* **81**, 3967 (1984).
- [99] R. Kosloff, *Annu. Rev. Phys. Chem.* **45**, 145 (1994).
- [100] M. Goerz, *Optimizing Robust Quantum Gates in Open Quantum System*, Ph.D. thesis, Universität Kassel, Heinrich Plett-Strasse, 34134, Kassel, Germany (2015).
- [101] C. Lanczos, *An iteration method for the solution of the eigenvalue problem of linear differential and integral operators* (United States Governm. Press Office Los Angeles, CA, 1950).
- [102] R. Mises and H. Pollaczek-Geiringer, *ZAMM-Journal of Applied Mathematics and Mechanics/Zeitschrift für Angewandte Mathematik und Mechanik* **9**, 58 (1929).
- [103] E. Koch, *The LDA+ DMFT approach to strongly correlated materials* (2011).
- [104] C. Leforestier, R. Bisseling, C. Cerjan, M. Feit, R. Friesner, A. Guldborg, A. Hammerich, G. Jolicard, W. Karrlein, H.-D. Meyer, N. Lipkin, O. Roncero, and R. Kosloff, *J. Comput. Phys.* **94**, 59 (1991).
- [105] J. P. Palao, R. Kosloff, and C. P. Koch, *Phys. Rev. A* **77**, 063412 (2008).
- [106] D. M. Reich, M. Ndong, and C. P. Koch, *J. Chem. Phys.* **136**, 104103 (2012).
- [107] E. Asplund and T. Klüner, *The Journal of Chemical Physics* **136**, 124118 (2012).
- [108] N. Khaneja, T. Reiss, C. Kehlet, T. Schulte-Herbrüggen, and S. J. Glaser, *Journal of Magnetic Resonance* **172**, 296 (2005).
- [109] K. C. Kiwiel, *Mathematical programming* **90**, 1 (2001).
- [110] M. Avriel, *Nonlinear Programming: Analysis and Methods*, Dover Books on Computer Science Series (Dover Publications, 2003).
- [111] J. Dennis and R. Schnabel, *Numerical Methods for Unconstrained Optimization and Nonlinear Equations*, Classics in Applied Mathematics (Society for Industrial and Applied Mathematics, 1996).
- [112] C. G. Broyden, *IMA Journal of Applied Mathematics* **6**, 76 (1970).
- [113] R. Fletcher, *The Computer Journal* **13**, 317 (1970).

- [114] D. Goldfarb, *Mathematics of computation* **24**, 23 (1970).
- [115] D. F. Shanno, *Mathematics of computation* **24**, 647 (1970).
- [116] R. H. Byrd, P. Lu, J. Nocedal, and C. Zhu, *SIAM Journal on Scientific Computing* **16**, 1190 (1995).
- [117] S. E. Sklarz and D. J. Tannor, *Phys. Rev. A* **66**, 053619 (2002).
- [118] M. Ndong, C. Koch, and D. Sugny, *Journal of Modern Optics* **61**, 857 (2014).
- [119] M. Ndong, H. Tal-Ezer, R. Kosloff, and C. P. Koch, *The Journal of chemical physics* **130**, 124108 (2009).
- [120] M. Ndong, H. Tal-Ezer, R. Kosloff, and C. P. Koch, *The Journal of chemical physics* **132**, 064105 (2010).
- [121] T. G. Kolda, R. M. Lewis, and V. Torczon, *SIAM review* **45**, 385 (2003).
- [122] O. Kramer, D. E. Ciaurri, and S. Koziel, in *Computational optimization, methods and algorithms* (Springer, 2011) pp. 61–83.
- [123] J. A. Nelder and R. Mead, *The Computer Journal* **7**, 308 (1964).
- [124] D. M. Olsson and L. S. Nelson, *Technometrics* **17**, 45 (1975).
- [125] K. Klein and J. Neira, *Computational Economics* **43**, 447 (2013).
- [126] K. I. McKinnon, *SIAM Journal on Optimization* **9**, 148 (1998).
- [127] J. C. Lagarias, J. A. Reeds, M. H. Wright, and P. E. Wright, *SIAM Journal on optimization* **9**, 112 (1998).
- [128] J. Dennis and D. J. Woods, *New computing environments: microcomputers in large-scale computing* **11**, 6 (1987).
- [129] C. J. Price, I. D. Coope, and D. Byatt, *Journal of optimization theory and applications* **113**, 5 (2002).
- [130] R. P. Brent, *Algorithms for minimization without derivatives*, 1st ed. (Prentice-Hall Inc., Englewood Cliffs, Princeton, New Jersey, 1973).
- [131] I. Loshchilov, M. Schoenauer, and M. Sebag, in *Proceedings of the 13th annual conference on Genetic and evolutionary computation* (ACM, 2011) pp. 885–892.
- [132] M. J. D. Powell, *The Computer Journal* **7**, 155 (1964).

- [133] K. R. Gegenfurtner, *Behavior Research Methods* **24**, 560 (1992).
- [134] P. Ghosh, *Introduction to photoelectron spectroscopy*, Chemical analysis (Wiley, 1983).
- [135] S. Hüfner, *Photoelectron spectroscopy: principles and applications* (Springer Science & Business Media, 2013).
- [136] P. van der Heide, *X-ray Photoelectron Spectroscopy: An introduction to Principles and Practices* (Wiley, 2011).
- [137] H. E. Schwarz, *Journal of Electron Spectroscopy and Related Phenomena* **21** (1980).
- [138] R. E. Goetz, A. Karamatskou, R. Santra, and C. P. Koch, *Phys. Rev. A* **93**, 013413 (2016).
- [139] R. Santra and L. S. Cederbaum, *Phys. Rep.* **368**, 1 (2002).
- [140] J. G. Muga, J. P. Palao, B. Navarro, and I. L. Egusquiza, *Physics Reports* **395**, 357 (2004).
- [141] X. M. Tong, K. Hino, and N. Toshima, *Phys. Rev. A* **74**, 031405 (2006).
- [142] A. Karamatskou, S. Pabst, Y.-J. Chen, and R. Santra, *Phys. Rev. A* **91**, 069907(E) (2015).
- [143] D. Varshalovich, A. Moskalev, and V. Khersonskii, *Quantum Theory of Angular Momentum: Irreducible Tensors, Spherical Harmonics, Vector Coupling Coefficients, 3nj Symbols*, 1st ed. (Word Scientific Co. Pte. Ltd., 687 Hartwell Street, Teaneck, NJ 07666, 1988).
- [144] M. Rose, *Elementary Theory of Angular Momentum*, 5th ed. (John Wiley & Sons, Inc., New York, 1967).
- [145] B. L. Silver, *Irreducible Tensor Methods: An Introduction or Chemists*, 1st ed., Vol. 36 (Academic Press, Inc.(London) LTD, 24/28 Oval Road, London NW1, 1976).
- [146] A. Edmonds, *Angular Momentum in Quantum Mechanics*, 4th ed. (Princeton University Press, Princeton, New Jersey, 1996).
- [147] S. J. Glaser, U. Boscain, T. Calarco, C. P. Koch, W. Köckenberger, R. Kosloff, I. Kuprov, B. Luy, S. Schirmer, T. Schulte-Herbrüggen, D. Sugny, and F. K. Wilhelm, *Eur. Phys. J. D* **69**, 279 (2015).
- [148] J. C. Light and T. Carrington, *Adv. Chem. Phys.* **114**, 263 (2007).

- [149] R. Kosloff, in *Dynamics of Molecules and Chemical Reactions*, edited by R. Wyatt and J. Zhang (Marcel Dekker, New York, 1996) pp. 185–230.
- [150] U. Peskin and N. Moiseyev, *J. Chem. Phys.* **99**, 4590 (1993).
- [151] M. Ndong, H. Tal-Ezer, R. Kosloff, and C. P. Koch, *J. Chem. Phys.* **132**, 064105 (2010).
- [152] H. Tal-Ezer, R. Kosloff, and I. Schaefer, *J. Sci. Comput.* **53**, 211 (2012).
- [153] E. Fattal, R. Baer, and R. Kosloff, *Phys. Rev. E* **53**, 1217 (1996).
- [154] V. Kokoouline, O. Dulieu, R. Kosloff, and F. Masnou-Seeuws, *J. Chem. Phys.* **110**, 9865 (1999).
- [155] K. Willner, O. Dulieu, and F. Masnou-Seeuws, *J. Chem. Phys.* **120**, 548 (2004).
- [156] S. Kallush and R. Kosloff, *Chem. Phys. Lett.* **433**, 221 (2006).
- [157] M. Nurhuda and F. H. M. Faisal, *Phys. Rev. A* **60**, 3125 (1999).
- [158] R. Heather and H. Metiu, *J. Chem. Phys.* **86**, 5009 (1987).
- [159] A. Keller, *Phys. Rev. A* **52**, 1450 (1995).
- [160] J. L. Krause, K. J. Schafer, and K. C. Kulander, *Phys. Rev. A* **45**, 4998 (1992).
- [161] S. Chelkowski, T. Zuo, O. Atabek, and A. D. Bandrauk, *Phys. Rev. A* **52**, 2977 (1995).
- [162] K. C. Kulander and B. W. Shore, *J. Opt. Soc. Am. B* **7**, 502 (1990).
- [163] P. Wopperer, *Electron photoemission from sodium and carbon clusters*, Theses, Université Paul Sabatier - Toulouse III ; Universität Erlangen-Nürnberg (2013).
- [164] Y. Ohtsuki, W. Zhu, and H. Rabitz, *J. Chem. Phys.* **110**, 9825 (1999).
- [165] E. Tiesinga, C. J. Williams, and P. S. Julienne, *Phys. Rev. A* **57**, 4257 (1998).
- [166] R. González-Férez and C. P. Koch, *Phys. Rev. A* **86**, 063420 (2012).
- [167] A. Crubellier, R. González-Férez, C. P. Koch, and E. Luc-Koenig, *New J. Phys.* **17**, 045020 (2015).
- [168] “Weak formulation of elliptic problems,” in *Elliptic Equations: An Introductory Course* (Birkhäuser Basel, Basel, 2009) pp. 35–42.

- [169] R. B. Lehoucq, D. C. Sorensen, and C. Yang, “Arpack users guide: Solution of large scale eigenvalue problems by implicitly restarted arnoldi methods.” (1997).
- [170] I. Schaefer, H. Tal-Ezer, and R. Kosloff, arXiv:1611.06707 (2017).
- [171] U. Peskin, R. Kosloff, and N. Moiseyev, *J. Chem. Phys.* **100**, 8849 (1994).
- [172] M. Ndong, H. Tal-Ezer, R. Kosloff, and C. P. Koch, *J. Chem. Phys.* **130**, 124108 (2009).
- [173] C. P. Koch and R. Moszyński, *Phys. Rev. A* **78**, 043417 (2008).
- [174] C. Joachain, N. Kylstra, and R. Potvliege, *Atoms in Intense Laser Fields* (Cambridge University Press, 2012).
- [175] A. de Bohan, P. Antoine, D. B. Milošević, and B. Piraux, *Phys. Rev. Lett.* **81**, 1837 (1998).
- [176] H. Niikura, D. M. Villeneuve, and P. B. Corkum, *Phys. Rev. Lett.* **94**, 083003 (2005).
- [177] J. C. Baggesen and L. B. Madsen, *J. Phys. B* **44**, 115601 (2011).
- [178] M. Lewenstein and A. L’Huillier, “Principles of single atom physics: High-order harmonic generation, above-threshold ionization and non-sequential ionization,” in *Strong Field Laser Physics* (Springer New York, New York, NY, 2009) pp. 147–183.
- [179] P. B. Corkum, *Phys. Rev. Lett.* **71**, 1994 (1993).
- [180] A. D. Bandrauk, S. Chelkowski, D. J. Diestler, J. Manz, and K.-J. Yuan, *Phys. Rev. A* **79**, 023403 (2009).
- [181] L. Keldysh, *Sov. Phys. JETP* **20**, 1307 (1965).
- [182] A. Gordon, R. Santra, and F. X. Kärtner, *Phys. Rev. A* **72**, 063411 (2005).
- [183] I. Schaefer and R. Kosloff, *Phys. Rev. A* **86**, 063417 (2012).
- [184] J. Solanpää, J. A. Budagosky, N. I. Shvetsov-Shilovski, A. Castro, A. Rubio, and E. Räsänen, *Phys. Rev. A* **90**, 053402 (2014).
- [185] J. B. Watson, A. Sanpera, X. Chen, and K. Burnett, *Phys. Rev. A* **53**, R1962 (1996).

- [186] S. Beaulieu, S. Camp, D. Descamps, A. Comby, V. Wanie, S. Petit, F. Légaré, K. J. Schafer, M. B. Gaarde, F. Catoire, and Y. Mairesse, *Phys. Rev. Lett.* **117**, 203001 (2016).
- [187] M. Lara-Astiaso, R. E. F. Silva, A. Gubaydullin, P. Rivière, C. Meier, and F. Martín, *Phys. Rev. Lett.* **117**, 093003 (2016).
- [188] I.-L. Liu, P.-C. Li, and S.-I. Chu, *Phys. Rev. A* **84**, 033414 (2011).
- [189] H. Z. Jooya, P.-C. Li, S.-L. Liao, and S.-I. Chu, *Phys. Lett. A* **380**, 316 (2016).
- [190] Z. Zhai, R.-F. Yu, X.-S. Liu, and Y.-J. Yang, *Phys. Rev. A* **78**, 041402 (2008).
- [191] J.-G. Chen, Y.-J. Yang, S.-L. Zeng, and H.-Q. Liang, *Phys. Rev. A* **83**, 023401 (2011).
- [192] L. Feng and T. Chu, *Phys. Lett. A* **376**, 1523 (2012).
- [193] G.-T. Zhang, *Mol. Phys.* **111**, 3117 (2013).
- [194] A. Chacón, M. F. Ciappina, and A. P. Conde, *Eur. Phys. J. D* **69**, 133 (2015).
- [195] K. Nasiri Avanaki, D. A. Telnov, and S.-I. Chu, *Phys. Rev. A* **94**, 053410 (2016).
- [196] S. Hüfner, *Photoelectron Spectroscopy, Principles and Applications*, 3rd ed. (Springer, 2003).
- [197] M. Meyer, D. Cubaynes, V. Richardson, J. T. Costello, P. Radcliffe, W. B. Li, S. Düsterer, S. Fritzsche, A. Mihelic, K. G. Papamihail, and P. Lambropoulos, *Phys. Rev. Lett.* **104**, 213001 (2010).
- [198] F. Fabre, P. Agostini, G. Petite, and M. Clement, *Journal of Physics B: Atomic and Molecular Physics* **14**, L677 (1981).
- [199] U. Becker and D. A. Shirley, *VUV and Soft X-Ray Photoionization*, 3rd ed. (Springer Science & Business Media, 1996).
- [200] G. Wu, P. Hockett, and A. Stolow, *Phys. Chem. Chem. Phys.* **13**, 18447 (2011).
- [201] C. I. Blaga, F. Catoire, P. Colosimo, G. G. Paulus, H. G. Muller, P. Agostini, and L. DiMauro, *Nature Phys.* **5**, 335 (2009).
- [202] F. Krausz and M. Ivanov, *Rev. Mod. Phys.* **81**, 163 (2009).

- [203] H. Wabnitz, L. Bittner, A. R. B. de Castro, R. Dohrmann, P. Gurtler, T. Laarmann, W. Laasch, J. Schulz, A. Swiderski, K. von Haefen, T. Moller, B. Faatz, A. Fateev, J. Feldhaus, C. Gerth, U. Hahn, E. Saldin, E. Scheidmiller, K. Sytchev, K. Tiedtke, R. Treusch, and M. Yurkov, *Nature Physics* **420**, 482 (2002).
- [204] P. Corkum and F. Krausz, *Nature Physics* **3**, 381 (2007).
- [205] E. P. Kanter, B. Krässig, Y. Li, A. M. March, P. Ho, N. Rohringer, R. Santra, S. H. Southworth, L. F. DiMauro, G. Doumy, C. A. Roedig, N. Berrah, L. Fang, M. Hoener, P. H. Bucksbaum, S. Ghimire, D. A. Reis, J. D. Bozek, C. Bostedt, M. Messerschmidt, and L. Young, *Phys. Rev. Lett.* **107**, 233001 (2011).
- [206] P. Duinker, *Rev. Mod. Phys.* **54**, 325 (1982).
- [207] K. L. Reid, *Annu. Rev. Phys. Chem.* **54**, 397 (2003).
- [208] C. Meier and V. Engel, *Phys. Rev. Lett.* **73**, 3207 (1994).
- [209] Z. Shen and V. Engel, *Chem. Phys. Lett.* **358**, 344 (2002).
- [210] M. Wollenhaupt, V. Engel, and T. Baumert, *Annu. Rev. Phys. Chem.* **56**, 25 (2005).
- [211] S. Gräfe, M. Erdmann, and V. Engel, *Phys. Rev. A* **72**, 013404 (2005).
- [212] H. Braun, T. Bayer, C. Sarpe, R. Siemering, R. de Vivie-Riedle, T. Baumert, and M. Wollenhaupt, *J. Phys. B* **47**, 124015 (2014).
- [213] T. Klamroth, *J. Chem. Phys.* **124**, 144310 (2006).
- [214] M. Mundt and D. J. Tannor, *New J. Phys.* **11**, 105038 (2009).
- [215] A. Castro, J. Werschnik, and E. K. U. Gross, *Phys. Rev. Lett.* **109**, 153603 (2012).
- [216] M. Hellgren, E. Räsänen, and E. K. U. Gross, *Phys. Rev. A* **88**, 013414 (2013).
- [217] C. W. McCurdy and T. N. Rescigno, *Phys. Rev. A* **56**, R4369 (1997).
- [218] F. Martín, *Journal of Physics B: Atomic, Molecular and Optical Physics* **32**, R197 (1999).
- [219] T. N. Rescigno and C. W. McCurdy, *Phys. Rev. A* **62**, 032706 (2000).
- [220] H. Bachau, E. Cormier, P. Decleva, J. E. Hansen, and F. Martín, *Reports on Progress in Physics* **64**, 1815 (2001).

- [221] C. W. McCurdy and F. Martín, *Journal of Physics B: Atomic, Molecular and Optical Physics* **37**, 917 (2004).
- [222] T. Rathje, A. M. Saylor, S. Zeng, P. Wustelt, H. Figger, B. D. Esry, and G. G. Paulus, *Phys. Rev. Lett.* **111**, 093002 (2013).
- [223] N. I. Shvetsov-Shilovski, E. Räsänen, G. G. Paulus, and L. B. Madsen, *Phys. Rev. A* **89**, 043431 (2014).
- [224] L. M. Smith, D. R. Keefer, and S. Sudharsanan, *Journal of Quantitative Spectroscopy and Radiative Transfer* **39**, 367 (1988).
- [225] M. J. J. Vrakking, *Review of Scientific Instruments* **72**, 4084 (2001).
- [226] V. Dribinski, A. Ossadtchi, V. A. Mandelshtam, and H. Reisler, *Review of Scientific Instruments* **73**, 2634 (2002).
- [227] D. Townsend, M. P. Minitti, and A. G. Suits, *Review of Scientific Instruments* **74**, 2530 (2003).
- [228] D. Strasser, X. Urbain, H. B. Pedersen, N. Altstein, O. Heber, R. Wester, K. G. Bhushan, and D. Zajfman, *Review of Scientific Instruments* **71**, 3092 (2000).
- [229] L. Dinu, A. T. J. B. Eppink, F. Rosca-Pruna, H. L. Offerhaus, W. J. van der Zande, and M. J. J. Vrakking, *Review of Scientific Instruments* **73**, 4206 (2002).
- [230] R. Toomes, P. Samartzis, T. Rakitzis, and T. Kitsopoulos, *Chemical physics* **301**, 209 (2004).
- [231] M. Wollenhaupt, M. Krug, J. Köhler, T. Bayer, C. Sarpe-Tudoran, and T. Baumert, *Applied Physics B* **95**, 647 (2009).
- [232] C. Smeenk, L. Arissian, A. Staudte, D. M. Villeneuve, and P. B. Corkum, *Journal of Physics B: Atomic, Molecular and Optical Physics* **42**, 185402 (2009).
- [233] J. P. Palao, D. M. Reich, and C. P. Koch, *Phys. Rev. A* **88**, 053409 (2013).
- [234] D. M. Reich, J. P. Palao, and C. P. Koch, *J. Mod. Opt.* **61**, 822 (2014).
- [235] U. Hohenester, P. K. Rekdal, A. Borzı́, and J. Schmiedmayer, *Phys. Rev. A* **75**, 023602 (2007).
- [236] J. P. Palao and R. Kosloff, *Phys. Rev. A* **68**, 062308 (2003).
- [237] R. Eitan, M. Mundt, and D. J. Tannor, *Phys. Rev. A* **83**, 053426 (2011).

- [238] G. Jäger, D. M. Reich, M. H. Goerz, C. P. Koch, and U. Hohenester, *Phys. Rev. A* **90**, 033628 (2014).
- [239] S. G. Schirmer and P. de Fouquieres, *New J. Phys.* **13**, 073029 (35pp) (2009).
- [240] S. Chelkowski, A. D. Bandrauk, and A. Apolonski, *Phys. Rev. A* **70**, 013815 (2004).
- [241] L. Young, D. A. Arms, E. M. Dufresne, R. W. Dunford, D. L. Ederer, C. Höhr, E. P. Kanter, B. Krässig, E. C. Landahl, E. R. Peterson, J. Rudati, R. Santra, and S. H. Southworth, *Phys. Rev. Lett.* **97**, 083601 (2006).
- [242] E. Goulielmakis, Z.-H. Loh, A. Wirth, R. Santra, N. Rohringer, V. S. Yakovlev, S. Zherebtsov, T. Pfeifer, A. M. Azzeer, M. F. Kling, S. R. Leone, and F. Krausz, *Nature* **466**, 739 (2010).
- [243] A. Wirth, M. T. Hassan, I. Grguraš, J. Gagnon, A. Moulet, T. T. Luu, S. Pabst, R. Santra, Z. A. Alahmed, A. M. Azzeer, V. S. Yakovlev, V. Pervak, F. Krausz, and E. Goulielmakis, *Science* **334**, 195 (2011).
- [244] F. Calegari, D. Ayuso, A. Trabattoni, L. Belshaw, S. De Camillis, S. Anumula, F. Frassetto, L. Poletto, A. Palacios, P. Decleva, J. B. Greenwood, F. Martín, and M. Nisoli, *Science* **346**, 336 (2014).
- [245] T. C. Weinacht, J. Ahn, and P. H. Bucksbaum, *Nature* **397**, 233 (1999).
- [246] R. Kienberger, M. Hentschel, M. Uiberacker, C. Spielmann, M. Kitzler, A. Scrinzi, M. Wieland, T. Westerwalbesloh, U. Kleineberg, U. Heinzmann, M. Drescher, and F. Krausz, *Science* **297**, 1144 (2002).
- [247] A. Borot, A. Malvache, X. Chen, A. Jullien, J. Geindre, P. Audebert, G. Mourou, F. Queré, and R. Lopez-Martens, *Nature Physics* **8**, 416 (2012).
- [248] D. Brinks, F. D. Stefani, F. Kulzer, R. Hildner, T. H. Taminiau, Y. Avlasevich, K. Müllen, and N. F. van Hulst, *Nature* **465**, 905 (2010).
- [249] L. Rybak, S. Amaran, L. Levin, M. Tomza, R. Moszynski, R. Kosloff, C. P. Koch, and Z. Amitay, *Phys. Rev. Lett.* **107**, 273001 (2011).
- [250] R. Santra, R. W. Dunford, and L. Young, *Phys. Rev. A* **74**, 043403 (2006).
- [251] U. V. Riss and H. D. Meyer, *J. Phys. B: Atomic, Molecular and Optical Physics* **26**, 4503 (1993).
- [252] G. Jolicard and E. J. Austin, *Chem. Phys. Lett.* **121**, 106 (1985).

- [253] S. Pabst, L. Greenman, and R. Santra, “XCID program package for multichannel ionization dynamics,” (Rev 1425, 2014).
- [254] T. Koopmans, *Physica* **1**, 104 (1934).
- [255] I. P. Grant, *Relativistic quantum theory of atoms and molecules : theory and computation*, Springer series on atomic, optical, and plasma physics, Vol. 40 (Springer, New York, 2007).
- [256] P. Doria, T. Calarco, and S. Montangero, *Phys. Rev. Lett.* **106**, 190501 (2011).
- [257] T. Caneva, T. Calarco, and S. Montangero, *Phys. Rev. A* **84**, 022326 (2011).
- [258] N. Rach, M. M. Müller, T. Calarco, and S. Montangero, *Phys. Rev. A* **92**, 062343 (2015).
- [259] M. H. Goerz, K. B. Whaley, and C. P. Koch, *EPJ Quantum Technology* **2**, 21 (2015).
- [260] M. T. Hassan, T. T. Luu, A. Moulet, O. Raskazovskaya, P. Zhokhov, M. Garg, N. Karpowicz, A. M. Zheltikov, V. Pervak, F. Krausz, and E. Goulielmakis, *Nature* **530** (2016).
- [261] S. W. T. L. Kelvin, *The molecular tactics of a cristal* (Oxford University Press Warehouse, Macmillan & CO., 66 Fifth Avenue, 1894).
- [262] B. Ritchie, *Phys. Rev. A* **14**, 359 (1976).
- [263] I. Powis, “Photoelectron circular dichroism in chiral molecules,” in *Advances in Chemical Physics* (John Wiley & Sons, Inc., 2008) pp. 267–329.
- [264] C. Lux, M. Wollenhaupt, T. Bolze, Q. Liang, J. Köhler, C. Sarpe, and T. Baumert, *Angew. Chem. Int. Ed.* **51**, 4755 (2012).
- [265] C. Lux, M. Wollenhaupt, C. Sarpe, and T. Baumert, *ChemPhysChem* **16**, 115 (2015).
- [266] A. Kastner, C. Lux, T. Ring, S. Züllighoven, C. Sarpe, A. Senftleben, and T. Baumert, *ChemPhysChem* (2016).
- [267] C. S. Lehmann, N. B. Ram, I. Powis, and M. H. M. Janssen, *J. Chem. Phys.* **139**, 234307 (2013).
- [268] M. H. M. Janssen and I. Powis, *Phys. Chem. Chem. Phys.* **16**, 856 (2014).

- [269] M. M. Rafiee Fanoood, M. H. M. Janssen, and I. Powis, *Phys. Chem. Chem. Phys.* **17**, 8614 (2015).
- [270] B. Ritchie, *Phys. Rev. A* **13**, 1411 (1976).
- [271] N. A. Cherepkov, *J. Phys. B* **16**, 1543 (1983).
- [272] L. Nahon and I. Powis, in *Chiral Recognition in the Gas Phase*, edited by A. Zehnacker (CRC Press, 2010).
- [273] S. N. Dixit and P. Lambropoulos, *Phys. Rev. A* **27**, 861 (1983).
- [274] P. R. Monson and W. M. McClain, *J. Chem. Phys.* **53**, 29 (1970).
- [275] W. M. McClain, *J. Chem. Phys.* **57**, 2264 (1972).
- [276] W. M. McClain, *Acc. Chem. Res* **7**, 129 (1974).
- [277] I. Tinoco Jr., *J. Chem. Phys.* **62**, 1006 (1974).
- [278] L. V. Keldysh, *Sov. Phys. JEPT* **20**, 1307 (1965).
- [279] F. H. M. Faisal, *J. Phys. B* **6**, L89 (1973).
- [280] I. Dreissigacker and M. Lein, *Phys. Rev. A* **89**, 053406 (2014).
- [281] Z. Amitay, A. Gandman, L. Chuntunov, and L. Rybak, *Phys. Rev. Lett.* **100**, 193002 (2008).
- [282] L. Levin, W. Skomorowski, L. Rybak, R. Kosloff, C. P. Koch, and Z. Amitay, *Phys. Rev. Lett.* **114**, 233003 (2015).
- [283] K. L. Reid., *Annu. Rev. Phys. Chem* **54**, 397 (2003).
- [284] J. Cooper and R. N. Zare, in *Lectures In Theoretical Physics*, Vol. 9, edited by Gordon and Breach (University of Colorado, New York, 1968) pp. 317–337.
- [285] N. Chandra, *J. Phys. B* **20**, 3405 (1987).
- [286] S. N. Dixit and V. McKoy, *J. Chem. Phys.* **82**, 3546 (1985).
- [287] H. A. Bethe and E. E. Salpeter, *Quantum Mechanics of One and Two-Electron Atoms*, 1st ed. (Academic Press Inc., 111, Fifth Avenue, New York 3, New York/USA, 1957).
- [288] C. Jin, A.-T. Le, S.-F. Zhao, R. R. Lucchese, and C. D. Lin, *Phys. Rev. A* **81**, 033421 (2010).

- [289] R. R. Lucchese, G. Raseev, and V. McKoy, *Phys. Rev. A* **25**, 2572 (1982).
- [290] B. M. Bishop, *Advances in Quantum Chemistry*, 1st ed., Vol. 3 (Academic Press Inc., Berkeley Square House, London W.1, 1967).
- [291] D. Dill, *J. Chem. Phys.* **65**, 1130 (1976).
- [292] C. M. Oana and A. I. Krylov, *J. Chem. Phys.* **131**, 124114 (2009).
- [293] B. Ritchie, *J. Chem. Phys.* **64**, 3050 (1976).
- [294] R. Goetz, T. Isaev, B. Nikoobakht, R. Berger, and C. Koch, *The Journal of chemical physics* **146**, 024306 (2017).
- [295] K.-N. Huang, *Phys. Rev. A* **22**, 223 (1980).
- [296] W. L. Peticolas, *Annu. Rev. Phys. Chem.* **18**, 233 (1967).
- [297] W. M. McClain and R. A. Harris, in *Excited States*, edited by E. C. Lim (Academic Press, 1977) pp. 1–56.
- [298] M. A. C. Nascimento, *Chem. Phys.* **74**, 51 (1983).
- [299] C. N. Yang, *Phys. Rev.* **74**, 764 (1948).
- [300] J. Pollmann, R. Franke, and J. Hormes, *Spectrochimica Acta Part A: Molecular and Biomolecular Spectroscopy* **53**, 491 (1997).
- [301] C. J. Harding, E. Mikajlo, I. Powis, S. Barth, S. Joshi, V. Ulrich, and U. Hergenhahn, *J. Chem. Phys.* **123**, 234310 (2005).
- [302] A. Kastner, T. Ring, B. C. Krüger, G. B. Park, T. Schäfer, A. Senftleben, and T. Baumert, *The Journal of Chemical Physics* **147**, 013926 (2017).
- [303] A. Kastner, private communication (2017).
- [304] T. Seideman, *Phys. Rev. A* **64**, 042504 (2001).
- [305] C. M. Oana and A. I. Krylov, *J. Chem. Phys.* **127**, 234106 (2007).
- [306] A. Humeniuk, M. Wohlgemuth, T. Suzuki, and R. Mitrić, *J. Chem. Phys.* **139**, 134104 (2013).
- [307] S. Gozem, A. O. Gunina, T. Ichino, D. L. Osborn, J. F. Stanton, and A. I. Krylov, *J. Phys. Chem. Lett.* **6**, 4532 (2015).
- [308] U. Boesl von Grafenstein and A. Bornschlegl, *ChemPhysChem* **7**, 2085 (2006).

- [309] R. Li, R. Sullivan, W. Al-Basheer, R. M. Pagni, and R. N. Compton, *J. Chem. Phys.* **125**, 144304 (2006).
- [310] H. G. Breunig, G. Urbasch, P. Horsch, J. Cordes, U. Koert, and K.-M. Weitzel, *ChemPhysChem* **10**, 1199 (2009).
- [311] D. Kröner, *Phys. Chem. Chem. Phys.* **17**, 19643 (2015).
- [312] E. D. Commins, *Physica Scripta* **36**, 468 (1987).
- [313] Y. B. Zel'dovich, *Sov. Phys. JETP* **9**, 682 (1959).
- [314] M. Bouchiat and C. Bouchiat, *Journal de Physique* **35**, 899 (1974).
- [315] M. Bouchiat and C. Bouchiat, *Journal de Physique* **36**, 493 (1975).
- [316] S. Gilbert, M. Noecker, R. Watts, and C. Wieman, *Physical review letters* **55**, 2680 (1985).
- [317] E. Wigner, *Gött. Nachr* **375** (1927).
- [318] M.-A. Bouchiat and C. Bouchiat, *Reports on Progress in Physics* **60**, 1351 (1997).
- [319] D. Budker, D. F. Kimball, and D. P. DeMille, *Atomic physics: an exploration through problems and solutions* (Oxford University Press, USA, 2004).
- [320] A. Bakasov, T.-K. Ha, and M. Quack, *The Journal of chemical physics* **109**, 7263 (1998).
- [321] R. Prentner, M. Quack, J. Stohner, and M. Willeke, *The Journal of Physical Chemistry A* **119**, 12805 (2015).
- [322] M. Quack, J. Stohner, and M. Willeke, *Annu. Rev. Phys. Chem.* **59**, 741 (2008).
- [323] J. K. Webb, M. Murphy, V. Flambaum, V. Dzuba, J. Barrow, C. Churchill, J. Prochaska, and A. Wolfe, *Physical Review Letters* **87**, 091301 (2001).
- [324] S. Weinberg, *Physical review letters* **19**, 1264 (1967).
- [325] M. Lintz, J. Guéna, and M.-A. Bouchiat, in *Proceedings of The 3rd Workshop From Parity Violation to Hadronic Structure and more...* (Springer, 2007) pp. 165–169.
- [326] J. Guéna, D. Chauvat, P. Jacquier, E. Jahier, M. Lintz, S. Sanguinetti, A. Wasan, M.-A. Bouchiat, A. Papoyan, and D. Sarkisyan, *Phys. Rev. Lett.* **90**, 143001 (2003).

- [327] J. Guéna, M. Lintz, and M.-A. Bouchiat, in *SFP05 Congrès de la SFP et de la BPS* (2005).
- [328] J. Guéna, M. Lintz, and M. Bouchiat, *Physical Review A* **71**, 042108 (2005).
- [329] S. Gilbert and C. Wieman, *Physical Review A* **34**, 792 (1986).
- [330] C. Wood, S. Bennett, D. Cho, B. Masterson, J. Roberts, C. Tanner, and C. E. Wieman, *Science* **275**, 1759 (1997).
- [331] S. Bennett and C. E. Wieman, *Physical Review Letters* **82**, 2484 (1999).
- [332] M. Quack, *Angewandte Chemie International Edition* **28**, 571 (1989).
- [333] M. Quack and M. Willeke, *The Journal of Physical Chemistry A* **110**, 3338 (2006).
- [334] M. Quack, *Chemical Physics Letters* **132**, 147 (1986).
- [335] M. Fabry, *Journal of quantitative spectroscopy and radiative transfer* **16**, 127 (1976).
- [336] P. M. Stone, *Physical Review* **127**, 1151 (1962).
- [337] D. DeMille, *Physical review letters* **74**, 4165 (1995).
- [338] E. Fermi, *Leipziger Vorträge* **95**, 111 (1928).
- [339] M. G. Mayer, *Physical review* **60**, 184 (1941).
- [340] C. F. Fischer, *Hartree–Fock method for atoms. A numerical approach* (John Wiley and Sons, Inc., New York, 1977).
- [341] B. Numerov, *Astronomische Nachrichten* **230**, 359 (1927).
- [342] L. G. Ixaru and M. Rizea, *Computer Physics Communications* **19**, 23 (1980).
- [343] H. A. Moses and A. Russek, *Physical Review* **135**, A1547 (1964).
- [344] E. U. Condon and G. H. Shortley, *The theory of atomic spectra* (Cambridge University Press, 1951).
- [345] U. Fano and J. Cooper, *Reviews of Modern Physics* **40**, 441 (1968).
- [346] A. Corney, *Atomic and laser spectroscopy*, Oxford science publications (Clarendon Press, 1977).
- [347] J. Köhler, M. Wollenhaupt, T. Bayer, C. Sarpe, and T. Baumert, *Optics express* **19**, 11638 (2011).

- [348] B. M. Patterson, J. F. Sell, T. Ehrenreich, M. A. Gearba, G. M. Brooke, J. Scoville, and R. J. Knize, *Phys. Rev. A* **91**, 012506 (2015).
- [349] M. Schöffler, C. Stuck, M. Waitz, F. Trinter, T. Jahnke, U. Lenz, M. Jones, A. Belkacem, A. Landers, M. Pindzola, *et al.*, *Physical review letters* **111**, 013003 (2013).
- [350] A. N. C. Laser Quantum, “Taccor Ultra: specifications,” (2017).
- [351] F. Krack, M. Goetz, and C. P. Koch, “QDYN program package for quantum dynamics and control,” (2.0dev, 2017).
- [352] M. Rayson, *Physical Review E* **76**, 026704 (2007).
- [353] M. Abramowitz and I. A. Stegun, *Handbook of Mathematical Functions with Formulas, Graphs and Mathematical Tables*, 10th ed. (National Bureau of Standards, Applied Mathematics Series 55, 20402, Washington D.C./USA, 1972).
- [354] G. Golub and G. Meurant, *Matrices, Moments and Quadrature with Applications*, Princeton Series in Applied Mathematics (Princeton University Press, 2009).
- [355] C. Aslangul, *Mécanique Quantique 2, Développements et applications à basse énergie*, 1st ed. (De Boeck S.A, Rue des Minimes 39, B-1000, Bruxelles, 2008).